ESTUARINE CONDITIONS AND WATER EXCHANGE IN FJORDS OF PRINCE WILLIAM SOUND, ALASKA

A Dissertation

by

SHELTON MANN GAY III

Submitted to the Office of Graduate and Professional Studies of
Texas A&M University
in partial fulfillment of the requirements for the degree of

DOCTOR OF PHILOSOPHY

Chair of Committee,	Steven F. DiMarco
Co-Chair of Committee,	David A. Brooks
Committee Members,	Timothy M. Dellapenna
	Antonietta S. Quigg
	Kenneth P. Bowman
Head of Department,	Piers Chapman

December 2013

Major Subject: Oceanography

ABSTRACT

This dissertation addresses spatial variation in physical properties of small fjords in Prince William Sound (PWS), Alaska between 1994 and 1997 and circulation and water exchange in 2007 and 2008 at Simpson Bay, a small subarctic fjord located in eastern PWS. Ancillary weather data were also collected at Simpson in both years. Principal component (*PC*) analysis is used to quantify variance in freshwater content (*FWC*) and temperature among sites and regression analysis is used to compare mean *FWC*s with watershed to fjord basin area ratios (WSR), watershed areas and maximum elevations. The results show that the principal components explaining > 90% of the variance in *FWC* occur in two statistical modes that respectively indicate total freshwater input from all sources and the vertical distribution from mixing, advection and in certain cases internal waves. The spatial variation of temperature is more complex due to local differences in solar heating combined with cooling effects of alpine runoff and subsurface water advected from tidewater glacial fjords. In 1994, this type of advection influenced the hydrography in western PWS possibly as far south as N. Elrington Pass, and in 1996 and 1997, fjords influenced by glacial advection again exhibit atypically high *FWC* values due to subsurface freshening.

The currents at Simpson Bay reveal a complex flow structure forced by tides interacting with bathymetry and moderated by stratification, tidal volume flux, internal waves and winds. Baroclinic currents form the principal mechanism forcing exchange, shown by both an imbalance in tidal volume transports and highly coherent low frequency variations in near-surface T/S properties. Surface exchange by both winds and currents are also inferred by low to high frequency oscillations in the T/S wavelet spectra, and internal waves are evident from fluctuations in both the pycnocline depths during tide cycles and by vertical oscillations of moored temperatures. Vertical diffusivity and the efficiency of work performed by mixing from internal waves in comparison to available tidal energy indicate that deep diffusivity exceeds the available tidal energy on O (10 to 100). As such, changes in deep density in both basins over time cannot be alone due to vertical mixing and must come from advection of subsurface water from outside the fjord, and possibly submarine ground water discharge in the northern basin.

DEDICATION

This dissertation is dedicated to my mother and father, who respectively showed me the true beauty in this world though music and encouraged my love of nature and scientific discovery at a young age. I would also like to dedicate this work to two dear friends who loved Prince William Sound as much as I do: Professor R. Ted Cooney of the University of Alaska at Fairbanks and Jack Babic, captain of the Miss Kayley. All of these people have unfortunately departed this world and are dearly missed.

ACKNOWLEDGEMENTS

The author wishes to express his appreciation to a large number of people who collected CTD data and to the captains and crews of the M/V Auklet, F/V Miss Kayley and the F/V Kyle David, who all helped make the various field programs a success. Special thanks are extended to Loren Tuttle, Andy Craig, Scott Pegau and James Thorne for their assistance in the field and especially to the late R. Ted Cooney for his friendship and leadership during the SEA program.

I would also like to thank my advisors Dr. Steve DiMarco and Dr. David Brooks for their guidance and help with the analyses and writing of the dissertation and my committee members Drs. Kenneth Bowman, Antonietta Quigg and Timothy Dellapenna for their comments on the manuscript.

This dissertation is the result a multidisciplinary research program, Sound Ecosystem Assessment, sponsored by the Exxon Valdez Oill Spill Trustee Council (EVOSTC) from 1994 to 1998, and more recent studies of juvenile Pacific herring *(Clupea pallasai*) nurseries sponsored also by EVOSTC in 2007 and 2008 (see Integrated Herring Restoration Plan at http://www.evostc.state.ak.us/Universal/Documents/Publications/).

.

TABLE OF CONTENTS

CHAPTER III CIRCULATION AND WATER EXCHANGE WITHIN SIMPSON BAY, A SMALL SUBARCTIC FJORD IN PRINCE WILLIAM SOUND, ALASKA: HYDROGRAPHY, CIRCULATION, WATER EXCHANGE AND INTERNAL TIDES………………………………... 38

CHAPTER IV CIRCULATION AND WATER EXCHANGE WITHIN SIMPSON BAY, A SMALL SUBARCTIC FJORD IN PRINCE WILLIAM SOUND, ALASKA: TIME-SERIES OF HYDROGRAPHY AND WINDS…………………………………………………….………… 65

LIST OF APPENDIX TABLES

LIST OF APPENDIX FIGURES

FIGURE Page

FIGURE Page

FIGURE Page

FIGURE Page

FIGURE Page

CHAPTER I

INTRODUCTION

Prince William Sound (PWS) (Fig. 1.1) is a large estuarine system that forms a boundary between the northern Gulf of Alaska (NGOA) and fjords located along the south central Alaskan coast (cf. Muench and Schmidt, 1975). The Sound has fjord-like physical properties due to its deep basins that are restricted relative to the NGOA shelf and high annual freshwater input. It also has a broad, deep (400*m*) central basin (Fig. 1.1) exhibiting circulation similar to a small marginal sea (Niebauer *et al.*, 1994; Vaughan *et al.*, 2001).

The primary drivers of the regional climate (Wilson and Overland, 1986) include seasonal interactions of the Aleutian Low and the Siberian and North Pacfic High pressure systems (Fig. 1.2). Freshwater input occurs from both rainfall and precipitation stored in snow and glacial ice fields, with a seasonal variation similar to the NGOA coast (Royer *et al.*, 1979). Surface runoff is maximal in autumn (September and October) and minimal in late winter and early spring (March and April). However, an additional source of coastal freshwater affecting PWS is the Copper River (Fig. 1.3) as part of the Alaska Coastal Current (ACC). The ACC is a westward flowing geostrophic-baroclinic current (Johnson *et al.*, 1988; Schumacher *et al.*, 1990; Weingartner *et al.*, 2005) that interacts with PWS via water exchange at Hinchinbrook Entrance (HE) and Montague Strait (MS) (Niebauer *et al.*, 1994; Vaughan *et al.*, 2001; Bang and Mooers, 2003).

Knowledge of how the various sources of glacial and non-glacial freshwater input influence PWS is limited mainly to sporadic observations of hydrography over time, leading to difficulties in accurately parameterizing freshwater flux in circulation models using a Princeton Ocean Model (POM) (Wang *et al.*, 1997, 2001; Bang *et al.*, 2005). As such, model predictions of buoyancy-forced flows during field experiments do not well match actual observations (Cox *et al.*, 2004). More recent modeling attempts using line sources of freshwater input into the Sound (Mooers *et al.*, 2009; Wu 2011) have made improvements to the predicted circulation and baroclinic-geostrophic flows, but a full validation of the freshwater flux is currently being sought by the Alaska Ocean Observing System (AOOS) and the Oil Spill Recovery Institute (OSRI) to support a new modeling effort using a Regional Ocean Model (ROM) led by Dr Yi Chou at the JPL Lab in Berkley, California (http://ourocean.jpl.nasa.gov/PWS/).

Hypothetically, the myriad of small fjords in PWS should constitute a significant source of freshwater input due to their extreme number and wide distribution around the mainland and major islands within the Sound (Fig. 1.1). However, at present, knowledge regarding the dynamics of estuarine conditions, circulation and water exchange between the small fjords and the Sound remains rudimentary (Gay and Vaughan, 2001; Muench and Heggie, 1978; Colonell, 1981). The hydrography of small PWS fjords varies significantly (see Fig. 2.2) and is moderated by local climatic conditions (Gay and Vaughan, 2001) and, in certain cases, possibly by offshore winds, watershed topography and size (area) relative to fjord basin area (see Chapter II). A complicating factor affecting these relationships, however, is a massive annual release of freshwater from ice fields within the Chugach Mountains into tidewater glacial fjords.

For example, Figure 1.3 shows glacial water (light turquoise in color due to suspended silt) discharging into PWS. This occurs via some rivers, such as in Port Valdez and eastern Orca Bay (Fig. 1.4), but the main sources come from basal discharge from under large tidewater glaciers (Walters *et al.*, 1988; Motyka, 2003) scattered across the northern and western Sound (Fig. 1.3 and 2.1A). Figure 1.4 gives a schematic representation of the advection from these sources and shows small fjords potentially affected by such large-scale geostrophic-baroclinic flows. In the figure, glacial water is shown propagating westward and southward as a quasi-coastal current. Additional features include inflow and retroflection of the ACC (i.e. Copper River water) at HE (Halverson *et al.*, 2013) and through-flow at Middle Ground Shoal, and northward (southward) propagation of ACC (Columbia Bay water); the latter sources believed to drive cyclonic circulation in the central Sound (Niebauer *et al.*, 1994; Vaughan *et al.*, 2001).

The presence of subglacial freshwater beyond the outer moraines (sills) of large tidewater glacial fjords, such as Columbia Bay, is typically signified by marked sub-surface temperature minima and maxima in the upper 10 to 30*m* (Walters *et al.*, 1988). In 1996, Gay and Vaughan (2001) observed similar thermal characteristics within Unakwik Inlet and Icy Bay, and more recently Gay (2011b) observed such anomalies within Columbia Bay. Advection of glacial water occurs across the northern and western regions of PWS, where tidewater glaciers are more common, and certain fjords located in these regions therefore exhibit remnants of the glacial signatures in their temperature profiles. More recent hydrography data (Gay 2011b) indicate the effects of glacial advection are intensifying within some of the small fjords in PWS and this pattern may represent accelerating rates of glacial ablation. Similar effects of increased glacial flux have been suggested recently for the NGOA coast by Royer and Grosch (2006). These authors attribute this to a positive feedback mechanism involving increases in poleward heat flux due to a strengthening of the ACC. The latter is occurring due to enhanced coastal runoff, and the increased heat transport is possibly intensifying the Aleutian Low Pressure system, which in turn is leading to greater storm activity and increased rates of glacial ablation. The latter effects of the ACC strengthening of the Aleutian Low are not yet unequivocal, however.

One of the goals of this investigation, therefore, is to provide a more comprehensive framework of the variation in hydrographic conditions among the small fjords in PWS and to ascertain the factors affecting freshwater contents within these basins, in particular glacial advection. This will aid in determining their potential contributions to freshwater input within PWS. Another goal is to determine the dynamics of water exchange at one intensively studied fjord located in eastern PWS, Simpson Bay (Fig. 1.1).

1. Review of estuarine circulation in relation to small PWS fjords

In most large fjords worldwide, upper layer circulation and water exchange are defined by the volume of freshwater discharge from significant point sources, such as large rivers, and a corresponding estuarine circulation (e.g. Pickard, 1967, 1971; Saelan, 1967; Farmer and Freeland, 1983). This usually takes on the form of an outwardly flowing fresh layer ($S \leq 5$), 1 to 5m in thickness, which eventually thickens and becomes increasingly brackish down-fjord due to entrainment of salty subsurface marine water. The stratification sequence is one of progressive changes along the estuary as opposed to one of local controls from tides and river flow (Hansen and Rattray, 1966). Following Knudsen's relations (Dyer, 1997) the salt flux due to mixing and transport within the out-flowing layer is typically balanced by a subsurface inflow of marine source water at the mouth. In addition to estuarine flow, however, density fluctuations due to winds and along-shore currents outside the mouths of certain fjords can cause baroclinic gradients having marked effects on the circulation and exchange of the intermediate water (Aure *et al.*, 1996; Klinck *et al.*, 1981). Likewise, internal waves produced by tidal flows over sills have an influence on water exchange (Valasenko *et al.*, 2002; Gillbrand and Amundrud, 2007).

Small fjords in PWS, by comparison, tend to have highly localized watersheds (Fig. 1.4; Appendix 3.3) and freshwater input, therefore, occurs from high order streams scattered along the basin periphery. This line-source causes freshwater to disperse over a surface layer, but the volume relative to the cross-sectional area yields negligible freshwater velocities: $u_f = R/A = O(0.0025 \text{ m s}^{-1})$, where R is the freshwater inflow relative to cross-sectional area, A, at the mouth or a constriction. This also causes very low densimetric (freshwater) Froude numbers (Hansen and Rattray, 1966) $Fr_f = u_f \big/ \sqrt{g' h}$ = O(10^{-4}). The tidal prisms also have a large range (Δh = 3 to 5*m*), and thus the small freshwater sources are non-conducive to estuarine flow. The controls on stratification and mixing appear to be strongly viscous as opposed to the hydraulic effects of sills or constrictions (Hetland, 2010), and recent research within Simpson Bay also indicates that a significant additional source of freshwater flux inside the inner basins of small fjords in PWS can occur from submarine ground water discharge (Swarzenski, *et al.*, 2009).

All of the above modes of freshening within small non-glacial fjords in PWS ultimately result in the formation of relatively brackish surface conditions (Gay and Vaughan, 2001). Therefore circulation is predominately driven by tides and baroclinic gradients, moderated by basin morphometery, internal waves and in certain cases by both offshore and along-fjord winds (Gay, 2011a). Offshore baroclinic gradients markedly affect circulation when small fjords are located downstream from tidewater glacial fjords. In such cases, advection of cold, brackish surface and subsurface glacial water into the outer basins appears to counter outward dispersal of freshwater by creating low-density fields at the mouths (i.e. reversed estuarine gradients). These conditions appear within fjords as upper layer intrusions of glacially derived water, causing frontogenesis within the main (outer) basins (Gay and Vaughan, 2001).

In addition to upper layer exchange, fjords with basin depths exceeding the level of minimum annual density variation within PWS (~100*m*) exhibit either exchange or renewal of deep water (Muench and Heggie, 1978; Colonell, 1981), the type depending on the sill depth and season. For example, extremely deep fjords (> 200*m*) lacking sills are open to exchange of deep water from PWS in the summer, but those with shallow sills (i.e. << 100*m* limit) only experience deep renewal in the winter (Muench and Heggie, 1978). All of these factors tend to cause baroclinic currents and water exchange within deep basins lacking sills to occur within numerous layers, with the strongest flows restricted to the mouths (Gay and Vaughan, 2001). In contrast, shallow fjords (< 60*m*) tend to exhibit more prominent secondary tidal flows, such as jets and full to partially closed eddies (Gay and Vaughan, 2001). However, even in the latter basins water exchange in the summer appears to occur in layers with little vertical exchange. Zaikof Bay (Fig. 1.1) is the one exception due to high amounts of vertical shear in the outer basin originating from strong cross-channel flows approaching 2.0$m\ s^{-1}$ in HE (Gay and Vaughan, 2001).

2. Research objectives

The main objectives of this study are to elucidate the nature of the factors controlling variability in the physical properties of small fjords in PWS and their affects on estuarine conditions, circulation and water exchange (primarily in the upper layers). A better understanding of these processes will aid in determining both the freshwater budget and its distribution within the Sound, both of which have proved problematic in the past for modeling circulation (Wu, 2011). In addition, the small basins within PWS serve as nurseries for commercially valuable juvenile fish species such as pink salmon (*Oncorhynchus gorbuscha*) and Pacific herring *(Clupea pallasai*) (Stokesbury *et al.*, 2000). The quality of the habitat for these fish is entirely dependent on availability of zooplankton food sources (Foy and Norcross, 1999b) and water temperatures, which affect metabolism and growth rates of age-0 fish (Paul and Paul, 1998; Foy and Paul, 1999). Factors influencing local primary production and advection of nutrients, plankton and larval fish into these basins are therefore quite important in determining which nurseries consistently have the highest survival and recruitment of juvenile fish into the adult population (Norcross *et al.*, 2001). This aspect of fisheries oceanography has recently become a major topic of interest, as over the past two decades following Exxon Valdez Oil Spill (in March 1989) Pacific herring stocks in PWS have remained at severely depressed levels.

To accomplish the above objectives this dissertation addresses the following topics: 1) factors controlling broad-scale variation in freshwater content and hydrography among various fjords across PWS, and 2) the dynamics of circulation and water exchange within one intensively surveyed location, Simpson Bay. The above topics constitute individual chapters in the dissertation, and a final section provides a synthesis and major conclusions of the research. The second chapter addresses patterns of variation observed in the hydrography of fjords located in various sub-regions of PWS. This is done by quantifying the variance of freshwater contents, salinities and temperatures into statistical modes through principal component analysis (Emory and Thompson, 2004). Descriptions of hydrography are shown for representative fjords and the underlying factors responsible for the observed variation are discussed in relation to watershed characteristics and effects of glacial advection. The third and fourth chapters address the results of intensive physical oceanographic surveys within Simpson Bay. The data include repeated transects measuring currents over diurnal and semidiurnal tidal cycles with a towed acoustic Doppler current profiler (ADCPs), hydrography from CTD casts performed during ebb and flood tides. Ancillary data include time-series of temperature and salinity from moored instruments and weather data collected at stations deployed at the mouth.

Analyses in chapter II involve calculations of transports across the sill region of Simpson Bay to determine net amounts of exchange and flushing rates within the main basin of the fjord. The temperature series at various depths are also analyzed for the presence of internal waves by removing the effects of tides and then determining changes in isotherm depths over time. Calculations of vertical diffusivity and work performed against the buoyancy forces are then made from density profiles to determine the energy available to internal waves from tides and the efficiency of internal wave dissipation in causing mixing below the pycnocline.

In the fourth chapter the T/S time-series from the moorings are analyzed by power spectral density, coherence, phase and wavelet power spectra to determine if and when periods of water exchange occur within the two basins and how the variation in physical properties within the near-surface and deep water relate statistically. The near-surface T/S series are also compared with wind data by performing cross-correlation and coherence to determine how diurnal wind events relate to surface and subsurface transport into the main and northern basins.

The final chapter provides both summaries and conclusions of the main topics and discusses the biological implications of the findings. This chapter also presents examples of on-going work and discusses apparent decadal variation in the freshwater contents and stratification within certain fjords, and how these trends may be driven in the future by current climate change that is profoundly impacting the Arctic.

CHAPTER II

VARIATION IN HYDROGRAPHY AND FRESHWATER CONTENTS OF SMALL FJORDS IN PRINCE WILLIAM SOUND, ALASKA IN RELATION TO LOCAL CLIMATE, WATERSHED TOPOGRAPHY AND GLACIAL ADVECTION

This chapter describes variation in hydrography and freshwater content (*FWC*) in the upper 100*m* of small fjords within Prince William Sound, Alaska between May 1994 and August 1997. Statistical modes of variance are derived by principal component analysis, and patterns in physical properties in the spring and summer are linked to differences in local climate, watershed characteristics and advection of glacially derived melt water within the Sound. Two principal components explain > 90% of the variance in salinity and freshwater content anomalies (*FWCA*) reflect the magnitude of surface freshening and the vertical structure of *FWCAs* respectively. Fjords with large positive mode 1 amplitudes all have high freshwater contents, and whereas large positive mode 2 values indicate high stratification, moderate to highly negative mode 2 amplitudes reflect subsurface freshening due to effects of allochthonous freshwater. In contrast, fjords with large negative mode 1 amplitudes are typically salty throughout the water column. The vertical structure of temperature anomalies (*TA*) is more complicated, and three statistical modes are required to explain > 90% of the variance. The causes of this include differences in solar heating (i.e. local climate) and the effects of cold alpine runoff and cold subsurface water advected from tidewater glacial fjords. Sub-regions influenced by this type of advection exhibit large positive mode 1 amplitudes of *FWCA* and negative mode 1 amplitudes of *TA*. In certain cases glacial advection results in reversed estuarine conditions in the outer basins, indicated by moderately negative mode 2 *FWCA* amplitudes. These sites also exhibit a very high *FWC* relative to their watershed to fjord basin area ratios.

1. Introduction

Prince William Sound is a small semi-enclosed sea, isolated from the Northern Gulf of Alaska (NGOA) by large barrier islands located along the south-central coast of Alaska (Fig. 2.1A). Due to its tectonic and glacial history, the interior shoreline forms a complex of fjords located along the mainland and on islands of differing size and elevation. The Chugach Mountains form a steep barrier along the coast with elevations rising abruptly from sea level to heights of 2000 to

4000*m*. The subarctic climate and adiabatic effect of these mountains has created extensive ice fields within the region, which frequently terminate as tidewater glaciers within many of the largest fjords located in the western arc between Port Valdez and Port Bainbridge (Fig. 2.1A).

Oceanographic research in PWS was first conducted in support of the Trans-Alaska oil pipeline terminal in Port Valdez, and early studies focused on the seasonal hydrography and circulation within Port Valdez and the hydrography within the oil transportation corridor (Muench and Nebert, 1973; Muench and Schmidt, 1975). Initial studies were also made at this time of water exchange between Port Valdez and PWS (Muench and Heggie, 1978; Colonell, 1981) and Hinchinbrook Entrance (HE) and the NGOA (Schmidt 1977; Muench and Heggie 1978). Since the 1990's further investigations of water exchange have been made at HE and Montague Strait (MS), as well as large-scale features of transport and circulation of NGOA water within the Sound (Niebauer *et al.*, 1994; Vaughan *et al.*, 2001, Halverson *et al.*, 2013). However, research of PWS fjords (other than Port Valdez) is limited to two studies that respectively describe deepwater renewal at Unakwik Inlet (Muench and Heggie 1978) and some unique features of hydrography and circulation within Columbia Fjord (Walters *et al.*, 1988).

Following the *T/V Exxon Valdez* oil spill (EVOS) in 1989, research of PWS fjords continued through the Sound Ecosystem Assessment (SEA) program (Cooney *et al.*, 2001). The results of SEA provided further knowledge regarding seasonal variation in the hydrography and circulation within PWS (Vaughan *et al.*, 2001; Wang *et al.*, 1997; 2001) and in many of its small fjords (Gay and Vaughan, 1998). From the SEA results Gay and Vaughan (2001) provided a detailed description of various factors affecting the physical oceanography of four PWS fjords routinely surveyed from 1994 to 1998. These factors included interannual and local climatic variation, watershed hydrology, watershed to fjord surface area ratios, winds, and tidal currents. In addition, freshwater from local tidewater glacial fjords, alpine glaciers, or the Alaska Coastal Current (ACC) was observed to create reversed density gradients at the mouths of certain fjords.

The present study addresses statistical modes of variation in hydrography of the upper 60*m* of fjords located throughout PWS, and the interaction of local and allochthonous mechanisms in causing significant temporal and geographic variation in temperatures and freshwater contents among sites. The discussion focuses on the effects of local climate and watershed hydrology. However, advection of glacial water exerts considerable effects on temperatures and estuarine conditions in the upper water column. Therefore, these factors are described in greater detail in comparison to previous reports and publications.

2. Study area

2.1. Regional climatic and oceanographic conditions

The regional climate of PWS is mostly influenced by the Aleutian Low (Wilson and Overland, 1986), which from early fall to late spring generates strong cyclonic winds over the northern GOA coast (see Fig. 1.2). During the winter, Ekman transport from these winds frequently causes surface layer inflow into PWS through Hinchinbrook Entrance (Fig. 2.1A) with a corresponding outflow through Montague Strait (Fig. 2.1A) (Niebauer, *et al.*, 1994; Vaughan *et al.*, 2001). In the summer, relaxation of wind stress and changes in coastal dynamic topography may result in either inflow (Royer *et al.*, 1979) or outflow (Vaughan *et al.*, 2001), but some common annual features of the circulation in the summer and fall include deep (> 200m) exchange at HE (Schmidt, 1977) and the formation of a cyclonic gyre in the central basin (Niebauer, *et al.*, 1994; Vaughan *et al.*, 2001). In the fall, extreme runoff along the northern GOA coast (Royer, 1979, 1982) is reflected in the seasonal increases in both local dynamic heights (0/100m) and the strength of the Alaska Coastal Current (ACC) (Fig. 2.1A). The flow of the ACC ranges from 0.25$m\ s^{-1}$ in the winter to 1.5$m\ s^{-1}$ in the fall (Johnson *et al.*, 1988). Under certain conditions portions of the ACC may become entrained in the general circulation within the Sound (Muench and Schmidt, 1975; Niebauer *et al.*, 1994).

2.2. Sub-regional climatic conditions

A detailed description of the sub-regional climatology within PWS from 1994 to 1998 is given in Gay and Vaughan (2001). These data include monthly means of air temperatures, cumulative precipitation, total monthly means and their variance (standard deviations) computed from daily noon observations collected at four PWSAC[1] salmon hatcheries and from hourly data taken at two NOAA CMAN stations located, respectively, in the central basin (Mid Sound Buoy) and at Potato Point in Valdez Narrows (Fig. 2.1A). The PWSAC stations are archived under COOP data at the Utah State University Climate Center http://climate.usurf.usu.edu/products/data.php) and the NOAA stations under (http://www.ndbc.noaa.gov/maps/Alaska_inset.shtml). A fourth data set came from the CFOS buoy (CLAB) deployed by the Institute of Marine Science at the University of Alaska at Fairbanks (UAF-IMS).

---

[1] Prince William Sound Aquaculture Corporation, main office located in Cordova, Alaska

2.3. Locations and geomorphology of PWS fjords

The fjords investigated for this study are shown in Figs. 2.1A to C. Fig. 2.1A is an overview of the entire Sound and shows the locations of most fjords surveyed across PWS, whereas Fig. 2.1B is an enlargement of the western and southwestern regions showing locations surveyed south of 60^{o} 46' N (i.e. from Culross Island to Port Bainbridge). The initial SEA hydrographic surveys were conducted in 1994 within western PWS, and to facilitate organization of these data and discussion of results this portion of the Sound is divided into five primary sub-regions (Fig. 2.1B). In 1995 and 1996 surveys were expanded across PWS to include four more sub-regions (Fig.2.1C). All inlets (except small passes) are collectively referred to as fjords, and when referring to locations by name the term “Bay” will mostly be omitted. The general basin dimensions (morphometry), sill depths and watershed topography are listed in Table 2.1.

Pritchard (1967) defined fjords as deep, highly stratified estuaries with steep sided basins that are typically U-shaped in cross section and frequently have shallow sills located near the mouth. Fjords in Norway (Saelan, 1967) and western Canada (Pickard, 1961; 1967) generally conform to Pritchard's definition, but they vary significantly in size from lengths of a few kilometers to extremely long basins such as the 176 *km* Sognefjord and the 115 *km* Portland Canal. Saelan (1967) also notes that the term "fjord" is applied very liberally to bodies of water in Norway, some of which are actually bays and Sounds. By comparison, Prince William Sound is a complex of fjords ranging from relatively large primary basins (> $1000 km^2$) to numerous secondary and tertiary basins (Fig 1A) that vary markedly in size and maximum depth (Table 2.1).

Although many PWS fjords tend to follow Pritchard's definition in terms of hydrography, they tend to have highly irregular basins due to reefs, ridges and pinnacles. Entrance sills, when present, vary from 4 to 100*m* in depth, and fall between the shallow and intermediate depth classes described by Muench and Heggie (1978). Certain basins (e.g. Simpson Bay) are also partially filled with glacially derived sediments (Noll *et al.*, 2008) and the hydrography indicates that stratification occurs briefly in late summer. Basins that do not strictly conform to Pritchard’s definition include South Bay, West Twin Bay, Ewan Bay, Paddy Bay, Sawmill Bay, Simpson Bay, Sheep Bay, Port Gravina and Zaikof Bay. These were classified as either shallow partially mixed fjords or bays (Table 2.1), but it should be noted that they are all estuaries due to generally high annual sub-regional freshwater input (Fig. 2.2A).

In PWS, the basins that conform most nearly to the classic definition of fjords are those containing tidewater glaciers (Fig. 2.1A). Unakwik Inlet and Icy Bay are two fjords in this group that were surveyed periodically. Both are relatively large (43-75km^2) and have deep (>200-300m) inner basins isolated by shallow to intermediate depth sills (Table 2.1).

3. Datasets and methods

3.1. Hydrography

The hydrography data used in this study were obtained from vertical profiles collected from May 1994 to March 1998 during the SEA program using SeaBird Electronics SBE19.03 conductivity, temperature and depth (CTD) profilers. Details of sensor resolution, accuracy and sampling methodology for the above instruments are given in Gay and Vaughan (2001). The observation dates and number of oceanographic stations surveyed per cruise are listed in Appendix 3.1. Station locations within each fjord are shown in Appendix 3.2.

3.2 Freshwater contents

The estuarine conditions within sites are derived by the same methods described in Gay and Vaughan (2001), but the analysis is expanded here by examining the relationship between freshwater content and the ratio of fjord watershed and basin area (*watershed ratios*) using least squares regression. The maximum elevation, area and ratio of watersheds are listed in Table 2.1. Conceptually, fjords with large watershed ratios should exhibit high concentrations of freshwater and vice versa for locations with small ratios. Contributing factors, such as aspects and hydrology (i.e. the extent of streams, lakes, alpine glaciers, etc.) were determined qualitatively from 1:24,000 scale USGS topographic maps (http://topomaps.usgs.gov).

The percent of freshwater content (*FWC*) at each station was derived by integrating the relative salinity variation over depth, as expressed by the following equations:

$$FWC(\%) = \frac{1}{z_0}\int_{1}^{z_0}(S_0 - S_i/S_0)dz \equiv \frac{1}{z_0}\left\{\sum_{1}^{z_0}\left[\left(S_0 - S_i\right)/S_0\right]\Delta z\right\} \qquad (2.1)$$

where S_0 is a base salinity determined from all casts during a cruise, S_i is the salinity at each depth increment, z_0 is the maximum depth of integrated by 1m increments (i.e. Dz = 1). To express *FWC* as a percentage the index is normalized by integration depth, z_0, and multiplied by 100. These indices are calculated for z_0 = 1, 10, 25 and 60m.

3.3. Principal component analysis

Principal component (PC) analyses are performed on temperature, salinity and *FWC* to derive statistical modes of variance or empirical orthogonal functions (EOFs). The modes are used to determine which sites are mainly affected by intrinsic factors such as local climate and watershed hydrology and which sites may also be influenced by extraneous factors, such as advection of cold, brackish water from glacial regions of the Sound. The reason for using this approach as opposed to other standard techniques, such as analysis of variance (ANOVA), is that the *PC* analysis provides the most comprehensive and succinct method of showing spatial variation in hydrography among sites (*FWC* in particular) and the differences in vertical structure as well. The EOFs are identical to those described by Emery and Thomson (2004); the difference being that in the present case the modes are spatial (i.e. over depth) as opposed to being temporal. The analyses are performed by first removing the means over all stations at each depth to derive monthly anomalies of temperature (*TA*), salinity (*SA*) and freshwater content (*FWCA*). The latter are then used to derive the EOFs, PC amplitudes (*PCAs*) and percent of variance explained by each statistical mode (eigenvalues). The results for salinity are not included here because the *SA*s and *PCA* s are essentially the inverse of results for the *FWCs*. The PC analyses were checked for consistency by removing means calculated from the mean of all profiles for each site (i.e. the mean of the sample means), and also by removing the means of the site means calculated over entire summers.

4. Results

4.1. Hydrography in the late spring and summer of 1994, 1996 and 1997

Figure 2.2 shows the hydrography of small fjords and some nearshore regions in late spring and summer of 1994, 1996 and 1997. The diagrams are comprised of means calculated from all CTD profiles taken within each site (Appendi x A), and symbols and plot lines are color coded according to sub-regions (Figs. 1B and C). Standard error bars are shown for the most variable layer, the surface, and points throughout the diagrams are plotted at standard depths of 1, 3, 5, 10, 15, 20, 30,…, 100, 120,140,…, >200*m*. Note that the plots in May span the upper 100*m* only.

In late spring (May) the temperature variation among fjords is relatively low (Fig. 2.2a,g), and this is expected as the seasonal weather begins to change from relatively cool conditions in late spring to warm conditions in early summer (June). For example, in 1994 and 1997 the surface temperatures in May range from 6.2 to 7.7°*C* and 6.1 to 8.7°*C* respectively. In June 1994 (Fig. 2.2b), temperatures have a similar range but rise dramatically (11.9 to 13.9°*C*) indicating that a significant increase in solar heating occurs between the two months (Gay and Vaughan, 2001). Water temperatures in June 1996 are lower by comparison (8.3-12°*C*), in part due to the surveys being conducted 10 to 20 days earlier than in 1994. However, mean air temperatures in June 1996 are also ~ 4°*C* lower in comparison to 1994 (Gay and Vaughan, 2001).

In contrast to temperature, the surface salinities in 1994 (Fig. 2.2a,b) indicate freshwater input varies markedly among sites in western PWS in both May (22.9-29.5) and June (20.3-27.3). For example, Culross and Main Bay exhibit cold, fresh surface layers in May but all other sites have relatively high salinities (Fig. 2.2a). In May 1997, spatial variation in salinity is more limited and saltier conditions prevail (27.9-31.3) in part due to significantly lower precipitation[2] relative to 1994 (13 vs. 45*cm*). In June, precipitation is similar in both 1994 and 1996 (17-18*cm*) but high air temperatures in 1994 year contribute to more alpine melting and runoff at certain fjords. This is indicated by a marked decrease in surface salinities at Main and Eshamy (-4 to -8) and large increases in surface temperatures (6-7°*C*). All other sites in 1994 vary between warm, brackish conditions and cold, fresh subsurface water (Fig. 2.2b). In June 1996, however, the salinities (Fig. 2.2d) are much higher by comparison, and this may be an attribute of the scant rainfall that occurs in May 1996 in comparison to 1994 (6 vs. 45*cm*). Relatively cool weather conditions also occur in 1996, contributing to less alpine melting, and all these factors help explain differences in surface salinity observed between the latter two years.

By mid to late summer (July and August) surface heating in PWS fjords typically reaches a maximum following a peak in air temperatures (Gay and Vaughan, 2001). Surface freshening also continues, but the magnitudes of both depend upon the annual sub-regional climate and the differential effects of precipitation, alpine runoff and subsurface glacial advection. For example, in July 1994 (Fig. 2c) some local warming and freshening occurs throughout sub-region 1A, and Herring continues to exhibit much cooler (13.2°*C*) and saltier (27) conditions relative to Drier (14.5°*C* and 24.6). Similar surface conditions (relative to Drier) occur at both Mummy (11.3°*C* and 28) and Little Bay (12.3°*C* and 27.1). In contrast, the sites in sub-region 4 exhibit relatively cool subsurface water, with temperature minima at about 15*m* in depth (Fig. 2.2b,c) due to advection of subsurface glacial water. These properties are most conspicuous at Whale where

---

[2] Mean monthly precipitation computed from weather stations reported in Gay and Vaughan (2001)

conditions at 10 to 15*m* are generally cold (5-7^{o}C) and brackish (27.7-28), but they also occur with decreasing intensity in the upper water columns of Bainbridge Pass and N. Flemming I. The coldest and saltiest conditions, however, occur in the far southwest at Lower Prince of Wales Pass and Twin Bays (Fig. 2.2c).

In July 1996, many fjords in the study area exhibit relatively high surface temperatures (Fig. 2.2e) but the range among sites is extreme (7.8 to 16.2^{o}C). Again, this is due to cold conditions at Whale and also to the two glacial fjords, Icy Bay and Unakwik Inlet. The surface salinities are low at Jack (18.4) and moderately low at Galena, Whale and Icy (22.9 to 23.7), and all the above properties along with warm, salty conditions in sub-region 8 (Port Gravina, Sheep and Simpson) contribute to a wider spatial variation in hydrography in comparison to 1994 (Fig. 2.2c). In August 1996 (Fig. 2.2f), all sites re-surveyed from July show increases in surface temperatures, with the largest changes occurring at Simpson (+2^{o}C) and minor changes occurring at Whale (1-1.3^{o}C). The surface salinities at Eaglek and Simpson decrease moderately by -3 and -3.4 respectively, but at Whale freshening occurs mainly in the subsurface water (3-5*m*) again due to effects of glacial advection from Icy Bay (Gay and Vaughan, 2001). This also creates much colder surface conditions in the main basin in comparison to the inner basin (10.8 vs. 13.2^{o}C).

In 1997, a marked transition in hydrography occurs between May and July (Fig. 2.2g,h). All sites exhibit strong solar heating but the magnitude of freshening differs significantly between the two deep fjords (Whale and Eaglek) and the two shallower basins (Simpson and Zaikof). For example, at Eaglek the surface salinities in July decrease by -6, and prominent subsurface temperature maxima at 10*m* in both the inner and outer basins indicate that freshwater input occurs from both local runoff and glacial advection from Unkawik Inlet. At Whale the decrease in surface salinity is even greater (-8 to -10), and like Eaglek glacial advection creates surface temperature inversions in the outer basin. The conditions at Whale are similar to August 1996, albeit at higher temperatures (12.3 vs. 14.8^{o}C). In August 1997 (Fig. 2.2i), the temperature maxima at Eaglek erode due to increased surface heating but minimal decreases occur in surface salinity. At Simpson the hydrography of the inner basin looks quite similar to Whale (Fig. 2.2i). However, the subsurface T/S values are generally higher by comparison. At Zaikof, both surface heating and freshening significantly increase in August 1997, but this fjord is consistently quite salty in comparison to all other sites (Fig. 2.2h,i).

4.2. Principal components of freshwater content

The two methods of deriving the *FWCA*s show that similar results are obtained whether the total mean *FWC* is calculated directly from profiles of all sites or if sample means from each site are used. However, expanding calculations over the entire spring and summer resulted in enhancing the temporal resolution at the expense of spatial resolution. The present study is primarily interested in the monthly variation in *FWC* among sites. Therefore it was concluded that removal of monthly means was most appropriate for the analyses.

The results are shown in Figures 2.3 to 2.11. There are four types of plots in the figures including: a) profiles of anomalies grouped by sub-regions; b) the mean profile used to derive *FWCA* and EOF modes 1 to 3 over depth; c) percentage of variance explained for modes 1 to 10, and d) spatial bar plots of *PC* amplitudes for modes 1 and 2. Unless shown otherwise, the scale of the mode 1 and 2 *PCA* bar plots is 0.125 and 0.25*cm* per unit amplitude *FWCA* respectively.

4.2.1 Late spring and summer of 1994

The *FWCA* profiles in 1994 show in all months there are sites with entirely positive (fresh) or negative (salty) profiles and sites with profiles falling in between (i.e. with either positive nearsurface water becoming negative in the subsurface, or vice versa). The EOFs in May 1994 (Fig. 2.3e) indicate mode 1 is entirely positive over depth and dominates the percentage of variance explained (Figs. 2.3f). Mode 2, by contrast, is positive in the nearsurface (5*m*) then switches sign over the remainder of the water column. Mode 3 is more complicated, exhibiting two zero crossings, but it also explains only a minor amount of the variance. The EOFs in June and July 1994 (Figs. 2.4f,g and 2.5f,g) follow similar patterns to May, but over time mode 2 shifts downward in depth (10-12*m*) and intensifies slightly.

In terms of physical mechanisms driving the statistical modes, mode 1 is an indicator of total freshwater input (from all sources), whereas mode 2 indicates how the freshwater is distributed vertically as a result of mixing, advection and internal waves. As such, the two modes must be evaluated together when interpreting the underlying physics. For example, in May 1994 sites with the highest freshwater contents (Culross and Main) have over 88% *FWCA* profiles > 0 and, hence, the mode 1 *PCA*s are large and positive (20-58). The mode 2 amplitudes vary in sign at both sites, and the reason for this is that both fjords show gradients from relatively fresh to brackish conditions (Fig. 2.3b,d). Thus for the former profiles, which show the effects of local runoff, the mode 2 *PCA*s are dominated by positive (green) values, whereas profiles with brackish (low runoff) conditions have negative (blue) values.

Other fjords, such as Eshamy and West Twin, exhibit negative mode 1 *PCA*s inferring a generally low freshwater input. However, at Eshamy the amplitudes are larger by comparison (-8 to -22) due to saltier (negative) subsurface *FWCA*s (Fig. 2.3c,d). For the same reason, the mode 2 amplitudes at Eshamy are entirely positive. There is one outlier, however, with large positive *PCA* values for both mode 1 and 2 (22 and 20), and this combination of amplitudes signifies strong stratification in this profile due to fresh surface water overlying salty subsurface water (Fig. 2.3d). In contrast, the mode 1 amplitudes at West Twin are all relatively small (-3 to -7) from offsetting effects of brackish subsurface water. The mode 2 amplitudes are also entirely negative but increase in value towards the mouth. This indicates that the outer basin has higher amounts of subsurface freshwater that may be the result of both advection and vertical mixing by storm-generated winds observed in this fjord in May. This is addressed further below in the Discussion (*section 5.2*).

The remaining sites have *PCA*s that are either predominately negative for both modes (Fig. 2.3g,h), such as the south side of Perry I. (-7 to -16), or vary between positive and negative *PCA*s, such as at Herring (-20 to 10). The latter is due to a split structure in the *FWCA*s (Fig. 2.3a), which also cause the mode 2 amplitudes to vary between positive and negative values (-7 to 6). Like Eshamy and West Twin, the small positive to large negative mode 1 *PCA*s in sub-regions 1 and 2 are attributes of generally limited runoff in these sites in May. However, the varied subsurface conditions result in mode 2 amplitudes ranging from small positive values where salty subsurface water occurs to large negative values in sites with brackish conditions.

In June 1994, both fjords in sub-region 3 increase significantly in freshwater contents throughout their water columns (Fig. 2.4d) and this manifests itself in large, positive mode 1 *PCA*s (25-61) (Fig.4h). The mode 2 amplitudes (Fig. 2.4i) differ in magnitude and sign, however, primarily due to variation in brackish subsurface conditions. Main, for example, has entirely positive amplitudes indicating it has greater stratification from saltier conditions, whereas at Eshamy the effects of higher surface freshening are partly offset by brackish subsurface water. This results in small mode 2 *PCA*s at Eshamy that vary in sign (Fig. 2.4i).

In sub-region 2, the *FWCA* profiles near the surface are either slightly positive or negative, indicating that these sites again have limited freshwater inputs. This results in small mode 1 *PCA*s (Fig. 2.4h) but the highest freshwater contents, where mode 1 amplitudes are all positive

(2-13), occur offshore around SE Perry I. and at the mouth of South Bay. Both sites also have small mode 2 *PCA*s (-3 to 2) due to the low magnitudes of the subsurface *FWCA*s, and the amplitudes are negative wherever the subsurface water is mostly brackish and vice versa for salty conditions (Fig. 2.4b). In contrast, all three fjords in sub-region 1 have moderate to small *FWCA*s that are negative throughout most of the basins (Fig. 2.4a). This gives them small to moderate, negative mode 1 *PCA*s (-6 to -30), but the mode 2 amplitudes are all positive from salty subsurface water, particularly at the head of Drier (Fig. 2.4i), indicating that these fjords are also slightly stratified. A similar situation occurs for sites in sub-region 5 (Fig. 2.4e,h) due mainly to highly negative nearsurface *FWCA*s in Prince of Wales Pass and Shelter Bay (Fig. 2.4e). Unlike sub-region 1, however, the mode 2 *PCA*s are all negative due to slightly fresher subsurface water, which could be the result of either vertical mixing or advection.

In sub-region 4, the *FWCA* profiles at Whale and Bainbridge (Fig. 2.4c) exhibit minimal effects of surface runoff, but large amounts of subsurface freshening result in moderately positive mode 1 and negative mode 2 *PCA*s (Fig. 2.4h). In contrast, mode 1 and 2 *PCA*s for N. Flemming are all negative (Fig. 2.4h) due to generally brackish conditions (Fig. 2.4c). At the two fjords, the highest mode 1 and 2 amplitudes (20-33) occur in the outer basins, indicating that much of the freshening in these sites is extraneous (i.e. allochthonous). However, Bainbridge exhibits a split between positive and negative mode 2 amplitudes in the inner and outer basins (Fig. 2.4i). This is due to progressively fresher subsurface conditions (negative mode 2 values) towards the mouth and higher stratification (positive mode 2 values) towards the head.

In July 1994, the *FWCA*s within sites re-surveyed in sub-regions 1A, 4 and 5A (Fig. 2.5a,c,d) are generally higher in comparison to June (Fig. 2.4a,c,e). This is partly due to a lack of sites in July with high surface freshening, such as Main and Eshamy. However, the mean *FWC* profile in July (Fig. 2.5f) is slightly saltier (fresher) in the nearsurface (subsurface) layers relative to June (Fig. 2.4f). Thus the anomalies in July are primarily due to changes within sites over time.

This can be seen in sub-region 4, where both Whale and Bainbridge exhibit marked increases in subsurface freshening (Fig. 2.5c) and N. Flemming I. shows an upward shift in *FWCA*s throughout the water column. All sites in sub-region 5A (Fig. 2.5d) also exhibit relatively fresh subsurface conditions and in Upper Prince of Wales Pass, stations well inside the mouth resemble profiles in the outer region of Bainbridge Pass and N. Flemming I. (Fig. 2.5c). The above sub-regions all have moderate to highly positive mode 1 and negative mode 2 *PCA*s (Fig. 2.5h), and fresh subsurface conditions now extend beyond N. Flemming I. (25-28) southward into Prince of Wales Pass (15-21). All these results indicate that fresh subsurface water (most likely from Icy Bay) markedly increased in July 1994 within southwestern PWS.

The remaining sub-regions primarily have negative *FWCA*s indicating they are relatively salty throughout their water columns (Fig. 2.5a,b,e), and this is also shown by their negative mode 1 *PCA*s (Fig. 2.5h). Drier is exceptional, however, and the moderately positive mode 1 and 2 *PCA*s for this fjord indicate that it is more stratified in comparison to Herring, Lower Herring and most sites in sub-region 1 B, except the northern portion of Long Channel. The latter instead shows a southward gradient from fresh to salty conditions in both the *FWCA*s and *PCA*s (Fig. 2b,h,i). In contrast, the sites in the extreme southwest (sub-region 5B) all have negative mode 2 amplitudes caused by the excessively salty upper water columns (Fig. 2.2c), which overwhelm the positive effects of the relatively fresh deep *FWCA*s (Fig. 2.5e). The latter combination infers that vertical mixing occurs in these sites and also in various profiles in sub-region 1A and B.

4.2.2 Summer of 1996

In June 1996, the differences in *FWCA* profiles for the three sites surveyed (not shown) generally follow the TS properties (Fig. 2.2d), and are fully positive at Eaglek and Simpson and fully negative at Zaikof. Mode 1 dominates the variance, and together with mode 2 explains > 98% of the variation (Table 2.2). The EOF modes are similar in vertical structure to July 1994, albeit with a much lower surface *FWC* (8 vs. 18%) and the mode 1 *PCA*s in 1996 (Fig. 2.6a) are, therefore, all positive at Eaglek (8-28) and Simpson (4-13). In contrast, amplitudes at Zaikof are all large and negative (-24 to -33) due to the salty water column (Fig. 2.2d). Mode 2 *PCA*s (Fig. 2.6b) are small at all sites (-5 to 7) but positive amplitudes indicate stations having higher surface freshwater input, whereas negative values indicate effects of brackish subsurface water.

The *FWCA* profiles in July 1996 (Fig. 2.7a to f) reflect a wide spatial variation in freshwater input across PWS (Fig. 2.2e), similar to June 1994, resulting in a large total variance ($\sigma^2 = 526$) that is 1.5 times greater than the variance in July 1994 ($\sigma^2 = 347$). The EOFs (Fig. 2.7g) are also similar in structure to July 1994, and 85% of the variance is dominated by mode 1 (Fig. 2.7h). Mode 2 is more substantial in 1996, however, contributing to 13% of the variance (Table 2.2). As in 1994, this is due to a large number of sites with positive *FWCA* values below10*m* that also have small to moderately positive mode 1 *PCA*s. The latter sites include Whale and Icy (10-32), Ewan, Paddy and Dangerous Pass (1-6) and the inner basin of Unakwik Inlet (9-12). These sites also show moderate to large amounts of subsurface freshening, indicated by the negative mode 2 amplitudes, but the magnitudes vary from small values at Whale and Dangerous Pass (-3 to -12) where the freshening is from extraneous mixing and advection, to large values in the inner basin of Unakwik (-18 to -19) where basal freshwater discharge occurs from Meares Glacier (Fig. 1A).

In contrast, Jack and Galena are the only two sites that have fully positive nearsurface *FWCA*s (Fig. 2.7a) and positive mode 1 *PCA*s (Fig. 2.7i). However, whereas Jack exhibits marked stratification shown by large positive *PCA*s for both modes 1 (26-46) and 2 (16-22), Galena exhibits mostly small amplitudes (6 to18 and -3 to 7) indicating that it is only moderately stratified. The sites in sub-regions 1 and 8 all have mostly negative *FWCAs* similar to salty sites in July 1994 and hence the mode 1 *PCA*s are all < 0. As a consequence, the stratification in these sites is relatively weak, but varies between sites as indicated by the mixed (positive to negative) mode 2 PCAs. In sub-region 6, Eaglek and Unakwik, exhibit both positive and negative *PCA*s (Fig. 2.7i) due to high variation in *FWCA*s throughout their basins (Fig. 2.7d). However, at Eaglek this occurs mainly in the nearsurface layer, whereas Unakwik exhibits much more brackish *FWCA*s in the outer basin that are similar to profiles in the outer basin at Eaglek (Fig. 2.7d). The two outer basins also have negative mode 1 and 2 *PCA*s (Fig. 2.8i,j) from slightly fresher subsurface water in comparison to sub-regions 1 and 8.

In August 1996, the *FWCA* profiles (Fig. 2.8a to c) indicate that freshwater input generally increases at most sites. The exception is Whale, where the *FWCA*s are more negative throughout the water column. This is partly an artifact of the monthly analyses, and Whale actually exhibits moderately large, positive mode 1 *PCA*s in August (10-23). Stratification also appears to be stronger in the outer basin where the largest positive mode 1 and 2 *PCA*s occur. However, the T/S plots (Fig. 2.2e,f) indicate that the mean salinity in Whale's outer basin is less than the inner basin and freshening is primarily in the subsurface layers. Similar properties are indicated by progressively negative (saltier) *FWCA* profiles towards the inner sill (Fig. 2.8a), where the *PCA* is ~ 0.5, and by the negative mode 2 amplitudes in the outer basin (Fig. 2.7h).

At Eaglek the *FWCA* profiles markedly increase throughout the upper water column in August (Fig. 2.8b) and the mode 1 *PCA*s are, therefore, mostly positive (8-23). Eaglek also has all positive mode 2 amplitudes indicating an increase in stratification as shown by the fresh near-surface profiles (Fig. 2.8b). Unakwik Inl*et al.*so exhibits large, positive mode 1 amplitudes, particularly within the inner basin, (36-44), but in contrast to Eaglek, the mode 2 *PCA*s are all negative and the amplitudes in the inner basin markedly increase towards the head (-17 to -27) due to an intensification of upwelling and mixing of sub-glacial freshwater discharge.

At Simpson and Zaikof the water columns are relatively salty, and all mode 1 *PCA*s are << 0 (-8 to -17 and -24 to -46 respectively). Two exceptions occur in the inner basin of Simpson (-1.6 and 0.4) where two stations have stratified *FWCA* profiles (Fig. 2.8c). In contrast, the water column of Zaikof is quite salty throughout the fjord (Fig. 2.9d), as shown by the fully negative mode 2 *PCA*s.

4.2.3 Late spring to late summer of 1997

In May1997, the *FWCA* profiles are again mostly positive at Eaglek and fully negative at Zaikof, as suggested by the T/S diagrams (Fig. 2.2g). At Simpson they are mainly negative, and this is partly due to Simpson's relatively salty water column. Inclusion of Whale, a relatively fresh fjord (Fig. 2.2g), however, also causes a negative shift in Simpson's *FWCA* values. The amplitudes of mode 1 (Fig. 2.9a) are positive at Eaglek, except for one station at the mouth (-3 to 20) and fully positive at Whale (10-16). Note also that the largest amplitudes occur in the outer basins of both fjords. The amplitudes at Simpson are moderately negative (-3 to -14) but at Zaikof they are highly negative (-18 to -22) again due to the extreme salty conditions (Fig. 2.2g). The mode 2 *PCA*s are all quite small (Fig. 2.9b) and as in prior months, they vary in sign depending on the relative values of the nearsurface and subsurface *FWCA*s. At Eaglek and Whale, however, negative mode 2 amplitudes occur in the outer basins, again indicating that in May 1997 subsurface freshening was already influencing their hydrography.

In July 1997, the *FWCA* profiles at Whale and Eaglek (Fig. 2.10a,b) show higher freshwater inputs relative to 1996 (+5 to 10%), also implied by the T/S diagrams (Fig. 2.2e,h), but at Whale the freshening is mainly in the nearsurface layer whereas at Eaglek it is throughout the water column. These properties are also evident in the *PCA*s, which are positive at both fjords for mode 1 (7- 14 and 4-12 respectively). In contrast, the *FWCA*s and *PCA*s at Simpson and Zaikof are markedly negative, particularly in the surface layers.

The EOF structure in July (Figs. 2.10e) is similar to previous years but the percentages of variance explained by modes 1 and 2 (Fig. 2.10f) are similar to May 1994 (> 95 and 3%), probably due to large differences in water column conditions in both months. The mode 1 *PCA*s are also lower in magnitude relative to 1996 due to the smaller nearsurface EOFs (Fig. 2.10e).

The mode 2 *PCA*s in July (Fig. 2.10h) are relatively small (similar to May), but the amplitudes are distinctly higher at Whale and Eaglek as a result of greater haline stratification in comparison to the other sites (Fig. 2.2h). The stratification is highest in the outer basin of Whale where the mode 2 values are positive (Fig. 2.10a), whereas at Eaglek the mode 2 amplitudes are nearly all negative due to the increased subsurface to deep freshening. At Simpson and Zaikof the mode 2 amplitudes are relatively small by comparison due to a greater offsetting by the mode 2 EOFs on their markedly negative *FWCA* profiles (Fig. 2.10c,d). However, the mode 2 values also vary in sign depending the relative amounts of freshwater in the nearsurface versus subsurface layers.

In August 1997, large changes in *FWCA*s occur relative to July among most sites (Fig. 2.11a to d). This is due to an unprecedented increase in upper layer freshening at Simpson (+10 to 30%), particularly within the inner basin (Fig. 2.2i), and it has two effects: 1) it shifts the mean *FWC* upward by ~10% at the surface (Fig. 2.11e) and 2) it causes a net reduction in the *FWCA*s at both Whale and Eaglek (Fig. 2.11a,b). Also, as in 1996, the mode 2 EOFs in 1997 explain a much higher amount of the variance relative to mode 1 (Table 2.2). At Zaikof the *FWCA*s are again highly negative, but they are also nearly uniform in value throughout the fjord within the nearsurface water (Fig. 2.11d).

The mode 1 *PCA*s (Fig. 2.11g) show the above variation in *FWCA*s among sites and also the distribution of freshwater content inside each fjord. For example, the mode 1 amplitudes at Simpson (Fig. 2.11g) indicate that the highest freshwater contents occur respectively in the inner and outer basins (33-37). Among the other stations, however, there is marked variation in the *PCA*s (-16 to 20). Whale also exhibits moderately high mode 1 PCAs throughout the fjord (14-20), whereas Eaglek is split between negative and positive amplitudes that coincide with saltier (-2 to -13) and fresher conditions (3-20) in the inner and outer basins respectively (Fig. 2.11b). Zaikof again has negative *PCA*s throughout the fjord, but the magnitudes in 1997 are extreme (-52 to -59) due in part to the strong surface freshening at Simpson.

Mode 2 amplitudes show the varied effects of stratification from runoff versus mixing and advection among sites. For example, at Whale the large positive mode 2 amplitudes indicate that all stations are more stratified in comparison to prior months and years, but whereas large values indicate saltier conditions, small values indicate stations with subsurface freshening. In contrast, positive amplitudes at Zaikof (Fig. 2.11h) generally infer salty subsurface conditions, but the larger values in both the inner basin and at the mouth also indicate that these stations have slightly higher subsurface freshwater contents. At both Simpson and Eaglek the mode 2 amplitudes are all negative, but the largest amplitudes coincide with the brackish conditions in both the near-surface and subsurface to deep water (Fig. 2.11b,c).

4.3. Principal components of temperature

In contrast to freshwater content, the EOFs of temperature (Fig. 2.12a to c) exhibit a more complicated vertical structure on both a monthly and annual basis. This is related to high spatial variability from thermal features such as surface inversions and subsurface minima and maxima (Fig. 2.2), caused by differences in local insolation and the influence of cold alpine and sub-glacial discharge (Gay and Vaughan, 2001). The percentage of variance explained by mode 1 (53.6 -79.2%) is considerably less with respect to the percentages for *FWC* (Table 2.2) and in all months, mode 2 is significant, explaining 9.7 to 33.5% of the variance.

Interpreting the physical significance of the EOF modes can be difficult since similar results can occur from much different vertical arrays of temperature anomalies (*TA*s). For example, in May 1994 the range in surface temperatures is relatively low ($\Delta\overline{T} \sim 1.5^{o}\,C$) and the variance in *TA*s among sites (Table 2.2) is only $6.3^{o}\,C^{2}$. The EOF of mode 1 (Fig. 2.12a) is, therefore, relatively homogeneous in distribution within the upper 60*m*. In contrast, the distribution of mode 1 June 1994 is almost entirely centered on a subsurface maximum at ~10*m*. The variance ($36.5^{o}\,C^{2}$) is more than 6 times the value in May, and the high variability and the unusual EOF structure are both undoubtedly related to the cold subsurface water in sub-region 4 (Fig. 2.2b) and also quite likely to marked subsurface *TA* maxima of +3 to $4^{o}\,C$ in sub-regions 2 and 3.

In June 1994, the sites in sub-regions 1 to 4 with positive mode 1 amplitudes (Fig. 2.13a) also have positive subsurface *TA*s (not shown), and the magnitudes of the *PCA*s in these sites are indicators of their respective amounts of thermal stratification. In contrast, sites with moderate to large, negative amplitudes have limited stratification due either to low surface heating (Herring) or cold subsurface glacial water (Whale and N. Flemming I.). Drier and Bainbridge both have many negligible mode 1 *PCA*s, but for very different reasons. Drier has moderate surface heating (*TA*s = 1-$1.8^{o}\,C$) over cool subsurface to deep water (*TA*s = -0.5 to +$0.2^{o}\,C$), thus causing an offsetting effect on the *PCA*s. At Bainbridge, the near-surface water is much warmer by comparison (*TA*s = 1.5-$3^{o}\,C$), but many of the profiles with these conditions are offset by cold subsurface glacial water (*TA*s = -1.5 to -$2^{o}\,C$) similar to Whale. In contrast, the *TA* structure at upper Prince of Wales Pass and Shelter Bay in sub-region 5 is inverted (i.e. cool nearsurface over warm water) giving these sites small *PCA*s that are mostly negative (Fig. 2.13a).

In July 1994, the variance ($36.4^{o}\,C^{2}$) is similar to June but the near-surface EOFs are negative (Fig. 2.12a). Glacial water in sub-region 4 still causes a subsurface maximum in the vertical EOF structure, but it is shifted downward by ~ 5*m*. The deep EOFs are also all now positive, and these changes along with the lack of sites with strong thermal stratification, such as SE Perry and Eshamy, result in a much different set of mode 1 *PCA*s (Fig. 2.13b). The effect is most profound at both N. Flemming I. and sites throughout sub-region 5, where the *PC* amplitudes are all positive. This is again due to marked inversions in the *TA* structure. Whale and Bainbridge both have negative amplitudes from cold subsurface water, but the fjords in sub-region 1 exhibit varied *PCA* magnitudes and signs. This results from moderate near-surface stratification in sub-region 5A, particularly at Drier, and poor to limited stratification in sub-region 5B (Fig. 2.2c).

The structure of mode 2 in 1994 bears some similarities to mode 2 EOFs of the freshwater contents (Fig. 2.12 d to f), but in May (Fig. 2.12a), the function crosses zero much deeper in the water column at ~ 16*m*. In June it rises to < 10*m*, following the subsurface maximum of the mode 1 EOF, but in July it shifts downward to 18*m* and remains closer to zero with depth. These latter changes result in the sign of mode 2 *PCA*s to fluctuate between June and July in sub-regions 4 and 5A (Fig. 2.13c,d), but in sub-region 5B large negative *PCA*s occur due to a marked inversion in *TA* structure ($|\Delta TA| \sim 5^{o}\,C$). This is also indicated in the TS plots (Fig. 2.2c).

In 1996, the mode 1 EOF structure again varies with depth (Fig. 2.12b), but the subsurface maxima observed in 1994 are absent and the variance of the *TA*s increases significantly (64.1, 58.1 and $98.6^{o}\,C^{2}$ in June, July and August respectively). The mode 1 *PCA*s (Figs. 14a,c) indicate how the variance in the upper 30*m* is generally distributed among sites, whereas mode 2 *PCA*s (Figs. 2.14b,d) show the effects of subsurface *TA* variation. For example, the mode 2 EOFs have large subsurface maxima that fluctuate in sign between months (Fig. 2.12b). In June the maximum is centered at ~ 30*m*, and this is likely due a change in vertical *TA* structure at Eaglek and Simpson from positive surface and subsurface values to negative deep *TA*s, and vice versa for Zaikof (Fig. 2.2d). In July, however, the mode 2 EOFs become positive above 10*m* and negative below, with a subsurface minimum again at about 30*m*. This fluctuation causes the mode 2 *PCA*s (Fig. 2.14b) to be negative at sites that are either entirely warm (*TA*s > 0), such as Port Gravina, Sheep, Eaglek and Ewan, or have cold surface inversions and subsurface maxima, such as Icy Bay, the outer basin of Whale and the inner basin of Unakwik (Fig. 2.2e).

Sites in July with mostly positive mode 2 *PCA*s are thermally stratified with subsurface water that is either cool (*TA*s < 0), such as Jack Bay, or neutral (*TA*s → 0), such as Galena, Drier, Dangerous Pass and Paddy. Other sites, by contrast, have varied mode 2 *PCA*s, particularly between the inner and outer basins. For example, the outer basin of Unakwik has slightly negative to neutral nearsurface *TA*s but the subsurface water is cool due to outflow of glacial water (Gay and Vaughan, 2001), thus the mode 2 *PCA*s in the outer basin are positive. In contrast, Whale's the inner basin has positive mode 2 *PCA*s mainly due to warmer nearsurface water relative to the outer basin and mouth.

In August 1996, the PCAs of mode 1 (Fig. 2.14c) show upper layer temperature variability among sites (Fig. 2.2e), just as in July, but the mode 2 EOFs fluctuate back to a structure similar to June. This results in mostly positive amplitudes at the sites with cold surface water (Whale and Unakwik). Zaikof also has highly positive mode 2 *PCA*s, but this is due to the effects of warm subsurface water (Fig. 2.2e), whereas Eaglek and Simpson have negative *PCA*s due to relatively warm nearsurface and cool subsurface water respectively (Fig. 2.2e).

In 1997, the total variance is low in May ($16^{o}\,C^{2}$) but is very high in both July ($137^{o}\,C^{2}$) and August ($83^{o}\,C^{2}$). The structure of mode 1 EOFs in May (Fig. 2.12c) is similar to mode 1 in July 1996, and the *PCA*s again generally reflect cold subsurface water at Whale and Zaikof and warm upper layers at Eaglek and Simpson (Fig. 2.2h). In July, however, the EOFs exhibit a subsurface maximum similar to June 1994 that is clearly related to the large ($+4^{o}\,C$) subsurface maxima at Eaglek and the surface inversion in the outer basin of Whale (Fig. 2.2h). The large magnitude of subsurface warming at Eaglek results in highly positive mode 1 *PCA*s (Fig. 2.15a), whereas all the other sites exhibit negative values. Mode 2 EOFs have a structure in July similar to 1996. This results in uniformly negative *PCA*s at Whale and small values at Eaglek and Simpson that vary in sign (Fig. 2.15b) due to effects of cold water in their outer basins. At Zaikof, the mode 2 *PCA*s are all highly positive due to the effects of relatively warm subsurface water (Fig. 2.2h).

In August 1997, the subsurface maximum of the mode 1 EOF deepens to ~ 30*m* but deceases in magnitude, following the same trend as the subsurface temperature variation among sites (Fig. 2.2i). The mode 1 PCAs (Fig. 2.15c) are positive for all sites except Whale, which again exhibits relatively cool upper layer conditions. The mode 2 EOFs also fluctuate, exhibiting a subsurface minimum between 20 to 30*m* and highly positive values in the upper 15*m* (Fig. 2.12c). As a result, the *PCA*s at Whale and Eaglek vary in sign (Fig. 2.15d) but the positive values at Whale all occur in the inner basin due to warmer water in the upper 10*m* (Fig. 2.2i). At Eaglek, the amplitudes vary throughout the fjord, but the warmest and coolest water occurs at the head and mouth respectively. Mode 2 *PCA*s at Simpson are all negative due to cool nearsurface water over the entire fjord (Fig. 2.2i), whereas the uniformly positive PCAs at Zaikof occur from marked warming of the upper water column (Fig. 2.2h,i).

4.4. Regressions of FWC in relation to watershed ratios, areas and maximum elevations

To examine the statistical relationship between the freshwater contents of fjords and their watershed characteristics, regression analyses are performed for *FWC* and watershed ratios (WSRs) in the spring and summer of 1994, and for *FWC* and watershed ratios, areas and maximum elevations in the summer of 1996. The regressions are conducted first by including all sites, and then omitting certain outliers that have some anomalous watershed characteristics or are suspected of being influenced by allochthonous sources of freshwater (i.e. extraneous to the system). For example, the regression for *FWC* integrated to 60*m* in May 1994 (Fig. 2.16a) has a low coefficient of determination ($R^2 = 0.14$) and is not statistically significant ($p = 0.414$), hence the slope is indistinguishable from zero. For most sites the mean *FWC* falls within the 95% confidence interval (C.I.), except Eshamy, which has peculiar features to its innermost basin and watershed. Removing this single outlier results in not only a significant correlation ($p = 0.003$) but also a very high R^2 (0.92) and a substantial narrowing of the 95% C.I. Similar results (not shown) occur for depths of 10 and 25*m* ($R^2 = 0.81$ for both).

In June 1994 (Fig. 2.16b) a similar situation occurs for Whale, which is markedly affected by allochthonous glacial water (see sections 4.1 and 4.2). The *FWC* is highly under-predicted for this fjord, but the regression is significant at the 5% level whether it is included ($R^2 = 0.45$, $p = 0.047$) or omitted ($R^2 = 0.73$, $p = 0.007$). Omitting Whale tightens the 95% C.I., however, and markedly improves the regressions at 10 and 25*m* ($R^2 = 0.83$, and 0.73). In July 1994, however, the regression including all sites is essentially non-existent due to two extreme outliers, Whale and Little Bay (Fig. 2.16c). However, removing Whale and the two sites with disproportionately low *FWC* values (Mummy Bay and Little Bay) only marginally improves the regression ($R^2 = 0.39$) and the correlation is only significant at the 20% level ($p = 0.183$).

For July 1996, the regressions are performed for *FWC* at 60*m* in both inner and outer basins (Fig. 2.17a). These results show a significant correlation at the 10% level ($p = 0.089$), but the R^2 value is quite small (0.15). When the regression is performed using the inner basins only, the R^2 doubles in value (0.32) and remains significant at the 10% level ($p = 0.07$). Furthermore, the regressions performed for *FWC* in the inner basins versus watershed areas and maximum elevations (Fig. 2.17b,c) show significant relationships only at the 10% ($p = 0.07$) and 20% level ($p = 0.18$) respectively. The R^2 values are also small to moderate in size (0.13 to 0.31).

As in 1994, a number of fjords have suspicious *FWC* values in 1996, including Whale, Ewan, Paddy, Eaglek and Simpson. The *PC* analysis (section 4.2.2) shows that the first four sites are influenced by allochthonous fresh (glacial) water, and at Simpson the inner basin responds dramatically to high precipitation in late summer and the outer basin can be influenced by extraneous freshwater within the Rude River plume (Gay and Vaughan, 2001). Figure 2.17e shows the same regressions performed as in Figure 2.17b, but with the above five sites omitted (black circles). The R^2 value is markedly improved (0.78) and the relationship is significant at the 5% level ($p = 0.016$). However, it should be noted here that the relationship of *FWC* to the watershed ratios is highly tenuous in 1996 due to the large number of outliers. Also, significance in the regression is achieved only by including the two glacial systems with extensive *WSR*s (Table 1). The significant relationships in May and June 1994 probably occur due to the close geographic proximity and similar watershed topography of the fjords being compared, whereas in 1996 the fjords are scattered across PWS. Thus there is a wider range of factors either intrinsic to their watersheds or extrinsic, such as advection of allochthonous glacial water into their basins. This is discussed below in greater detail.

5. Discussion

5.1 Temporal variation in EOF modes of FWC

The changes over time in EOFs of mode 1 and 2 for the anomalies of temperature (*TA*) and freshwater content (*FWCA*) are shown for 1994, 1996 and 1997 in Figure 2.12d-f. From these plots it can be seen that the structure of the *TA* modes is much more complicated than the modes for *FWCA*. The structure of temperature is affected by variation in insolation and the effects of cold alpine runoff, as well as diffusive, viscous and advective mechanisms (Muench and Nebert, 1973; Muench and Schmidt, 1975; Muench and Heggie, 1978). In contrast, the stabilizing effects of high *FWC* on density stratification in the Northern Gulf of Alaska (NGOA) region (Royer, 1979) makes the vertical structure of salinity more predictable.

The changes in mode 1 EOFs of *FWCA* over time primarily show the seasonal changes in surface salinity through progressive amounts of runoff from rainfall and melting of stored precipitation, and subsurface changes due to advection. Mode 2, however, infers differences in vertical structure of *FWC* and is, therefore, affected by subsurface and deep freshening due to vertical mixing and/or advection. For example, in 1994 the temporal changes in both modes are affected by the downward mixing of freshwater, but in May the structure of mode 1 reflects the high *FWCA*s at Culross and Main (Fig. 2.3b,d). In June mode 1 shows a greater influence of subsurface freshwater on the variance, implying that mixing and/or advection occurs in fjords with surface and subsurface freshening, such as Eshamy and Main in sub-region 3 (Fig. 2.4d). The high *FWC* in the above fjords in June also results in the percent of variance explained by mode 1 to increase to over 95%, similar to the pattern in salinity (Table 2.2). The absence of observations from Eshamy and Main in July reduces the mode 1 percent of variance explained to < 90% (Table 2.2). In contrast, mode 2 increases markedly in July for both salinity and *FWC* due to the high subsurface *FWC* within sub-regions 4 and 5A.

In 1996 the changes in EOF structure between June and July is reversed for both modes (Fig. 2.12b), due likely to a paucity of sites surveyed in June in comparison to July. It also is due to a general lack of haline stratification (Fig. 2.2d) caused by very dry conditions in May and only moderate increases in precipitation in June (Gay and Vaughan, 2001). The EOF modes in July bear a remarkable similarity to those in May 1994, however, mainly as a result of haline stratification in Galena and Jack in sub-region 7 (Fig. 2.7e). In August, both EOF modes increase in depth since none of the sites surveyed exhibit highly stratified conditions over their entire basins. Furthermore, the depth increase of mode 2 exceeds mode 1 due to a greater influence of subsurface freshwater, particularly in sub-region 6 (Fig. 2.8b).

In 1997, the vertical structure of the mode 1 EOFs (Fig. 2.12c) is similar in all months due to consistent differences in upper water column salinities among the four SEA fjords (Fig. 2.2g,h,i). This results in similar spatial variation in *FWCA* and *PCA* values in June and July (Figs. 2.9 to 2.10). However, in August, the EOFs shift slightly higher (lower) in value for the near-surface (subsurface) water due to the large FWCAs in Simpson's inner basin (Fig. 2.11c). The mode 2 EOFs also exhibit an interesting reversal at ~ 2*m* depth, apparently caused by a negative shift in the nearsurface *FWCA*s at Whale and Eaglek due to Simpson's extreme freshening (Fig. 2.2i).

5.2. Spatial variation in TAs and FWCAs and the physical context of mode 1 and 2 variation

As aforementioned in section 4.2.1, mode 1 *FWCA* variation is an indicator of total freshwater input from all sources, including runoff, direct precipitation and advection from outside fjord systems. In contrast, mode 2 variation infers the vertical distribution of freshwater as a result of processes such as stratification, mixing, interleaving (due to advection) or internal waves. For example, Culross and Main exhibit moderate to large, positive mode 1 *PCA*s in May 1994 due to relatively strong local freshwater input. However, the mode 2 amplitudes (Fig. 2.3h) are positive where the *FWCA* profiles show haline stratification and negative at stations exhibiting saltier conditions (Fig. 2.3b,d). The high spatial variation in *FWCA*s within both fjords is partly due to a scattered distribution of the small (high order) streams that discharge into PWS fjords (see Fig 19 and Appendix 3.3). However, winds and tidal currents also contribute to spatial variability by creating convergences, observed as surface tide rips that move within basins during the tide cycles. Runoff in the spring is typically cold, and this results in negative surface *TA*s at both sites. At Culross, however, the subsurface TAs below 20*m* are also markedly negative indicating that the deep freshening there (Fig. 2.3b) could be due to advection from northern glacial sub-regions, such as College Fjord.

In early summer, glacial advection begins to have a strong impact on the hydrography of certain fjords. Two prime examples include Whale and the outer portions of Bainbridge Pass in both June and July 1994 (Figs. 4h,i and 5h,i). At Whale, the mode 1 *PC* amplitudes of the *TA*s (Fig. 2.13a,b) are large and negative in both months due to the effects of cold subsurface water, and at Bainbridge the *PCA*s are small to negligible in June and all negative in July. In 1996 and 1997, the *TA PCA*s are again highly negative at Whale (Figs. 14 and 15) and the amplitudes of *FWCA*s are consistently large and positive (Figs. 7 to 11). The freshwater content at Whale is also very high in relation to the watershed ratio, making it an outlier in all regression analyses (Figs. 2.16 and 2.17). All of the above results suggest that the subsurface freshening at this fjord (and other sites to the south and east) occurs from advection from a nearby glacial fjord, Icy Bay. Two small fjords north of Icy Bay, Ewan and Paddy, also exhibit atypically fresh conditions in July 1996 (Fig. 2.7b,i,j) possibly caused by glacial advection from the north.

In May 1994, the temperature variation is small in comparison to salinity (Fig. 2.2a). This is also shown in vertical sections of temperature for sub-regions 3 and 1 (Fig. 2.18a-d). Most sites, therefore, have either fully positive or negative *PCA*s of temperature, but as discussed above, the amplitudes of *FWCA*s exhibit relatively high intra-site variation and in some cases the *PCA*s change sign indicating marked local variation in freshwater content. At Main Bay the latter is due to a near-surface salinity gradient (S = 23-26) that extends towards the mouth of the fjord (Fig. 2.18a). Eshamy, by contrast, has negative PCAs due to salty near-surface water (S = 29-30) except for one station located inside the outer sill, where fresher water (S = 23) appears to be pooled (Fig. 2.18b) causing the mode 1 *FWCA PCA* there to be >> 0.

The fjords in sub-region 1 exhibit high surface salinities in May 1994 (Fig. 2.18c,d) and also large negative mode 1 amplitudes of *FWC* (Fig. 2.3g). They both have mixed +/- *PCA*s within their basins, and the vertical sections of salinity reveal that positive values at Herring result from a large concentration of low salinity water in middle of the fjord, whereas at Lower Herring they occur mainly in a small side arm and near the mouth (Fig. 2.3g). The mode 2 *PCAs* at Herring also vary in sign and have positive amplitudes where the subsurface water above ~ 15*m* is salty and vice versa for where it is fresh. This is expected on the basis that the relatively brackish surface salinities (28-30) show that less stratification occurs at Herring in comparison to Main, where positive values occur for both modes. The mode 2 *PCA*s at Lower Herring, by contrast, are all negative following the nearly uniform horizontal distribution of salinity, but near the mouth where shoaling of isohalines occurs near the sill they diminish in magnitude (Fig. 2.18d).

It is uncertain as to exactly what process creates the vertical fluctuations in the water column at Herring, but since they are evident in both T and S structures they may represent effects of internal waves. Although herring has no entrance sill, the winds during the survey were blowing southwards into the fjord against an ebbing tide and a distinct convergence zone was observed across a shelf break at the mouth formed by depths > 220*m* shoaling to 150*m*. The winds also formed Langmuir cells, visible as wide streaks O(100*m*), which could also be responsible for concentrating the surface freshwater measured along the CTD line (Fig. 2.18c).

In June 1994, the fjords in sub-region 3 are both warm and thermally stratified, particularly Eshamy, as indicated by both the vertical sections of temperature (Fig. 2.18e,f) and mode 1 *TA* PCAs (Fig. 2.13a). Both fjords also show moderate to highly positive mode 1 amplitudes for *FWC* (Figs. 3g and 4h), but the changes at Eshamy are dramatic suggesting that in June freshwater rapidly enters the main basin. The lowest surface salinities within Eshamy occur towards the head (Fig. 2.18f) but in general freshwater is well distributed throughout the basin. In contrast, the mode 1 *PCA*s at Main are higher in the outer basin, where low salinity water is again concentrated over the outer sill (Fig. 2.18e). The mode 2 *PCA*s at Main are all positive indicating that it has higher stratification relative to Eshamy, whereas the latter site has small mode 2 values that vary in sign due to deeper freshening (Fig. 2.4d).

Runoff in the early summer includes a greater contribution from stored precipitation (Gay and Vaughan, 2001), and the increased volume results in a broad dispersal of surface freshening within both fjords in sub-region 3 (Fig. 2.2b). However, they also have relatively fresh subsurface water (Fig. 2.4d), and moderate to highly positive mode 1 *TA* amplitudes (Fig. 2.13a) at both fjords suggest that the bulk of this freshening probably comes from local sources. This means there must be some additional mechanism of rapidly mixing freshwater into the subsurface layers, particularly at Eshamy. Both fjords have mid-depth (50*m*) sills (Table 2.1) and internal waves generated by tidal flows across these obstructions (Stigebrandt, 1976) could potentially cause turbulence that deepens the pycnoclines (Stigebrandt and Aure, 1989). This process occurs at Simpson Bay and is addressed below in detail in Chapter III.

At Herring and Lower Herring the spatial variation of mode 1 *PCA*s within diminishes In June but the negative amplitudes (Fig. 2.4h) indicate that the total freshwater content is low in comparison to sites with positive *PCA*s. Furthermore, the former fjords have positive mode 2 values as a result of salty subsurface water (Fig. 2.4a). Vertical sections (Fig. 2.18e,f) indicate there is some stratification at both fjords in June, but the conditions at Lower Herring are distinctly warmer and fresher in comparison to Main, and similar conditions occur at Drier (Fig. 2.4h,i). The sign of the *PCA*s of modes 1 and 2 for *FWCA* are in phase at all three fjords in June, but in July this changes as the differences in *FWCA* among the three fjords intensifies (Fig. 2.5h,i). The variation in magnitude of the *PCA*s is mainly due to differences in local runoff, which is highest at Drier. However, the *FWC* does not strictly follow the respective watershed ratios until possibly in July (Fig. 2.16). This may be related to the generally low freshwater input exhibited by these fjords in 1994, and occurs again in July 1996 for Drier (Fig. 2.7i,j).

5.3 Allochthonous sources of glacial water

The results of this study show some fjords and nearshore regions in PWS have consistently high *FWCAs* and mode 1 *PCA*s in relation to both their watershed hydrology (Fig. 2.19) and WSRs (Fig. 2.16 and 2.17). The mode 2 amplitudes at these sites are also typically negative due to the effects of subsurface freshwater, and in sub-region 4 the physical properties suggest that the fresh conditions are caused by allochthonous water that is glacial in origin. For example, in June and July 1994 the hydrography at Whale (Fig. 2.2b,c) exhibits subsurface temperature minima at about 15*m*, and beneath this layer the water is very cold and isothermal (5.1 to 5.4^{o} *C*). During the same months, temperatures in the outer basin at Bainbridge Pass and around N. Flemming I. exhibit similar subsurface minima. Vertical sections from transects in June (Fig 20a to d) indicate that these temperature anomalies are in fact comprised of fine-scale minima and maxima, that are distributed intermittently at Whale to depths of 50*m* over the entire outer basin (Fig. 2.20c,d). In contrast, the anomalies at Bainbridge exist just beneath the thermocline inside the mouth (Fig. 2.20c,d). Similar properties occur in both fjords in July (not shown).

The temperature anomalies within the above two fjords resemble similar sub-thermocline temperature minima and maxima within fjords containing tidewater glaciers observed by Pickard (1967; 1971) in southeast Alaska and southern Chile. He attributed the number and depth of such features to the relative input of glacial meltwater. Additional research of other glacial fjords in Alaska has shown that these unique subsurface characteristics are actually caused by cooling from both the large ice mass (Matthews and Quinlan, 1975) and upwelling of nearly $0^{o}C$ meltwater from under the base of tidewater glaciers (Walters *et al.*, 1988; Motyka, 2003). For example, Walters *et al.* (1988) found that by early summer (June) upwelling of sub-glacial water in Columbia Bay far exceeds surface runoff. This water mixes in the upper water column and exits across the terminal moraine as a subsurface plume, where it interleaves with marine source water to create distinct subsurface temperature minima and maxima within the seaward basin.

Similar properties can be seen in the T/S diagrams for outer basin of Unakwik Inlet in July and August 1996 (Fig. 2.2e,f) and also in Eaglek in August 1996 and 1997 (Fig. 2.2f,i). At Icy Bay the effects of glacial water appear confined to the upper water column in July 1996 (Fig. 2.2e) but at Whale this creates a distinct subsurface temperature minimum. Although the tidewater glaciers at Icy Bay and Unakwik Inlet are from 15 to 19*km* from their terminal moraines (Table 2.1), cold glacial water is evident in their inner and outer basins, and in March and July 1996 this water creates subsurface temperature minima and maxima at Icy and Whale (Fig. 2.20e-h). Vertical sections at Unakwik and Eaglek indicate that similar temperature anomalies also exist in these fjords in the late winter and summer of 1996 (Fig. 2.21a-d) and in the summer of 1997 (Fig. 2.21e,f). The watershed of Bainbridge (Fig. 2.19d) has virtually no alpine glaciers contributing to runoff, and those at Whale are insignificant. At Eaglek, the hydrography of the inner basin indicates that alpine glaciers (Fig. 2.19) probably provide a large amount of runoff in late summer (Gay and Vaughan, 2001) but in 1997, effects of allocthonous glacial water in the outer basin are relatively high, as shown by large mode 1 amplitudes of *FWCA* in May and August and negative mode 2 amplitudes near the mouth in all months (Figs. 2.9 to 2.11). Like Whale, subsurface water near the mouth is cooler than in the inner fjord (Fig. 2.21d,e,f), and this is also shown by the *PCA*s of temperature (Figs. 2.14 and 2.15).

The allocthonous freshwater in the outer basins of the above fjords most likely comes from adjacent fjords containing tidewater glaciers. Advection from Icy Bay into Whale is not only indicated by the hydrography, but also by the motions of sheet ice and small bergs observed respectively in the late winter and summer. Gay and Vaughan (2001) describe the currents responsible for advection into Whale, and the observations of ice motion within lower Dangerous Pass are consistent with the southerly extent of the effects of glacial water in June and July1994 on *FWC* (Figs. 2.4 and 2.5) and temperatures (Fig. 2.13). In July, there are also marked discontinuities in T/S properties between sub-regions 4 and 5A and those of 5B (Fig. 2.5c,d and e). Southerly flow within KIP has been shown by ADCP data collected in 1989 (Niebauer *et al.*, 1994) and drifter buoy trajectories in both 1976 (Royer *et al.*, 1979) and 1997 (Vaughan *et al.*, 2001). Perhaps this current diverges at Chenega I. (Fig. 1B), thus providing a mechanism for southward advection of glacial water from Sub-Region 4. In northern PWS, the prevailing circulation in the summer is from east to west (Royer *et al.*, 1979; Vaughan *et al.*, 2001). Therefore, subsurface glacial water within Eaglek most likely originates from Unakwik Inlet and possibly also (under certain conditions) from Columbia Bay.

5.4. Estuarine conditions in relation to watershed topography and ratios

The regression analyses demonstrate that many small fjords in PWS have anomalous estuarine conditions with respect to the watershed ratios (WSR) (Figs. 16 and 17). Furthermore, in 1996 the correlations for watershed areas and maximum elevations are quite poor if the extensive watersheds of Icy Bay and Unakwik Inlet are not included. This suggests that a combination of intrinsic and extrinsic factors plays a role in controlling the timing and magnitude of seasonal freshwater flux in these sites. So, the question is what causes the *FWC* in many fjords to deviate so unexpectedly?

The answer lies apparently in factors pertinent to their watersheds as well as the influence of allochthonous sources of freshwater, particularly from sub-regions with tidewater glaciers.

Table 2.1 gives the relative size, elevation ranges and watershed ratios for all the fjords described herein, and Figure 2.19 shows some of the major hydrological features[3]. The watersheds of sites surveyed in 1994 are all generally small (Table 2.1) and only two fjords, Drier and Eshamy, have watersheds exceeding $50 km^2$ in size. Sub-region 2, in particular, has minor watershed areas, yet in May 1994 Culross exhibits large, positive mode 1 amplitudes of *FWCA*s (Fig. 2.7a) following the WSR (Fig. 2.16a). West Twin, by contrast, has only small, negative mode 1 values but as a result of higher than average subsurface *FWCA*s both fjords exhibit moderate to large, negative mode 2 amplitudes (Fig. 2.3h). Given the generally salty subsurface conditions at most fjords in May and the very small watersheds of both fjords (Fig. 2.19), it is doubtful that the relatively fresh subsurface to deepwater at these fjords originates entirely from local runoff. Instead, it is possible that glacial water from the north, such as from

---

[3] Note that larger scale versions of the same maps are given in Appendix 3.3.

Port Wells (Figs. 1.4 and 2.1), enters their outer basins. This type of advection from tidewater glaciers is exemplified by estuarine conditions within Unakwik Inlet in 1996 (Figs. 2.7 and 2.8).

A similar situation occurs on the south side of Perry I. in June 1994. At this time, thermal and haline stratification increase significantly (Fig. 2.2b, 2.4h and 2.13a) but the highest mode 1 *PCA*s occur in the nearshore area, whereas inside South Bay the mode 1 amplitudes are negative. In addition, both the mouth of the bay and the offshore sites all have negative mode 2 amplitudes (Fig. 2.4i). All of the above properties are inconsistent with the watershed hydrology of Perry Island. (Fig. 2.19), and the only other explanation is that they arise from advection, possibly from the glacial sub-regions either to the northeast or northwest (Fig. 1.4).

In sub-region 3, Eshamy had a relatively low *FWC* in May 1994 (Fig. 2.16a) but in June, the estuarine conditions surpass those of Main Bay (Fig. 2.16b). The watersheds are similar in elevations (Table 2.1) and freshwater input in June also tends to follow the respective WSRs. However, the watershed at Eshamy is nearly twice the size of Main (56 vs. 27km^2) and the fjord basin is also 1.7 times larger by comparison. In PWS, the low subarctic solar angle and steep, mountainous topography create large differences in insolation depending on slope aspects, and at Eshamy the slopes are northerly and southerly, whereas at Main they are easterly and westerly (Fig. 2.19). As such, both heat and freshwater flux from snowmelt should be higher at Eshamy, and in June 1994, this was indeed the case as indicated by higher, positive amplitudes of both *FWC* (Fig. 2.4h) and *TA* (Fig. 2.13a). However, the marked lag in freshening at the latter fjord may be an attribute of hydrology. For example, in both systems runoff initially drains into large lakes (Fig. 2.19), but at Eshamy discharge from its lake first enters a long (5*km*), moderately deep (> 60*m*) lagoon. This inner estuary is separated from the main fjord by a narrow entrance with a shallow sill (~ 6*m*), and this constriction may provide a buffer to initial freshwater dispersal into the outer fjord.

The other fjords in sub-region 3, Ewan and Paddy, exhibit relatively brackish surface water in July 1996, as expected from their watershed characteristics (Table 2.1 and Fig. 2.19), but they also have relatively high subsurface *FWCAs* that result in positive mode 1 *PCA*s within both outer basins and in Dangerous Pass (Fig. 2.7b,i). The mode 2 *PCA*s in the outer basins are also negative, similar to Icy and Whale (Fig. 2.7j), but unlike the latter two fjords, the temperatures at Ewan and Paddy exhibit positive mode 1 and 2 *PCA*s (Fig. 2.14a,b). This indicates that the subsurface water in their outer basins does not come from Icy Bay, to the south, but instead must arise from advection of water from farther north. This is consistent with past observations of southerly flow in Knight Island Pass (KIP) from drifter trajectories by Royer *et al.* (1979) and ADCP data by Niebauer *et al.* (1994) and Vaughan *et al.* (2001). It is also inferred by strong positive phasing of maximum surface freshening throughout KIP observed in August 2006 and 2007 by Okkonen and Belanger (2008).

All of the above studies suggest that allochthonous freshwater from northern sub-regions, such as Port Wells and Port Nelly Juan, could potentially reach Ewan and Paddy. However, some of the freshwater in western KIP could also come from Main and Eshamy. In 1994, this is indicated by a local decrease in salinity offshore of these two fjords observed in June (Fig. 2.22) and July (not shown), and again in the summers of 2006 and 2007 (Okkonen and Belanger, 2008). For example, the PCAs of *FWCA* for the stations shown in Figure 2.22 are positive for mode 1 (Fig. 2.23a) in the region of low salinity extending from SEA11 to 23 (S = 26-21) and mostly negative where the surface water is brackish (S > 28). The vertical section of salinity also shows a wave-like structure similar to Herring Bay in May 1994 (Fig. 2.18a) and the amplitudes of mode 1 are reduced wherever the subsurface is salty but mode 2 *PCA*s increase (Fig. 2.23b). However, note that the highest positive amplitudes occur at SEA16, where the water column is most stratified.

Sub-region 4 is an area of PWS markedly influenced by glacial advection from Icy Bay, and in 1994 the *PCA*s of *FWCA* indicate the glacial water extends throughout this area and into sub-region 5A as well. For example, the *FWC* at Whale is very high in all years relative to the watershed ratio (Figs. 2.16 and 2.17) and the mode 1 *PCA*s are large and positive (Figs. 2.4, 2.5 and 2.7 to 2.11). The mode 2 amplitudes are also large and negative, indicating that subsurface freshening is high in all months; the one exception occurs in July and August 1997 when freshwater is concentrated in the nearsurface layer. The watershed at Whale is only moderate in size (Table 2.1) and highly localized (Fig. 2.19) and the cold, fresh upper water column over time is inconsistent with the hydrology. However, the proximity of Whale to Icy Bay explains this anomaly and the circulation (Gay and Vaughan, 2001) shows how these conditions prevail in the main outer basin due to anticyclonic inflows during ebb tides. These inflows cause cool, fresh (low density) subsurface conditions in Whale's outer basin.

In northern PWS many of the fjords surveyed have large watersheds (Table 2.1) that are 2 to 10 times greater in size relative to the watersheds of small fjords surveyed in the western and southwestern Sound (Fig. 2.19). These sites, including Eaglek, Jack, Galena and Simpson, also have alpine glaciers at high elevations (Table 2.1) ranging from 1300 to > 1500*m*. However, the

TS properties of these fjords vary significantly in July 1996 (Fig. 2.2e), and in all subsequent surveys Eaglek and Simpson also differ markedly in hydrography (Fig. 2.2f to i).

Eaglek Bay has a similar WSR to that of Whale (2.3 vs. 2.1), and in consideration of the above characteristics, freshwater input should surpass Whale. However, the effects of runoff at Eaglek vary considerably between years (Gay and Vaughan, 2001), and the only time the *FWC* possibly exceeds Whale is in May 1997 when mode 1 amplitudes are relatively high (Fig. 2.9a). The distribution of alpine runoff at Eaglek is highly skewed to the northwest (glacial) portion of the watershed (Fig. 2.19), and this may explain the large positive mode 1 *PCA*s at mid fjord in June 1996 (Figs. 2.6a) and in May and July 1997 (2.9a, and 2.10g). The positive mode 2 amplitudes in June 1996 (Fig. 2.6b) indicate the subsurface water is relatively salty, but in all months of 1997 the mode 2 values are negative (Figs. 2.9b, 2.10h and 2.11h) indicating that the subsurface *FWCA*s are significantly fresher over much of the fjord. As discussed above, the water in the lower basin is also much cooler than in the upper fjord, and like Whale, these conditions cannot be explained solely by watershed hydrology. Thus, the physical properties in the outer basin appear to also be influenced by glacial water emanating (most likely) from Unakwik Inlet (Gay and Vaughan, 2001).

In northeast PWS (sub-region 7), Jack and Galena have mostly positive mode 1 and 2 *PCA*s in July 1996 (Figs. 2.7i,j). This indicates that freshwater is concentrated mostly in the upper water column and hence these fjords are more stratified in comparison to the other sites. At Jack the haline stratification is substantial by comparison (Figs. 2.2e and 2.7e), but at Galena the 60*m* *FWC* surpasses Jack (Fig. 2.17) due to greater amounts of subsurface freshening. Galena is also significantly warmer by comparison (Figs. 2.2e and 2.14a), but given that the fjords are adjacent to each other and have similar watershed aspects and elevations, there is no obvious reason why the local climates should differ. The variation in estuarine conditions, however, may be linked to intrinsic attributes of the hydrology that affect the timing of runoff.

For example, at Jack runoff occurs directly from alpine glaciers in the watershed (Fig. 2.19), and thus the cool, highly stratified conditions probably reflect the beginning of peak alpine discharge, which in Port Valdez coincides with maximum insolation in July (Carlson *et al.*, 1969). In contrast, Galena's watershed (Fig. 2.19) has one primary ice field and numerous lakes that serve as interior catchments, similar to Eshamy and Main. The watershed discharges mostly into the inner basin and virtually all alpine runoff enters Silver Lake prior to entering the fjord. Thus at Galena, the cooling and freshening effects of alpine discharge may be moderated by its lentic (lake) system of hydrology. However, the outer basin of Galena also shows small, negative or positive mode 2 *PCA*s due to higher subsurface *FWCA*s, properties suggesting it may also be influenced by allochthonous freshwater possibly originating from the Shoup Glacier in Port Valdez or from Columbia Bay.

In eastern PWS, Simpson Bay does not exhibit high *FWCA*s, except in August of 1996 and 1997. Given the relatively large, high elevation watershed of this fjord (Table 2.1) it should exhibit coupling between the local climate and its glacial hydrology (Fig. 2.19). This only occurs in late summer, however, when the hydrography responds dramatically to increased precipitation in both August 1996 and 1997 (Gay and Vaughan, 2001). In 1997, the magnitude of surface freshening in the late summer is excessive (Fig. 2.2i), particularly within the inner (northern) basin (Fig. 2.11c,g). This basin is also affected by submarine groundwater discharge (Swarenski *et al*., 2009), and this possibly contributes to consistent freshening observed in the lower portion of the inner basin (Gay and Vaughan, 2001).

The PC amplitudes of the mode 1 *FWCA*s (Fig. 2.11g) also show high, positive values occurring in the outer basin and mouth (Fig. 2.8c) due to both surface and subsurface freshening. The source of this water is likely the Rude River (Fig. 2.18f), which drains a large glaciated region in the Chugach Mountains (Noll *et al.*, 2008). This glacial water propagates westward as a plume each summer creating fronts (see Chapter III) routinely observed in eastern Orca Bay (Fig. 2.1A). In August 1996 low-density fronts (possibly from this water) were observed in nearsurface (5-10*m*) and subsurface (20-30*m*) layers by a towed, undulating CTD (Gay and Vaughan, 2001).

6. Summary and conclusions

This chapter addresses spatial variation in physical properties of small fjords in Prince William Sound (PWS), Alaska in relation to local climate, watershed topography and broad-scale advection of glacial water. Principal component (*PC*) analysis is used to quantify the variance in freshwater content (*FWC*) and temperature among sites in the spring and summer, and regression analysis is used to compare mean *FWC*s integrated over the upper 60*m* with watershed to fjord basin area ratios (WSR), watershed areas and maximum elevations.

The results show that the principal components explaining > 90% of the variance in *FWC* occur in two statistical modes that respectively indicate total freshwater input from all sources and the vertical distribution from mixing, advection and in certain cases internal waves. As such, fjords with large, positive mode 1 and 2 *PC* amplitudes (*PCA*s) tend to be well stratified from high amounts of surface freshening, whereas fjords with large, positive mode 1 and negative mode 2 *PCA*s are less stratified due to relatively high subsurface *FWC*. In contrast, fjords with large, negative mode 1 *PCA*s typically exhibit saltier, oceanic conditions.

The vertical structure of the temperature anomalies (*TA*) is more complex relative to *FWC* due to differences in solar heating (i.e. local climate) and the cooling effects of alpine runoff and cold subsurface glacial water, and at least three EOF modes are required to explain 90% of the variance. The cold glacial freshwater creates both surface temperature inversions and sub-surface minima and maxima, and sub-regions influenced by this type of advection typically exhibit large positive mode 1 amplitudes of *FWC* and negative mode 1 *TA* amplitudes.

The regression analyses indicate there is a poor relationship of *FWC* to either watershed ratios or topography unless outliers due to either intrinsic factors of the watersheds or the effects of glacial advection are removed. The latter process results in reversed estuarine conditions in the outer basins of certain sites, indicated by moderately negative mode 2 *PC* amplitudes. In the summer of 1994 this type of advection influenced hydrographic conditions in southwestern PWS possibly as far south as N. Elrington Pass and Sawmill Bay. In 1996 and 1997, fjords influenced by glacial advection again exhibit high *FWC* values due to subsurface freshening, and in 1996 high subsurface *FWC* in Dangerous Pass and the outer basins of Ewan and Paddy Bay indicate that advection of subsurface freshwater potentially also occurs from glacial regions to the north.

In conclusion, small fjords located within the same geographical sub-regions have similar patterns of heat and freshwater input due to shared climatic and watershed characteristics. The *FWC* among individual basins is influenced by local topographic factors such as watershed aspects, hydrology and the WSR. However, the broad-scale relationship between estuarine conditions and watersheds appears random due to varied intrinsic factors of watersheds and effects of glacial water advected through PWS. In many cases, advection of allochthonous glacial water supersedes runoff from local watersheds, and in at least one case (Whale) this advection creates extreme fresh conditions relative to the WSR in all years of this study.

CHAPTER III

CIRCULATION AND WATER EXCHANGE WITHIN SIMPSON BAY, A SMALL SUBARCTIC FJORD IN PRINCE WILLIAM SOUND, ALASKA: HYDROGRAPHY, CIRCULATION,WATER EXCHANGE AND INTERNAL TIDES

This chapter addresses currents and hydrography measured in the summers of 2007 and 2008 over diurnal (26*h*) and semidiurnal (13*h*) tidal periods respectively and temperature and salinity time-series collected in 2007 within Simpson Bay, located in eastern Prince William Sound (PWS) Alaska. Ancillary data include air temperatures, winds and precipitation collected in 2007 and 2008 and tides in August 2005. The two summers vary significantly ($p < 0.001$) in both air temperatures and precipitation, with 2007 being relatively warm and dry (13.4°*C* and 3*cm*)[1] and 2008 being cool and wet (11°*C* and 17.2*cm*). Strong up-fjord winds ($4\text{-}7 m\ s^{-1}$) occur diurnally, and in 2007 these winds are higher in both magnitude and frequency in comparison to 2008. The hydrography follows similar patterns as the climate, and in 2008 the pycnocline is ~10*m* deeper relative to 2007. Although the vertical density structure differs between years, the patterns in circulation were consistent between cruises, thus allowing data in 2007 to be a representative for calculations of seasonal transport and diffusivity, and analyses of internal waves.

The current data reveal a complex flow structure forced mainly by tides interacting with bathymetry, moderated by stratification, tidal volume flux, internal waves and winds. The principal mechanisms initiating circulation are inflowing (outflowing) baroclinic tidal jets ($0.3\text{-}0.4 m\ s^{-1}$) that accelerate during the flood (ebb) tide across two sills (30 to <60*m* and <10 to 30*m*) located respectively at the mouths of the main and northern basins. The circulation near the mouth of the main basin occurs in multiple layers that frequently reverse in direction, whereas in the northern basin the circulation is more fjord-like, with maximum inflows (outflows) occurring in the near-surface layer, and one to two flow reversals deeper in the water column. Transport calculations indicate that baroclinic currents during flood tides advect PWS water inward at a rate in excess of the tide volume flux that is not balanced by reciprocal baroclinic exchange during ebb tides. The result is a net inflow into the main fjord at rates ranging from 194 to 1363 $m^3\ s^{-1}$, with respective flushing periods of 16.4 to 2.3 days.

---

[1] Air temperatures are means for June, July and August, and precipitation is a total for July and August.

Internal waves in phase with semidiurnal tides are evident from vertical oscillations of both pycnocline depths measured from CTD data and temperatures measured by thermistors moored at various depths in 2007. Changes in the vertical structure of the currents during the tide cycles are possibly linked to these waves progressing through the lower basin, so that during the flood (ebb) stages the maximum currents begin in the upper layer then gradually deepen during the course of the tide cycle to become subsurface inflows (outflows). Calculations of vertical diffusivity κ_v and the efficiency of work performed against buoyancy by mixing from internal waves (W) are compared to available tidal energy (E_2) by flux Richardson numbers ($R_f = W/E_2$). In all cases, the results indicate that deep diffusivity exceeds available tidal energy on O(10 to 100), and density changes below sill depth are, therefore, the result of additional processes such as tidal and wind driven advection. Also, deep freshening in the northern arm over time cannot be alone due to vertical mixing of the lower halocline by internal waves and must come from some additional source, possibly such as submarine ground water discharge.

1. Introduction

Following the Exxon Valdez Oil Spill (EVOS) in March of 1989, oceanographic studies of Prince William Sound, Alaska began in 1994 under Sound Ecosystem Assessment (SEA) (Cooney *et al.*, 2001). The objectives of the SEA program were to ascertain the importance of various ecological factors affecting growth and survival of two commercially valuable fish species damaged by the spill; pink salmon (*Oncorhynchus gorbuscha*) (Willette *et al.*, 2001) and Pacific herring (*Clupea pallasi*) (Norcross *et al.*, 2001). During SEA, four small (nursery) fjords were selected for intensive oceanographic study from fall 1995 to late winter 1998 (Gay and Vaughan, 2001). The primary objective of the fjord surveys was to quantify the seasonal changes in water temperature, salinity and density over a period of several years (Gay and Vaughan, 2001). These features of hydrography potentially impact the survival of juvenile herring in two ways: first, annual stratification from heat and freshwater input influences the local production and availability of plankton food sources (Foy and Norcross, 1999b), and second, water temperature directly affects larval growth rates in the summer and metabolism and feeding behavior of juveniles during the winter (Foy and Norcross 1999a; Foy and Paul, 1999). A secondary objective was to measure currents to identify regions of convergence, divergence, shear and ephemeral fronts associated with the tides. Larval herring and zooplankton are advected to various nursery sites by the general circulation within the Sound (Wang *et al.*, 2001;

Norcross *et al.*, 2001), but the role of the currents in either their advection or retention within nurseries had not been quantified.

After a hiatus of nearly nine years, hydrographic (CTD) surveys of the four SEA fjords resumed in 2007 and 2008. At Simpson this research also involved a comprehensive program to quantify physical processes affecting circulation and water exchange in the summer, including measurements of currents and hydrography over full tidal cycles, temperature and salinity (T/S) time-series from moored instruments in 2007, and ancillary weather data collected at the mouth in both years. In 2008 a similar comprehensive study was conducted at Whale Bay (Fig. 3.1a).

This chapter addresses the dynamics of hydrography and circulation at Simpson in 2007, and focuses on the following features: 1) the patterns in circulation during sequential tidal cycles and the effects of horizontal shear in creating marked cross-channel variation in the flows; 2) the role of baroclinic currents associated with stratification and bathymetry on water exchange and flushing rates within the outer (main) basin; and 3) evidence of internal tides and their affects on vertical diffusivity.

2. Study area

Prince William Sound (PWS), located along the Northern Gulf of Alaska (NGOA) coast (Fig. 3.1a), is comprised of a complex of small to large fjords scattered along the mainland and on large islands of varying size. However, the Sound also has deep primary basins that exhibit estuarine conditions from high annual freshwater input and fjord-like properties due their restriction from the NGOA shelf by sills at Hinchinbrook Entrance (HE) and Montague Strait (MS) (Fig. 3.1a). In addition, PWS also has a broad, deep (400*m*) central basin with horizontal circulation similar to a small marginal sea (Niebauer *et al.*, 1994; Vaughan *et al.*, 2001).

The regional climate is mostly influenced by the strength and positions of the Aleutian Low and the Siberian High (Wilson and Overland, 1986, Stabeno *et al.*, 2004); the former generating strong cyclonic (westward) winds over the NGOA from fall to spring. In the summer the westward winds relax or at times reverse, leading to a general paradigm of westward (eastward) winds driving coastal convergence (divergence) reflected in upwelling indices (Bakun, 1973; Royer, 2005). Within PWS the local wind fields are complicated by coastal orography and the passage of storm systems, however. For example, Olsson *et al.* (2003) describe local katabatic winds in the winter at Wells Passage that frequently accelerate into eastward low-level jets reaching speeds of 25 m s^{-1}. Other orographic effects on winds within PWS include gap-winds and ‘wiliwaws’ generated during storms, and summer seabreezes.

Simpson Bay is a small fjord situated in the eastern Sound, close to Cordova (Fig. 3.1a), and is classified oceanographically as a partially mixed fjord estuary (Gay and Vaughan, 2001) and geologically as a macrotidal ($Dh > 5m$) turbid outwash fjord (Noll *et al.*, 2008). Simpson’s morphometry is comprised of a main (western) basin and two inner basins (arms) located in the north and southeast respectively (Fig. 3.1b). The western basin is relatively shallow with depths ranging from 25 to 55*m*, but on the eastern side of the mouth a 100+*m* channel extends into the southeastern arm and depths in the southern portion of the northern (inner) basin reach nearly 80*m* (Fig. 3.1b). The bathymetry of the western basin is highly irregular due to the presence of topographic obstructions (Noll *et al.*, 2008), such as an outer sill (ranging from 30 to 60*m* in depth), interior ridges and a shallow reef (< 10*m*); the latter forming a boundary between the northern arm and main basin. Consequently, over the summer the main basin tends to exhibit vertical T/S gradients to depth, whereas the northern arm tends to remain highly stratified (Gay and Vaughan, 2001). Turbulent mixing (primarily from bottom friction) possibly affects the deep portion of the water column, but mixing within the upper pycnocline is inhibited by stratification.

The watershed at Simpson is relatively large (170 km^2) and contains numerous alpine glaciers at moderately high in elevations (1200-1500*m*) (Fig. 3.2). The watershed to fjord surface area ratio is about 6:1 for the entire fjord (Gay and Vaughan, 2001), but the ratio for the northern arm is closer to 13:1 (Noll *et al.*, 2008). Since runoff primarily enters the northern arm (Fig. 3.2) this leads to relatively high concentrations of surface freshwater within the latter basin, particularly in late summer to early fall when precipitation begins to increase (Gay and Vaughan, 2001; see also Chapter 2). Other sources of freshwater that potentially affect Simpson’s inner basin come from submarine ground-water discharge (Swarzenski, *et al*., 2009) that emerges from benthic areas near small streams in the northern arm, particularly at high tides.

In contrast to the northern (inner) basin, the main basin of Simpson is periodically influenced by glacial water advected westward from the Rude River (Fig. 3.2a). Fronts from this plume (Fig. 3.3) are frequently observed at Salmo Point and Channel Island (Gay, 2008) and its presence in the lower main basin of Simpson was observed occasionally during cruises in 2007. In August 1996, relatively low water densities at 5 to 10*m* and 20 to 30*m* over the sill and the western side of the mouth respectively were most likely due to the presence of Rude River water

(Gay and Vaughan, 2001). This water may also be responsible for relatively high freshwater contents (*FWC*) in the upper 60*m* within the lower main basin in both July 1996 and August 1997 (see Chapter II). Similar hydrographic conditions occur at mouth of Simpson in August 2011, following a marked seaward advection of Rude River water into Orca Bay (Gay, 2011b).

The local climate at Simpson Bay is similar to Cordova, Alaska, which is situated about 12*km* to the southeast in Orca Inlet (Fig. 3.1). However, precipitation is much higher in the town due to the orography of the Heney Mountains. Winds, air temperatures and rainfall measured at Simpson over the summers of 2007 and 2008 are described below in the results.

3. Datasets and methods

3.1. Currents and hydrography

The data on currents and hydrography were obtained in 2007 and 2008 by methods similar to those described in Gay and Vaughan (2001). In contrast to the earlier years, however, the new surveys used an RDI Direct Reading 600 kHz acoustic Doppler current profiler (ADCP) mounted on a Biosonics tow sled (Fig. 3.4). The ADCP was towed at a depth of ~ 0.5*m* at speeds of 2 to 2.5 $m\ s^{-1}$. Bottom tracking was generally attainable over the entire fjord and temporal averaging of 20 water pings per ensemble resulted in segments of absolute velocities every 16 to 20*m* with standard deviations < 1$cm\ s^{-1}$. Data were averaged vertically into 1*m* bins with valid data ranging from 2 to ~ 50*m* in depth. In 2007 the ADCP was operated continuously over 26 hr (diurnal) tidal periods resulting in 11 to 12 ADCP transect sets per survey (Table 3.1).

Hydrography profiles were collected using an SBE19-*plus* conductivity, temperature and depth (CTD) profiler (Fig. 2.4) with a combination fluorometer/turbidimeter (WetLabs ECOfluorometer). The layout of the ADCP transects and oceanographic stations occupied during the surveys is shown in Figure 3.4. The CTD data were collected on every other set of transects resulting in 4 to 6 sets of casts per cruise (Table 3.1). In 2008, the oceanographic cruises were conducted using similar methods as in 2007, the exception being that transects were surveyed over 13*hr* (~ semidiurnal) tidal periods. This effectively reduced of the number of repeated ADCP transects and CTD casts per cruise to half the number in 2007.

3.2. CTD moorings and weather stations

In 2007, two sets of moored instruments (Fig. 3.5a,b) were deployed respectively at 80*m* in the deep portion of the northern arm and at 50*m* on the western side of the main lower basin. The basic design (Fig. 3.5f-i) consisted of a surface spar buoy housing a near-surface (2-3*m*) CT, comprised of either a SB16.03 Seacat or a SB37 Microcat, and two subsurface floats located respectively at 10*m* and 40-70*m* above the bottom. The deep buoys had either a CT or CTD hung just below them, and thermistors were set between the two subsurface buoys approximately every 10*m*. Calibrations of the CTs were performed by SBE Inc. prior to and after the deployments to determine offset and drift in the sensors. To maintain the weather station anemometer (Fig. 3.5a) at a low angle under strong wind and current conditions the spar buoy at the mouth was designed with a tether (Fig. 3.5g). The tether was clamped onto the spar at the approximate center of pressure given a 1.0$m\ s^{-1}$ current and a 10$m\ s^{-1}$ wind.

Weather data were collected synoptically with the CTD moorings from June through August 2007 at two stations located respectively on the mooring buoy (Fig. 3.5a,g) and an island located on eastern side of the mouth (Fig. 3.5c,e). The console and battery for operating each station were set up inside waterproof cases either attached to the mast of the buoy (Fig. 3.5g,i) or set under the station tripod. In 2008, the shore-based weather station was set up at the same site as in 2007. In both years the sensors on the stations consisted of Davis Instruments (DI) anemometers and thermistors, and a DI rain gauge placed at the shore station. The anemometers have no internal compasses, so the shore station was set up primarily to obtain true directions for the winds. This was done using a standard procedure for DI gauges of aligning the instrument (by compass) until the direction of the anemometer vane and the readings match.

3.3. Tide gauges in 2005

Sea surface elevations were measured in August 2005 over a period of nearly ten days at two stations located in the northern arm and main basin (Fig. 3.1b). The data were collected using Seabird SBE26 Tide and Wave gauges, set to measure water levels every 5*min*, with continuous integration of the pressure to average out waves. Waves were also measured by burst sampling to obtain 1024 samples per measurement at 0.25*sec* intervals, giving a minimum (Nyquist) period ($2\Delta t$) of 0.5*sec* at amplitudes of 1-2*cm*. Only tide data are reported here, however.

The raw data were adjusted for barometric pressure using data collected at a NOAA NOS station #945050 (http://tidesandcurrents.noaa.gov) located at Cordova, Alaska. These data were then corrected for differences in deployment depth and synchronized (by interpolation) for comparison with 6*min* tide data from the Cordova NOS station. Harmonic analysis using the first four semidiurnal (M_2, S_2, N_2, K_2) and three diurnal constituents (K_1, O_1, P_1) was performed on the Simpson tide data to determine their relative contribution to the tidal potential by comparing the fitted and measured tides. The least squares coefficients were derived by the MATLAB function, cyc_opt[1], which uses the method of cyclic descent (Bloomfield, 1976). The two sets of adjusted and corrected tidal elevations were then compared to determine if any significant anomaly occurs between the heights within inner and outer basins.

3.4. Data processing and analysis

The hydrography (CTD) data were post-processed using standard SBE algorithms to convert, filter, align and average the data into 1*m* bins. These data were used to derive additional parameters for subsequent calculations, such as depth, density, and buoyancy frequencies (N^2).

The ADCP data were post-processed by first horizontally averaging every two consecutive profiles into segments and then removing depth bins according to the following thresholds: 1) percentage of valid water echoes < 80%, 2) error velocities > 5 $cm\ s^{-1}$ and 3) vertical velocities > 10 $cm\ s^{-1}$. In certain cases, the deletion criteria were relaxed in order to compare segments in question with adjacent profiles to determine if data were actually good. In general profiles with > 20% of bins missing were removed entirely, however, and gaps in the remaining segments were filled in with linear interpolation. Additional screening included flagging bins in which the absolute value of the difference in either the u or v components between successive depth bins exceeded 20$cm\ s^{-1}$. In such cases the bins were only deleted after segments were examined from plots of vertical sections containing the questionable data. Bins exhibiting unusually high accelerations typically occur at the very bottom of profiles, and these were always removed.

3.4.1. Volume transport calculations

The velocities for two consecutive ADCP transects located respectively along the outer sill and immediately to the north in Sections B and C (see Fig. 3.10A) were used to calculate volume

---

[1] MATLAB function written by S. DiMarco, Texas A&M Oceanography September, 2002

transports. The procedure was done by first rotating *u* and *v* axes 35° clockwise into cross and along channel components (*u', v'*), and then numerically integrating the *v'* velocities over each section to derive a net total volume transport:

$$Q_{xz} = \iint_{xz} v'dxdz = \sum_{i=1}^{N}\sum_{j=1}^{M} v'_{ij}\Delta x\Delta z \;\; (m^3\, s^{-1}). \tag{3.1}$$

To calculate transports within the bottom layer (between the base of profiles and the fjord bottom) the velocities are estimated using a standard logarithmic profile (Dyer, 1997):

$$U(z) = \frac{u_*}{\kappa}\ln\left(\frac{z}{z_0}\right) \tag{3.2}$$

where k is the von Karman constant (= 0.4), z_0 the bottom roughness length, and u_* the friction velocity $= \left(\tau_0/\rho\right)^{1/2}$. Because τ_0 is equal to the bottom stress ($\rho C_d u^2$), u_* can be estimated for the upper boundary layer using the drag coefficient (C_d) and flow magnitude at the bottom of profiles (*U*) as $\sqrt{C_d}U$. The nominal values for C_d and z_0 used in this study were 0.006 and .03*m* respectively, and were based on ranges derived empirically from bottom current measurements over the Oregon continental shelf by Chriss and Caldwell (1982). The latter study shows that for depths well above a viscous sublayer (>0.02*m*), z_0 is a large-scale parameter influenced by both small-scale topography and skin friction. If form drag is not significant then the mean flow in the upper boundary layer is expected to follow the logarithmic law (eq. 3.2) and z_0 will be mainly a function of bed stress.

The bottom regions over Sections B and C at Simpson are relatively flat and comprised of relict glacial deposits of coarse, gravelly sand and mud (Noll *et al.*, 2008). In contrast, the seabed over the region studied by Chriss and Caldwell (1982) is comprised of silty sands. So, to account for the higher bed friction at Simpson, values of z_0 more than double the maximum found in the latter study (0.015*m*) were used to derive the bottom velocity profiles. The value for C_d given above (0.006) is the mean at 1.0*m* derived by Chriss and Caldwell (1982). However, using values ranging from 0.003 to 0.01 for the drag coefficient and 0.03 to 0.06*m* for the roughness length had little effects on the velocity profiles. Examples of profiles derived by the above method are shown below (see Figure 3.13).

3.4.2. Net baroclinic and barotropic transports

In most cases, the currents during this study were strongly baroclinic, and determining their contribution to the net volume transport required calculating and removing the tidal volume flux (i.e. barotropic transport). This was done by first determining the changes in water column height during a given transect period according to two methods: 1) using an equation for a progressive shallow water wave, and 2) interpolating data from a NOAA tide station located in Cordova. The first method makes use of the following equation:

$$h(t) = H_0 + \left[H_a - \left(H_a \cos(\phi)\right)\right], \tag{3.3}$$

where H_0 is the initial tidal elevation (relative to mean sea level), H_a is the tidal amplitude (= one half the total tide height) and ϕ is the *phase*, which is based on the relative portion of tidal period (T) in *sec* covered by a transect. Phase is given as $\phi = \left(t_i/T\right)2\pi$, where t_i is the elapsed time of the start (or end) of a transect relative to the tidal period, taken as peak to peak for ebb tides and trough to trough for floods. Once the phase has been assigned for the start and end times of transects, t_1 and t_2, the heights at each time are found using eq. 3.3. The tidal volume flux (Q_T) for a given transect is then determined by multiplying the change in height, $\Delta h_t = \left|h_{t2} - h_{t1}\right|$ by the appropriate basin surface area (SA) (Table 3.1) and dividing by the transect period, $Tr = t_2 - t_1$:

$$Q_T = (\Delta h_t)(SA)/Tr. \tag{3.4}$$

The baroclinic transport is then simply the net transport less the tidal volume flux:

$$Q_{bc} = Q_{yz} - Q_T \tag{3.5}$$

3.4.3. Vertical diffusivity and tidal energy available to internal waves and surface jets

Stigebrandt and Aure (1989), from hereon referred to as SA, present a method for calculating vertical diffusivity (k_v) within the deep basin water of silled fjords due to dissipation of internal waves. The calculations require repeated observations of density, and knowledge of sea surface elevations and fjord surface areas over depth. The method is applied here to density data collected in June, July and August 2007, and tidal elevations and hypsographic data were taken respectively from the CMAN station in Cordova, and from bottom profiles estimated using a NOAA nautical chart with a scale of 1:80,000 *in*. The empirical equation for deriving κ_z is based on a budget method described in detail by Gargett (1984), and given by SA (3) as

$$\kappa_{z=u} = 1/\left(A\delta\rho/\delta z\right)_{z=u} \int_b^u \delta\rho/\delta t A dz\,, \tag{3.6}$$

where $A = A(z)$ is the basin surface area inside the sill over depth, b is the deepest region where no diffusive flow of mass occurs and u is the upper integration level. The gradients $\delta\rho/\delta \mathrm{t}\,,\delta\rho/\delta \mathrm{z}$ are horizontal averages found from measurements of salinity and temperature profiles repeated at various stations over time. The vertical profiles of κ_z obtained by eq. 3.6 are then used to determine the total work performed by turbulent wave dissipation against the buoyancy forces due to stratification ($W = wV_b$), where V_b is the volume of the basin below sill depth and w is the mean work defined by SA (4) as

$$w = (1/V_b)\int_b^i \rho\kappa_z N^2 A dz\,. \tag{3.7}$$

According to Stigebrandt (1976), the main source of energy transferred to internal waves in fjords comes from the barotropic tide losing some energy due to the non-viscous form drag created by sills. Progressive internal tides occur on both sides of the sill and their dissipation inside the fjord is thought to occur by wave breaking against the sloping fjord bottom and by turbulence generated over the sill region (Stigebrandt, 1999). The mean energy flux from the tide in a two-layer system is defined by SA (15) (cf Stigebrandt, 1976) as

$$E_2 = 0.5\rho\omega^2 a_0^2 A_f^2 H_2 c_i / A_s(H_1 + H_2) \tag{3.8}$$

where a_0 and ω are the tidal amplitude and frequency, A_f and A_s are the surface area of the fjord and cross-sectional (vertical) area over the sill, H_1 and H_2 are the depths of the upper and lower layers respectively and c_i is the baroclinic mode wave speed $c_i = \left(g' H_1 H_2/(H_1 + H_2)\right)^{1/2}$. The total work and mean energy flux from eqs. 3.7 and 3.8 can be used to estimate the efficiency of the work performed against the buoyancy forces by a flux Richardson number (R_f), defined by SA (21) as the ratio W/E_2. In addition to internal waves, tidal flows across sills may also generate jets, with a mean kinetic energy (E_j) approximated by SA (19) as

$$E_j \approx \left\{0.42(1/4)\rho\omega^3 a_0{}^3 A_f{}^3\right\}/A_s{}^2\,. \tag{3.9}$$

The constant ¼ arises due to jets flowing into the fjord only half the tidal period $(1/2)^2$ and 0.42 is the approximate time average of $\left|\cos(\omega t)^3\right|$. Whether a fjord is strictly a jet or a wave basin depends on the densimetric Froude number (F_d) = $\alpha H_2/H_1 c_i$, where α is the amplitude of the tidal currents over the sill (Us_0) = $(A_f/A_s)a_0\omega$. Wave basins occur when $F_d << 1.0$ and jet basins occur when $F_d > 1.0$, indicating subcritical and supercritical flow, respectively.

4. Results

4.1 Weather conditions and hydrography in 2007 and 2008

In order to facilitate discussion of the ADCP results, observations of the meteorology and hydrography in the summers of 2007 and 2008 are presented first. The weather records at Simpson (Fig. 3.6) indicate that climatic conditions are much warmer and drier in 2007 in comparison to 2008. For example mean summer air temperatures for the two years (13.4 and 11.1^{o}C) differ significantly ($p < 0$) and the total precipitation in July and August is 2.7*cm* in 2007 versus 17*cm* in 2008. The same trends in air temperatures can be seen in the noon observations at Cordova, which exhibit less variation in 2008. The precipitation at Cordova is also much higher by comparison in both years, and at certain times in 2008 rainfall exceeds Simpson by a factor of 3 to 6. A long-term climatology for Simpson Bay is lacking, but records at Main Bay (Gay, 2013) show similar trends in air temperatures in 2007 and 2008, with a difference in means in July of -2 and -2.6^{o}C at Main and Simpson respectively. Over the past two decades, records at Main Bay also indicate that mean air temperatures in July 2007 fell close to the climatological mean (~13^{o}C), whereas in 2008 they are well below average (~11^{o}C).

The difference in climate between years is also reflected in the relative thermal and haline stratification. For example, in early June the water column at Simpson is slightly cooler in 2007 relative to 2008, but by mid July solar heating in 2007 advances well beyond that in August of the later year (Fig. 3.7a to f). Also, in 2007 freshwater appears to be concentrated more in surface lenses in the northern arm, whereas in 2008 it is much more dispersed both horizontally and vertically. This produces a noticeably deeper vertical salinity gradient in 2008, and hence a deeper pycnocline. With respect to long-term hydrographic records, the relatively deeper heating and freshening in 2008 is similar to the hydrography in 1997 (Gay and Vaughan, 2001), with the exception that near-surface temperatures are much cooler by comparison in 2008 (10 vs. 12+^{o}C) following the trend in climate.

Winds in the summer at Simpson (Figs. 3.8 and 3.9) vary highly in magnitude, but also exhibit regular periods of relatively high speeds peaking at 5 to 7$m\ s^{-1}$. A low variability of these winds is indicated by the close fit between the 10hr low pass filter line and the hourly data. Figure 9 also shows that the wind directions are principally either up or down-fjord, varying between diurnal periods of inflow during the day followed by lower magnitude outflow at night. The strongest northerly winds occur during periods of high solar heating under clear skies, indicated in 2007 by frequent periods when air temperatures peak rapidly to maximum values exceeding

18 to 20+^{o}C (Fig. 3.6). They also tend to occur over 2 to 4 day periods, coinciding with stable high pressure over the region. In 2007, the northerly wind events are more frequent and higher in magnitude (Fig. 3.9c), and the mean velocity ($2m\ s^{-1}$) differs significantly ($p < 0.007$) from 2008 ($1.7m\ s^{-1}$). Winds from other directions are variable and relatively weak. However, prolonged periods of moderate southerly (down-fjord) winds (Fig. 3.9a,b) are often accompanied by precipitation (Fig. 3.6).

4.2. Horizontal and vertical structure of baroclinic currents

To illustrate the spatial variation in the flow field over the tide cycles, horizontal vectors from ADCP data for the 2*m* layer are described here along with selected vertical sections of the along-channel flows (*v'*) for two consecutive semidiurnal tides in July 2007 (Table 3.1). The location of transects in relation to the fjord's bathymetry and the winds and tides occurring during the July cruise are shown in Figures 3.10A and B respectively.

The near-surface currents at Simpson (Fig. 3.11) exhibit considerable spatial complexity over consecutive tide phases. In general, the horizontal flow fields appear to be forced mainly by the interaction of stratified tidal currents with the bathymetry, caused by accelerations in flows across the two sills. For example, during the early portion of flood tide 1 (Fig. 3.11a) an inflow jet ($0.25\text{-}0.30m\ s^{-1}$) forms over the outer sill located at the mouth and continues northward into the fjord mainly as a sub-surface current (Fig. 3.11b,c). This surface pattern is repeated on flood tide 2 but during flood tide 3 the inflow jet is much stronger over the entire main basin (Fig. 3.11h,i and n). During the same tide stages a southward flow reversal also occurs along the eastern shoreline of the main basin in conjunction with outflow from the southeast arm (Fig. 3.11a-e,h-k). Vertically, the currents are also highly variable within the main basin (Figs. 12 and 13). For example, during the early portion of flood tide (Fig. 3.12A) both the inflowing baroclinic jet and the outflow reversals are clearly visible in Sections A to D. These currents are also associated with an anticyclonic eddy that forms at the mouth (Gay and Vaughan, 2001).

As the flood tides progress the nearsurface expression of the inflows (Fig. 3.11d,e,j,k) either weakens or reverses in direction, particularly at the mouth. The baroclinic inflows continue as deep subsurface currents, however, and the velocities in Section B across the sill (Fig. 3.13A) approach $0.35m\ s^{-1}$. In Section C, the velocities also exhibit a change from near-surface inflows early in the flood tides to deeper subsurface currents as the tides progress. However, later in the flood tides the deepest inflows are limited entirely to the eastern side. They are also much weaker in comparison to flows at Section B (Fig. 3.13A). Note also that the flows on the western side of Section C reverse direction, but at nearly the same time the flows across the sill in Section B are entirely inward and quite strong. These opposing flows must produce a deep region of convergence in the lower fjord late in the flood tide stages.

At the onset of ebb tide 1 (Fig. 3.11e) weak near-surface currents initially flow from the northern arm, but as the tide progresses, the outflow accelerates over the west side of the reef southward into the upper main basin (Fig. 3.11f). A similar pattern occurs during ebb tide 2 (Fig. 3.11k,l), but the outflows are stronger by comparison and penetrate farther into the lower fjord. As there is little wind during the latter transect (Fig. 3.10B,c), this flow pattern must mainly be a result of the relatively large tidal prism (Fig. 3.10B,d). Figure 3.12B shows the vertical structure of the currents in the main basin for the same period as Figure 3.11f. In Sections E and F the outflow is initially concentrated within the upper 10*m* on the western side of the upper main basin, but in response to this current inflows occur on the far eastern side in the near-surface layer and across the much of the deep channel. Down-fjord in Sections C and D, the near-surface currents decelerate and the outflows become concentrated in a subsurface layer, with deeper inflow reversals beneath. In contrast, currents near the mouth in Sections A and B exhibit inflows over much of the upper layer, which converge with subsurface outflow over the sill in Section B. This convergence forces the outflows over the sill to form a deep baroclinic jet that exits across the western side at speeds of nearly -0.35$m\ s^{-1}$ (Fig. 3.12B and 13B).

Another major feature of the ebb tides is a cyclonic eddy that forms from outflows around the reef region in the upper main basin (Fig. 3.11g,m). This eddy is a consistent feature during later portions of the ebb tides, and its surface expression is affected by tidal elevations relative to the depth of the reef, which is exposed at mid basin (Fig. 3.10A) whenever ebb tides exceed mean sea level. The eddy remains intact into the tide change (Fig. 3.11h,n) and the flow cycle is then completed by entrance of the next flood tide jet.

4.3. Winds in relation to near-surface currents in July 2007

Wind speeds, vectors and tidal elevations during the July 2007 cruise are shown in Figure 10B. At the start of the cruise the winds are consistently up-fjord at speeds of 5 to 6 $m\ s^{-1}$. These northerly (diurnal) winds continue throughout flood tide 1 and into ebb tide 2, and although the near-surface (2*m*) currents are initially influenced by the winds, the effects are short-lived. For example, relatively strong inflows at the mouth (Fig. 3.11a) are initially aligned with the channel and then diverge (relative to the subsurface jet) within the upper main basin, and flow to the north and northwest. This may be a response to cyclonic turning of the winds; a tendency due to positive local vorticity (K. Bowman, pers. comm.) induced by the mountainous topography bordering the western periphery of the fjord (Fig. 3.1). However, as the flood tide progresses the effects of the winds at 2*m* become negligible (Figs. 11d,e). Indeed, although there are still strong inflowing currents over the reef into the northern arm later in the tide (Fig. 3.11d), the current speeds in the lower main basin remain quite weak and the near-surface flows at the mouth exhibit reversals on both sides. At the mouth the outflows occur to depths of 10 to15*m* on both sides of the sill in Section B and also on the eastern side of Section C (Fig. 3.13A).

At the turn of the tide (1600*hr*) the up-fjord winds remain strong (Fig. 3.10B,c) but by 1800*hr* they begin to relax. At this time the currents within the fjord shift to a marked upper-layer outflow from the northern arm due to the obstruction of the reef (Figs. 11f and 12B); a pattern typical of most ebb tides observed during the study. In the present case, however, these currents may also be enhanced by an increase in sea-surface elevation in the upper fjord due to earlier surface transport by the winds and (as shown below) possibly by tidal amplification in the northern basin during flood tides. This sea surface slope (albeit quite small, +1*cm*) may assist in generating strong tidal flows out of the northern arm.

As ebb tide 1 progresses, the wind speeds remain weak (Fig. 3.10B,c) until the passage of a front between 2130 and 2300*hr*. This brings a brief period east winds that blow down-fjord at speeds of 2 to 3$m\ s^{-1}$, with gusts reaching 7 to 8$m\ s^{-1}$ (Fig. 3.10B,b). These winds coincide with the inflowing tidal jet in the lower fjord at the start of flood tide 2 and the down-fjord winds possibly contribute to surface convergence at mid-basin (Fig. 3.11f). However, with the exception of a brief period of up-fjord winds from 0200 to 0400*hr*, winds during the remainder of the cruise are weak ($\leq 1m\ s^{-1}$) and any effects on the near-surface currents are negligible.

4.4 Sea surface elevations in 2005

Figure 3.14 shows sea surface elevations measured at two stations in Simpson Bay and a NOAA CMAN station #9454050 in Cordova, Alaska (http://tidesandcurrents.noaa.gov) from August 10th to the 24th, 2005. Elevations for the two series at Simpson represent both the height changes due to the tides and water depth at the times of deployment, whereas the data at Cordova are relative to mean low sea level. All three series bear a remarkable similarity, and a close correspondence of the two stations in Simpson (Fig. 3.14b) suggests that the tides are principally standing waves throughout the fjord. Also, the synchronization of the tides with the Cordova station means that the latter can be used as a predictor of sea surface elevations in the fjord.

Harmonic analysis (not shown) indicates that all four semidiurnal constituents (M_2, S_2, N_2, K_2) and at least the first three diurnal constituents (K_1, O_1, P_1) are required to nearly replicate either tide series. To accurately replicate the tides at Cordova, however, the NOAA analysis lists a total of 34 constituents (Appendix 3.10), only one of which, the SA (solar annual) constituent, has a major contribution in addition to the seven primary constituents listed above.

Figure 14b also shows the tide height variation between the two stations in Simpson. This plot suggests that regular cyclical fluctuations in sea surface heights occur between the two basins. When the mean is removed and the data are low-pass filtered to remove instrument noise [2], the anomaly is only ~ ± 1 *cm* and tends to be positive in the northern arm during flood tides and vice versa during the ebb tides. Although quite small this anomaly is within the accuracy of the tide gauge (0.3*mm*) and it may reflect a slight amplification of the tide wave within the northern (inner) basin. The natural period of oscillation for Simpson, estimated using Merian's formula (Pond and Pickard, 1983) in the form of a quarter wave oscillator: $T = 4L/(gH)^{1/2}$, where L is the total length of the fjord to the outer shelf (~ 7.5*km*) and *H* is the average depth of about 50*m*, is about 22.5*min*, or about 3% of the average semidiurnal tidal period (12.5*hr*). This would result in ~ 6*cm* of amplification of a 2*m* tide. The same period calculated for the inner basin only (*L* = 3.5*km* and *H* = 60*m*) is ~ 10*min*, which is about 1.3% of the tidal period. This would result in an amplification of about 2*cm*. The unfiltered oscillations (Fig. 3.14b) fall within the above range, hence tidal resonance could be a possible factor in causing the slight height increase and decrease in the northern basin relative to the outer basin near the sill.

4.5. Net total transports and baroclinic and barotropic flow

Based on the equations given in section 3.3.1, the net total, baroclinic and barotropic transports were calculated for Sections B and C in June, July and August 2007 (Appendices 3.4 to 3.9). Each of the monthly data sets was then integrated over the tidal periods to derive a flushing rate based solely on the differences between baroclinic and barotropic flows. Over the sill region these two currents should sum to zero (Stigebrandt, 1976), and any net positive

---

[2] Low-pass filter is a Lanczos kernal spanning 24*hr* with a frequency of 6hr^{-1}

amount during the flood tide would require additional outflow to achieve a balance and vice versa for the ebb.

Figure 15 shows a quasi time-series of all three transports along with the tide heights measured at Cordova, Alaska. The results indicate that a strong positive relationship exists between the net total transports (due to baroclinc flows) during flood tides over the sill. In July these currents cause a large net positive exchange of water during flood tides that is not balanced by baroclinc outflows during the ebb tides. This is shown even more clearly in plots of fitted and measured transports in Figure 16a. Note that in the latter Figure the barotropic and baroclinic flows were fitted by a sine function, with amplitudes based on the measured transports. In July and August the fitted and measured baroclinic flows are considerably higher than the barotropic tidal flows, and the flushing rates vary accordingly at 1363 and 711$m^3\ s^{-1}$ respectively. The exchange rate in June is much smaller (194 $m^3\ s^{-1}$) and the corresponding times of total replacement of water in the main basin are 16.4, 2.3 and 4.5 days respectively in June, July and August (Table 3.2).

For the time-series at Section C (Fig. 3.15b), the fitted versus measured tidal and baroclinic transports (Fig. 3.16b) show a similar pattern to Section B with inflow occurring each month, albeit with much lower magnitudes (Table 3.2). As expected, the corresponding flushing rates are lower in all three months at 145, 180 and 403$m^3\ s^{-1}$, with times of total flushing increasing to 22, 17.7 and 7.9 days respectively. However, one caveat is that the transports north of the sill either reverse in direction or are negligible during the first half of the flood phases, and during the ebb phases the baroclinic exchange is northward in all months. The transports at Section C also drop by nearly an order of magnitude relative to the sill proper (Table 3.2), and taken as whole this possibly indicates that periods of divergence and convergence occur within this region of the fjord. This hypothesis is also supported by evidence of internal tides in both fjord basins, and being progressive in nature their passage could certainly cause reversing flow patterns within portions of the fjord during a given tide phase. The effects of internal waves are discussed in detail in the following section.

4.6. Evidence of internal tides from hydrography in 2007

The approximate timing of the ADCP transects with CTD stations is summarized for surveys in 2007 in Figure 17. The hydrographic measurements are not evenly spaced over the tide cycles due to differences in transit times for transects with and without casts. For this reason, some

CTD series fall well within a given tide phase while others span across the transition between ebb and flood stages. Figure 18 shows a quasi time-series of salinity vertical sections beginning with a flood tide in July and ending with an ebb tide in August. Distances in the plots start from station 7 in the northern basin and end at station 2c over the outer sill (Fig. 3.10A). Throughout this series the isohaline depths (and hence isopycnal depths) exhibit vertical changes during the tide cycles showing the generation of what appear to be internal waves, caused by stratified tidal flows over sills (Stigebrant, 1976; 1978 and 1979). In June (not shown), the stratification is restricted to the upper 5*m* and the internal waves are relatively low in amplitude, but by mid July this layer expands vertically and the waves are relatively large and conspicuous, particularly below 30*m*. For example, during the ebb tides (run B and E in July and A and D in August) a wave shown by rising of isopycnals downstream of the inner sill that separates the northern (inner) and southern (outer) basins (Fig. 3.10A). During the transition from ebb to flood tides (runs C and F in July, and run B in August) the pattern reverses, and a rising of isopycnals occurs in the inner basin. At this time a thickening of the subsurface layers occurs in the lower basin that is synoptic with an inflowing jet over the outer sill (Fig. 3.11h and n).

The patterns described above are basically repeated during most tides in 2007 and 2008, albeit with modulations due to differences in tidal prisms and density stratification. The reversed patterns in the isopyncals during the late stages of the tides may be due to lee waves traveling upstream from the inner sill. The presence of these waves is explored further in the next section by analyses of time-series from moored subsurface thermistors and deep CTDs in the two fjord basins near station 4b and 6b respectively (Fig. 3.10A). The effectiveness of internal waves in causing turbulent mixing in the deep water below the pycnocline is also addressed in section *4.8* by calculations of vertical diffusivity, tidal energy and flux Richardson numbers.

4.7. Evidence of internal waves from moored thermistors in 2007

Figure 19 shows time-series of temperatures collected at various depths at moorings A and B (for locations see Fig. 3.5). All the series show a gradual (seasonal) increase in water temperatures from solar heating and low frequency events that possibly signify periods of advection. Superimposed on the latter are oscillations that appear to be tidal in period. The two exceptions are the series at 45*m* and 70*m* at mooring B in the northern basin (Fig. 3.19B), in which low frequency changes are subdued but high frequency fluctuations are still evident. Also, the high frequency oscillations near the surface (3*m* and 2*m*) are more irregular by comparison, and since the data at these depths were collected with CTs attached to surface buoys (Fig. 3.5) they are not subject to vertical changes due to the tides as are the subsurface sensors. Therefore, the near-surface temperature variations indicate the affects of horizontal tidal and wind advection and possibly mixing by wave action during periods of strong diurnal up-fjord winds (Fig. 3.8).

To explore the presence of internal waves each series was first de-meaned and de-trended, and the data were low-pass filtered with a lancos kernal spanning 40*hr* to separate the tidal and other high frequencies from the low frequency advective events. The high-pass data are shown for 2*m* and 3*m* in Figure 20A along with subsurface pressure variations due to the tides. The high-pass series for all other depths at moorings A and B are shown in Figures 20B and C respectively. Also shown in these plots are vertical temperature fluctuations due to the tides, calculated from vertical gradients over depth determined from CTD casts during the cruises in June, July and August. The data from the cruises were fitted with a linear function using least squares (Emory and Thomson, 2004) and the pressure changes measured by the deep (40*m*) CTD (Fig. 3.5) were applied to the changes in vertical gradients over time to determine the equivalent temperature changes shown in the Figures. In all cases, the vertical oscillations due to the barotropic tides comprise less than half of the total vertical variation in temperatures.

To discern the power of the various frequencies comprising the total variance, spectral analyses were conducted on each of the high-pass series. The spectra for the two near-surface series are given in Figure 21A. From these results it can be seen that the power of the high frequencies near the surface is very low in general, with the highest contribution to the variance being at a frequency near the diurnal (0.032*cph* or 30*hr*). However, the frequency preserving form of the spectra indicates that the power is spread across a wide number of frequencies, with the small peak at the quarter diurnal period (~ 6*hr*) standing out that corresponds to the duration of the sustained up-fjord wind events. In contrast, the subsurface pressure series shows three spectral peaks at diurnal, semidiurnal and quarter diurnal periods, with only the semidiurnal peak truly standing out in the variance preserving spectra.

The spectra for remaining depths, shown in Figures 21B and C, indicate that the high frequency variation in subsurface temperatures is almost strictly tidal in nature, with the semidiurnal clearly standing out at all depths. The power of the spectra below 20*m* diminishes considerably due to smaller vertical T/S gradients at these depths (Figs. 7 and 18). However, this does not mean the internal waves at these depths are inconsequential. For example, when the vertical changes in temperature due to the tides are removed and the equivalent depth changes are derived from the temperature gradients at each depth, the largest oscillations (10-20*m*) occur in the deepest layers (Fig. 3.22). From the spectral analyses it is clear that these wave phenomena are strongly semidiurnal in nature, as would be expected from internal tides (Stigebrandt, 1976, 1979 and 1989). However, there are also oscillations at the diurnal period and higher harmonics at the half and quarter semidiurnal periods (~ 6 and 3*hr* respectively), and the latter two periods may signify the presence of internal lee waves caused by upstream trapping of waves near the inner sill. Descriptions of similar lee waves and their implications on water exchange are given by Vlasenko *et al.* (2002) and Gillibrand and Amundrud (2007).

From the above analyses, it is clear that internal tides and (possibly) lee waves occur in Simpson, and these waves may be responsible for creating the subsurface current reversals observed in the ADCP transects through vertical changes they cause in the depths of inflow and outflow during the tide cycles (Figs. 12 and 13). The pressure gradients induced by these waves may be inferred from the spatial variation in density within the lower basin. Figure 23 shows vertical sections of salinity and profiles of density anomalies at stations 5b, 4b and 2c within the lower basin for the first flood and ebb tides (F1 and E1) in July 2007. During the F1 tide the slopes of the isohalines vary in sign over depth within the lower basin, and the effects of this can be seen in the density anomalies (Fig. 3.23b). For example, over the central portion of the sill there are three regions of salty (hence dense) water and one region of fresher (lower density) water in comparison to the other stations. This produces at least two baroclinic modes alternating between inflow and outflow over the outer sill, with the main inflow occurring at 20 to 25*m*. A similar pattern occurs for station 3b, just shifted slightly higher in the water column. The latter baroclinic modes are also inferred by the along-channel velocities during the F1 tide at 14:25*hrs* from 0 to ~ 0.4*km* across Section B (Fig. 3.13A). During the E1 tide the isohalines also exhibit variation in slope within the upper water column, with stronger negative slopes from 10 to 30*m* relative to the F1 tide (Fig. 3.23c). This results in a thick region of relatively low-density subsurface water over the sill (Fig. 3.23d). In contrast, a marked positive density gradient at the surface suggests that outflow occurs from the upper fjord during the first portion of the ebb tides (Figs. 11d,m and 12B). However, due to the low density of subsurface water over the sill the outflows are forced to exit from the fjord as a deep jet (Figs. 12B and 13B, lower left panel).

4.8. Calculations of total work and tidal energy available to internal waves and jets

In the following section, the methods outlined in section 3.3.2 are used to calculate vertical profiles of diffusivity (κ_v) from temporal changes in density below sill depth within both the inner and outer basins of Simpson. The calculations are made from CTD data collected for various tide phases in July and August 2007 (Fig. 3.17). The value of A_f for the outer (inner) basin is 7.85 (5.66) km^2 respectively from Noll *et al.* (2008), and values for A_s for the outer sill are means of the cross-sectional areas described in section 3.3.1 (see Appendix 3.4). The areas for the inner (northern) sill and hypsographic data are estimated from nautical charts.

The results of the analyses, including values of work and energy normalized by the fjord basin surface areas at sill depth (A_b), are listed in Table 3.3 along with flux Richardson numbers (*Rf*). The calculations include layers from sill depth to near-bottom (Table 3.3a) and layers within 10 to 15*m* of the bottom (Table 3.3b). When the layers are near the bottom the efficiencies are reduced by an order of magnitude. However, in all cases the mixing efficiencies shown by the *Rf* values indicate that the work performed against the buoyancy forces far surpasses the available tidal energy available to internal waves and is also only a tiny fraction of the energy available to jets. Thus the changes in density of the deep basin water over successive tide phases represent work from additional processes, such as advection and possibly the effects of internal waves themselves on the density structure. This is particularly true for the outer (main) basin where the *Rf* values during the flood to ebb transitions in July are more than 10 times the values of the inner basin (Table 3.3). The relatively low efficiency within the inner basin is also due to significantly greater amounts of energy (nE_2) generated by the tidal flow across the shallow inner sill. In July, this energy exceeds the available amounts at the outer sill by ~ 6 to 9 times, and in August it is more than an order of magnitude greater (Table 3.3a). The tidal energy imparted to jets is probably also grossly overestimated by (12). This is indicated by the ADCP data, which shows the jet flow to occur for < 1/4 of the tidal periods. This means that the actual available energies are $< 0.25nE_{2j}$, ranging from 200 to 1300$mW\,m^{-2}$. However, the values of the densimetric Froude numbers shown in Table 3.4 are all << 1, and this clearly indicates that both basins at Simpson are predominately wave basins.

By using horizontal averages of the density it was hoped to remove most of the effects of the internal waves. However, the long waves that result from the stratified tidal flow possibly cause variation in the mean density between tide phases (and between the two basins) and hence the implied diffusive changes are related to more than just turbulent dissipation. Phase differences of the internal tides over the fjord may also be indicated by the tendency for the sign of the density changes to reciprocate between the two basins. This is also indicated by the differences in mode 1 internal wave speeds, which are much higher within the inner basin for both successive and individual tide phases shown in Tables 3 and 4.

The only calculation that definitively eliminates effects of internal waves is the comparison using average density over all tides for July and August (see Fig. 3.17). In this case the deep water of the outer basin exhibits an increase in density over time, whereas the inner basin shows a decrease (Table 3.3). These results are consistent with the temporal variation in deep hydrography within both basins, and they indicate that the deep water of the outer basin is influenced more by advection from outside the fjord. The inner basin, by contrast, is affected more by turbulent diffusion of local freshwater. However, even within the bottom 10*m* in the northern arm the mixing of freshwater is over 10 times the efficiency of tidal energy imparted to internal waves. Characteristics of the deep hydrography are discussed further in the next section.

5. Discussion

5.1. Horizontal and vertical flow structure

The horizontal currents described in section 4.2 have similar flow patterns during all periods of observation in 2007 and 2008, with differences in amplitude and phase being modulated by density stratification, tidal volumes and possibly winds. In Figure 3.11 the flows can be seen to form a cycle over the semidiurnal tides, in which inflows in the outer basin start out during the flood stages as jets in the upper layer but then deteriorate rapidly into areas of slack water and outflow over the sill. This pattern then reverses during the ebb tides. The moderating effects on the tidal jets by smaller tidal prisms can be seen for both the 1st ebb and 2nd flood stages (Fig. 3.11,f-h). Other features of the residual circulation moderated by changes in tidal volume include the anticylonic and cyclonic eddies that form respectively at the mouth during the flood tides and around the inner sill (reef) during ebb tides (Fig. 3.11,a,g,h,m and n).

A numerical study of Loch Torridon (Gillibrand and Amundrud, 2007), a Scottish fjord bearing some similarity to Simpson Bay, shows many of the same features of residual barotropic circulation. These features include accelerated jet flows with antcyclonic and cyclonic vortices induced by cross-channel shear during inflows and outflows respectively caused by a shallow (20*m*) sill and a lateral constriction between the inner and middle basins. Some of the features persist in simulations of the mean baroclinic flows, but they are strongly modulated by estuarine (gravitational) outflow from the inner basin. The latter effect differs markedly from the inner basin of Simpson, where the surface currents are always in phase with the tides (Fig. 3.11).

Another feature of the Loch Torridon study is the generation of internal tides caused by stratified tidal flow across the sill. These waves are very similar to the depth variations in salinity observed during the tide cycles at Simpson (Fig. 3.18). The modeled baroclinic velocities of Loch Toriridon also indicate that current reversals in the inner basin of Loch Torridon occur at various depths due to depression of the isopycnals by internal waves during flood tides. The baroclinic flows seaward of the inner sill resemble a mode 1 baroclinic response, whereas the currents in the inner basin develop a three-layer structure, similar to baroclinic flows in Simpson's northern basin (Gay, 2011a). The vertical structure of the flows within Simpson's main basin (Fig. 3.12) show the flood jet persisting as a subsurface current northwards of the outer sill (Fig. 3.11a-c), whereas the ebb jet rapidly deteriorates southwards due to surface convergence at the mouth (Fig. 3.11f). As a result, the outflow is forced into a deep baroclinic jet over the western side of the outer sill. The changes in vertical flow structure over the sill at Section B (Fig. 3.13) indicate that with time the flood tide j*et al.*so deteriorates into a deep inflow across the sill. So what starts out as a mode 1 baroclinic flow becomes a mode 2 (three layer) flow. Section C starts out with much the same flow pattern as B, but later in tide it exhibits deep outflows on the western side resembling the flow structure during ebb tides. The reciprocal changes in flow structure in the main basin at Simpson during the semidiurnal tides are probably baroclinic responses to propagating internal waves, similar to Loch Torridon. This is discussed further below, following the next section on wind effects.

5.2. Water exchange and effects of internal waves

The calculations of water exchange (Table 3.2) from the ADCP data measured over the outer sill and an adjoining transect just to the north (Figs. 15and 16) show that during flood tides baroclinic currents generate inflows in excess of the tidal currents that are not reciprocated during the ebb tides. The excess inflows, therefore, must be counter-balanced by outflows not measured by the ADCP. Some of the outflow could occur in the bottom layer estimated by logarthmic profiles and the 0.5-0.6*m* surface layer above the instrument, but some of the excess flow likely occurs in the end-regions beyond the transects.

The potential processes generating the baroclinic flows at Simpson are garnered from an extensive literature regarding fjord hydrography and circulation (e.g. Gillibrand and Amundrud, 2007; Farmer and Freeland, 1983; Stigebrandt, 1976; 1980; 1999; Stigebrandt and Aure, 1989; Vlasenko *et al.*, 2002; Stacey *et al.*, 1995; Stacey, 1999). All of the above studies focus on processes including internal waves generated by stratified flows over sills and their effects on water exchange, vertical mixing and baroclinic wave drag due to bottom friction.

In two of the more recent studies (Vlasenko *et al.*, 2002; Gillibrand and Amundrud, 2007), internal waves are predicted by numerical models to occur in two forms: 1) internal tides at the same frequency as the M2 tides, and 2) shorter lee waves, which can be either steady or unsteady. The displacement of isopyncnals due to the internal tides varies greatly between the two studies, with the amplitudes being only 1*m* in the upper Tronheimsfjord in Norway (Vlasenko *et al.*, 2002) and over 32*m* in Loch Torridon in Scotland (Gillibrand and Amundrud, 2007). In both cases, however, the models also predict stationary lees waves that grow to large amplitudes by gaining energy from the tides (e.g. Stigebrandt, 1976 to 1999). As the tidal flows slacken, these waves freely propagate upstream within the fjords, and in both models the water exchange across the sills is strongly regulated by residual currents caused by the lee waves.

At Simpson Bay, the internal tides appear to be on a similar scale as the Loch Torridon model, with maximum deep amplitudes of 10 to 20*m* inferred from the isotherm displacements (Fig. 3.22A,B). The changes in isohaline depths during the tide cycles (Fig. 3.18) also give the impression that long period internal tides and possibly shorter lee waves occur that grow in amplitude by gaining energy from the tides. Since the Froude numbers for the two basins at Simpson (Table 3.4) are all highly subcritical (<< 1.0), none of the long waves should be trapped by topography. In fact, the model of Vlasenko *et al.* (2002) shows the first three baroclinic tidal modes for waves in the upper Trondheimsfjord have very long wave lengths (21.5-60.5*km*) and phase speeds of 0.5 to 1.4*m s-1*, which are in the same range as the wave speeds calculated for Simpson (Table 3.4). The growth and propagation of lee waves at Simpson, however, appears to begin following a break-down of the jets that initially commence at the onset of the flood and ebb tides (Fig. 3.11a,f,h,l,n). Some of the Froude numbers in Simpson's outer basin (Table 3.4) also exceed 0.33, the critical value for continuous stratification (Dyer, 1997), so perhaps after garnering enough energy from the barotropic tides, the growth of lee waves ultimately interferes with the jet flow causing it to dissipate. At this point, the latter aspects are speculative, but during calm conditions visual observations show that by the middle of a tide stage the progressive internal waves show surface expressions in the form of slack water, indicating surface divergence (slicks), and areas of convergence seen as surface tide rips, probably from waves propagating in both directions from the sills. As such, these characteristics give Simpson a mixed classification as that of a jet and a wave fjord; which Stigebrandt and Aure (1989) state is common among the diverse fjord basins in Norway.

Another feature of the internal waves at Loch Torridon is the tendency for the lee waves to be much larger during flood tides than during the ebbs due to presence of dense deep water below the sills that inhibits the growth of the waves. However, during the flood tides the rising of intermediate water 35 to 40*m* over the sill increases the density of water entering the upper basin, thereby enhancing deep water exchange. At the Tronheimsfjord, residual currents caused by lee waves also result in water exchange into the fjord at sill depth. This type of exchange probably also occurs at Simpson, but the densest marine source water would initially enter the main basin, and this apparently happens during later portions of the flood tides when the inflows switch to the deep water column (Fig. 3.13A). This pattern could very well represent the downward displacement of dense water moving over the sill, similar to effects shown in the model for Loch Torridon. The regular exchange of deep water across the outer sill is also indicated by the cyclical low frequency changes on the O(3-5*d*) in both the thermistor data at 30*m* (Fig. 3.19A) and the deep T/S properties at 40*m* (Fig. 3.23C).

5.3. Vertical diffusivity and changes in deep density

Methods from one of the early studies (Stigebrandt and Aure, 1989) were used to estimate the vertical diffusivity in the deep waters at Simpson and the work performed against buoyancy by tidal energy available to internal waves. The results are summarized in flux Richarson numbers that clearly indicate that the efficiency of internal wave dissipation is too great to account for large changes in the deep density over short time intervals (i.e. tide cycles) and also over longer periods. Other processes such as deep advection (i.e. water exchange) must occur as well as sub-pycnocline mixing. However, due to different sources of water being exchanged and mixed within the two basins, the density over time decreases in the inner basin due to mixing of localized freshwater and increases in the outer basin due to advection from outside the fjord. Despite periodic water exchange of dense (salty) water from the outer basin into the northern arm, the deep water of the latter basin becomes warmer and fresher over time in the summer. This pattern follows the same differences in hydrography observed in prior years by Gay and Vaughan (2001) and suggests that additional freshwater sources, such as submarine groundwater discharge (Swarzenski *et al.*, 2009), possibly exist around the deep portion of the delta at the head of the basin for internal wave action to mix it into the deep water.

5.4. Estuarine conditions in relation to overmixing

Due to the dispersed nature of freshwater input at Simpson Bay, the circulation and water exchange in the summer is driven primarily by large tidal prisms (Δh = 1.5 to 2.5m), internal waves and winds. The freshwater velocity is given as $u_f = Q_f / A$, where Q_f is the freshwater discharge (~100 to 150$m^3\ s^{-1}$) and A is the cross-sectional area above the inner sill (~14,090m^2). In midsummer u_f ranges from 7.1 x 10^{-3} to 10.6 x 10^{-3} $m\ s^{-1}$, and thus the densimetric Froude numbers, given as $Fr_f = u_f \big/ \sqrt{g'_f\, H}$, are quite small (0.002 – 0.0024). The cross-sectional area at the outer sill is ~ 5 times greater than that of the inner sill, and the above parameters are an order of magnitude smaller at the outer control section of the fjord (3.5x10^{-4} to 5.2x10^{-4} $m\ s^{-1}$).

In terms of estuarine overmixing (Hetland, 2010), normalized reduced gravity ($g' \big/ g'_f$) ranges from 0.08 to 0.105 $m\ s^{-2}$ at the mouth (based on g' values in Table 4.4). Equation (4) in Hetland (2010), therefore, suggests Simpson is overmixed and close to the limit in terms of maximum exchange flow, in which the normalized upper layer thickness (h_1/H) is about half the maximum depth (30m/60m). This is the same limit to maximum subcritical flow (Farmer and Armi, 1986), in which the composite Froude number of the two layers: $G^2 = F_1^2 + F_2^2$ is ~ 0.3. The latter is also close to the critical value of 0.33 given by Dyer (1997) for continuous stratification, which actually fits the density profiles at Simpson much better than a two layer approximation.

Finally, when the normalized reduced gravity is plotted against the densimetric Froude number (Fig. 3.24), Simpson falls well into the viscous control side according to Figure 5 in Hetland (2010). This result shows how differently subarctic fjords in PWS behave in comparison to temperate zone estuaries in terms of density driven circulation. Although there appears to be viscous control, gradual mixing within the upper stratified layer and extreme vertical diffusivity calculated herein indicate that the exchange flow is governed primarily by advection due to the hydraulics of the sills and the concomitant internal waves generated by the stratified tidal flows.

6. Summary and conclusions

Chapter III describes patterns in circulation and water exchange from towed ADCP, CTD and moored T/S data collected in the summers of 2007 and 2008 at Simpson Bay, a small subarctic fjord located in eastern PWS (Figs. 2.1A and 3.1). Ancillary data include air temperatures (*Ta*), winds and precipitation (*P*) collected in 2007 and 2008 and tides in August 2005. Between years air temperatures vary significantly ($p < 0$), with relatively warm, dry conditions in 2007 ($\overline{Ta} = 13.4^{o}C$; $P = 2.7cm$), followed by cool wet conditions in 2008 ($\overline{Ta} = 11.1^{o}C$; $P = 17cm$), The hydrography closely follows the annual patterns in the climate, and higher *FWC* in 2008 causes the pycnocline to be ~ 10*m* deeper relative to 2007. Winds at Simpson are highly varied in magnitude but strong up-fjord diurnal winds (4-7$m\ s^{-1}$) occur over periods of 6 to 8*hr* during the day, followed by light (< 2$m\ s^{-1}$) down-fjord winds at night. In 2007, the diurnal winds are higher in both magnitude ($p < 0.007$) and frequency, but in 2008 prolonged periods of down-fjord winds occur during storm activity.

The circulation within both basins has a complex horizontal structure forced mainly by tides interacting with bathymetry, moderated by stratification, tidal volumes, internal waves and winds. The principal mechanism initiating circulation within the fjord is an inflowing (outflowing) baroclinic tidal jet (0.3-0.4$m\ s^{-1}$) that accelerates during the flood (ebb) tides across two sills (30 to <60*m* and <10 to 30*m* in depth) located respectively at the mouths of the main and northern basins. Secondary flows associated with the tidal jets include southward currents along the eastern shoreline of the main basin during the flood tides that are partly re-circulated via entrainment by an anticyclonic eddy at the mouth and outflows from the northern basin during ebb tides, that become cyclonic due to cross-channel shear around the reef/sill.

The circulation in the lower fjord occurs in multiple layers that frequently reverse in direction, but vertical exchange between layers is limited by high stratification relative to vertical current shear (i.e. *Ri* numbers >> 0.25). In contrast, the circulation in the northern basin is more fjord-like, with maximum inflows and outflows occurring in the near-surface layer, and one to two flow reversals deeper in the water column. Transport calculations for flows across the lower sill and adjacent flows to the north show that the flood tide baroclinic jet advects PWS water inward at a rate in excess of the tide volume flux that is not balanced by reciprocal baroclinic exchange during ebb tides. The result is a net inflow of PWS water into the main fjord at rates ranging from 194 to 1363 $m^3\ s^{-1}$, with associated flushing periods of 16.4 to 2.3 days respectively.

Internal waves, evident in vertical displacements of isohalines over consecutive tide cycles (Fig. 3.18), have maximum deep amplitudes of 10 to 20*m* inferred from isotherm displacements (Fig. 3.22A,B). The waves are similar in scale to waves shown in a numerical model of Loch Torridon, Scotland (Gillibrand and Amundrud, 2007), and Froude numbers for both basins (Table 3.4) are highly subcritical (<< 1.0), indicating that none of the long waves should be trapped by topography. As these waves progress through the lower basin they appear to change the vertical structure of the currents, so that during the flood (ebb) stages the maximum currents that begin in the upper layer gradually deepen during the course of the tide cycle to become subsurface inflows (outflows) across the outer sill. Calculations of vertical diffusivity in the deep water of both basins and work performed against buoyancy relative to available tidal energy show changes in deep density occur over sequential tide cycles and longer (monthly) periods that cannot be solely due to vertical mixing of a stagnant layer beneath the pycnocline.

In conclusion, the principal mechanisms forcing circulation and water exchange at Simpson Bay are large tidal prisms moving stratified water across sills. This is shown by an imbalance in the baroclinic flows that strongly favor the flushing of the main (outer) basin during flood tides. The circulation patterns are relatively consistent over time, and at the start of each tide cycle are initially comprised of flood and ebb jets that eventually become subsurface flows due to effects of internal waves and winds (described in Chapter IV). Internal waves in phase with semidiurnal tides are a common feature of circulation. These waves appear as regions of slack water in the near-surface currents and occur concurrently with a breakdown of the tidal jets. This gives Simpson a mixed classification as that of a jet and a wave fjord (Stigebrandt and Aure, 1989).

Vertical mixing beneath the pycnocline is caused by internal waves within the two fjord basins. However, high efficiencies shown by large flux Richardson numbers (R_f) indicate that other processes, such as advection, must play a role in increasing deep density over time within the outer basin. In contrast, the deep density in the inner basin decreases over time. The R_f values there indicate that mixing efficiencies are 10 times greater than the tidal energy available to internal waves, thus the deep freshening in this basin must come from additional sources of local freshwater input other than surface runoff.

CHAPTER IV

CIRCULATION AND WATER EXCHANGE WITHIN SIMPSON BAY, A SMALL SUBARCTIC FJORD IN PRINCE WILLIAM SOUND, ALASKA: TIME-SERIES OF HYDROGRAPHY AND WINDS

This chapter focuses on additional features of circulation and water exchange at Simpson Bay inferred from time-series of the moored T/S data and winds. Power spectra and wavelet analyses performed on all the data show that highly coherent ($\gamma^2 > 0.7$) low frequency oscillations (64-256*hr* periods) occur in the near-surface T/S properties of both the main (outer) and northern (inner) basins due to water exchange driven by a combination of tides, internal waves and up-fjord winds. The results for the winds indicate that the diurnal, up-fjord winds have a much greater impact on surface transport in 2007, and both wind and tidally related events the northern basin are evident as diurnal and semidiurnal peaks in power, particularly for salinity. Smaller spectral peaks also occur at periods of 8, 6 and 4*hr*. By contrast, the near-surface T/S series at the mouth exhibit fewer distinct spectral peaks, and the variance is evenly spread over a range of periods spanning from diurnal to 6-7*h*. However, phase differences indicate that T/S variation either leads or lags between the basins depending upon frequency. In both the inner and outer basins the deep T/S series exhibit marked spectral peaks at semidiurnal periods associated with tides and internal waves, but the outer basin also has significant power for low frequency events (128*hr*) linked to periods of water exchange from outside the fjord. In contrast, the deep sensors in the northern arm show generally weak spectral energy associated with gradual temporal changes. However, deep salinity changes in both basins are coherent at periods of 36 to 64*hr* and at semidiurnal periods. The wavelet spectra show episodes of T/S perturbations at the above periods in which increases in deep density in the northern basin occur due to advection of saline water from the outer basin related to periods of both down-fjord and up-fjord (diurnal) winds.

1. Introduction

In the previous chapter (Part A) the history and recent objectives of the oceanographic research at Simpson Bay, Alaska (see Fig. 3.1) are described along with examples of the meteorology and hydrography in the summers of 2007 and 2008. The circulation within the fjord over sequential tide cycles is also described and water exchange at the outer sill is calculated from vertical sections of along-channel velocities derived from towed ADCP data.

To summarize, at the start of each tide cycle the circulation is primarily driven by tidal jets accelerating across the two sills, but as the tides progress the surface jets dissipate and the flows become deep sub-surface currents. Other secondary features of circulation include anticyclonic and cyclonic eddies associated with cross-channel shear and entrainment. Integrated transports over time show that the water exchange process over outer sill is dominated by baroclinic inflows during flood tides that are not balanced by reciprocal baroclinic outflows during ebb tides, thus leading to flushing of the outer basin.

Internal tides formed by stratified flows across both sills are mainly in phase with semidiurnal tides, but higher frequency harmonics in the power spectra of high-pass temperatures possibly indicate the presence of lee waves. The evidence of internal waves is observed in their effects on the vertical structure of salinity (and other properties) over sequential tide cycles and from temporal oscillations in subsurface temperatures measured at ~ every 10*m*. Following methods given by Stigebrandt and Aure (1989), calculations of vertical diffusivity (κ_v) are used to determine the work performed against the buoyancy forces (W) by such internal waves. These data along with calculations of available tidal energy (E_2) are used to derive flux Richardson numbers ($R_f = W/E_2$), which quantify the efficiency of turbulent mixing by the internal tides.

The present chapter (Part B) addresses additional features of circulation and water exchange between the main basin and northern basin. These processes are explored through standard time-series analyses and wavelet power spectra of moored T/S data within the two basins and synoptic winds measured at the mouth.

2. Study area

Simpson Bay is a small fjord situated in the eastern Prince William Sound (PWS), close to Cordova, Alaska (see Fig. 3.1a). A detailed description of the fjord and its watershed is given in chapter III. Simpson is classified as a partially mixed fjord estuary (Gay and Vaughan, 2001), with a morphometry comprised of a main (western) basin and one inner basin (arm) located in the north, and a third separate basin located in the southeast (see Fig. 3.1b). This study concerns the T/S conditions in the former two basins only. The maximum depths of these two basins (see Table 3.1) vary from ~56 to 80*m* respectively and both have sills located at their mouths (see Fig. 3.1b). The outer and inner basins have nearly the same lengths (3.7 vs. 3.5*km*) but the northern arm is much narrower and, therefore, has a much smaller surface area (7.85 vs. 5.66km^2). Simpson's watershed is relatively large (170 km^2) and contains alpine glaciers at moderately high elevations (1200-1500*m*) (see Fig. 3.2). The watershed to fjord surface area ratio (WSR) is about 6:1 for the entire fjord (Gay and Vaughan, 2001). However, the ratio for the northern arm is closer to 13:1 (Noll *et al.*, 2008). Since runoff primarily enters the northern arm this leads to relatively high concentrations of surface freshwater within the latter basin, particularly in late summer to early fall when increasing precipitation adds to glacial melting (Gay and Vaughan, 2001).

3. Datasets and methods

3.1. Moored T/S and wind time-series

The instruments used on the CT moorings and weather stations are described in detail in chapter III. The moored data sets consist of near-surface (2-3*m*) and deep (40-70*m*) temperatures and salinities (T/S), and temperatures collected from thermistors strung at depths of 10, 20 and 30*m* in the main basin and at depths of 10, 30 and 45*m* in the northern basin (see Fig. 3.5). The wind data were collected in the main basin at mooring A and also at a shore-based station on the east side of the outer sill (see Fig. 3.5). The shore station was aligned by compass so as to measure winds relative to true north. Speeds and directions in 2007 and 2008 are averaged over 15 and 30*min* intervals respectively. Directions measure where the winds are coming from.

3.2. Data processing and time-series analysis

In 2007, all time-series were collected at 15*min* sample intervals and then averaged into hourly observations during post-processing. The wind data were converted to true vectors and rotated ~ 25° clockwise from true north to obtain the along-fjord components v'. Standard power spectra (Emory and Thomson, 2004) are performed on all the time-series to determine the statistical power (i.e. variance) of the frequencies comprising each series. Coherence and phase are also calculated to determine if the temporal variation in hydrography has any statistical correlations at the same depths between basins or between the surface and deep water within a given basin, and also the time lags that occur between them.

Averaging the data in 2007 and 2008 ($\Delta t = 0.25hr$ and $0.5hr$) into hourly series reduces the respective Nyquist frequencies from 48 and 24*cpd* to 12*cpd*. Thus aliasing from variance at periods < $2h$ should be reduced. The power spectra are obtained for the hourly data using 256 Fourier coefficients for the entire T/S series and 128 coefficients for the monthly wind series. In all cases, Kaiser-Bessel windows are applied with a 50% overlap, resulting in 14 windows (DOF = 28) for the T/S series, and 7 to 19 windows (DOF = 14-38) for the various wind series (Emory and Thomson, 2004). In addition, wavelet transforms are performed on all the series using a standard Morlet wavelet (Emory and Thomson, 2004) $g_{a\tau}(t) = (1/\sqrt{a})g\left[a^{-1}(t-\tau)\right]$ where $g(t) = e^{-t^2/2}e^{ikt}$, with scales (a) ranging from 2 to 256*hr*.

The wavelet computations are performed using a standard MATLAB package written by Torrence and Compo (1998), and the spectra are used to track the amplitudes locally of all the prominent frequencies in the time-series identified by the global power spectra. Corrections to the wavelets are made following a formalization given by Liu *et al.* (2007). This involves normalizing the square of the wavelet transform coefficients by the scales (periods) over which the power is calculated, thus allowing a comparison of spectral power across different scales. Without this correction, Liu *et al.* (2007) show that the software of Torrence and Compo (1998) has a bias towards low frequencies in the wavelet calculations, even if all frequencies in the spectra have the same amplitude. Dividing the transform coefficients by the scale factor 2^{-j}, where j is a given suboctave level, corrects this problem by providing a conservation of variance across scales.

4. Results

4.1. Power and wavelet spectra of winds in 2007 and 2008

The power spectra for the along-fjord (*v'*) wind velocities in the summers of 2007 and 2008 are shown respectively in Figures 4.1A and B. In both years the spectra indicate that the winds are primarily diurnal in frequency (0.05-0.04*cph*) with periods ranging from 20 to 25*hr*, and with exception of June 2008 the diurnal spectral power in 2007 is nearly double the power of 2008. This is shown more clearly in the variance preserving plots, which also indicate the presence of smaller spectral peaks at the semidiurnal period (~11.7hr) and at a period of 8*hr*.

The marked diurnal character of the winds is also shown by the time-series of the *v'* velocities and the associated wavelet spectra (Fig. 4.2b-f), the latter indicating when the winds have significant average variance ($p < 0.05$). The periods of significance occur in a band of 16 to 32*hr*, and in July and August 2007 these periods are 2 to 3 days longer and 1 to $3(m\ s^{-1})^2$ higher in average variance in comparison to the same months in 2008. In contrast, June 2008 (Fig. 4.4d) shows three periods of sequential diurnal up-fjord winds from the 7th to the 21st. The magnitudes are similar to July 2007, with maximum speeds close to or exceeding $4m\ s^{-1}$, and the peaks in average variance are also comparable between years being >5 and 2 to $2.5(m\ s^{-1})^2$. However, the average *v'* components in July and August 2007 (0.8 and $0.6m\ s^{-1}$) are 4 to 26 times greater than the averages in 2008 (-0.03 and $0.15m\ s^{-1}$). Indeed, the smaller average speeds in 2008 are partly a result of prolonged periods of down-fjord winds, which in 2008 are typically accompanied by periods of precipitation (see Fig. 3.6).

From June 14 to July 7, 2007, the wind directions were not accurately measured at mooring A due to buoy rotation, and the wavelet spectrum is, therefore, calculated using the wind speeds with the mean removed. The method is crude but it does result in showing high power of the diurnal winds over three days from June 26 to 29. In an attempt to discern the wind directions during this period at Simpson, wind vectors from the mid-Sound buoy (MSB in Fig. 2.1A) are compared with the wind speeds at Simpson from mid June to early July 2007 (Fig. 4.3a-c). For example, during the first 7 days westerly to southerly winds occur at the MSB (Fig. 4.3a). When the wind directions are from the southwest, maximum speeds at Simpson exceed $4m\ s^{-1}$ but when the directions turn from the south, speeds drop to < $2m\ s^{-1}$. When the winds at the buoy turn back from the west the maximum speeds at Simpson again reach 4 to $5m\ s^{-1}$.

The above patterns occur in conjunction with relatively high barometric pressure (1020-1025*mb*), and this probably signifies a period when the winds at Simpson are predominately up-fjord. The strongest bursts occur synoptically with the west winds, but following this is a 2 to 3 day period when winds at the MSB are from the southeast (Fig. 4.3a,b). Low barometric pressure offshore of PWS usually draws air out of fjords (Olson *et al.*, 2003). However, the decrease in air pressure during the above period is minimal (e.g. 1010 to 1015*mb*), just as it is throughout most of 2007, and as can be seen, the air pressures at this time actually rise and then fall again. Therefore, the winds at Simpson are likely down-fjord when winds at the MSB are easterly, even though the pressures are rising. This is indeed indicated during other months when similar synoptic changes in pressure and wind directions occur (Fig. 4.3b-f).

One of the more interesting types of diurnal winds at Simpson follows immediately after the above period of southeast winds. This occurs from June 26th to the 29th, when for 3 consecutive days the winds are strongly up-fjord and with average speeds exceeding 6 to $7m\ s^{-1}$ (Fig. 4.3b). At this time the barometric pressure again increases to 1024*mb* and the winds at the buoy are initially from the north before turning back to the west and southwest (Fig. 4.3b). Although the MSB wind speeds are weaker at this time in comparison to earlier in the month, the response in eastern Orca Bay and at Simpson is dramatic (pers. observation). It should be noted that these conditions typically occur under clear skies, and the effects of diurnal solar heating of the steep topography (see Fig. 3.1) may contribute to afternoon sea-breeze effects that amplify the diurnal winds. However, the atmospheric dynamics creating these wind events remains undocumented.

For the remainder of the time up until mid July the MSB winds are highly variable but the directions are frequently northerly (Fig. 4.3b,c). The wind response at Simpson is less obvious at these times, but from June 29th to July 7th there appear to be four periods when winds may be up-fjord in response to southwesterly and northwesterly winds at the MSB. At other times when the winds at the buoy are easterly, Simpson's winds have a mixed response (up or down-fjord).

4.1.1. Wind vectors in July-August 2007 and June-August 2008

The above inferences regarding winds at Simpson Bay in relation to the mid-Sound buoy (MSB) are shown more clearly in plots of vectors at both locations through the remainder of 2007 (Fig. 4.3e-g). For example, from July 14 to 17 diurnal, up-fjord winds at Simpson occur when the MSB winds are from the southwest to northwest (westerly). During the short period when MSB winds are from the southeast to northeast (easterly), the wind speeds at Simpson decrease and the air pressures over PWS also decrease. However, following this is a lengthy period (~5*d*) of diminished velocities that are mostly down-fjord from July 23 to 26 (Fig. 4.3e). At this time, the MSB winds are easterly in direction, but the air pressure in the Sound increases to moderately high values (≥ 1010mb). This mixed response of the winds at Simpson continues until mid to late August, when down-fjord winds occur there in association with relatively low barometric pressure and easterly winds at the MSB (Fig. 4.3g).

In 2008, the meteorological conditions at the MSB and Simpson (Fig. 4.4) follow a different pattern in comparison to 2007. For one, periods of diminished barometric pressure over the Sound are more frequent and intense, with the lowest values falling well below 1000*mb* in July and August. In response, Simpson's diurnal winds are less frequent (particularly after mid June), lower in magnitude and have a larger cross-fjord component in comparison to 2007. At times when the air pressures are increasing and the MSB winds are southerly, the winds at Simpson are either weakly up or down-fjord (Fig. 4.4a). Just as in 2007, however, there are periods in July and August when both down-fjord winds and southeast winds occur respectively at Simpson and the MSB, even though the air pressure is rising. In both years the latter pattern may be related to eastward motions of the low pressure center (see Fig. 1.2). This would explain why in both years air pressures inside the Sound tend to increase when winds are still easterly. When the low pressure center moves northward towards the Sound the pressures would drop.

4.2. Time-series analyses of moored T/S data

Time-series of the near-surface (3-2*m*) and deep (40-70*m*) temperatures and salinities with the mean and trend removed are shown in Figure 4.5A and B. As expected, the T/S variation is generally highest in amplitude for the surface water and relatively low in amplitude within the subsurface water, particularly for the deep salinities in the northern basin. These data were also low-pass filtered at 40*hr* using a Lanczos cosine kernel with 96 points on either side of the window to remove all frequencies above the tides (Fig. 4.5C). An interesting trend in all four series is the tendency for temperature and salinity to vary inversely. This creates high coherence between both variables and phase differences of ~ 180^o, particularly for the subsurface water.

The power spectra of the surface T/S series (Fig. 4.6) show spectral peaks in the northern arm to be well resolved, particularly at the diurnal and semidiurnal frequencies and also at 3, 4 and 6*cpd* (i.e. periods of 8, 6 and 4*hr*). In contrast, the temperature spectrum at 3*m* in the main basin is relatively white (Fig. 4.6a), and with exception of the low frequencies only one higher frequency at 4*cpd* stands out. The diurnal frequency is not resolved and the semidiurnal is bracketed between periods ranging from 15.4 to 11.8*hr*. The salinity at 3*m* (Fig. 4.6c) is well resolved at the diurnal frequency in comparison to the semidiurnal, and vice versa for the northern arm (Fig. 4.6d); differences that show up quite well in the variance preserving plots. In the northern arm, spectral peaks at 3 and 6*cpd* also stand out, whereas in the main basin the highest power (i.e. variance) for salinity occurs at 4*cpd* (6*hr*).

The deep T/S series in both basins (Fig. 4.7) exhibit much lower spectral power in relation to the surface as expected, but the variance of temperature in the northern arm is nearly an order of magnitude larger than that of the salinity and is concentrated in the semidiurnal band. This pattern is very similar to the spectra for the high-pass temperature series described above for internal waves in section *4.5.1* of Chapter III. In contrast, the spectra of the deep T/S series in the main basin are nearly one to two orders of magnitude greater than that of the northern arm. In both basins, however, most of the variance is concentrated in the semidiurnal band (Fig. 4.7). In the main basin there are also smaller peaks centered at 0.4*cpd* (2-3*d*) and 4*cpd* (6*hr*).

The variation in surface T/S spectral peaks between the two basins appears to be related to differential effects of winds and tides within the two basins, but the cause of the marked power at 4*cpd* (6*hr*) for both variables is less certain. It is within the range of high frequency variation in the winds (Figs. 8 and 9), and the actions of internal waves at a harmonic of the M2 tide could also be a possible driving mechanism. The strong influence of semidiurnal tides on the surface salinity in the northern arm is quite obvious from the marked spectral peak (Fig. 4.6d), whereas the peaks at higher frequencies may be related to winds, internal waves and possibly shallow water constituents of the tides, which for Cordova occur at frequencies of 4, 6 and 8*hrs*.

The maximum low frequency variation for the surface series (Fig. 4.5C) occurs at 0.094*cpd*, or a period of 256*hr* (~11*d*), which is shorter than the fortnightly tidal period of ~14*d* (Fig. 3.20). There are also higher, superimposed frequencies at ~ 0.4 to 0.3*cpd* or periods of 64 to 80*hr* (2-3*d*) that are much stronger for temperature. The latter also exhibits high power at 0.188*cpd* (128*hr* or 5.3*d*). The deep water in the outer basin also exhibits low frequency variation, but the power is centered at the 128*hr* period. There is also moderate power at 80*hr* (3*d*). In the northern arm the low frequencies are negligible in comparison to the semidiurnal frequency, as are the higher frequencies (Fig. 4.7). In all cases, however, the T/S values appear to vary inversely over the 2 to 3*d* periods, and for the surface series the low frequency periods (256 to 128*hrs*) are in fact highly coherent for the two basins.

4.2.1. Coherence and phase

Figure 4.8 shows the coherency of T/S variation for the near-surface (3-2*m*) and deep (40-70*m*) water, and variation between the surface and deep water within each basin. These results indicate that the physical properties of the surface water in both basins are highly coherent ($\gamma^2 >$ 0.7) at low frequencies (0.09 - 0.19*cpd*) corresponding to periods of 256 to 128*hr*. Moderate coherence ($\gamma^2 > 0.5$) occurs for both variables at 64*hr* (0.375*cpd*) and for temperature at ~5.5 and 4.2*hr* (4.2 and 5.8*cpd*). There is also minor, albeit significant, coherence for both series near the diurnal and semidiurnal frequencies (0.84 to 2*cpd*) at periods of ~28 to 12*hr* and for a number of high frequencies (2.6 to 7.6*cpd*) at periods ranging from 9.2 to 3.2*hr*.

The phase of the cross-spectra (Fig. 4.9) shows that all the low frequencies (< 0.5*cpd*) have zero phase, but the higher frequencies exhibit periods in which the phase of one basin or depth leads the other (+ϕ) or vice versa (-ϕ). For example, the 3 to 2*m* temperatures are in phase near the diurnal period (20*hr*) with the outer basin lagging the inner basin by 18° (~1*hr*), whereas at the semidiurnal period they become out of phase, lagging by 127^0 (> 4*hr*). The phase of salinity (Fig. 4.9B,a) exhibits a much different pattern than temperature. For example, at 3 and 2*m* the outer basin initially leads the inner basin by 39^o to 45^o at the diurnal periods (28-24*hr*) and then at the semidiurnal periods (13.5-12*hr*) outer basin lags slightly (-16^o) or has nearly zero phase. At higher frequencies the phase gradually cycles between the outer basin lagging as much as -130^o to -147^o at 2.6 to 3.5*cpd* (9 to 7*hr*) and then increasing in phase to lead the inner basin by 53^o to 61^o at 6*cpd* or periods close to 4*hr*.

The large number of coherent frequencies at 3 and 2*m* indicates that the near-surface T/S properties of both basins are affected by similar physical processes. However, temperature has more coherency than salinity, particularly at frequencies above the tides. This is expected on the basis that solar heating is much more ubiquitous over the fjord in comparison to freshwater discharge. But there are also a greater number of processes affecting the spatial variation of temperature. This was discussed in Chapter II.

The temperatures at 3 and 40*m* in the outer basin (Fig. 4.8A,b) show slight coherence for only one low frequency (0.19*cpd*) at a period of 128*hr*, but moderate coherence for periods of 6.2 and 4.3*hr* (3.8 and 5.5*cpd*). In contrast, the salinity (Fig. 4.8B,b) has only one significant coherence ($\gamma^2 > 0.5$) that is in common with temperature or a period of 6.2*hr* (3.8*cpd*). As noted above, however, the T/S spectra at 3*m* in the outer basin (Fig. 4.6) are both relatively white in comparison to the other spectra, indicating that a variety of physical processes affect the near-surface T/S properties in the outer basin.

The phase for the 3 and 40*m* temperatures (Fig. 4.9A,b) shows the surface leading the deep water over most of the series, but at certain frequencies (0.8, 2.6 and 3.4) the phase decreases to slightly ≤ 0. Also, there is a large perturbation at 4.7 to ~4.8*cpd* in which the phase cycles from 130^o to -170^o and back to 180^o. The phase for frequencies around the semidiurnal (1.5 to 2.5*cpd*) is nearly constant, however, showing that the surface is out of phase and leads the deep water by ~120^o. The remaining frequencies are mostly in phase with the surface temperatures still leading by 45^o to 90^o, but for frequencies above 6*cpd* the pattern reverses and the 3m temperatures gradually lag by 180^o at 7.25*cpd*. The phase for the 3 and 40m salinities is quite complicated by comparison, and initially it cycles rapidly between 3*m* lagging ($-\phi$) and leading ($-\phi$) 40*m* respectively, up to ~1.6*cpd*. After this the phase increases from -160^o to $+150^o$ and then remains relatively constant at 135^o to 120^o through the semidiurnal periods up to 2.5*cpd*. At frequencies higher than the latter it again cycles widely between -/+ values up to 3.5*cpd* (6.9*hr*), and at the remaining frequencies the phase gradually changes from ~54° at 3.5*cpd* to > -135° at 6.4*cpd* then again exhibits a cyclical pattern through the highest frequencies.

In contrast to the surface, the deep temperatures at 40 and 70*m* exhibit significant coherencies (Fig. 4.8A,c) clustered around the semidiurnal tidal period (10.2-13.5*hr*) and one significant coherency at the 36*hr* period. Above the tides, however, only three significant periods occur respectively at 8, 6 and 5*hr*. The deep salinities also exhibit coherence around the semidiurnal period (12.2-13.5*hr*), but there is also greater coherence at the low frequencies at periods of 128 to 36*hr*. The phase for the deep temperatures starts with 40*m* leading 70*m* and then becoming out of phase and reversing to a negative phase (-48° to -49°) close to the semidiurnal (1.5-2.5*cpd*). The phase at 40*m* continues to lag 70*m* up to ~5.5*cpd*, but the large perturbations again occur at both ~3.4cpd and 4.7 to 4.8*cpd*. At the highest frequencies (5.6-8*cpd*) 40*m* either leads by 65 to 135° or is in phase at angles from 0 to 20°. The pattern in phase for the deep salinities initially resembles the pattern for the surface depths, but at ~2.7*cpd* the phase cycles from -180° to +180° and gradually diminishes to 135o and then drops -149o at 3.5*cpd*. After this it the phase rises to ~90° and remains there up 4.4*cpd*. From there it rises to +90° and remains positive up to 6*cpd* and then cycles between –/+ values and back to -140°.

The coherence of temperatures at 2 and 70*m* in the inner basin (Fig. 4.8A,d) exhibits a much different pattern in comparison to all the other spectra, and other than minor significance near the semidiurnal period (11.6*hr*) the coherence is skewed towards the high frequencies, at periods ranging from 7.1 to 3.2*hr*. A similar pattern occurs for salinity, with the exception that minor significance occurs at periods slightly greater than the semidiurnal (14.2-15*hr*). Also, two frequencies with a $\gamma^2 > 0.5$ occur at periods of 4.9 and 9.8*hrs*.

The phase of the 2 and 70*m* temperatures initially switches back and forth with 2m either lagging or leading by -135 and 45° respectively up to 1.5*cpd*, after which the phase is nearly -170° with 70m leading 2m through the semidiurnal frequencies up to 2.5*cpd*. Above the latter frequency the phase changes by 350° to 2*m* leading 70*m* again and gradually diminishing to a negative phase at 4.5cpd with 70m leading 2m for all remaining frequencies except 6.6 to 6.9*cpd*, where the phase is nearly zero.

4.3. Wavelet spectra of T/S time-series in 2007

Wavelet analyses for the near-surface and deep temperature and salinity time-series are shown in Figures 4.10 to 4.13. In each case, the top panel shows the time-series, followed respectively by panels showing the wavelet power spectrum and scale-averaged variances. For the 2-3*m* series (Figs. 4.10 and 4.11) the outstanding features are the significant power of the low frequencies relative to the high frequencies; the latter showing scattered periods of significance ($p < 0.05$) mainly for salinity. The power of the low frequencies is also higher in the main (outer) basin, where two events occur in which temperatures vary at periods of 64 to 128*hr* (2.6 to 5.3*d*). In late June to early July these fluctuations are quite strong and a second, shorter period with less power occurs in late July. At 128*hr*, these cycles exhibit minor coherence with the along-fjord winds (Table 4.1). The salinities in both basins exhibit significant power mainly at periods ≥ 128*hr*, but scattered fluctuations do occur at high frequencies ranging from 2 to > 10*hr* (Fig. 4.11). These isolated periods of significant high frequency ($p < 0.05$) are associated with short, ephemeral negative trends in salinity O(6-12*hr*).

Although in the wavelet analyses the high frequency variation in T/S properties of the near-surface water is overwhelmed by strong significance in the low frequencies, the series in Figure 4.5 do show some significant ($p < 0.05$) relationships with the winds. For example, in the main basin temperatures are coherent with along-fjord winds at periods ranging from 2.8 to 7.1*hr* (Table 4.1), whereas salinity variation has minor coherence with winds at only one high frequency (4.3*hr*). However, relatively strong coherence (0.68-0.74) occurs for periods ranging from 13.5 to 25.6*hr*, suggesting that there is a marked response of salinity to the diurnal, up-fjord winds. In the northern basin, coherence of the near-surface temperatures with the winds occurs for either very high frequencies (periods of 2.4 to 3.1*hr*) or at diurnal frequencies ranging from 21.3 to 25.6*hr* (Table 4.1). The salinities exhibit a similar pattern, but there is also coherence close to the semidiurnal period of 11.1*hr*.

The wavelet analysis for the deep series (Figs. 4.12 to 4.13) shows that most of the power for temperatures at 40*m* in the main basin occurs at low frequencies at periods of 128 to 256*hr*. Beginning in mid July, however, there are scattered events in which significant variation occurs around the semidiurnal period (10-16*hr*). In contrast, significant power of the deep T/S series at 70*m* in the northern basin occurs over two main periods: one in late June to early July and the other is sporadically throughout August. During these periods, the power is significant over two ranges: 2 to 16*hr* and 64 to 128*hr*, both with very low average variances (Figs. 4.12 to 4.13).

The nearly identical patterns of significance in the wavelets for temperature and salinity in both basins is due to a high coherence of the two variables (not shown), particularly at periods of 64 to 128*hr*, diurnal, semidiurnal and 6*hr* ($\gamma^2 = 0.8$ to > 0.9). The high frequencies also show coherence with the along-fjord winds (Table 4.1). In the main basin, this occurs for both T/S series at periods of 5 to 19.7*hr*, whereas in the northern arm coherence with winds occurs for temperature at 3.9 to 11.1*hr* and for salinity at 2.8 and 10.7*hr*. The deep temperature variation in the northern basin is also coherent with winds at the diurnal period (25.6*hr*) but the salinity variation is instead coherent only at the lowest frequency with a period of 256*hr* (Table 4.1).

5. Discussion

5.1. Winds in relation to circulation and hydrography

The winds primarily affecting water exchange at Simpson are the sustained up-fjord winds that are diurnal in frequency (Figs. 3.9 and 4.1). The wavelet spectra in 2007 (Fig. 4.2a-c) show the periods when these winds are significant statistically, but the only time when ADCP currents were measured synoptically with a prolonged diurnal wind event is in July 2007 (Fig. 3.10B). However, direct effects of these winds on circulation are uncertain from these data, and during all other cruises winds were generally light and variable in direction. In many cases, the currents at 2*m* in July 2007 (Fig. 3.11) are either very weak in the middle of the main basin or out of phase at the mouth with respect to the wind direction. Examples of this occur during both flood tides (Fig. 3.11d,e,h-j).

The low correlation of the near-surface currents with the winds may be related to the high stratification in the surface layer (Fig. 3.18), which tends to trap wind stress. For example, in a study of circulation in response to diurnal winds in the Jøsenfjord, located in southwest Norway, Svendson and Thompson (1978) found wind stress to be confined to the upper 2*m.* This was determined by the ratio: $\rho_a C_D U_a^2 /(\rho_w g \varsigma_x)$, where ρ_a is the density of air, *CD* is the drag coefficient (= 1.3 x 10^{-3}), *Ua* is the wind speed, ρ_W is the density of the surface water, *g* the acceleration due to gravity and ζ_x is the sea-surface slope measured at tide gauges located nearly 100*km* apart at Stavanger and Förre. Applying the above ratio to Simpson Bay, using 1.25*kg* m^{-3} for the air density, 1020*kg* m^{-3} for the surface water density and ζ_x = 0.02*m*/7700*m* from the sea surface elevation difference between basins described in Chapter III, the depth of wind stress is also found to range from 0.25 to 2*m* under typical up-fjord winds ranging from 2 to 6*m* s^{-1}.

In the Norwegian study, the average diurnal period response of the currents is highly coherent with wind stress (0.86-0.93) for 1.5, 5 and 10*m* at phase lags of 3, 13 and 10*hr* respectively. The deeper responses (20-40*m*) showed less coherence (0.64-0.66) but the phase is also much shorter

(1-4*hr*). The large phase jump for the currents between 1.5 and 5*m* (~10*hr*) also occurred for temperatures at the same depths. An ad hoc analysis of the winds and T/S data at Simpson was performed using methods similar to Svendson and Thompson (1978) by averaging hourly data over 24*hr* segments of the synoptic series between July 14th and August 21st for a total of 22 days when winds were predominately diurnal. The results, shown in Figure 4.18, indicate the near-surface series have a lagged response to the winds, similar to the Norwegian study, but the sub-surface responses are dominated by the semidiurnal tides.

Harmonic analysis performed at frequencies ranging from 0.96 to 1.143*cpd* (25-21*hr*) is used to obtain the amplitude and phase of the diurnal components of the winds and all temperature series and the surface and deep salinities. Examples of these components are shown in Figures 4.19 and 4.20. From these plots it can be seen that with exception of the winds the diurnal amplitudes of temperatures at all depths are quite small in relation to the total variation. In fact, the percentage of variance explained is 58.5% for the winds but for both the temperatures and salinities the range is only 1.7 to 3.7%. The coherence and phase of the most significant ($p < 0.05$) diurnal T/S components are listed in Table 4.2. For both temperature and salinity at 2 and 3*m* and for temperature at 45*m* there are significant correlations with the diurnal winds, particularly for salinity, at frequencies ranging from 0.2 to 1.1*cpd* at periods of 128 to 21.3*hr*. Coherencies at the other depths only occur at frequencies ≥ 1.7*cpd* or periods ≤ 14.2*hr*. The longest period close to the diurnal (25.6*hr*) exhibits zero phase lag, but at periods of 21.3 to 12.8*hr* the temperatures in the main and northern basins lag the wind by 3.9 to 2.3*hr* and 5.5 to 3.3*hr* respectively. This would be expected since the diurnal winds affect the fjord in a progressive manner starting at the mouth. The salinity at 3*m* in the main basin is highly coherent with the diurnal winds and exhibits phase lags ranging from 8 to 2.5*hr* for periods of 21.3 to 6.1*hr*, but at 2*m* in the northern basin the coherence at 21.3*hr* is not significant (0.33) and the phase lag is < 0 (-1.9*hr*). Negative lags also occur for all other significant coherencies at higher frequencies (Table 4.2) and also for the coherencies of temperatures at 45*m*.

The reason for the near-surface salinity variation in the northern basin to lead the winds is uncertain, but it may be related to the wind energy being trapped in the surface layer. For example, the maximum diurnal wind effects occur in the outer basin and beyond the mouth in Orca Bay, but in the northern arm the diurnal winds diminish rapidly past the inner reef. The depth of surface mixing by breaking waves (i.e. white caps) may be estimated by a surface roughness length (*z0*) derived by Stacey (1999). In this parameterization *z0* is related to the friction velocity (*u**) at the air-sea interface $\{z_0 = a(u_*^2/g)\}$, but the relationship is also expressed in terms of wind speeds (*U*) as $z_0 \approx 0.2(U^2/g)$. The latter expression is also ~ O(*Hs*), where $H_s \approx 0.3(W^2/g)$ is an empirical expression for significant wave height given unlimited fetch. Using typical wind speeds at the peak of diurnal winds at Simpson (4-7$m\ s^{-1}$) one finds that *z0* ranges from 0.3 to 1*m* and *Hs* ranges from 0.5 to 1.5*m*. The latter values fall well within the ranges of fully developed waves observed in 2007. This would result in surface mixing in the outer basin near mooring A, but in the inner basin, surface transport across the reef would cause the subsurface water (2-3*m*) to move outward at the depth of the CT at mooring B, thus producing changes opposite of those at mooring A. This is also inferred by the differences in phase at diurnal frequencies between the temperature and salinity in the two basins (Fig. 4.9) and is discussed further below under the time-series analyses.

Given the small amplitudes of the diurnal components, it appears that the direct effects of winds are markedly overpowered by the tides and internal waves. This is also shown in the T/S power spectra for all depths except 3*m* in the outer basin, in which the spectrum of temperature is relatively white (Fig. 4.6a). The wind effects, therefore, appear to be confined mainly to low frequency signals exhibiting high spectral power in the synoptic band (i.e. 3-5*d*). One direct effect of surface transport by diurnal winds, however, could be downwelling inside the inner sill, resulting in enhanced deep outflow from the main basin. This can be seen during ebb tide 1 in July 2007, in which the strongest outflows during the cruise (0.35$m\ s^{-1}$) occur over the western side of the sill at 18:35 local time (Fig. 3.13B) when the wind is still up-fjord (Fig. 3.10B).

5.2. Advective processes inferred from the T/S time-series

The high coherence of the low frequencies for the near-surface (2-3*m*) T/S properties (Fig. 4.8A) and strong statistical significance in the de-trended wavelet spectra (Figs. 4.10 and 4.11) suggest that over time regular exchanges of surface water may occur within the main and northern basins. The advection of near-surface water of differing properties is also evident in the T/S changes in relation to the winds, shown in Figure 4.21. In the Figure the near-surface properties frequently exhibit inversions between T/S values that are coherent at low frequencies, suggesting that either intrusions of marine source water occur from outside the fjord during up-fjord wind events or advection from the northern arm occurs in response to down-fjord winds. For example, the fetch from central PWS through Orca Bay is O(70*km*) and during periods of strong up-fjord winds ($\geq 4m\ s^{-1}$) the wave field in eastern Orca Bay becomes fully developed, with breaking waves > 2*m* in height. This results in surface mixing down to the level of the sensors on both moorings, so that the surface T/S properties in Simpson become warmer and fresher if the source water is from the Rude River plume and cooler and saltier if it comes from farther west in Orca Bay. Conversely, during prolonged down-fjord wind events fresh (i.e. low density) surface water from the northern basin propagates southward generating a baroclinic response (i.e. flow reversal) beneath the surface layer. During the up-fjord wind events the sign of the gradients in physical properties will depend on the strength of surface mixing and whether the response at the moorings is due to a thick intrusion or simply a subsurface baroclinic response. Good examples of the latter occur during down-fjord winds in which T/S values decrease and increase in phase.

Further complicating the near-surface T/S properties is the interaction of winds with the baroclinic tidal jets (Figs. 3.11, 3.12A and 3.13A) and internal waves in both basins (Figs 3.18 and 3.22). This can be seen in the high-pass wavelet spectra for both physical properties, in which variation is significant at periods ranging from 2 to 16*hr*, but the patterns over time for the T/S series differ as a result of low coherence of the variables. This is probably also why the spectra for the outer basin are white in comparison to the inner basin where direct wind effects are not as strong. In addition, many of the significant spectral peaks and coherencies for both temperature and salinity occur at periods close to or within the range of the diurnal and semidiurnal tidal constituents for Cordova (23.9-28*hr* and 11.98-12.9*hr* respectively). Furthermore, all significant coherency for frequencies higher than the semidiurnal are close to the shallow water overtide constituents, including the 4 to 6*hr* principal lunar (M4 and M6) and solar (S4 and S6), quarter diurnal (MN4), and 8.2-8.4*hr* terdiurnal and luner terdiurnal (MK3 and M3). The tidal constituents for Cordova are listed in Appendix 3.10. It should be noted that all the shallow water constituents other than the M4, M6, S4 and MN4 have negligible amplitudes and, therefore, probably have very little affect on the T/S variation. All the frequencies at these harmonics are typically non-significant statistically and are most likely noise in the spectra.

For the deep water (40 and 70*m*) the low frequency variation for the T/S values is highly coherent in both basins ($\gamma 2 = 0.85\text{-}0.98$), and in the outer basin this extends over all higher frequencies as well. Therefore, the wavelet spectra for the de-trended full and high-pass series (Figs. 4.12 to 4.13 and 4.16 to 4.17) show identical significance ($p < 0.05$) for both properties in the outer basin and very similar patterns of significance for the inner basin. Unlike the near-surface properties, however, low frequency variation of the deep physical properties is not highly coherent between the two basins, but there is moderate coherence at the semidiurnal and some higher frequencies (Fig. 4.8A,B). In addition, the phase is similar for both properties, particularly at the semidiurnal (Fig. 4.9A,B), probably due to the fact that both depths are markedly affected by internal waves of similar frequencies (Fig. 3.22).

The coherent, low frequency inversions of the T/S values in the two basins are shown in Figure 33 in relation to wind speeds and along-fjord velocities in 2007. In the outer basin these oscillations are higher in amplitude from mid July through August, similar to the periods of significance shown in the wavelet spectra (Fig. 4.12 to 4.13). In the inner basin the highest amplitude changes appear to be correlated with periods of strong diurnal winds that occur in late June and mid to late August, also shown in the wavelet series. In such cases, the salinity increases but the temperature decreases, both of which being indicators of deep water exchange from the outer basin. Smaller amplitude T/S changes of the same sign also occur in mid July in the inner basin. In the outer basin, however, the response to diurnal wind periods is just the opposite, and reciprocal changes in T/S values frequently occur in relation to changes in deep properties in the inner basin. This is an indication that down-welling may occur at the reef at head of the outer basin, and the effects on vertical velocities may force dense water through the 40*m* channel on the eastern side of the reef and into the northern basin where it sinks to the level of the deep sensors. Southward (reversed) outflow of deep water could show up as the reciprocal T/S changes at the outer mooring. Advection into the inner basin may also occur during prolonged periods of down-fjord winds. The moderating factor that determines whether the water sinks or remains buoyant above the deep sensors is the density of the marine source water outside the fjord, as described above. Recent evidence from CTDs collected in August 2011 indicates that water from the Rude River can impact salinities and temperatures as deep as 60*m* across the mouth (Gay, 2013).

6. Summary and conclusions

This chapter describes additional features of circulation and water exchange at Simpson Bay determined by time-series analyses of moored T/S data in 2007 and winds in both 2007 and 2008. Power spectra and wavelet analyses performed on all the data show low frequency oscillations (64-256*hr*) occur in near-surface physical properties in the outer basin that are highly coherent ($\gamma^2 > 0.7$) with those of the inner basin just north of the sill, indicating that regular periods of surface water exchange occur between the two basins. Diurnal winds also play a role in forcing surface exchange into the fjord, as suggested by coherence of physical properties both at low frequency periods (2-5*d*) (Fig. 4.8) and for near-surface salinity in the main (outer) basin at diurnal periods, and for both temperature and salinity in the northern basin (Table 4.2). The duration and strength of the winds varies annually (Figs. 3.8 and 3.9) as do other meteorological conditions, such as air temperatures and precipitation (Fig. 3.6). The diurnal component explains ~59% of the variation in along-fjord winds during periods when the directions are predominately up-fjord. However, the percentage of variance explained by diurnal T/S components during the same periods is negligible (1.7-3.7%), and even though they are coherent this means that much of the wind effects on physical properties are contained within the low frequency variation in both the near-surface and deep layers.

In both the inner and outer basins the deep T/S series exhibit marked spectral peaks at semidiurnal periods associated with tides and internal waves, but the outer basin also has significant power for low frequency events (128*hr*) linked to periods of water exchange from outside the fjord. Variation in the marine source water entering the fjord further complicates the response patterns of the near-surface physical properties in both basins. These differences are apparent in patterns in near-surface properties changing from being cool and saline when sources are from PWS (i.e. western Orca Bay) to slightly warmer and fresher when advection is from the east (i.e. Rude River water). Glacial water in the Rude River plume is a surface discharge that is advected over 18*km* before reaching Simpson. This causes some vertical diffusion in the fresh layer but it also traps heat due to the enhanced buoyancy (T. C. Royer, pers. comm.). Due to the latter, the effects of wind mixing are also limited to the near-surface layer as in certain Canadian and Norwegian fjords (Stacey, 1999; Svendsen and Thompson, 1978). Conversely, when winds predominately blow out of the fjord over a period of days the response appears to be baroclinic reversals beneath a surface outflow where the wind energy is trapped. This causes a reciprocal pattern in the T/S variation in both basins relative to periods of mild up-fjord winds.

Deep salinity changes in both basins are also coherent at periods of 36 to 64*hr* and at semidiurnal periods. The wavelet spectra show episodes of T/S perturbations at the above periods in which increases in deep density in the northern basin occur due to advection of saline water from the outer basin related to periods of both down-fjord and up-fjord (diurnal) winds.

CHAPTER V

SUMMARY AND CONCLUSIONS

1. Estuarine conditions of PWS fjords

The first part of this dissertation addresses differences in estuarine conditions in the spring and summer among small fjords in Prince William Sound (PWS), Alaska. Principal component (*PC*) analysis is performed on monthly anomalies of relative freshwater contents (*FWC*) to quantify the variance in the estuarine conditions among sites. Least squares regression is also performed to compare the mean *FWC*s integrated over the upper 60*m* with watershed to fjord surface area ratios (WSR) and watershed areas and maximum elevations. The *FWC*s are based on reference values equal to the maximum salinity at 100*m* found from hydrographic data within all fjords in a given month. The latter depth was chosen since it is the approximate level of annual minimum density variation in PWS used in descriptions of deep water exchange (Muench and Heggie, 1978) and calculations of dynamic topography and geostrophic-baroclinic flows (Niebauer *et al.*, 1994; Vaughan *et al.*, 2001).

The results of the regressions show that outliers consistently affect the relationships between estuarine conditions and WSRs, and the latter are statistically significant only when fjords having atypically high or low *FWC*s are omitted from the analyses. For western PWS (Fig. 2.16), this required omitting only one site in both May and June 1994, but in July, many of the sites surveyed in the extreme southwest with small to moderate WSRs exhibit highly varied estuarine conditions, hence there is no evident relationship between freshwater input and the watershed characteristics. A similar situation occurs for July 1996 (Fig. 2.17) when *FWC*s over a broad spectrum of fjords are compared with either watershed areas, maximum elevations or the WSRs.

In some cases, the above poor relationships can be traced to intrinsic factors within specific watersheds, such as the large interior lagoon at Eshamy or system of lakes at Galena that may delay maximum surface freshening and possibly also cause preheating prior to discharge into the fjord basins. In contrast, other sites such as Main, Jack and the fjords located on the northwestern side of Knight Island, all exhibit estuarine conditions roughly in accordance to their watershed topography, hydrology and WSRs. The most extreme cases, however, are the fjords affected by allochthonous glacial water, which consistently exhibit much higher *FWC*s than expected.

The *PC* analyses provided further clarity to the situation by quantifying the wide range of T/S conditions among fjords, and showing that > 90% of the variance in salinity and *FWCA* occur in two statistical modes respectively representing: 1) the magnitude of freshening from all sources, including local runoff, direct precipitation and advection from outside fjord systems, and 2) the vertical structure of *FWC* as a result of processes such as stratification, mixing, interleaving (due to advection) and internal waves. For example, fjords such as Eshamy and Jack have large positive mode 1 and 2 *PC* amplitudes (*PCA*s) indicating they are well stratified from high amounts of local freshwater overlying saltier subsurface water, whereas fjords with large positive mode 1 and negative mode 2 *PCA*s, such as Whale, Bainbridge and Eaglek are less stratified since much of the high *FWC* at these sites is due to subsurface advection of extraneous freshwater. Interleaving of baroclinic tidal flows at Whale was documented in 1996 by Gay and Vaughan (2001) and the dynamics of this process for Simpson is described in chapter III. In contrast, sites with large negative mode 1 *PCA*s, such as the western side of Knight Island (sub-region 1), southwestern PWS (sub-region 5) and eastern PWS (sub-region 8) are typically brackish to salty throughout the water column, but the mode 2 amplitudes vary in sign depending on extent of deep mixing (i.e. if some deep freshening exists mode 2 will be negative and vice versa for very salty conditions).

The vertical structure of temperature anomalies (*TA*) is much more complicated, and at least three statistical modes are required to explain > 90% of the variance. The causes of this include differences in solar heating (i.e. local climate) and the effects of cold alpine runoff and cold subsurface water advected from tidewater glacial fjords. The glacially derived water creates both surface temperature inversions and sub-surface minima and maxima. Sub-regions influenced by this type of advection typically exhibit large positive mode 1 amplitudes of *FWCA* and negative mode 1 *TA* amplitudes.

The flow of glacial water within PWS, shown schematically in Figure 1.4, is inferred from the MODIS satellite image in August 2003 (Fig. 1.3). Many of the flow patterns in these two figures corroborate the results of the *PC* analyses, showing turbid glacial water moving westward in the northern Sound and southwards in western PWS as a quasi coastal current. Advection from the tidewater glacial regions is also quite evident, and the *PC* analyses in 1994 show subsurface freshening (most likely from Icy Bay) influencing hydrographic conditions in the southwestern Sound as far south as Flemmng I. and possibly to N. Elrington Pass and Sawmill Bay. In 1996 and 1997, fjords affected by glacial advection, such as Eaglek and Whale, exhibit consistently high *FWCA*s due to surface and subsurface freshening, and in 1996, high subsurface *FWC* in Dangerous Pass and the outer basins of Ewan and Paddy Bay (shown by *PCA*s of mode 1 > 0 and mode 2 < 0) indicate that advection potentially also occurs from glacial regions to the north. In 1994, similar subsurface conditions were observed in the northwest at Perry Pass.

In Figures 1.3 and 1.4, Copper River (ACC) water can be seen moving northward through HE and retroflection of this water is shown by anticyclonic eddies in the turbid water. This type of flow, also observed by Halverson *et al.* (2013) and predicted by a circulation model by Bang and Mooers (2003), may cause intrusions of ACC water into the mouth of Zaikof, shown periodically in the *PCA*s as relatively brackish subsurface water at the mouth (mode 2 < 0). Also shown in the schematic is Rude River water propagating westward towards Simpson. The effects of this water on the hydrography at the latter fjord are described in detail in chapter IV.

In conclusion, although many fjords located within the same geographical sub-regions have similar patterns of heat and freshwater input due to shared climatic and watershed characteristics, the freshwater content among individual basins is highly influenced by local topographic factors such as basin and watershed aspects, hydrology, and the *WSR*s. Furthermore, the outflow (and inflow) of relatively fresh surface and subsurface glacial water not only influences circulation in northern and western PWS (Okkonen and Belanger, 2008) but also the hydrography of many small fjords and nearshore sites along its path.

2. Circulation and water exchange at Simpson Bay

The second portion of the dissertation describes patterns in circulation and water exchange at Simpson Bay, a small subarctic fjord located in eastern PWS (Figs. 2.1A and 3.1). In many respects, the drivers of circulation at Simpson and other PWS fjords differ from those of large fjord systems, such as in Scandinavia and western Canada. This is due primarily to the fact that freshwater input within the small subarctic basins of PWS is scattered more as a line source from small streams rather than large fluvial point sources; the latter normally driving estuarine (gravitational) circulation (Farmer and Freeland, 1983). The dispersed freshwater discharge and small volume relative to large macrotidal tidal ranges causes the latter to be the principal forcing mechanism of circulation and water exchange. This is shown by an imbalance in the baroclinic exchange flows that strongly favor the flushing of Simpson Bay's lower basin during flood tides (Table 3.2 and Figs. 15 and 16). Furthermore, the low frequency changes in near-surface physical properties in the outer basin are highly coherent with those of the inner basin just north of the sill, indicating that regular periods of surface water exchange occur between the two basins. This is also inferred by statistically significant low and high frequency T/S variation in the power spectral density (Figs. and wavelet spectra (.

Diurnal winds (Figs. 4.1 to 4.3) also play a role in forcing surface exchange into the fjord, as suggested by coherence of physical properties in both basins at low frequency periods (2-5*d*) (Fig. 4.8) and for near-surface salinity in the main (outer) basin at diurnal periods (Table 4.1), and for both temperature and salinity in the northern basin (Tables 4.1.and 4.2). The duration and strength of these winds varies annually (Figs. 3.8 and 3.9) as do other meteorological conditions, such as air temperatures and precipitation (Fig. 3.6). The diurnal component explains ~ 59% of the variation in along-fjord winds during periods when the directions are predominately up-fjord. However, the percentage of variance explained by diurnal T/S components during the same periods is negligible (1.7-3.7%), even though they are coherent (Table 4.2), and this means that much of the wind effects are likely contained in the low frequency variation of the T/S properties in both the near-surface and deep layers.

Variation in marine source water entering the fjord further complicates the response patterns of the near-surface physical properties in both basins. These differences are apparent in patterns in near-surface properties changing from being cool and saline when sources are from PWS (i.e. western Orca Bay) to slightly warmer and fresher when advection is from the east (i.e. Rude River water). Advection of this glacial water (Fig. 1.3 and 1.4) begins as a surface discharge and propagates over 18*km* before reaching Simpson, which causes some vertical diffusion in the fresh layer but it also traps heat due to the enhanced buoyancy (T. C. Royer, pers. comm.). Due to the latter, the effects of wind mixing are also limited to the near-surface layer as in certain Canadian and Norwegian fjords (Stacey, 1999; Svendsen and Thompson, 1978). Conversely, when winds predominately blow out of the fjord over a period of days the response appears to be baroclinic reversals beneath a surface outflow where the wind energy is trapped. This causes a reciprocal pattern in the T/S changes in both basins relative to periods of mild up-fjord winds.

Internal waves at Simpson Bay with the same frequency as the semidiurnal tides (Stigebrandt, 1976) are evident in vertical displacements of isohalines over consecutive tide cycles (Fig. 3.18). They also appear to have a similar scale to waves shown in a numerical model of Loch Torridon, Scotland (Gillibrand and Amundrud, 2007), with maximum deep amplitudes of 10 to 20*m* inferred from the isotherm displacements (Fig. 3.22A,B). Froude numbers for both basins at Simpson (Table 3.4) are highly subcritical (<< 1.0), indicating that none of the long waves should be trapped by topography. The growth and propagation of these waves, however, appear in the near-surface currents as regions of slack water occurring concurrently with a break-down of the tidal jets that commence at the onset of the flood and ebb tides (Fig. 3.11a,f,h,kl,n), giving Simpson a mixed classification as that of a jet and a wave fjord (Stigebrandt and Aure, 1989).

Calculations of vertical diffusivity in the deep water of both basins and work performed against buoyancy relative to tidal energy available to internal waves show that changes in deep density occur over sequential tide cycles and longer (monthly) periods that cannot come solely from vertical mixing beneath the pycnocline. The short term fluctuations in density between tide phases are probably in part artifacts of the internal waves themselves, but the high efficiencies shown by large flux Richardson numbers (R_f) indicate that other processes, such as advection by deep baroclinic inflows, play a role in increasing deep density over time within the outer basin. In contrast, the deep density in the inner basin decreases over time, despite periodic intrusions of salty water. The R_f values in the inner basin indicate that mixing efficiencies are 10 times greater than the tidal energy available to internal waves, thus this deep freshening is must come from additional sources of local freshwater input other than surface runoff.

The outflow of freshwater laden with glacial sediments is evident from the surface turbidity in Simpson's northern basin in most months (Fig. 5.1). However, a possible source of the deep freshwater input is submarine groundwater discharge (Swarzenski *et al.*, 2009). Such water has been documented to rise from the bottom of small stream deltas in the northern basin when submerged at high tides. If similar upwelling occurs from the main river delta at the head of the fjord, it would be mixed vertically into the deep water by internal wave dissipation. The latter process is supported by observations of turbid water accumulating throughout the bottom layers in both 2007 and 2008 (Fig. 5.1). Another possible source of turbid bottom water at the mooring site (SB6b) is re-suspension of bottom sediments within the outer basin. Noll *et al.* (2008) describe these sites as potential hydraulic jumps, where evidence of scouring over obstructions to deep flow indicates a re-suspension of glacial silt deposits on the leeward sides. Re-suspension of sediments in the outer basin is evident in the turbidity data in all months, but is most obvious at station 5 in July 2007 and at station 4 in July and August 2008 (Fig. 5.1). Re-suspension of sediments by accelerated flows through the channel east of the shallow reef (Fig. 3.10A) is also a potential source of turbidity (Noll, pers. comm.). Such sediments would be advected mainly into the northern basin by the cyclonic flows around the reef (Fig. 3.11), and when accompanied by intrusions of dense salty water (Figs. 4.13 and 4.17) these sediments would sink into the deep region behind the reef.

3. Water exchange in relation to phytoplankton biomass and larval transport

3.1. Phytoplankton biomass

One of the objectives of the research in 2007 and 2008 was to compare the oceanographic conditions within two highly dissimilar juvenile herring nursery fjords: Simpson and Whale Bay (Fig. 3.1). Gay and Vaughan (2001) show that these two fjords differ considerably in terms of geographic location, bathymetry, local climate, watershed hydrology and effects of allochthonous glacial water (described also in Chapter II) and, therefore, they also exhibit significant variation in physical properties, circulation and water exchange.

At Whale, for example, the currents in the upper layer are dominated by offshore density gradients that force upper layer baroclinic flows into the fjord during ebb tides (Gay and Vaughan, 2001). Due to Whale's much deeper (300*m*) outer basin and the lack of an entrance sill, these inflows can reach 40+*m* in depth and the outflow from the fjord occurs in a deep 60 to 90*m* layer. In 2008, similar inflows at Whale were observed from ADCP transects (Gay, 2011a), but the glacial water is more concentrated in the near-surface layer causing shallow turbidity in the outer basin (Fig. 5.2). This in turn appears to reduce primary productivity in the outer fjord in comparison to the inner basin (Fig. 5.3).

At Simpson, the water exchange process is facilitated by tidal jets, internal waves and anticyclonic and cyclonic eddies located at the mouth and around the shallow mid-fjord reef respectively (Fig. 3.11). Diurnal winds (described in Chapters III and IV) also markedly affect surface transport, and this factor in conjunction with the smaller basin volumes and high flushing rates (Table 3.2) are probably responsible for the significantly higher phytoplankton biomass in comparison to Whale in 2008 (Fig. 5.3). The outer basin at Simpson also has a relatively lower turbidity, hence the effects of light inhibition on phytoplankton growth are nil (Quigg *et al.*, 2013). The marked differences in chlorophyll between the two fjords continue throughout the summer of 2008, and in late August the phytoplankton biomass appears to intensify again at Simpson to 4-5 $\mu g\ l^{-1}$. The latter increase in chlorophyll is consistent with a late summer bloom of small diatoms observed by A. S. McInnes *et al.* (unpubl. data) (see Quigg *et al.* 2013).

In 1996, all the SEA fjords except Zaikof exhibit relatively high fluorescence in late winter (Fig. 5.4), but in the late summer and fall most sites have only scant amounts of chlorophyll. The exception is Simpson, which exhibits a mid-fall bloom (Fig. 5.5). The latter pattern is repeated at Zaikof in March 2010 (Fig. 5.6) but in April 2011, the inner basin of this fjord exhibits an extreme phytoplankton biomass (40μg l^{-1}) that exceeds all other fjords (Fig. 5.7). This bloom is quite unprecedented but diminishes rapidly over time (Campbell, 2013), however.

The water exchange at Zaikof bears some similarities to that of Simpson due to its shallow (50-60*m*) shelf and silled inner basin. However, in all months phytoplankton are well dispersed within the water column in the outer basin where the physical properties are more homogeneous due to strong vertical shear in the currents (Gay and Vaughan, 1998; 2001). Storms also result in ephemeral bursts of freshwater input within the inner basin (Gay, 2013). This input mixes rapidly, but in the spring it also imparts some stability. One of these events occurred in mid April (see Fig. 5.8). Remnants of this freshening were observed in slight haline stratification during the survey, and this early stability likely supported the large phytoplankton bloom in April.

At Simpson, maximum fluorescence in April 2011 (15μg l^{-1}) occurs in the outer basin and across the mouth similar to March 1996 (Gay, 2013). This characteristic occurs again in other months and is consistent with the water exchange mechanism observed at the mouth. It also indicates that in the late winter and spring, both nutrients and phytoplankton may be advected into the lower fjord. Exceptions to this pattern did occur in October 1996, March 2010 and August 2011 (not shown), however, and a higher biomass in the inner basin in these months further illustrates the complex interrelationship between hydrodynamic, nutrient and biological controls of primary productivity (Quigg *et al.* 2013).

At Whale and Eaglek the phytoplankton in April 2011 are distributed in narrow depth bands (Fig. 5.5). Whale has the lowest maximum fluorescence of all sites (12μg l^{-1}) but this occurs mostly in the outer basin. Eaglek, by contrast, has one profile in the inner basin showing high fluorescence (40μg l^{-1}) and biomass over the remainder of the fjord is relatively sparce. Since turbidity from glacial advection at Whale is limited in the spring the higher fluorescence in the outer basin in 2011 could be from productivity outside the fjord. This is also suggested by the distribution of fluorescence in March 1996. In more recent years, however, the largest spring blooms tend to occur within the southern (inner) basin (Campbell, 2013), and this may have some relationship to recent observations of increased intrusions of glacial water (Gay, 2013).

At Eaglek, moderate fluorescence is distributed through most of the fjord in 1996 and 1997, closely following T/S fronts that develop towards the mouth. The exchange process at this fjord is highly uncertain due to marked spatial variation in the currents (Gay and Vaughan, 1998). However, the bloom conditions appear to be changing, and in recent years relatively high phytoplankton biomass occurs mainly in the inner basin, and occasionally near the mouth. This may be related to increased stratification at all sites in general, which is discussed further below.

3.2. Larval transport and retention mechanisms

Another physical feature of Simpson Bay that may be very important biologically is a potential mechanism of advection of larval herring into the nursery area of the northern basin. A key part of this mechanism is the up-fjord winds in relation to the westerly wind field in Orca Bay. The latter may be the primary mode of transport of herring larvae from the closest major spawning site, located in the western side of the mouth of Port Gravina (Fig. 2.1A). For example, during years when westerly winds occur in high frequency in Orca Bay, as indicated at the MidSound Buoy in June 2007 (Fig. 4.3), herring larvae are probably advected from the spawning areas eastward into Orca Bay. If they reach the mouth of Simpson then surface currents generated by diurnal winds would create a natural mechanism of transport into the fjord, particularly if they remain in the surface layer, which is where they are typically found (E. Brown, pers. comm.). Age 0 herring could also be advected by the system of surface jets and eddies that develop through the tidal cycles. In this case, the herring may exhibit selective tidal transport (Townsend *et al.,* 1986) and thus be advected up-fjord by the flood tide jets and then continue into the northern basin by taking advantage of the cyclonic eddy at the reef. A caveat to this is a tradeoff between the meteorological conditions favorable to eastward transport of age 0 herring into Simpson Bay that are possibly not conducive to production of ample zooplankton food sources. Thus a high mortality rate of age 0 herring could occur due to food competition and low lipid reserves in the following winter (Norcross *et al.*, 2001).

The question of whether retention mechanisms function within the bays and fjords of PWS originated from the past research within the Gulf of Maine and Britain, which points to the importance of tidal mixing and frontal formation within these regions on stocks of Atlantic herring (*Clupea herringus*). Iles and Sinclair (1982) suggest that the size of individual adult spawning populations of Atlantic herring are determined by the geographic area of the tidally mixed regions and that they serve as important retention areas of the larvae. However, a study of larval drift within the Gulf of Maine by Townsend *et al.* (1986) indicate that herring larvae are gradually dispersed from spawning areas into stratified regions farther inshore by the residual (nontidal) flow. These authors found that abundance of zooplankton within the stratified regions is much greater than concentrations within the tidally mixed regions and, therefore, the dispersal of larval herring from the spawning sites is highly advantageous to their growth and survival.

In PWS, larval drift of newly hatched herring occurs from tidally mixed spawning regions located along the northwestern coast of Montague Island and the aforementioned area at Port Gravina (Fig. 2.1A). Advection of these larvae into various bays and fjords was investigated during the SEA program (Norcross *et al.*, 2001). Although the advective mechanism causing initial dispersal from the main spawning aggregations remains uncertain, features of circulation within fjords such as Simpson and Whale indicate that mechanisms of retention may exist in the form of flow reversals over depth. Frontal formation within the outer basins of Whale and Eaglek (Gay and Vaughan, 2001) may also serve to retain locally spawned fish. At Zaikof, however, this same feature occurs from strong cross-channel flows intruding from Hinchinbrook Entrance. Although the currents during the flood tide are conducive to transporting fish into mid-fjord, the ebb flows could in fact inhibit advection by trapping fish in anticyclonic eddies that form at the mouth (Gay and Vaughan, 2001). Also, in contrast to the layered inflows at Simpson and Whale, larvae entering Zaikof would be subjected to strong vertical current shear. As such, they would need to quickly reach the sheltered waters of the silled inner basin or risk being swept back out of the bay. For this very reason, age 0 herring reside within the inner basins of all nursery fjords (Stokesbury *et al.*, 2000) where currents are relatively weak (Gay and Vaughan, 2001).

4. Recent and future work

4.1. Moored CT deployments from 2010 to 2012

The most recent research of juvenile herring nurseries involves deployment of CT moorings in the inner basins of the four SEA fjords (Fig. 3.1) from March 2010 to May 2012. The mooring designs are similar to the deployments at Simpson and in 2007 (Fig. 3.5) and at Whale in 2008 (Gay, 2011a). In addition, hydrography data were collected twice each year during maintenance cruises, typically in late winter/spring (March-May) and summer (August). The results of this work are summarized in a final report to EVOSTC (Gay, 2013).

The time-series of T/S data from this research are shown for the near-surface and deep sensors in Figure 5.8. In all cases, there is a similar general response in the hydrography to the annual meteorology but significant differences ($p<0.05$) occur among sites. For example, mean surface temperatures in the summer (June to September) are higher in 2011 (12.1-15.1^{o}C) in comparison to 2010 (10.8-13.4^{o}C). Surface freshening is also slightly greater in 2011, but the mean salinities have a similar range among sites each year (22.9-29 vs. 23.6-28.8). In winter, the minimum surface temperatures decrease each year, with ranges of 3 to 4.25^{o}C in 2010 falling to 0.25 to 2.5^{o}C in 2012. The hydrographic profiles from CTD casts show similar variation in T/S properties among the four nurseries in both summers and in late winter to spring. However, there are significant differences between years at all sites, particularly in temperature minima and maxima in the summer signifying the presence of subsurface glacial water at Whale and Eaglek.

The effects of tides in each series appear as high frequencies in the background, but at Eaglek and Whale these signals have relatively high amplitudes that contribute to substantial variation in the physical properties. This is illustrated in both plots of power spectra (not shown) and normalized autocovariance functions (Fig. 5.9), and it effectively shortens the integral time scales at these two sites in comparison to the other two basins. Episodic perturbations similar to Simpson in 2007 also occur with periods on the order of weeks. These fluctuations are possibly linked to changes in offshore T/S conditions during large-scale meteorological events in the Sound. As shown from the work at Simpson, this water may be advected into fjords by enhanced baroclinic currents during fortnightly tides or periods of sustained winds.

In the deep sensors, the amplitudes of the seasonal and intermediate signals are highly dampened relative to those of the near surface layer: the exception being for intermediate frequencies at Eaglek in 2011. However, whereas the two shallow basins (Simpson and Zaikof) exhibit nearly monotonic subsurface warming in early spring, the two deep fjords (Eaglek and Whale) have relatively constant T/S properties until late summer. At this time, there are at least three large-scale perturbations in deep temperature at Eaglek in 2011 that continue into mid fall. In each of these events, subsurface warming is accompanied by freshening. Whale exhibits similar patterns in deep T/S conditions 2011, albeit at much lower amplitudes. However, in 2010 there is only one of these events at both fjords.

The deep T/S changes at the above two fjords are possibly linked to broad scale storms within PWS. For example, the marked perturbations in the fall of 2010 took place during a storm that lasted from 3 to 4 days. This was indicated by high wind speeds at the MidSound Buoy that reached gusts ~20$m\ s^{-1}$ (http://www.ndbc.noaa.gov/station_page.php?station=46060). In 2011, storm generated winds of similar magnitude also co-occur with the marked variations in deep T/S properties at both the above fjords (Gay, 2013).

4.2. Changes in FWC between 1996 and 2012

One of the more interesting comparisons of the recent hydrography with that of the 1990's is the pattern in freshwater content anomalies over time at the four SEA fjords. Quasi time-series of the *FWCA* profiles for these sites are shown respectively for Simpson, Zaikof, Eaglek and Whale in Figures 5.10 to 5.13. In all cases, there appear to be increases in freshwater content in more recent years and increased stratification at Simpson and Eaglek. The largest increases occur at Whale over the entire upper 60m, but increased subsurface freshening is also evident at the other fjords as well. At all sites the high *FWC* in August 1997 is an anomaly related to large increases in precipitation along with high air temperatures during that month (Gay and Vaughan, 2001). In most other months during the SEA years the FWC is lower in comparison to later years from 2007 to 2011. Another unprecedented anomaly is the large amount of freshwater at Zaikof in June 2008 (Fig. 5.10). This occurred in the inner basin and is probably related to a combination of rainfall and runoff of low elevation snowmelt, described for Simpson Bay in Chapter III. A record amount of snow accumulation of 13*m* at sea level occurred at Main Bay, Alaska from November 2011 and March 31, 2012 (http://climate.usurf.usu.edu/products/data.php). This may be a future trend in PWS, as shown by increasing precipitation over the past two decades at Main Bay, Alaska in Figure 5.14. In the figure, the precipitation from 1991 to 2000 is more evenly spread across the months, whereas from 2001 to 2010 not only does the precipitation increase, it also becomes stronger in the late fall and winter. The difference between the decadal means (39.4 vs. 46.3*cm*) is significant at the 98% level and the extreme events become more frequent. This trend is also continues into 2013 (Gay, 2013).

A climatological factor affecting Alaska, and one that is also having a major influence on extreme winter conditions at mid latitudes (Greene and Monger, 2012), is a weakening of the polar cyclonic vortex at high altitudes over the Arctic. This in turn is shifting the Arctic Oscillation (AO) to a predominately negative phase. The trigger for these changes is a loss in Arctic sea ice that has significantly increased since 2007, producing what Overland *et al.* (2008) term the recent Arctic warm trend. The reduction in ice cover results in less ice-albedo feedback and hence more solar heating of the ocean over the summers that releases the excess heat in the early fall. The net result is increased atmospheric pressure and moisture, which favor a weakening of the polar vortex and the jet stream. These conditions have less constraint on southward intrusions of cold, moist Arctic air, which can cause large amounts of snowfall along the south-central to southeast Alaskan coast, as well as over mid-latitudes of the continental US.

Of course, the short hydrographic record for the PWS fjords does not make these conclusions unequivocal, but given the above climate effects in the Arctic, such as sea ice loss, the melting of permafrost with its concomitant releases of methane (Walter *et al.*, 2010) and the rapid ablation of Alaskan glaciers (Arendt *et al.*, 2002) the hydrographic record certainly points to the possibility that climate driven changes similar to the NGOA (Royer and Grosch, 2006) are occurring within PWS. Therefore, there is a strong need for continued data collection at these sites in order to determine the actual long-term trends. The effects of increased stratification in enhancing the background baroclinic-geostrophic circulation of the Sound could also alter the through-flow characteristics and basic productivity of PWS, and where this may be heading in the future is very uncertain.

Finally, a fjord in PWS that is attracting much attention by glaciologists is the Columbia, which is forming due to the rapid retreat of the Columbia Glacier (O'Neel *et al.*, 2010; Walter *et al.*, 2010). Although the Columbia has undergone a lengthy retreat of over 16*km* since it lost hold of its terminal moraine in 1978 (Walters *et al.*, 1988) the outflow of subsurface glacial water is still quite strong, as observed recently by CTD casts performed in the new inner basin by the author in 2011 (PWSSC *Breakwater*, Spring 2012 http://pwssc.org/breakwater-2/). Future work is anticipated to include proposals to study the interrelationship of the Columbia Fjord with the oceanography of the Sound, and how the eventual loss of PWS tidewater glaciers will affect the physical properties and circulation. Other work will involve re-establishing the ADCP/CTD moorings in Hinchinbrook Entrance and Montague Strait to monitor water exchange between PWS and the Gulf of Alaska.

5. General conclusions

The following overarching conclusions are based on the results of the two major research topics regarding the physical oceanography of small fjords in Prince William Sound, Alaska:

1) The physical properties and freshwater contents of small fjords in PWS are highly varied in the late spring and summer, depending on the geographic location (affecting local climate),

topography of the watersheds (maximum size, elevations and presence of lakes and alpine glaciers), watershed ratios, circulation and inputs of allochthonous freshwater.

2) As such, most fjords with small, localized watersheds do not contribute significantly to freshwater input in the Sound in the summer and hence have little affects on the baroclinic-geostrophic flows observed in the past within PWS from drifters and ADCP data. Instead, the latter flows are governed mostly by glacial advection and freshwater dispersal from certain key small fjords with large watershed ratios (e.g. Main and Eshamy Bay).

3) Given the above constraints, the main (outer) basins of most small fjords are essentially inland extensions of PWS and behave like stratified embayments, whereas if there are secondary, silled inner basins the latter will exhibit more fjord-like dynamics due to the bulk of freshwater entering these basins and the obstruction to deep water exchange caused by the sills.

4) Due to the dispersed nature of the freshwater input (i.e. from small streams) the circulation in both types of basins is driven primarily by large tidal prisms and winds, the latter being highly variable depending on local topography and the response to geostrophic winds within PWS. The flows can be modulated by the maximum depth and presence of sills through the action of internal waves, however, and at one location, Simpson Bay, an imbalance in baroclinic tidal flows between flood and ebb tides results in net inflows and flushing of the main basin. This same process likely also occurs at other small, shallow fjords, such as Zaikof and Sheep Bay.

In conclusion, all of the above factors lead to a complex system of physical properties in secondary (and higher) basins in PWS, which range from small, brackish fjords and bays affected mainly by local watershed and climatic conditions to large, cold fjords with high subsurface freshwater inputs from basal discharge from tidewater glaciers. In between are many small basins with high subsurface freshwater contents caused by the dispersal of glacial water from large systems, such as Columbia Bay, Unakwik Inlet, College Fjord, Port Nelly Juan and Icy Bay, and others with high stratification from local runoff, such as Main and Eshamy. Due to highly varied effects of the physical oceanography on primary and secondary production in these subsystems the habitat quality for juvenile fish is also quite diverse. In addition, recent research since 2007 indicates that small PWS fjords are all becoming more stratified due to high amounts of freshwater discharge from snowmelt in late spring/early summer and later in the summer from enhanced glacial inputs. This may be a trend driven in the future by climate change in the Arctic, and the long-term effects of this on circulation in PWS are uncertain.

REFERENCES

Arendt, A., Echelmeyer, K.A., Harrison, W.D., Lingle, C.S., Valentine, V.B., 2002. Rapid wastage of Alaska glaciers and their contribution to rising sea level. *Science*, 297 (5580), 382-386.

Aure, J., Molvaer, J., Stigebrandt, A., 1996. Observations of inshore water exchange forced by a fluctuating offshore density field. *Mar. Pollution Bulletin*, 33 (1-6), 112-119.

Bang, I., Mooers, C.N.K., 2003. The influence of several factors controlling the interactions between Prince William Sound, Alaska, and the Northern Gulf of Alaska. *Journal of Physical Oceanography* 33, 19–36.

Bang, I., Vaughan, S.L., Mooers C.N.K., 2005. Initial steps toward validation of a seasonal cycle simulation for Prince William Sound circulation (flow and mass) fields. *Cont. Shelf Res.* 25 (2005), 901–934.

Bloomfield, P. 1976. *Fourier analysis of time series: an introduction.* New York: Wiley.

Campbell, R.W. 2013. PWS herring survey: Plankton and oceanographic observations. *Exxon Valdez Oil Spill Restoration Project Final Report* (Restoration Project 10100132A - retrieve from http://www.evostc.state.ak.us).

Carlson, R.F., Wagner, J., Hartman, C.W., Murphy, R.S., 1969. Freshwater studies. In: *Baseline data survey for Valdez pipeline terminal environmental data study:* 7-41. Institute of Marine Science, University of Alaska, Fairbanks, Rept. R69-17

Chris, T.M., Caldwell, D.R. 1982. Evidence for the influence of form drag on bottom boundary layer flow. *J. of Geophys. Res*, 87 (6), 4148-4154.

Colonell, J. M. 1981. Deep Water Renewal in a Subarctic Fjord. *Journal of the Waterway, Port, Coastal and Ocean Division*, Proceedings of the Society of Civil Engineers, 107 (No.WW4), 223-231.

Cooney, R.T., Allen, J.R., Bishop, M.A., Eslinger, D.L., Kline, T.C., Jr., McRoy, C.P., Milton, J., Norcross, B.L., Olsen, J., Patrick, E.V., Salmon, D., Scheel, D., Thomas, G.L., Vaughan, S.L., Willette, T.M., 2001. Ecosystem controls of pink salmon (*Oncorhynchus gorbushcha*) and Pacific herring (*Clupea pallasi*) production in Prince William Sound, Alaska: a Sound Ecosystem Assessment (SEA) synthesis. *Fish. Oceanogr.* 10 (Suppl. 1), 1-13.

Cox, W., Okkonen, S., Gay, S.M. III, Belanger, C., Mooers, C., Bang, I., Wu, I., Olsson, P., Yi, H., Musgrave, D., Statscewich, H., Whitney, J., Reed, M., Hetland, B., Watabayashi. G., Beegle-Krause, CJ., O'Connor, C. 2004. *The 2004 Lagrangian Field Experiment.* PWSSC and OSRI Report pp.108 (retrieve from http://www.pws-osri.org).

Dyer, K. R. 1997. *Estuaries: A Physical Introduction*, 2nd Ed. John Wiley & Sons, London, New York, Sydney, Toronto.

Emory W.J. and R.E. Thomson 2004. *Data Analysis Methods in Physical Oceanography*. second ed. Elsevier, Amsterdam, 638 pp.

Farmer D.M., Armi, L., 1986. Maximal two-layer exchange over a sill and through the combination of a sill and a contraction with barotropic flow. *J. Fluid Mech*. 164, 53-76.

Farmer D.M., Freeland H.J. 1983. The Physical Oceanography of Fjords. *Prog. Oceanog.* 12, 147-220.

Foy, R.L., Norcross, B.L. 1999a Feeding behavior of herring (*Clupea pallasi*) associated with zooplankton availability in Prince William Sound, Alaska. *Ecosystem Consideration in Fisheries Management. Proceedings of the International Symposium on Ecosystem Consideration in Fisheries Management. Alaska Sea Grant College Program Report No. 99–01*. University of Alaska Fairbanks, Alaska, 129–135.

Foy, R.L., Norcross, B.L. 1999b. Spatial and temporal variability in the diet of juvenile Pacific herring (*Clupea pallasi*) in Prince Willliam Sound, Alaska. *Can. J. Zool.* 77, 697-706.

Foy, R.L., Paul, A.J. 1999. Winter feeding and changes in somatic energy content for age 0 Pacific herring in Prince William Sound, Alaska. *Trans. Am. Fish. Soc.* 128, 1193-1200.

Gargett, A.E. 1984. Vertical eddy diffusivity in the ocean interior. *J. of Mar. Res.*, 42, 359-393.

Gay, S. M. III, Vaughan, S.L. 1998. Descriptive physical oceanography of bays and fjords in Prince William Sound, Alaska used as nursery habitat by juvenile Pacific Herring *(Clupea pallasi)*. *Exxon Valdez Oil Spill Restoration Project Final Report* (Restoration Project 96320-M) Prince William Sound Science Center, Cordova AK. 8**,** 94-165 (retrieve from http://www.evostc.state.ak.us).

Gay, S.M. III and S.L.Vaughan 2001. Seasonal hydrography and tidal currents of bays and fjords in Prince William Sound, Alaska. *Fish. Oceanogr.* 10 (Suppl. 1), 159-193.

Gay, S.M. III. 2008. Physical Oceanographic Characteristics of Sites in Orca Inlet Surveyed as Alternative Locations for Disposal of Fish Offal from Cordova Seafood Processors. In: Thorne *et al.*, 2008 *Impacts of Seafood Waste Discharge in Orca Inlet, Prince William Sound*. *Exxon Valdez* Oil Spill Gulf Ecosystem Monitoring and Research Project Final Report, (GEM Project 040725 - retrieve from http://www.evostc.state.ak.us).

Gay, S.M. III. 2011a. Physical Oceanographic Factors Affecting Productivity in Juvenile Pacific Herring Nursery Habitats. Final Report for Exxon Valdez Oill Spill Restoration Project Number Restoration Project Number 070817.

Gay, S.M. III. 2011b. *Annual Report to EVOS Trustee Council*, Restoration Project Number Restoration Project Number 10100132-E.

Gay, S.M. III. 2013. Physical Oceanographic Characteristics of Nursery Habitats of Juvenile Pacific Herring. *Exxon Valdez* Oil Spill Restoration Project Final Report (Restoration Project. 10100132-E, retrieve from http://www.evostc.state.ak.us).

Gillbrand, P.A., Amundrud, T.L., 2007. A numerical study of the tidal circulation and buoyancy effects in a Scottish fjord: Loch Torridon. *J. Geophys. Res.* 112 (C05030), 1-22.

Greene, C.H., Monger, B.C. 2012. An Arctic wildcard in the weather. *Oceanography*, 25 (2),7-9.

Halverson M. J., Be´langer C., Gay, S. M., III, 2013. Seasonal transport variations in the straits connecting Prince William Sound to the Gulf of Alaska. *Cont. Shelf Res.* 63 (Suppl. 15), 63-78.

Hansen, D.V., Rattray, M. Jr., 1966. New dimensions in estuary classification. *Limnol. Oceanog*. 11, 319-326.

Hetland, R.D. 2010. Estuarine Overmixing. *Journal of Physical Oceanography* 40, 199-211.

Johnson, W.R., Royer, T. C., Luick, J. L., 1989. On the seasonal variability of the Alaska Coastal Current. *J. Geophys. Res* 93, 12423-12438.

Klinck, J. K., O'Brien, J. J. , Svendsen, H., 1981. A simple model of fjord and coastal circulation interaction. *Journal of Physical Oceanography* 11, 1612-1626.

Liu, Y., Liang X.S., Weisberg, R.H., 2007. Rectification of the Bias in the Wavelet Power Spectrum. *J. Atmos. Oceanic Technol*., 24, 2093–2102.

Matthews, J.B., Quinlan, A.V., 1975. Seasonal characteristics of water masses in Muir Inlet, a fjord with tidewater glaciers. *J. Fish. Res. Bd. Canada,* 32, 1693-1703.

Motyka, R.J., L. Hunter, K.A. Echelmeyer, and C. Connor 2003. Submarine melting at the terminus of a temperate tidewater glacier, LeConte Glacier, Alaska, U.S.A., *Ann. Glaciol.*, 36, 57–65.

Muench, R.D., Nebert, D.L., 1973. Physical Oceanography, *Environmental Studies of Port Valdez*, D. W. Hood, W. E. Shiels, and E. J. Kelly, eds., University of Alaska, Fairbanks, Alaska, 103-149.

Muench, R.D., Schmidt, G.M., 1975. Variations in the hydrographic structure of Prince Sound. *Sea Grant Report R75-1.* Institute of Marine Science Report, R75-1, University of Alaska, Fairbanks, 135 pp.

Muench, R.D., Heggie, D.T., 1978. Deep Water Exchange in Alaskan Subarctic Fjords. In *Estuarine Transport Processes*. (Kjerfve, B., ed.) The Belle W. Baruch Library in Marine Science, 7, 239-267.

Mooers C.N.K, Wu X., Bang I., 2009. Performance of a nowcast/forecast system for Prince William Sound, Alaska. *Cont. Shelf Res.* 29, 42–60.

Niebauer, H.J., Royer, T.C., Weingartner, T.J. 1994. Circulation of Prince William Sound, Alaska. *J. of Geophys. Res.* 99, (C7), 14,113-14,126.

Noll C.J., Dellapenna, T.M., Gilkinson A., Davis R.W. 2008. A high resolution geophysical investigation of sediment distribution controlled by catchment size and tides in a multi-basin turbid outwash fjord: Simpson Bay, Prince William Sound, Alaska. *Geo-Mar Lett* 29, 1−16.

Norcross, B.L., Brown, E.D., Foy, R.J., Frandsen, M., Gay, S.M. III, Kline, T.C. Jr., Mason, D.M., Patrick, E.V., Paul, A.J., Stokesbury, K.D.E., 2001. A synthesis of the early life history and ecology of juvenile Pacific herring in Prince William Sound, Alaska. *Fish. Oceanogr.* 10 (Suppl. 1), 42-57.

Okkonen, S. R. and Be´langer C., 2008. Annual period temperature and salinity signals of surface waters in Prince William Sound, Alaska. *Geophys. Res. Letters,* 35, L14604.

Olsson, P. Q., Volz , K. P., Yi, H., 2003. Numerical Simulations of Coastal Wind Events in the North Gulf of Alaska. *10th Conference on Mesoscale Processes*. Amer, Meteor. Soc., Portland, Oregon. 23-27.

O'Neel, S., W.T. Pfeffer, I.M. Howat, H. Conway, 2010. Exploring tidewater glacier retreat using past and current observations at Columbia Glacier, Alaska, *American Geophysical Union Fall meeting*, 12/2010 (retrieve from http://sites.agu.org/).

Overland, J.E., Wang, M., Slao, S., 2007. The recent Arctic warm period. *Tellus,* 60 (4), 589-597.

Pickard, G.L. 1961. Oceanographic features of inlets in the British Columbia Coast. *J. Fish. Res. Bd. Canada,* 18 (6), 907-999.

Pickard, G.L. 1967. Some oceanographic characteristics of the larger inlets of Southeast Alaska. *J. Fish. Res. Bd. Canada,* 24, 1475-1505.

Pickard, G.L. 1971. Some physical oceanographic features of inlets in Chili. *J. Fish. Res. Bd. Canada*, 28, 1077-1066.

Pritchard, D.W. 1967. What is an estuary: physical viewpoint. In *Estuaries:* 3-5. G. H. Lauff (editor). American Association for the Advancement of Science Publication No. 83: Baltimore MD: Horn-Shafer, 3–5.

Royer, T.C. 1979. On the effect of precipitation and runoff on coastal circulation in the Gulf of Alaska, *Journal of Physical Oceanography*, 9, 555-563.

Royer, T.C., Hansen, D.V., Pashinki, D.J., 1979. Coastal flow in the northern Gulf of Alaska as observed by dynamic topography and satellite tracked drogued drift buoys. *Journal of Physical Oceanography* 9, 555-563.

Royer, T. C. 1982. Coastal fresh water discharge in the northeast Pacific. *J. of Geophys. Res.* 87, 2017-2021.

Royer, T.C., 2005. Hydrographic responses at a coastal site in the northern Gulf of Alaska to seasonal and interannual forcing. *Deep-Sea Research* II, 52, 267-288.

Royer, T.C., Grosch, C.E. 2006. Ocean warming and freshening in the northern Gulf of Alaska. *Geophys. Res. Letters,* 33, L16605.

Saelan, O.H. 1967. Some features of the hydrography of Norwegian fjords. In: *Estuaries:* 63-70. G.H. Lauff (ed.). American Association for the Advancement of Science Publ. No. 83.

Schmidt, G.M. 1977. The exchange of water between Prince William Sound and the Gulf of Alaska, M.S. Thesis, University of Alaska at Fairbanks, 116 pp.

Schumacher, J.D., Stabeno, P., Roach, A.T., 1990. Volume transport in the Alaska Coastal Current. *Continental Shelf Research* 9, 1071–1083.

Stabeno, P.J., Bond, N.J., Hermann, A.J., Kachel, N., Mordy, C.W., Overland, J.E., 2004. Meteorology and Oceanography of the northern Gulf of Alaska. *Continental Shelf Research* 24, 859–897.

Stacey, M.W., Stephen, P., Nowak, Z.P., 1995. A numerical model of the circulation in Knight inlet, BC, Canada. *Journal of Physical Oceanography*. 25, 1037–1062.

Stacey, M.W. 1999. Simulation of the wind-forced circulation in Knight Inlet: a parameterization of the roughness length. *Journal of Physical Oceanography.* 29, 1363-1367.

Stigebrandt, A. 1976. Vertical diffusion driven by internal waves in a sill fjord. *Journal of Physical Oceanography,* 6, 486-495.

Stigebrandt, A. 1979. Notes and Correspondence: Observational evidence for vertical diffusion driven by internal waves of tidal origin in the Olsofjord. *Journal of Physical Oceanography.* 9, 435-441.

Stigebrandt, A. 1980. Some aspects of tidal interaction with fjord constrictions. *Estaurine and Coastal Marine Science,* II, 151-166.

Stigebrandt, A., Aure, J., 1989. Vertical mixing in basin waters of fjords, *Journal of Physical Oceanography.* 19, 917– 926.

Stigebrandt, A. 1999. Resistence to barotropic tdal flow in straits by baoclinic wave drag. *Journal of Physical Oceanography.* 29, 191-197.

Svendsen, H., Thompson, R. 1978. Wind-driven circulation in a fjord. *Journal of Physical Oceanography* 8, 703-712.

Torrence, C., Compo, G.P. 1998: A practical guide to wavelet analysis. *Bull. Amer. Meteor. Soc.,* 79**,** 61–78.

Townsend, D.W., Graham, J.J., Stevenson, D.K., 1986. Dynamics of Larval Herring (*Clupea harengus*) Production in Tidally Mixed Waters of the Eastern Coastal Gulf of Maine. In *Tidal Mixing and Plankton Dynamics*. (M.J. Bowman, C.M. Yentsch and W.T. Peterson, eds.) Springer-Verlag, Berlin Heidelberg. 253-277.

Vlasenko, V., Stashchuk, N., Hutter K., 2002. Water exchange in fjords induced by tidally generated internal lee waves. *Dynamics of Atmospheres and Oceans* 35, 63–89.

Vaughan S. L., Mooers, C.N.K., Gay, S.M. III, 2001. Physical variability in Prince William Sound during the SEA Study. *Fish. Oceanog.* 10 (Suppl 1), 58-80.

Walter, F., S. O'Neel, D. McNamara, W. T. Pfeffer, J. N. Bassis, and H. A. Fricker 2010. Iceberg calving during transition from grounded to floating ice: Columbia Glacier, Alaska. *Geophys. Res. Lett*., 37, L15501.

Walter Anthony, K.M., Anthony, P., Grosse, G., Chanton, J., 2011. Geologic methane seeps along boundaries of Arctic permafrost thaw and melting glaciers *Nature Geoscience* 5, 419- 426.

Walters, R.A., Josberger, E.G., Driedger, C.L., 1988. Columbia Bay, Alaska: an 'Upside Down' Estuary. *Estuarine, Coastal and Shelf Science* 26, 607-617.

Wang, J., Moores, C.N.K., Pattrick, E.V., 1997. A three dimensional tidal model for Prince William Sound, Alaska. In: Computer Modeling of Seas and Coastal Regions III. J.R. Acinas and C.A. Brebbia (eds.) Computational Mechanics Publications, Southhampton, 95-104.

Wang, J., Jin, M., Patrick, E.V., Allen, J.R. Moores, C.N.K. Eslinger, D.L., Cooney, R.T. 2001. Numerical simulations of the seasonal circulation patterns and thermohaline structure of Prince William Sound, Alaska. *Fish. Oceanog.* 10 (Suppl 1),132-148.

Weingartner, T.J., Danielson, S.L., Royer, T.C. 2005. Freshwater variability and predictability in the Alaska Coastal Current. *Deep-Sea Research II* 52, 169-191.

Willette, T.M., Cooney, R.T., Patrick, V., Mason, D.M., Thomas, G.L., Scheel, T.D. 2001. Ecological processes influencing mortality of juvenile pink salmon (*Oncorhynchus gorbuscha*) in Prince William Sound, Alaska. *Fish. Oceanogr*. 10 (Suppl. 1), 14–41.

Wilson, J.G., Overland, J.E., 1986. Meteorology. In *The Gulf of Alaska, Physical Environment and Biological Resources.* (D.W. Hood and S.T. Zimmerman, ed.) Alaska Office, Ocean Assessments Division, National Oceanic and Atmospheric Administration, U.S. Dept. of Commerce, No. MMS 86-0095, pp. 31.

Wu, X. 2011. Transport through Prince William Sound: numerical study in a nowcast/forecast system. *Ocean Dynamics.* 61, 449–46.

APPENDIX 1

TABLES

Table 2.1 General morphometry and watershed topography for fjords surveyed within Prince William Sound, Alaska May 1994 to March 1998.

Location	***(Code)***	***Median Width (km)***	***Maximum Length (km)***	***Basin Area (km)***	***Depth[1] (m)***	***Sill Depth (m)***	***Watershed: Elevations† (m)***	***Area (km)***	***Ratio[§]***
Sub-Region 1:									
Herring Bay [f]	(HB)	3.70	9.3	20.9	230	unsilled	278-720	25.4	1.2
Lower Herring [f]	(LHB)	1.85	7.4	7.1	200	100	307-720	16.4	2.3
Drier Bay [f]	(DB)	2.80	11.1	19.1	180	40 - 60	360-887	50.9	2.7
Long Channel [p]	(LC)	0.75	6.0	---	80	unsilled	---	---	---
Mummy Bay [sf]	(MBY)	1.80	5.9	10.0	120	unsilled	580-620	25	2.5
Little Bay	(LB)	1.10	2.3	2.5	60	unsilled	240-600	12	4.8
Sub-Region 2:									
Culross Bay [f]	(CB)	0.65	3.0	1.9	170	unsilled	583-700	9.8	5.2
Southeast Perry I.	(SEP)	---	---	---	140	---	---	---	---
South Bay	(SBY)	1.85	3.2	5.3	160	unsilled	298-380	6.6	1.3
W. Twin Bay	(WTB)	0.90	5.0	4.4	80	unsilled	334-380	7	1.6
Sub-Region 3:									
Main Bay	(MB)	1.40	5.2	6.6	160	50	400-760	27.3	4.1
Eshamy Bay	(EB)	1.85	3.2	11.1	200	50 - 70	320-916	56.4	5.1
Ewan Bay	(EW)	1.00	5.6	6.8	100	unsilled	375-916	25.9	3.8
Paddy Bay	(PB)	0.74	4.1	4.6	100	unsilled	367-590	13.0	2.8
Sub-Region 4:									
Nassau Fjord	(NF)	1.90	5.4	~10.3	350	20 - 30	900-1800	---	---
Icy Bay	(IB)	1.80	18.5	~33.0	200	30	same as abov	> 500	12.0
Whale Bay	(WB)	2.80	11.6	25.7	300	unsilled	450-890	54.1	2.1
Bainbridge	(BP)	2.00	6.3	18.8	340	unsilled	400-800	50	2.6
N. Flemming I.	(FI)	---	---	---	120	---	---	---	---
Sub-Region 5A:									
U. Prince of Wales Pass	(PWP)	3.00	10.0	---	200	unsilled	---	---	---
Shelter Bay	(SHB)	0.50	4.6	6.0	100	unsilled	240-310	15	2.5
Sawmill Bay	(SM)	0.70	4.8	5.7	160	40-70	390-595	10.9	1.9
N. Elrington	(NEP)	2.00	5.0	---	130	unsilled	---	---	---

Table 2.1 Continued

Location	*(Code)*	*Median Width (km)*	*Maximum Length (km)*	*Basin Area (km)*	*Depth[1] (m)*	*Sill Depth (m)*	*Watershed: Elevations† (m)*	*Area (km)*	*Ratio§*
L. Bainbridge Pass	(LBP)	0.50	10.0	---	150	20 - 30	---	---	---
N. & S. Twin Bays	(TBS)	1.2-1.4	2.3-2.8	6.4	70	unsilled	300-550	4.9	0.8
Hogg Bay	(HGB)	2.85	7.0	20.0	200	unsilled	400-600	40.0	2.0
Sub-Region 6									
Eaglek Bay	(EGB)	3.70	14.4	50.0	200	50 - 100	480-1300	114.3	2.3
Unakwik (ib)	(UI)	1.86	15.7	~23.2	300	4 - 10	1200-2100	>460	17.0
Unakwik (ob)	(UI)	3.48	14.8	~51.5	280	unsilled	300-750	47.0	0.9
Sub-Region 7									
Jack Bay (ib)	(JB)	0.60	6.5	---	135	30	670-155	138.5	9.7
Jack Bay (ob)	(JB)	1.68	3.7	14.3	250.0	---			
Galena Bay (ib)	(GBY)	2.80	3.3		120	25	630-1790	155.1	8.5
Galena Bay (ob)	(GBY)	1.47	5.0	18.3	220.0	---			
Sub-Regions 8 and 9									
Simpson Bay	(SB)	1.70	9.5	27.9	60-80	30-60,<10	610-1542	169.8	6.1
Sheep Bay	(SH)	3.50	13.8	42.4	80	unsilled	450-1470	95.2	2.3
Port Gravina	(PG)	5.00	24.0	120.0	150-195	115 - 130	150-660	54.9	2.1
Zaikof Bay	(ZB)	3.00	12.9	26.1	100	unsilled	450-890	54.1	2.1

Legend: f = fjord, gf = glacial fjord, sf = shallow fjord, p = pass, ns = near-shore region, all other locations are classified as shallow bays, mp means sills are located at mid pass.

Basin depths are either medians or ranges for the deepest regions of main basins.

‡ Data for main basin only at WB and BP; at WB widths of NW and S arms of the fjord are 1.5 and 1.3 km respectively, and lengths are 5.9 and 7.4 km. Total length is given above; at BP widths of S arm and narrows at SW inlet are 1.5 and 0.7 km respectively, and lengths are 4.1 and 11 km. Length is from mouth to narrow outlet to the SW.

1 These fjords lack entrance sills, but have interior sills: Whale - 60m entrance to the S. Arm, Bainbridge Pass - 60 to 100m entrance to the narrow outlet to the SW and 20-30m at mid pa

^ Basin areas are combined totals for inner and outer basins.

† Elevation ranges are for the maximum heights of the majority of peaks within each watershed.

§ Watershed to fjord basin surface area ratios described in the text.

Table 2.2 Percent of variance explained by EOF modes 1 to 10 for temperature and salinity from May 1994 to August 1997.

Temperature

Mode	May 94	Jun 94	Jul 94	Jun 96	Jul 96	Aug 96	May 97	Jul 97	Aug 97
1	68.08	55.83	55.11	73.13	68.57	53.59	79.18	73.21	72.44
2	14.36	27.80	33.45	22.03	16.21	32.20	9.69	14.90	12.79
3	11.72	9.05	3.73	2.38	6.89	7.91	6.84	5.27	6.68
4	1.79	2.80	2.58	0.78	4.20	2.84	1.46	3.93	3.79
5	1.38	1.25	1.35	0.52	1.24	0.99	1.05	0.88	1.83
6	1.05	0.91	1.19	0.28	0.70	0.63	0.50	0.60	0.64
7	0.38	0.66	0.72	0.25	0.51	0.52	0.41	0.33	0.34
8	0.24	0.41	0.44	0.16	0.33	0.38	0.24	0.23	0.31
9	0.19	0.29	0.32	0.09	0.24	0.19	0.15	0.17	0.26
10	0.14	0.18	0.21	0.08	0.18	0.14	0.12	0.11	0.17
Var.*	6.34	36.47	36.44	64.05	58.11	98.63	16.65	136.97	82.64
				Salinity					
1	72.33	84.65	68.43	92.16	69.77	59.82	86.54	85.75	52.43
2	17.15	7.43	19.53	5.18	18.64	30.36	5.45	9.31	27.92
3	5.71	3.32	4.84	0.96	5.82	5.23	4.16	1.95	12.93
4	2.23	1.41	2.51	0.80	1.98	1.82	1.40	1.48	3.63
5	1.15	1.24	1.50	0.28	1.51	0.94	0.74	0.58	1.21
6	0.50	0.71	1.04	0.20	0.87	0.41	0.49	0.21	0.45
7	0.33	0.32	0.57	0.11	0.31	0.37	0.30	0.19	0.40
8	0.18	0.19	0.33	0.08	0.29	0.29	0.29	0.13	0.26
9	0.10	0.16	0.27	0.05	0.18	0.19	0.16	0.09	0.17
10	0.08	0.11	0.21	0.04	0.14	0.12	0.14	0.07	0.14
Var.*	14.70	27.46	19.73	19.69	22.12	42.15	9.59	67.61	50.49
				FWC					
1	90.43	95.97	87.55	97.63	84.99	88.00	96.81	95.99	84.66
2	7.96	2.98	10.36	1.93	13.26	9.66	2.11	3.33	10.76
3	1.08	0.66	1.43	0.24	1.25	1.89	0.75	0.43	3.72
4	0.34	0.22	0.39	0.16	0.31	0.33	0.22	0.19	0.54
5	0.12	0.11	0.15	0.02	0.11	0.06	0.07	0.04	0.21
6	0.04	0.03	0.07	0.01	0.05	0.03	0.02	0.02	0.08
7	0.01	0.02	0.02	0.00	0.01	0.01	0.01	0.01	0.01
8	0.01	0.01	0.01	0.00	0.01	0.01	0.01	0.00	0.01
9	0.00	0.00	0.01	0.00	0.00	0.00	0.00	0.00	0.00
10	0.00	0.00	0.00	0.00	0.00	0.00	0.00	0.00	0.00

*Total variance of data with means removed: Tpr, Spr and FWCpr

Table 3.1 General morphometry, survey dates, number and times of transects and CTDs.

Location within the fjord	***Median Width (km)***	***Maximum Length[1] (km)***	***Basin Area (km^2)***	***Depth[2] (m)***	***Sill Depth[3] (m)***	***Sill Width[3] (m)***
Entire Fjord	1.7	7.5	27.90	60-80	35-150	2400
Main (lower) basin	2.0	3.7	7.85	50-60	30-50	1850
Northern (inner) basin	0.9	3.5	5.66	50-80	0-40	1100

Month, Day and Tides		***Transects***	***Sections[4]***	***Start***	***End***	***CTDs***
June 21	Flood1	13	N-A	14:12	16:38	
	Flood1	13	A-N	16:39	19:08	
	Ebb1	13	N-A	19:16	22:24	10
	Ebb1	13	A-N	22:25	0:29	
June 22	Flood2	13	N-A	0:30	5:14	10
	Flood2	13	A-N	3:30	5:14	
	Flood2	13	N-A	5:19	8:17	10
	Ebb2	13	A-N	8:18	10:20	
	Ebb2	13	N-A	10:26	13:00	10
	Flood3	13	A-N	13:01	14:52	
	Flood3	13	N-A	14:53	16:54	
July 16	Flood1	17	SE1- 4,A-N	10:07	12:30	
	Flood1	13	N-A	12:32	15:00	10
	Flood1/Ebb1	12	B'-N	15:01	16:40	
	Ebb1	13	N-A	16:41	19:20	10
	Ebb1	12	B'-N	19:21	20:50	
	Ebb1/Flood2	13	N-A	20:51	23:20	10
	Flood2	12	B'-N	23:21	0:48	
July 17	Flood2	13	N-A	0:49	3:32	10
	Flood2/Ebb2	12	B'-N	3:33	5:05	
	Ebb2	13	N-A	5:06	7:00	10
	Ebb2	12	B'-N	7:00	9:00	
	Flood3	14	N-B'	9:01	11:35	10
August 18	Flood1/Ebb1	17	SE1- 4,A-N	15:43	18:20	
	Ebb1	13	N-A	18:21	20:56	10
	Ebb1	12	B'-N	21:05	22:36	
August 19	Ebb1/Flood2	13	N-A	22:37	1:26	10
	Flood2	12	A-N	1:27	3:20	
	Flood2	13	N-A	3:21	6:08	10
	Ebb2	12	B'-N	6:14	7:39	
	Ebb2	13	N-A	7:40	10:13	10
	Ebb2/Flood3	12	B'-N	10:16	11:53	
	Flood3	13	N-A	11:54	14:47	10
	Flood3	12	B'-N	14:48	16:15	
	Flood3	13	N-A	16:16	18:06	

---

[1] Maximum length is taken from the mouth at the outer shelf to the head of the Northern Arm where the river delta enters.

[2] The basin depths are ranges for bottom depths within each basin.

[3] Sill depths are ranges for the mouth, the outer sill to the Main Basin, and the shallow reef/sill at the mouth of the N. Arm.

[4] Section labels are shown in Figure 10A.Note that the SE Arm has 4 transects that were run only once per cruise.

Table 3.2 Total exchange volume, flushing rates and times for Sections B and C in 2007.

Section B

Month	*Total Exchange Volume (m^3)*	*Flushing Rate (m^3/s)*	*Transect Times: (sec)*	*(hr)*	*(days)*
June	21,411,030	194	1,418,981	394	16.4
July	150,662,700	1363	201,655	56	2.3
August	78,631,340	711	386,384	107	4.5
	Section C				
June	15,977,460	145	1,901,545	528	22.0
July	19,907,162	180	1,526,177	424	17.7
August	44,655,960	404	680,354	189	7.9

Table 3.3a Total work and tidal energy calculations in July and August 2007. Also listed are baroclinic internal wave speeds and mean tidal currents over the lower sill region.

Tidal Periods	**nW (mW/m^2)**	**nE2 (mW/m^2)**	**Rf**	**sill depth (m)**	**lower depth (m)**	**Hu (m)**	**Hb (m)**	**Ci [#] (m/s)**	**Us0 [#] (m/s)**
		Tidal energy to internal waves (E2)							
Main Basin July 2007									
F1/E1	327	1.1	294	30	48	30	20	0.523	0.024
E1/F2a	-72	0.9	-78	30	48	30	20	0.537	0.022
F2a/F2b	-91	1.0	-91	30	48	30	20	0.563	0.021
F2b/E2	246	1.3	186	30	48	30	20	0.521	0.025
E2/F3	-10	1.4	-7	30	47	30	20	0.522	0.027
F1/F3	255	1.1	233	30	47	30	20	0.522	0.025
Northern Basin July 2007									
F1/E1	-87	8.2	-11	30	75	25	50	0.747	0.10
E1/F2a	347	6.4	55	30	74	25	50	0.700	0.09
F2a/F2b	-414	6.5	-63	30	74	25	50	0.715	0.09
F2b/E2	86	8.9	10	30	64	25	50	0.724	0.11
E2/F3	592	9.0	66	30	64	25	50	0.670	0.11
F1/F3	40	8.8	46	30	73	25	50	0.704	0.11
		Tidal energy to surface jets (E2j)							
Main Basin July 2007									
F1/E1	327	4264	0.04	30	48	30	20	0.523	0.024
E1/F2a	-72	3113	-0.02	30	48	30	20	0.537	0.022
F2a/F2b	-91	3206	-0.03	30	48	30	20	0.563	0.021
F2b/E2	246	4971	0.05	30	48	30	20	0.521	0.025
E2/F3	-10	5945	0.00	30	47	30	20	0.522	0.027
F1/F3	40	4589	0.06	30	47	30	20	0.522	0.025
Northern Basin July 2007									
F1/E1	-87	9804	-0.01	30	75	25	50	0.747	0.10
E1/F2a	347	7161	0.05	30	74	25	50	0.700	0.09
F2a/F2b	-414	7374	-0.06	30	74	25	50	0.715	0.09
F2b/E2	86	11431	0.01	30	64	25	50	0.724	0.11
E2/F3	592	13672	0.04	30	64	25	50	0.670	0.11
F1/F3	401	11917	0.03	30	73	25	50	0.704	0.11
		Mean *Kv* between July and August 2007*							
Main Basin	675	0.9	750	30	48	30	20	0.570	0.02
Northern Arm	-1267	5.5	-232	30	75	25	50	0.720	0.08

[#] Internal wave speeds and mean tidal currents are based on average tidal amplitudes for semidiurnal periods

* Means for each month are tidal averages

Table 3.3b Total work and tidal energy calculations based on observations in July and August 2007. Calculations are for layers 10 to 15*m* above the bottom.

Tidal energy to internal waves (E2)

Tidal Periods	***nW (mW/m^2)***	***nE2 (mW/m^2)***	***Rf***	***sill depth (m)***	***lower depth (m)***	***Hu (m)***	***Hb (m)***
Main Basin July 2007							
F1/E1	-18.6	1.1	-16.80	30	48	40	8
E1/F2a	7.2	0.9	7.80	30	48	40	8
F2a/F2b	-42.6	1.0	-42.80	30	48	40	8
F2b/E2	54.7	1.3	41.50	30	48	40	8
E2/F3	-10.9	1.4	-7.70	30	47	40	7
F1/F3	-3.4	1.1	-3.10	30	47	40	7
Northern Basin July 2007							
F1/E1	-5.9	8.2	-0.72	30	75	65	10
E1/F2a	5.8	6.4	0.92	30	74	65	9
F2a/F2b	-17.0	6.5	-2.60	30	74	65	9
F2b/E2	2.1	8.9	0.24	30	64	60	4
E2/F3	4.1	9.0	0.46	30	64	60	4
F1/F3	-0.1	8.8	-0.01	30	73	65	8
		Mean Kv between July and August 2007*					
Main Basin	355	0.9	395	30	50	40	10
Northern Arm	-221	5.5	-41	30	75	65	10
Main Basin	229	0.9	254	30	50	45	5
Northern Arm	-59	5.5	-11	30	75	70	5

Internal wave speeds and mean tidal currents are based on average tidal amplitudes for semidiurnal periods

* Means for each month are tidal averages.

Table 3.4 Mean tidal currents, internal baroclinic wave speeds and Froude Numbers in July 2007.

Location	***Tide Phase(s)****	***Umx***[a] (c***m/s***)	***Us0***[c] (c***m/s***)	***Uva***[b] (c***m/s***)	***g'*** ***m/s^2***	***Ci***[a] (c***m/s***)	***Fr1***	***Fr2***	***Fr3***
M. Basin	Flood 1a	15.4	2.4	6.9	0.023	53.37	0.217	0.045	0.131
	Flood 1b	53.4	2.4	4.3	0.023	53.40	0.140	0.045	0.080
	Flood 1c/Ebb 1a	11.9	2.4	6.8	0.023	51.10	0.161	0.043	0.133
	Ebb 1b	19.7	2.2	9.8	0.021	51.10	0.237	0.043	0.191
	Ebb 1c	18.8	2.2	4.8	0.021	56.00	0.261	0.038	0.087
	Ebb 1d/Flood 2a	19.6	2.1	3.5	0.025	58.20	0.246	0.036	0.060
	Flood 2b	18.7	2.1	3.9	0.025	53.80	0.268	0.039	0.073
	Flood 2c	17.2	2.1	5.2	0.022	53.80	0.150	0.039	0.097
	Flood 2d/Ebb 2a	14.8	2.5	12.9	0.019	50.20	0.277	0.050	0.257
	Ebb 2b	22.2	2.5	20.2	0.019	50.20	0.421	0.050	0.402
	Ebb 2c	47.3	2.5	14.7	0.019	48.90	0.417	0.051	0.300
	Ebb 2d/Flood 3a	24.0	2.7	14.5	0.024	54.90	0.397	0.049	0.264
N. Arm	Flood 1a	21.0	10.1	6.9	0.035	76.00	0.121	0.132	0.091
	Flood 1b	20.9	10.1	6.7	0.035	76.00	0.120	0.132	0.090
	Flood 1c/Ebb 1a	15.1	10.1	6.1	0.035	73.20	0.126	0.123	0.084
	Ebb 1b	17.1	9.0	8.6	0.032	73.20	0.146	0.123	0.117
	Ebb 1c	16.6	9.0	9.6	0.032	69.10	0.201	0.130	0.139
	Ebb 1d/Flood 2a	13.1	9.0	3.1	0.029	69.30	0.124	0.130	0.045
	Flood 2b	21.6	9.0	18.5	0.029	73.50	0.278	0.123	0.252
	Flood 2c	20.3	9.0	14.5	0.032	73.50	0.223	0.123	0.197
	Flood 2d/Ebb 2a	15.3	10.6	9.5	0.032	69.90	0.151	0.157	0.136
	Ebb 2b	20.3	10.6	14.8	0.029	69.90	0.220	0.157	0.212
	Ebb 2c	28.3	10.6	13.3	0.029	68.90	0.211	0.160	0.193
	Ebb 2d/Flood 3a	12.9	10.6	6.9	0.025	63.90	0.129	0.172	0.108

---

* Tide phases correspond to ADCP transect series shown in Fig. 11.

a Means for maximum flows are for all currents > 10 cm s-1 in the Main Basin and Northern Arm.

b Surface tidal currents derived from mean tidal amplitudes as in Table 3.

c Surface currents based on the vector average flows within the respective basins.

Table 4.1 Coherence* of temperature and salinity with along-fjord winds in July and August 2007

Location	***Depth***	***T(^{o}C)*** ***γ^2***	***freq. (cpd)***	***Period (hr)***	***Phase (hr)***	***S*** ***γ^2***	***freq. (cpd)***	***Period (hr)***	***Phase (hr)***
M. Basin	3m	0.53	8.40	2.8	1.4	0.42	5.60	4.3	1.6
		0.42	7.20	3.3	0.8	0.68	1.78	13.5	4.6
		0.54	5.90	4.1	0.0	0.68	1.03	23.3	6.3
		0.47	4.90	4.9	-2.1	0.74	0.94	25.6	7.0
		0.47	3.38	7.1	-0.7	0.42	0.84	28.4	7.3
		0.46	0.19	128.0	0.0	0.41	0.56	42.7	-21.1
	40m	0.47	6.00	4.0	-0.4	0.53	8.53	2.8	-1.1
		0.47	4.80	5.0	-0.9	0.43	4.70	5.1	2.1
		0.44	1.22	19.7	-4.5	0.45	1.22	19.7	5.8
		---	---	---	---	0.41	0.19	128.0	0.0
N. Arm	2m	0.42	9.90	2.4	-0.1	0.41	8.350	2.9	-1.1
		0.42	7.90	3.0	0.1	0.49	3.840	6.2	-0.7
		0.49	7.78	3.1	0.1	0.56	3.375	7.1	-1.5
		0.59	1.13	21.3	7.6	0.41	2.160	11.1	-5.3
		0.76	1.03	23.3	8.3	0.51	1.030	23.3	-2.2
		0.42	0.94	25.6	7.7	0.43	0.750	32.0	-5.3
	70m	0.43	6.20	3.9	-1.5	0.40	8.400	2.8	0.1
		0.43	5.20	4.7	-1.4	0.71	2.250	10.7	1.3
		0.41	4.70	5.1	-1.5	0.50	0.094	256.0	0.0
		0.49	2.20	11.1	-4.8	---	---	---	---
		0.41	0.94	25.6	10.7	---	---	---	---

---

*Coherencies >= 0.4 are significant at the 95% level

Table 4.2 Coherence and phase of the diurnal components of temperature and salinity versus the winds for various depths in 2007.

Location and <u>Depth</u>		***T(^oC) γ^2***	***freq. <u>(cpd)</u>***	***Period <u>(hr)</u>***	***Phase <u>hrs</u>***
Main Basin	3m	0.40	0.6	42.7	0.0
		0.45	0.9	25.6	0.0
		0.47	1.1	21.3	3.9
		0.54	1.7	14.2	2.6
		0.45	1.9	12.8	2.3
		0.61	3.2	7.5	0.5
	10m	0.42	4.5	5.3	-1.3
	20m	0.38	4.5	5.3	-0.6
	30m	n/s	n/s	n/s	n/s
	40m	0.48	1.7	14.2	0.5
		0.40	3.2	7.2	-0.1
Northern Arm	2m	0.47	0.8	32.0	0.0
		0.57	0.9	25.6	0.0
		0.52	1.1	21.3	5.5
		0.65	1.7	14.2	3.7
		0.62	1.9	12.8	3.3
		0.68	3.9	6.1	1.3
	10m	n/s	n/s	n/s	n/s
	30m	0.39	1.5	16.0	4.2
	45m	0.58	0.8	32.0	0.0
		0.47	0.9	25.6	0.0
		0.53	1.5	16.0	-0.9
		0.49	1.7	14.2	-0.8
		0.48	1.9	12.8	-0.7
		0.44	3.2	7.5	-0.1
	70m	0.38	1.7	14.2	6.7

Location and <u>Depth</u>		***S γ^2***	***freq. <u>(cpd)</u>***	***Period <u>(hr)</u>***	***Phase <u>hrs</u>***
Main Basin	3m	0.40	0.2	128.0	0.0
		0.50	0.4	64.0	0.0
		0.88	0.8	32.0	0.0
		0.87	0.9	25.6	0.0
		0.67	1.1	21.3	8.0
		0.84	1.7	14.2	5.3
		0.84	1.9	12.8	4.8
		0.76	2.1	11.6	4.4
		0.79	3.9	6.1	2.5
	40m	0.50	1.7	14.2	-6.8
		0.38	3.2	7.5	3.6
Northern Arm	2m	0.45	0.4	64.0	0.0
		0.47	0.6	42.7	0.0
		0.63	0.8	32.0	0.0
		0.57	0.9	25.6	0.0
		0.54	1.7	14.2	-1.2
		0.43	1.9	12.8	-1.1
		0.42	3.0	8.0	-0.5
		0.50	3.2	7.5	-0.3
		0.56	3.4	7.1	-0.2
		0.57	3.6	6.7	-0.2
	70m	n/s	n/s	n/s	n/s

APPENDIX 2

FIGURES

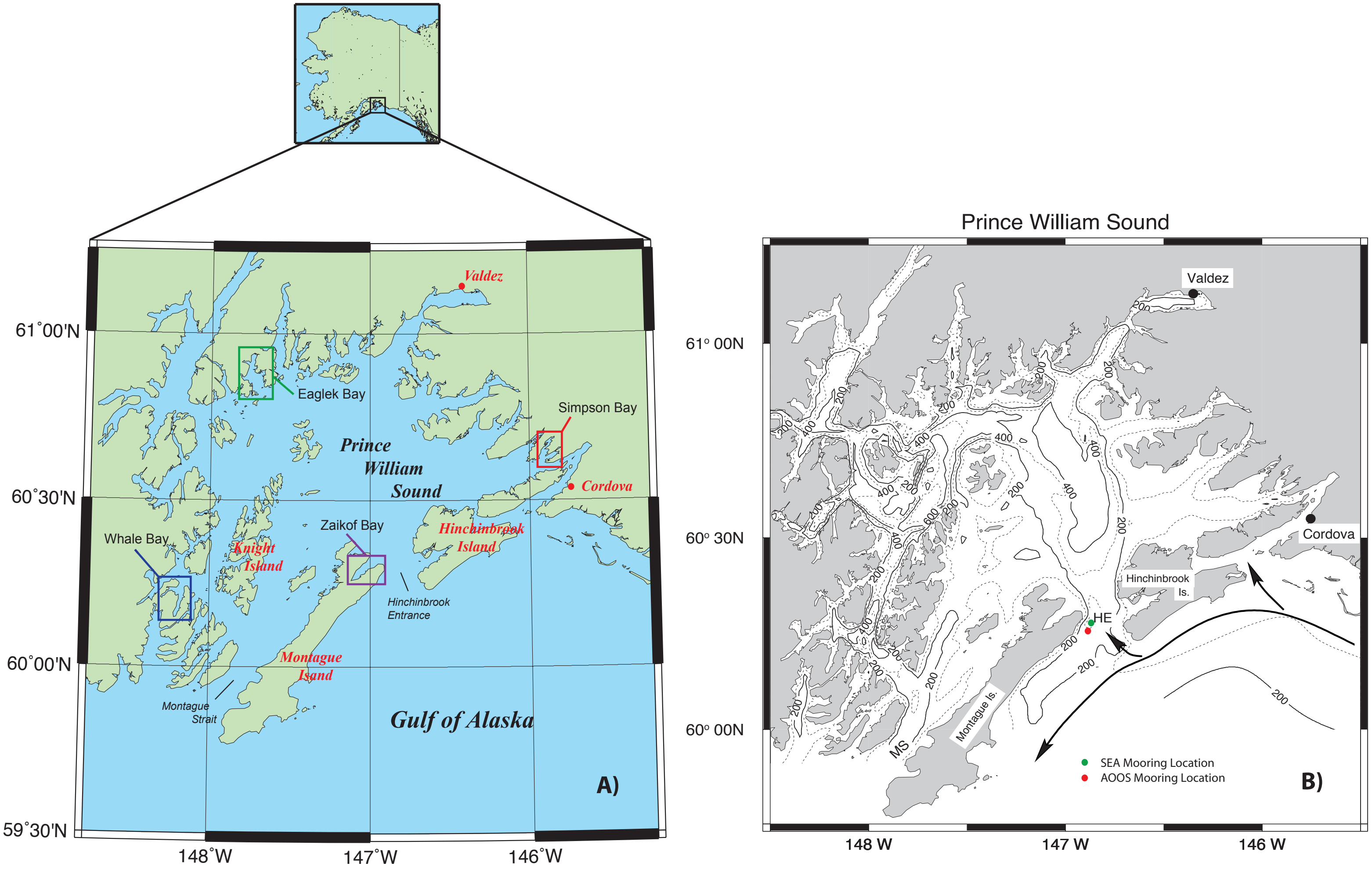

Fig. 1.1. a) Location of Prince William Sound, Alaska along the North Gulf of Alaska coast, the two major inlets (Hinchinbrook Entrance and Montague Strait) and the four fjords surveyed during the SEA program; b) Major features of bathymetry and a schematic of the ACC (Copper River water) flowing westward along the coast and into PWS.

a) Fall 2009: Nov. 5

b) Fall 2009: Nov. 6

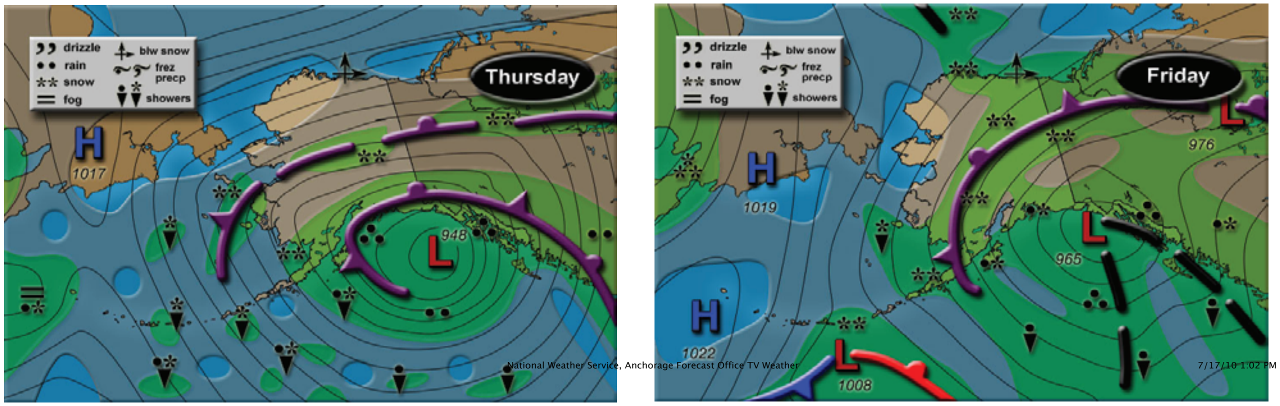

c) Late Winter 2010: Mar. 9

d) Summer 2010: July 17

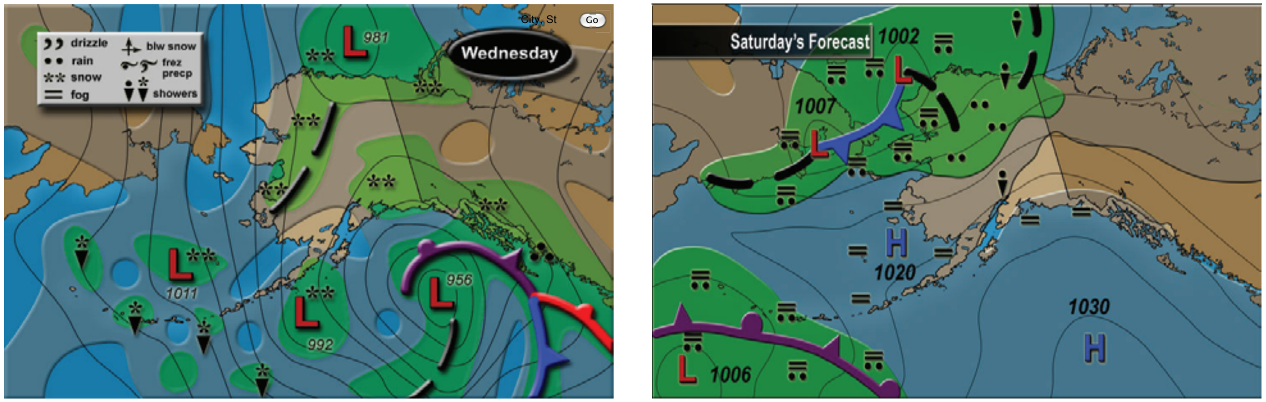

Fig. 1.2. Climatic scenarios in mid fall 2009 (a,b), late winter 2010 (c) and summer 2010 (d). Upper panels show examples of the Aleutian Low Pressure system in November, which generates cyclonic winds (≥ 20 mps) along coast. The presence of the Siberian High to the west causes southward streaming of arctic air (b). Cyclonic winds in the Gulf of Alaska are also shown in March (panel c). In the summer, (July) pressure gradients and wind speeds diminish during periods dominanted by the North Pacific High Pressure System. All images are from the National Weather Service web site (http://pafc.arh.noaa.gov/tvwx.php).

Fig. 1.3. MODIS satellite image of Prince William Sound in August 2003 showing a large extent of glacial water within the sound by late summer. Many of the features of advection described in Chapter II can be seen in the image. In particular the outflow of glacial water in western PWS emanating from College Fjord, Port Nellie Juan and Icy Bay. Note the large amount of glacial water coming from Icy Bay, extending past Prince of Wales Pass into N. Elrington Pass. Glacial outflows can also be seen in the north from Unakwik Inlet and Columbia Bay, and in the east from the Rude River. Northern inflow of Copper River water is also evident on the eastern side of Hinchinbrook Entrance , and in conjunction with southward flow from Columbia Bay the two freshwater sources create a cyclonic circulation in central PWS. *Image from the gallery of MODIS Land Response Team (http://rapidfire.sci.gsfc.nasa.gov/).*

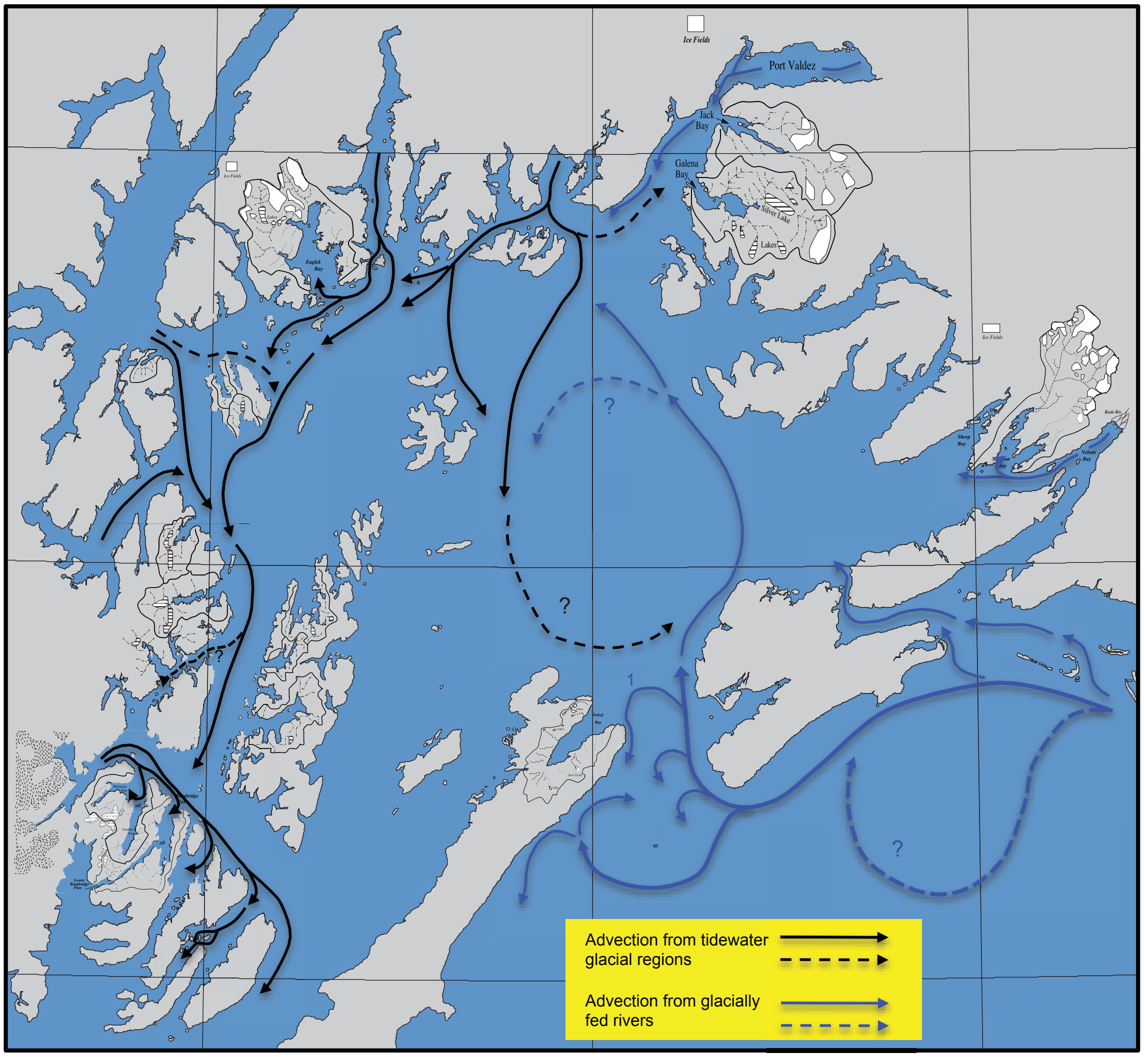

Fig. 1.4. Schematic representation of advection shown in the MODIS image in Fig. 1.3 with respect to watersheds of small PWS fjords. Advection from regions containing tidewater glaciers is shown as black arrows and flow from glacial fed rivers is shown as blue arrows. The latter include rivers emptying into Port Valdez in the north, the Rude River in the east and the Copper River to the south. Also shown are watersheds of small PWS fjords and locations that exhibit effects of the extraneous glacial water entering their basins as described in Chapter II. Dashed lines represent flows that possibly result from large scale changes in wind direction from the west (Olsson et al., 2003) or are uncertain (?) based on the satellite image. Retroflection in flows at Hinchinbrook Entrance (1) are based on the MODIS image, observations of Halverson et al. (2012) and a circulation model developed by Bang and Mooers (2003).

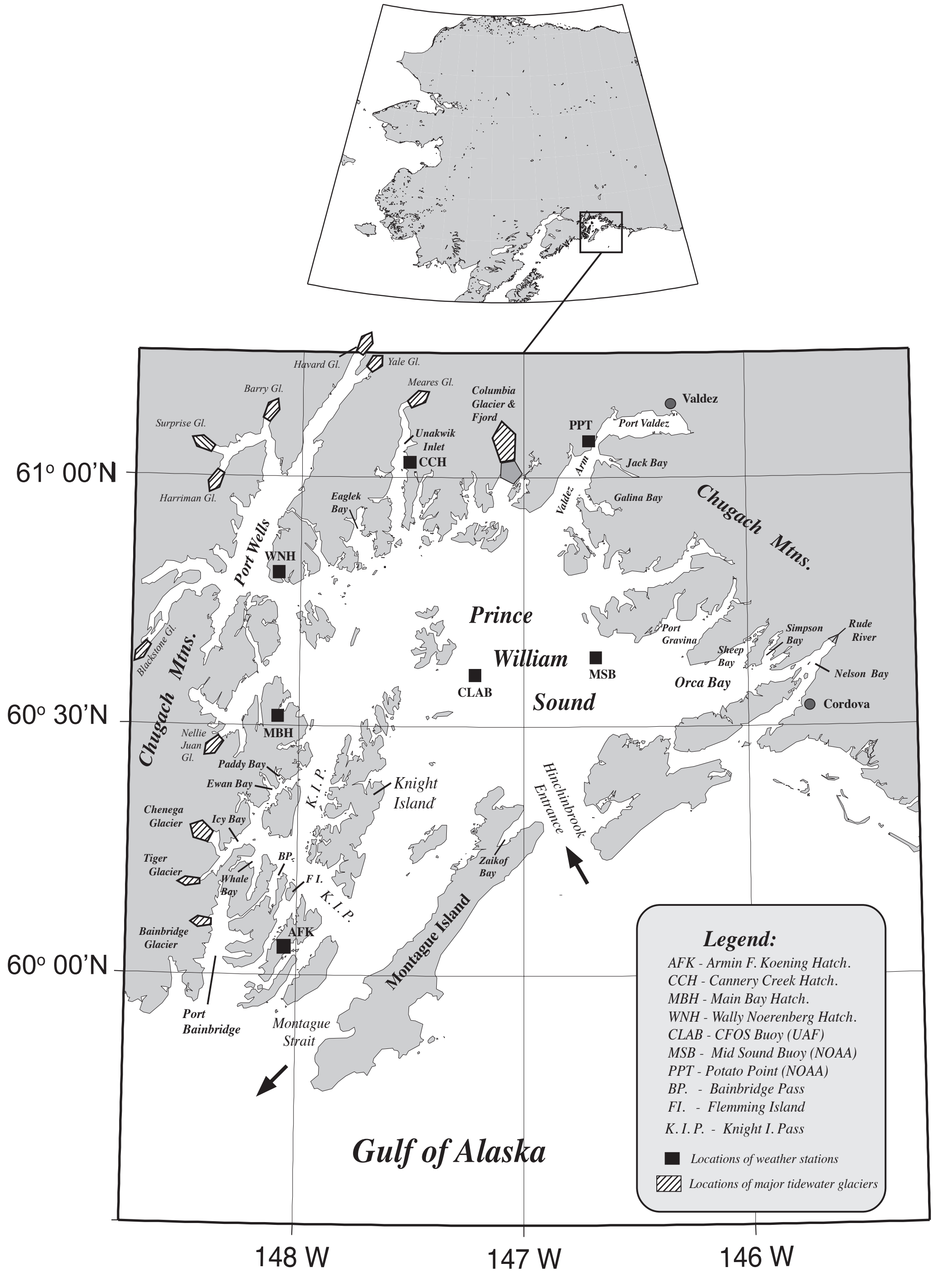

Fig. 2.1A. Location of Prince William Sound along the south-central coast of Alaska and major geographic features, including principal islands, inlets and tidewater glaciers. Also shown are weather stations and fjords surveyed from 1996 to 1998 during the Sound Ecosystem Assessment (SEA) program*. Note the large arrows denote locations of general inflow into and outflow from the sound.

*Reprinted with permission from "Seasonal hydrography and tidal currents of bays and fjords in Prince William Sound, Alaska" by Gay, S.M. III and S.L.Vaughan Fish. Oceanogr. 10 (Suppl. 1), 159-193, Copyright 2001 by John Wiley and Sons.

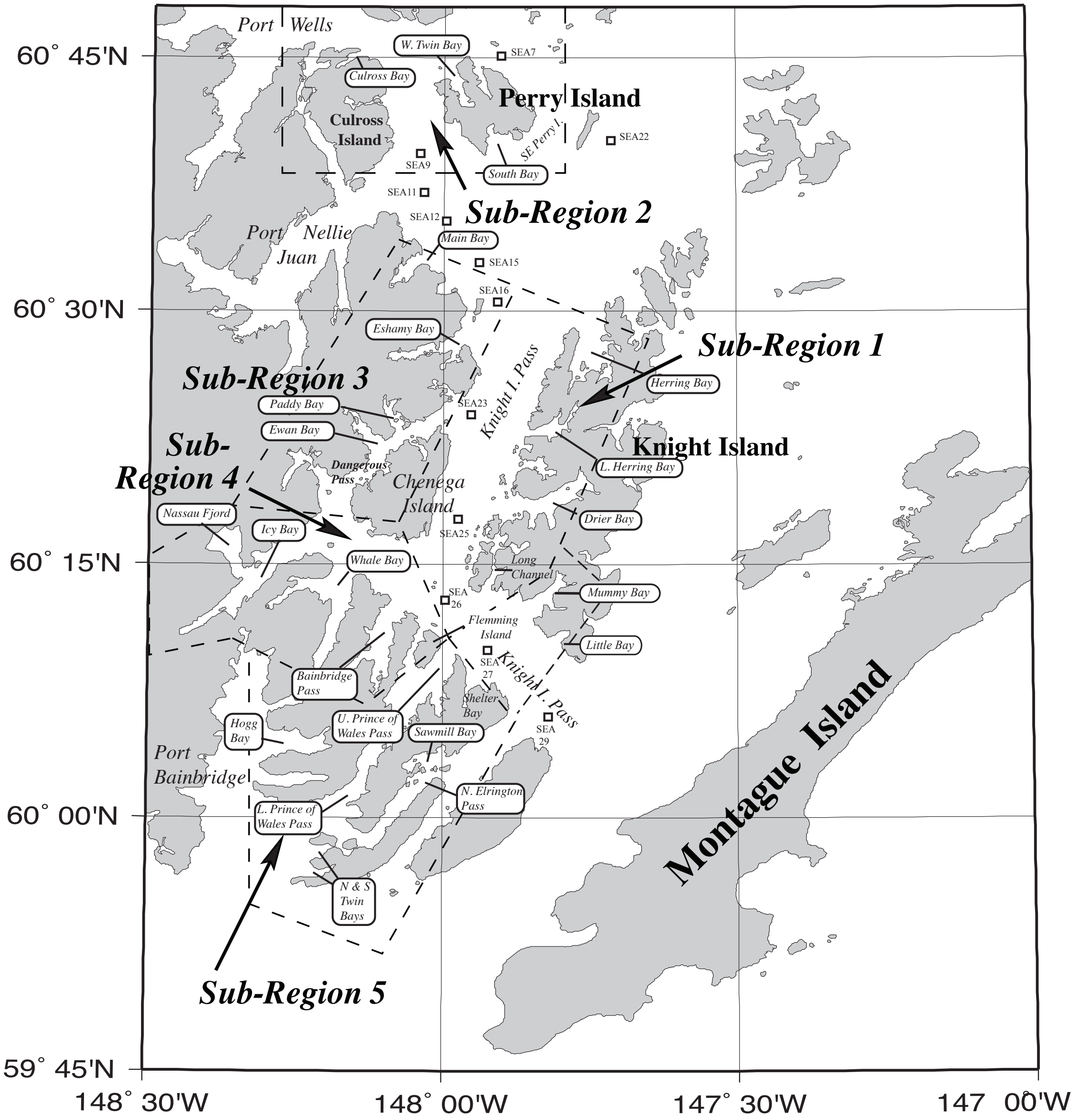

Fig. 2.1B. Locations of five sub-regions in southwestern Prince William Sound and small fjords and inlets surveyed within them in the spring and summer of 1994. Also shown are the SEA oceanographic stations established within the major passes surveyed during the same time period.

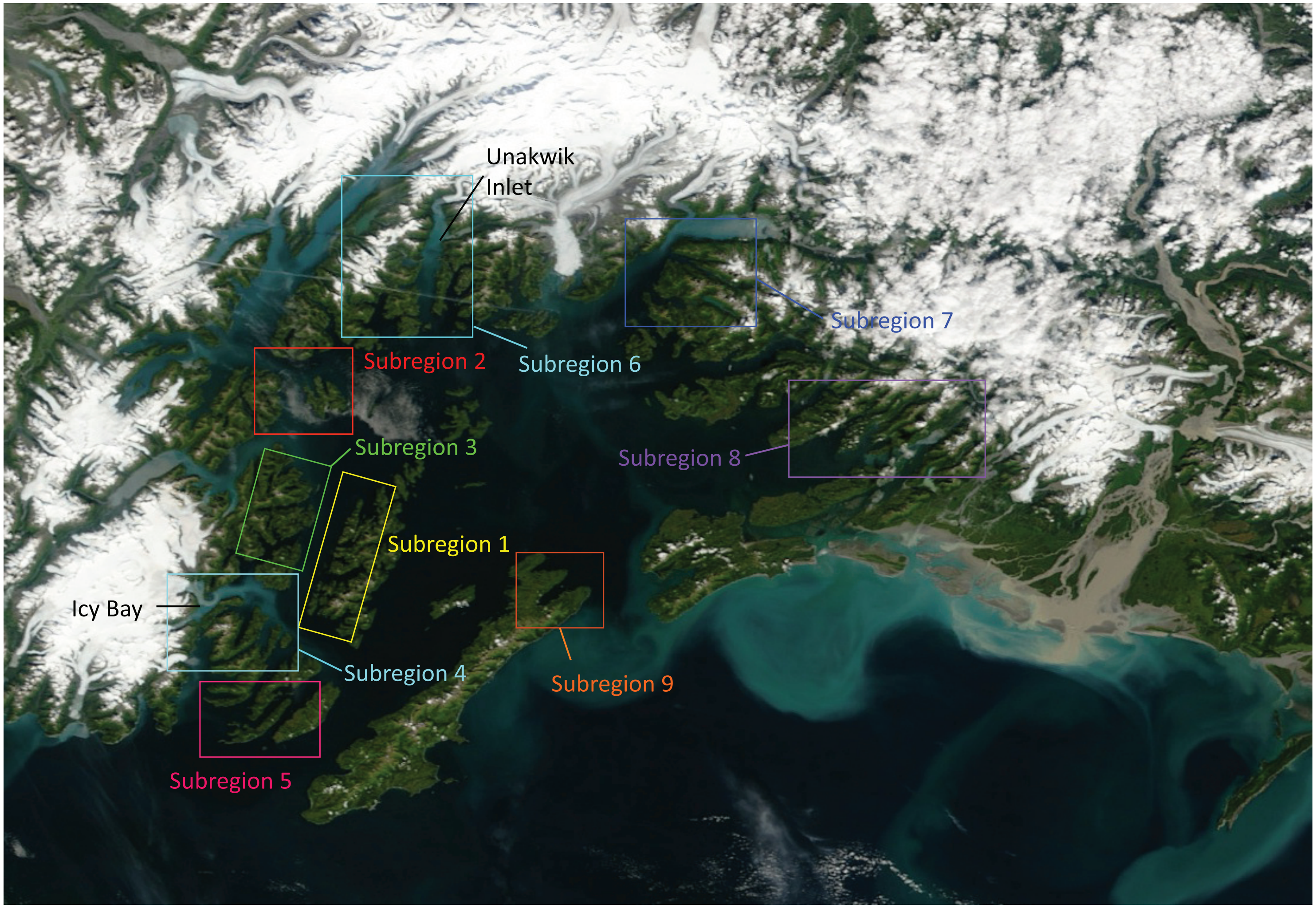

Fig. 2.1C. Subregions in PWS surveyed from May 1994 to March 1998. Note, these are referred to in the text by the number designation.

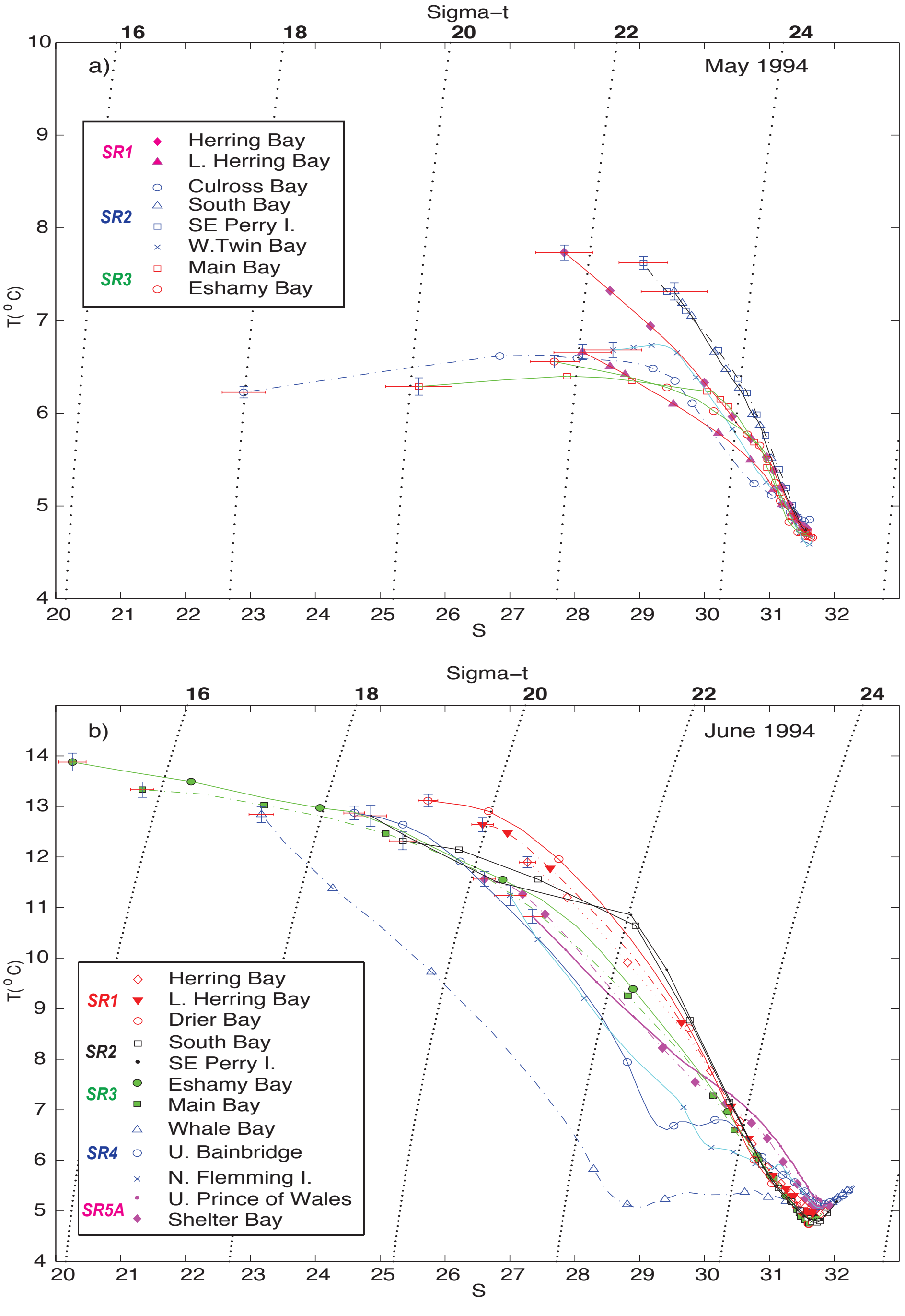

Fig. 2.2. Mean temperature versus salinity for all locations surveyed in 1994 (a-c), 1996 (d-f) and 1997 (g-i). Means are for the upper 100 to 200m with symbols at standard depths given in the text. Points and lines are color-coded according to sub-regions, and error bars for the surface 1m bin are standard errors. Plots for August 1996 (f) and July and August 1997 (h,i) include inner and outer basins shown as circles and pluses respectively.

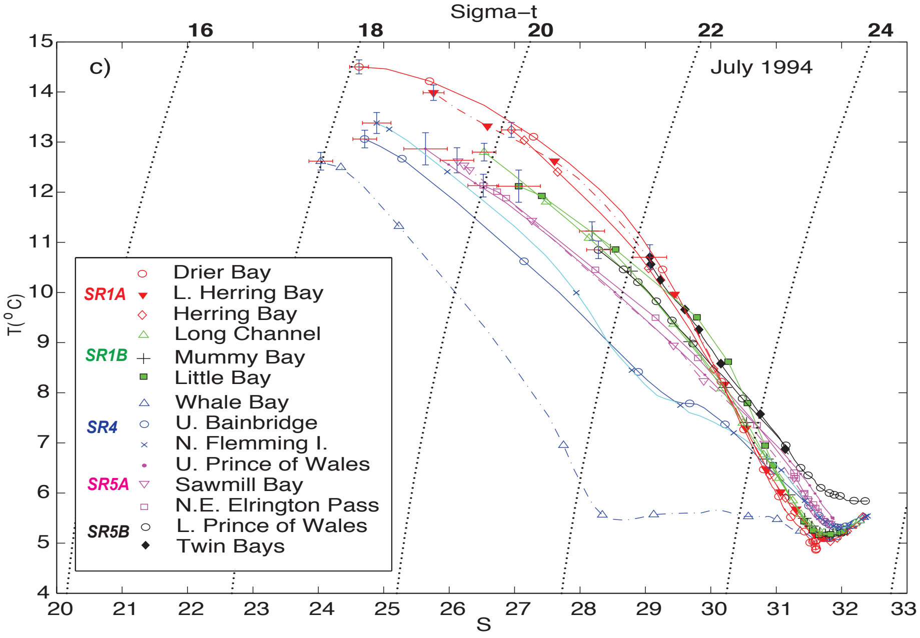
Sigma–t
16
18
20
22
24
c)
July 1994
T(°C)
S
Drier Bay
SR1A
L. Herring Bay
Herring Bay
Long Channel
SR1B
Mummy Bay
Little Bay
Whale Bay
SR4
U. Bainbridge
N. Flemming I.
U. Prince of Wales
SR5A
Sawmill Bay
N.E. Elrington Pass
SR5B
L. Prince of Wales
Twin Bays

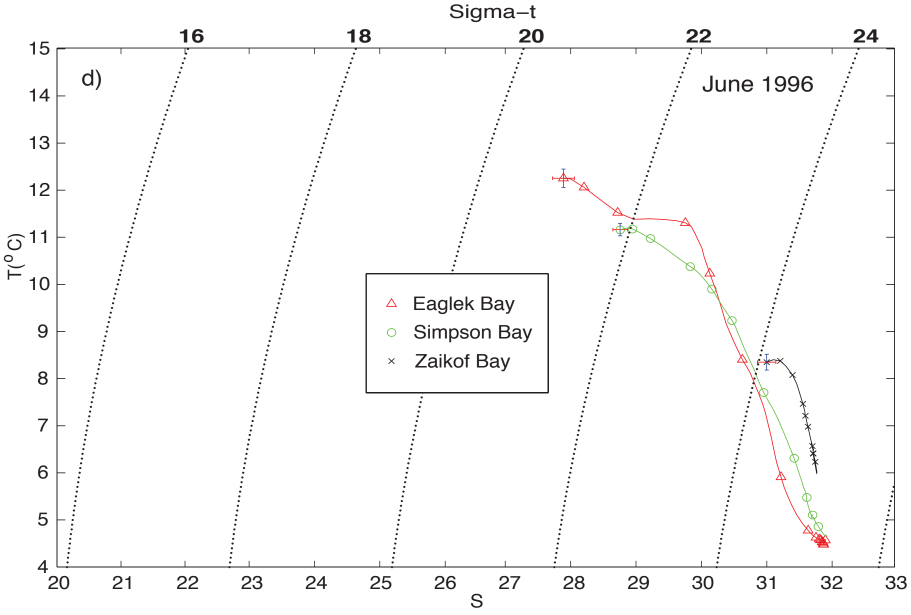
Sigma–t
16
18
20
22
24
d)
June 1996
T(°C)
S
Eaglek Bay
Simpson Bay
Zaikof Bay

Fig. 2.2 (cont).

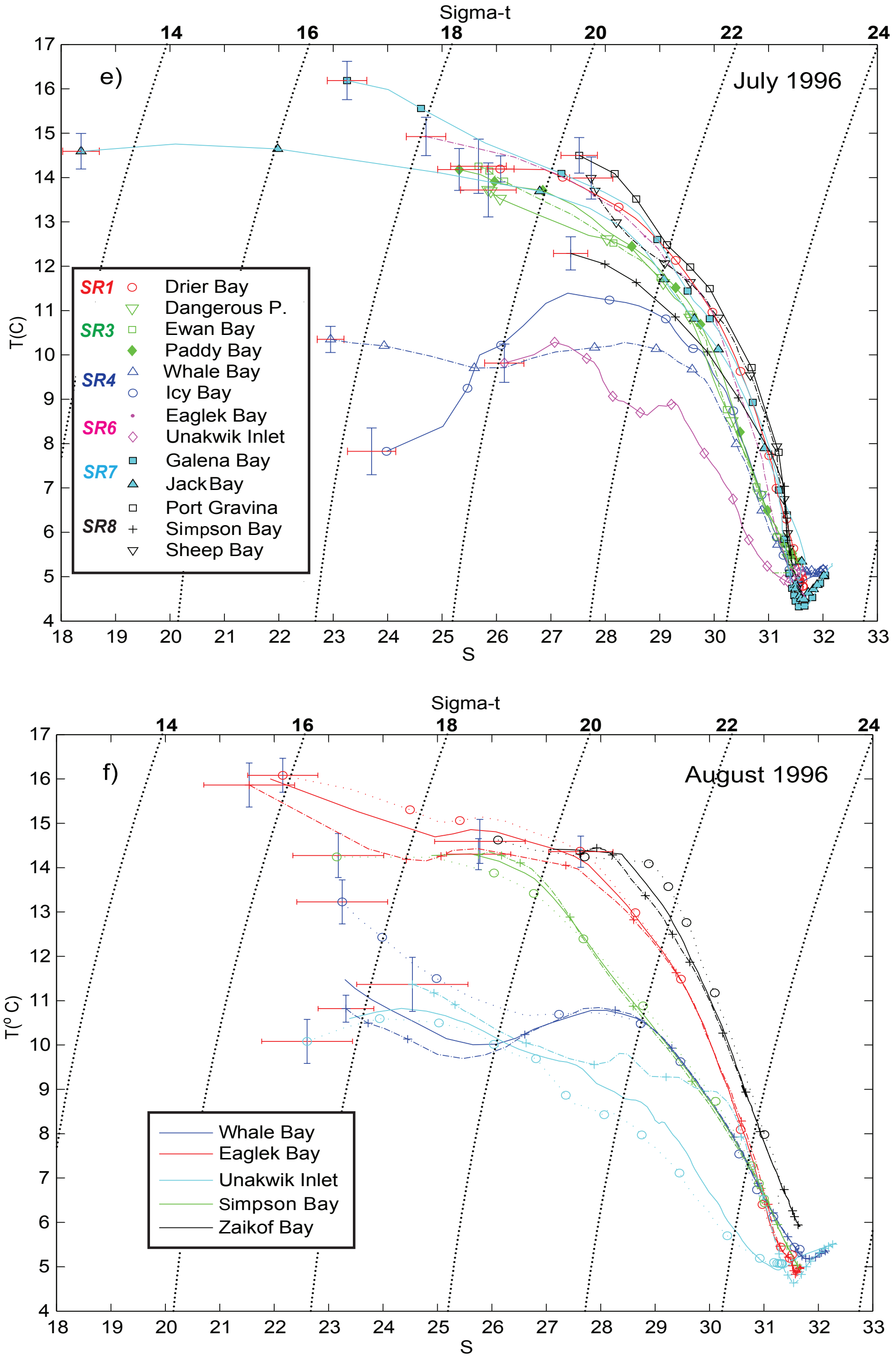
Sigma-t
14
16
18
20
22
24
e)
July 1996
T(C)
S
17
16
15
14
13
12
11
10
9
8
7
6
5
4
18
19
20
21
22
23
24
25
26
27
28
29
30
31
32
33
SR1 ○ Drier Bay
▽ Dangerous P.
SR3 □ Ewan Bay
◆ Paddy Bay
SR4 △ Whale Bay
○ Icy Bay
SR6 • Eaglek Bay
◇ Unakwik Inlet
SR7 ■ Galena Bay
▲ Jack Bay
□ Port Gravina
SR8 + Simpson Bay
▽ Sheep Bay
Sigma-t
14
16
18
20
22
24
f)
August 1996
T(°C)
S
Whale Bay
Eaglek Bay
Unakwik Inlet
Simpson Bay
Zaikof Bay

Fig. 2.2 (cont).

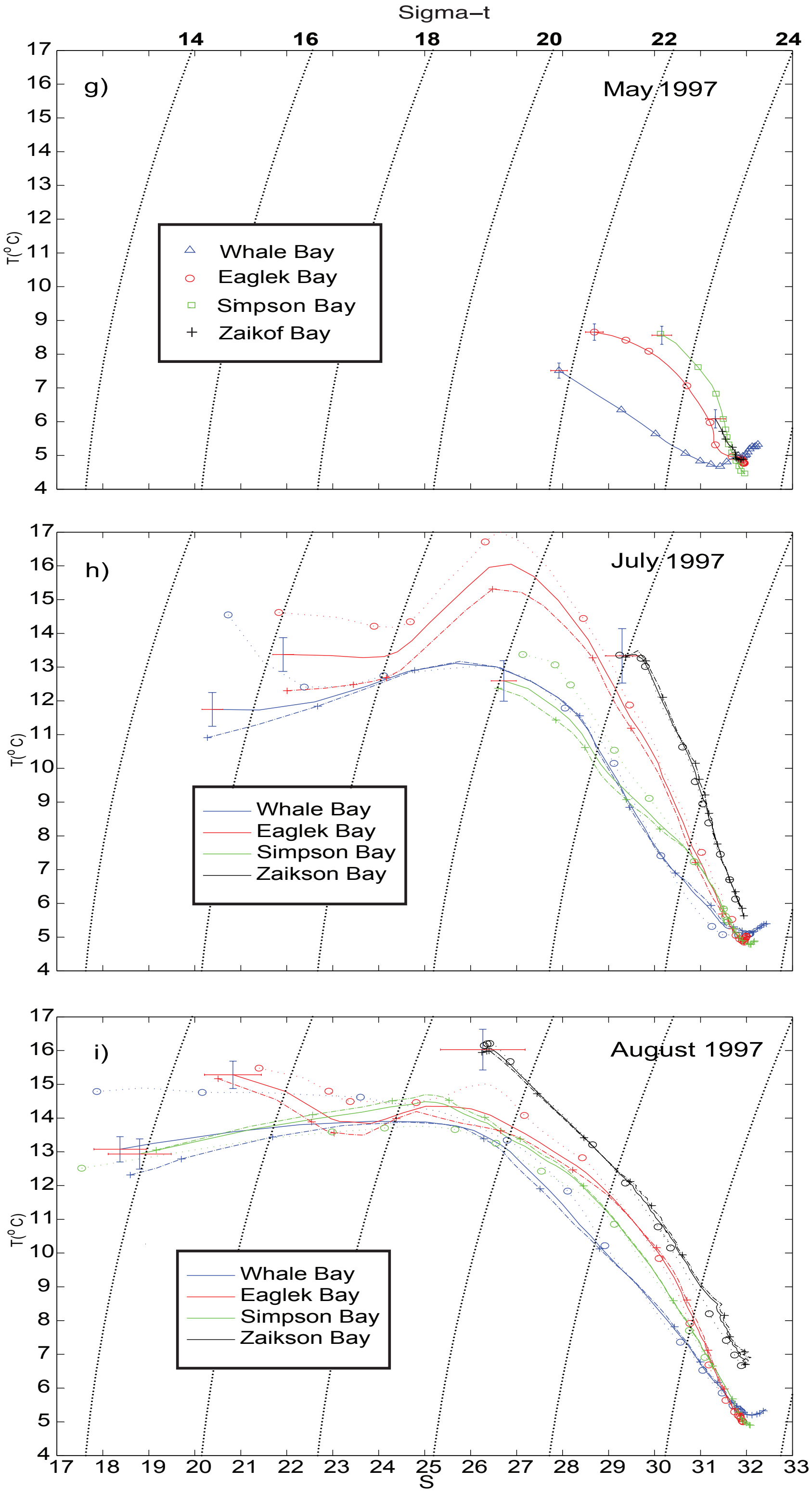
Sigma–t
14
16
18
20
22
24
g)
May 1997
△ Whale Bay
○ Eaglek Bay
□ Simpson Bay
+ Zaikof Bay
h)
July 1997
Whale Bay
Eaglek Bay
Simpson Bay
Zaikson Bay
i)
August 1997
Whale Bay
Eaglek Bay
Simpson Bay
Zaikson Bay
T(°C)
4
5
6
7
8
9
10
11
12
13
14
15
16
17
17
18
19
20
21
22
23
24
25
26
27
28
29
30
31
32
33
S

Fig. 2.2 (cont).

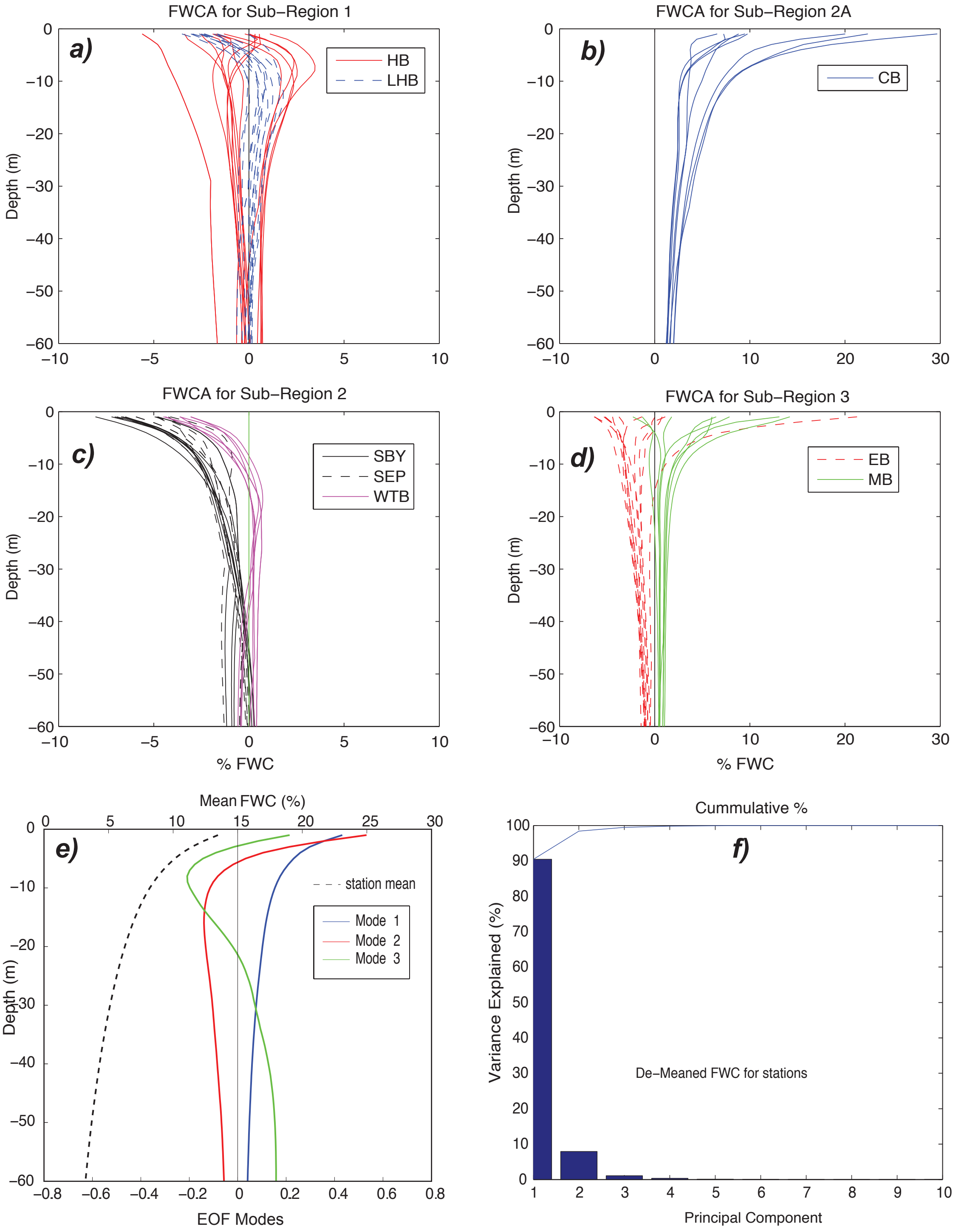

Fig. 2.3. May 1994 freshwater content anomalies (FWCA), eigenvectors of modes 1 to 3 and principal component amplitudes (PCAs) for sub-regions 1 to 3. Profiles (a-d) consist of FWC with the mean profile in (e) removed. Also shown are percentages of the variance explained by modes 1 to 10 (f). Red and green PCAs (g,h) are for positive for modes 1 and 2 respectively, and blue is negative for both modes. Location codes for the above plots are given in Table 2.1.

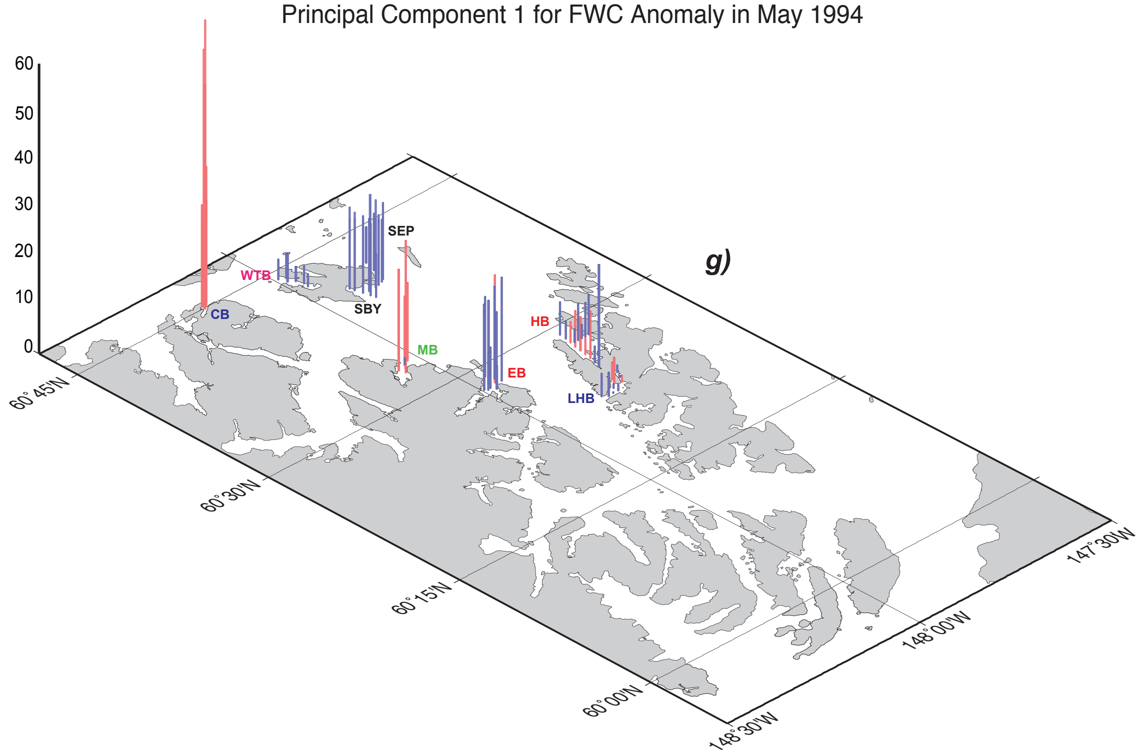
Principal Component 1 for FWC Anomaly in May 1994

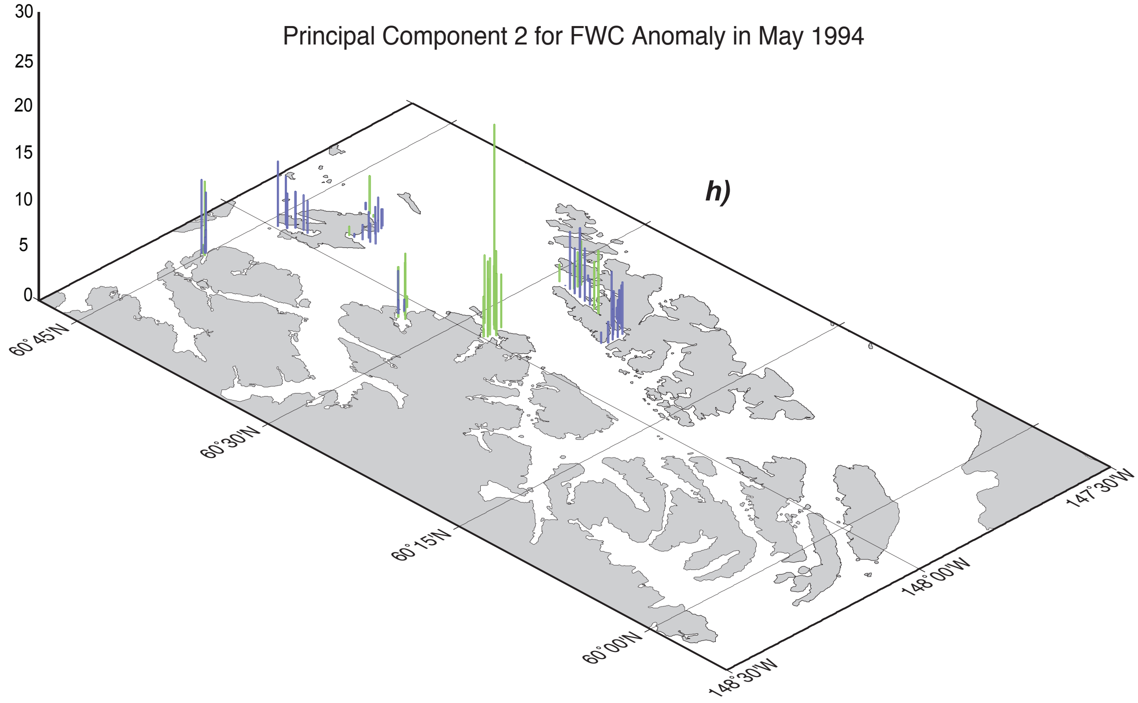
Principal Component 2 for FWC Anomaly in May 1994

Fig. 2.3 (cont.).

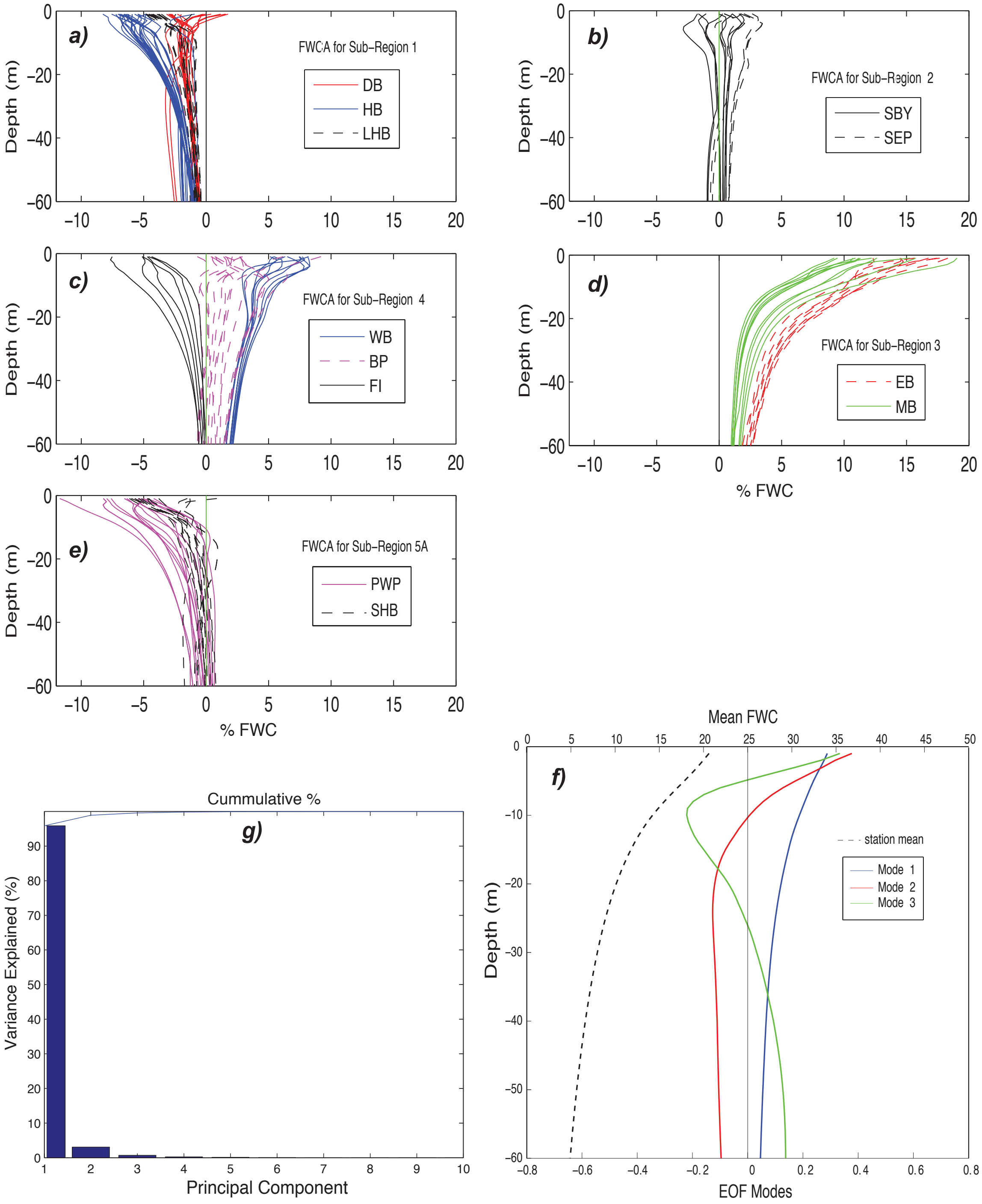

Fig. 2.4. June 1994 freshwater content anomalies (FWCA), eigenvectors of modes 1 to 3 and principal component amplitudes (PCAs) for sub-regions 1 to 5A. Profiles (a-e) consist of FWC with the mean profile in (f) removed. Also shown are percentages of the variance explained by modes 1 to 10 (g). Red and green PCAs (h,i) are positive for modes 1 and 2 respectively, whereas blue is negative for both modes.

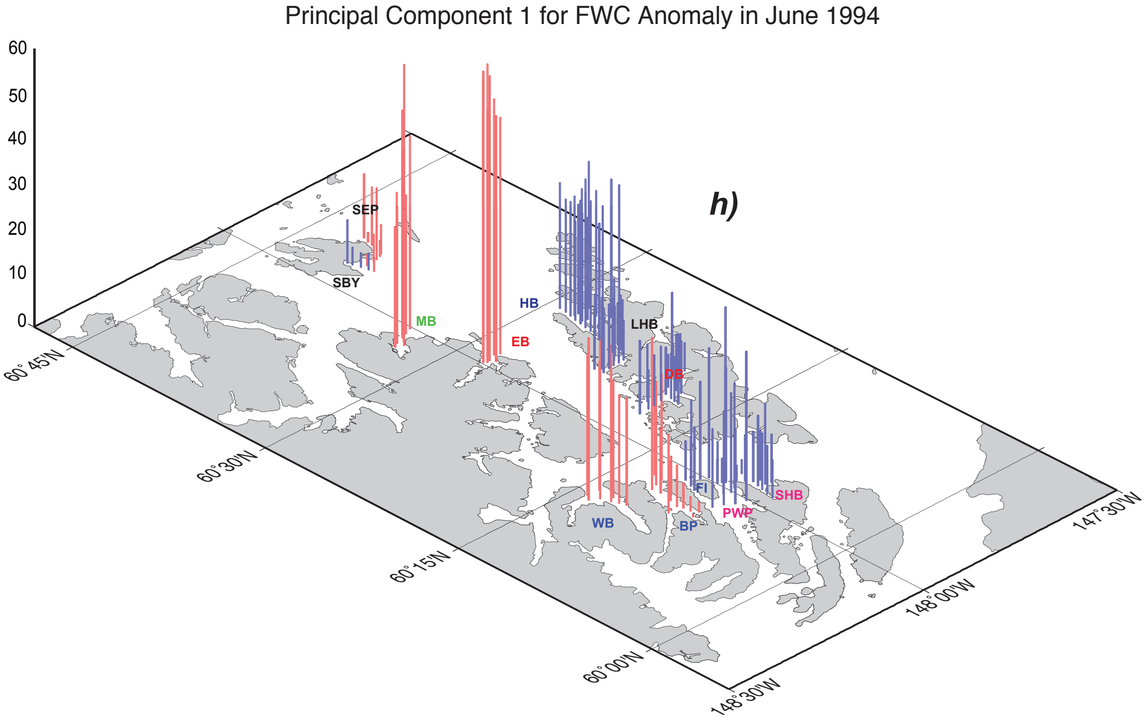
Principal Component 1 for FWC Anomaly in June 1994
60
50
40
30
20
10
0
h)
SEP
SBY
MB
HB
EB
LHB
DB
FI
SHB
PWP
WB
BP
60° 45'N
60°30'N
60°15'N
60°00'N
148°30'W
148°00'W
147°30'W

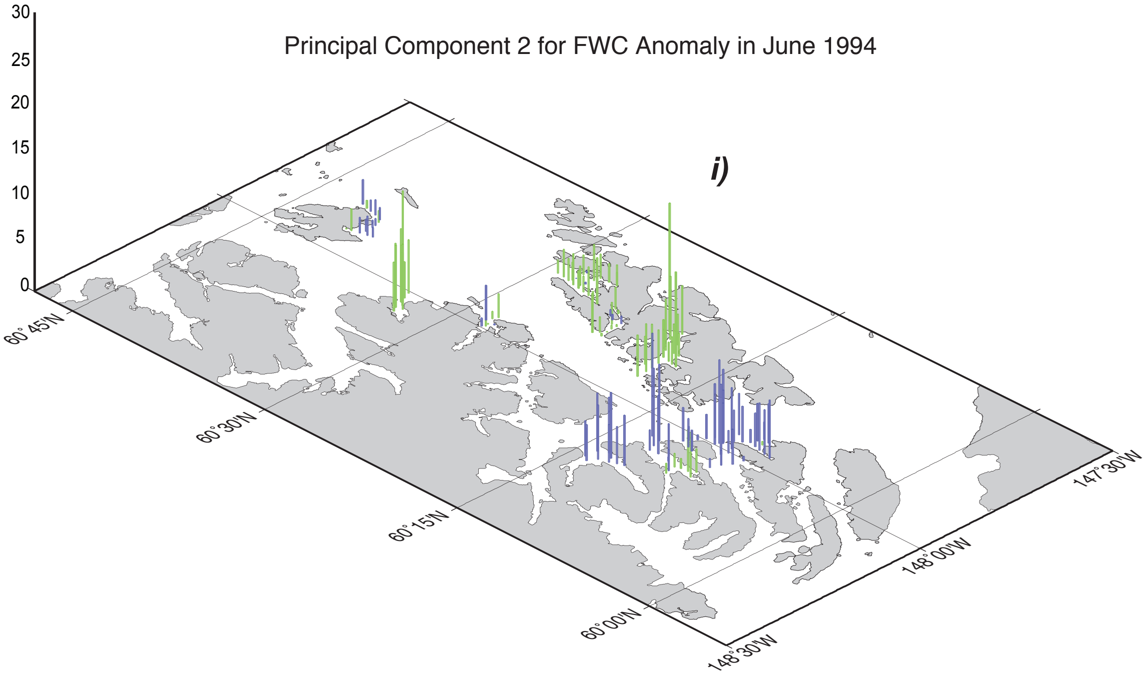
Principal Component 2 for FWC Anomaly in June 1994
30
25
20
15
10
5
0
i)
60° 45'N
60°30'N
60°15'N
60°00'N
148°30'W
148°00'W
147°30'W

Fig. 2.4 (cont.).

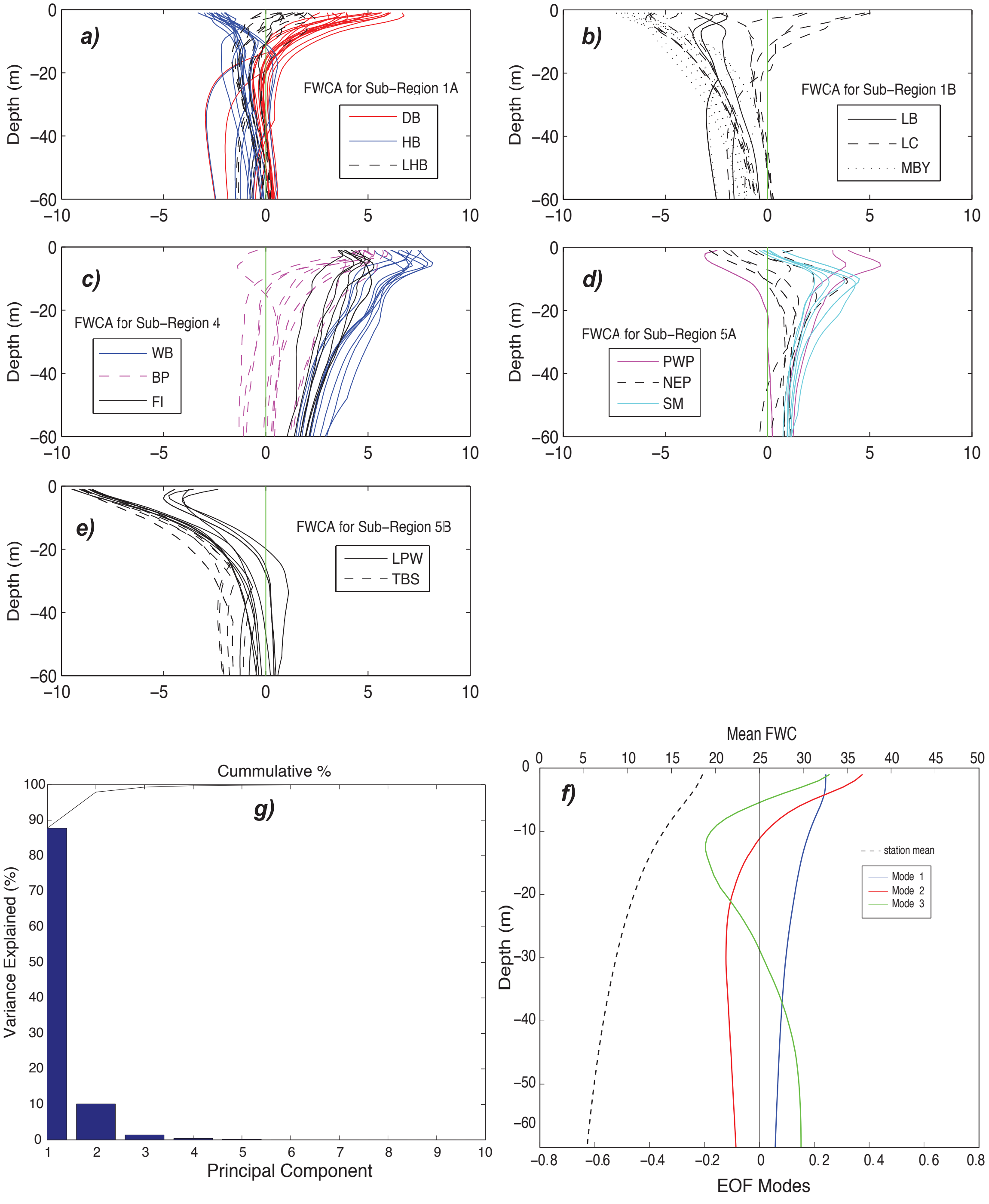

Fig. 2.5. July 1994 freshwater content anomalies (FWCA), eigenvectors of modes 1 to 3 over depth and principal component amplitudes (PCAs) for sub-regions 1A,B, 4 and 5A,B. Profiles (a-e) consist of FWC with the mean profile in (f) removed. Also shown are the percentages of the variance explained by modes 1 to 10 (g). Red and green PCAs (h,i) are positive for modes 1 and 2 respectively, and blue PCAs are negative for both modes.

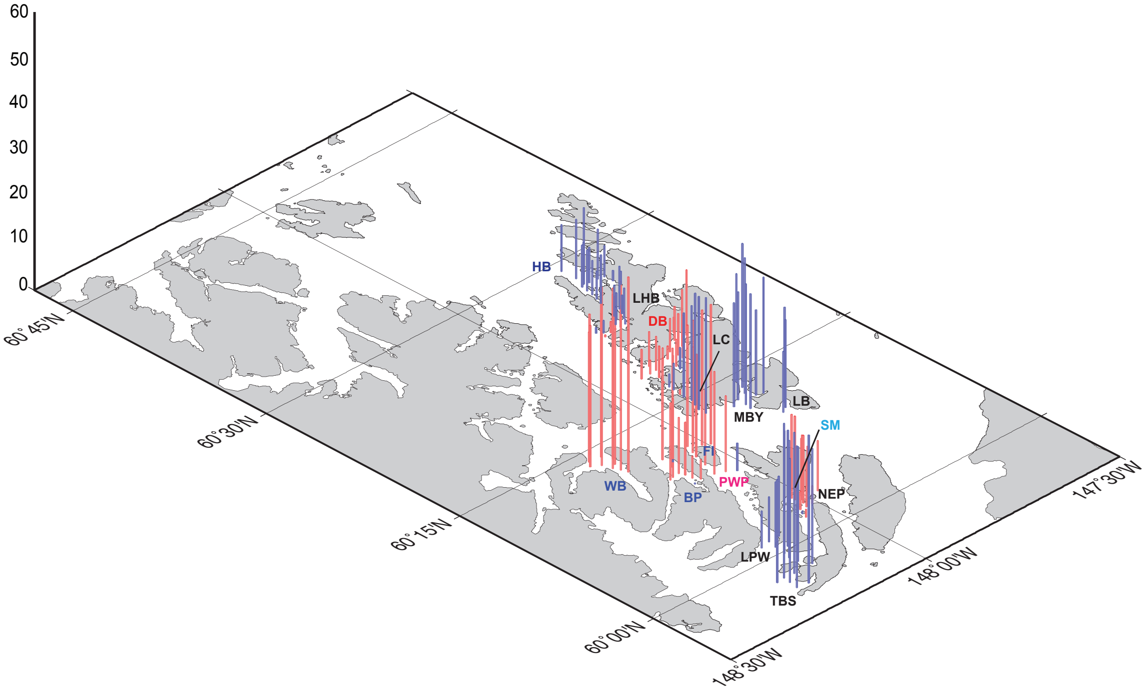

Principal Component 1 Amplitudes for FWC Anomaly July 1994

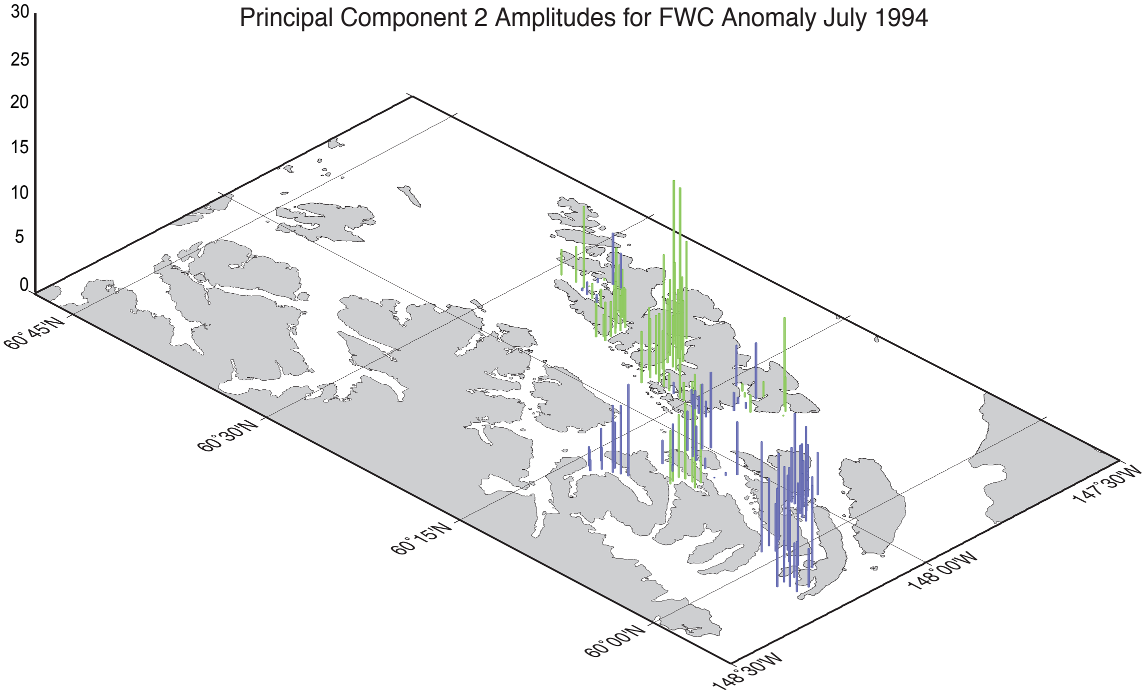

Principal Component 2 Amplitudes for FWC Anomaly July 1994

Fig. 2.5 (cont.).

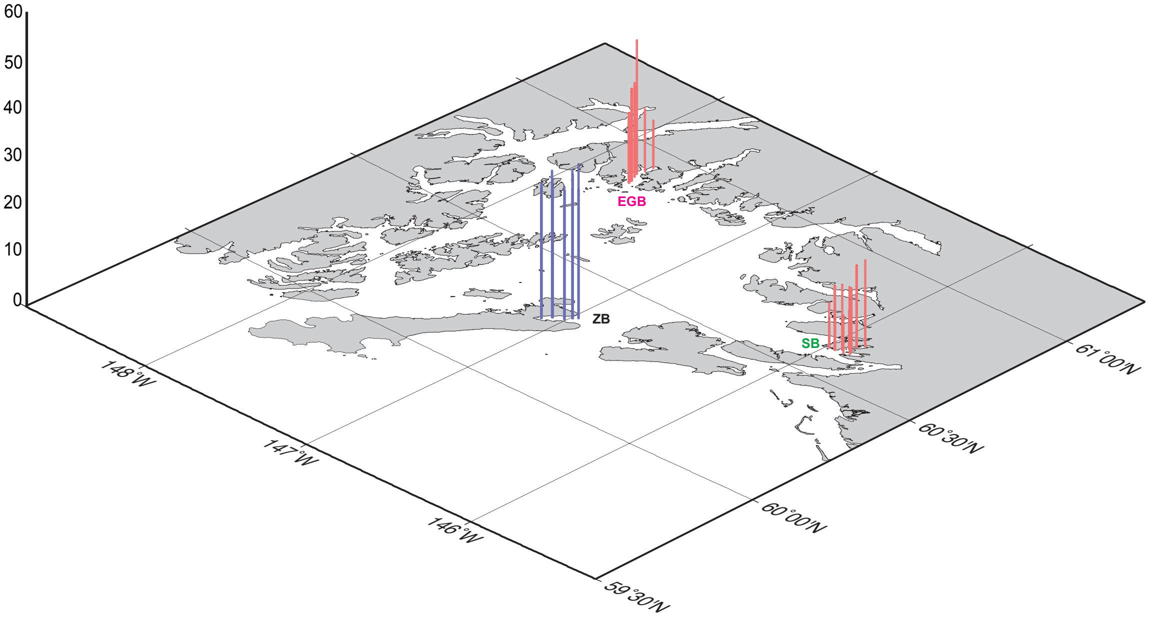
Principal Component 1 Amplitudes for FWC Anomaly June 1996

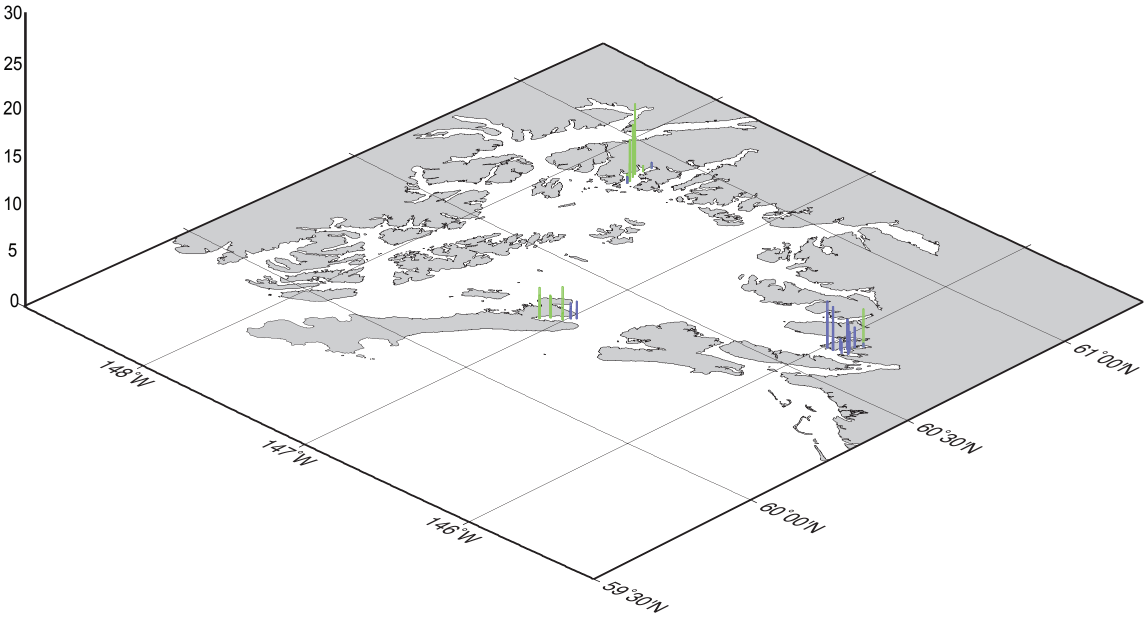
Principal Component 2 Amplitudes for FWC Anomaly June 1996

Fig. 2.6. Principal component amplitudes for FWC anomalies in sub-regions 6, 8 and 9 in June 1996. Red and green are positive for mode 1 and 2 respectively, and blue is negative for both modes.

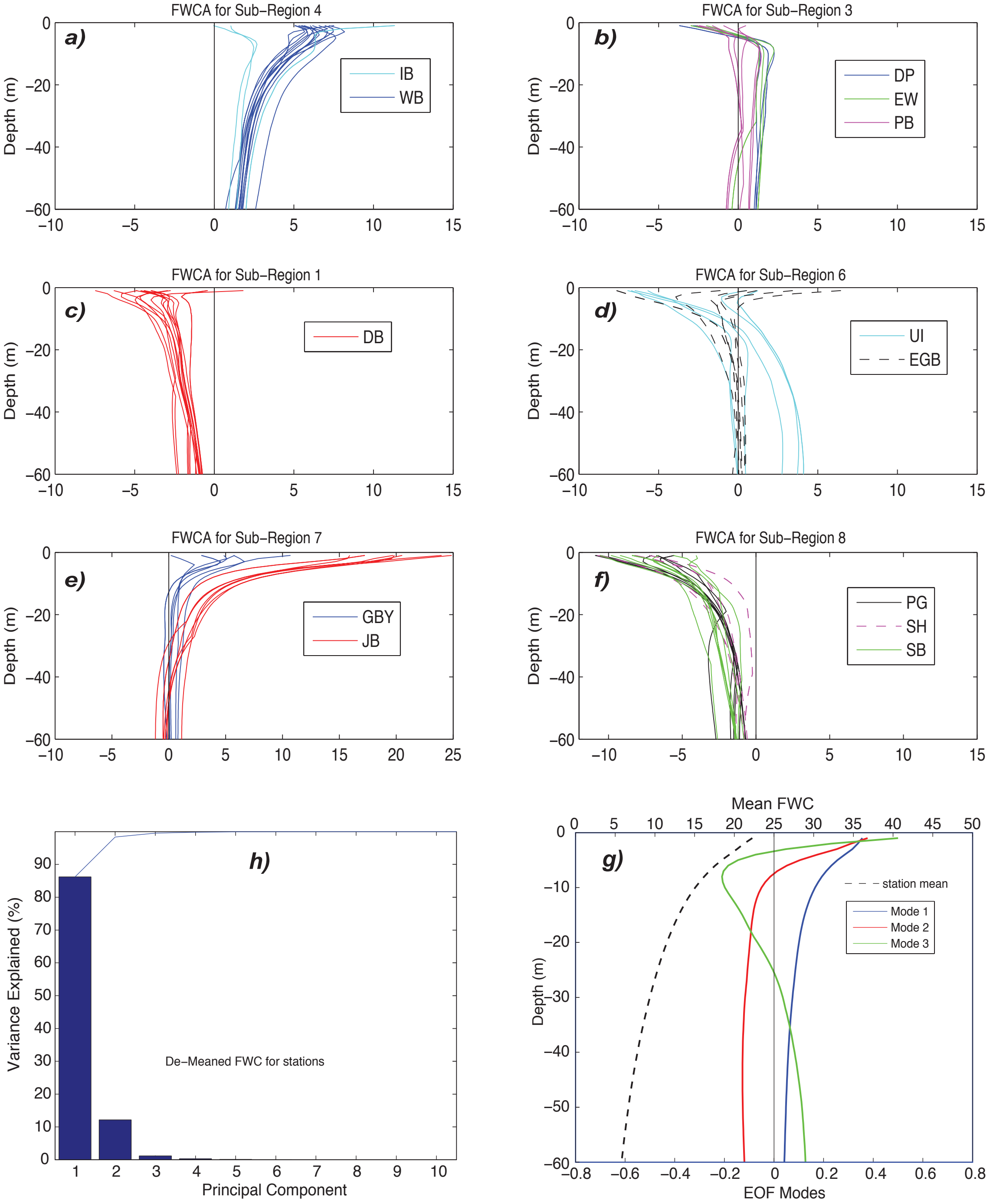

Fig. 2.7. July 1996 freshwater content anomalies (FWCA), eigenvectors of modes 1 to 3 over depth and principal component amplitudes (PCAs) for sub-regions 1, 3, 4, 6, 7 and 8. Profiles (a-f) consist of FWC with the mean profile in (g) removed. Also shown are the percentages of the variance explained by modes 1 to 10 (h). Red and green PCAs (i,j) are positive for modes 1 and 2 respectively, and blue PCAs are negative for both modes.

Principal Component 1 Amplitudes for FWC Anomaly July 1996

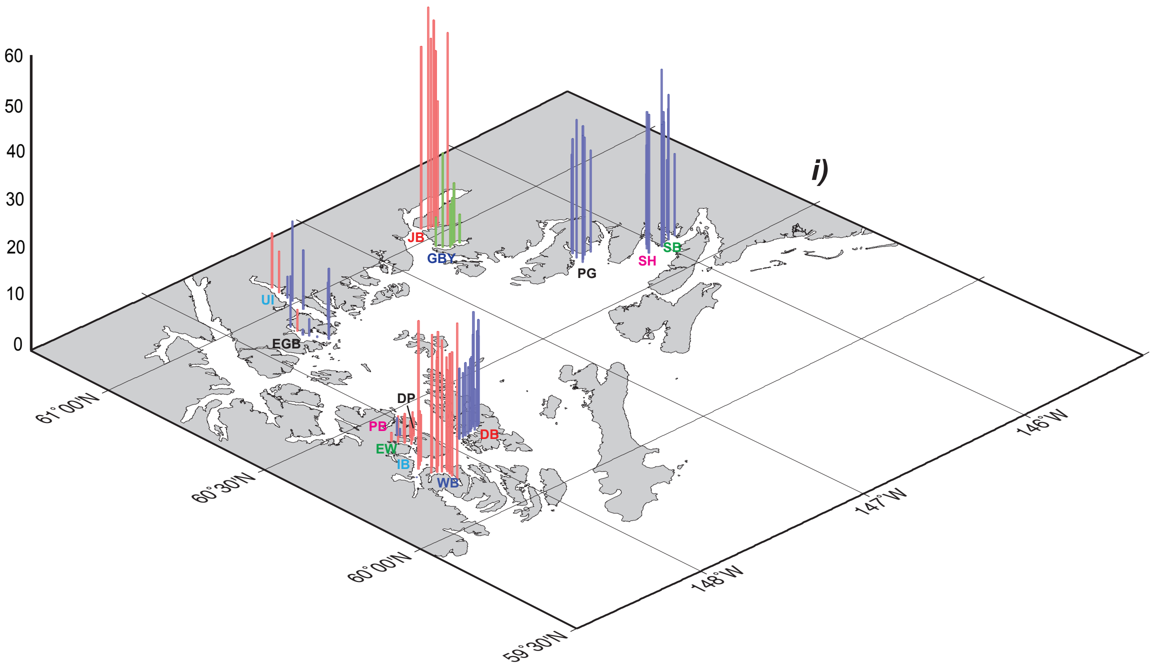

Principal Component 2 Amplitudes for FWC Anomaly July 1996

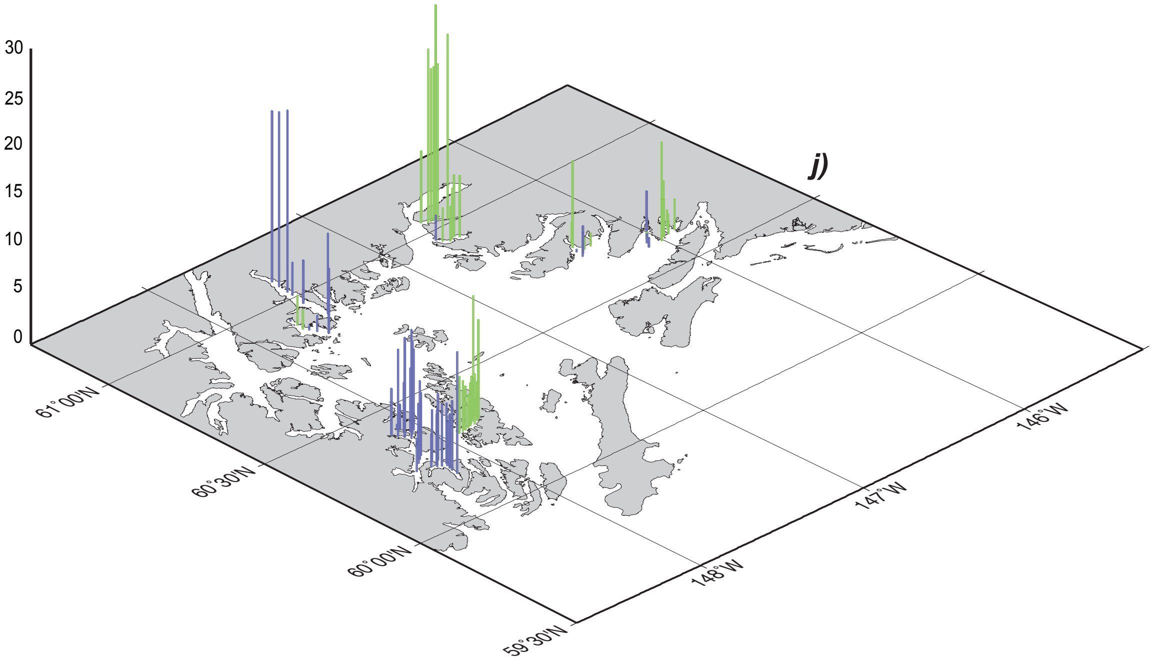

Fig. 2.7. (cont.).

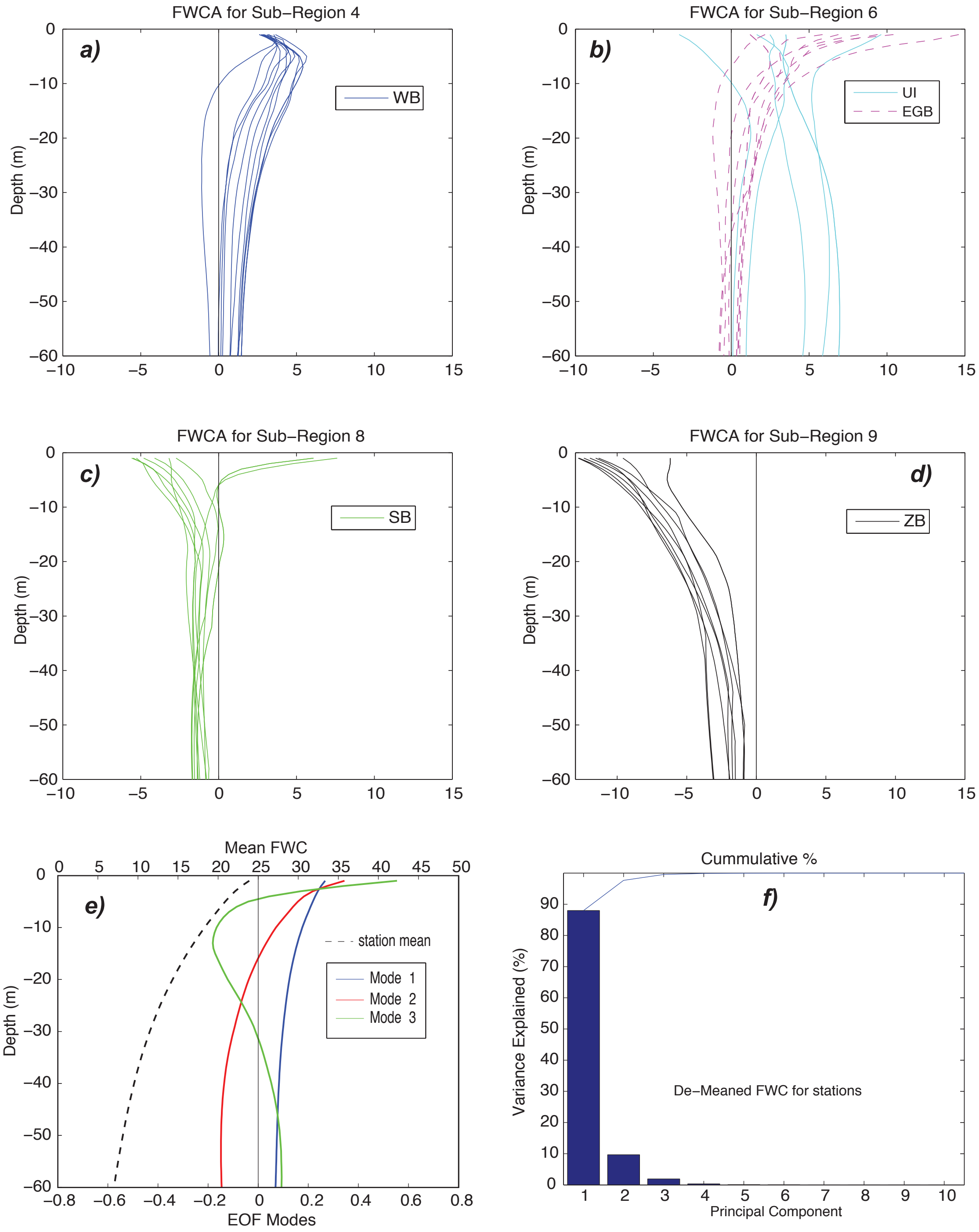

Fig. 2.8. August 1996 freshwater content anomalies (FWCA), eigenvectors of modes 1 to 3 over depth and principal component amplitudes (PCAs) for sub-regions 4, 6, 8 and 9. Profiles (a-d) consist of FWC with the mean profile in (e) removed. Also shown are the percentages of the variance explained by modes 1 to 10 (f). Red and green PCAs (g,h) are positive for modes 1 and 2 respectively, and blue PCAs are negative for both modes.

Principal Component 1 Amplitudes for FWC Anomaly Aug 1996

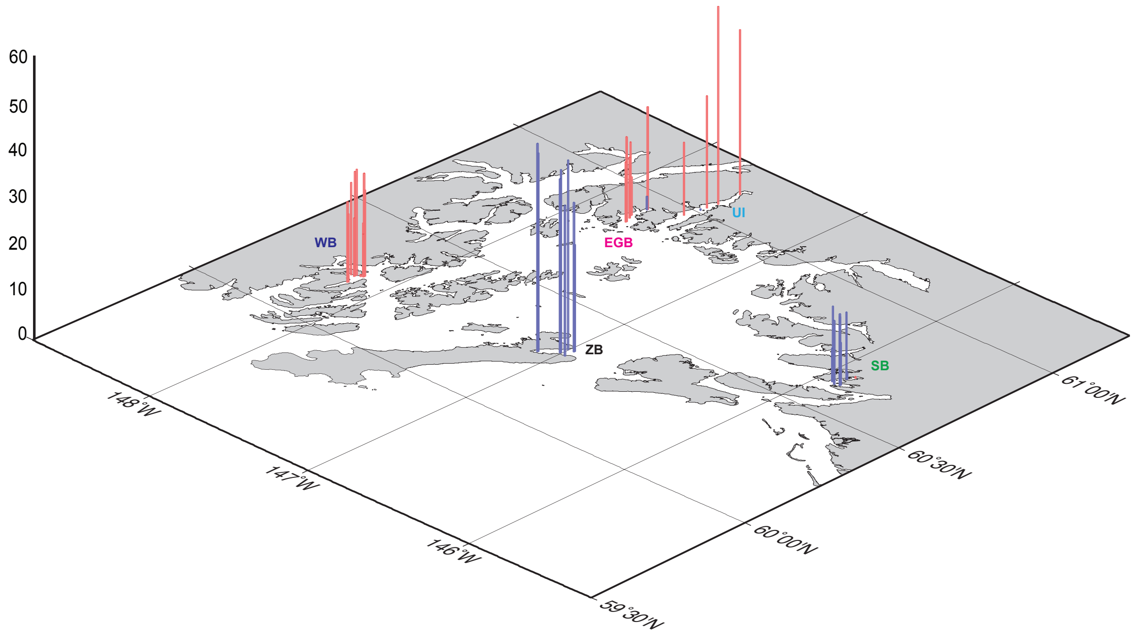

Principal Component 2 Amplitudes for FWC Anomaly Aug 1996

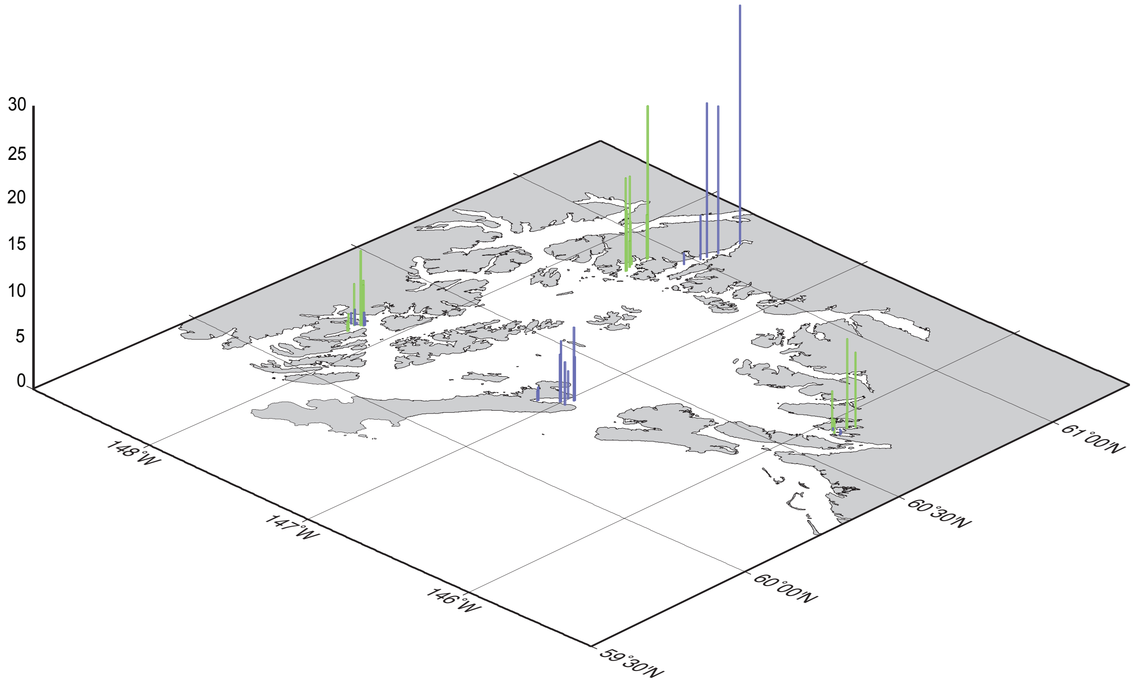

Fig. 2.8. (cont.).

Principal Component 1 Amplitudes for FWC Anomaly May 1997

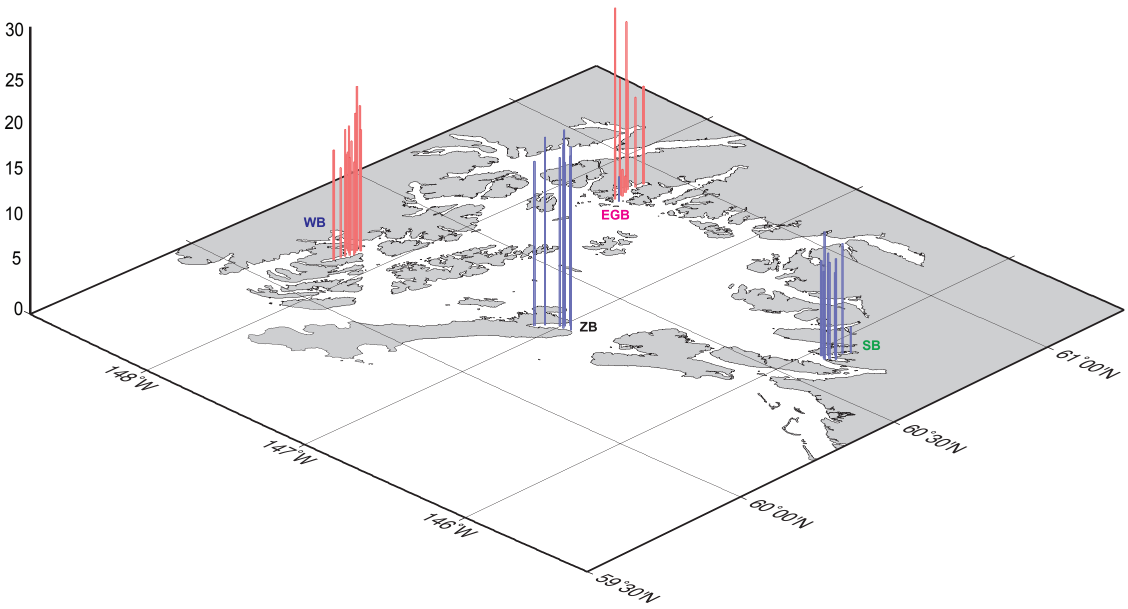

Principal Component 2 Amplitudes for FWC Anomaly May 1997

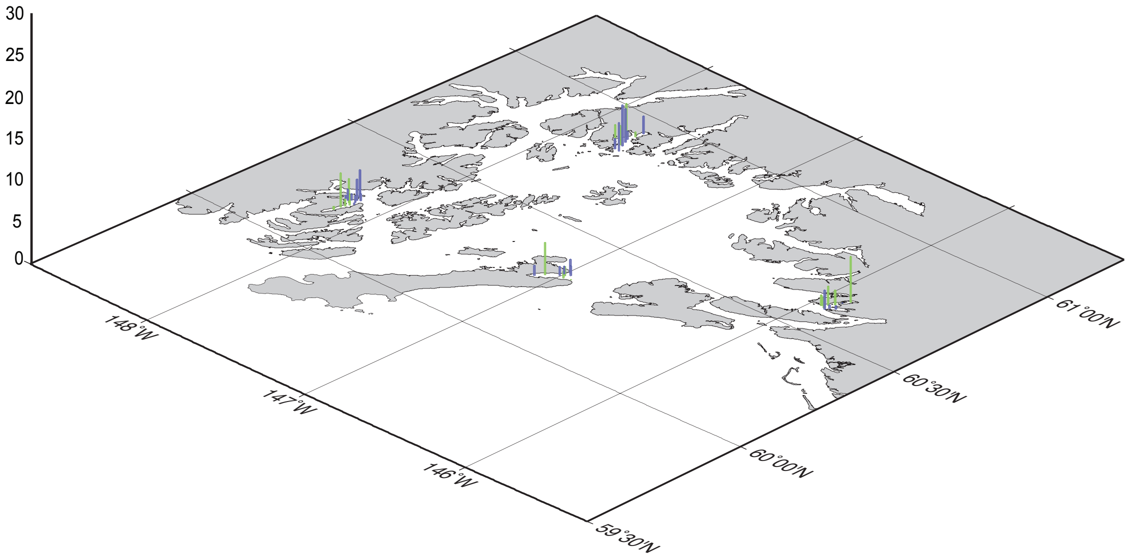

Fig. 2.9. Principal component amplitudes for FWC anomalies in sub-regions 4, 6, 8 and 9 in May 1997. Red and green are positive for mode 1 and 2 respectively, and blue is negative for both modes. Note that the scale for mode 1 = 0.25cm per unit amplitude, which is double that of previous months.

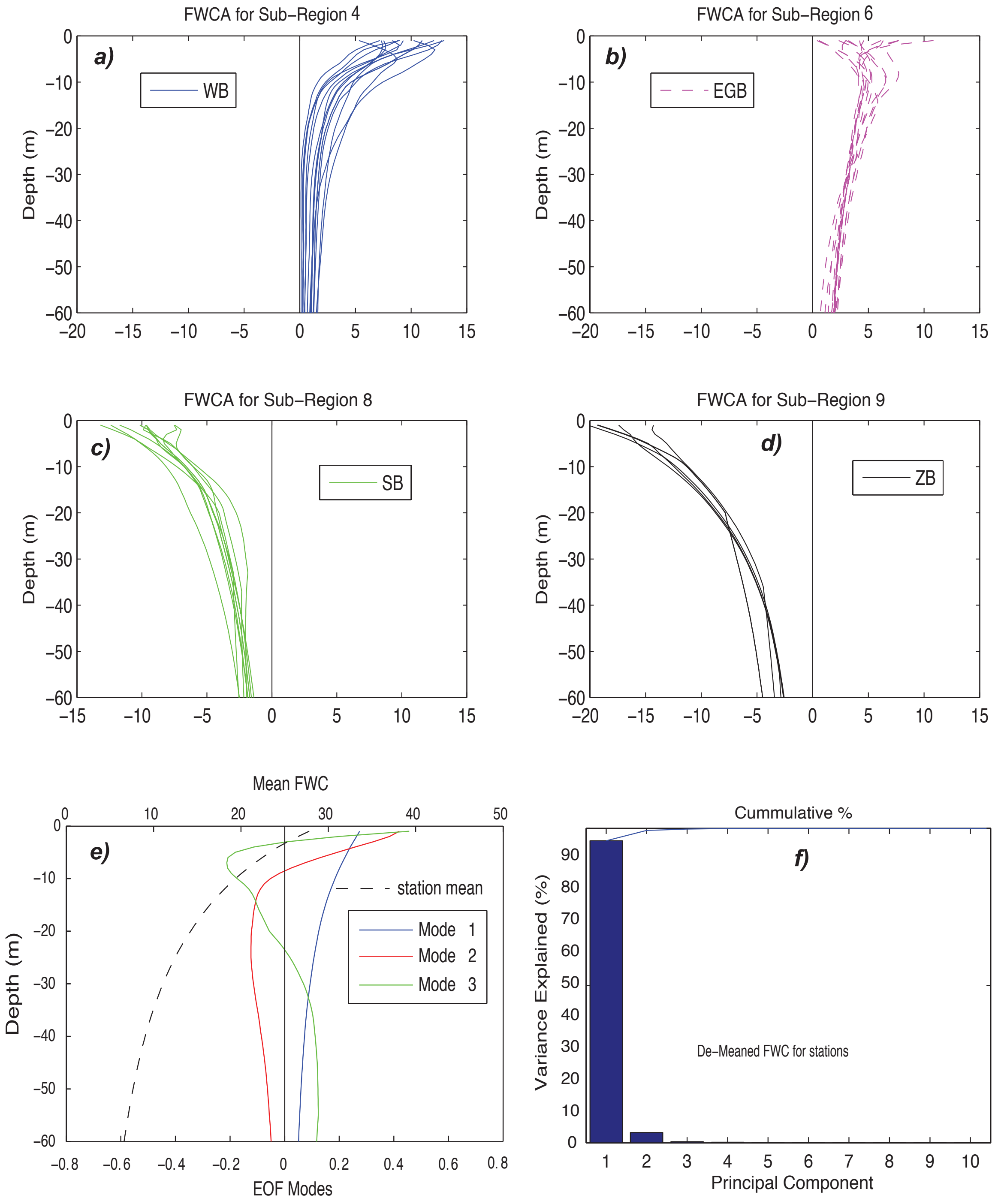

Fig. 2.10. July 1997 freshwater content anomalies (FWCA), eigenvectors of modes 1 to 3 over depth and principal component amplitudes (PCAs) for sub-regions 4, 6, 8 and 9. Profiles (a-d) consist of FWC with the mean profile in (e) removed. Also shown are the percentages of the variance explained by modes 1 to 10 (f). Red and green PCAs (g,h) are positive for modes 1 and 2 respectively, and blue PCAs are negative for both modes.

Principal Component 1 Amplitudes for FWC Anomaly July 1997

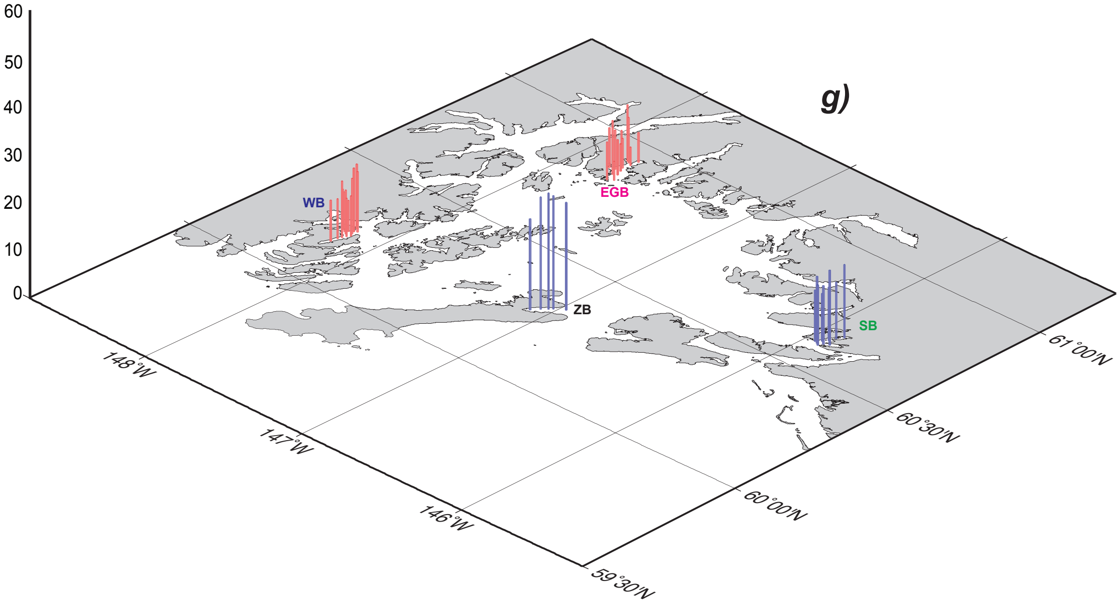

Principal Component 2 Amplitudes for FWC Anomaly July 1997

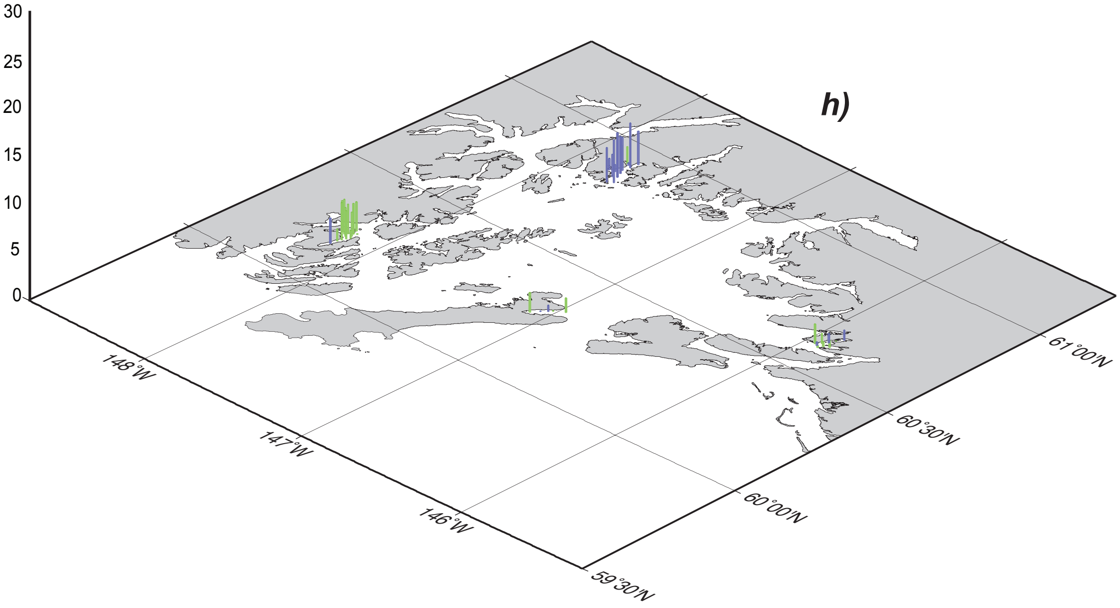

Fig. 2.10 (cont.).

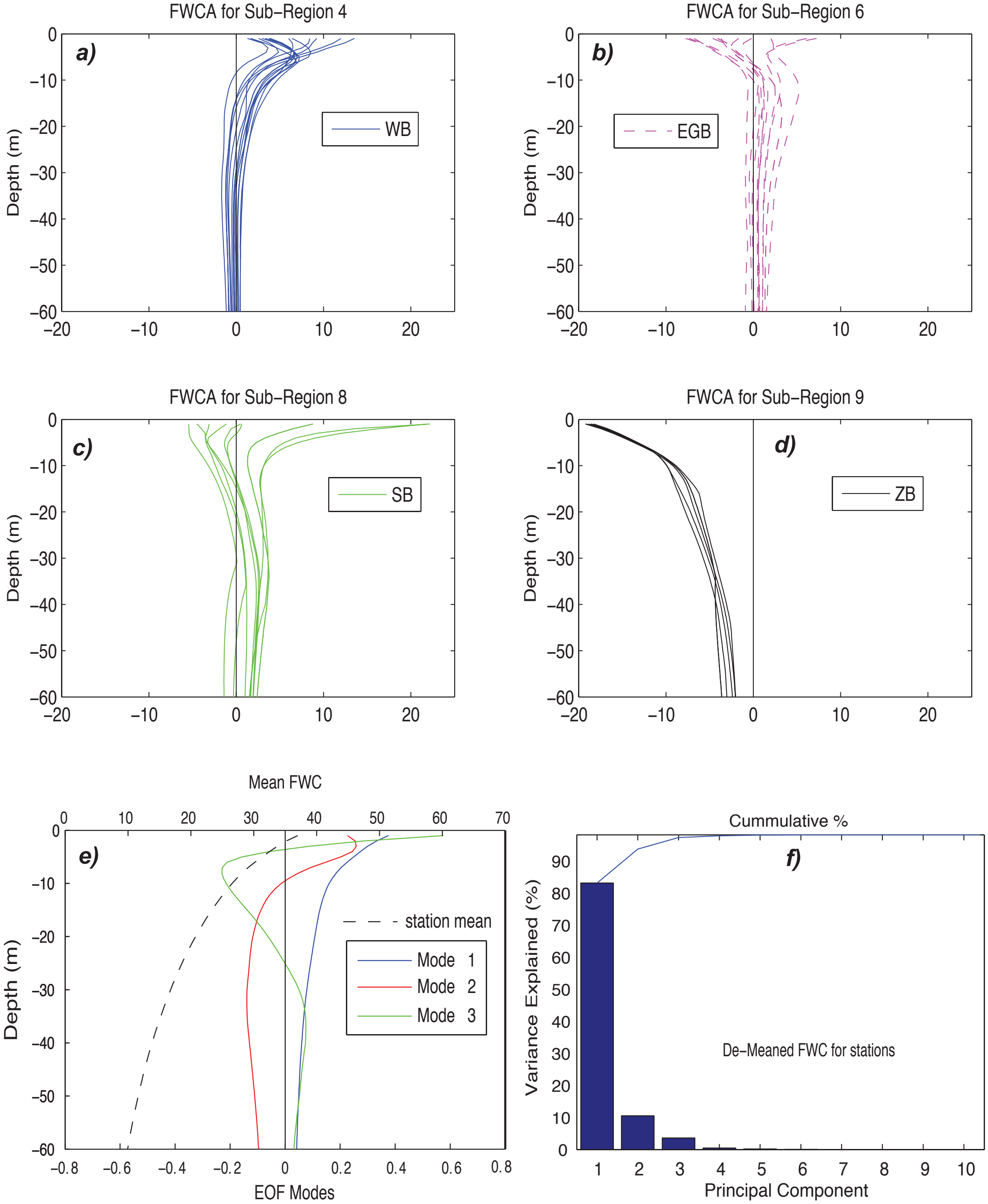

Fig. 2.11. August 1997 freshwater content anomalies (FWCA) and eigenvectors of modes 1 to 3 over depth. Profiles (a-d) consist of FWC with the mean profile in (e) removed. Also shown are the percentages of the variance explained by modes 1 to 10 (f). Red and green PCAs (g,h) are positive for modes 1 and 2 respectively, and blue PCAs are negative for both modes.

Principal Component 1 Amplitudes for FWC Anomaly Aug 1997

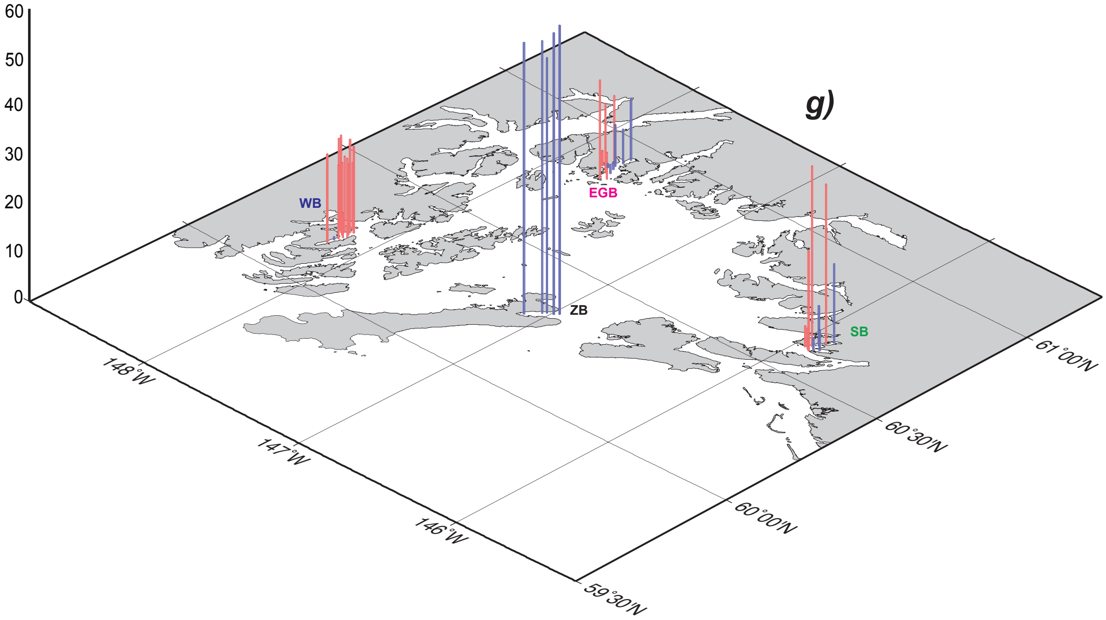

Principal Component 2 Amplitudes for FWC Anomaly Aug 1997

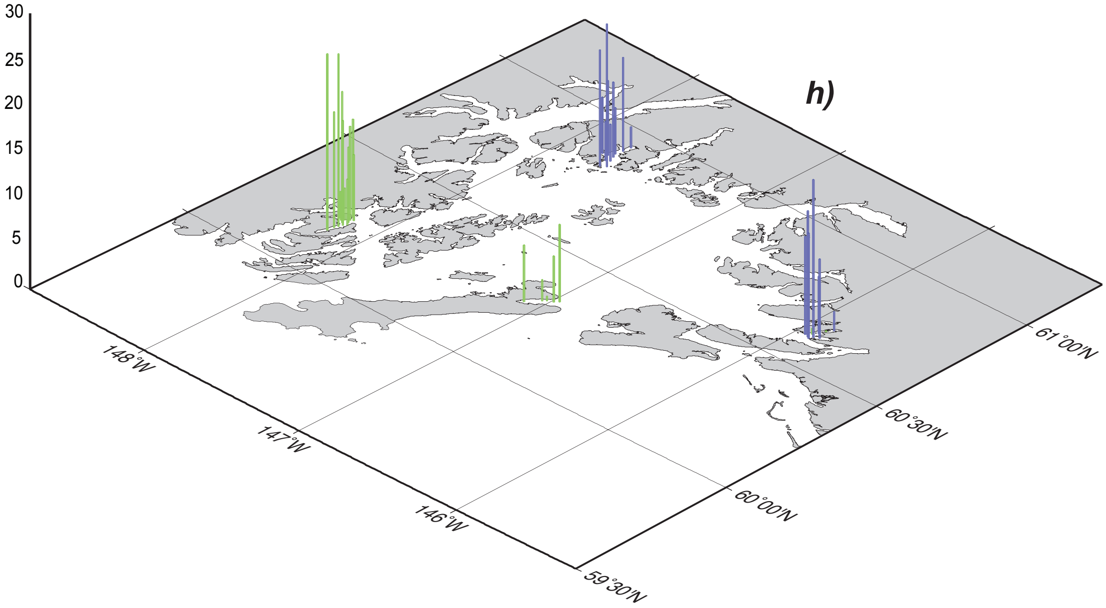

Fig. 2.11 (cont.).

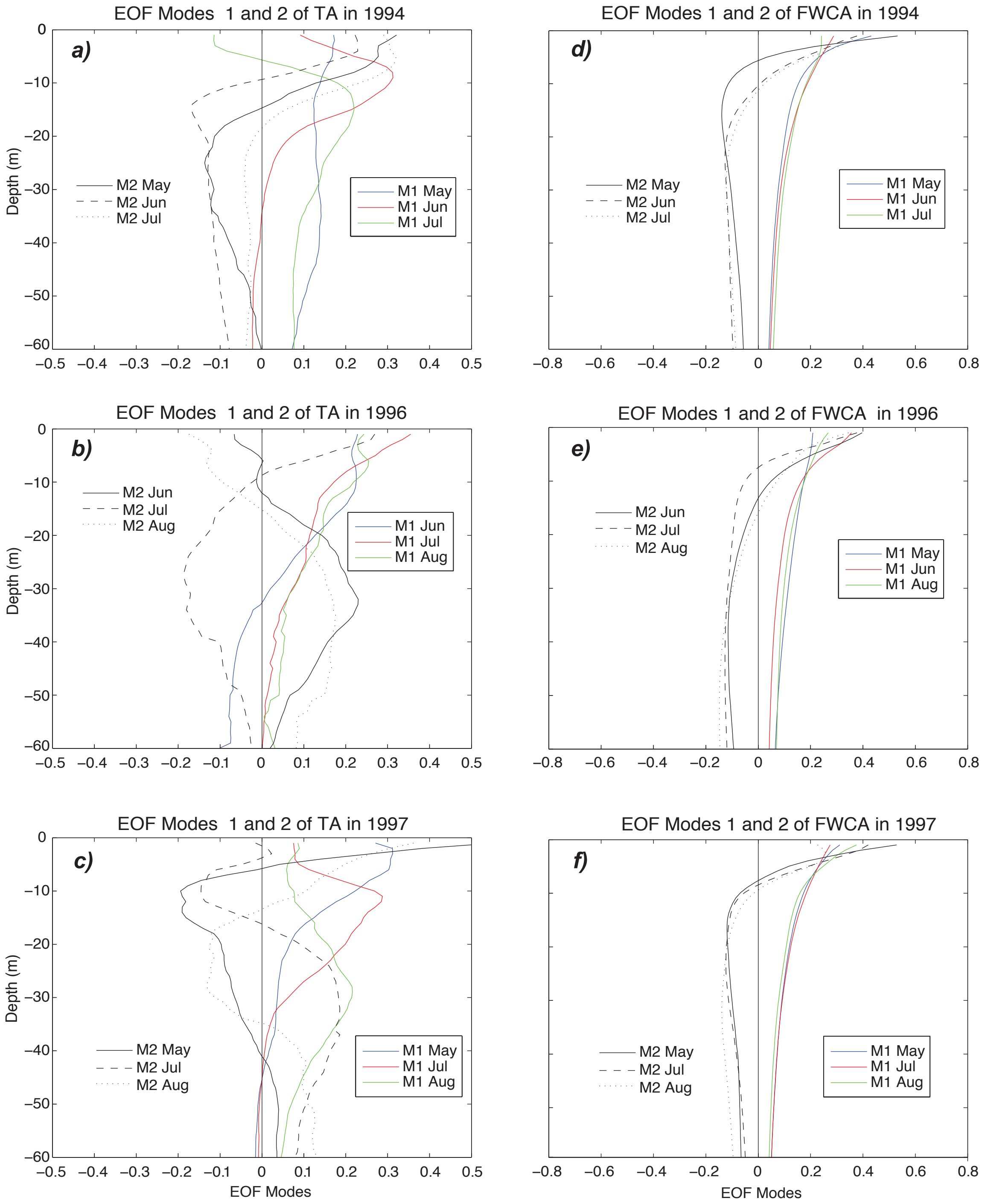

Fig. 2.12. EOFs over depth for anomalies of temperature (a-c) and FWC (d-f) in 1994, 1996 and 1997. Mode 1 is delinated by blue, red and green lines and mode 2 by black solid, dashed and dotted lines.

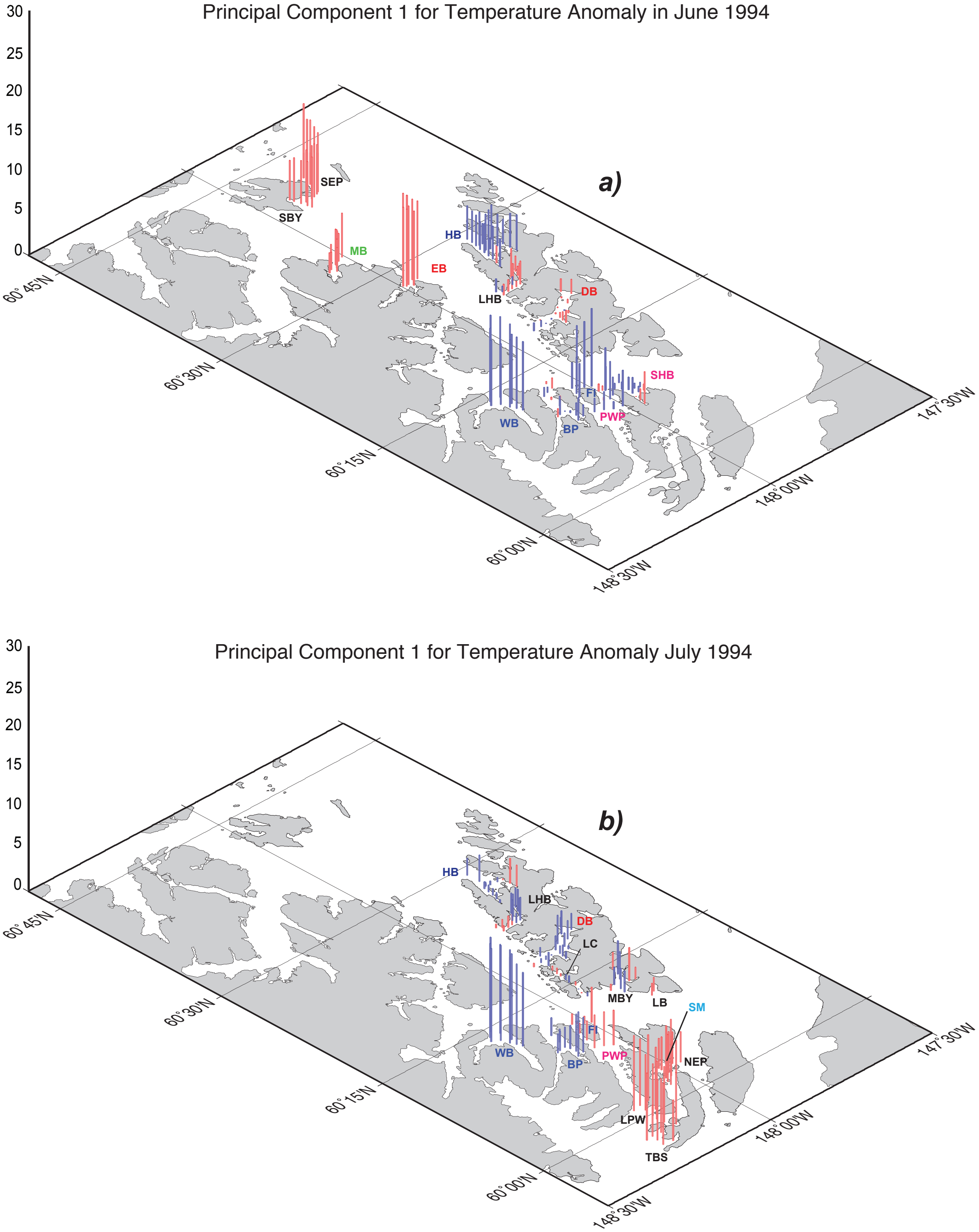

Fig. 2.13. Principal component amplitudes in June and July 1994 for temperature anomalies in sub-regions 1 to 5: a,b) PCAs of mode 1 and c,d) PCAs of mode 2. Note that the units are ^{o}C and the scale of mode 1 is half that of FWC. Red and green denote positive values for modes 1 and 2 respectively, whereas blue values are negative for both modes.

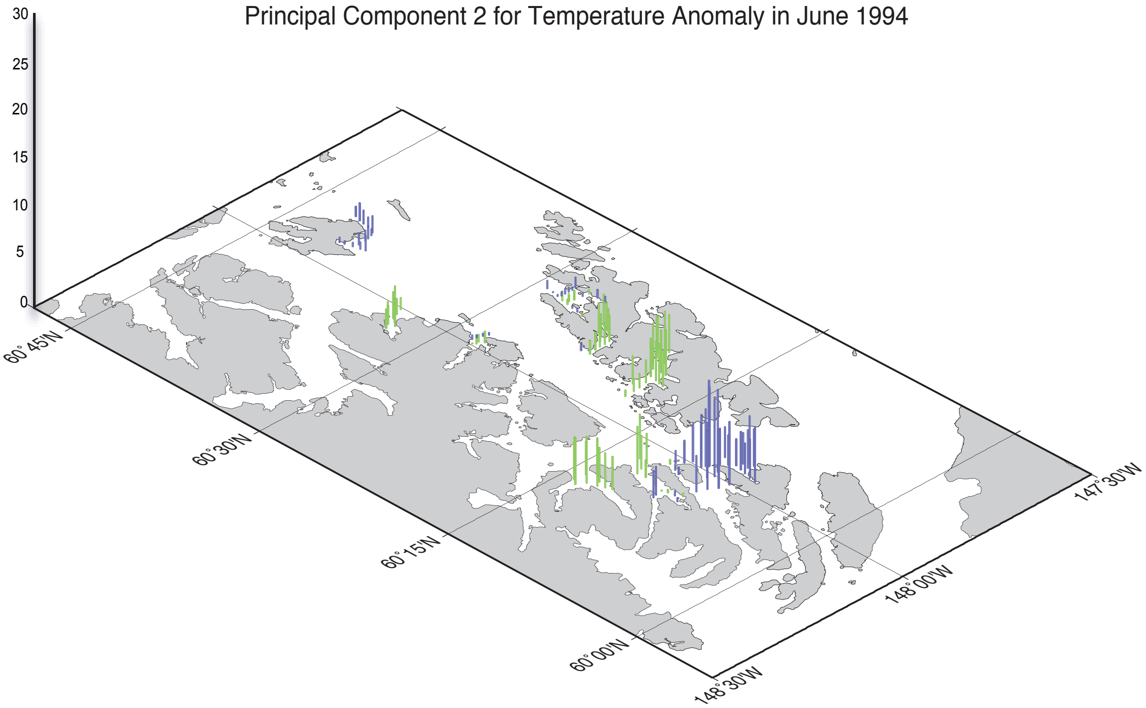

Principal Component 2 for Temperature Anomaly in June 1994

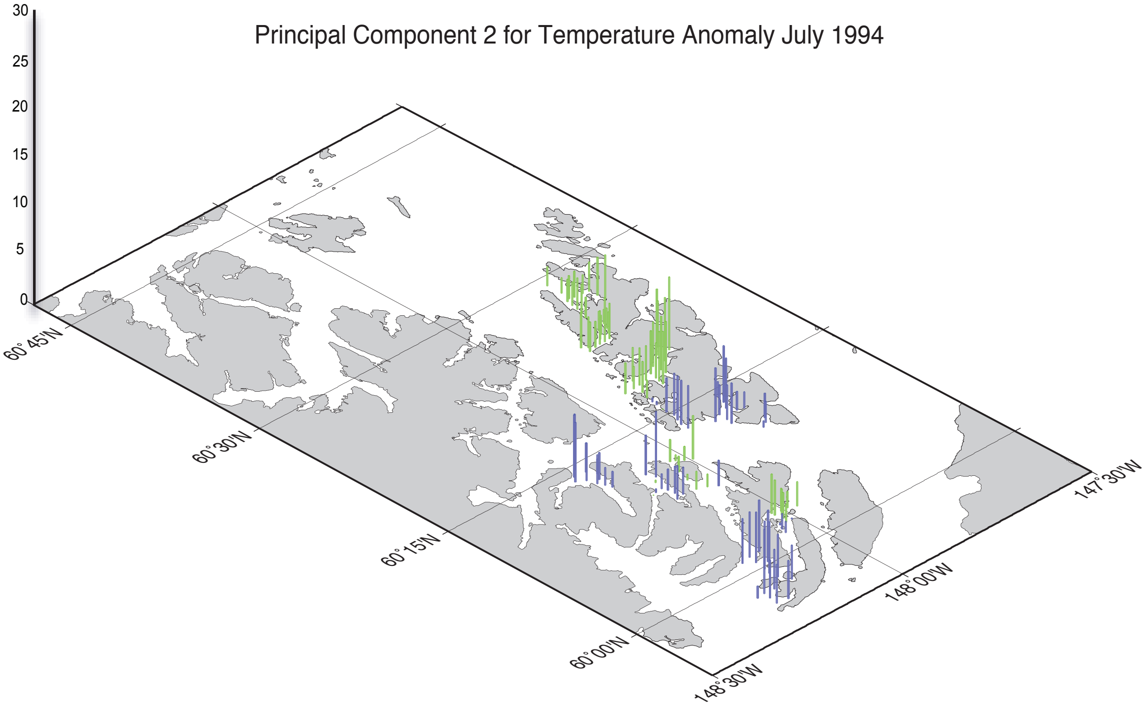

Principal Component 2 for Temperature Anomaly July 1994

Fig. 2.13 (cont.).

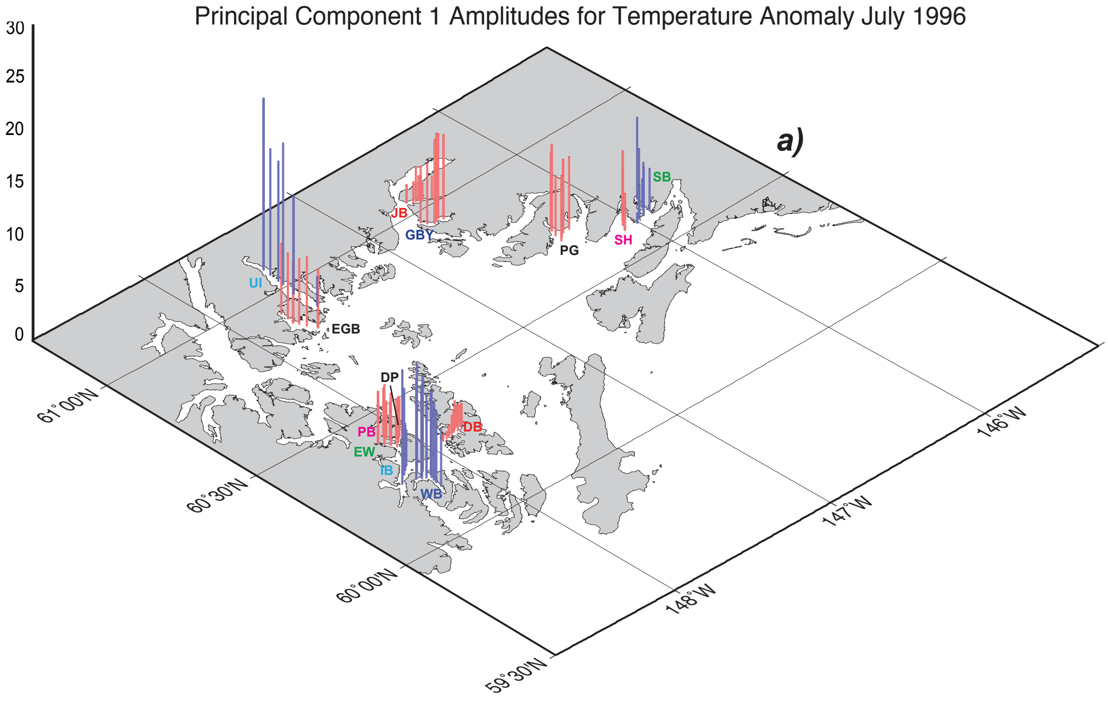
Principal Component 1 Amplitudes for Temperature Anomaly July 1996

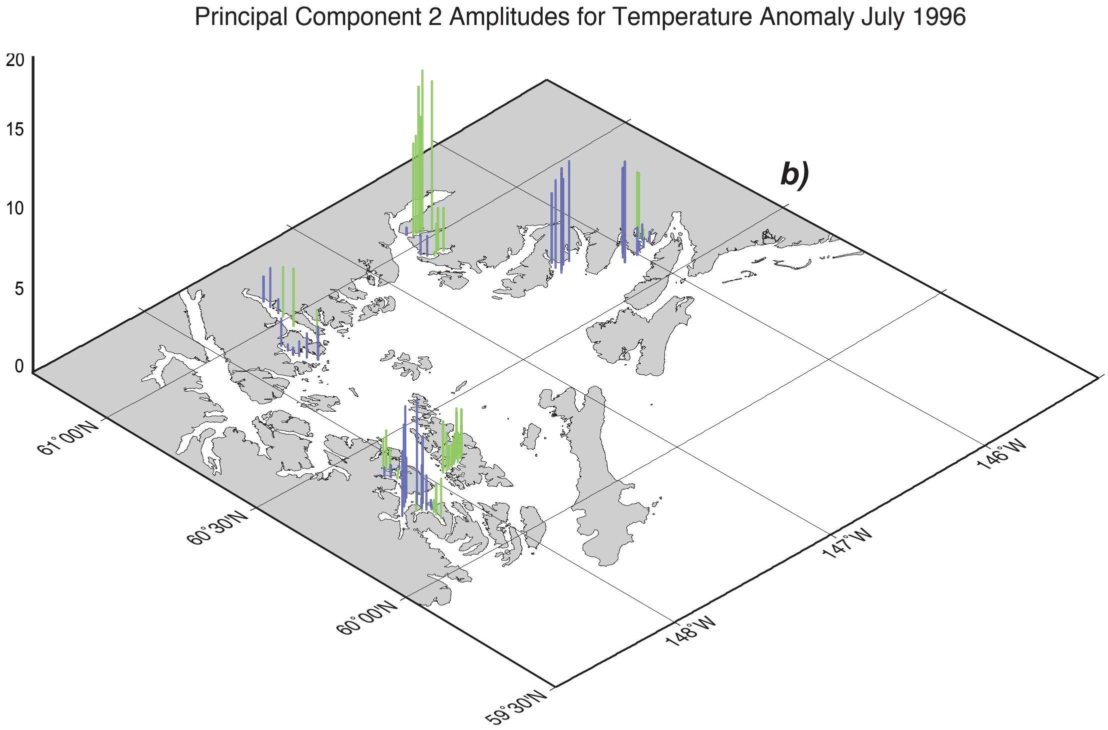
Principal Component 2 Amplitudes for Temperature Anomaly July 1996

Fig. 2.14. Principal component amplitudes for temperature anomalies in sub-regions across PWS in July (a,b) and August (c,d) 1996. Red and green are positive for modes 1 and 2 respectively, whereas blue is negative for both modes. Note the scale for mode 2 in July is expanded by 1.3x to show more contrast.

Principal Component 1 Amplitudes for Temperature Anomaly Aug 1996

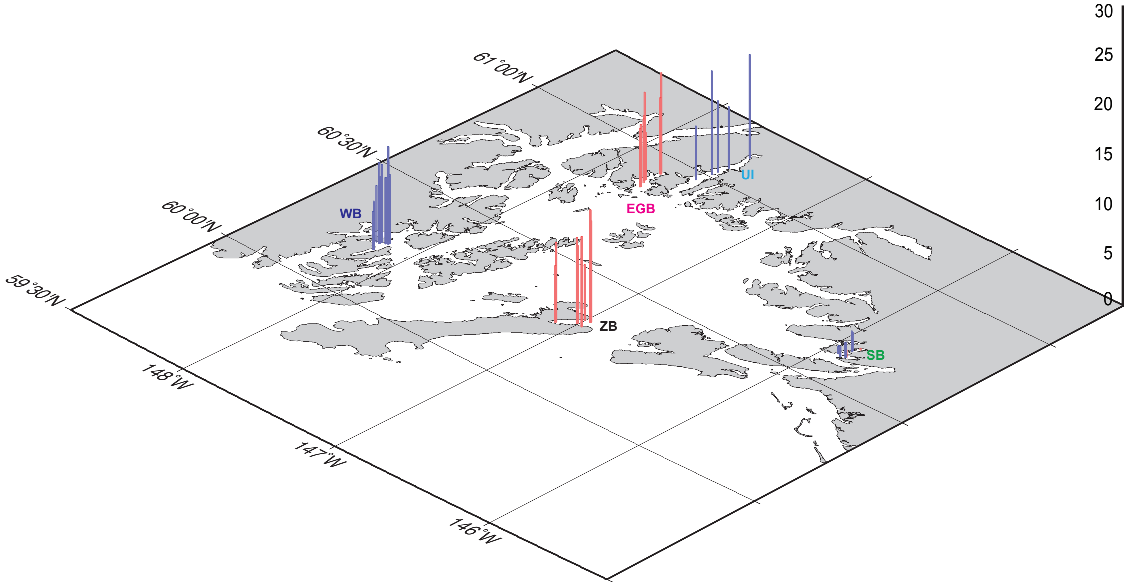

Principal Component 2 Amplitudes for Temperature Anomaly Aug 1996

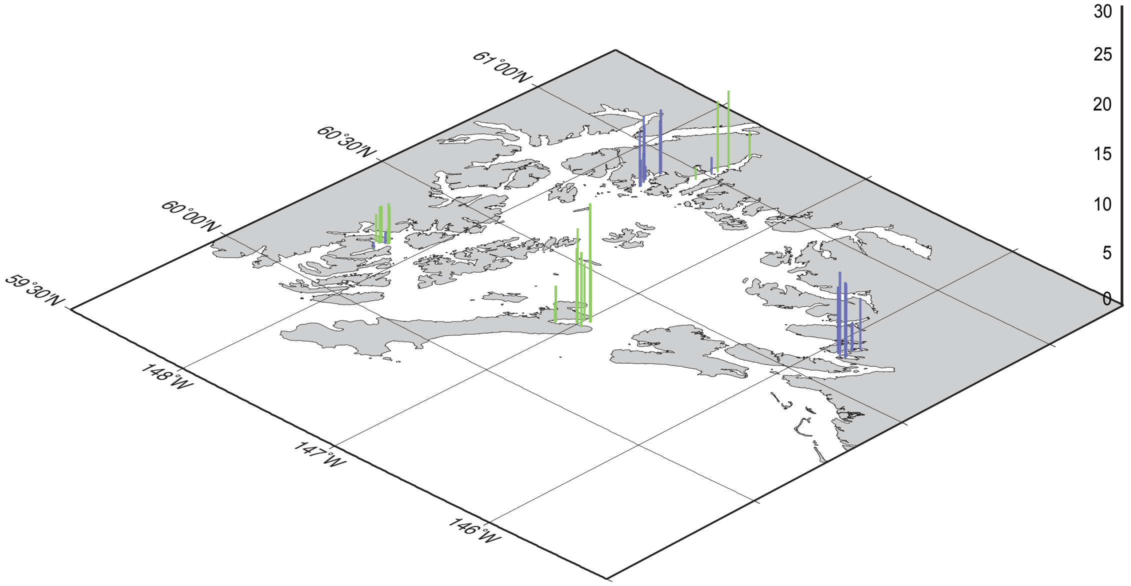

Fig. 2.14 (cont.).

Principal Component 1 Amplitudes for Temperature Anomaly July 1997

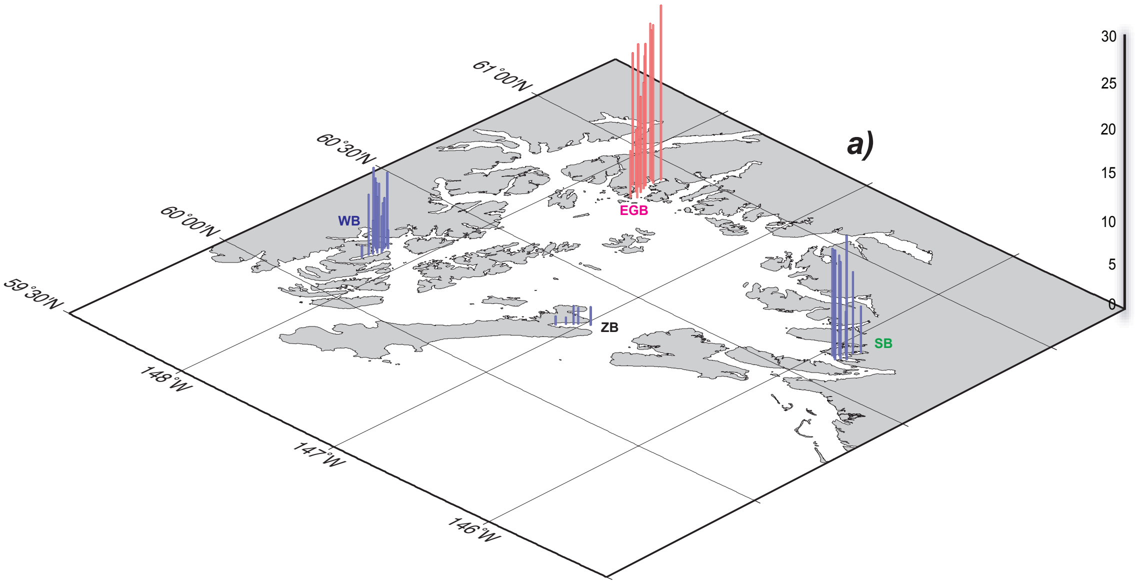

Principal Component 2 Amplitudes for Temperature Anomaly July 1997

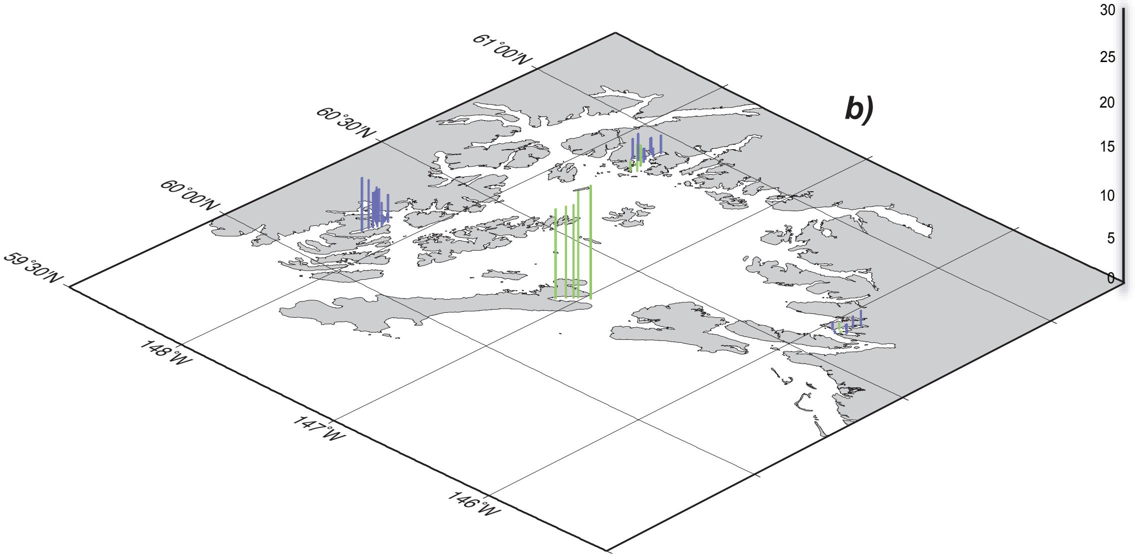

Fig. 2.15. Principal component amplitudes for temperature anomalies in sub-regions across PWS in July (a,b) and August (c,d) 1997. Red and green are positive for modes 1 and 2 respectively, whereas blue is negative for both modes. Note the scale for mode 2 in August is expanded by 1.3x to show more contrast.

Principal Component 1 Amplitudes for Temperature Anomaly Aug 1997

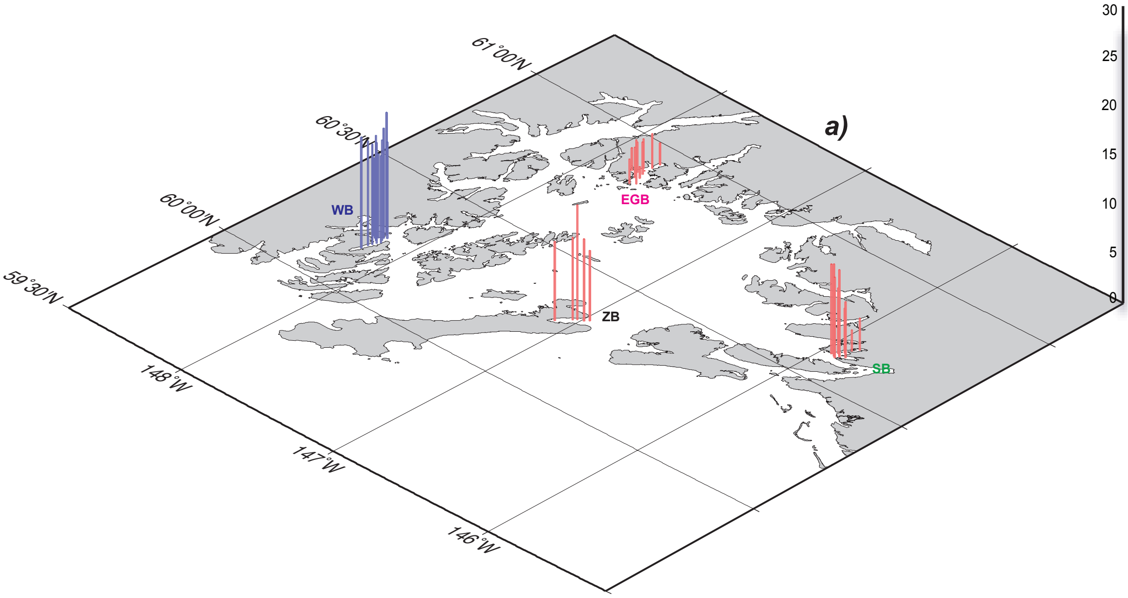

Principal Component 2 Amplitudes for Temperature Anomaly Aug 1997

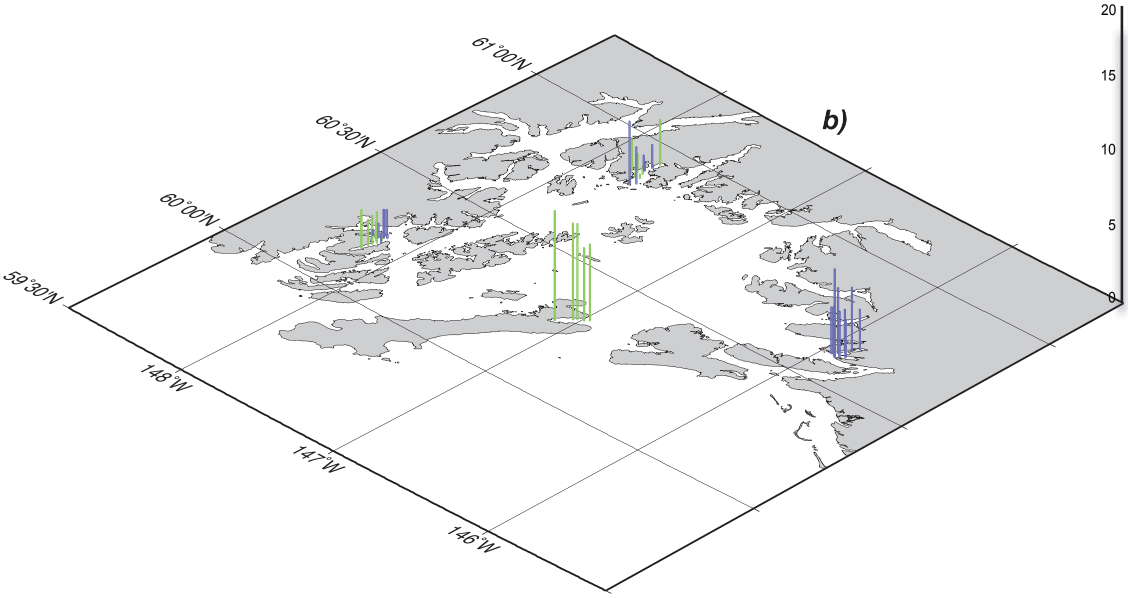

Fig. 2.15. (cont.).

a) May

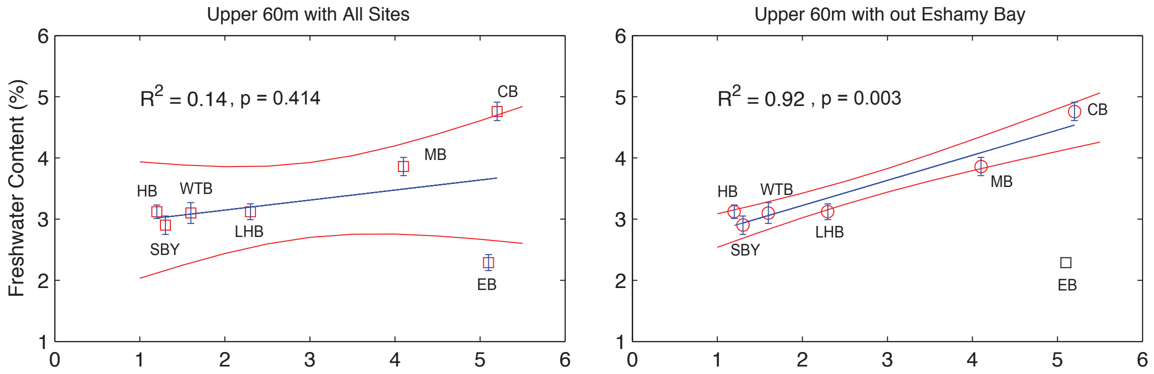

b) June

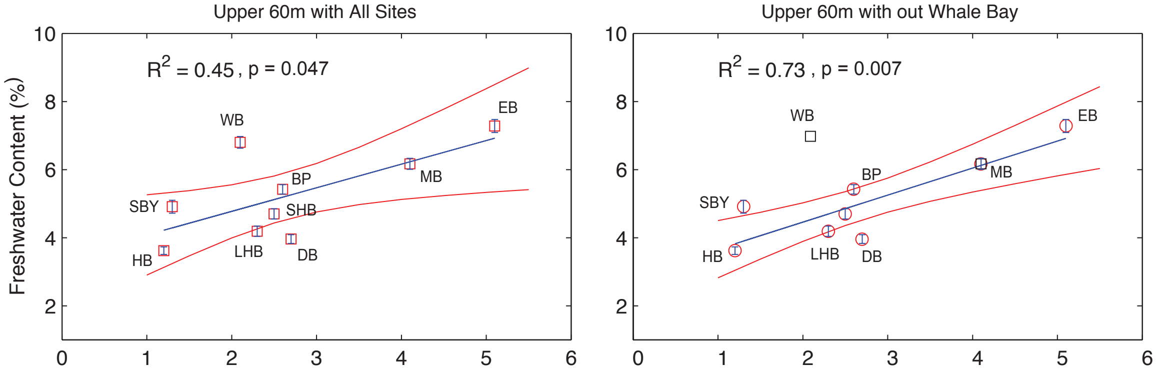

c) July

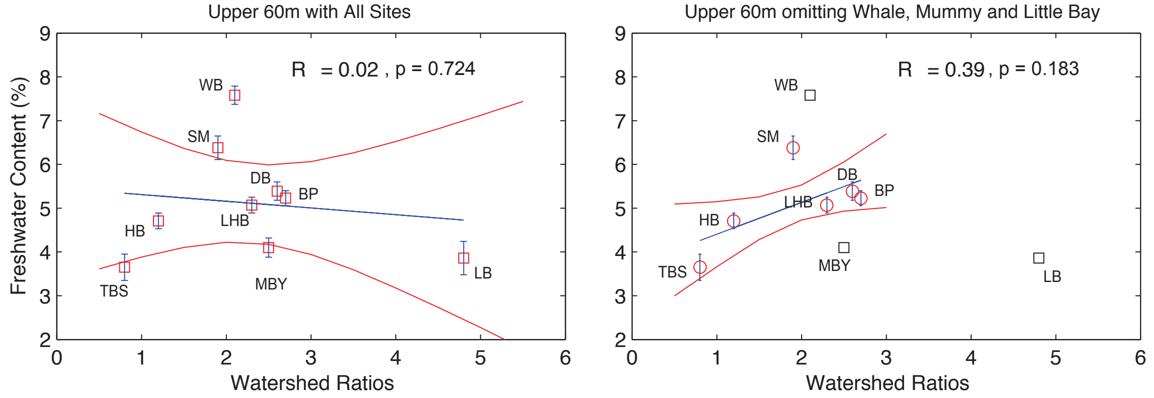

Fig. 2.16. Least squares regression of freshwater contents (*FWC*) in the upper 60*m* in 1994 and watershed ratios in a) May, b) June, and c) July. The regressions in May and June are enhanced significantly when single outliers are removed that are either anomalously high or low in *FWC* value, but the regression in July is very poor when all sites are included and removing outliers only moderately improves the results. Red lines are 95% confidence limits and error bars for the mean freshwater contents are standard errors.

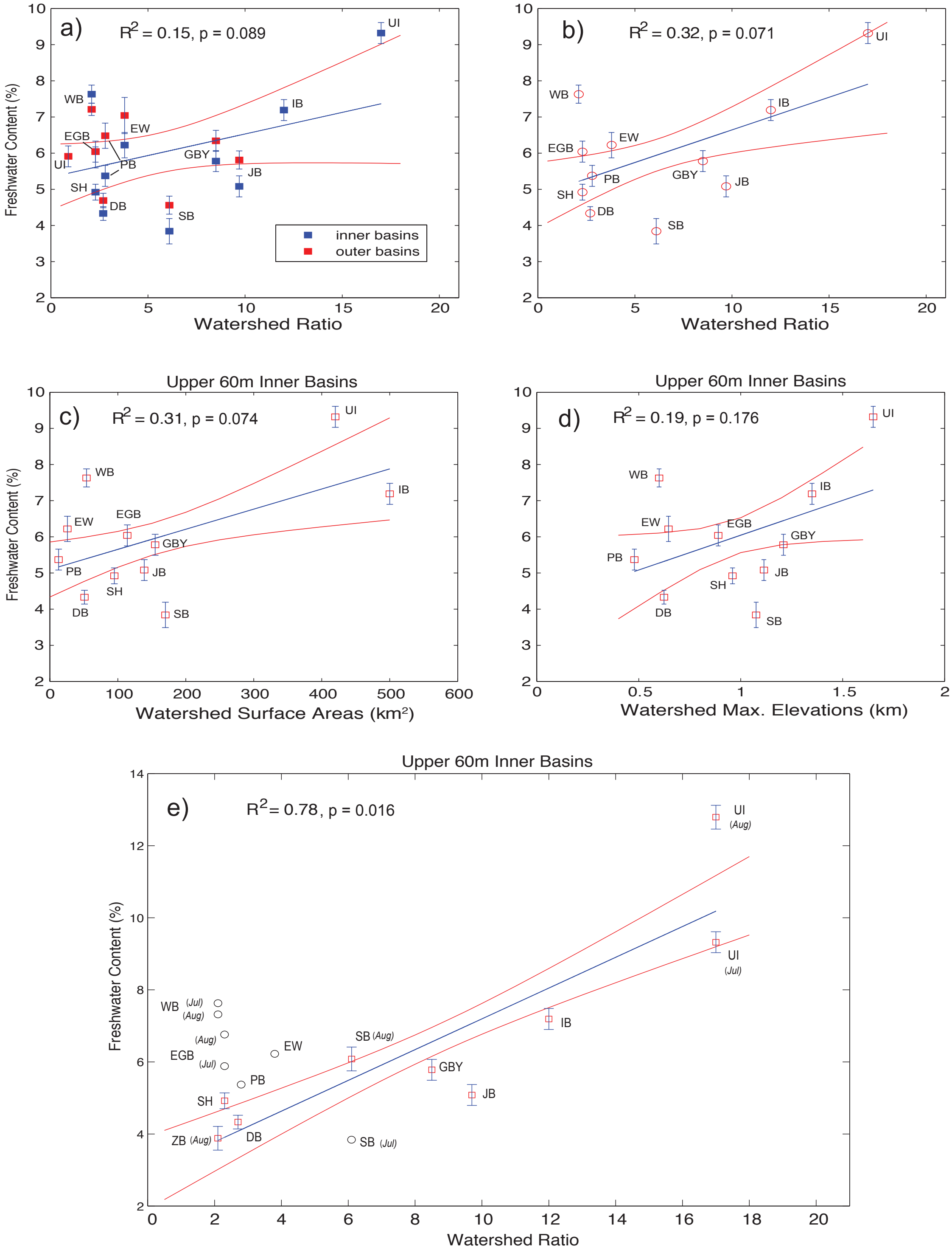

Fig. 2.17. Least squares regression of upper 60*m* freshwater contents in July 1996. a) inner and outer basins vs. watershed ratios, b) inner basins only vs. watershed ratios, c) watershed areas, d) maximum elevations, and e) watershed ratios with sites removed that are affected by allochthonous freshwater or exhibit a strong response to changes in precipitation. Error bars in the plots are standard errors.

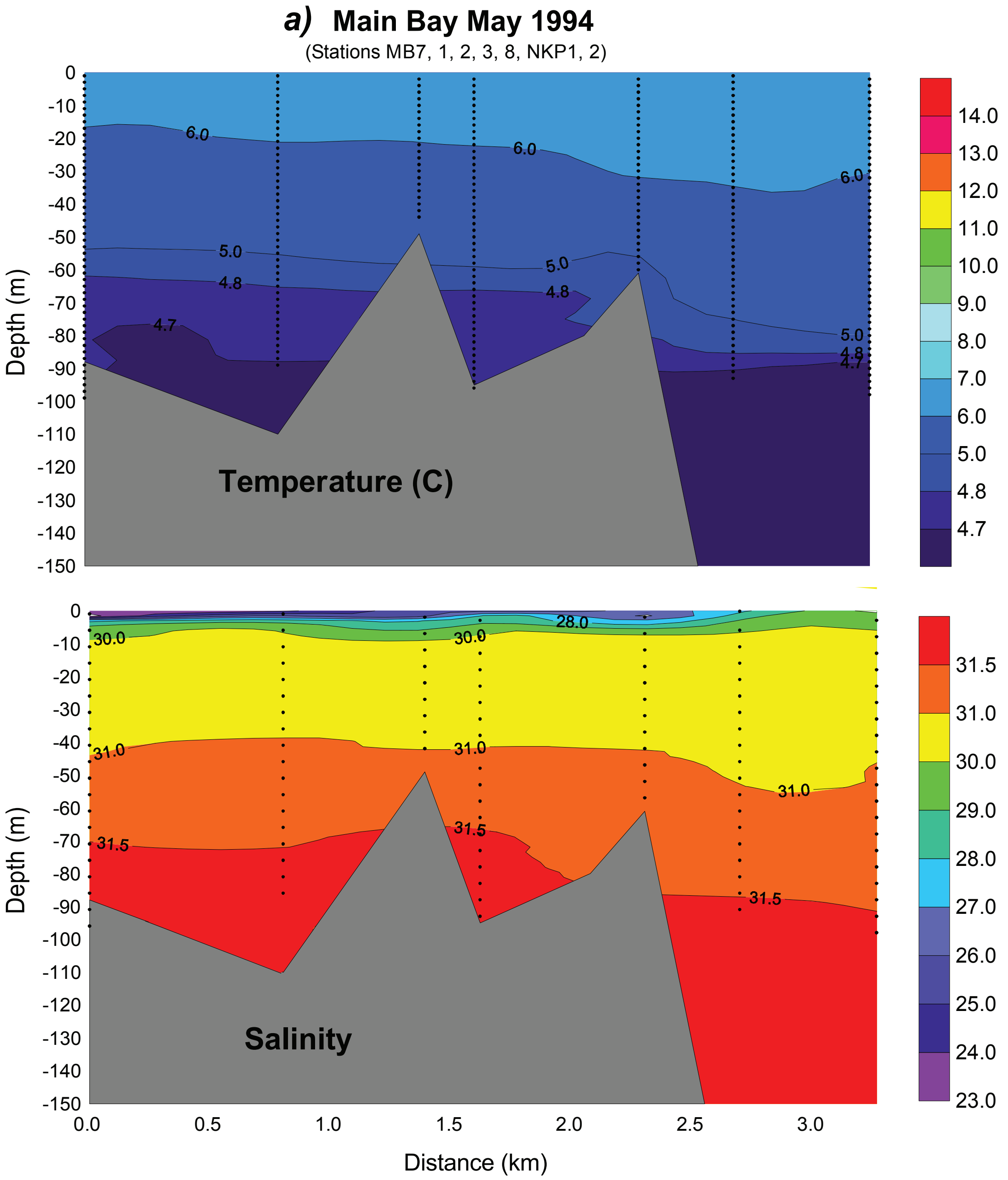

Fig. 2.18. Vertical sections of temperature and salinity in May and June 1994. a,b) Main and Eshamy in May; c,d) Herring and Lower Herring in May; e,f) Main and Eshamy in June; and g,h) Herring and Lower Herring in June.

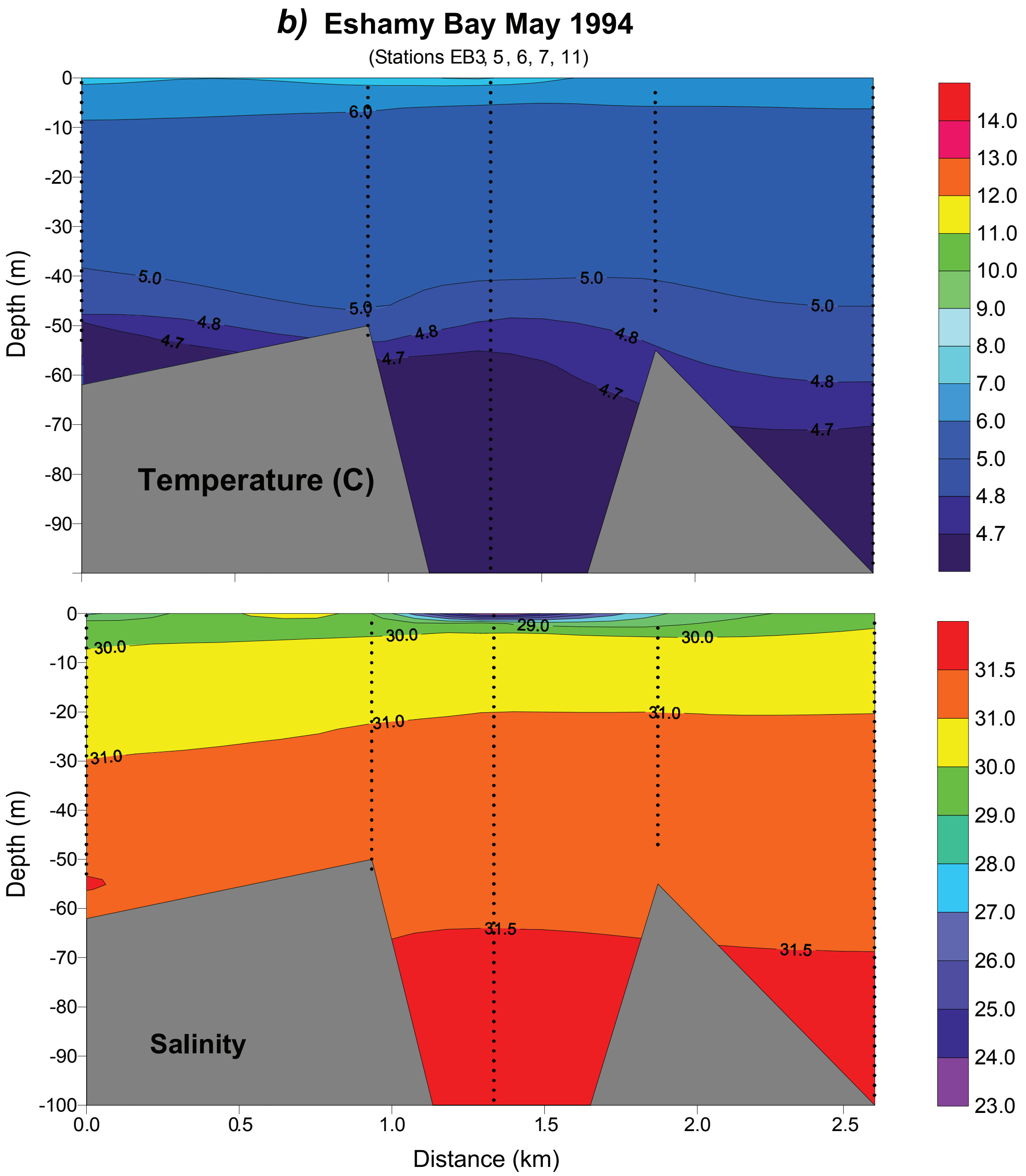
b) Eshamy Bay May 1994
(Stations EB3, 5, 6, 7, 11)
Depth (m)
0
-10
-20
-30
-40
-50
-60
-70
-80
-90
6.0
5.0
4.8
4.7
Temperature (C)
14.0
13.0
12.0
11.0
10.0
9.0
8.0
7.0
6.0
5.0
4.8
4.7
Depth (m)
-100
30.0
29.0
31.0
31.5
Salinity
0.0
0.5
1.0
1.5
2.0
2.5
Distance (km)
31.5
31.0
30.0
29.0
28.0
27.0
26.0
25.0
24.0
23.0

Fig. 2.18 (cont.).

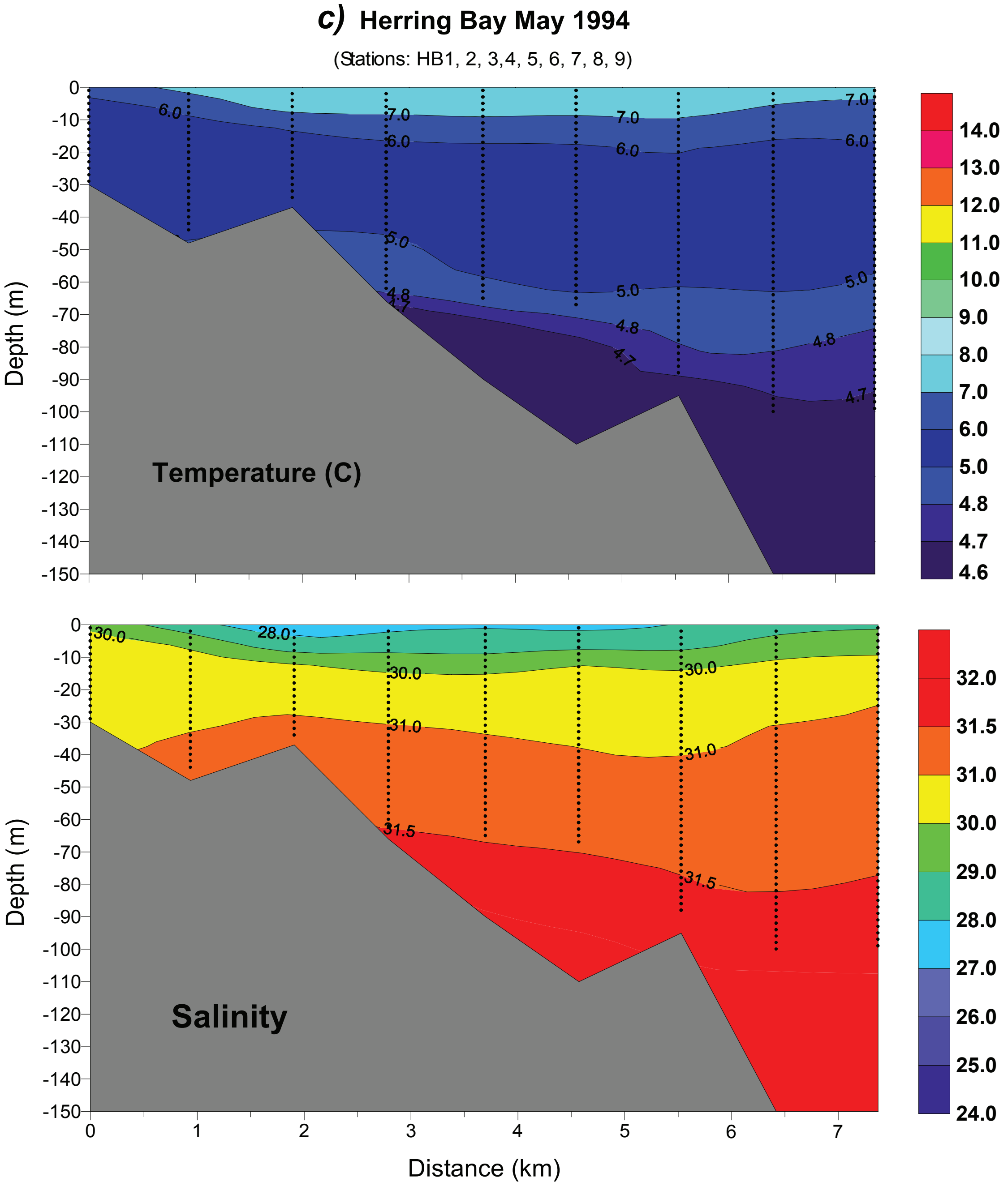
c) Herring Bay May 1994
(Stations: HB1, 2, 3,4, 5, 6, 7, 8, 9)
Temperature (C)
Salinity
Depth (m)
Distance (km)
0
-10
-20
-30
-40
-50
-60
-70
-80
-90
-100
-110
-120
-130
-140
-150
0
1
2
3
4
5
6
7
6.0
7.0
5.0
4.8
4.7
14.0
13.0
12.0
11.0
10.0
9.0
8.0
4.6
30.0
28.0
31.0
31.5
32.0
29.0
27.0
26.0
25.0
24.0

Fig. 2.18 (cont.).

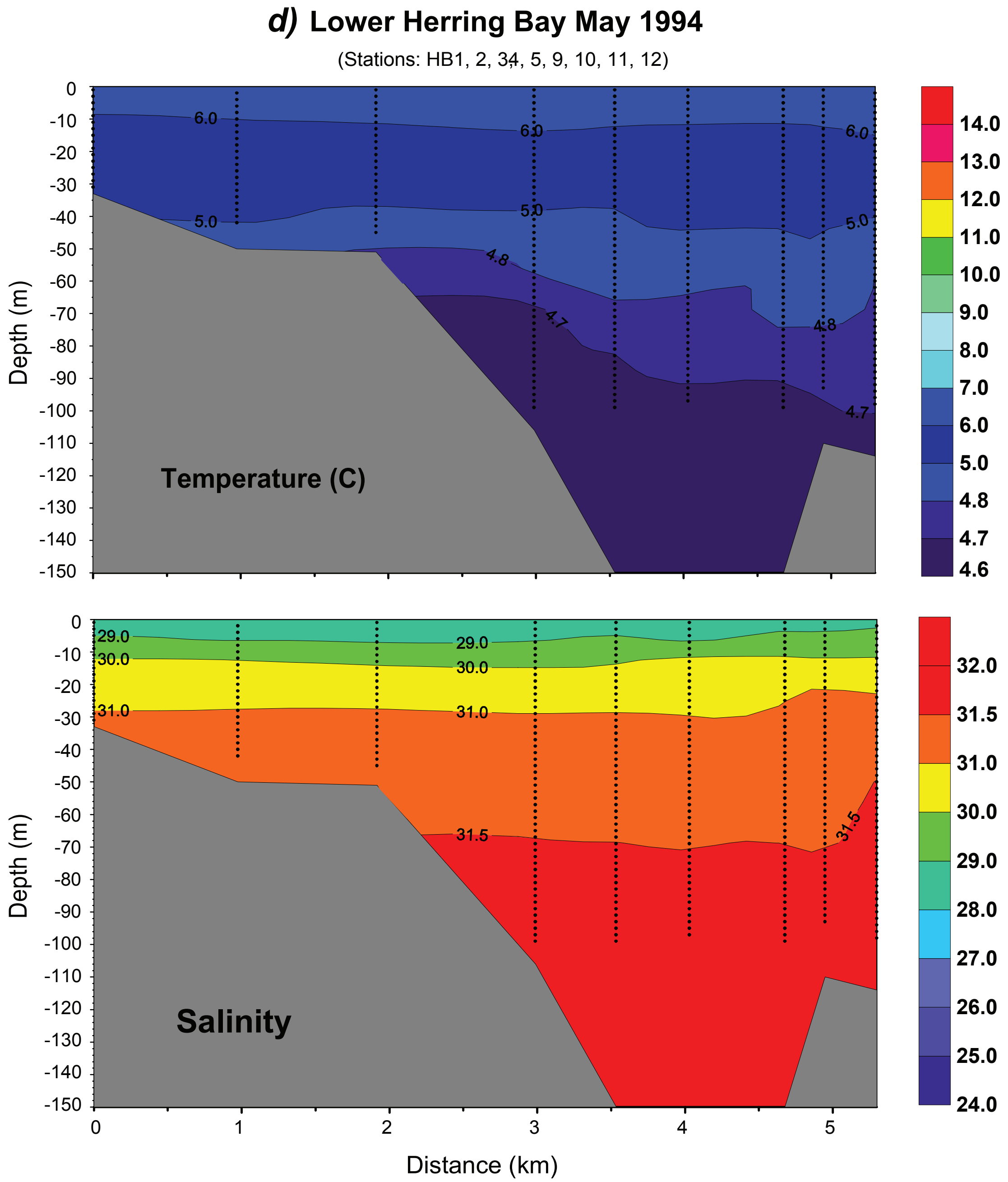
d) **Lower Herring Bay May 1994**

(Stations: HB1, 2, 3,4, 5, 9, 10, 11, 12)

Temperature (C)

Salinity

Fig. 2.18 (cont.).

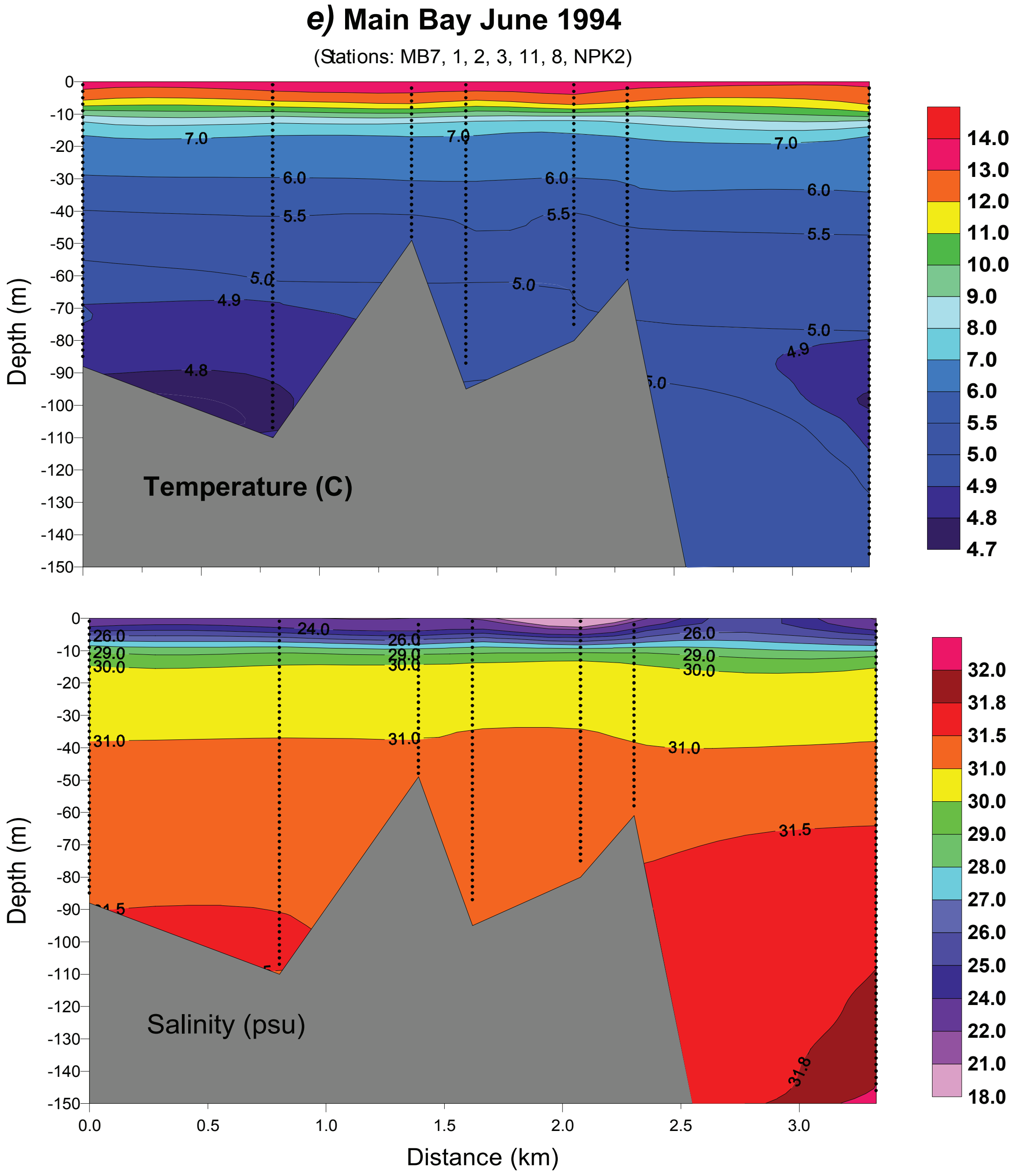

e) **Main Bay June 1994**

(Stations: MB7, 1, 2, 3, 11, 8, NPK2)

Fig. 2.18 (cont.).

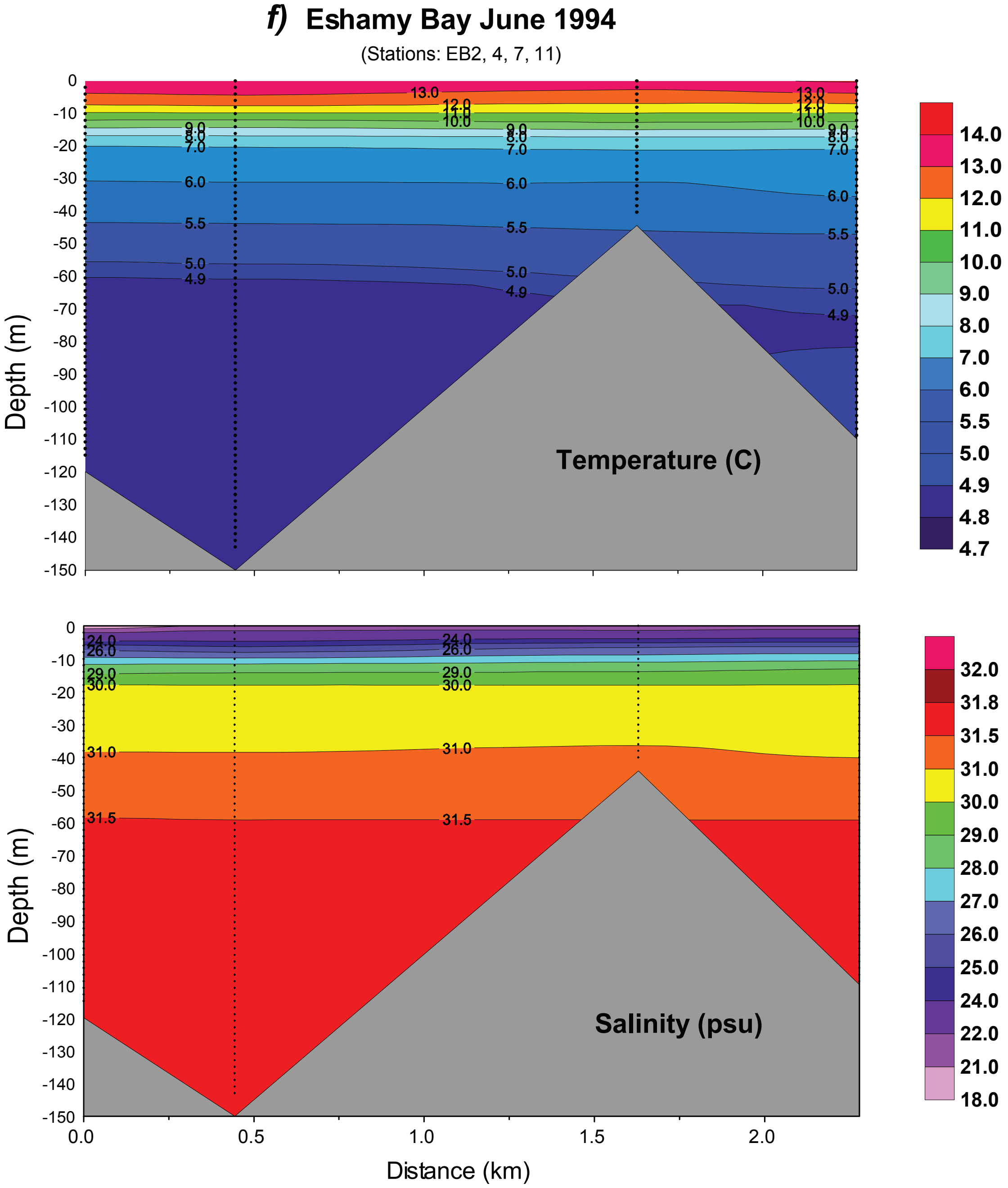

***f)* Eshamy Bay June 1994**

(Stations: EB2, 4, 7, 11)

Fig. 2.18 (cont.).

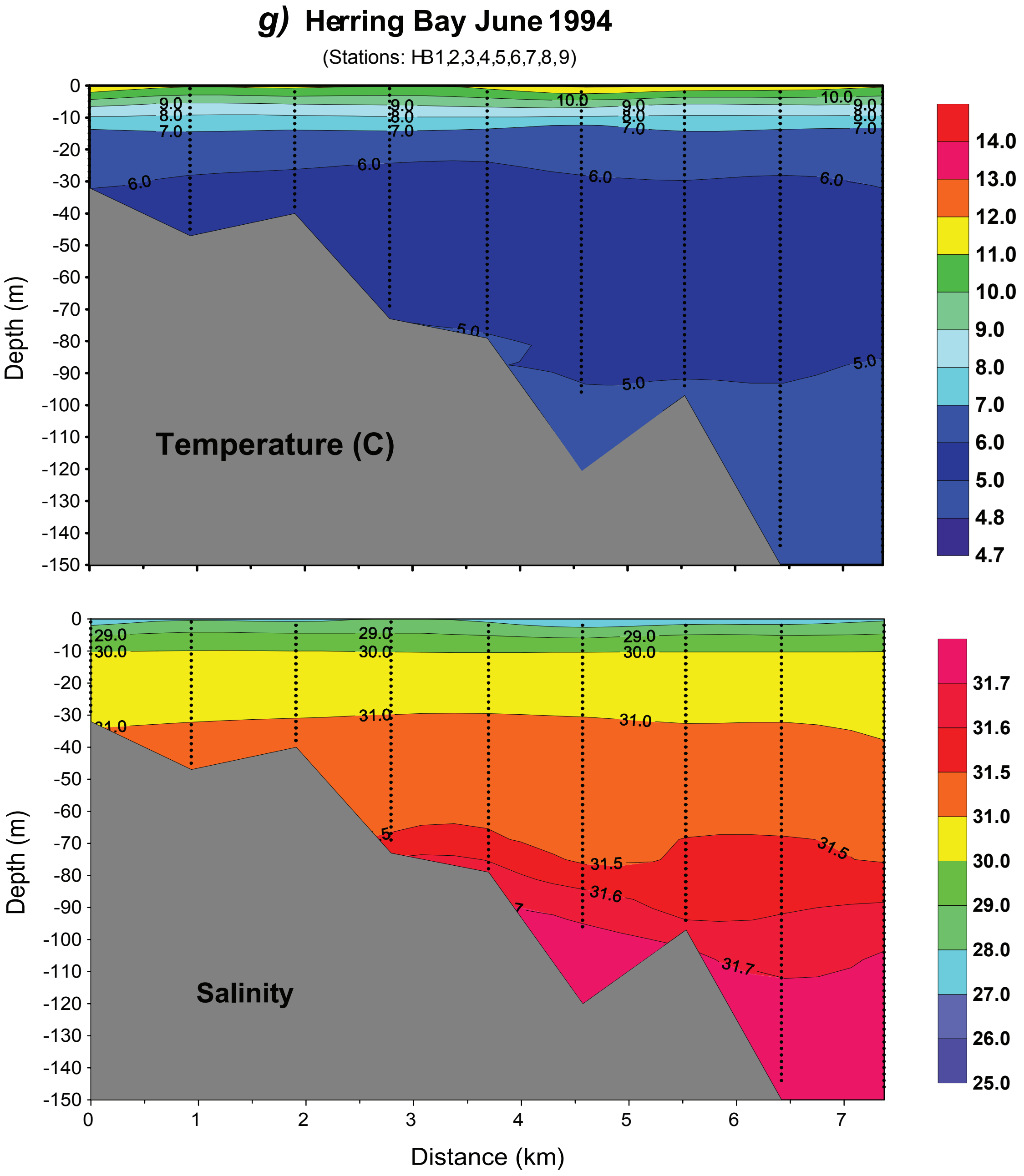
g) Herring Bay June 1994
(Stations: HB1,2,3,4,5,6,7,8,9)
Temperature (C)
Depth (m)
0
-10
-20
-30
-40
-50
-60
-70
-80
-90
-100
-110
-120
-130
-140
-150
9.0
8.0
7.0
10.0
6.0
5.0
14.0
13.0
12.0
11.0
10.0
9.0
8.0
7.0
6.0
5.0
4.8
4.7
Salinity
29.0
30.0
31.0
31.5
31.6
31.7
31.7
31.6
31.5
31.0
30.0
29.0
28.0
27.0
26.0
25.0
0
1
2
3
4
5
6
7
Distance (km)

Fig. 2.18 (cont.).

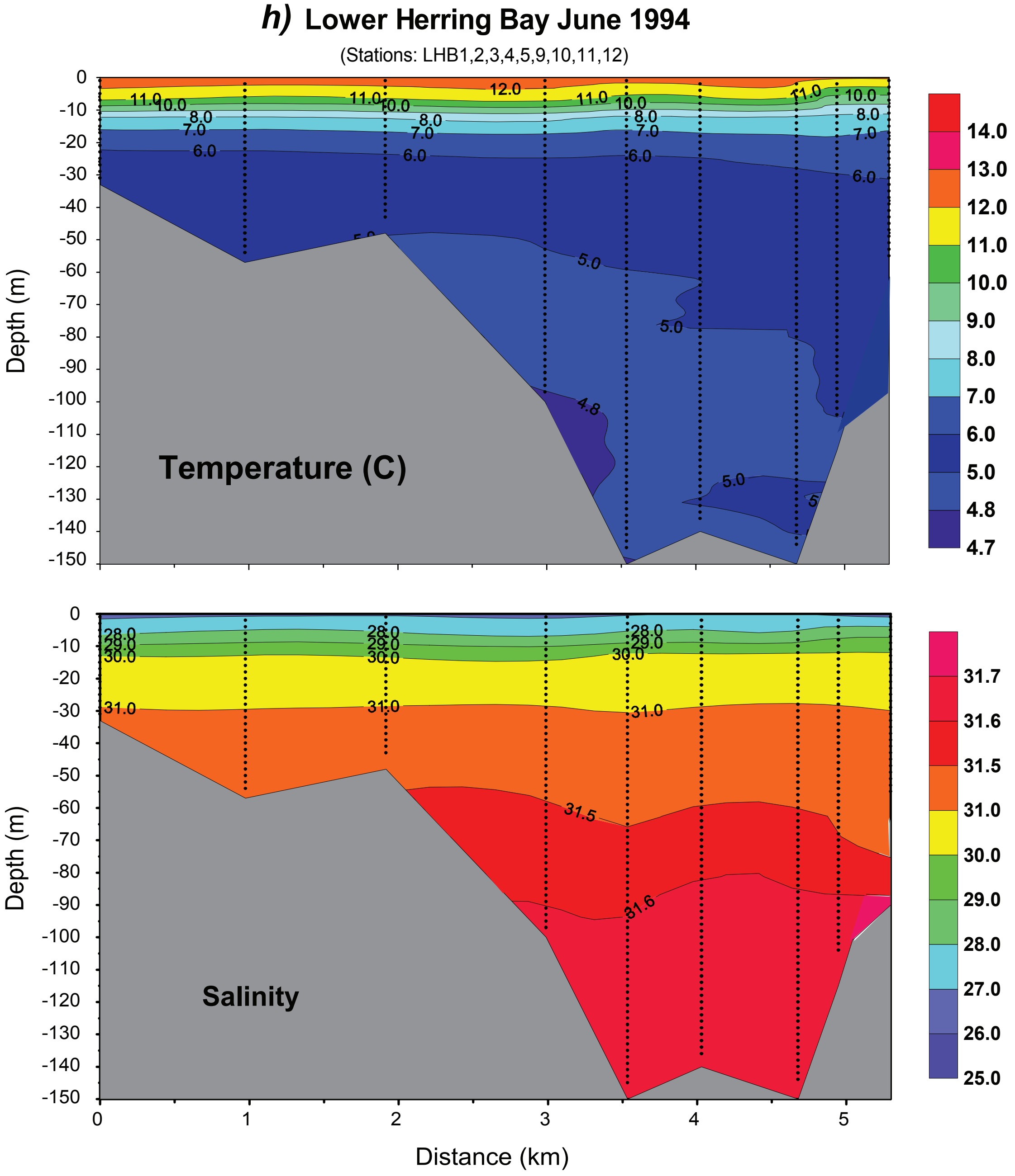

h) **Lower Herring Bay June 1994**

(Stations: LHB1,2,3,4,5,9,10,11,12)

Fig. 2.18 (cont.).

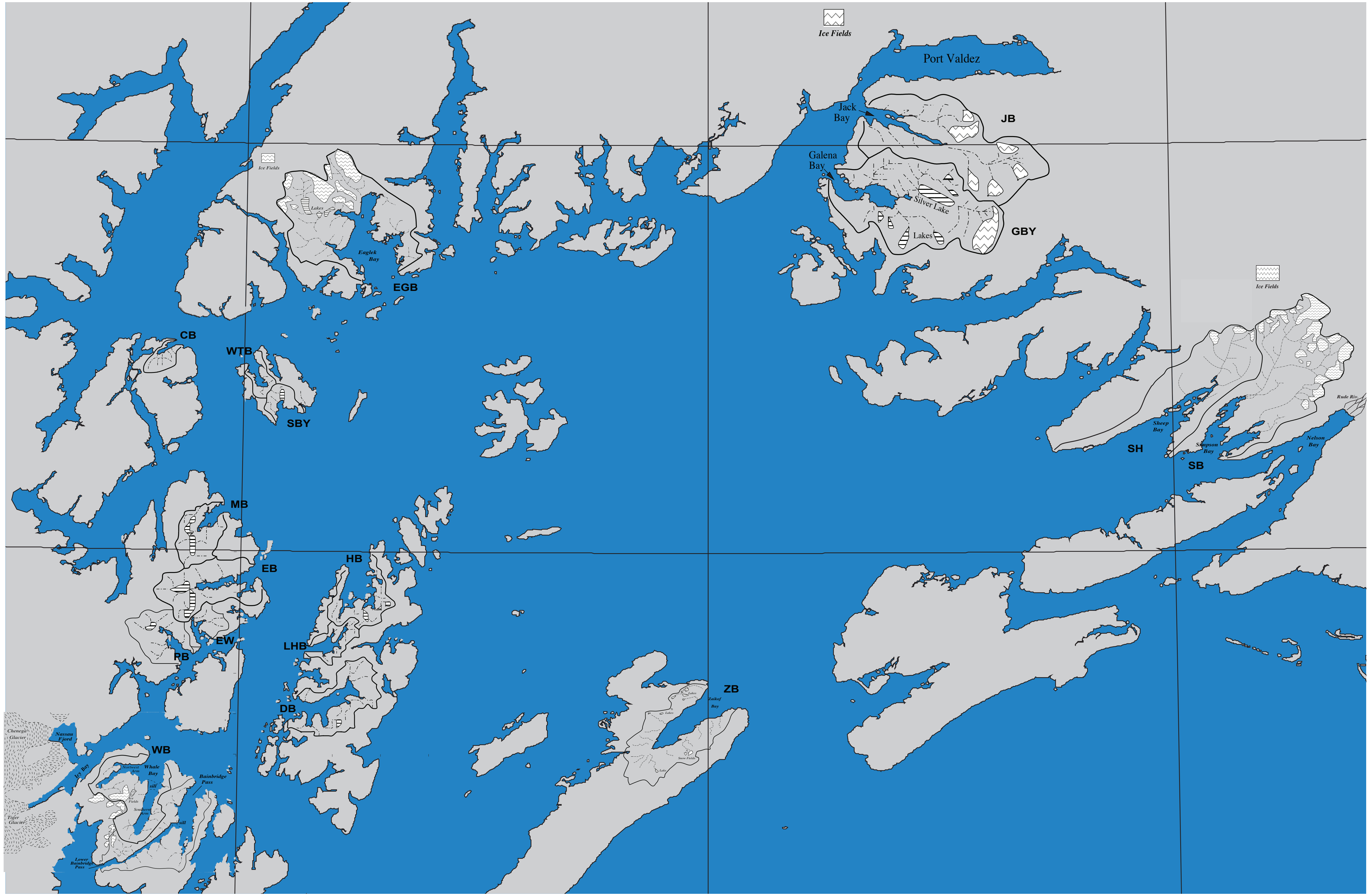

Fig. 2.19. Examples of watersheds of small PWS fjords. White areas with stippling denote alpine glaciers, striped areas lakes and small lines drainages. Location codes are given in Table 2.1.

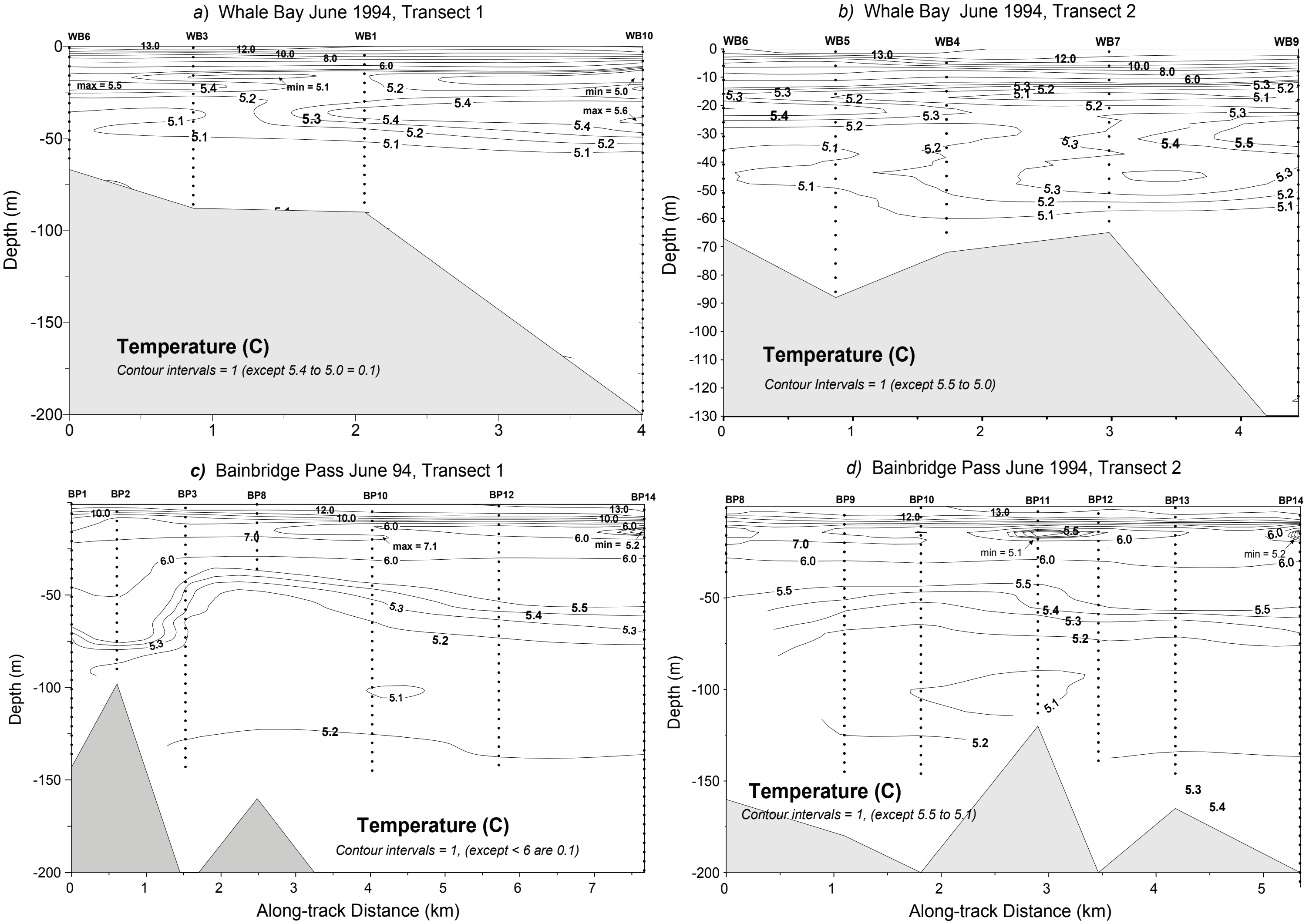

Fig. 2.20. Vertical sections of temperature at Whale Bay and Bainbridge Pass in June 1994 (a,b), Icy Bay and Whale Bay in March 1996 (e,f), and Icy Bay and Whale Bay in July 1996 (g,h). Locations of transects used in the contour plots are shown in Appendix 3.2.

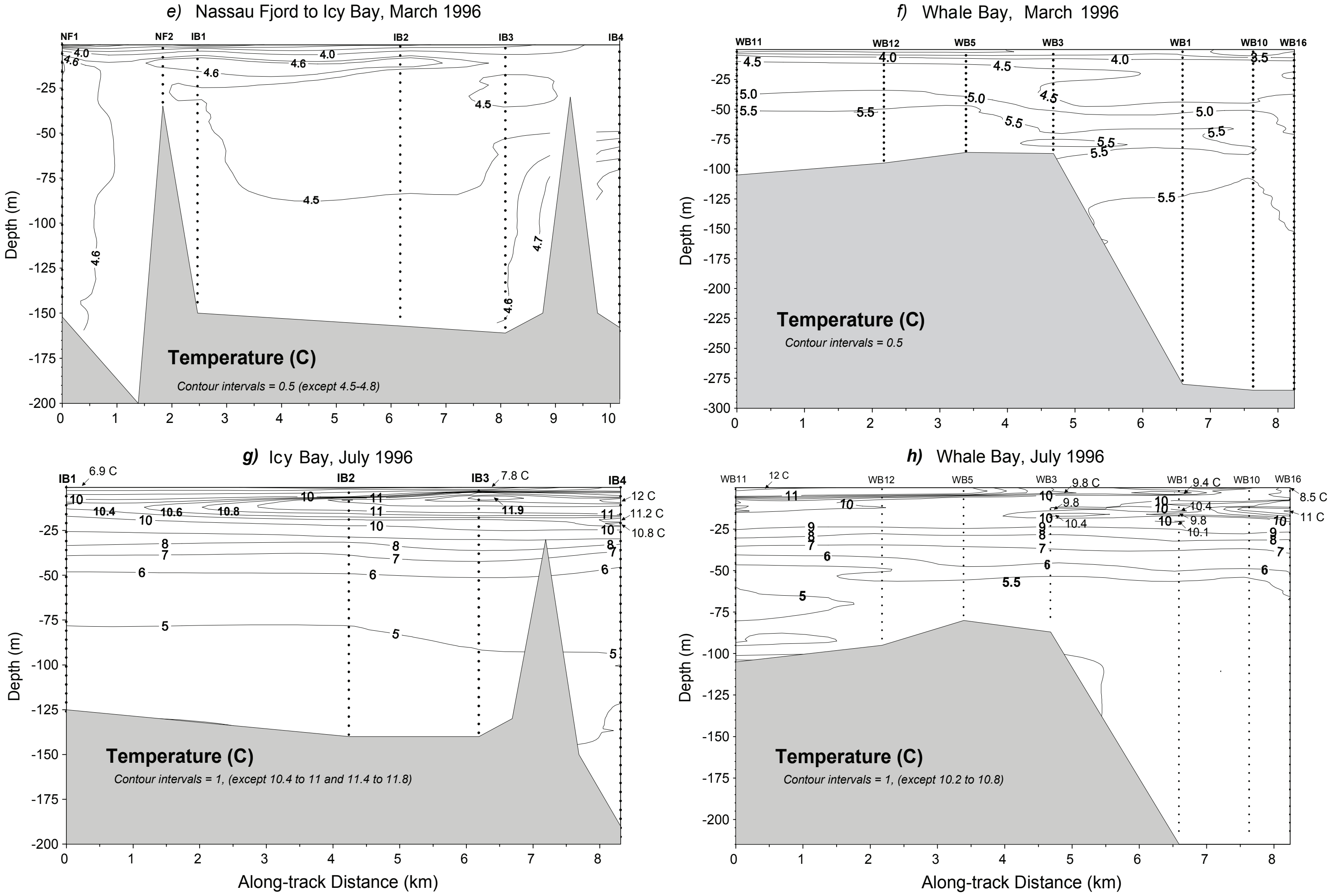

e) Nassau Fjord to Icy Bay, March 1996

f) Whale Bay, March 1996

g) Icy Bay, July 1996

h) Whale Bay, July 1996

Fig. 20 (cont.).

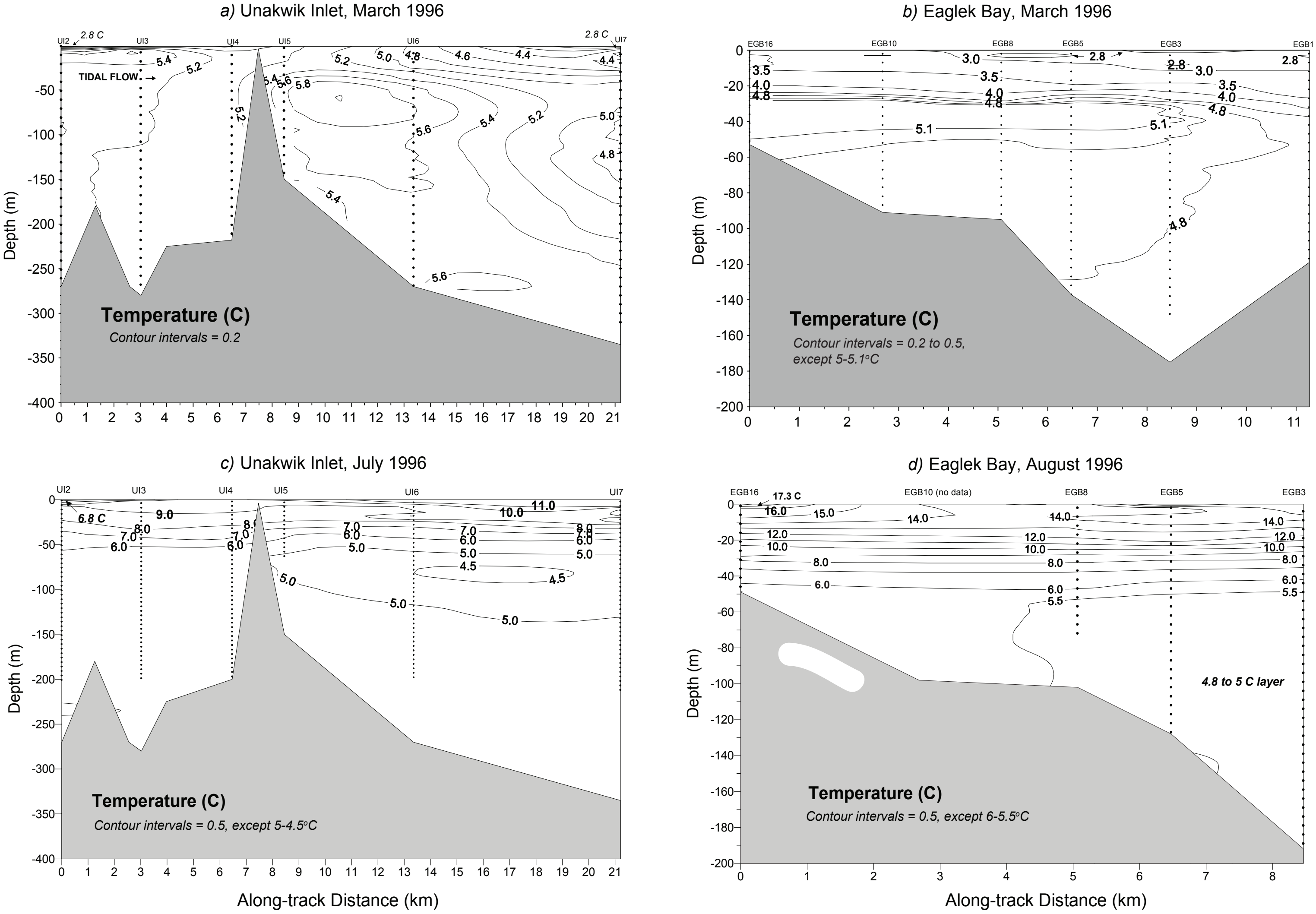

Fig. 2.21. Vertical sections of temperature at Unakwik Inlet and Eaglek Bay in March 1996 (a,b), and in July and August 1996 (e,f), Eaglek Bay in July and August 1997 (e,f) and Unakwik Inlet in August 1996 (g). Locations of transects used in the contour plots are shown in Appendix 3.2.

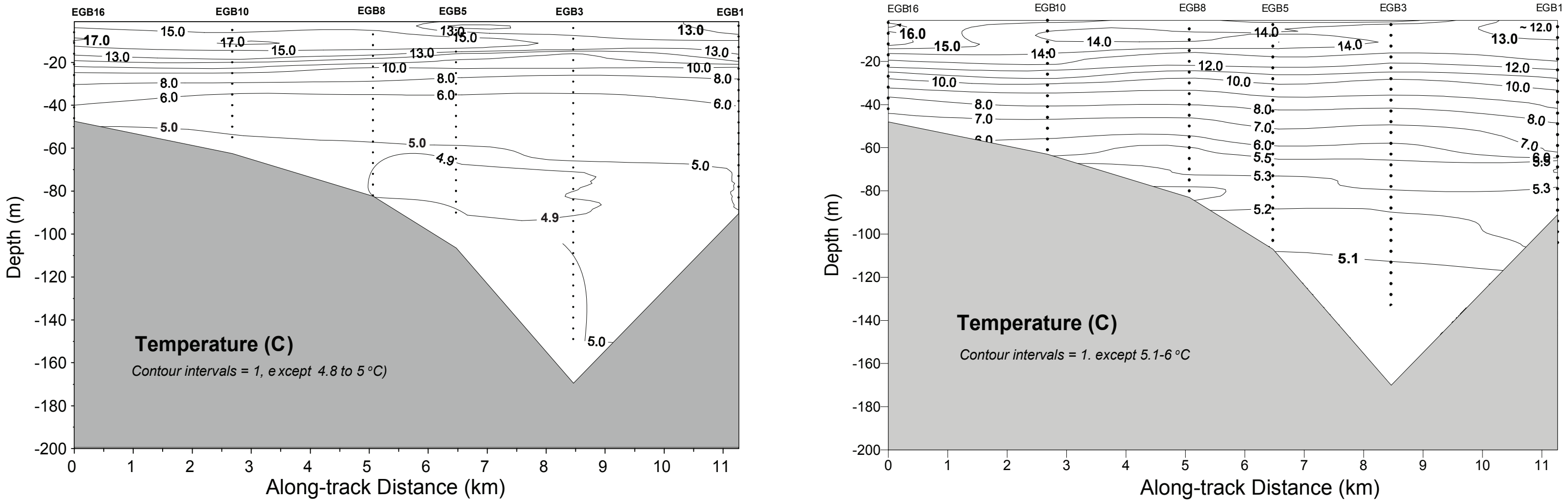

e) Eaglek Bay, July 1997

f) Eaglek Bay, August 1997

g) Unakwik Inlet, March 1996

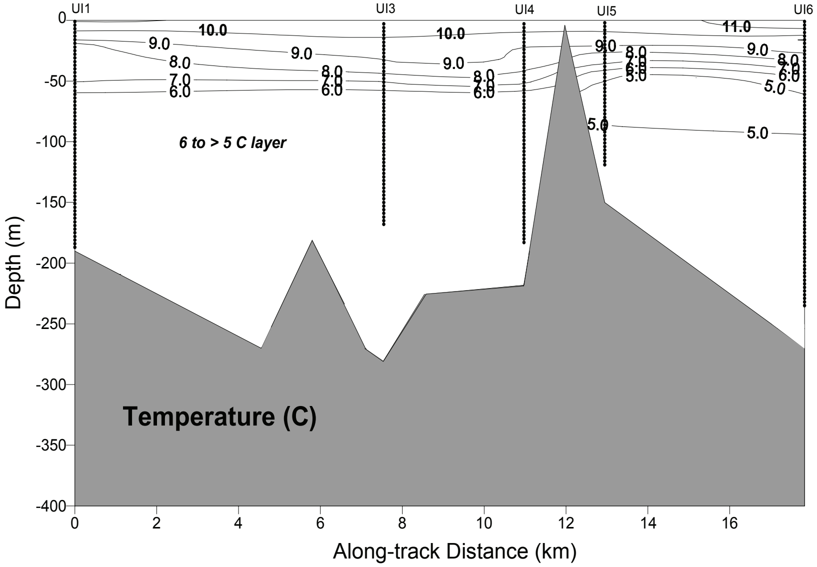

Fig. 21 (cont.).

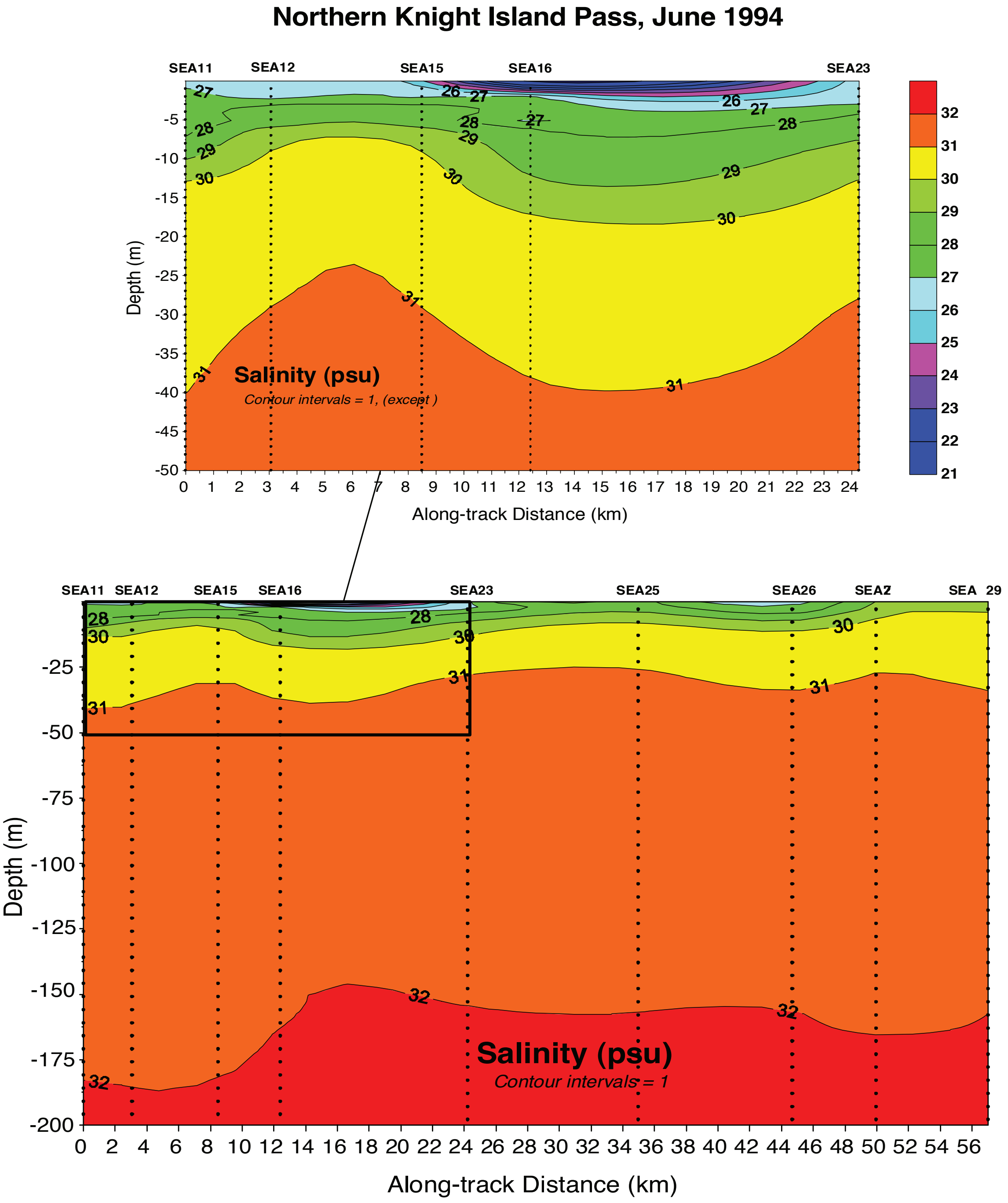

Fig. 2. 22. Vertical sections of salinity within northern Knight Island Pass in June 1994 from SEA stations shown in Figure 1B. Note the upper panel is a magnification of the inset for stations 11 to 23.

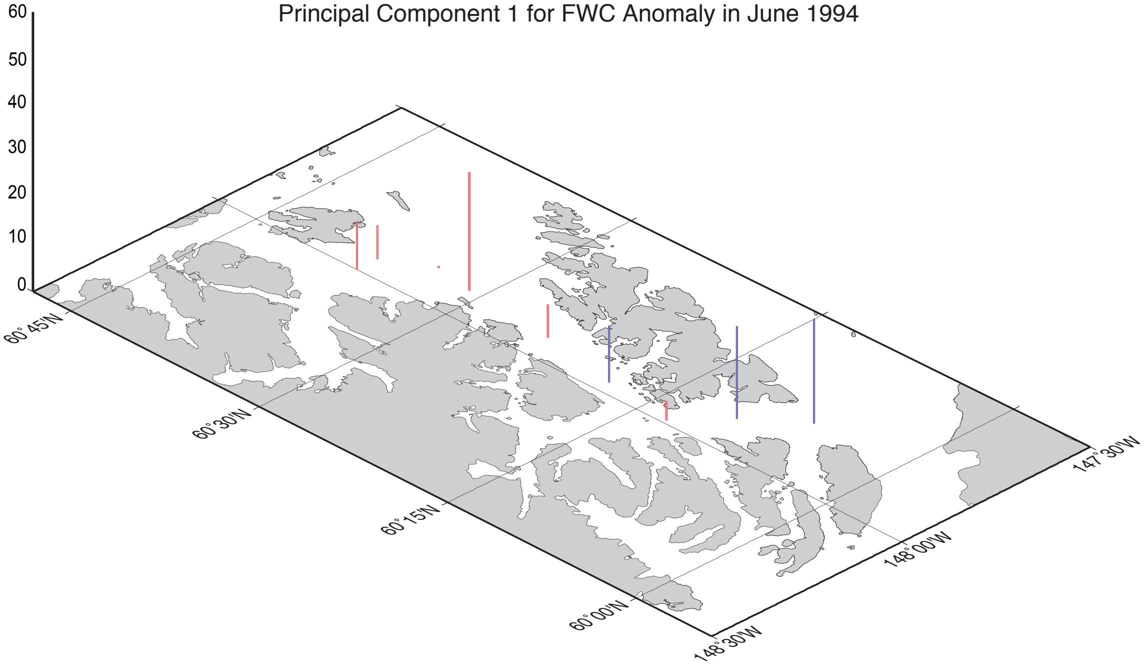

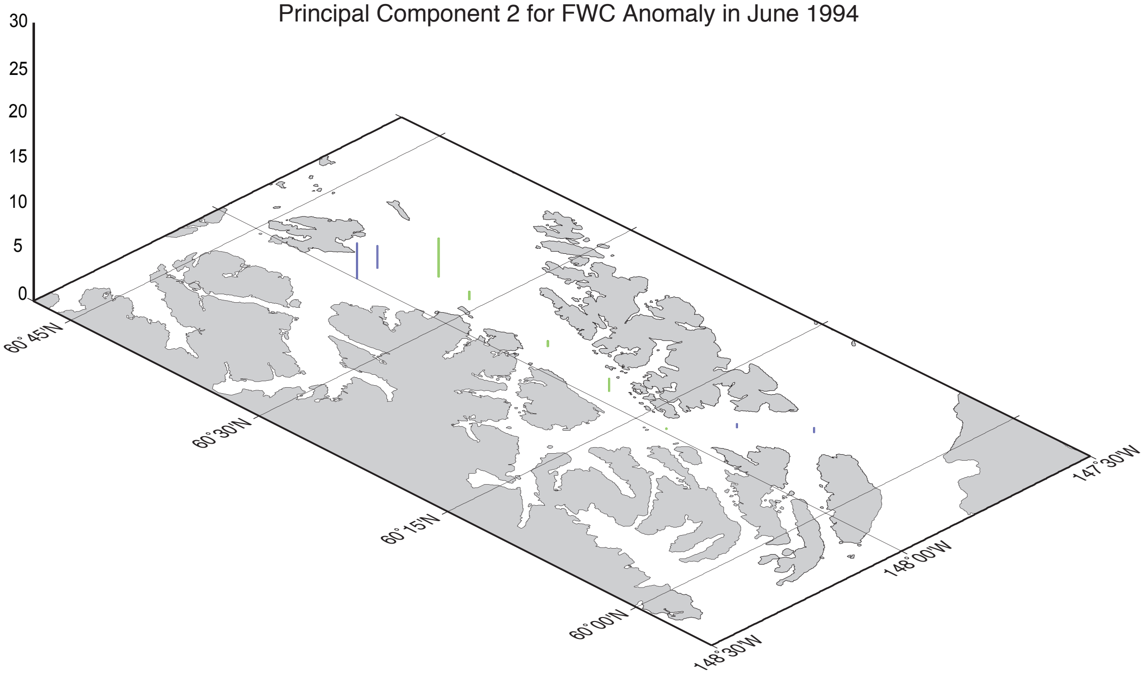

Fig. 2.23. Principal component amplitudes for FWC anomalies in Knight Island Pass in June 1994. Red and green are positive for modes 1 and 2 respectively, whereas blue is negative for both modes.

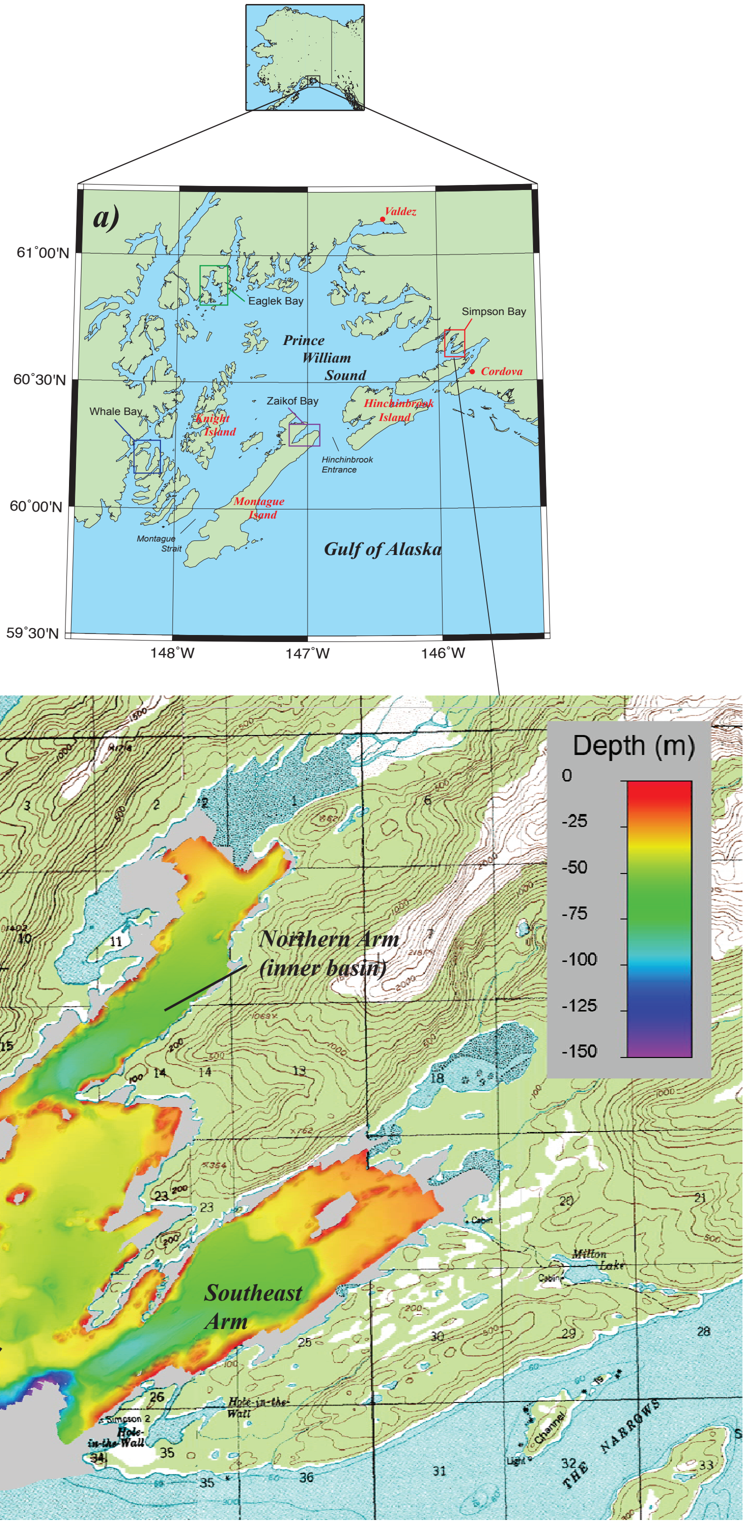

Fig 3.1. a) Location of Prince William Sound, Alaska and small fjords surveyed during the Sound Ecosystem Assessment Program and b) bathymetry of three basins that form Simpson Bay.*

*Reprinted with permission from “A high resolution geophysical investigation of sediment distribution controlled by catchment size and tides in a multi-basin turbid outwash fjord: Simpson Bay, Prince William Sound, Alaska” by Noll CJ, Dellapenna TM, Gilkinson A, Davis RW Geo-Mar Lett 29: 1−16, Copyright 2008 by Springer.

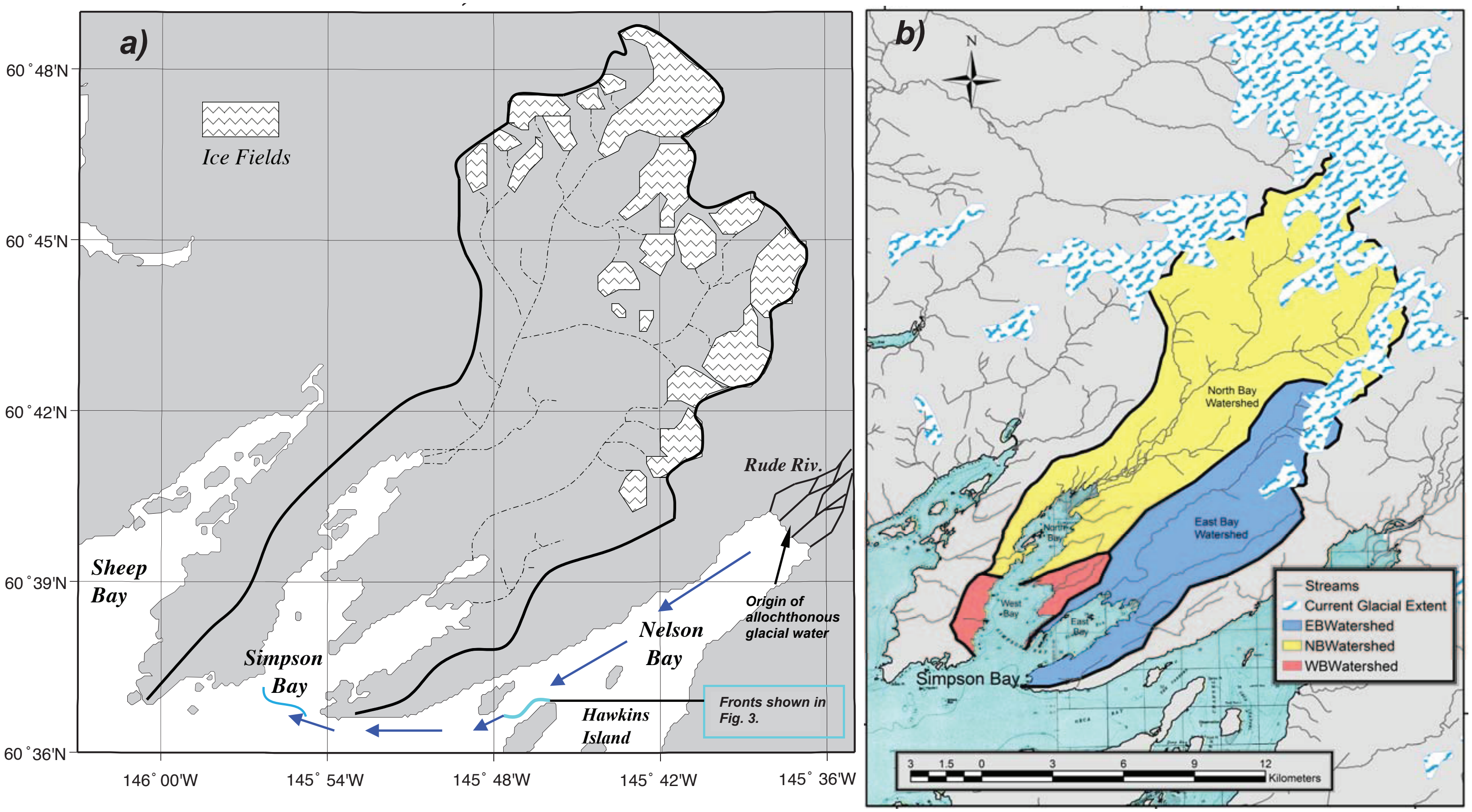

Fig 3.2. Watershed area and topography at Simpson Bay. a) total watershed area with high elevation alpine glaciers*; b) three sub-watersheds showing the primary drainages into the northern and southeast arms. The main basin, by contrast, has very little drainage area. Also shown is the potential source of allochthonous freshwater from the Rude River and locations of fronts observed in 2007 and 2011.#

*a) reprinted with permission from "Seasonal hydrography and tidal currents of bays and fjords in Prince William Sound, Alaska" by Gay, S.M. III and S.L.Vaughan Fish. Oceanogr. 10 (Suppl. 1), 159-193, Copyright 2001 by John Wiley and Sons. # b) reprinted with permission from "A high resolution geophysical investigation of sediment distribution controlled by catchment size and tides in a multi-basin turbid outwash fjord: Simpson Bay, Prince William Sound, Alaska" by Noll CJ, Dellapenna TM, Gilkinson A, Davis RW Geo-Mar Lett 29: 1–16, Copyright 2008 by Springer.

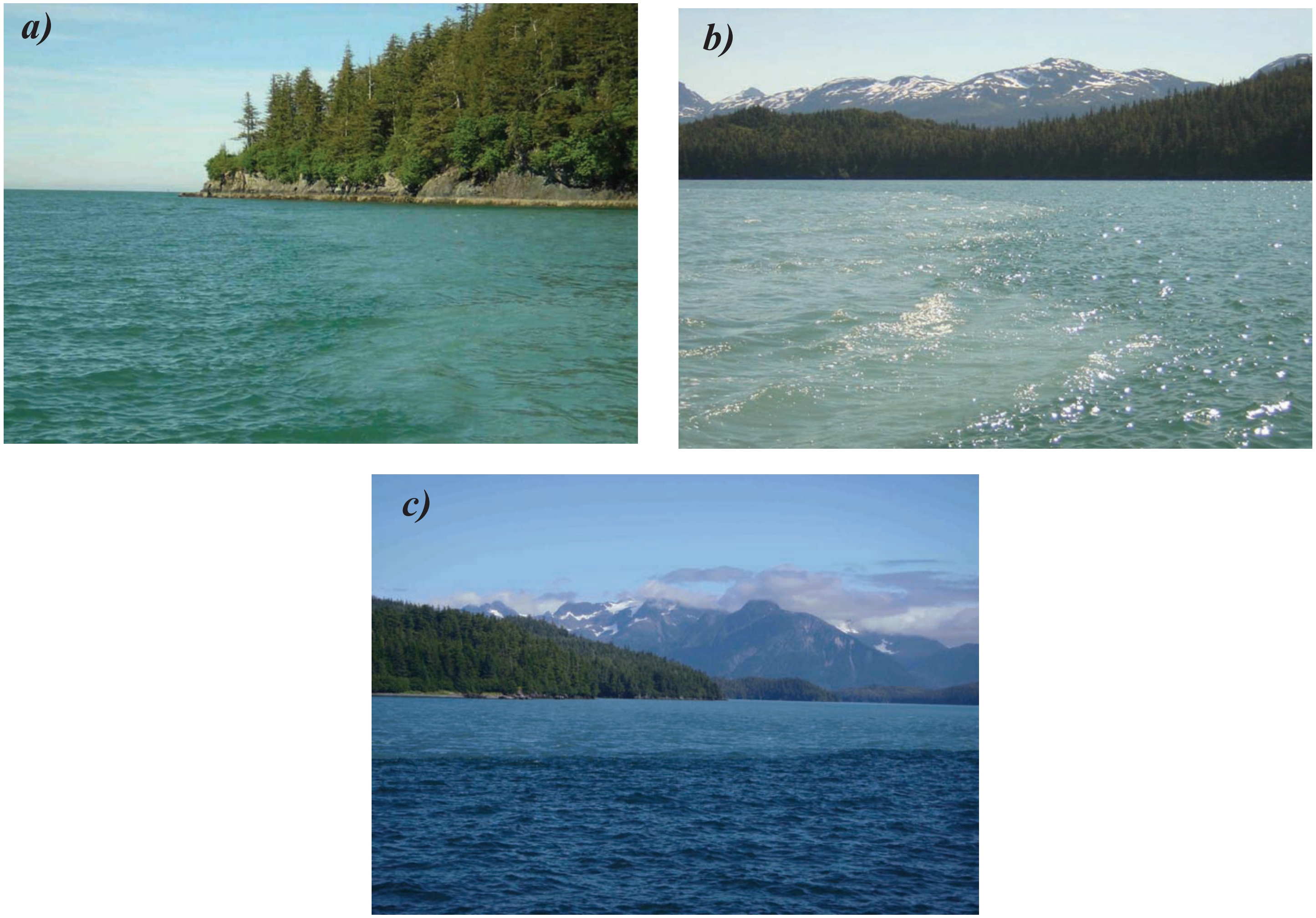

Fig. 3.3. Glacial water originating from the Rude River propagating westward within Orca Bay. a) view in June 2007 to the west past the outer tip of the Channel Islands; b) view in June 2007 towards Hawkins Island (see Fig. 2) and c) view in August 2011 from Simpson Bay eastward towards the Channel Islands. Locations of frontal zones are shown in panel-a of Fig. 2, where arrows indicate the potential path of Rude River glacial water.

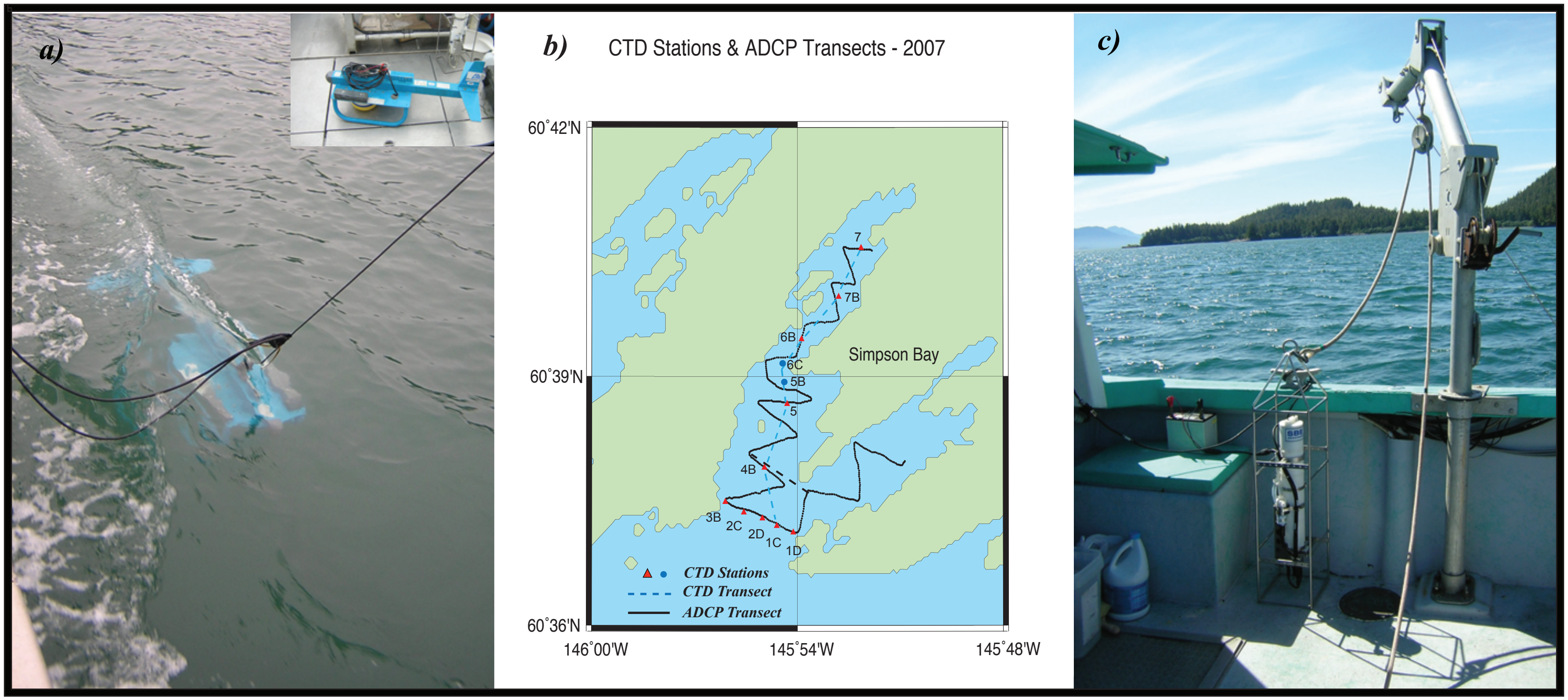

Fig. 3.4. Oceanographic instruments, transects and stations for cruises in 2007 and 2008. a) 600 kHz acoustic Doppler current profiler (ADCP) towed with a Biosonics acoustic towsled to collect data on currents; b) layout of ADCP transects and oceanographic stations; c) SBE19plus CTD used to collect hydrography data (CTD, Fluorescence and Turbidity). Also shown in (b) are stations included in CTD vertical sections and an alternate transect back across the main basin (black dashed line) during northward runs into the Northern Arm. Note also that two addtional stations (5B and 6C) shown as blue dots were established in 2008.

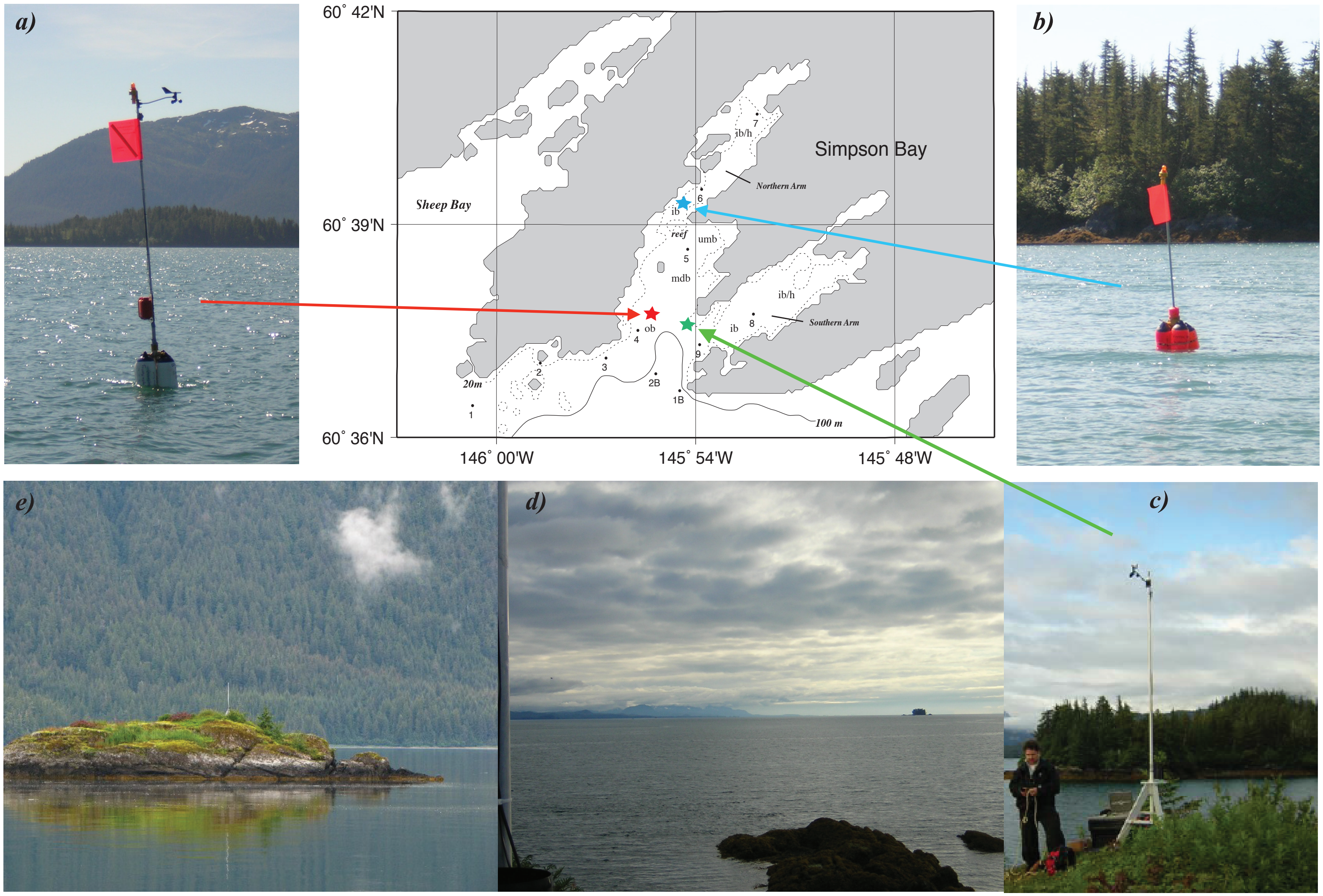

Fig. 3.5. CT moorings and weather stations deployed at Simpson Bay. a,b) moorings located in the lower (main) basin (red star) and mouth of the Northern Arm (blue star); c) shore-based weather station with rain gauge located on an island on the eastern side of the main basin (green star); d,e) respective views from the shore station to the west-southwest and across the station to the south; f) schematic of mooring components including surface CT, subsurface CTD, and thermistors described in the text; g) details of surface buoy and tow briddle; h) Danforth anchor and chains; and i) Pelican case housing weather data logger and battery.

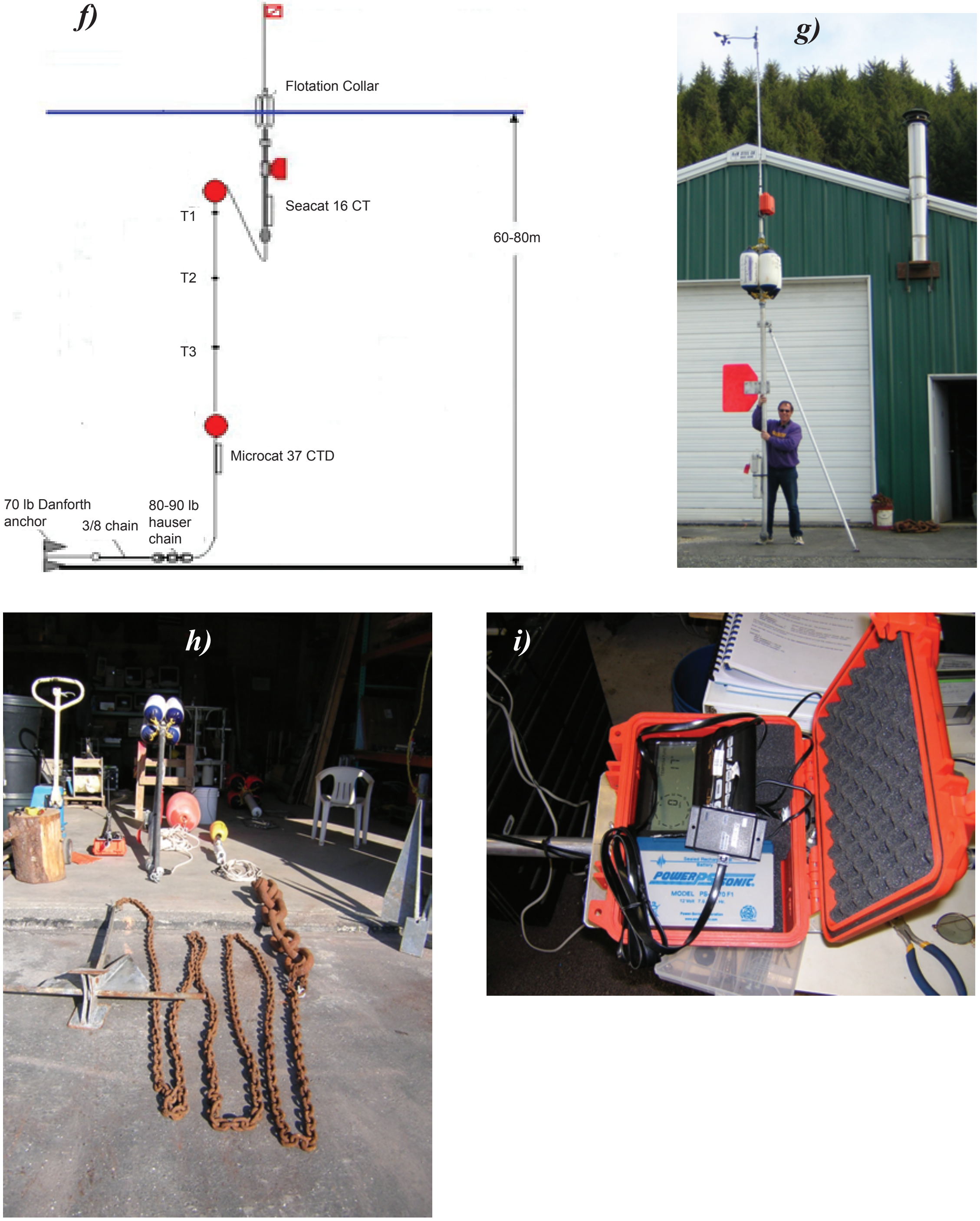
f)
Flotation Collar
Seacat 16 CT
T1
T2
T3
60-80m
Microcat 37 CTD
70 lb Danforth anchor
3/8 chain
80-90 lb hauser chain
g)
h)
i)
POWER-SONIC

Fig. 3.5 (cont.).

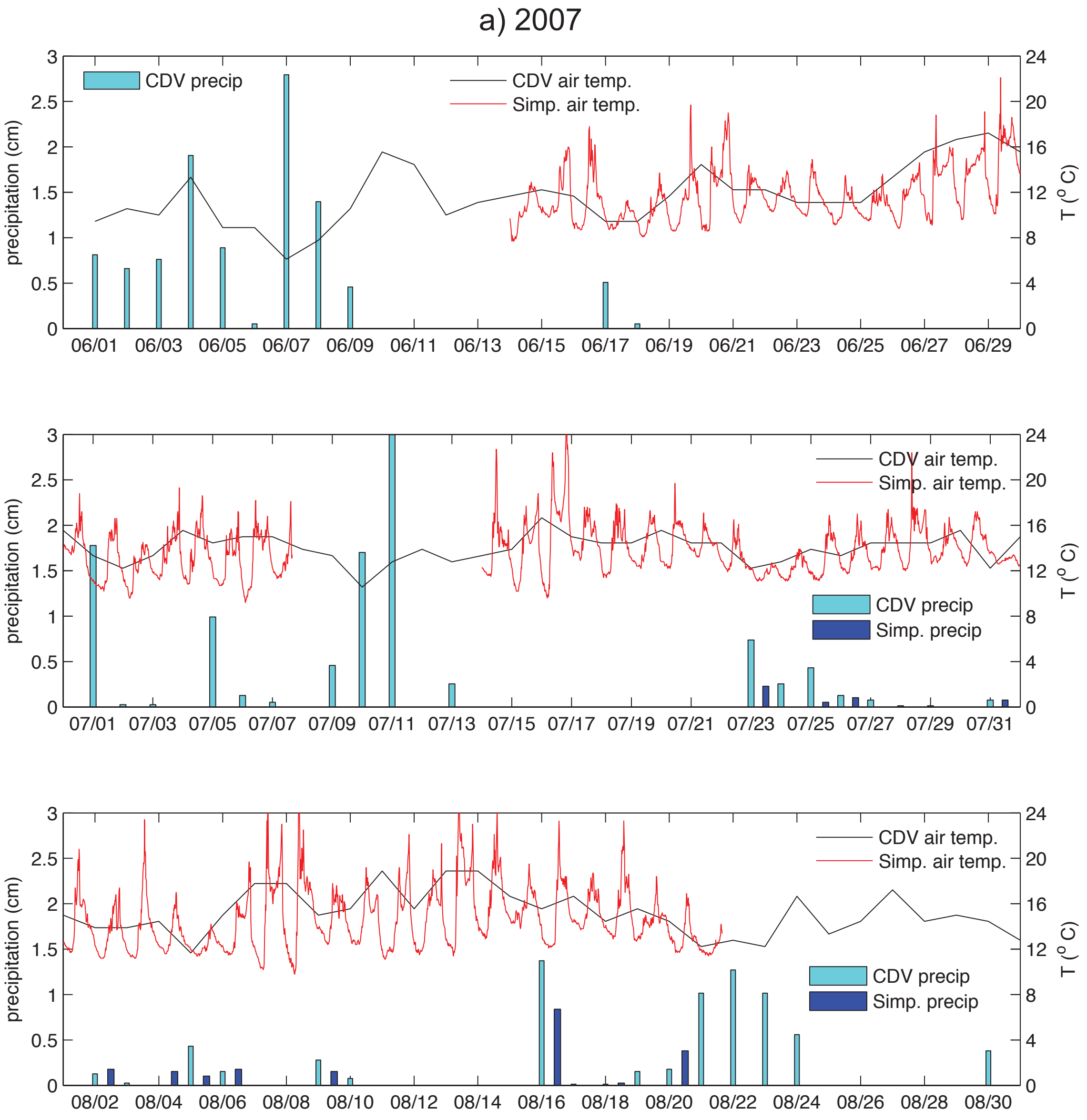

Fig. 3.6. Precipitation and air temperatures at Simpson Bay and Cordova, Alaska in the summers of 2007 (a) and 2008 (b). Air temperatures at Cordova are single observations made daily at noon, whereas at Simpson measurements are shown for 15 min. intervals. Precipitation at both locations are daily totals. Also, note that the scales are larger in both July and August 2008.

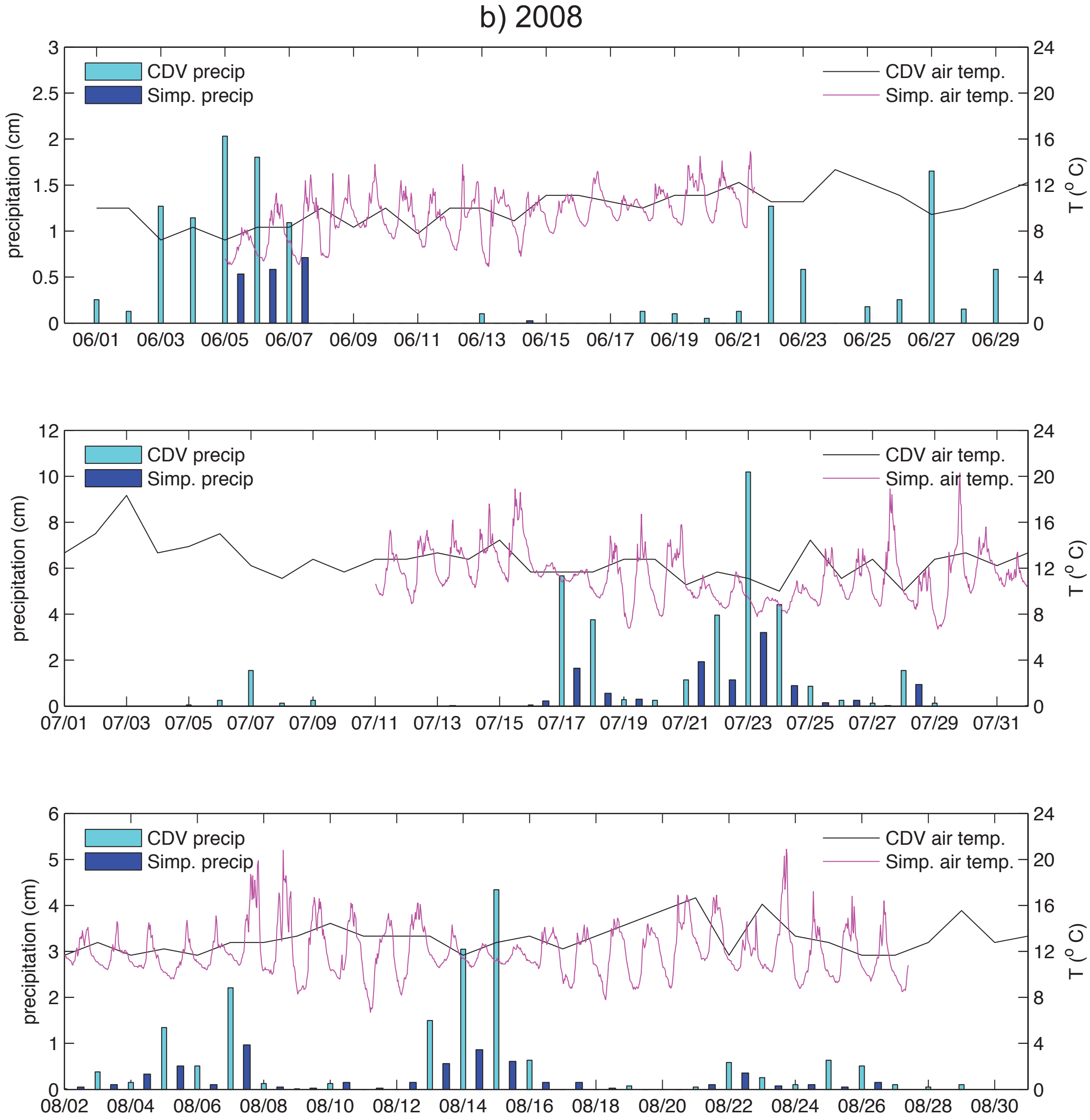
b) 2008
CDV precip
Simp. precip
CDV air temp.
Simp. air temp.
precipitation (cm)
T (^{o}C)
0
0.5
1
1.5
2
2.5
3
0
4
8
12
16
20
24
06/01
06/03
06/05
06/07
06/09
06/11
06/13
06/15
06/17
06/19
06/21
06/23
06/25
06/27
06/29
CDV precip
Simp. precip
CDV air temp.
Simp. air temp.
precipitation (cm)
T (^{o}C)
0
2
4
6
8
10
12
0
4
8
12
16
20
24
07/01
07/03
07/05
07/07
07/09
07/11
07/13
07/15
07/17
07/19
07/21
07/23
07/25
07/27
07/29
07/31
CDV precip
Simp. precip
CDV air temp.
Simp. air temp.
precipitation (cm)
T (^{o}C)
0
1
2
3
4
5
6
0
4
8
12
16
20
24
08/02
08/04
08/06
08/08
08/10
08/12
08/14
08/16
08/18
08/20
08/22
08/24
08/26
08/28
08/30

Fig. 3.6 (cont).

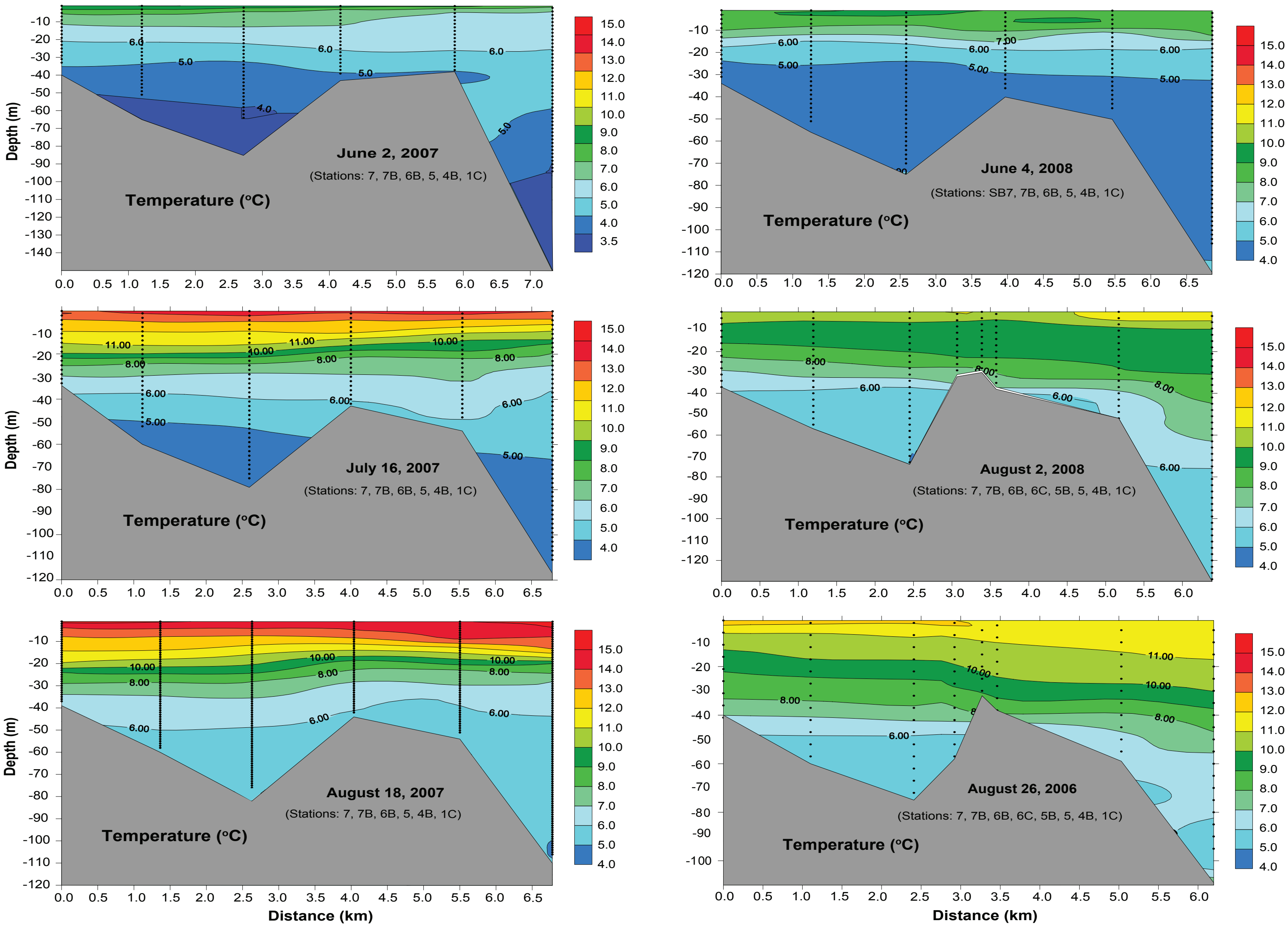

Fig. 3.7. Vertical sections of temperature and salinity at Simpson Bay in the summers of 2007 and 2008. Stations used in contour plots are shown in Fig. 3.4.

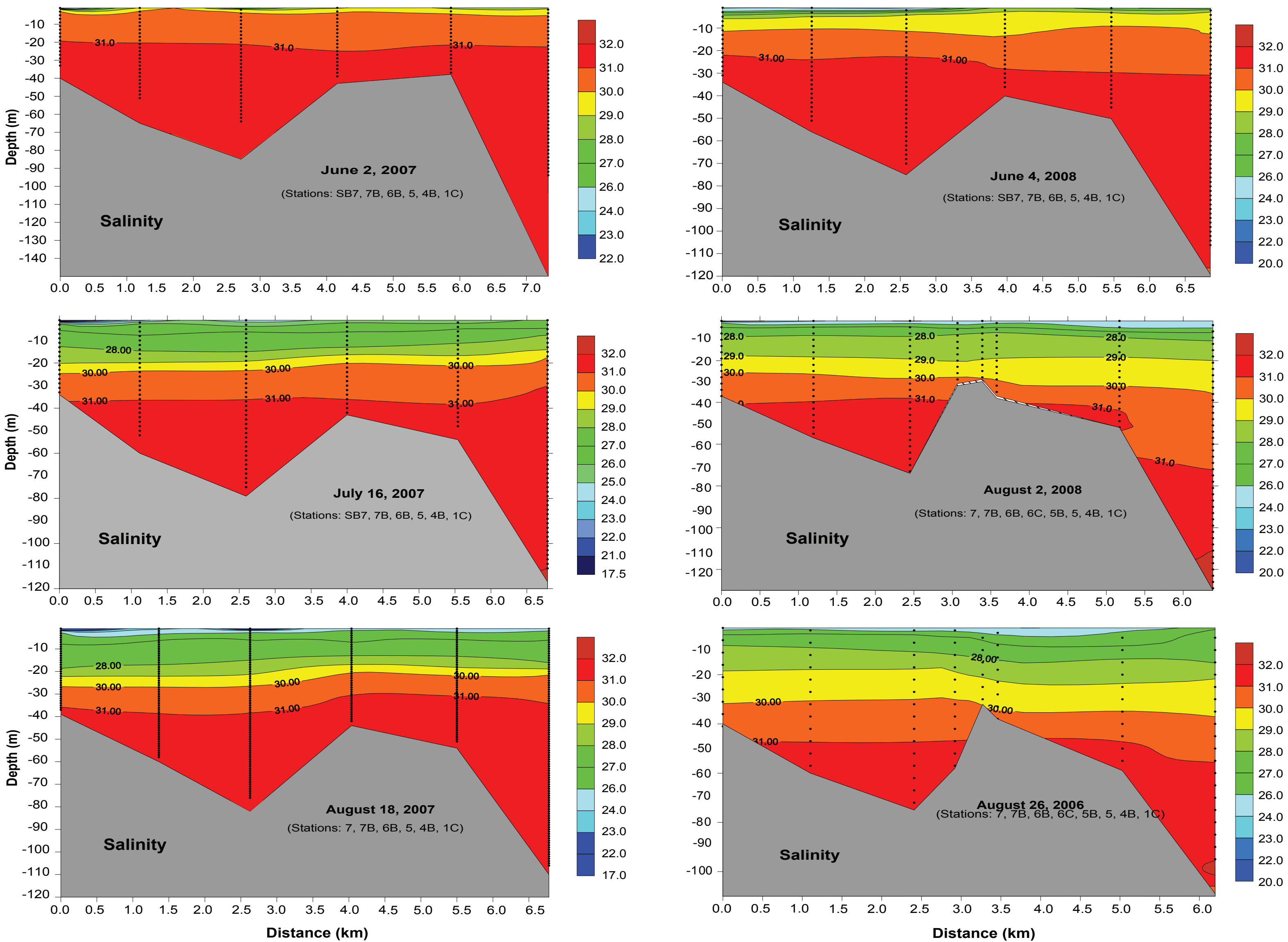
June 2, 2007
(Stations: SB7, 7B, 6B, 5, 4B, 1C)
Salinity
June 4, 2008
(Stations: SB7, 7B, 6B, 5, 4B, 1C)
Salinity
July 16, 2007
(Stations: SB7, 7B, 6B, 5, 4B, 1C)
Salinity
August 2, 2008
(Stations: 7, 7B, 6B, 6C, 5B, 5, 4B, 1C)
Salinity
August 18, 2007
(Stations: 7, 7B, 6B, 5, 4B, 1C)
Salinity
August 26, 2006
(Stations: 7, 7B, 6B, 6C, 5B, 5, 4B, 1C)
Salinity
Depth (m)
Distance (km)
28.00
29.0
30.00
31.00
31.0
32.0
27.0
26.0
25.0
24.0
23.0
22.0
21.0
20.0
17.5
17.0

Fig. 3.7 (cont.).

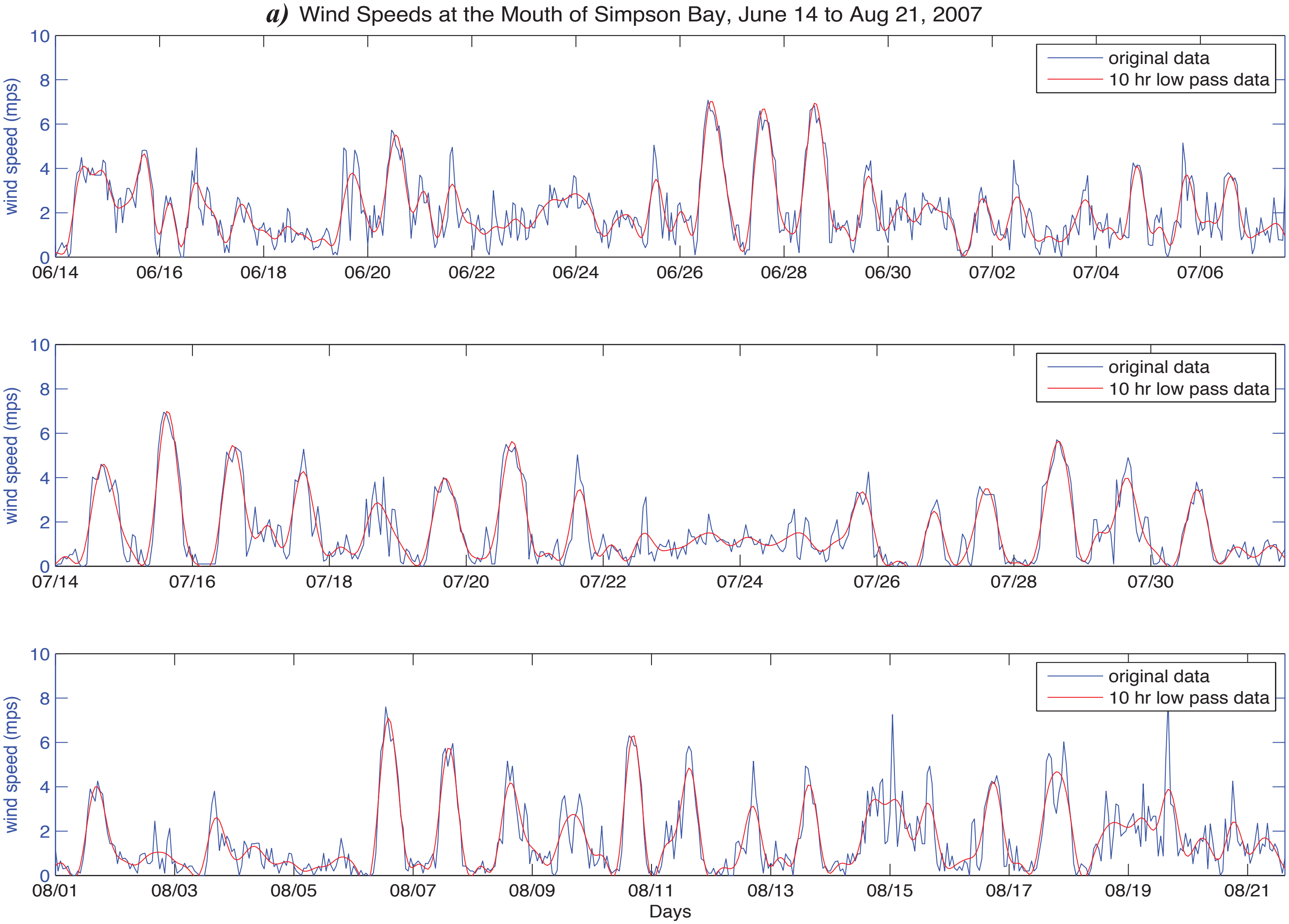

Fig. 3.8. Hourly and 10 hr low-pass filtered wind speeds measured at the mouth of Simpson Bay in the summers of a) 2007 and b) 2008.


b) Wind Speeds at the Mouth of Simpson Bay, June 5 to Aug 27, 2008
wind speed (mps)
original data
10 hr low pass data
0
2
4
6
8
10
06/05
06/07
06/09
06/11
06/13
06/15
06/17
06/19
06/21
07/11
07/13
07/15
07/17
07/19
07/21
07/23
07/25
07/27
07/29
07/31
08/01
08/03
08/05
08/07
08/09
08/11
08/13
08/15
08/17
08/19
08/21
08/23
08/25
08/27
Days

Fig. 3.8. (cont.).

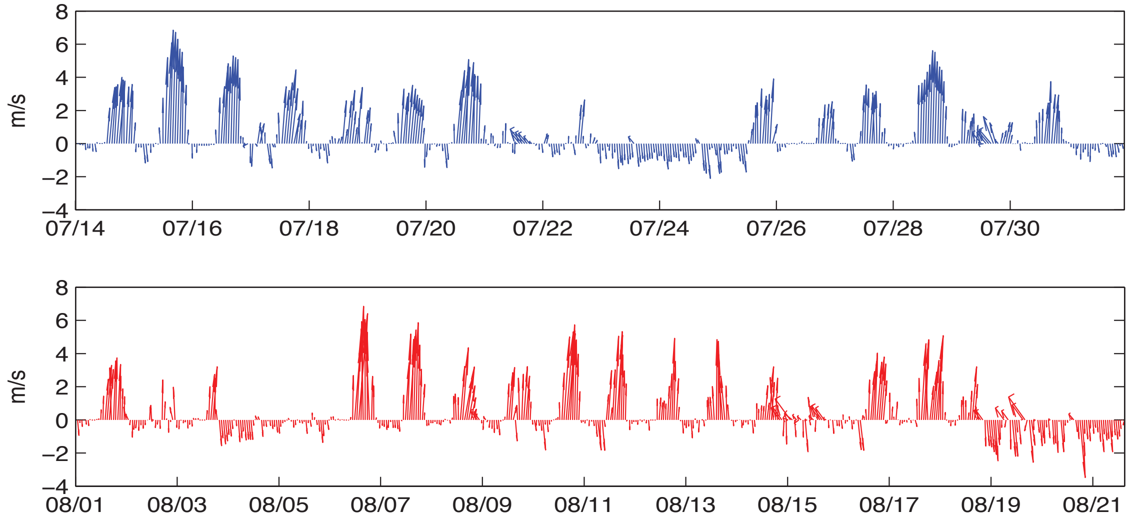

a) Along–Fjord Wind Velocities in July and August 2007

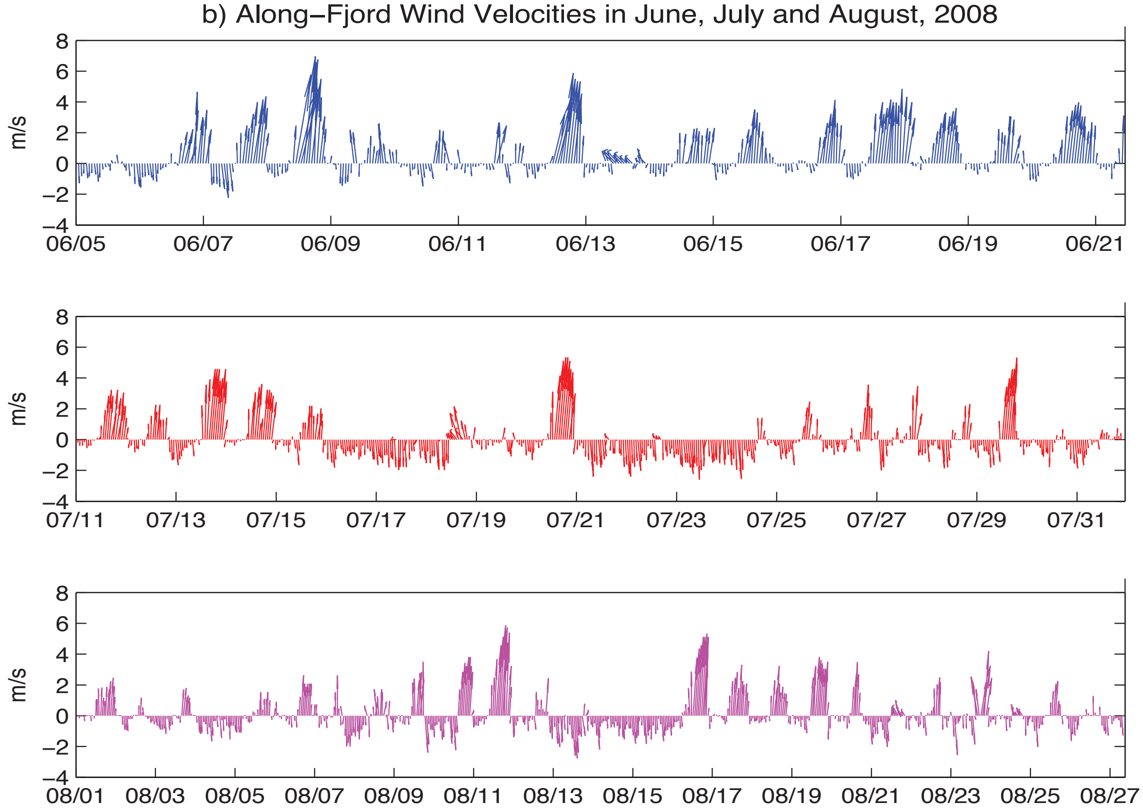

b) Along–Fjord Wind Velocities in June, July and August, 2008

Fig. 3.9. Wind vectors rotated to an along-fjord axis (NNE) measured at the mouth of Simpson Bay in the summer of 2007 (a) and 2008 (b), and histograms of along-fjord winds in July and August of 2007 (c) and 2008 (d). Note the higher frequency of winds > 2m s^{-1} in 2007.

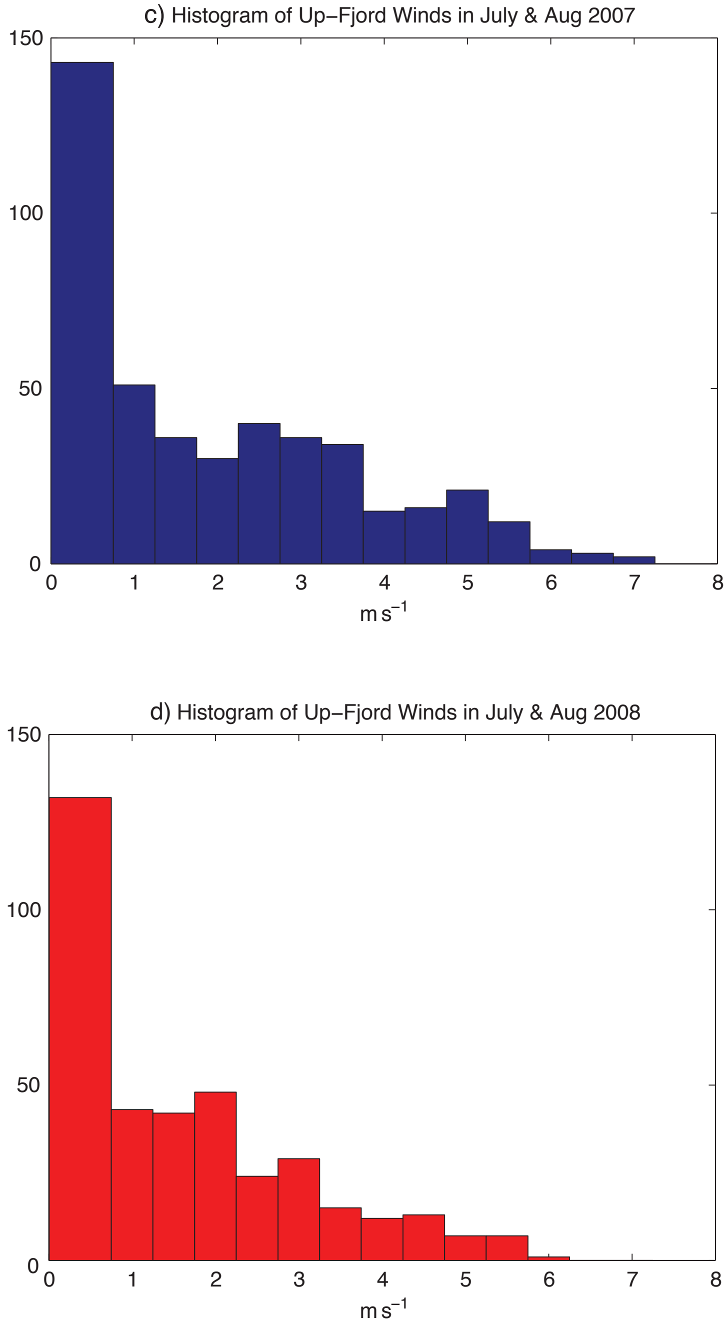
c) Histogram of Up−Fjord Winds in July & Aug 2007
150
100
50
0
0
1
2
3
4
5
6
7
8
m s^{-1}
d) Histogram of Up−Fjord Winds in July & Aug 2008
150
100
50
0
0
1
2
3
4
5
6
7
8
m s^{-1}

Fig. 3.9 (cont.).

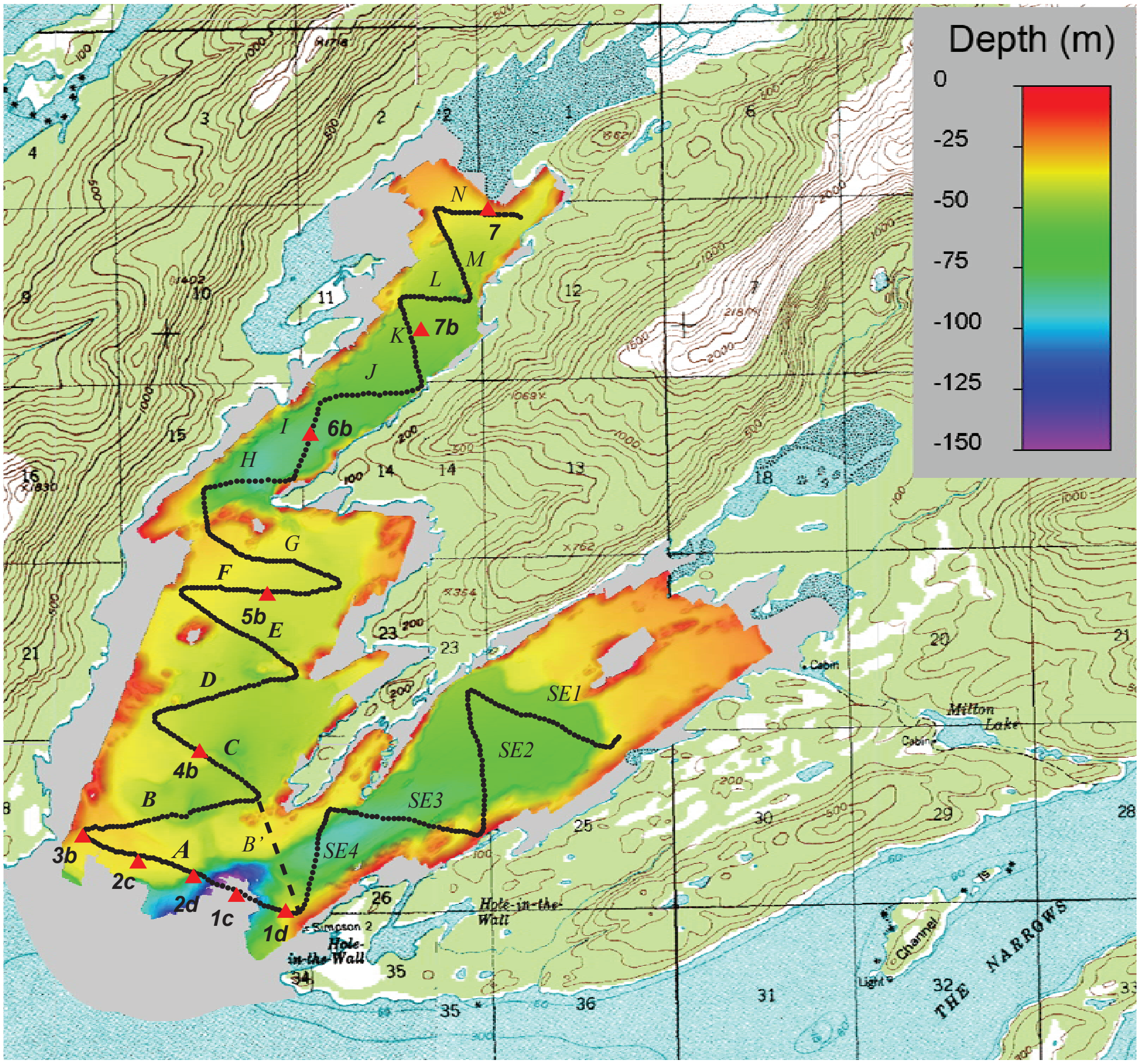

Fig. 3.10A. Locations of ADCP transects and CTD stations (red triangles) in relation to the bathymetry of Simpson Bay*. The stations are numbered from 1 to 7 with lower case letters, and transects are labled *SE1 to 4* in the *Southeast Arm*, *A to G* in the *Main Basin* and *H to N* in the *Northern Arm*. Transect *B'* was used when returning up-fjord.

*Bathymetry reprinted with permission from "A high resolution geophysical investigation of sediment distribution controlled by catchment size and tides in a multi-basin turbid outwash fjord: Simpson Bay, Prince William Sound, Alaska" by Noll CJ, Dellapenna TM, Gilkinson A, Davis RW Geo-Mar Lett 29: 1−16, Copyright 2008 by Springer.

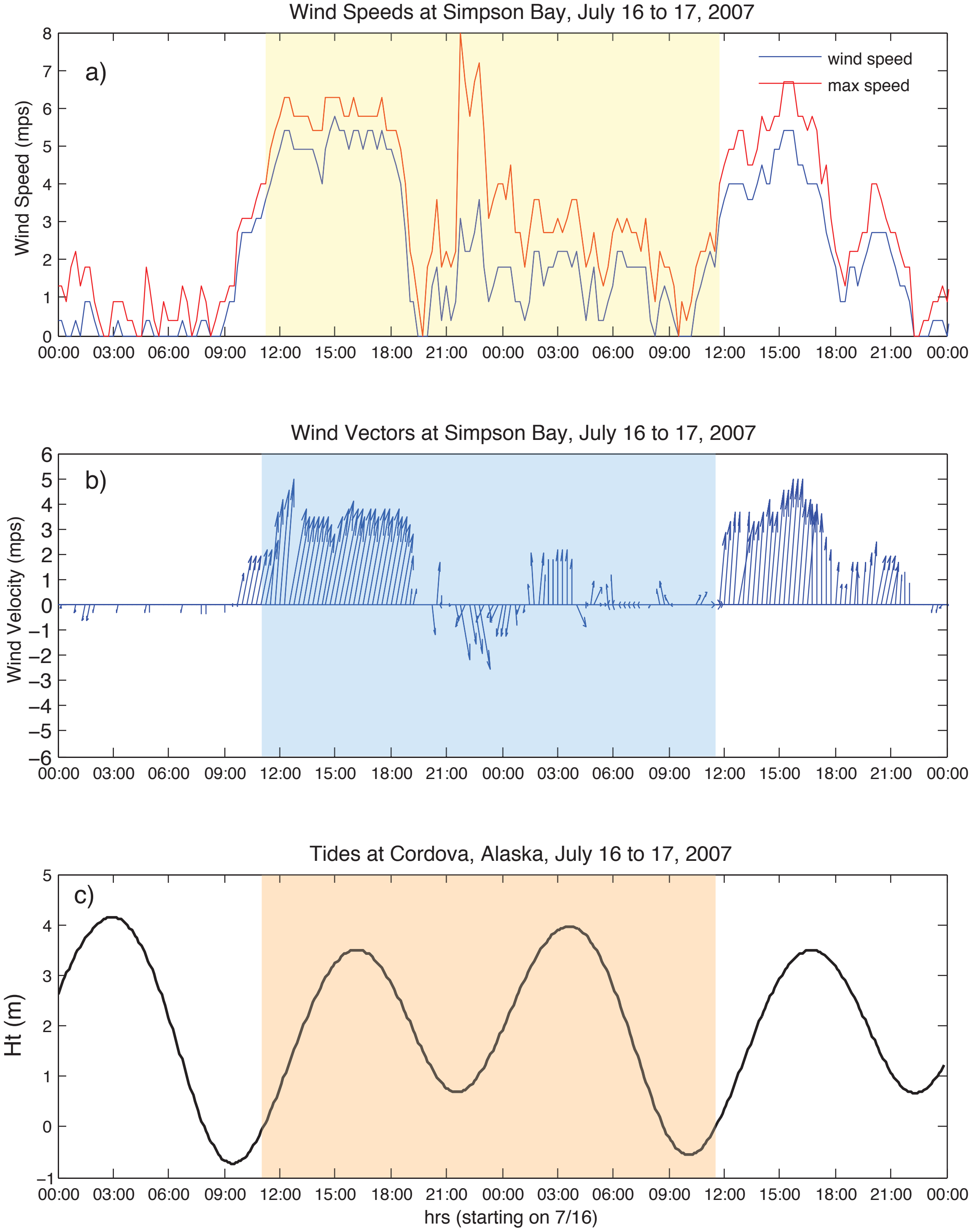

Fig. 3.10B. Wind speeds (a), directions (b) at Simpson Bay and tide heights (c) at Cordova, Alaska during the cruise on July 16 and 17, 2007. Note that the shaded areas denote the period for ADCP data collection. Transects begin at 10:42*hrs* on 7/16 and end at 11:42*hrs* on 7/17.

Fig. 3.11. Currents at Simpson Bay during the first semidiurnal tidal cycle in July 2007: *a*) vectors at 2*m* during flood tide 1 from 1007 to 1230*hr*; *b,c*) same period as panel *a* but with currents vertically averaged from 5 to 10*m* and 10 to 20*m* respectively. *d,e*) vectors at 2*m* during flood tide 1 ending ~ 0.5*hr* into ebb tide 1 at 1640*hr*; *f-h*) vectors at 2*m* during ebb tide 1 ending ~1.8*hr* into flood tide 2 at 2320*hr*; *i,j*) flood tide 2 ending at 0332*hr*, ~ 0.13*hrs* prior to the start of ebb tide 2; *k*) flood tide 2 ending ~1.4*hrs* into ebb tide 2 at 0505*hr*; *l* to *n*) ebb tide 2 ending ~1.5*hrs* into flood tide 3 at 1135*hr*. Note - transects in panels *a* to *c* start in the Southeast Arm and end at the head of the Northern Arm. In panel *d* they follow a reversed pattern southward from the head of the fjord to the mouth, and then in panel *e* they return using an alternate route (Fig. 3.10A) across the Southeast Arm and lower main basin, and then back to the head of the Northern Arm. They repeat this pattern four more times in panels *f* to *m*, then return back down-fjord and across the mouth, ending across the mouth of the Southeast Arm.

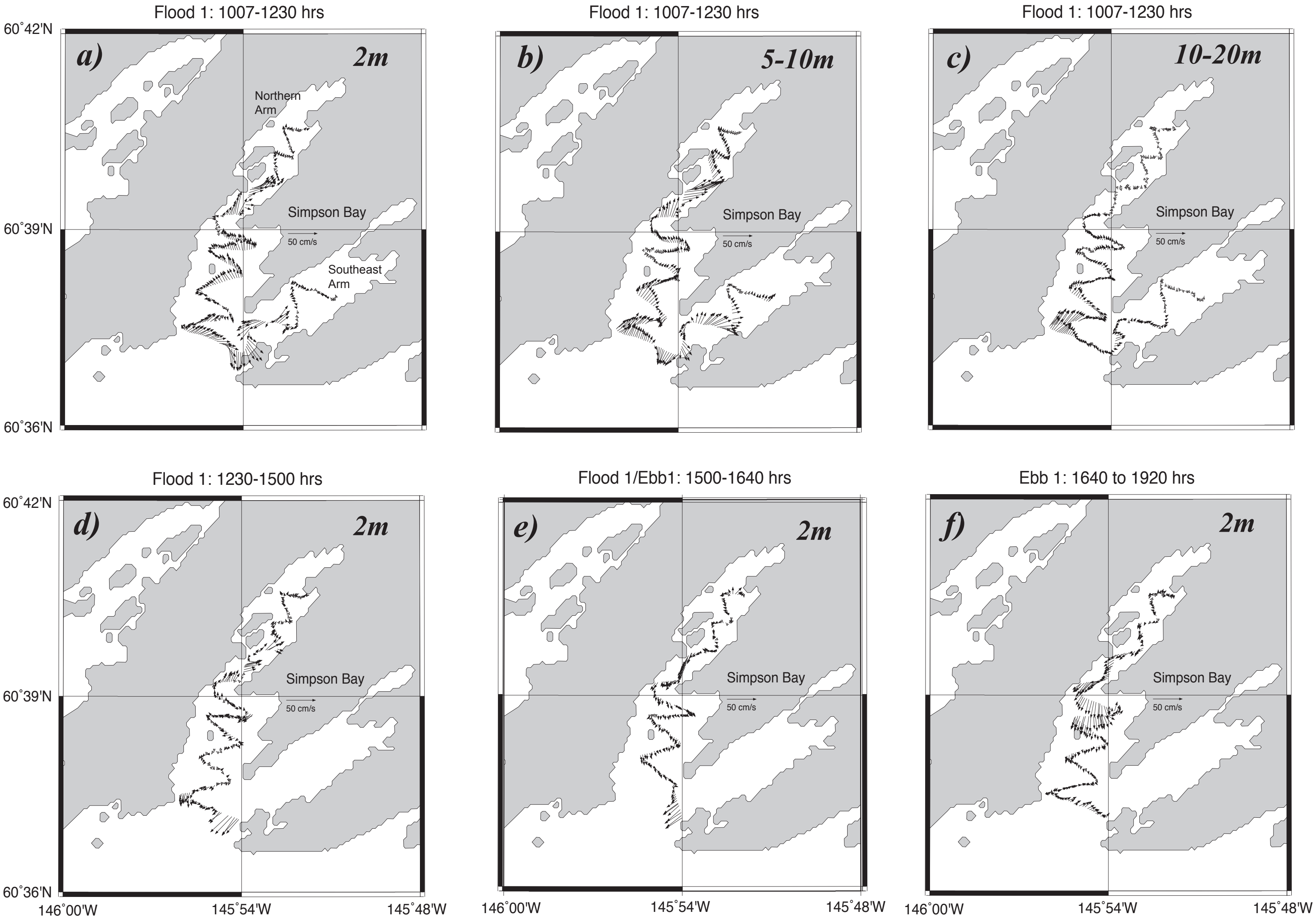

Flood 1: 1007-1230 hrs
a)
2m
Northern Arm
Simpson Bay
50 cm/s
Southeast Arm
Flood 1: 1007-1230 hrs
b)
5-10m
Simpson Bay
50 cm/s
Flood 1: 1007-1230 hrs
c)
10-20m
Simpson Bay
50 cm/s
Flood 1: 1230-1500 hrs
d)
2m
Simpson Bay
50 cm/s
Flood 1/Ebb1: 1500-1640 hrs
e)
2m
Simpson Bay
50 cm/s
Ebb 1: 1640 to 1920 hrs
f)
2m
Simpson Bay
50 cm/s
60˚42'N
60˚39'N
60˚36'N
146˚00'W
145˚54'W
145˚48'W

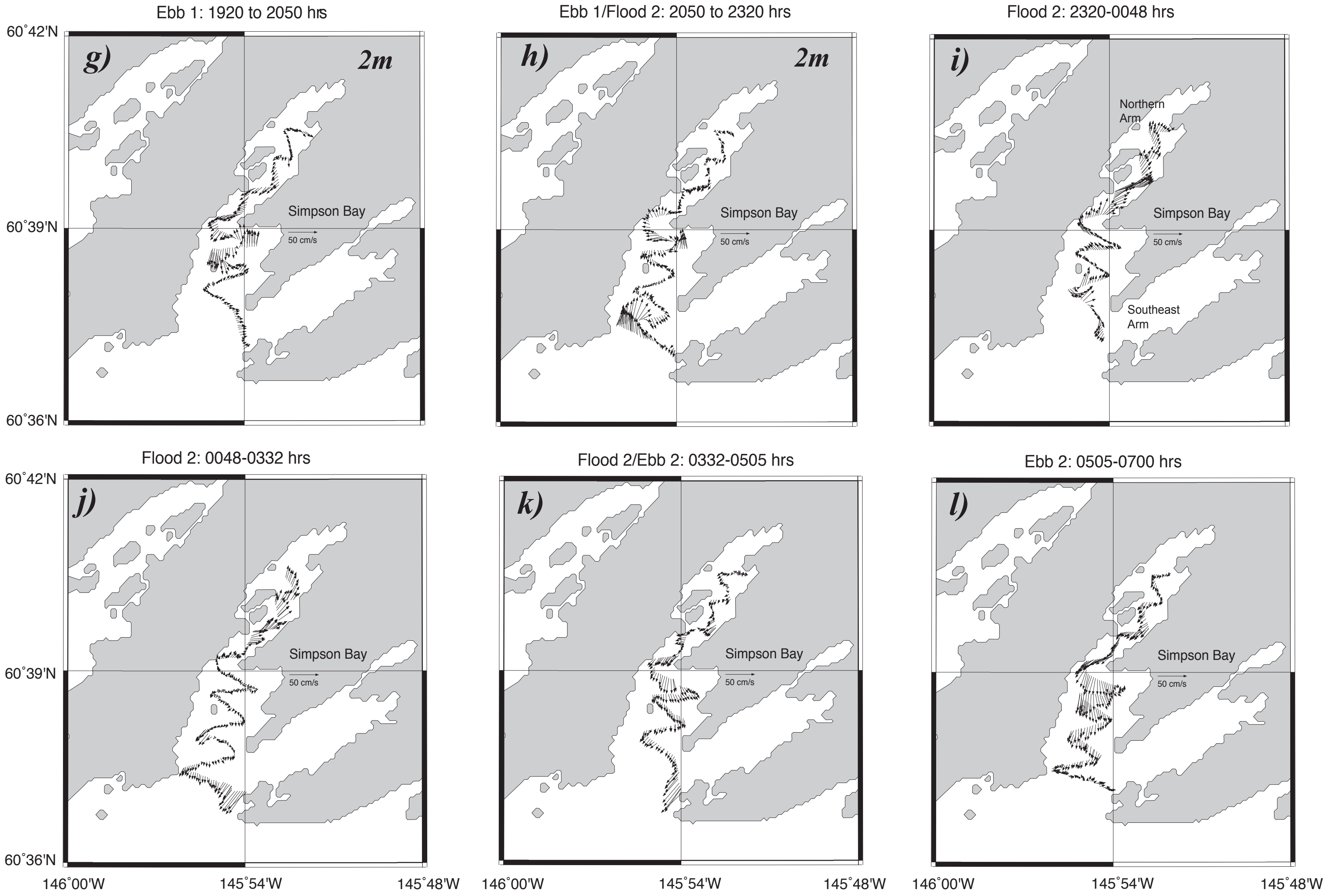

Ebb 1: 1920 to 2050 hrs

Ebb 1/Flood 2: 2050 to 2320 hrs

Flood 2: 2320-0048 hrs

Flood 2: 0048-0332 hrs

Flood 2/Ebb 2: 0332-0505 hrs

Ebb 2: 0505-0700 hrs

Fig. 3.11 (cont.).

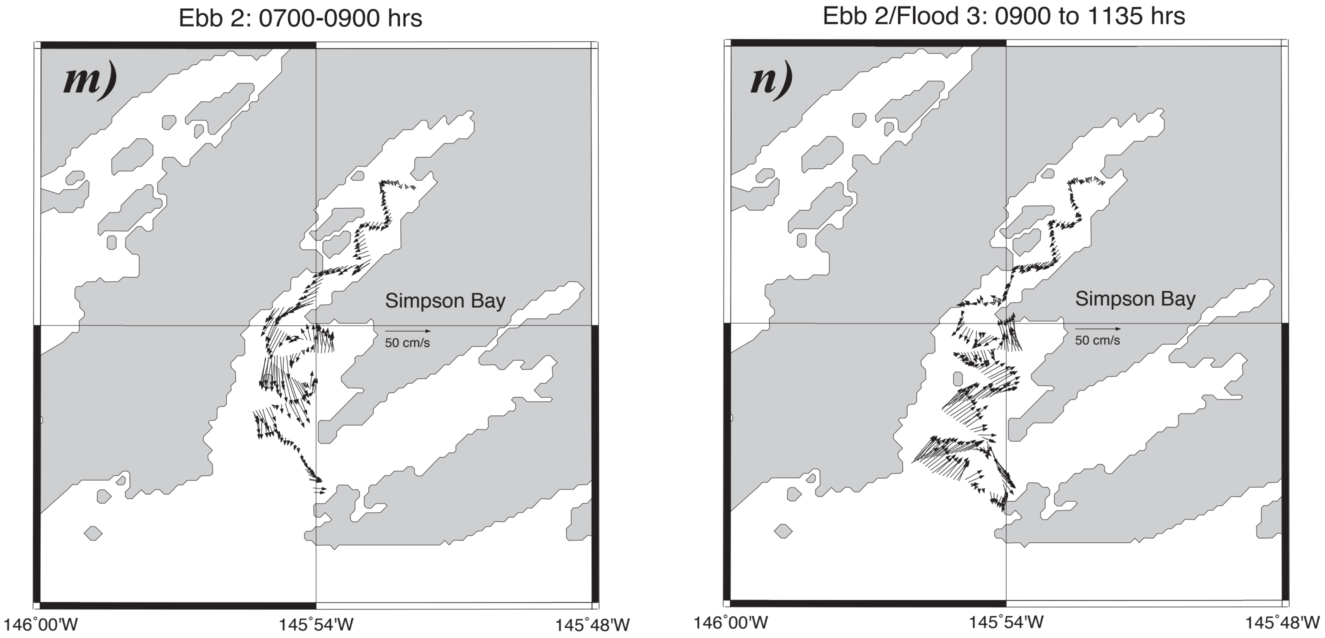
Ebb 2: 0700-0900 hrs
m)
Simpson Bay
50 cm/s
146˚00'W
145˚54'W
145˚48'W
Ebb 2/Flood 3: 0900 to 1135 hrs
n)
Simpson Bay
50 cm/s
146˚00'W
145˚54'W
145˚48'W

Fig. 3.11 (cont.).

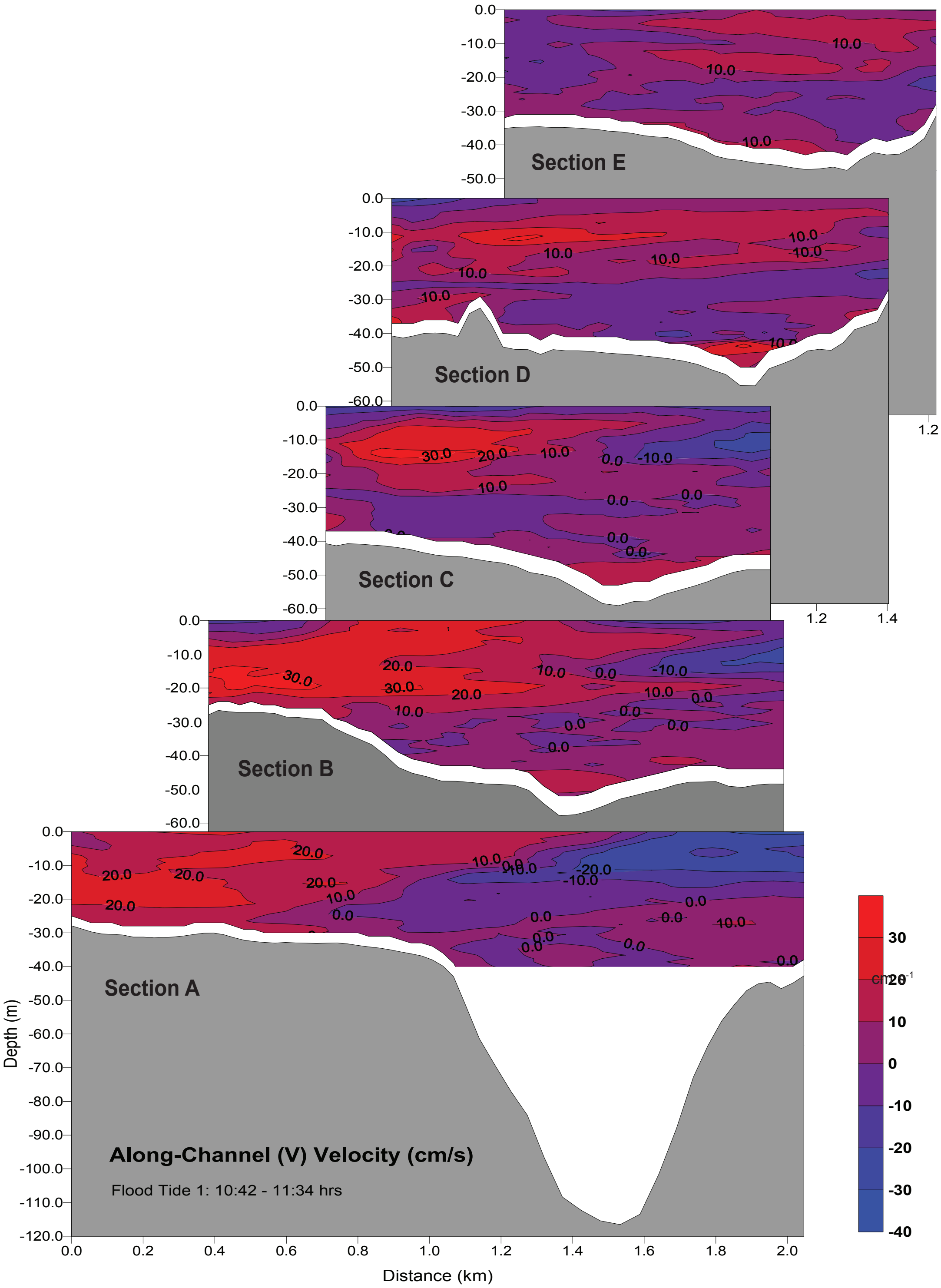

Fig. 3.12A. Along-channel ADCP velocities in July 2007 showing the vertical structure of flows within the main lower basin during the early portion of flood tide 1 from 1042 to 1134hrs. Note that transects start at the mouth on the right-hand side of Section A and progress northwards.

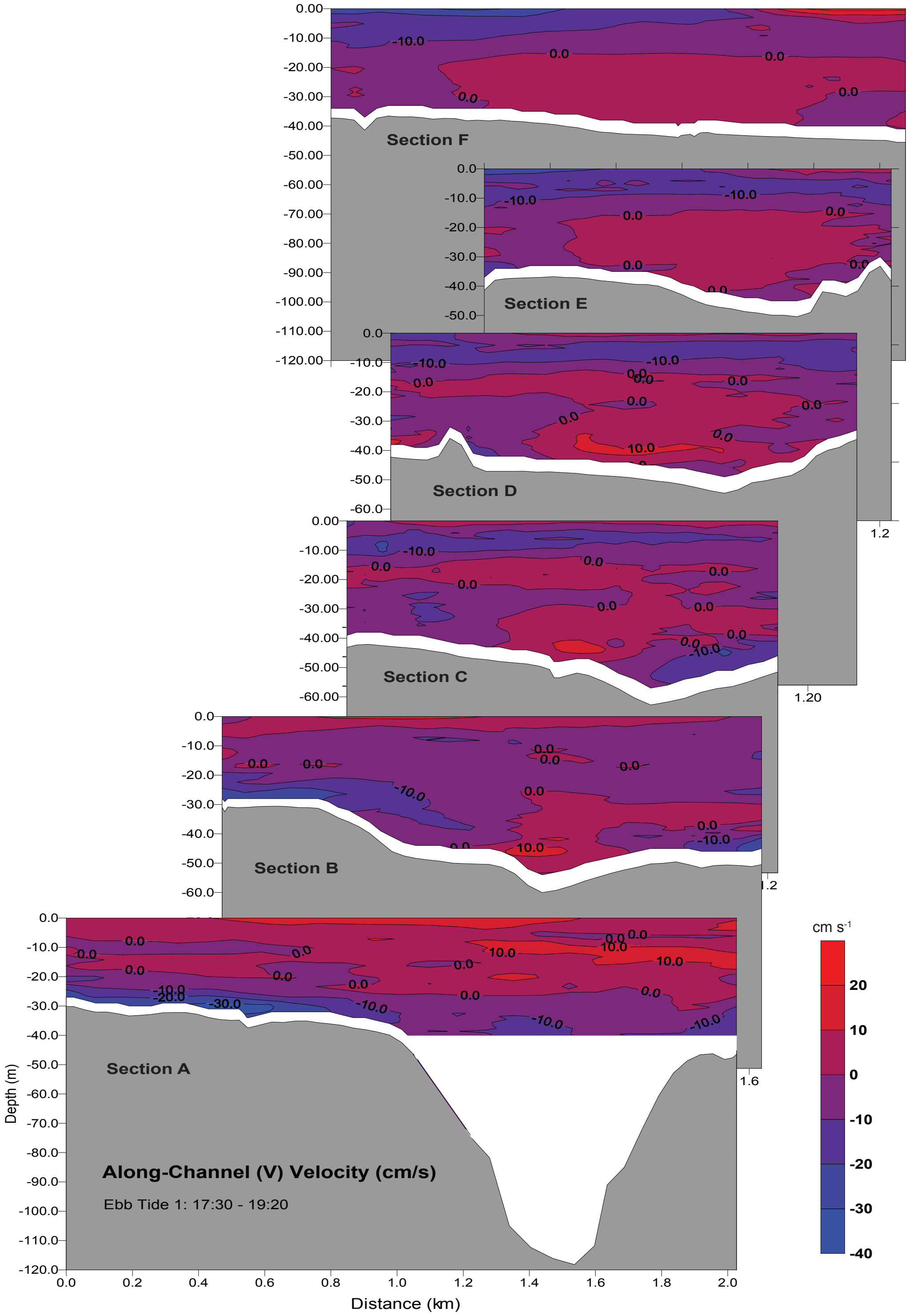

Fig. 3.12B. Along-channel ADCP velocities in July 2007 showing the vertical structure of flows during the early portion of ebb tide 1 from 1730 to 1920hrs. Note that transects start in the upper basin on the right-hand side of Section F and progress southwards.

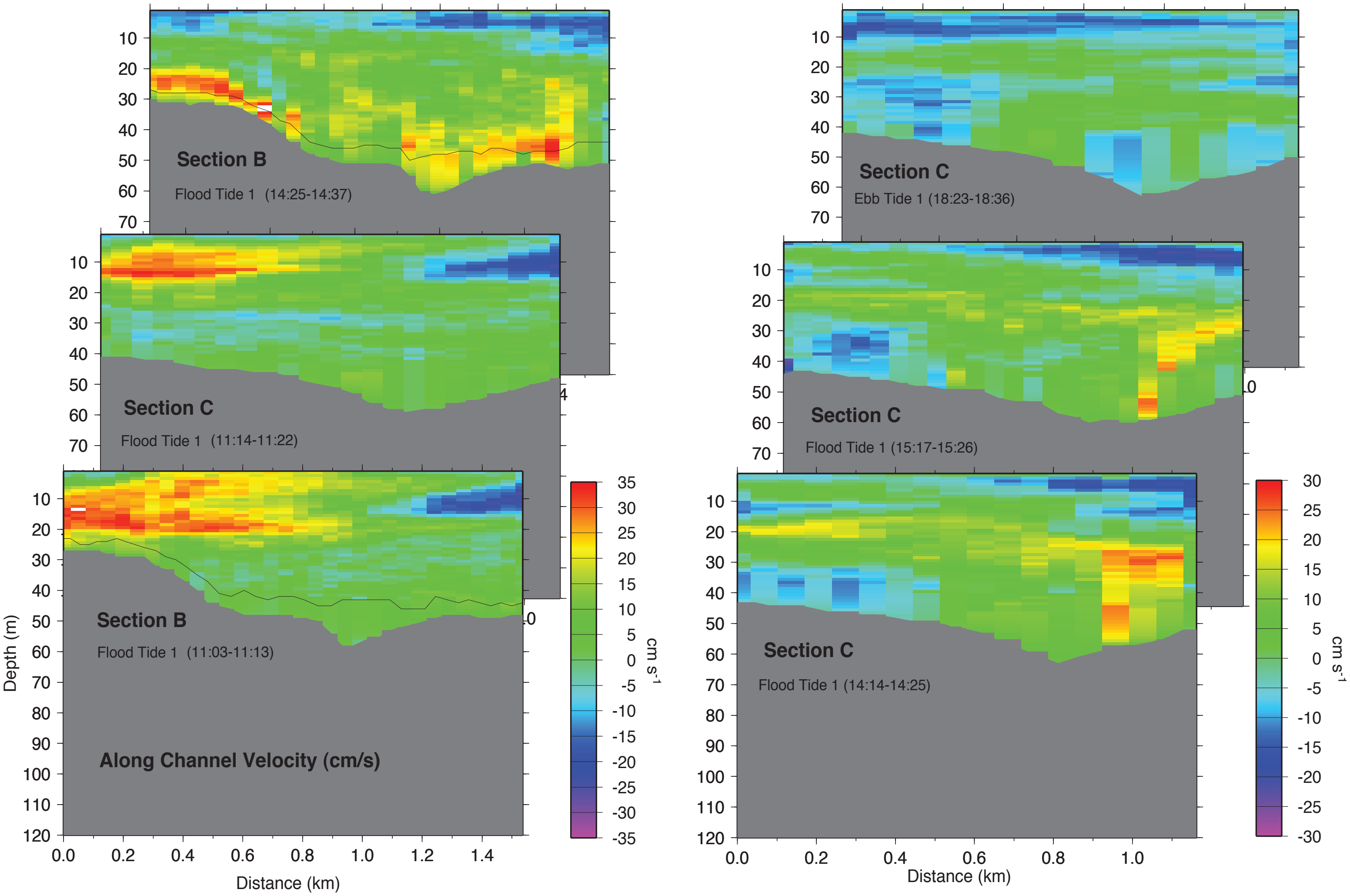

Fig. 3.13A. Along-channel velocities for Sections B and C during flood tide 1 and the start of ebb tide 1. In all panels the bottom currents are estimated by logarithmic profiles described in the text. The two panels for Section B show lines that delineate the estimated bottom layer regions.

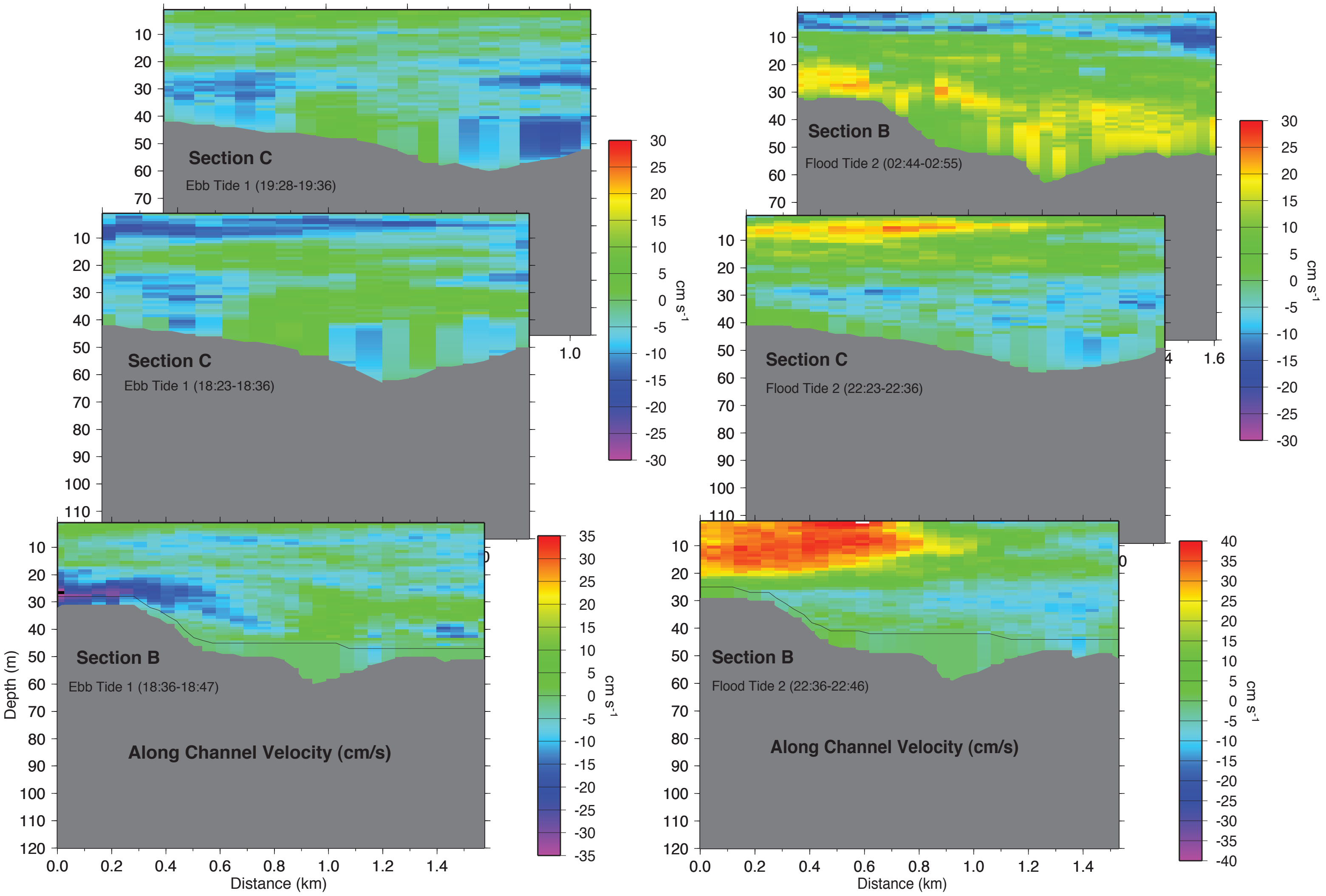

Fig. 3.13B. Along-channel velocities for Sections B and C during ebb tide 1 and part of flood tide 2. In all panels the bottom currents are estimated by logarithmic profiles described in the text. The two lower panels (for Section B) show lines that delineate the estimated bottom layer regions.

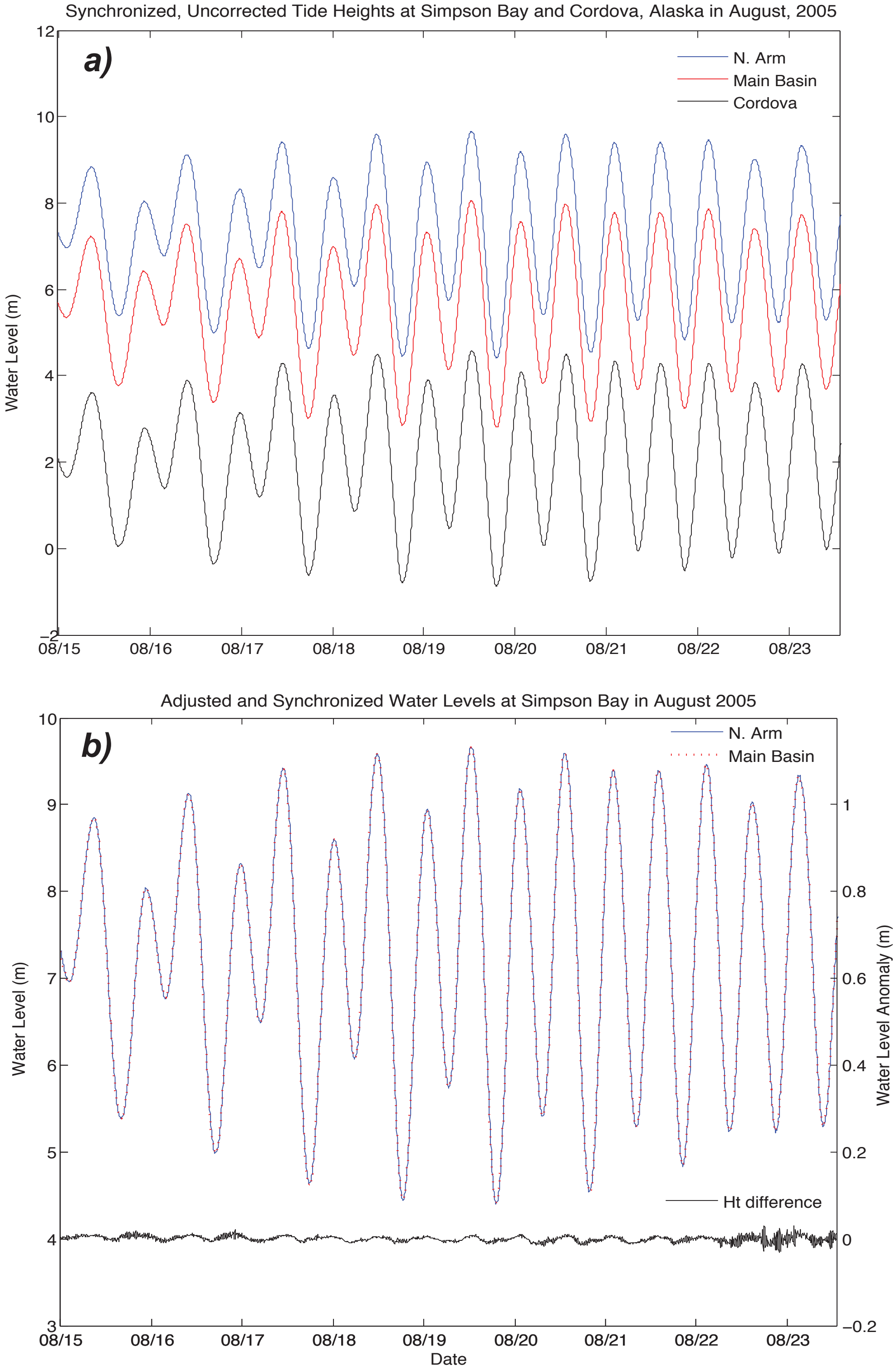

Fig. 3.14. Sea surface elevations measured at Simpson Bay and Cordova, Alaska in August 2005. a) Un-adjusted water levels in Simpson's inner and outer basins and at Cordova; b) adjusted water levels and variation in height between the two basins at Simpson.

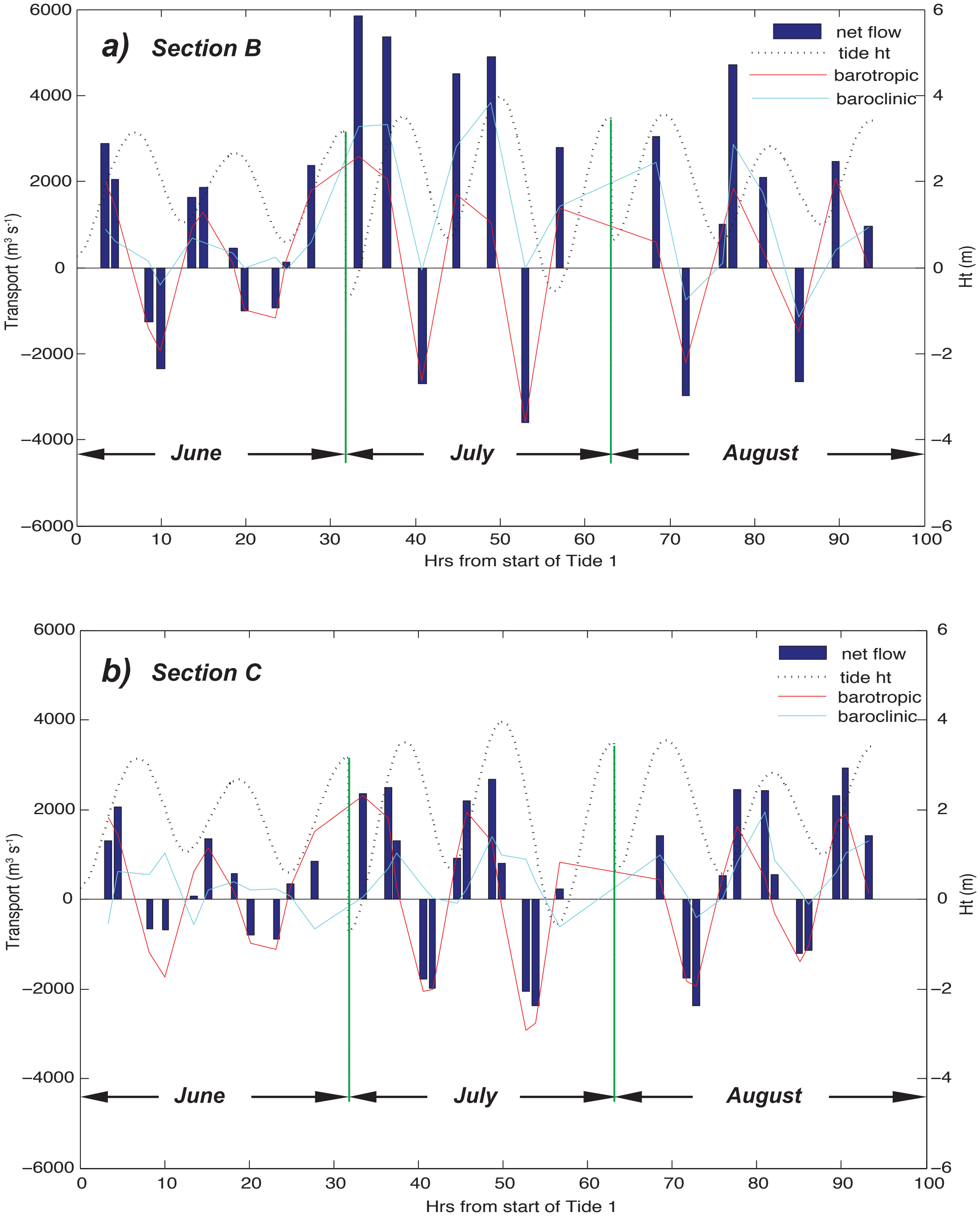

Fig. 3.15. Net total, baroclinic and barotropic transports calculated from ADCP data collected at sections B (a) and C (b) in Simpson Bay and tide heights at Cordova, Alaska in the summer of 2007.

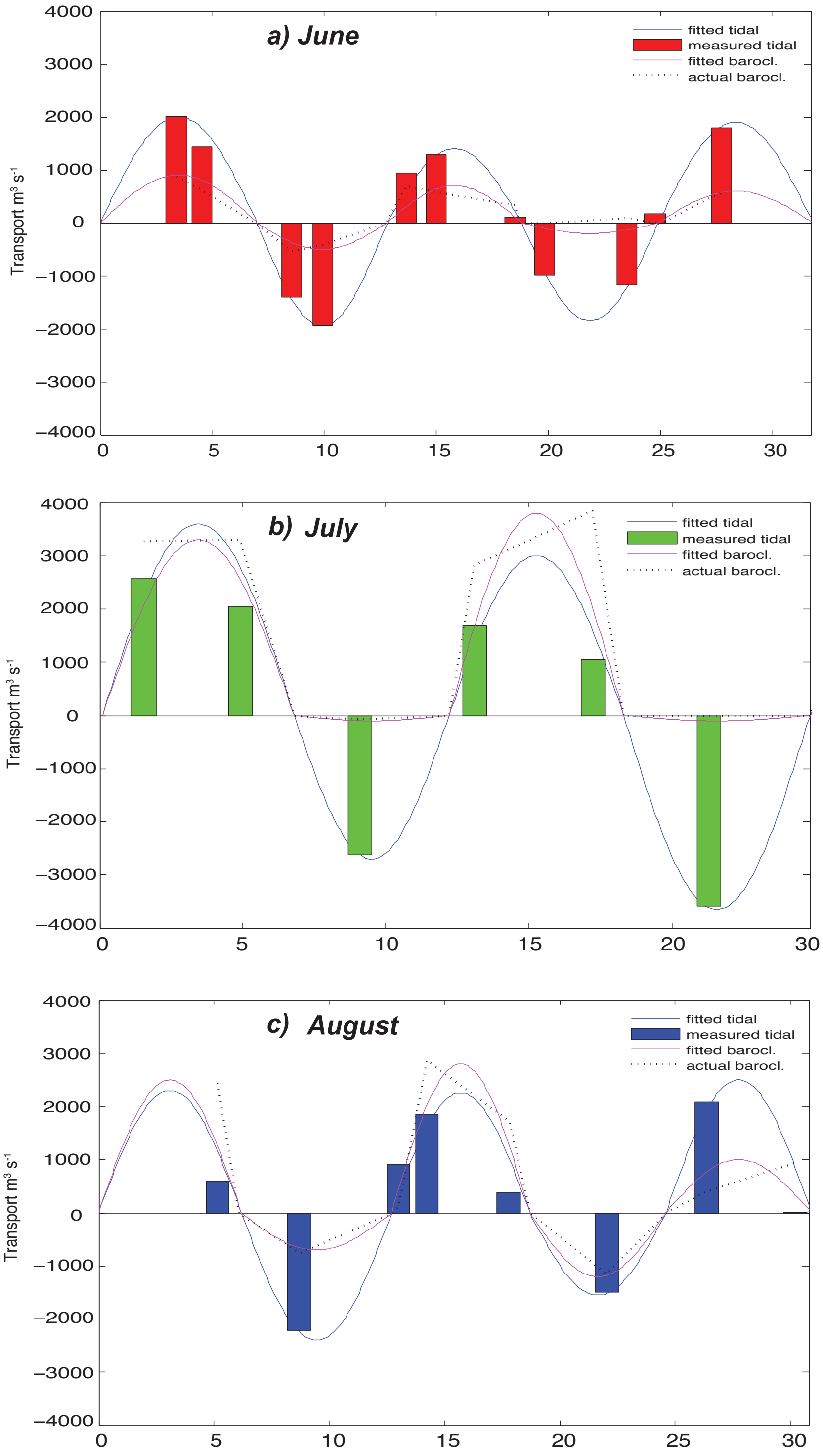

Fig. 3.16A. Fitted and measured tidal and baroclinic transports for Section B in a) June, b) July and c) August 2007. Signifcantly higher baroclinic flows during flood tides relative to ebb tides, particularly in July and August, lead to a marked imbalance in water exchange favoring the flood phases.

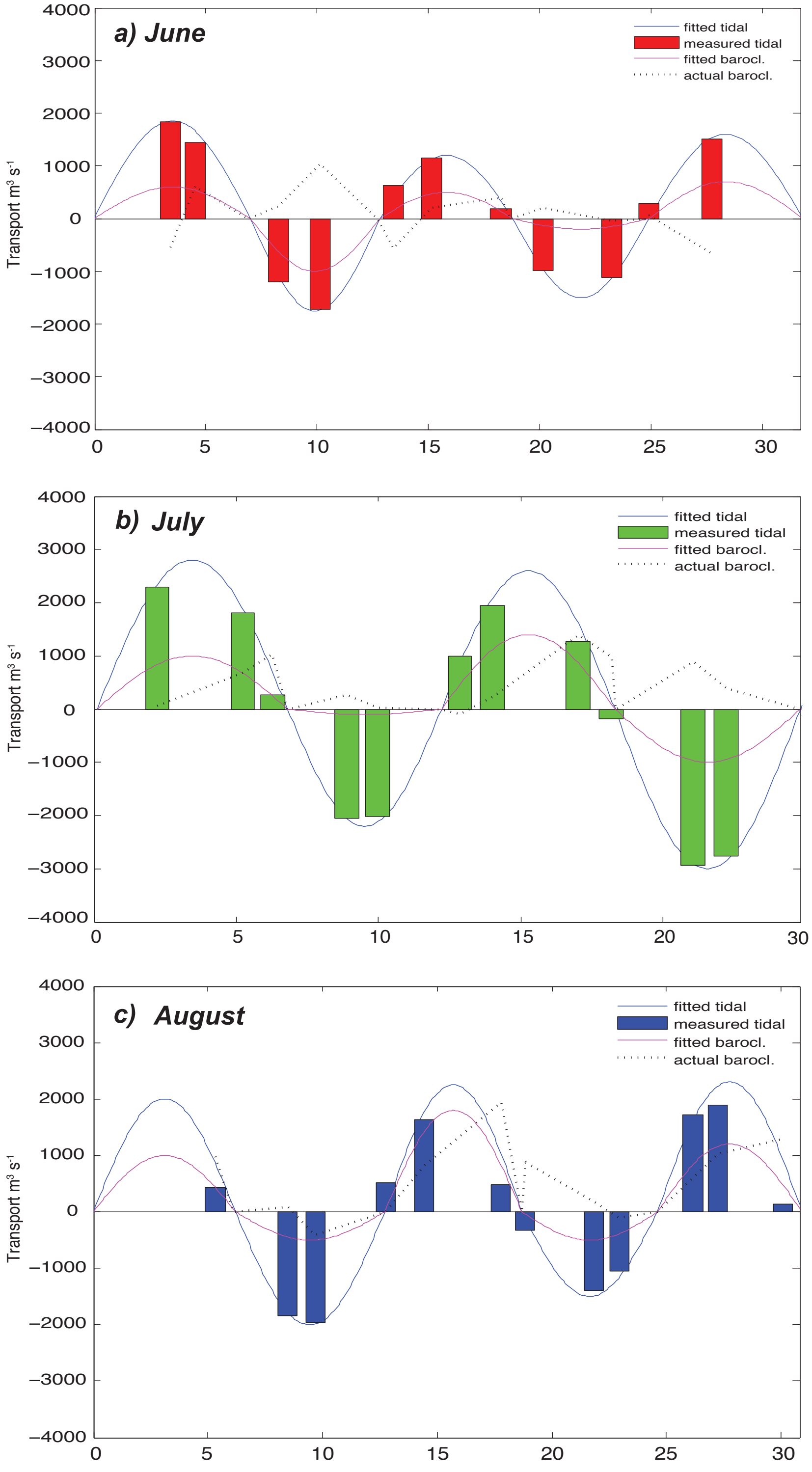

Fig. 3.16B. Fitted and measured tidal and baroclinic transports for Section C in a) June, b) July and c) August 2007. Baroclinic flows are generally lower in comparison to Section B, but they remain stronger during flood tides relative to ebb tides and thus water exchange still markedly favors the flood phases.

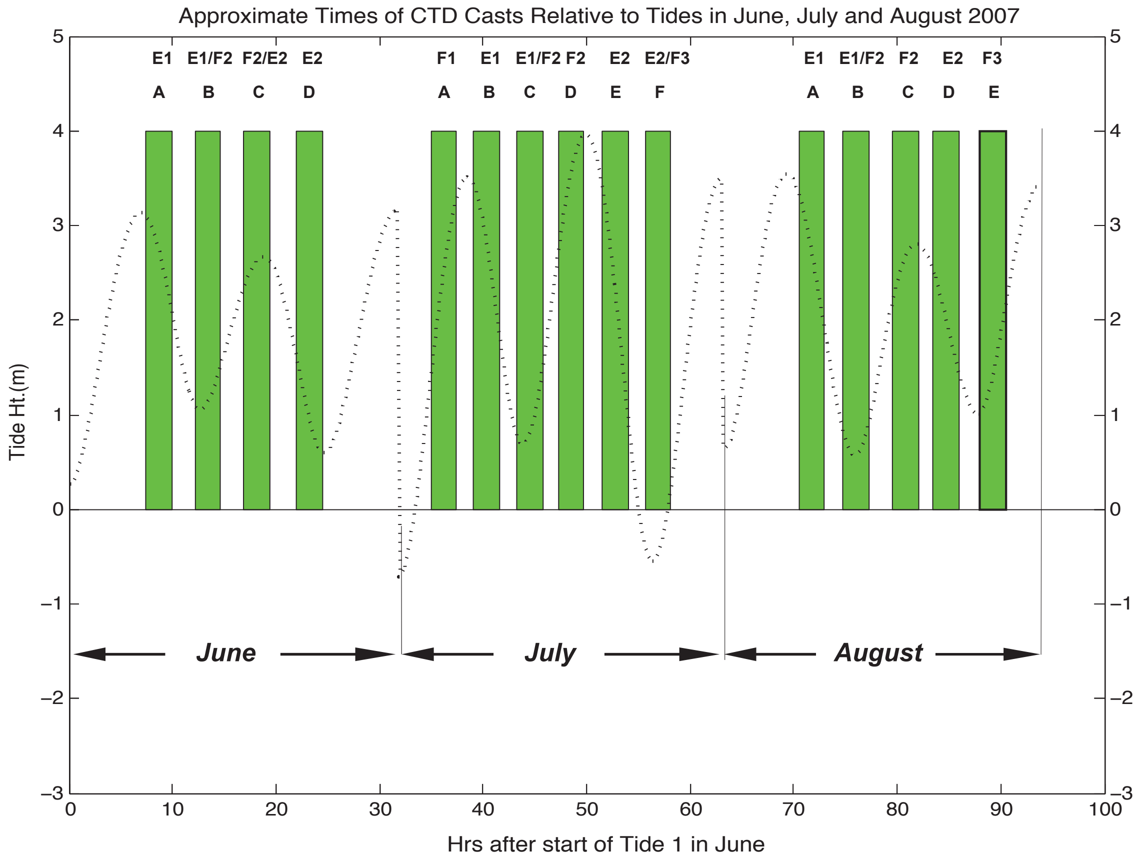

Fig. 3.17. Timing of hydrographic measurements during CTD surveys in June, July and August 2007. *Legend:* E and F are respective ebb and flood tide stages, and the numbers refer to the sequence of tides during the ADCP transects. Capital letters A to F refer to individual sets of vertical sections shown in Figure 3.18.

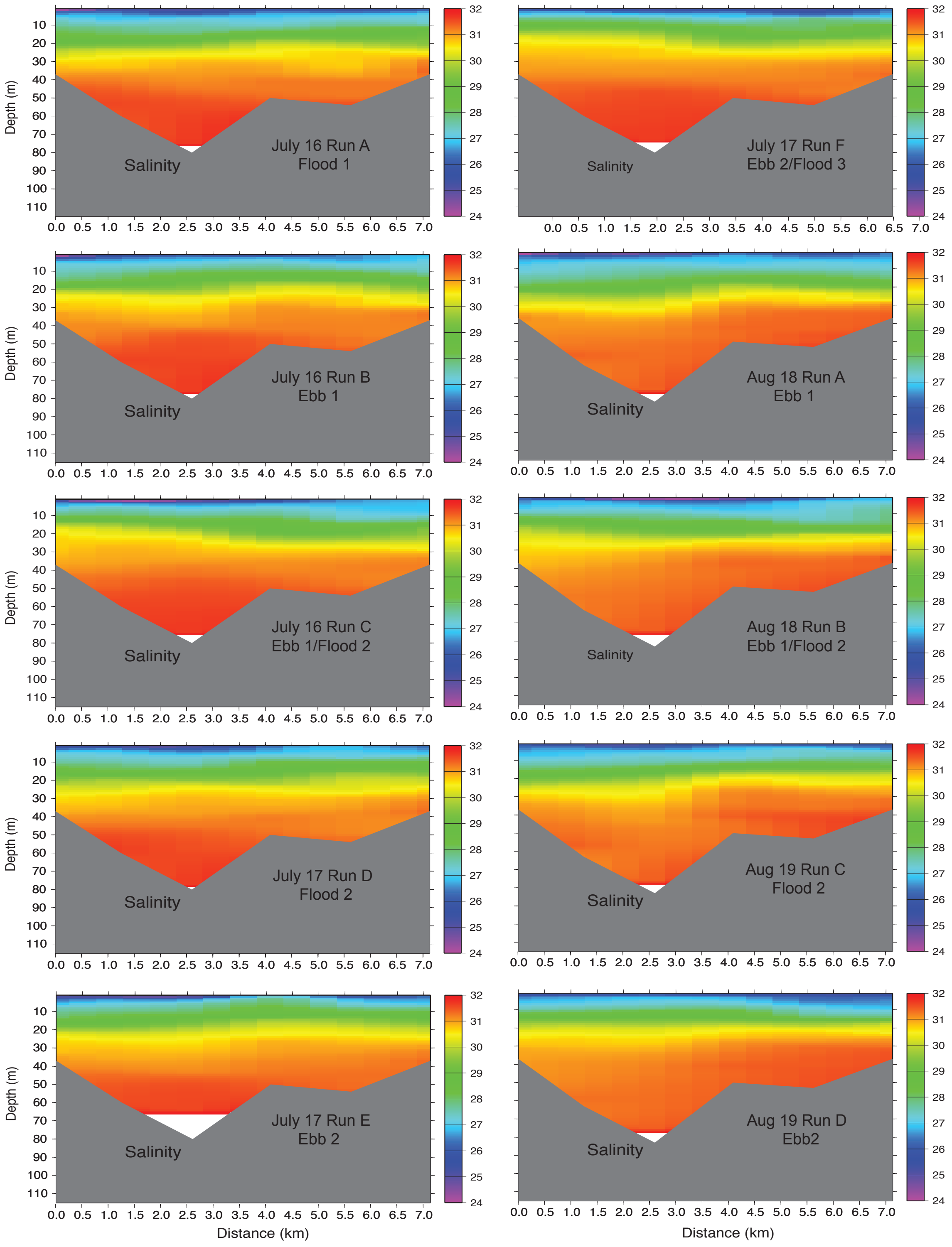

Fig. 3.18. Vertical sections of salinity from CTD surveys in July and August, 2007 showing changes in the halocline (and hence the pycnocline) during the flood and ebb tides. The approximate periods of data collection relative to the tidal periods for each panel are given in Figure 17.

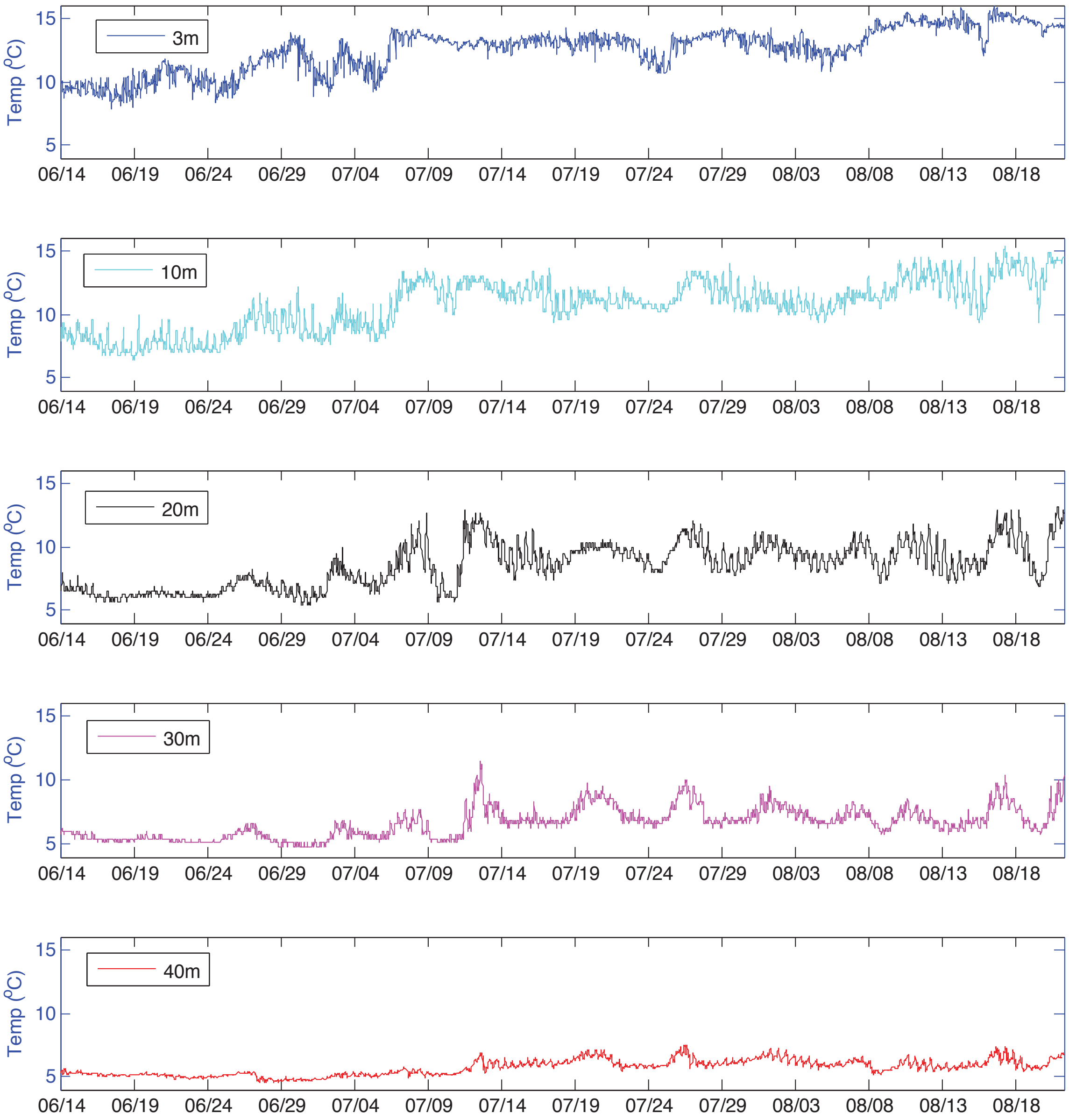

Fig. 3.19A. Temperatures at 3, 10, 20, 30 and 40m measured from June 14 to August 22, 2007 at mooring A, located near the mouth of Simpson Bay (see Fig. 5). The near-surface measurements were collected by a CT mounted to a surface buoy and, therefore, vertical tidal fluctuations do not affect the measurements. All other data were collected by either thermistors (10-30m) or a CTD (40m) attached beneath subsurface buoys (see schematic in Fig. 5.). Subsurface pressure changes due to the tides were measured by the deep CTD at 40m.

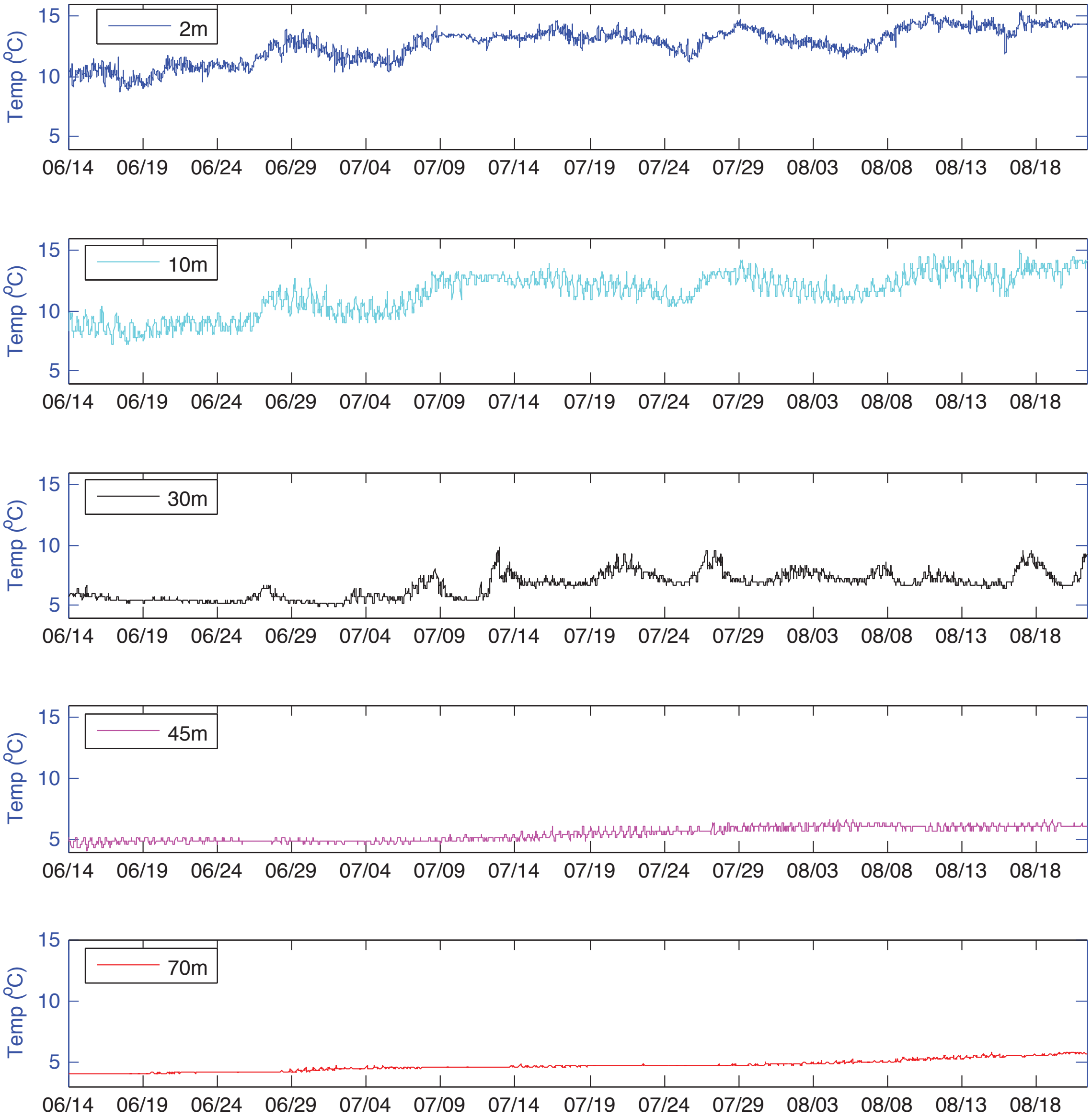

Fig. 3.19B. Temperatures at 2, 10, 30, 45 and 70m measured from June 14 to August 22, 2007 at mooring B, located north of the shallow reef at the mouth of the Northern Basin of Simpson Bay (see Fig. 5). The near-surface measurements were collected by a surface buoy, similar to mooring A, and, data at the other depths were collected by either thermistors (10-45m) or a CT (70m) attached beneath subsurface buoys (see schematic in Fig. 5.).

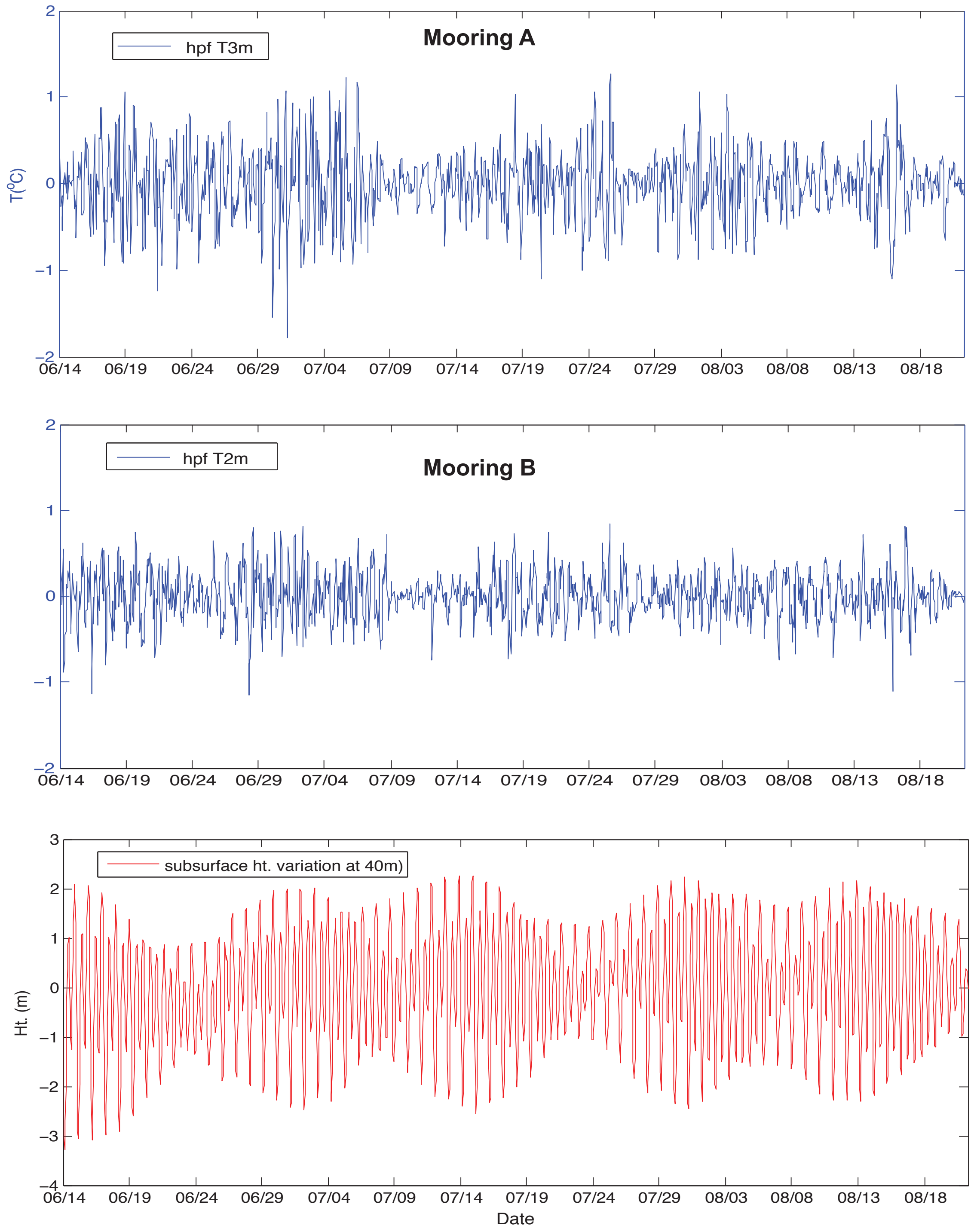

Fig. 3.20A. High-pass filtered near-surface temperatures (blue) measured at the surface buoys at moorings A and B, and subsurface depth changes due to tides measured at 40m by the deep CTD on mooring A. Note that the near-surface temperature series are rather noisy in comparison to the tides. This is shown in more detail in power spectra of the three series (see Fig. 3.23).

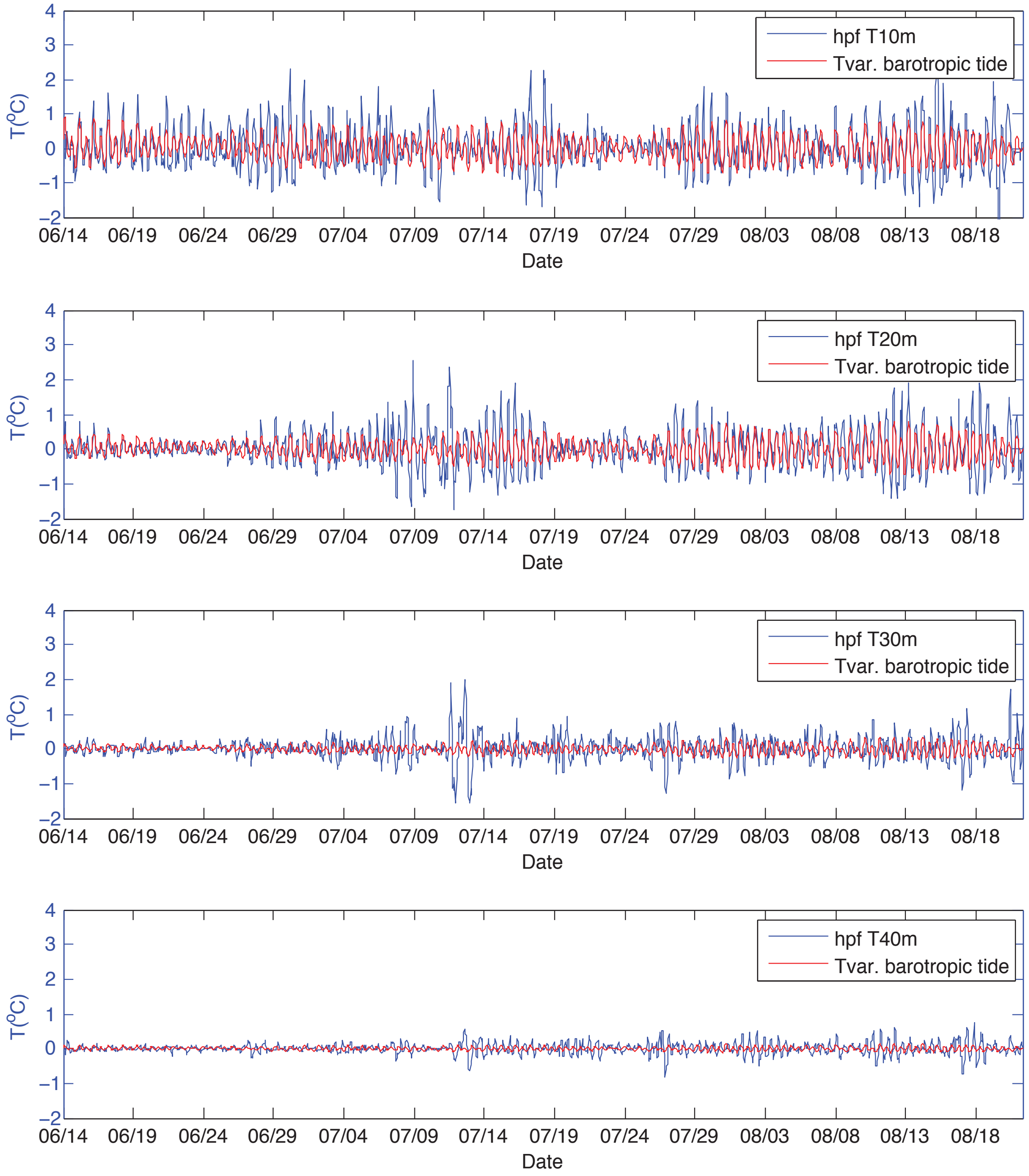

Fig. 3.20B. High-pass filtered temperature (blue) and temperature oscillations due to barotropic tides (red) at 10, 20, 30 and 40m measured at mooring A. Note that the tidal fluctuations measured by the deep CTD were removed from the high-pass data prior to deriving equivalent depths of motion due to internal waves (see Fig. 24).

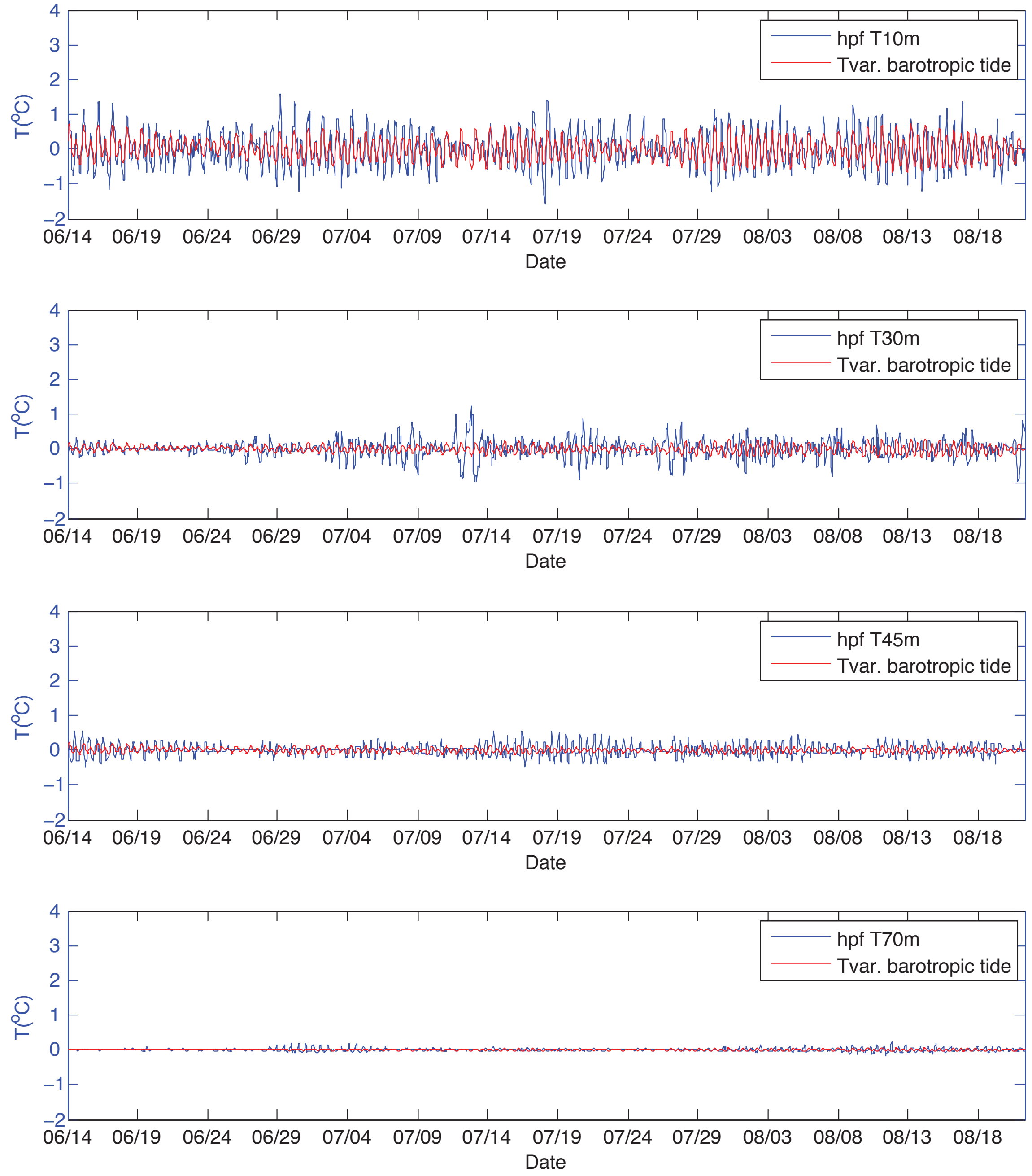

Fig. 3.20C. High-pass filtered temperature (blue) and temperature oscillations due to barotropic tides (red) at 10, 30, 45 and 70m measured at mooring A. Note that the tidal fluctuations measured by the deep CTD at mooring A were removed from the high-pass data prior to deriving the equivalent depths of motion due to internal waves (see Fig. 24).

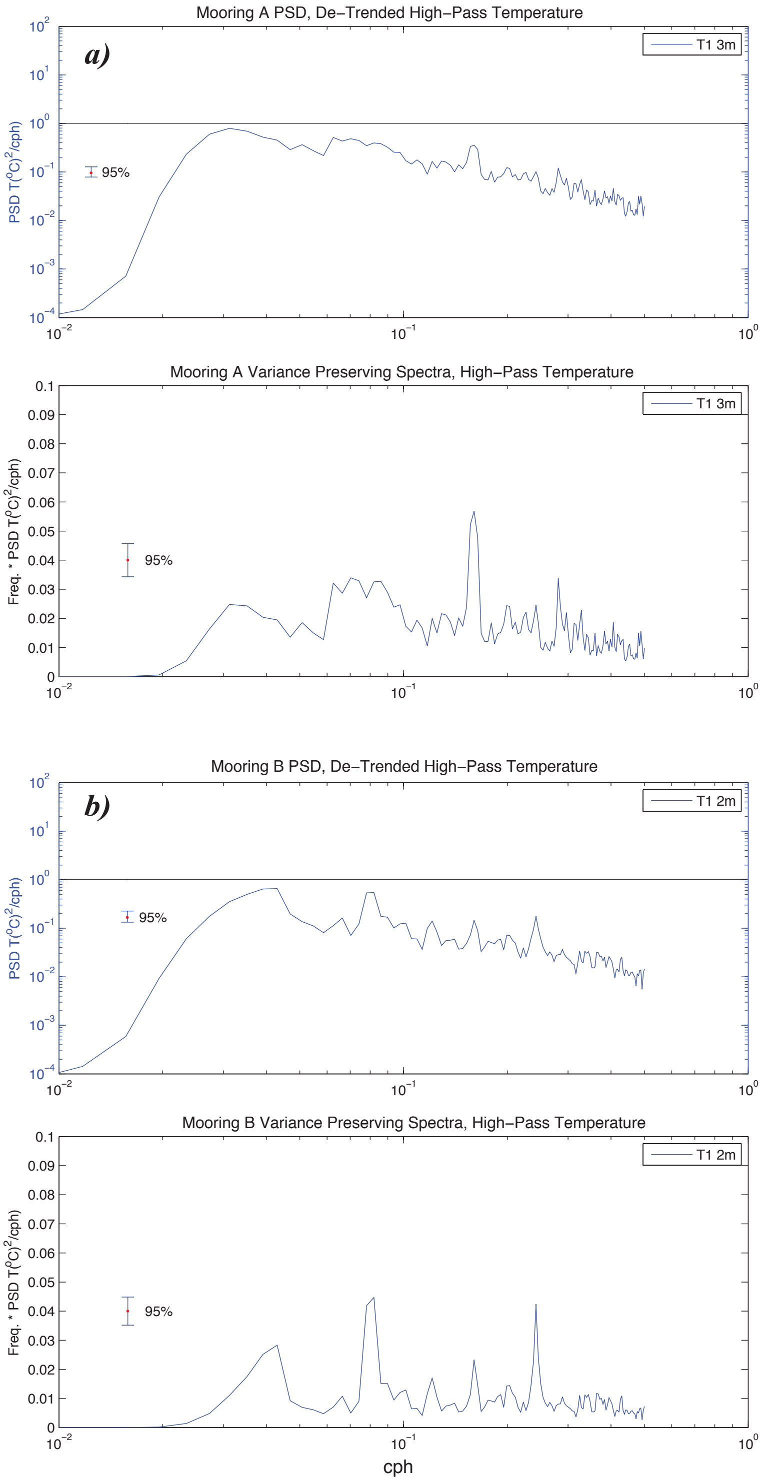

Fig. 3.21A. Power spectral density and variance preserving spectra for high-pass temperatures: a) 3m at mooring A, and b) 2m at mooring B. All spectra are calculated using 256 Fourier coefficients and Kaiser-Bessel windows with 50% overlap. Zero padding is used to limit end effects and obtain series lengths at 2^n values. Confidence limits are shown for the 95% level.

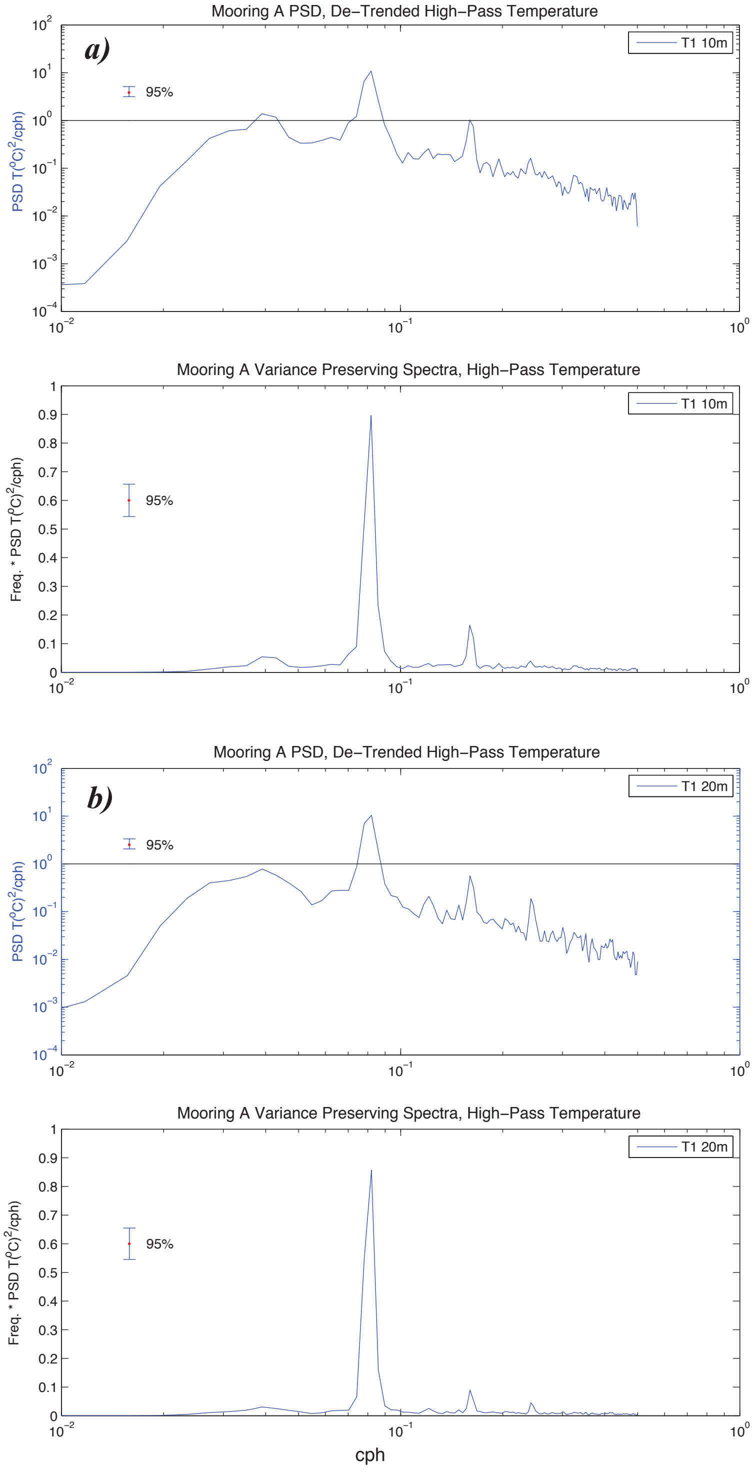

Fig. 3.21B. Power spectral density and variance preserving spectra of high-pass temperatures at mooring A: a) 10m, b) 20m, c) 30m and d) 40m. Note the large amplitudes of the semidurnal spectral peaks at 10 and 20m, particularly for the variance preserving spectra, and the presence of secondary peaks at the half and quarter semidiurnal periods (~6 and 3hr). The latter are very low in power, particularly at 40m.

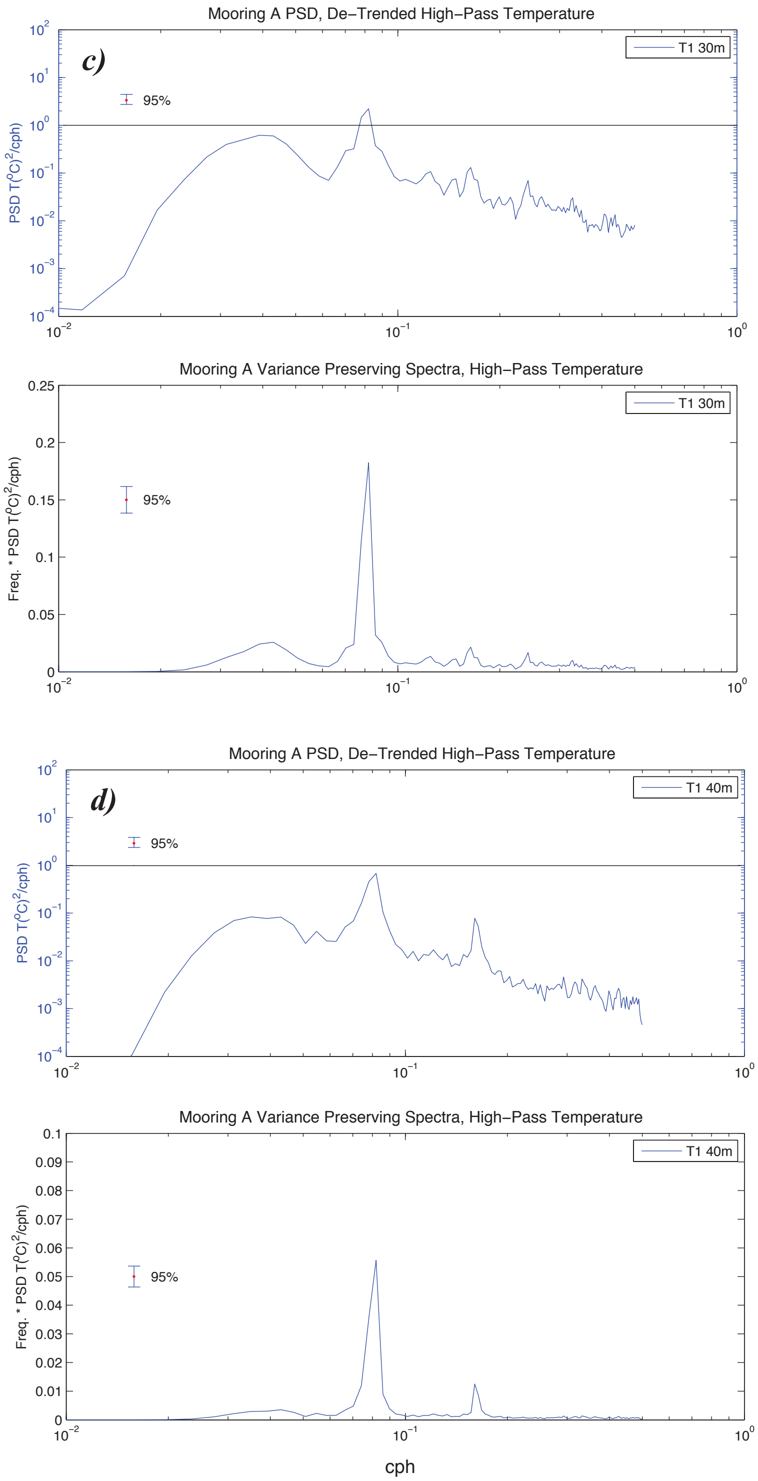

Fig. 3.21B (cont.).

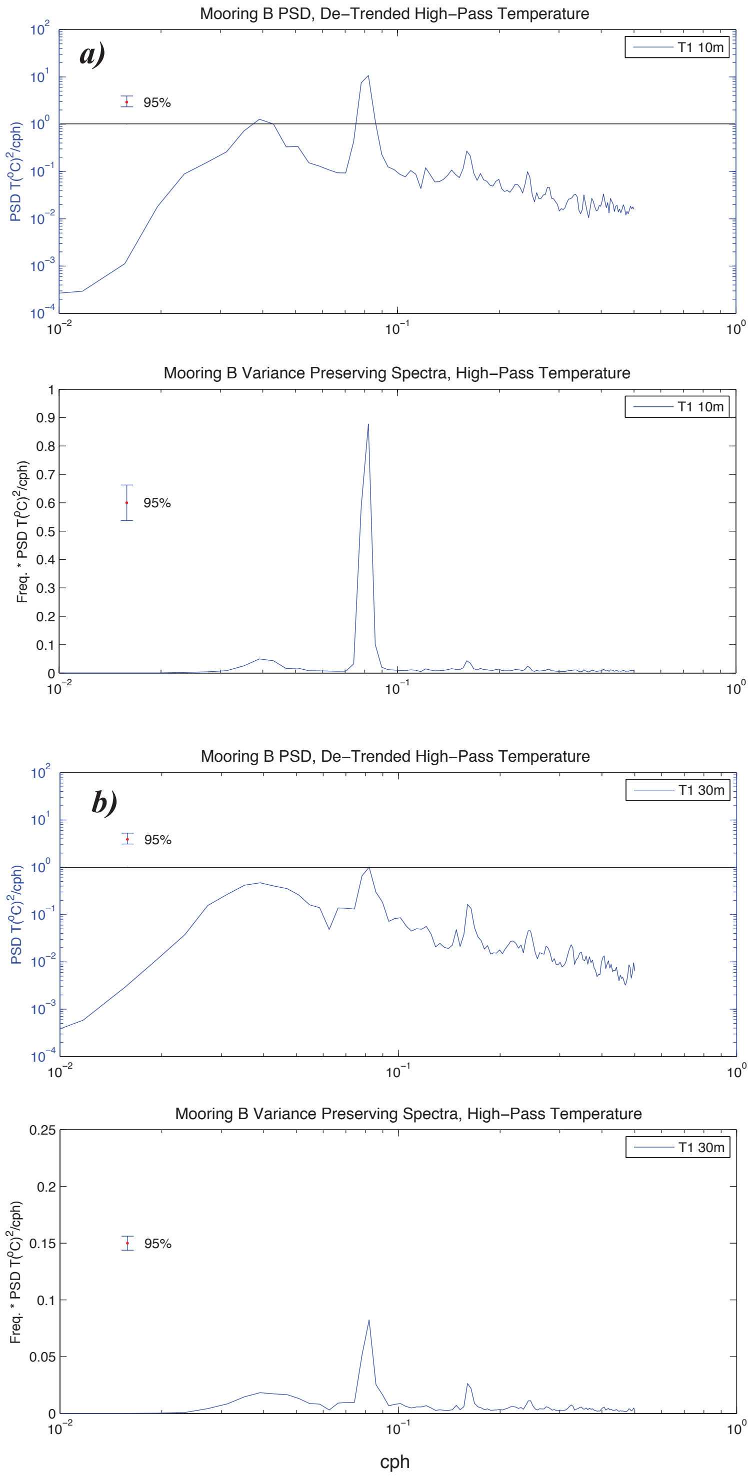

Fig. 3.21C. Power spectral density and variance preserving spectra of high-pass temperatures at mooring B: a) 10m, b) 30m, c) 45m and d) 70m. Large amplitudes occur for the semidurnal spectral peaks at 10m, similar to mooring A, particularly for the variance preserving plot, and secondary peaks also occur at the half and quarter semidiurnal periods (~6 and 3hr). The power diminishes rapidly with depth, however.

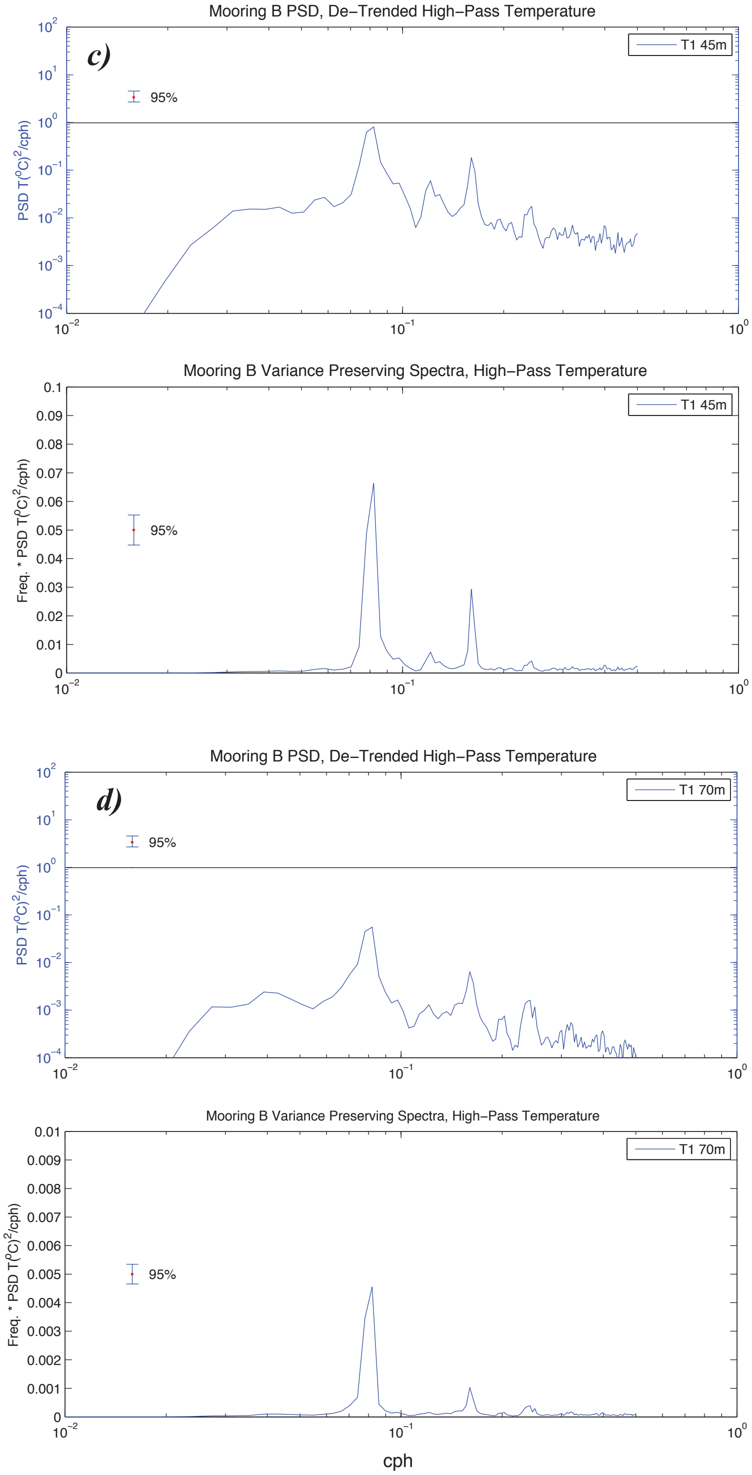

Fig. 3.21C (cont.).

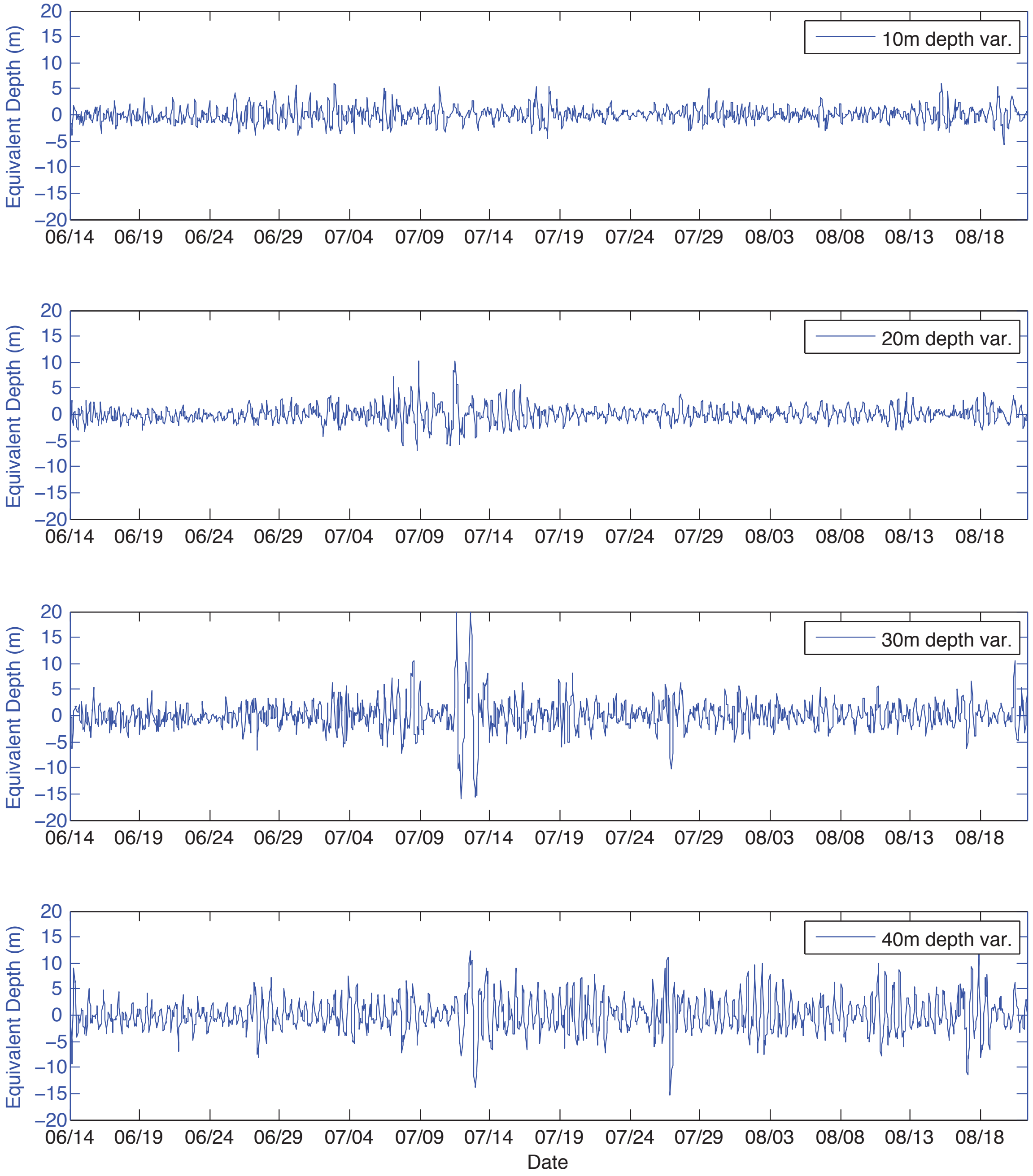

Fig. 3.22A. Vertical oscillations at 10, 20, 30 and 40m equivalent to the motions of vertical temperature gradients at the same depths from June 14 to August 22, 2007 at mooring A. Note that the hydrostatic effects of the tides on vertical height fluctuations of temperature were removed prior to deriving wave amplitudes.

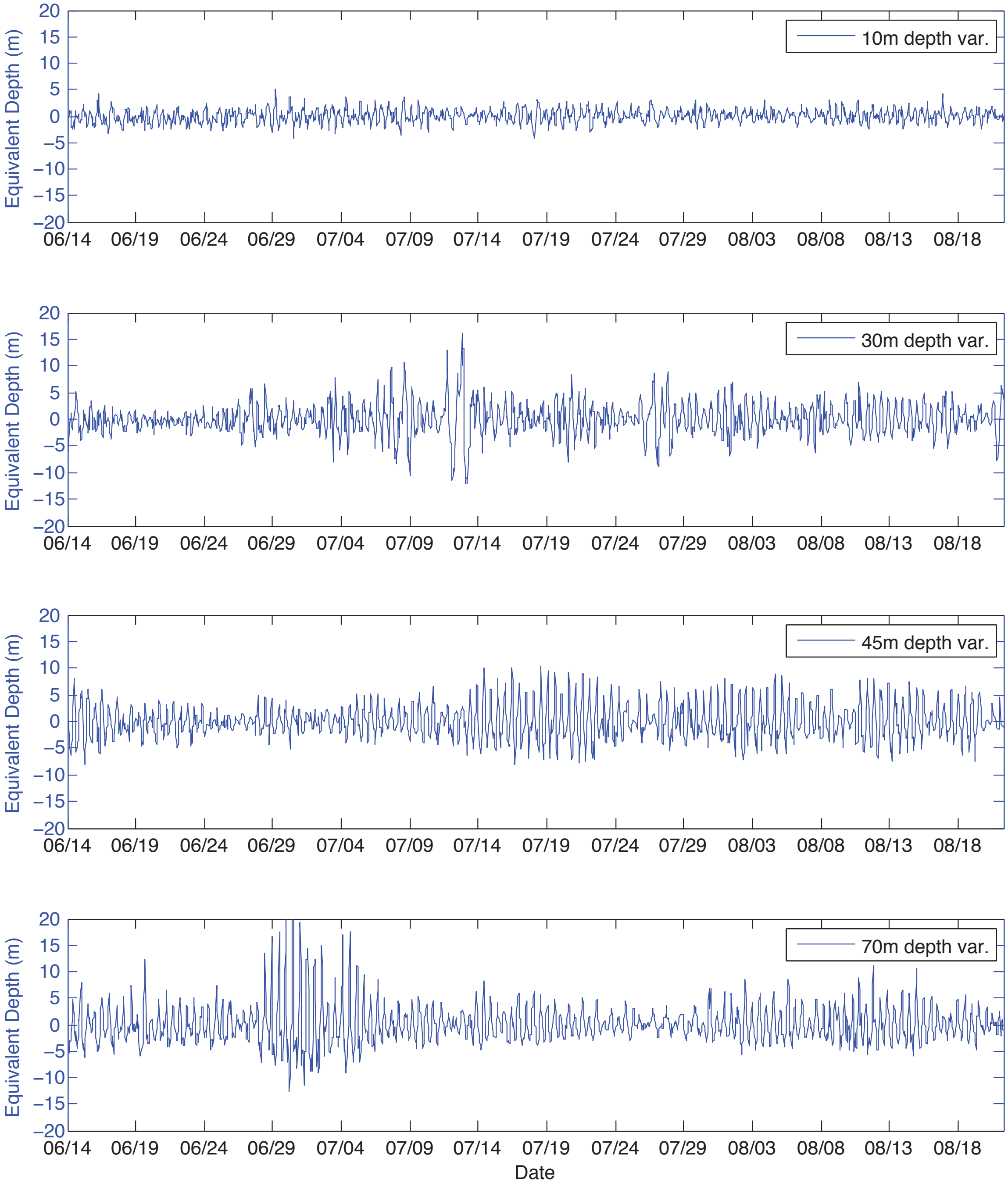

Fig. 3.22B. Vertical oscillations at 10, 30, 45 and 70m equivalent to the motions of vertical temperature gradients at the same depths from June 14 to August 22, 2007 at mooring B. Note that the hydrostatic effects of the tides on vertical height fluctuations of temperature were removed prior to deriving wave amplitudes.

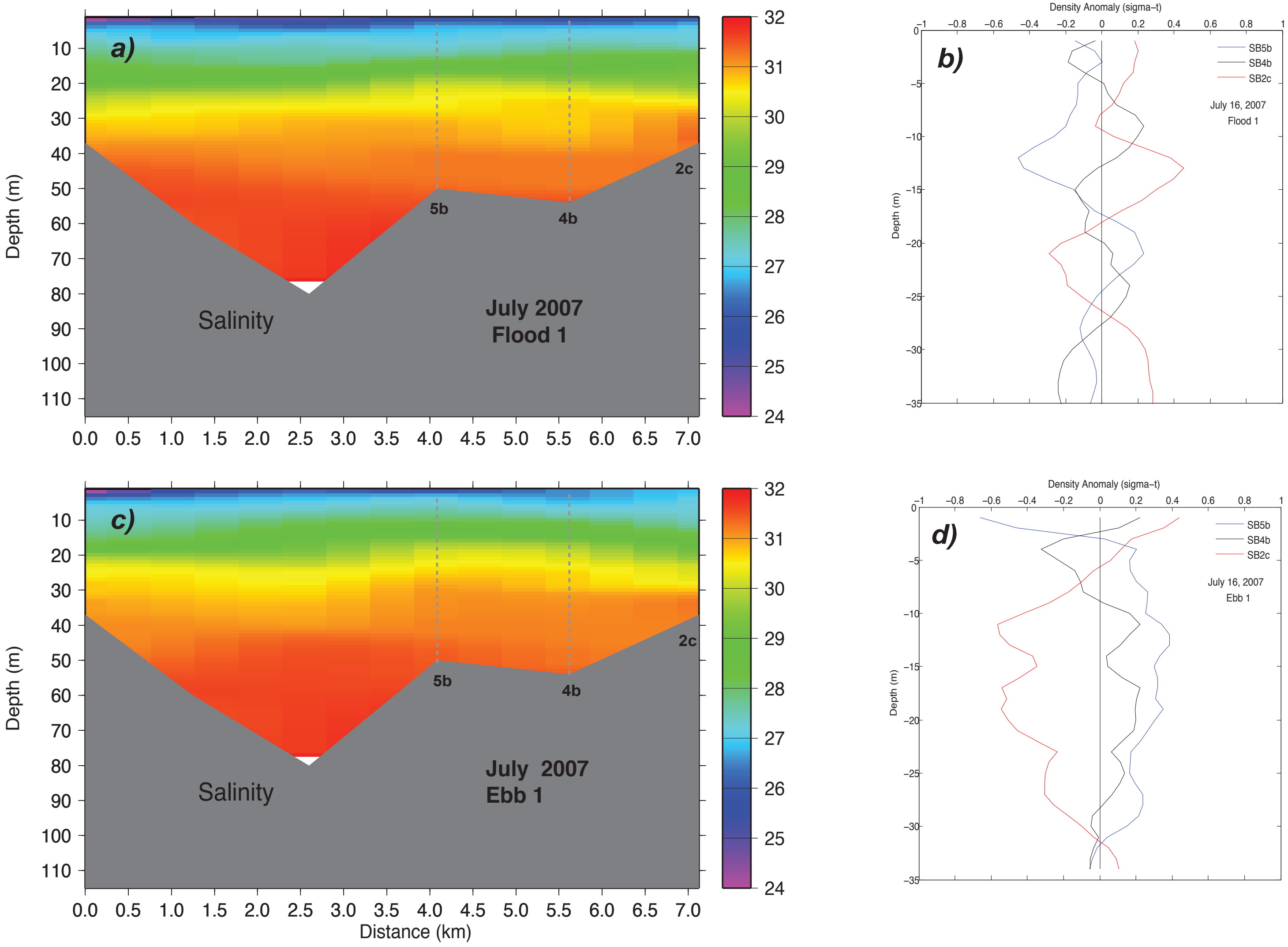

Fig. 3.23. Vertical sections of salinity and profiles of density anomalies within the main basin and central portion of the outer sill in July 2007 during flood tide 1 (a,b) and ebb tide 1 (c,d). Stations corresponding to the density anomaly profiles are shown in the salinity sections as dashed grey lines, and locations of all stations used in the plots are shown in Fig. 10.

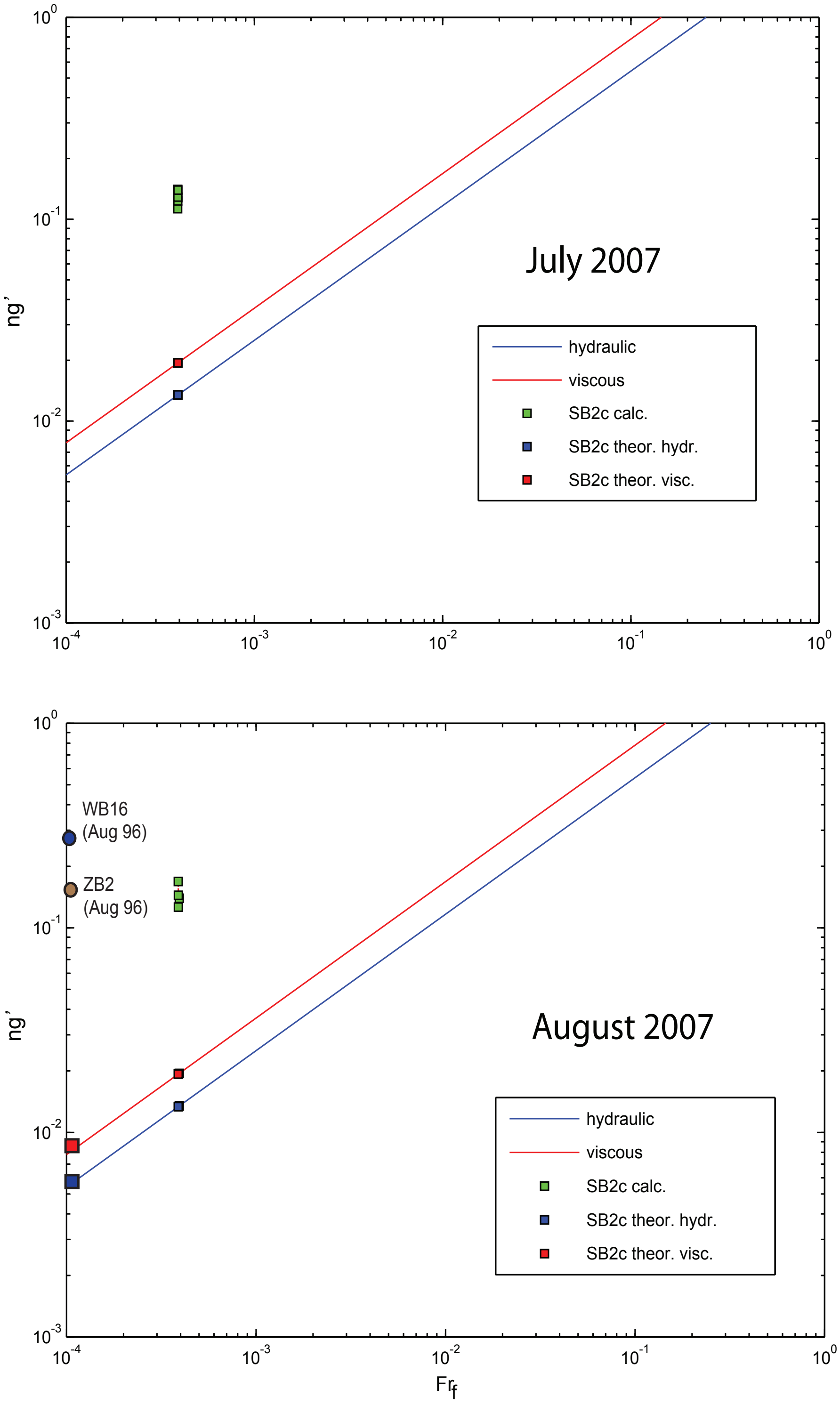

Fig. 3.24. Calculations of normalized reduced gravity (ng') versus densometric Froude Number (Fr_f). The solid lines represent the theoretical limits of hydraulic vs. viscous control of exchange flow based on eq. (6) and (7) respectively in Hetland (2010). The red and blue squares show the two solutions for Simpson, and the green squares and colored circles show the same relationship based on calculated values of ng' and Fr_f for Simpson, Zaikof and Whale Bay.

a) 2007

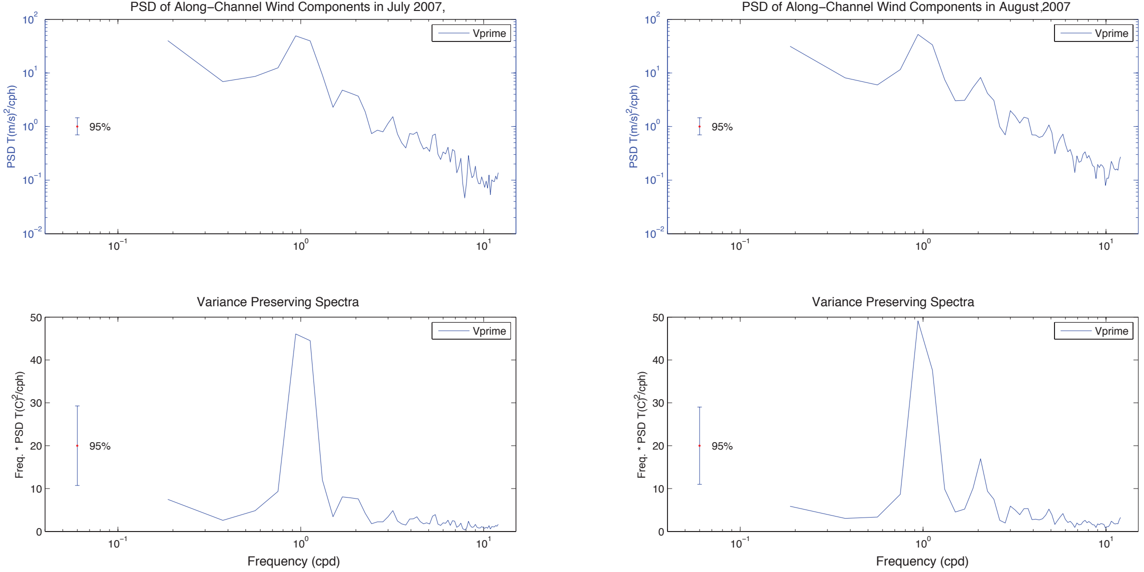

b) 2008

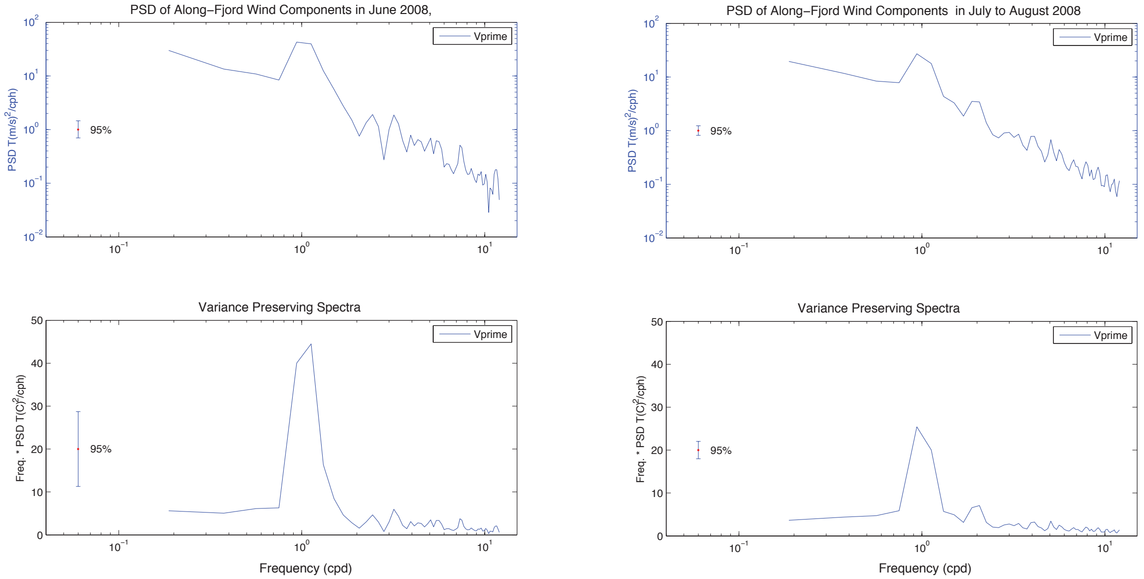

Fig. 4.1. Power spectra and variance preserving spectra for along-fjord winds in a) 2007 and b) 2008. In both years large spectral peaks occur corresponding to low frequency (diurnal period) up-fjord winds, the power in July and August 2007 being nearly double that of 2008. Secondary peaks also occur for the semidiurnal period. All spectra are calculated using 128 Fourier coefficients and Kaiser-Bessel windows with 50% overlap. Zero padding is used to limit end effects and obtain series lengths at 2^n values. Confidence limits are shown for the 95% level.

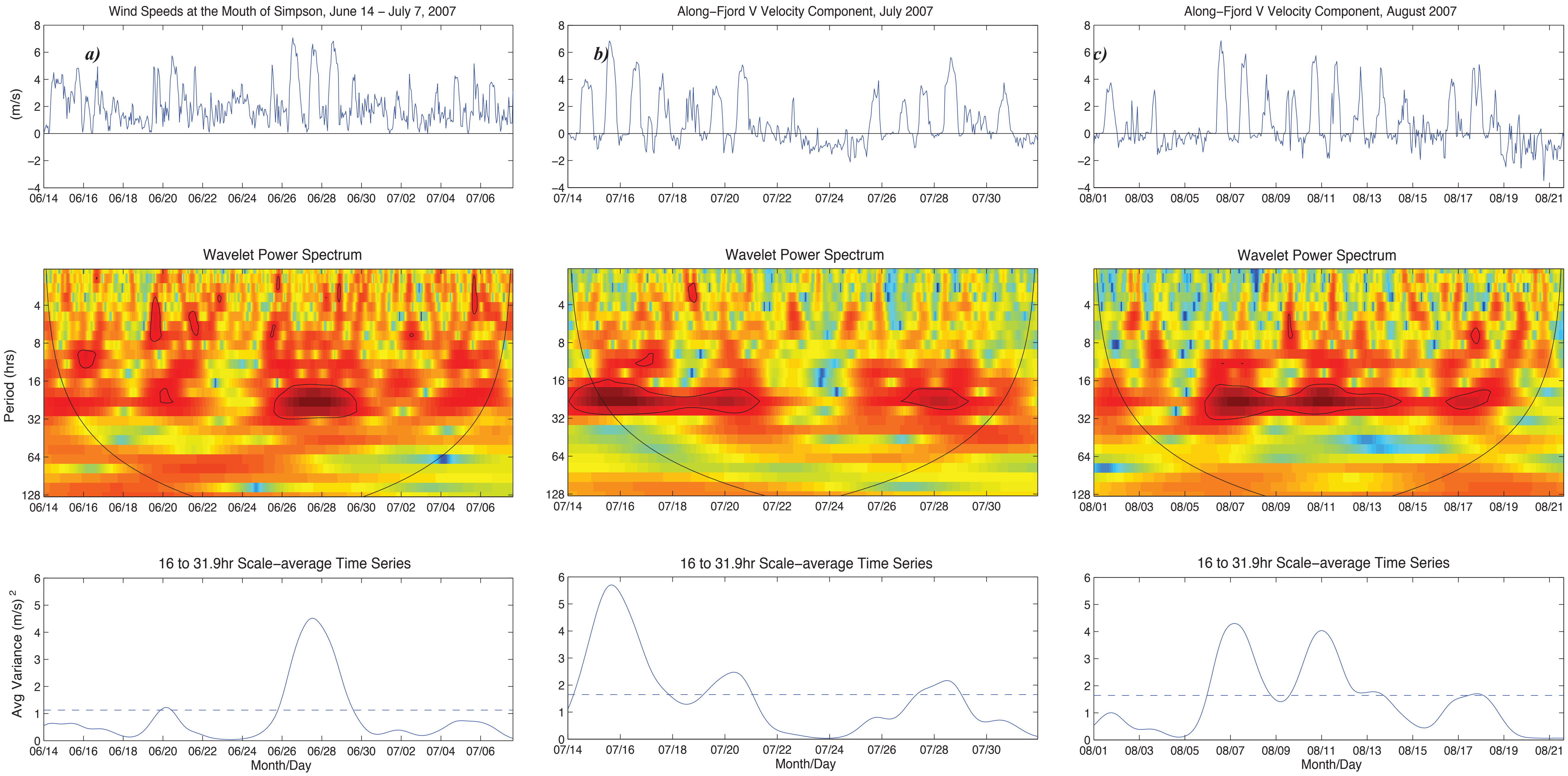

Wind Speeds at the Mouth of Simpson, June 14 – July 7, 2007

Along–Fjord V Velocity Component, July 2007

Along–Fjord V Velocity Component, August 2007

Wavelet Power Spectrum

16 to 31.9hr Scale–average Time Series

Fig. 4.2. Wavelet spectra for winds in 2007 (a-c) and 2008 (d-f) showing a greater influence of diurnal period up-fjord winds in 2007. In 2008 winds at higher frequencies (< = semidiurnal periods) are more frequent in July and August, in part due to greater storm activity.

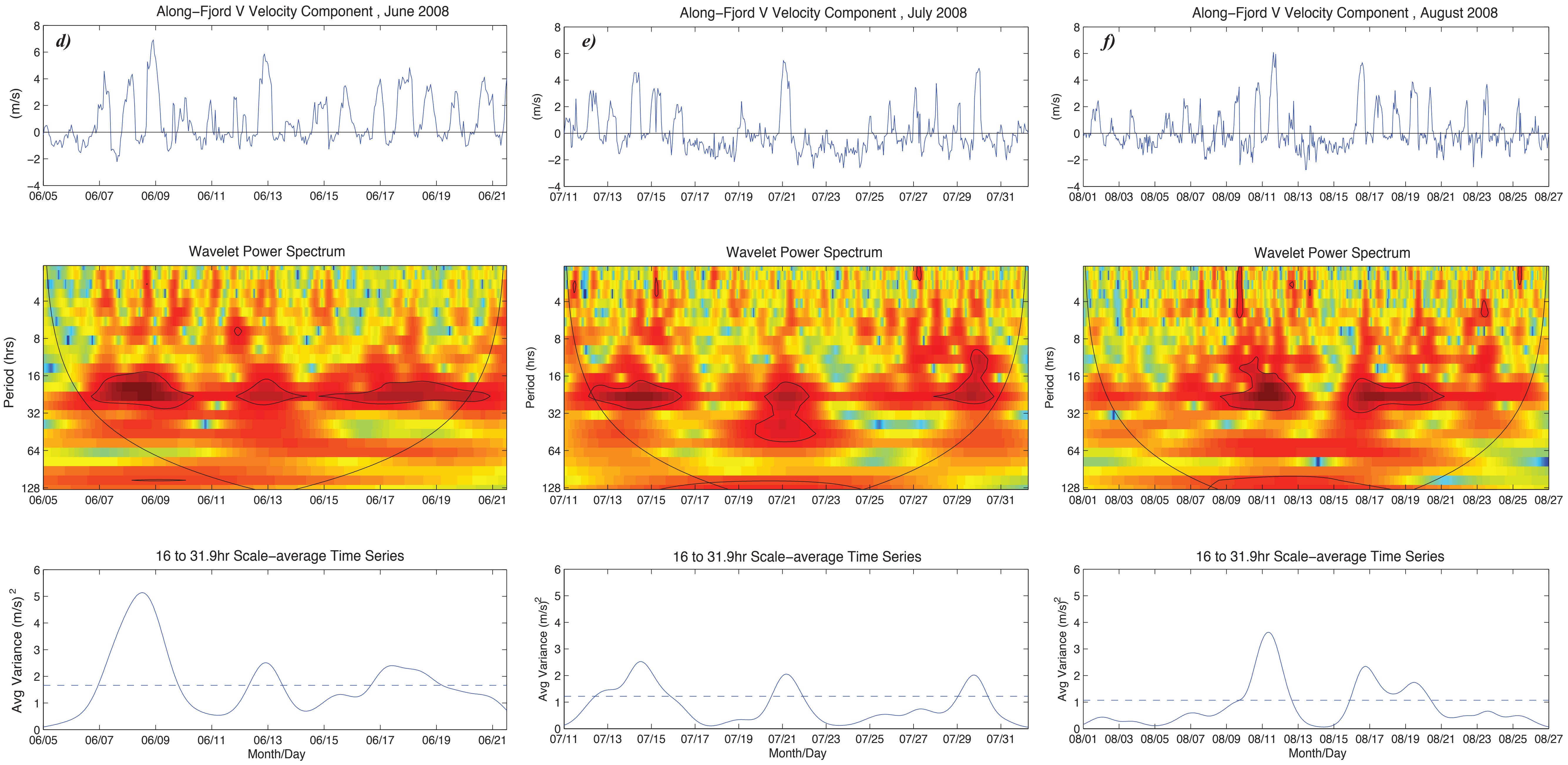
Along–Fjord V Velocity Component , June 2008
Along–Fjord V Velocity Component , July 2008
Along–Fjord V Velocity Component , August 2008
d)
e)
f)
(m/s)
8
6
4
2
0
−2
−4
06/05
06/07
06/09
06/11
06/13
06/15
06/17
06/19
06/21
07/11
07/13
07/15
07/17
07/19
07/21
07/23
07/25
07/27
07/29
07/31
08/01
08/03
08/05
08/07
08/09
08/11
08/13
08/15
08/17
08/19
08/21
08/23
08/25
08/27
Wavelet Power Spectrum
Period (hrs)
4
8
16
32
64
128
16 to 31.9hr Scale–average Time Series
Avg Variance (m/s)^2
0
1
2
3
4
5
6
Month/Day

Fig. 4.2. (cont.)

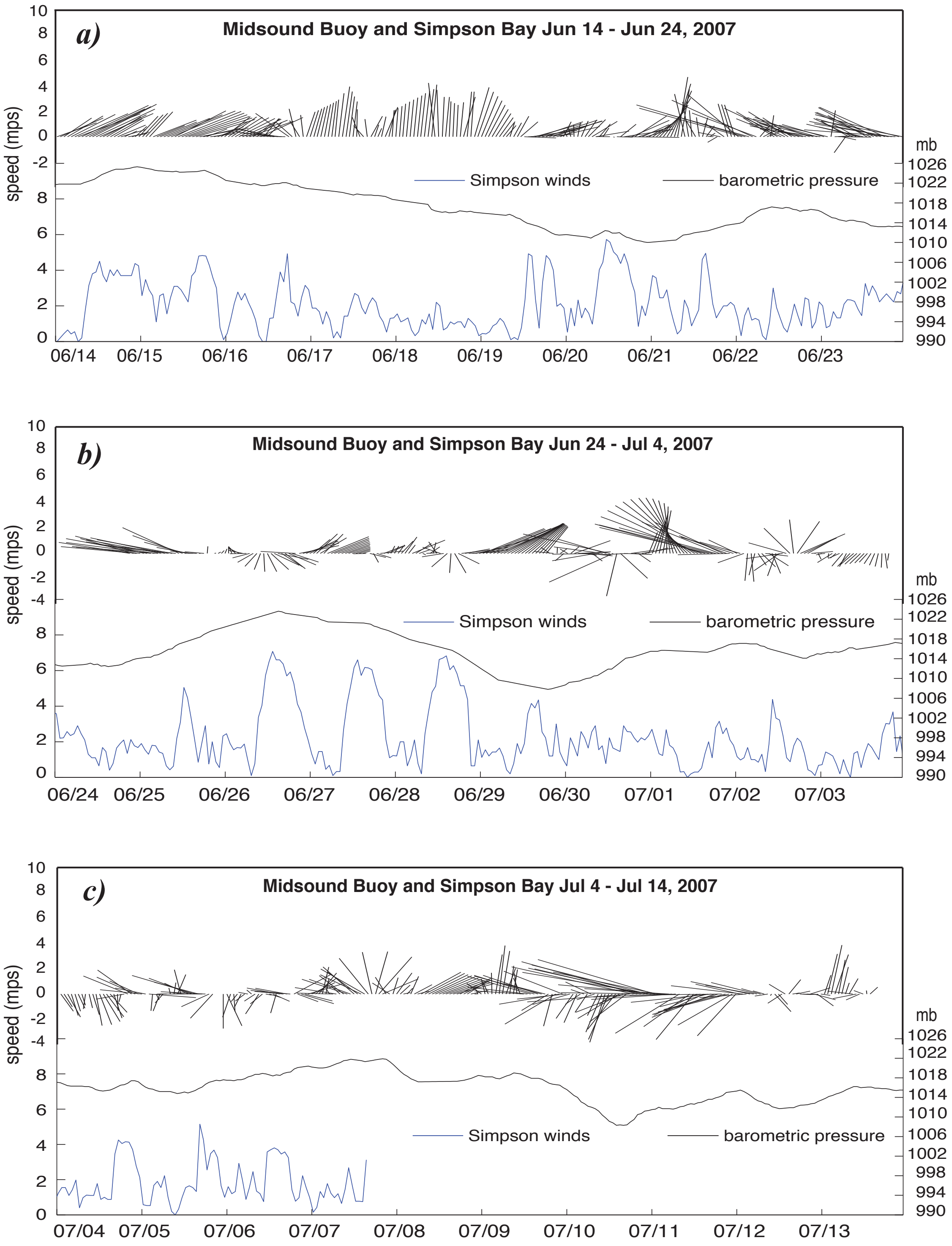

Fig. 4.3. Wind vectors and barometric pressure at the Midsound Buoy, and wind speeds at Simpson Bay from June to August, 2007. a) June 14 to 24, b) June 24 to July 4, c) July 4 to 14, e) July 14 to 27, f) July 27 to Aug. 9, and g) Aug. 9 to 22.

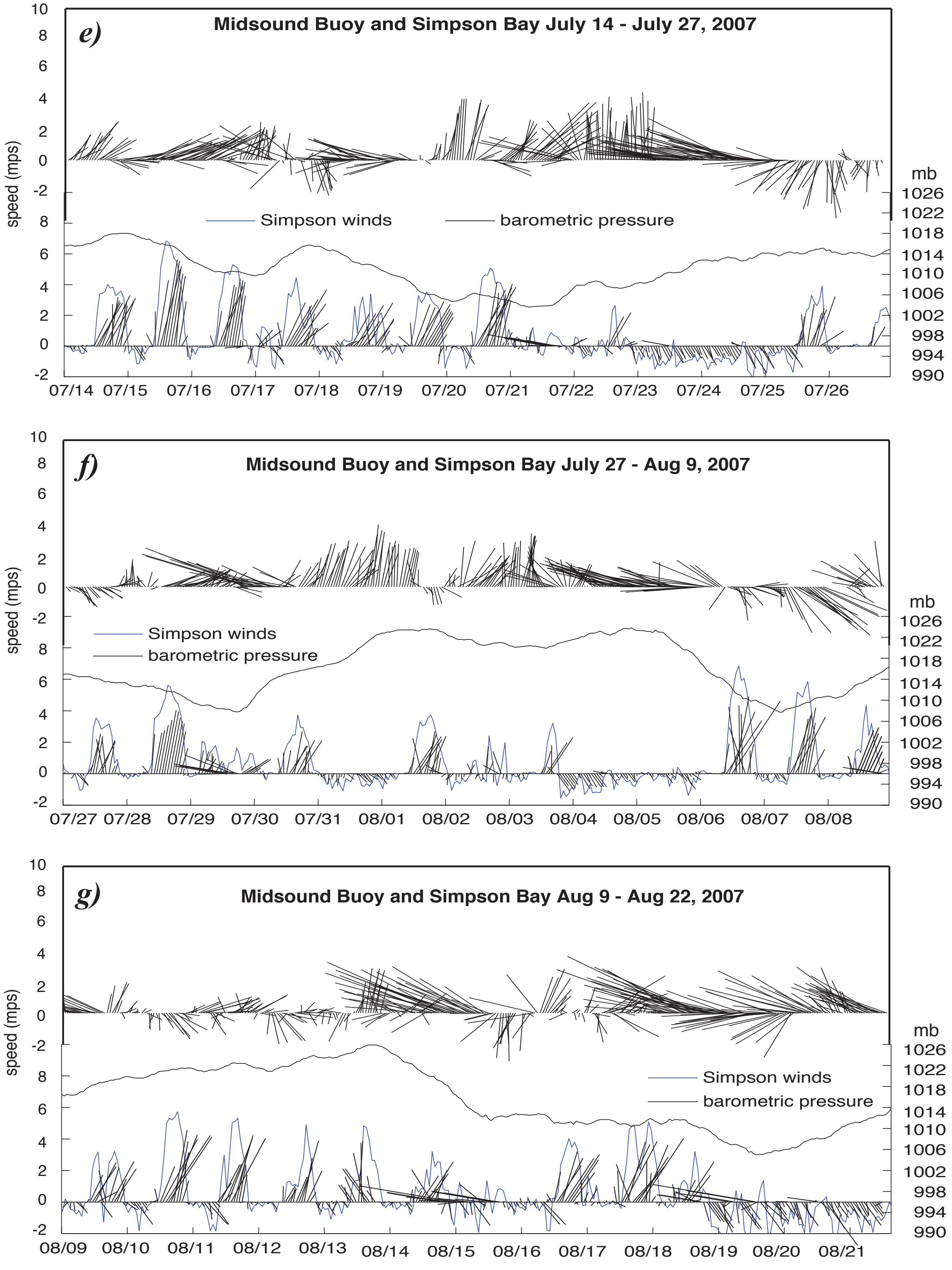
e)
Midsound Buoy and Simpson Bay July 14 - July 27, 2007
speed (mps)
Simpson winds
barometric pressure
mb
10
8
6
4
2
0
-2
1026
1022
1018
1014
1010
1006
1002
998
994
990
07/14
07/15
07/16
07/17
07/18
07/19
07/20
07/21
07/22
07/23
07/24
07/25
07/26
f)
Midsound Buoy and Simpson Bay July 27 - Aug 9, 2007
07/27
07/28
07/29
07/30
07/31
08/01
08/02
08/03
08/04
08/05
08/06
08/07
08/08
g)
Midsound Buoy and Simpson Bay Aug 9 - Aug 22, 2007
08/09
08/10
08/11
08/12
08/13
08/14
08/15
08/16
08/17
08/18
08/19
08/20
08/21

Fig. 4.3 (cont.).

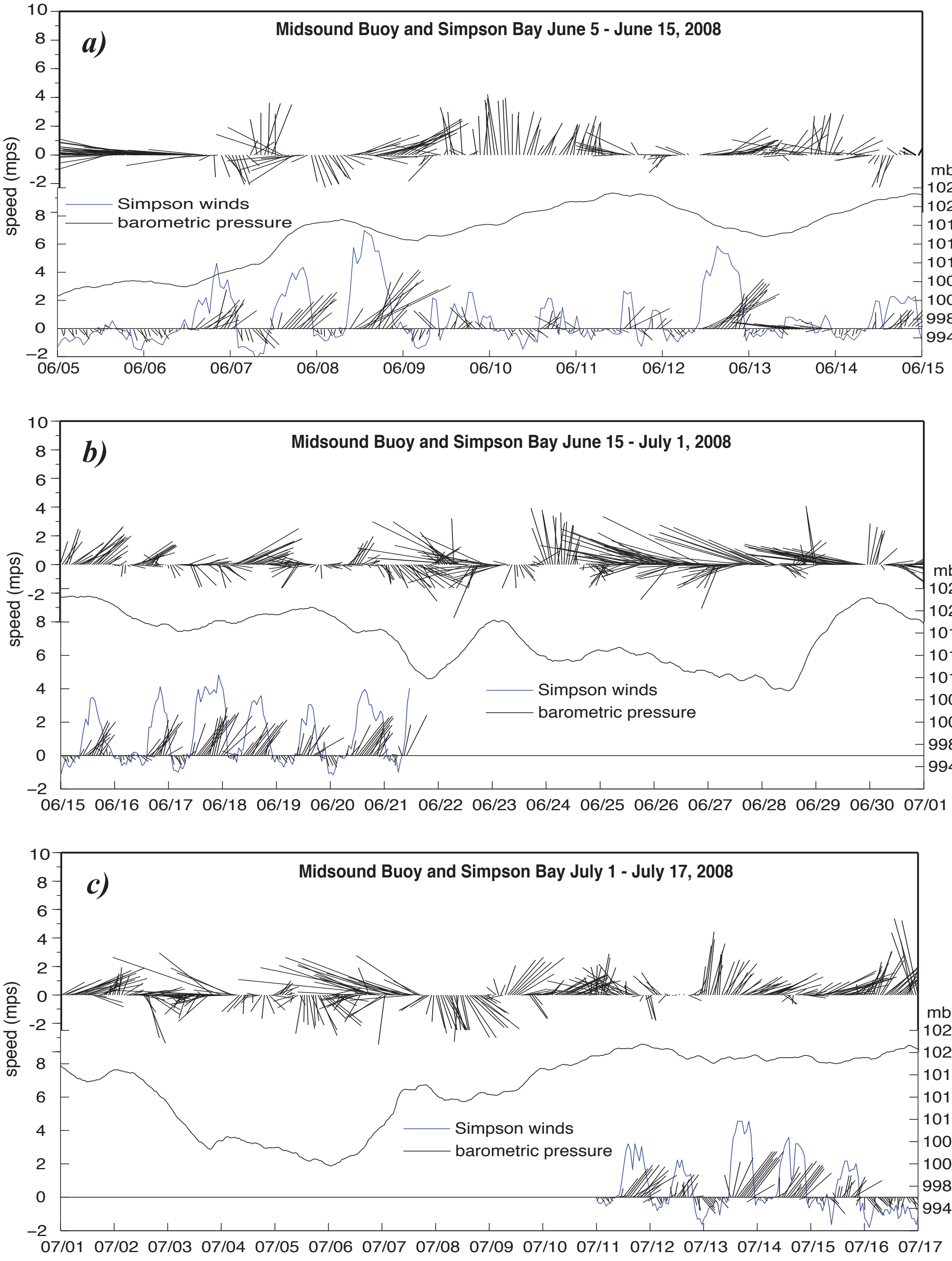

Fig. 4.4. Wind vectors and barometric pressure at the Midsound Buoy, and along-fjord winds at Simpson Bay from June 5 to August 27, 2008. a) June 5 to 15, b) June 15 to July 1, c) July 1 to 17, d) July 17 to Aug. 1, e) Aug. 1 to Aug 14, and f) Aug. 14 to Aug 27.

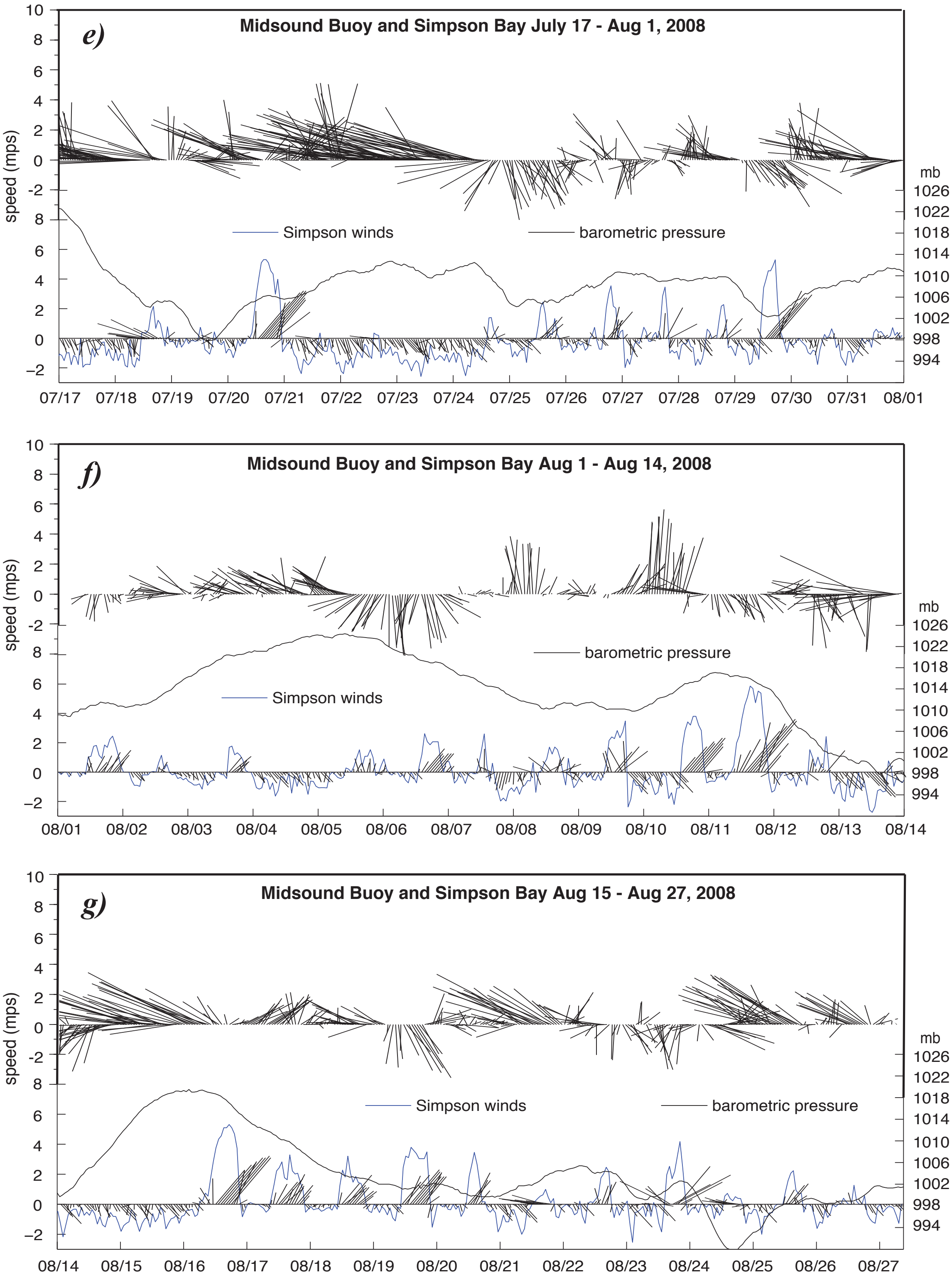
e)
Midsound Buoy and Simpson Bay July 17 - Aug 1, 2008
speed (mps)
10
8
6
4
2
0
-2
8
6
4
2
0
−2
mb
1026
1022
1018
1014
1010
1006
1002
998
994
Simpson winds
barometric pressure
07/17
07/18
07/19
07/20
07/21
07/22
07/23
07/24
07/25
07/26
07/27
07/28
07/29
07/30
07/31
08/01
f)
Midsound Buoy and Simpson Bay Aug 1 - Aug 14, 2008
speed (mps)
barometric pressure
Simpson winds
08/01
08/02
08/03
08/04
08/05
08/06
08/07
08/08
08/09
08/10
08/11
08/12
08/13
08/14
g)
Midsound Buoy and Simpson Bay Aug 15 - Aug 27, 2008
speed (mps)
Simpson winds
barometric pressure
08/14
08/15
08/16
08/17
08/18
08/19
08/20
08/21
08/22
08/23
08/24
08/25
08/26
08/27

Fig. 4.4 (cont).

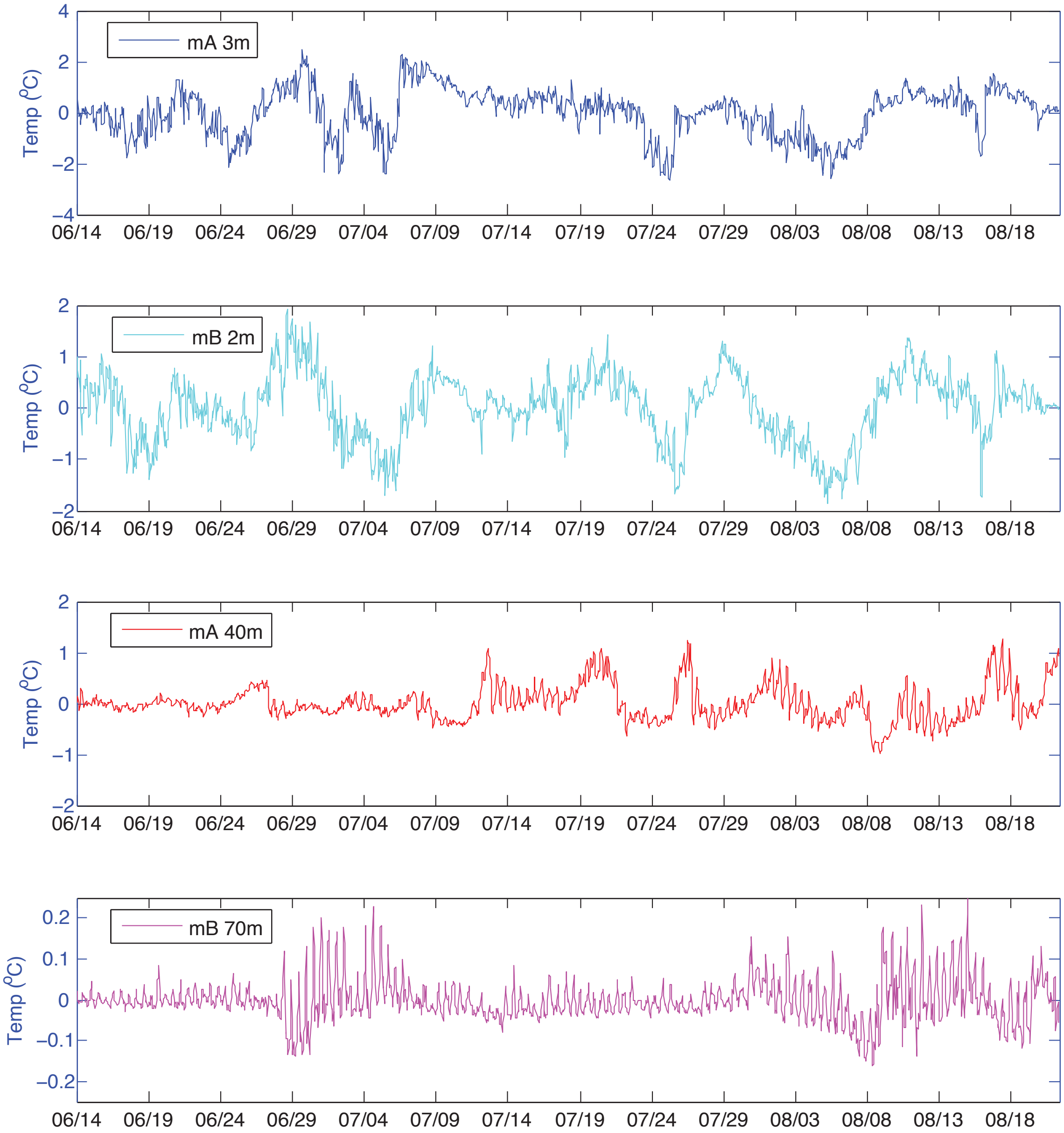

Fig. 4.5A. De-meaned and de-trended temperature series for the near-surface (3-2m) and deep (40-70m) CTs at moorings A and B in the summer of 2007.

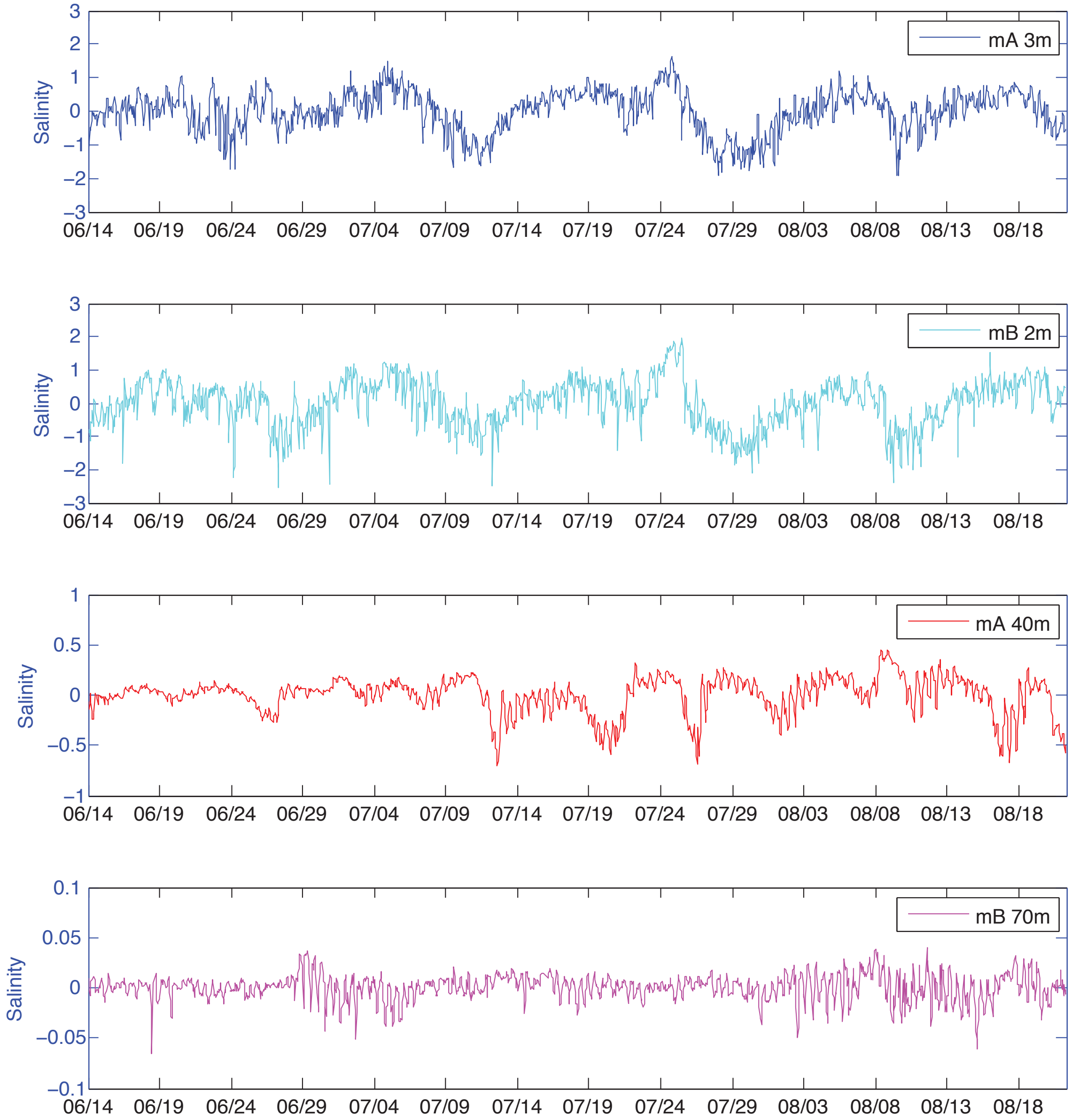

Fig. 4.5B. De-meaned and de-trended salinity series for the near-surface (3-2m) and deep (40-70m) CTs at moorings A and B in the summer of 2007.

Fig. 4.5C. Low-pass filtered temperatures and salinities at at moorings A and B: a) 3m, b) 2m, c) 40m and d) 70m.

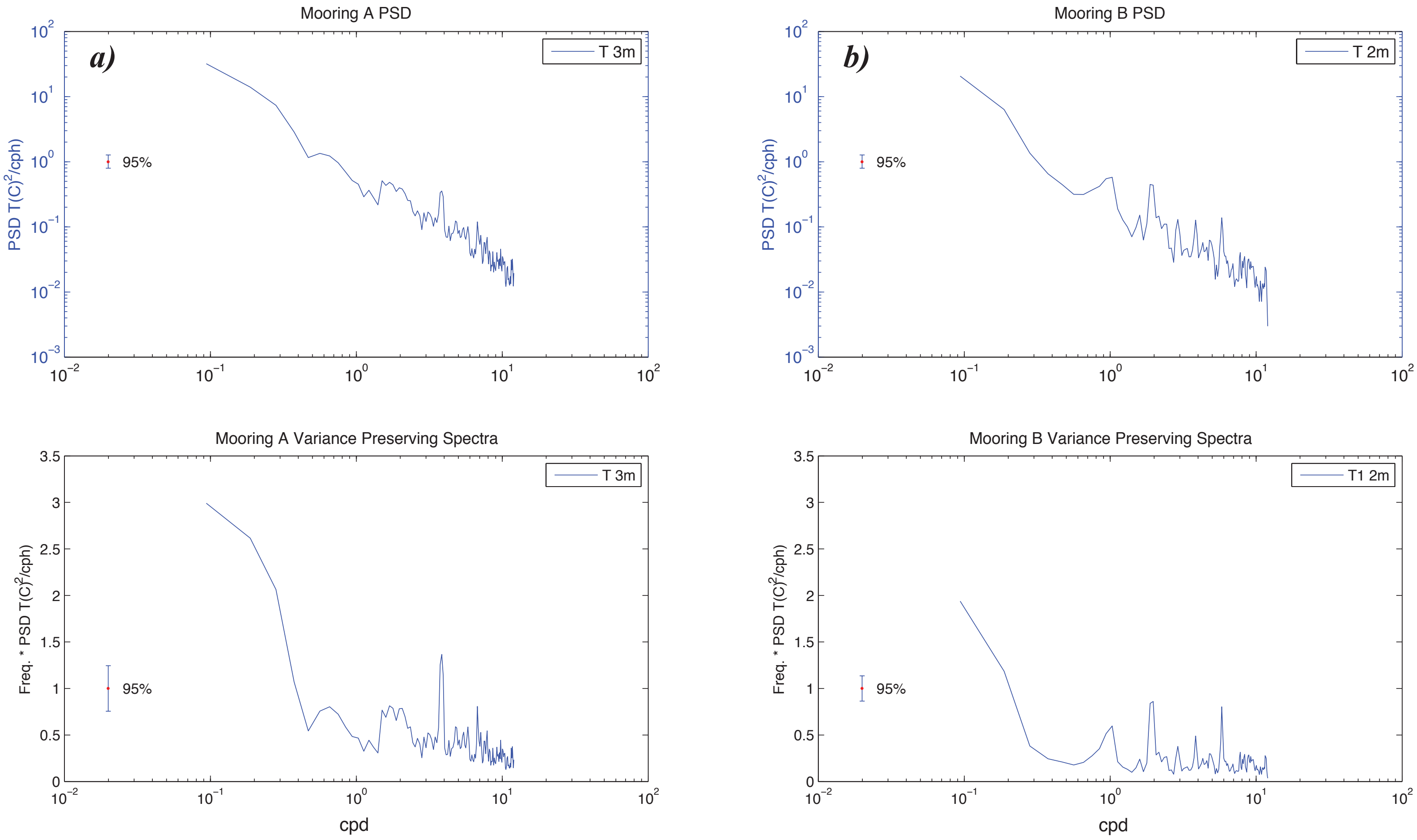

Fig. 4.6. Power spectral density and variance preserving spectra of time-series for near-surface temperature (T) and salinity (S): a) T (3m) at mooring A, b) T (2m) at mooring B, c) S (3m) at mooring A, and d) S (2m) at mooring B. All spectra are calculated using 256 Fourier coefficients and Kaiser-Bessel windows with 50% overlap. Zero padding is used to limit end effects and to obtain series lengths at 2^n values. Confidence limits are shown for the 95% level.

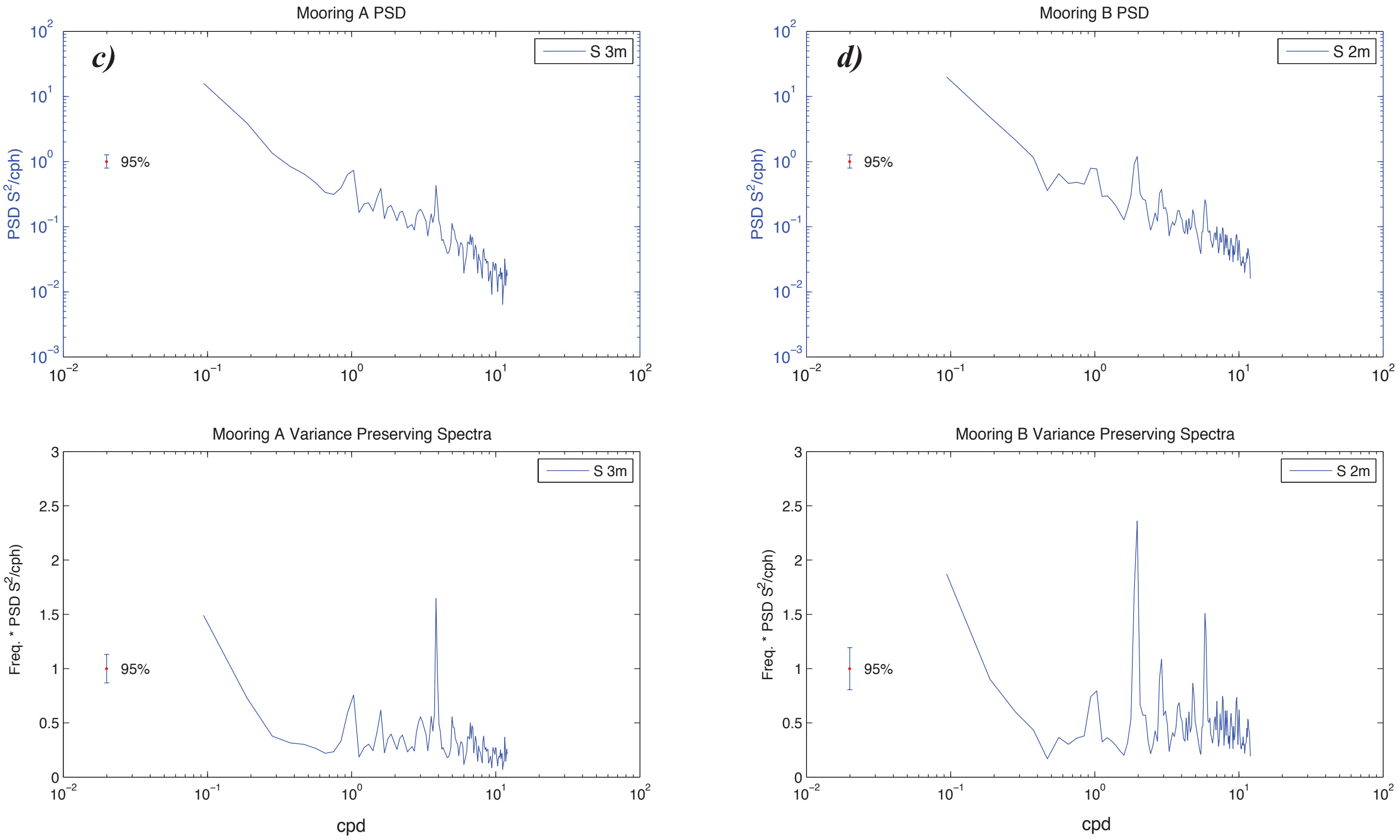
Mooring A PSD
c)
S 3m
95%
PSD S^2/cph)
10^2
10^1
10^0
10^{-1}
10^{-2}
10^{-3}
10^{-2}
10^{-1}
10^0
10^1
10^2
Mooring B PSD
d)
S 2m
95%
PSD S^2/cph)
Mooring A Variance Preserving Spectra
S 3m
95%
Freq. * PSD S^2/cph)
3
2.5
2
1.5
1
0.5
0
cpd
Mooring B Variance Preserving Spectra
S 2m
95%
Freq. * PSD S^2/cph)
cpd

Fig. 4.6 (cont).

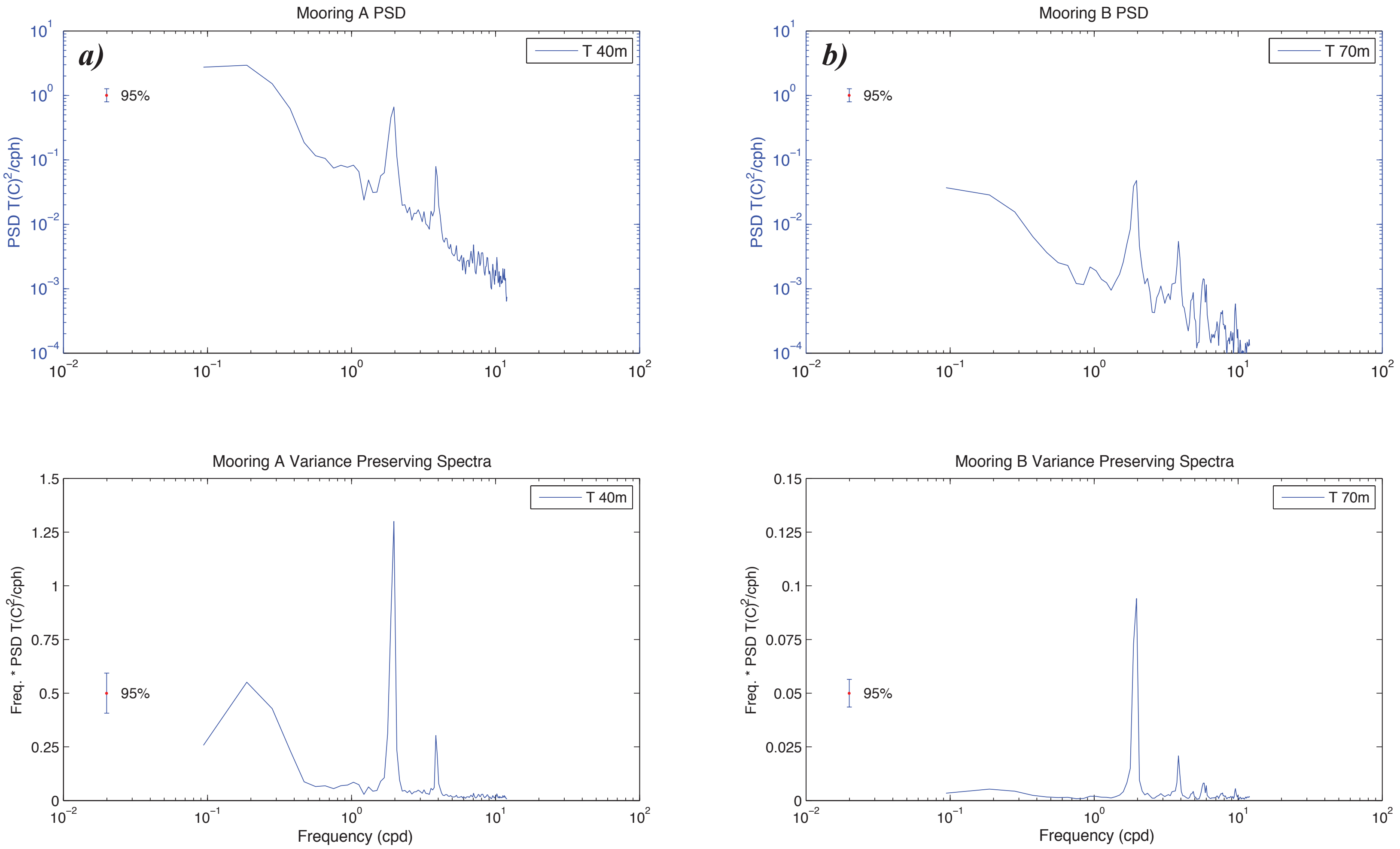

Fig. 4.7. Power spectral density and variance preserving spectra of deep temperature (T) and salinity (S): a) T (40m) at mooring A; and b) T (70m) at mooring B; c) S (40m) at mooring A; and d) S (70m) at mooring B. All spectra are calculated using 256 Fourier coefficients and Kaiser-Bessel windows with 50% overlap. Zero padding is used to limit end effects and obtain series lengths at 2^n values. Confidence limits are shown for the 95% level.

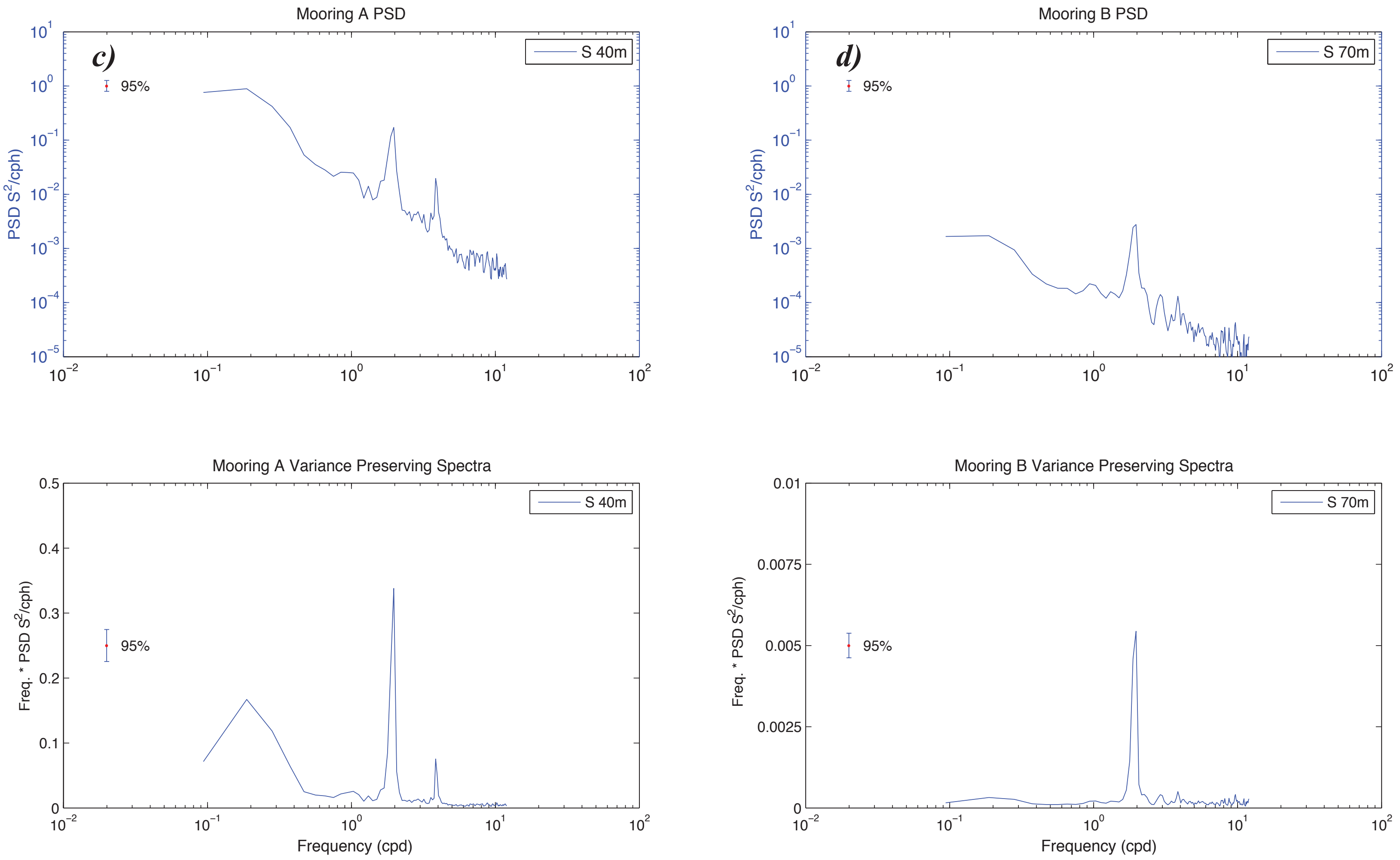
Mooring A PSD
c)
S 40m
95%
PSD S^2/cph)
10^1
10^0
10^{-1}
10^{-2}
10^{-3}
10^{-4}
10^{-5}
10^{-2}
10^{-1}
10^0
10^1
10^2
Mooring B PSD
d)
S 70m
95%
PSD S^2/cph)
Mooring A Variance Preserving Spectra
S 40m
95%
Freq. * PSD S^2/cph)
0.5
0.4
0.3
0.2
0.1
0
Frequency (cpd)
Mooring B Variance Preserving Spectra
S 70m
95%
Freq. * PSD S^2/cph)
0.01
0.0075
0.005
0.0025
0
Frequency (cpd)

Fig. 4.7 (cont).

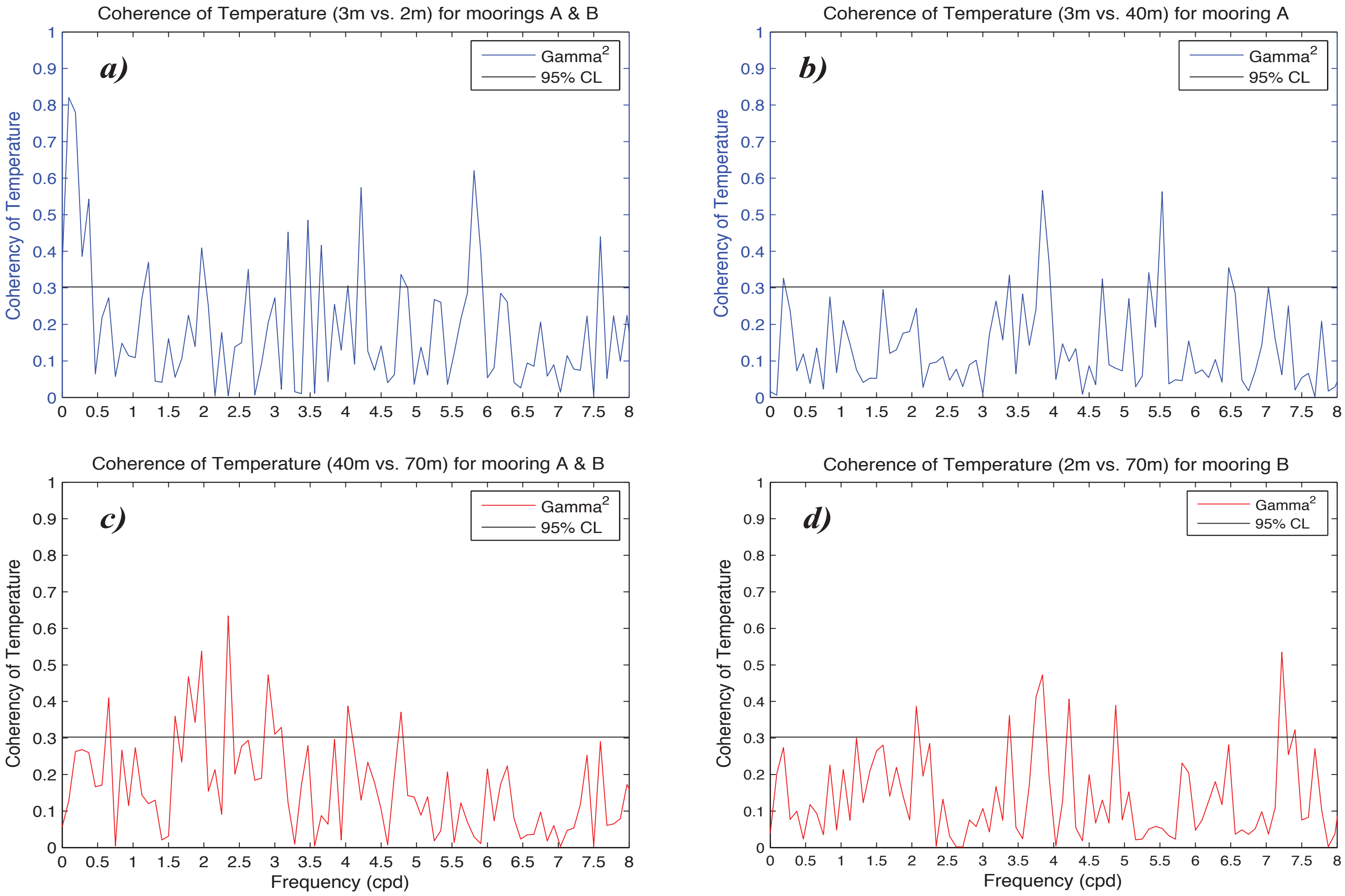

Fig. 4.8A. Coherence spectra of temperature: a) near-surface (3m vs. 2m) at moorings A and B; b) near-surface (3m) vs. subsurface (40m) at mooring A; c) subsurface (40m vs. 70m) at moorings A and B; and d) near-surface (2m) vs. subsurface (70m) at mooring B. All cross-spectra are calculated using 256 Fourier coefficients and Hamming windows with 50% overlap. Zero padding is used to limit end effects and to obtain series lengths at 2^n values. Confidence limits are shown for the 95% level.

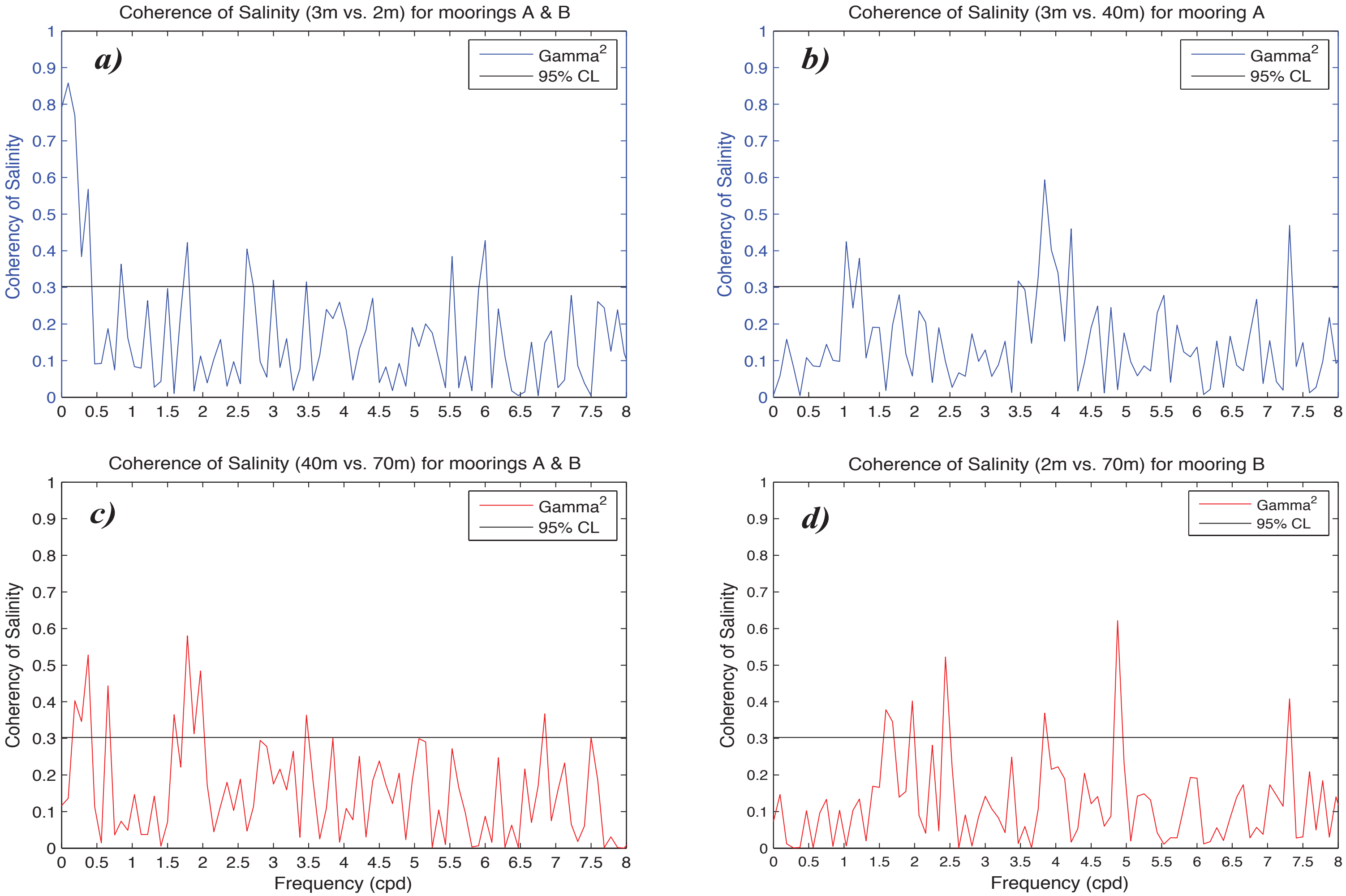

Fig. 4.8B. Coherence spectra of salinity: a) near-surface (3m vs. 2m) at moorings A and B; b) near-surface (3m) vs. subsurface (40m) at mooring A; c) subsurface (40m vs. 70m) at moorings A and B;and d) near-surface (2m) vs. subsurface (70m) at mooring B. All cross-spectra are calculated using 256 Fourier coefficients and Hamming windows with 50% overlap. Zero padding is used to limit end effects and to obtain series lengths at 2^n values. Confidence limits are shown for the 95% level.

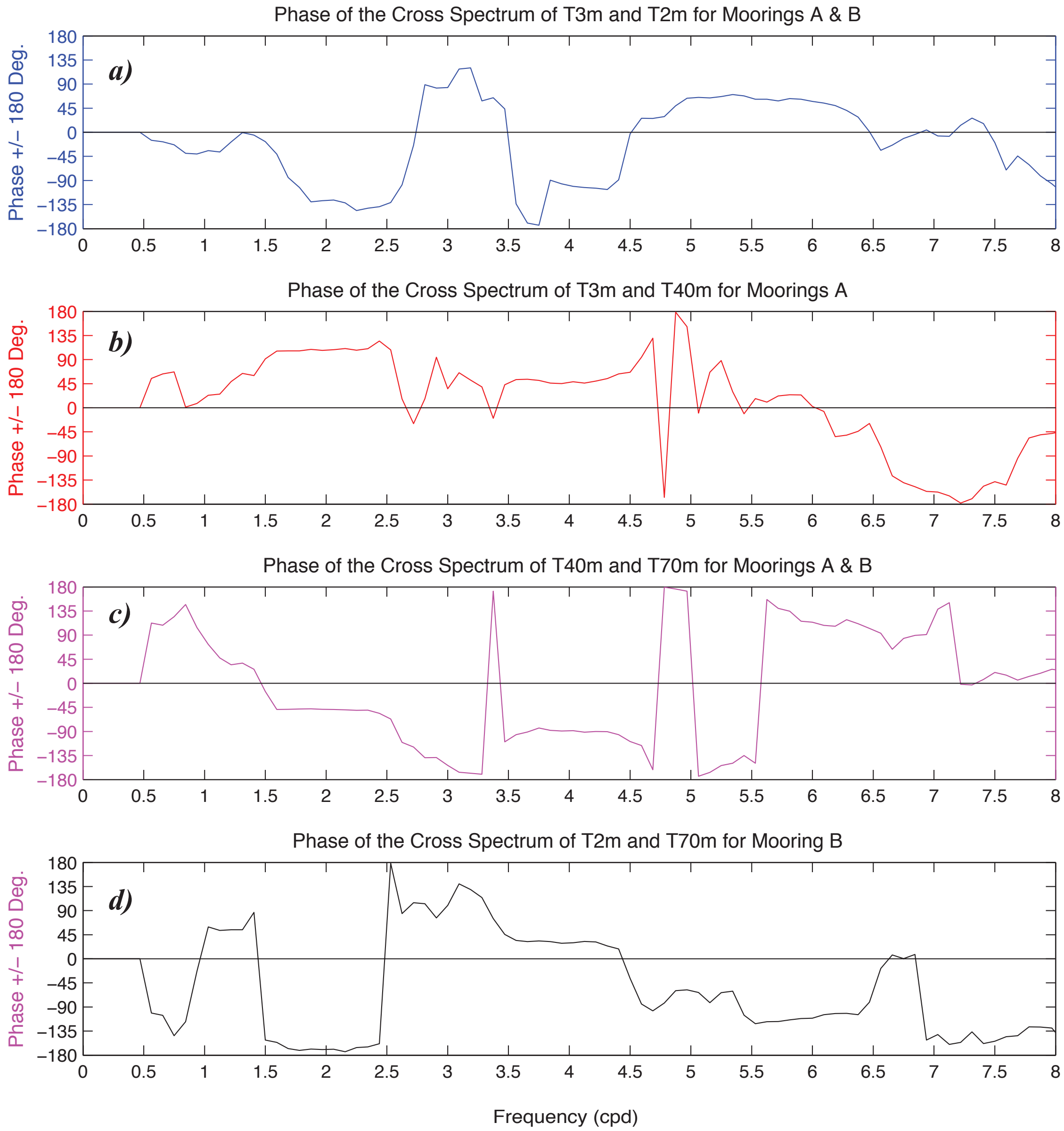

Fig. 4.9A. Phase of the coherence spectra of temperature: a) near-surface depths (3 vs. 2m) at moorings A and B; b) near-surface (3m) vs. subsurface (40m) depths at mooring A; c) deep water (40 vs. 70m) at moorings A & B; and d) near-surface (2m) vs. deep water (70m) at mooring B.

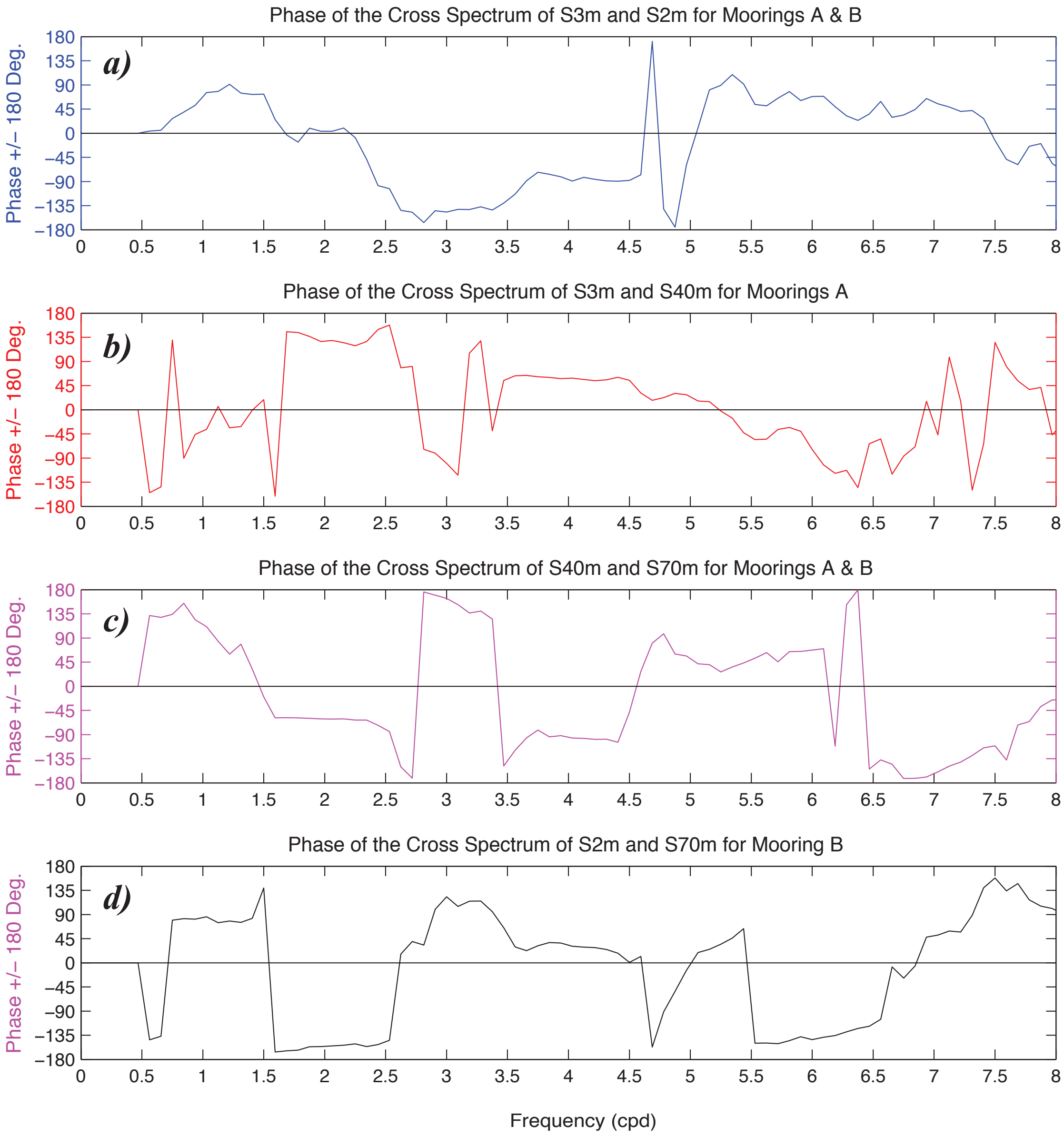

Fig. 4.9B. Phase of the coherence spectra of salinity: a) near-surface depths (3 vs. 2m) at moorings A and B; b) near-surface (3m) vs. subsurface (40m) depths at mooring A; c) deep water (40 vs. 70m) at moorings A & B; and d) near-surface (2m) vs. deep water (70m) at mooring B.

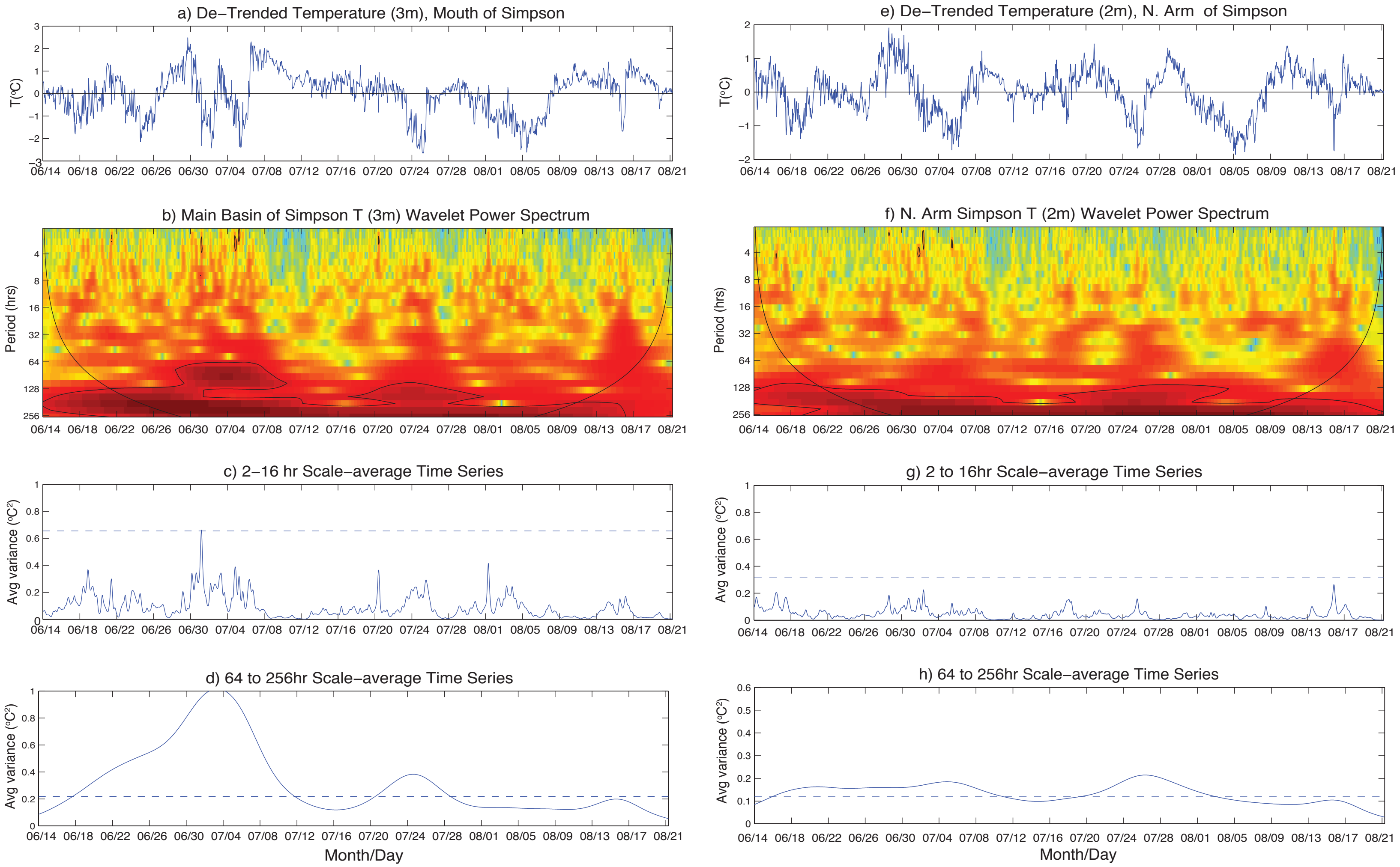

Fig. 4.10. Wavelet analysis of de-meaned and de-trended near-surface (3-2m) temperatures at mooring A (a-d) and mooring B (e-h). The wavelet power spectra in panels b and f are for all periods ranging from 2 to 256hr, whereas the scale averages are the average variances for the ranges given in the titles. Note the smaller significance levels for the low frequencies in comparison to the high frequencies.

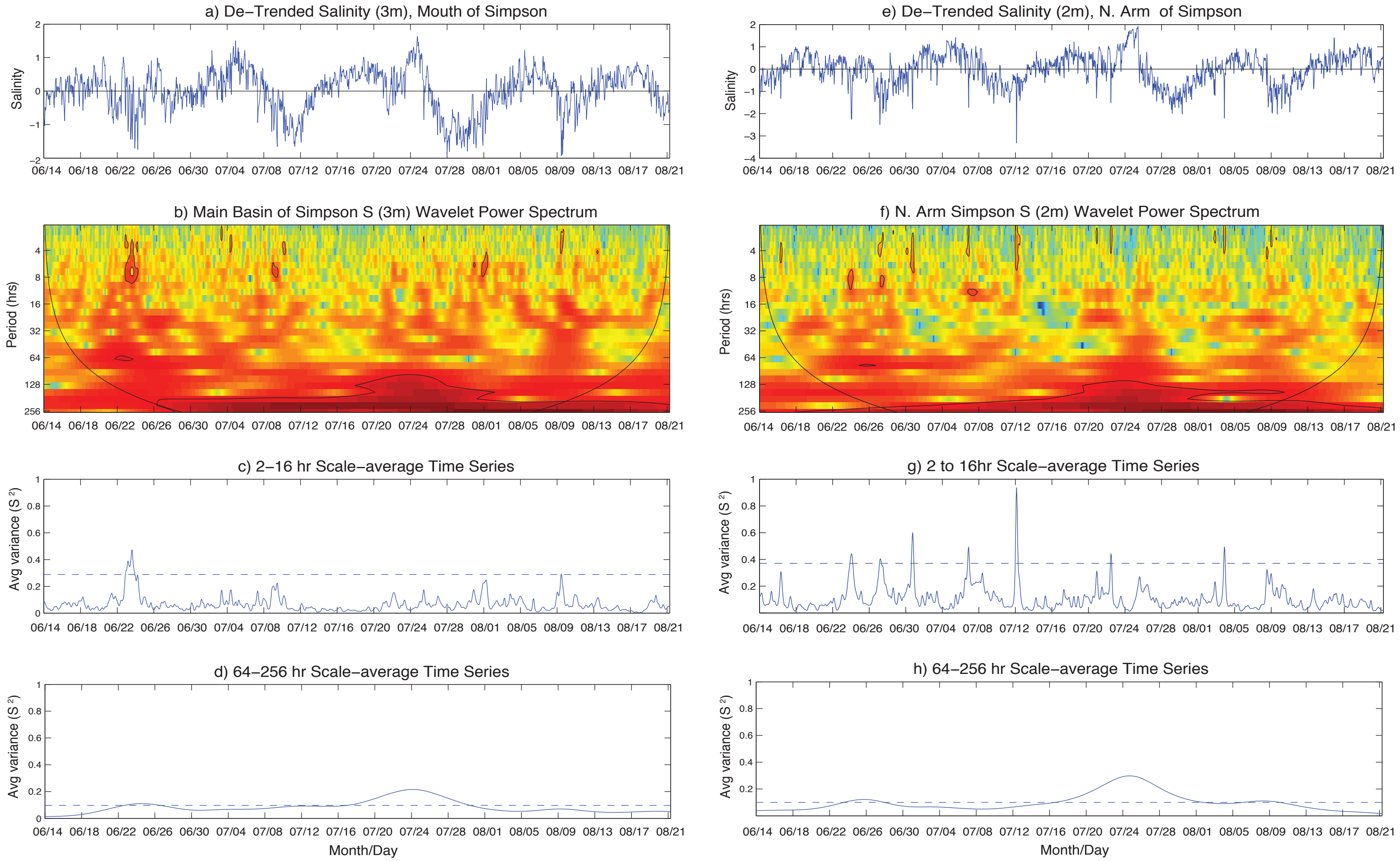

Fig. 4.11. Wavelet analysis of de-meaned and de-trended near-surface salinity at mooring A (a-d) and mooring B (e-h). The wavelet power spectra in panels b and f are for all periods ranging from 2 to 256hr, whereas the scale averages are the average variances for the ranges given in the titles. Note the smaller significance levels for the low frequencies in comparison to the high frequencies.

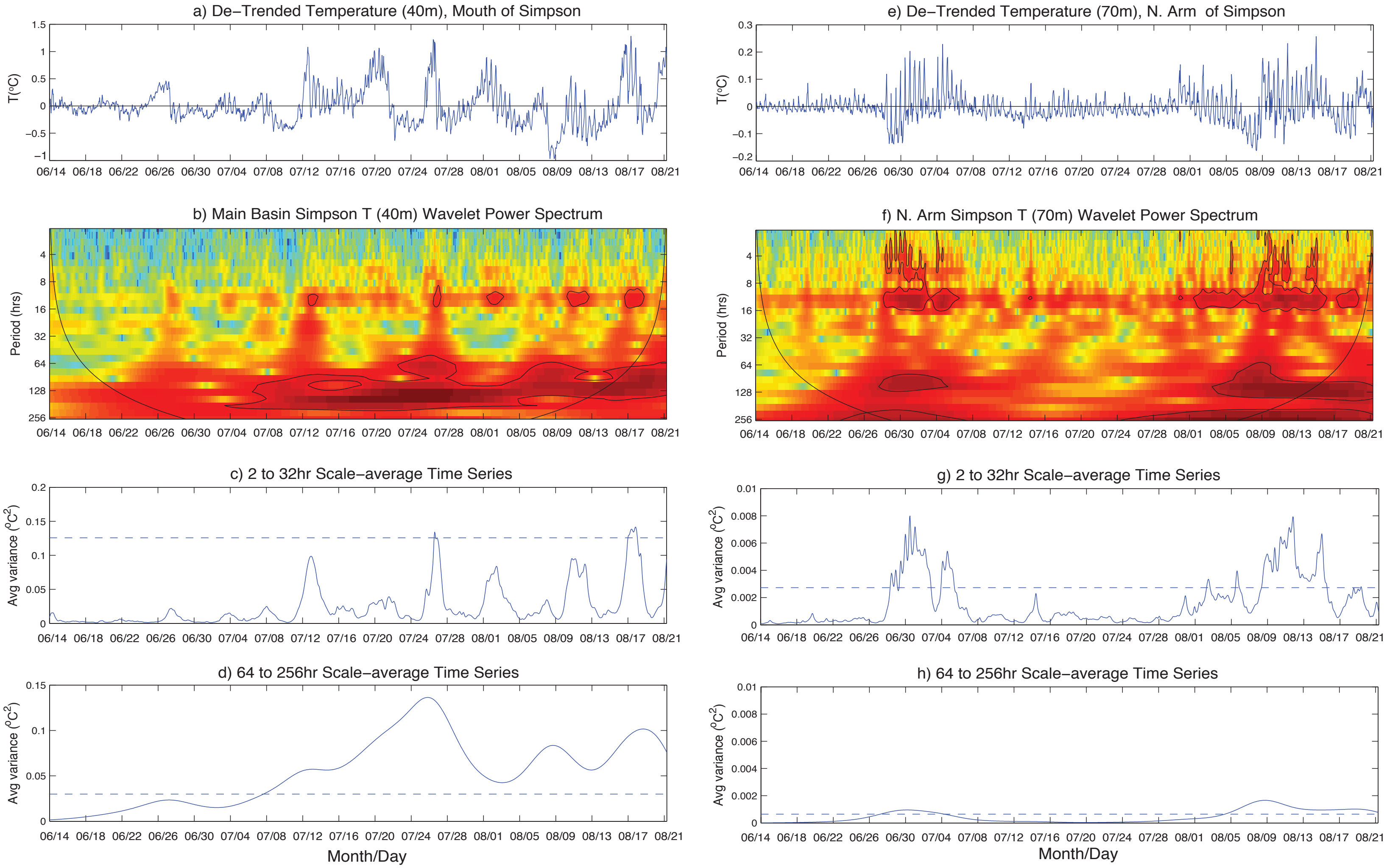
a) De–Trended Temperature (40m), Mouth of Simpson

e) De–Trended Temperature (70m), N. Arm of Simpson

b) Main Basin Simpson T (40m) Wavelet Power Spectrum

f) N. Arm Simpson T (70m) Wavelet Power Spectrum

c) 2 to 32hr Scale–average Time Series

g) 2 to 32hr Scale–average Time Series

d) 64 to 256hr Scale–average Time Series

h) 64 to 256hr Scale–average Time Series

Fig. 4.12. Wavelet analysis of de-meaned and de-trended deep temperatures at mooring A (a-d) and mooring B (e-h). The wavelet power spectra in panels b and f are for all periods ranging from 2 to 256hr, whereas the scale averages are the average variances for the ranges given in the titles. Note the smaller significance levels for the low frequencies in comparison to the high frequencies.

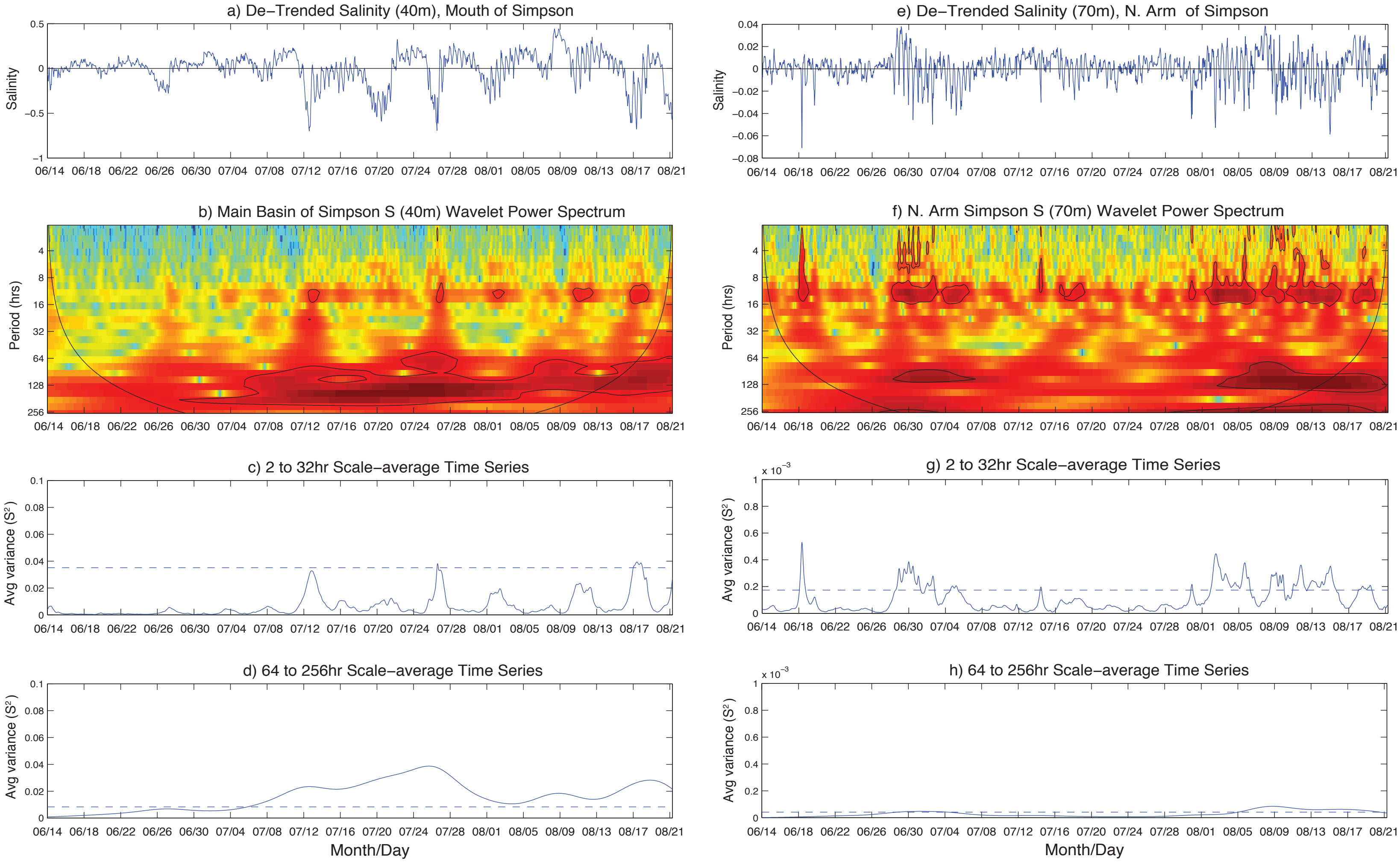

Fig. 4.13. Wavelet analysis of de-meaned and de-trended deep salinity at mooring A (a-d) and mooring B (e-h). The wavelet power spectra in panels b and f are for all periods ranging from 2 to 256hr, whereas the scale averages are the average variances for the ranges given in the titles. Note the smaller significance levels for the low frequencies in comparison to the high frequencies.

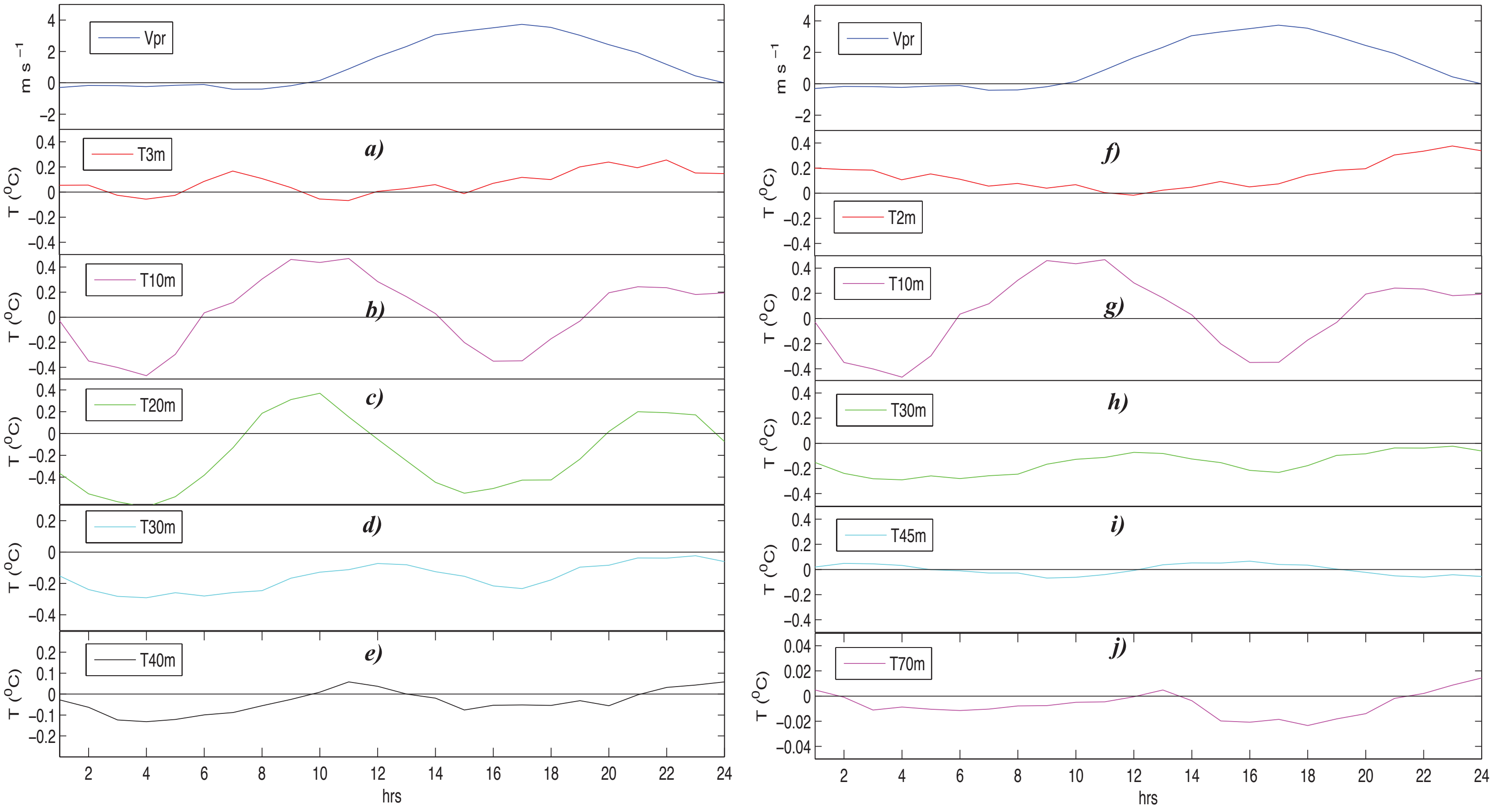

Fig. 4.14. Average diurnal variation of along-fjord winds (Vpr) in top panels and temperatures at Simpson Bay from 3 to 40m in the Main Basin (a-e) and at 2 to 70m in the Northern Arm (f-j). The plots represent averages for 22 days of diurnal winds over the period from July 14 to August 21, 2007 (Fig. 3.9).

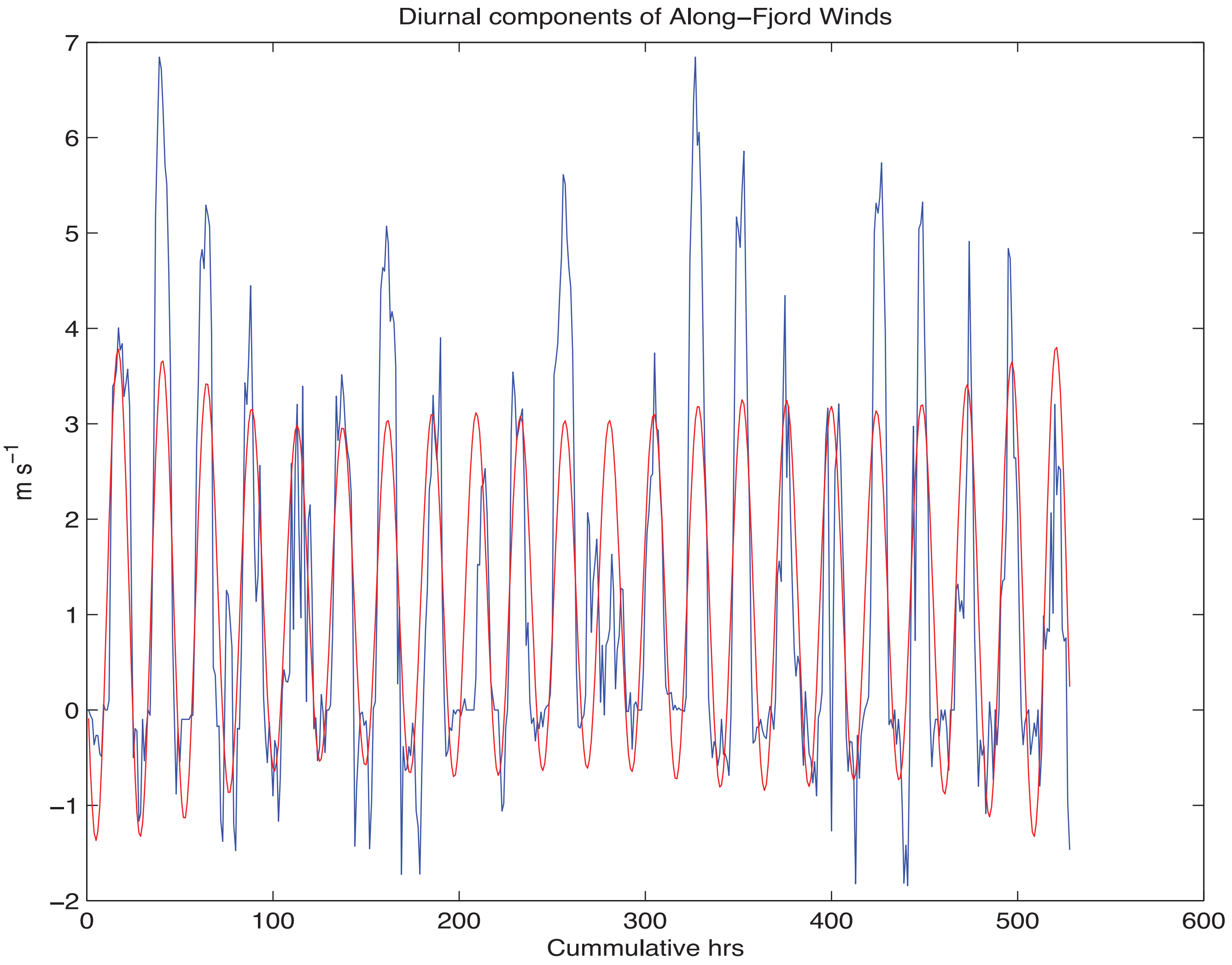

Fig. 4.15. Diurnal components of along-fjord winds during periods when winds are primarily up-fjord and large in amplitude. The plot represents 22 days of diurnal winds over the period from July 14 to August 21, 2007 (see Fig. 3.9).

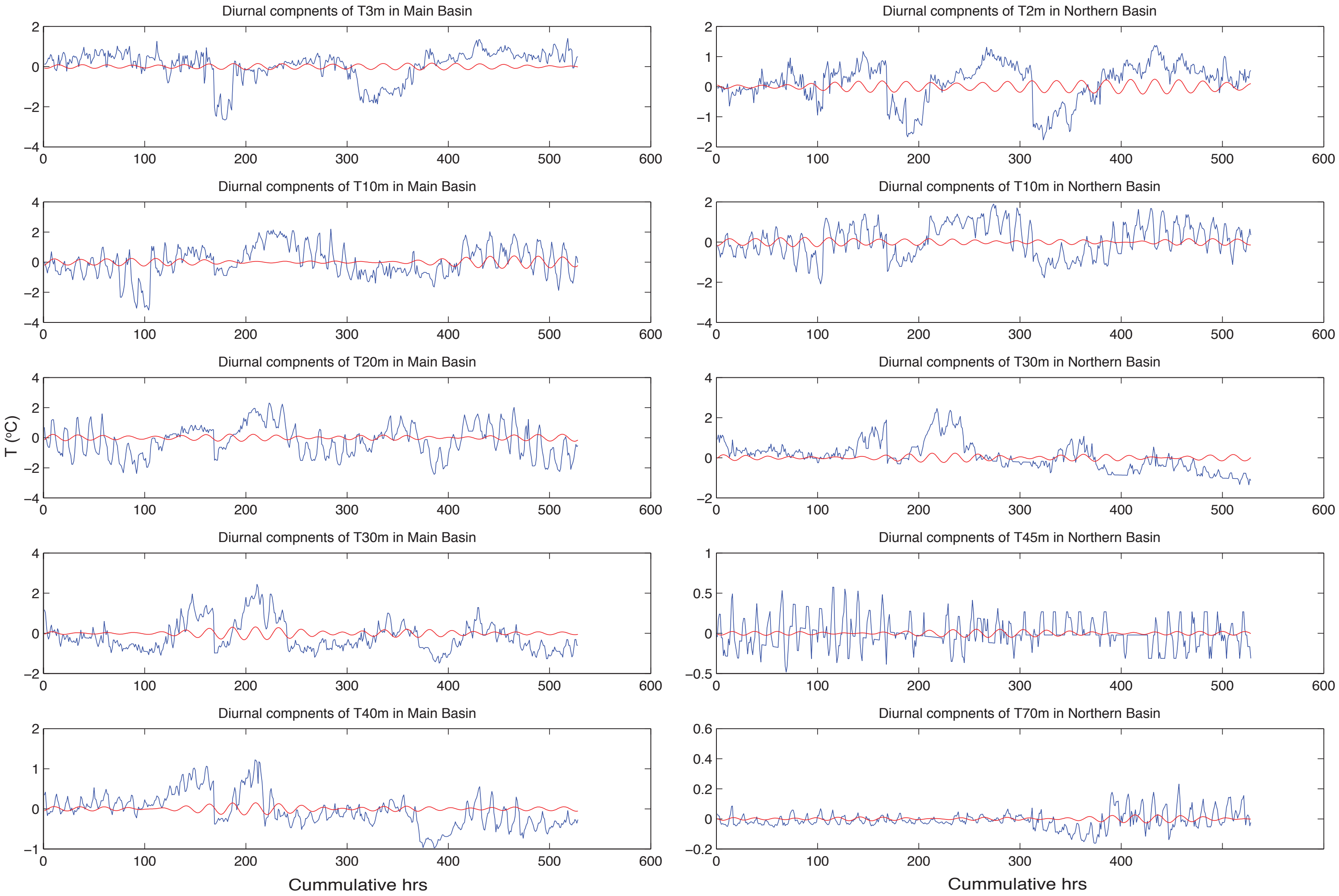

Fig. 4.16. Diurnal components of temperatures during periods when winds are primarily diurnal, up-fjord and large in amplitude. The plots represent 22 days of diurnal winds over the period from July 14 to August 21, 2007 (see Fig. 32A). Note the very small diurnal amplitudes in comparison to total variation, which typically explain only 1 to 2% of the variances described in the text.

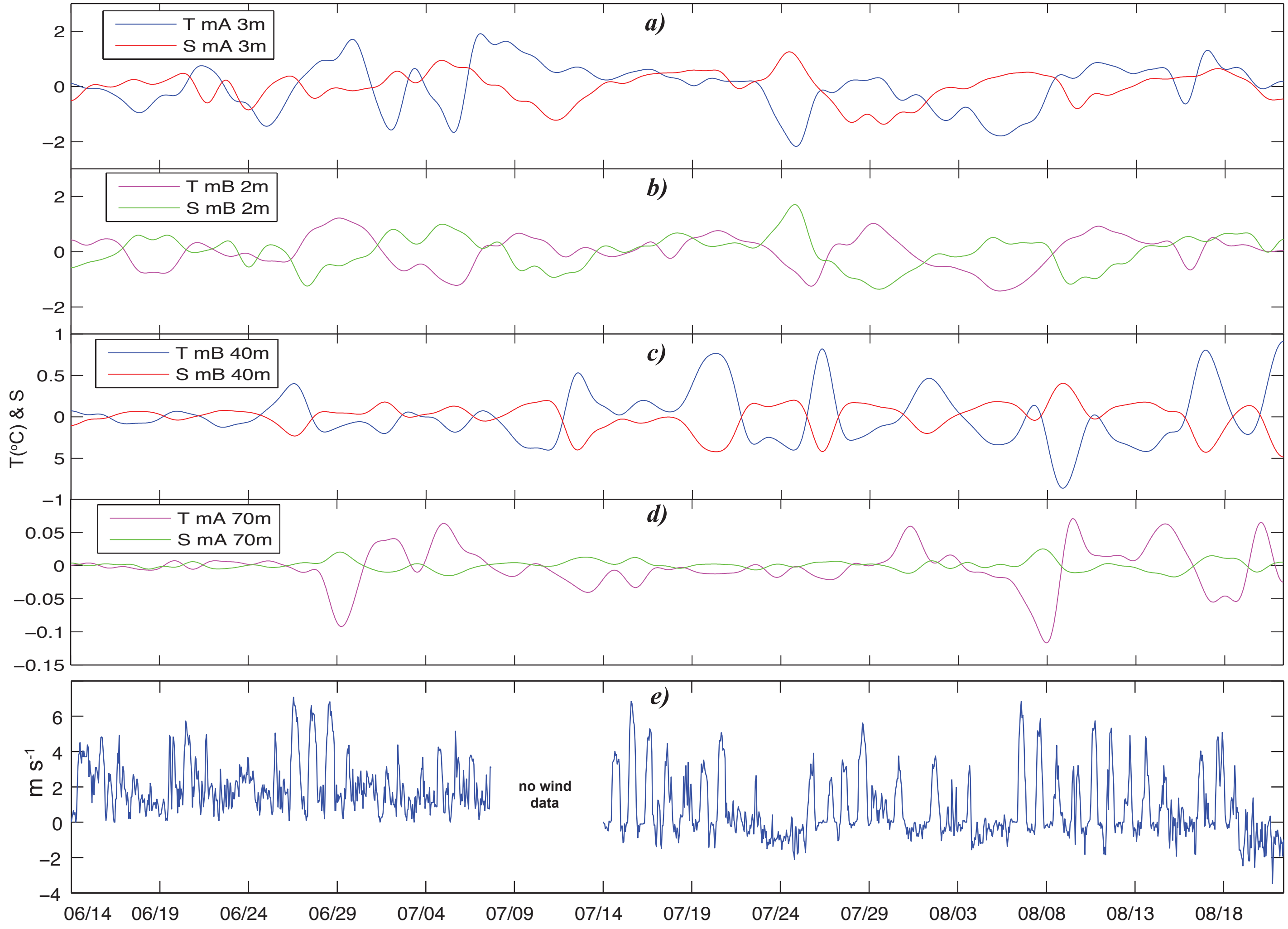

Fig. 4.17. Low-pass filtered temperatures and salinities at at moorings A and B: a) 3m, b) 2m, c) 40m and d) 70m, and e) wind speeds in mid June to early July and along-fjord winds from July 14 to August 21, 2007.

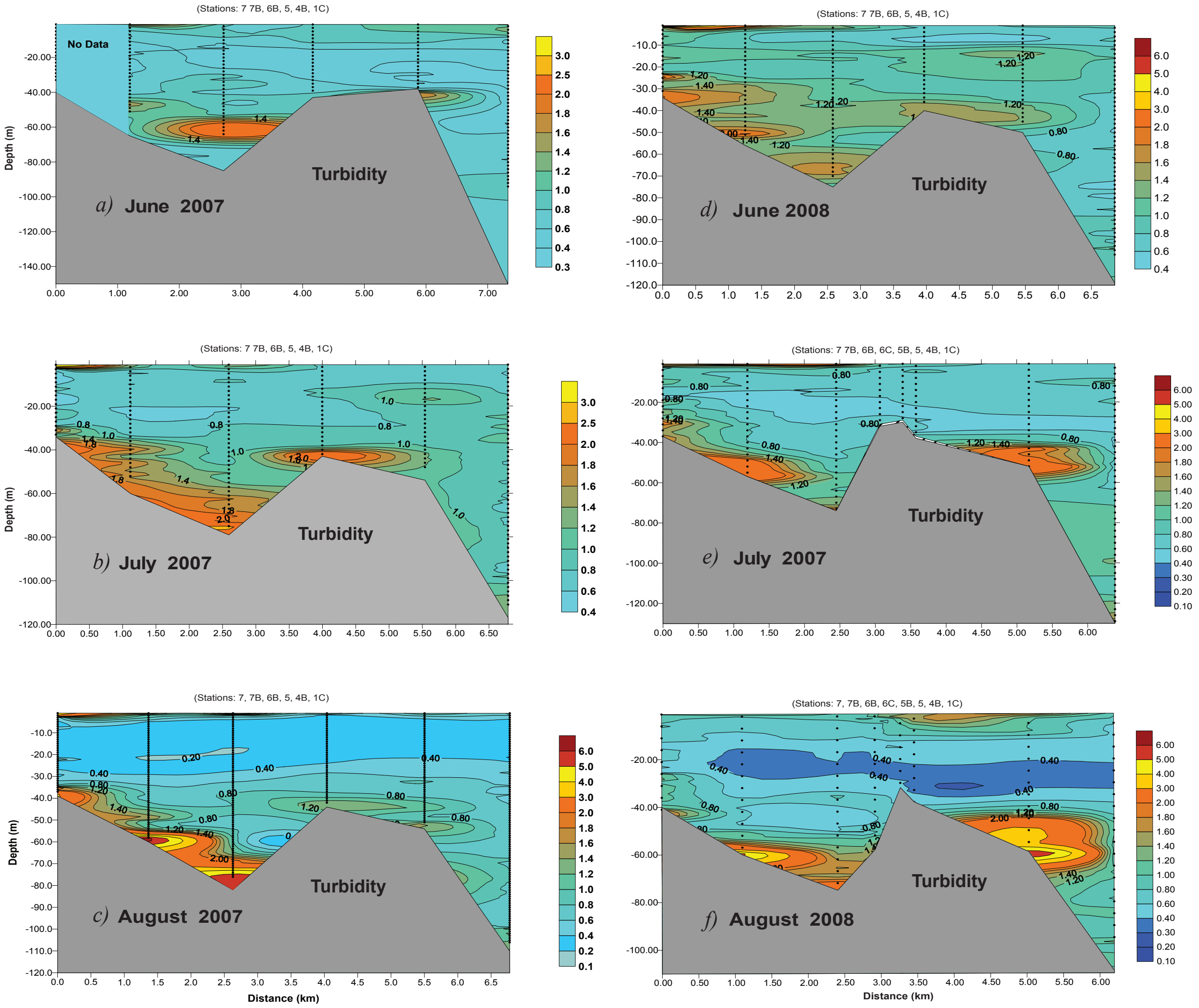

Fig. 5.1. Turbidity in the summers of 2007 (a-c) and 2008 (d-f) showing turbid surface and deep layers in both years. Note that measurement units in both years are normalized turbidity units (NTUs).

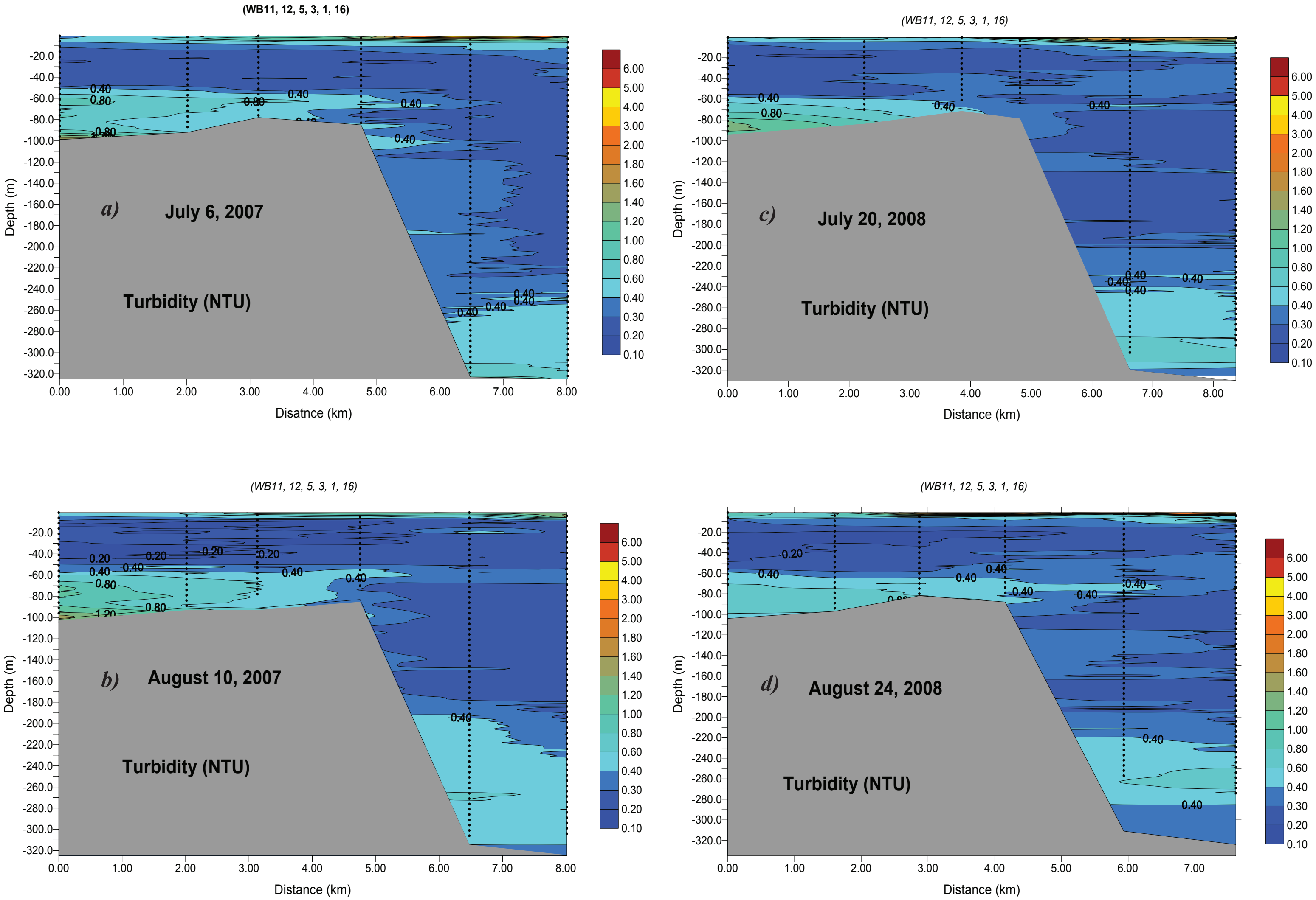

Fig. 5.2. Turbidity at Whale Bay in the summers of 2007 (a-b) and 2008 (c-d) showing turbid surface layers mostly in the outer basin in both years due to inflow of glacial water from Icy Bay.

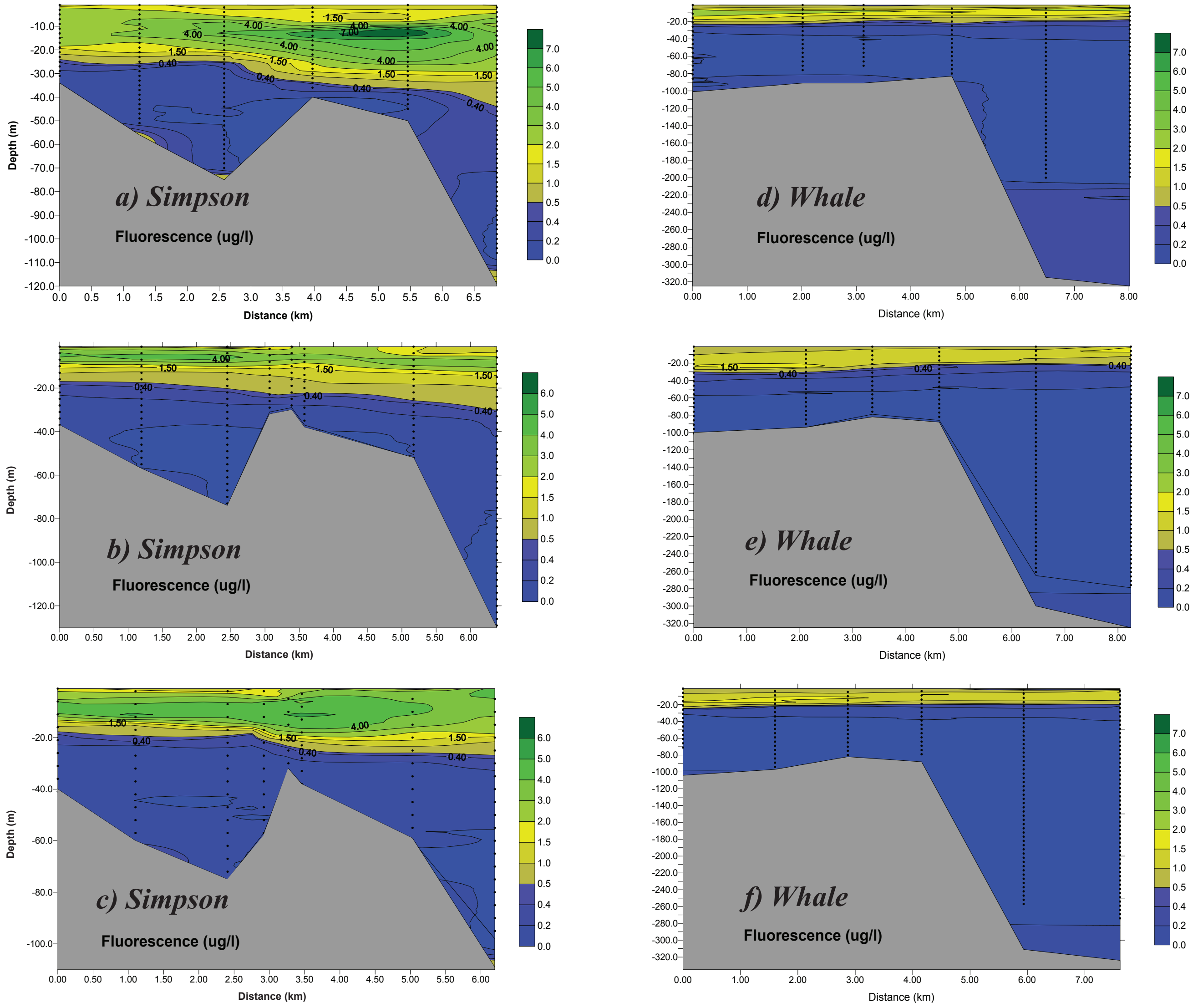

Fig. 5.3. Fluorescence measured at Simpson Bay (a-c) and Whale Bay (d-f) in the summer of 2008 showing much higher phytoplankton biomass at Simpson during a year of meteorological conditions more conducive to primary production.

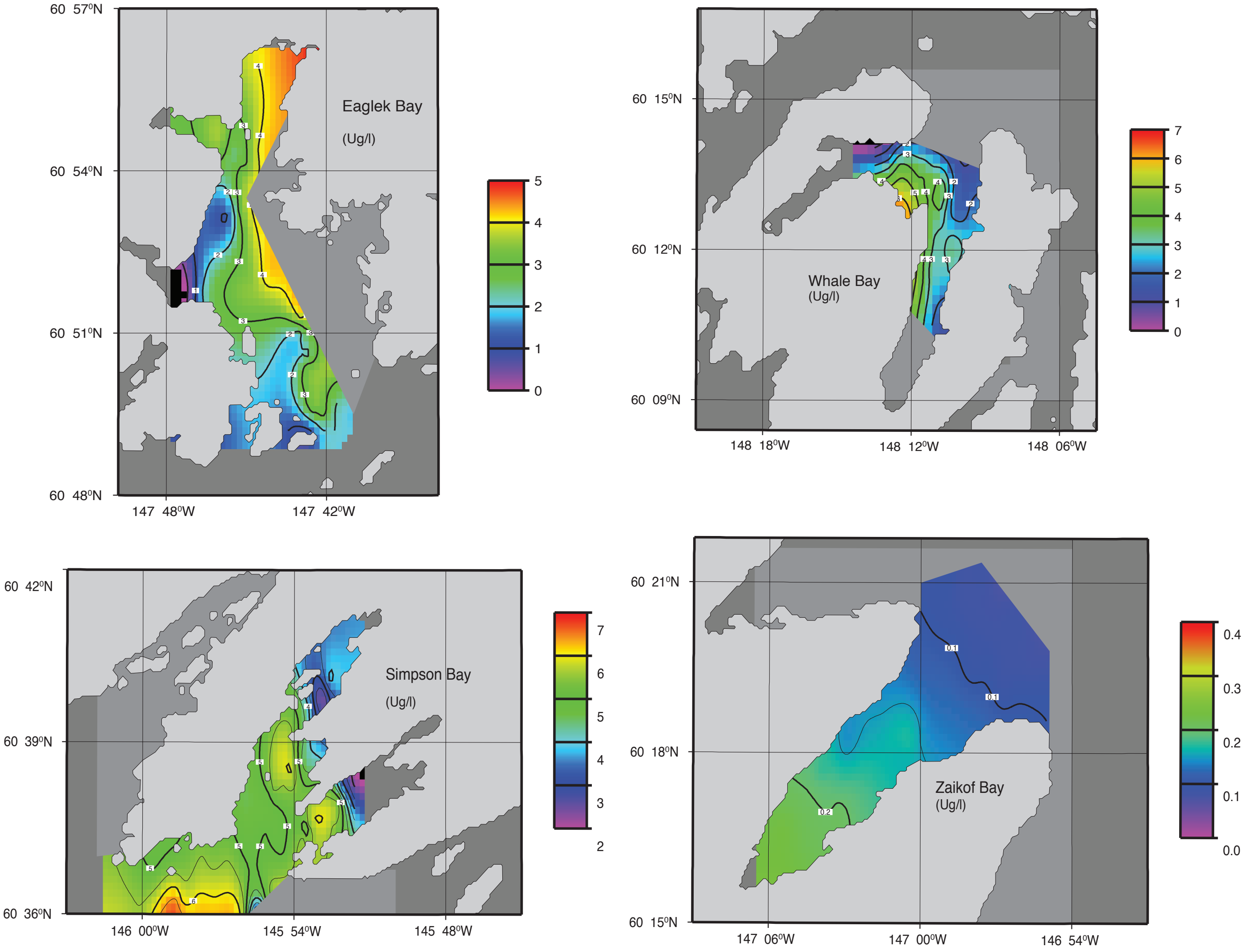

Fig. 5.4. Horizontal contours of average fluorescence from 5 to 10*m* in the four SEA fjords in March 1996.

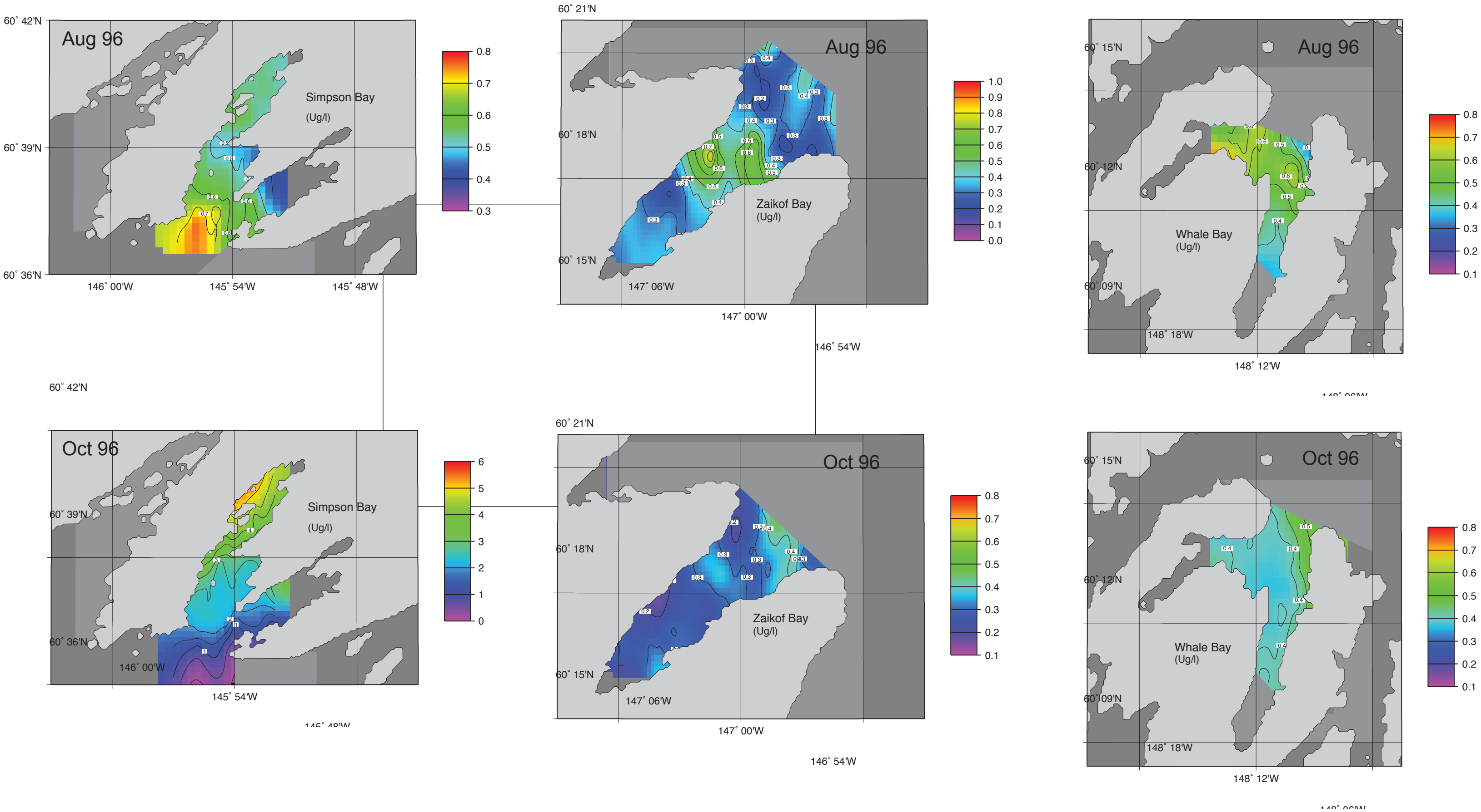

Fig. 5.5. Horizontal contours of average fluorescence from 5 to 10*m* in the four SEA fjords in 1996 in August (top panel) and October (bottom panel).

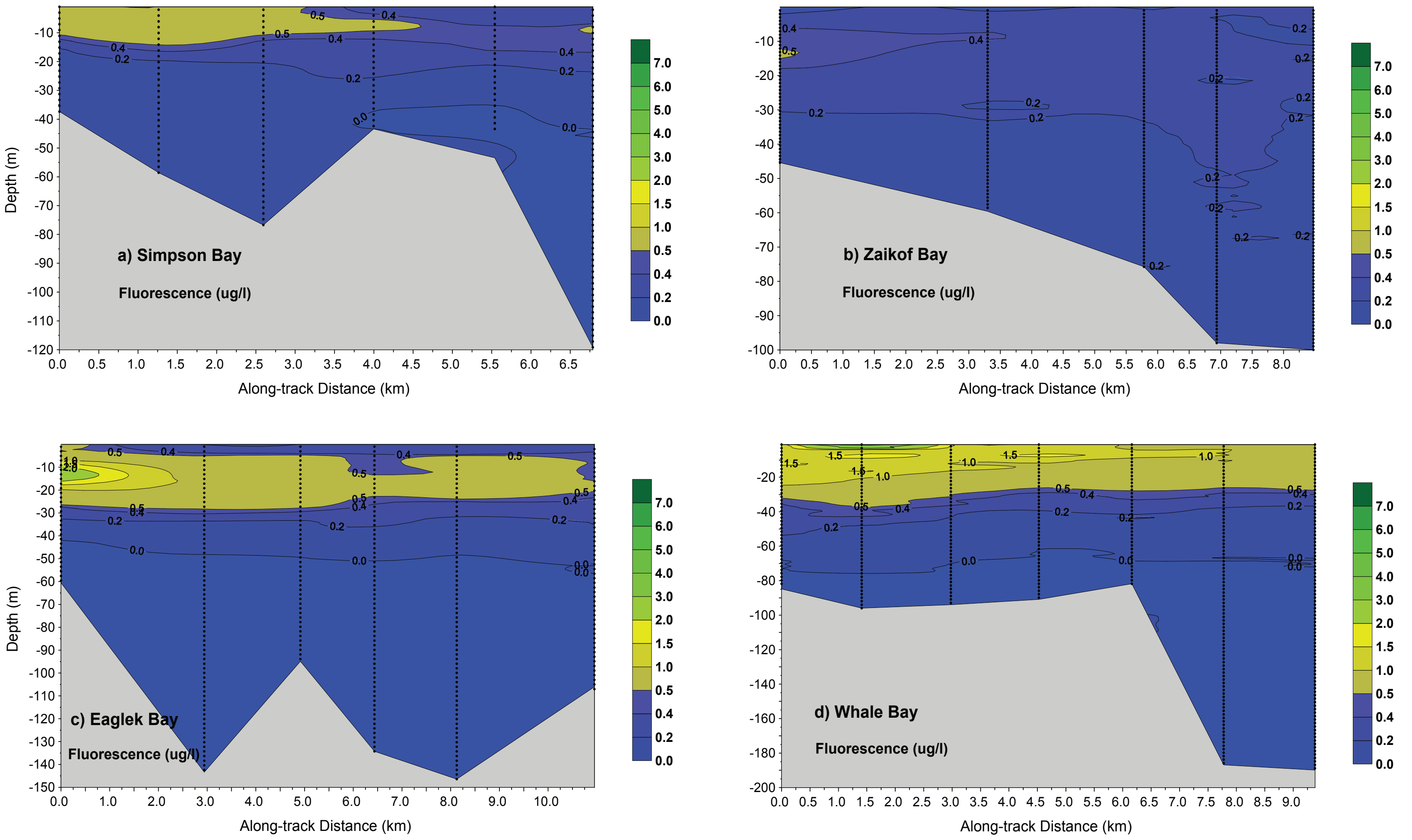

Fig. 5.6. Fluorescence measured in March 2010 at a) Simpson Bay, b) Zaikof Bay, c) Eaglek Bay, and d) Whale Bay showing examples of late winter phytoplankton blooms in recent years. Note that as in other years Zaikof has the most limited biomass.

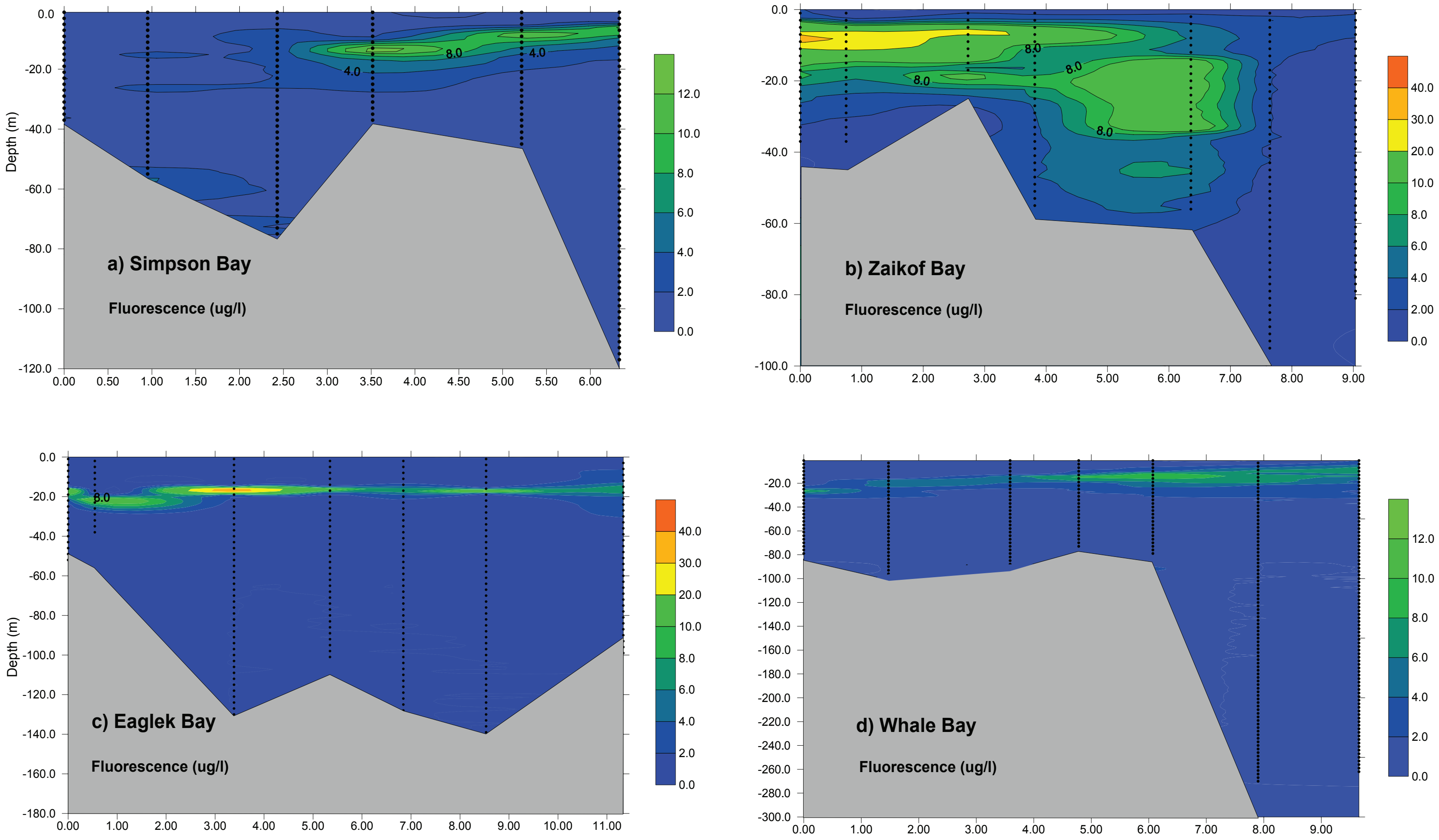

Fig. 5.7. Fluorescence measured in April 2011 at a) Simpson Bay, b) Zaikof Bay, c) Eaglek Bay, and d) Whale Bay showing an example of markedly increased spring phytoplankton blooms in recent years.

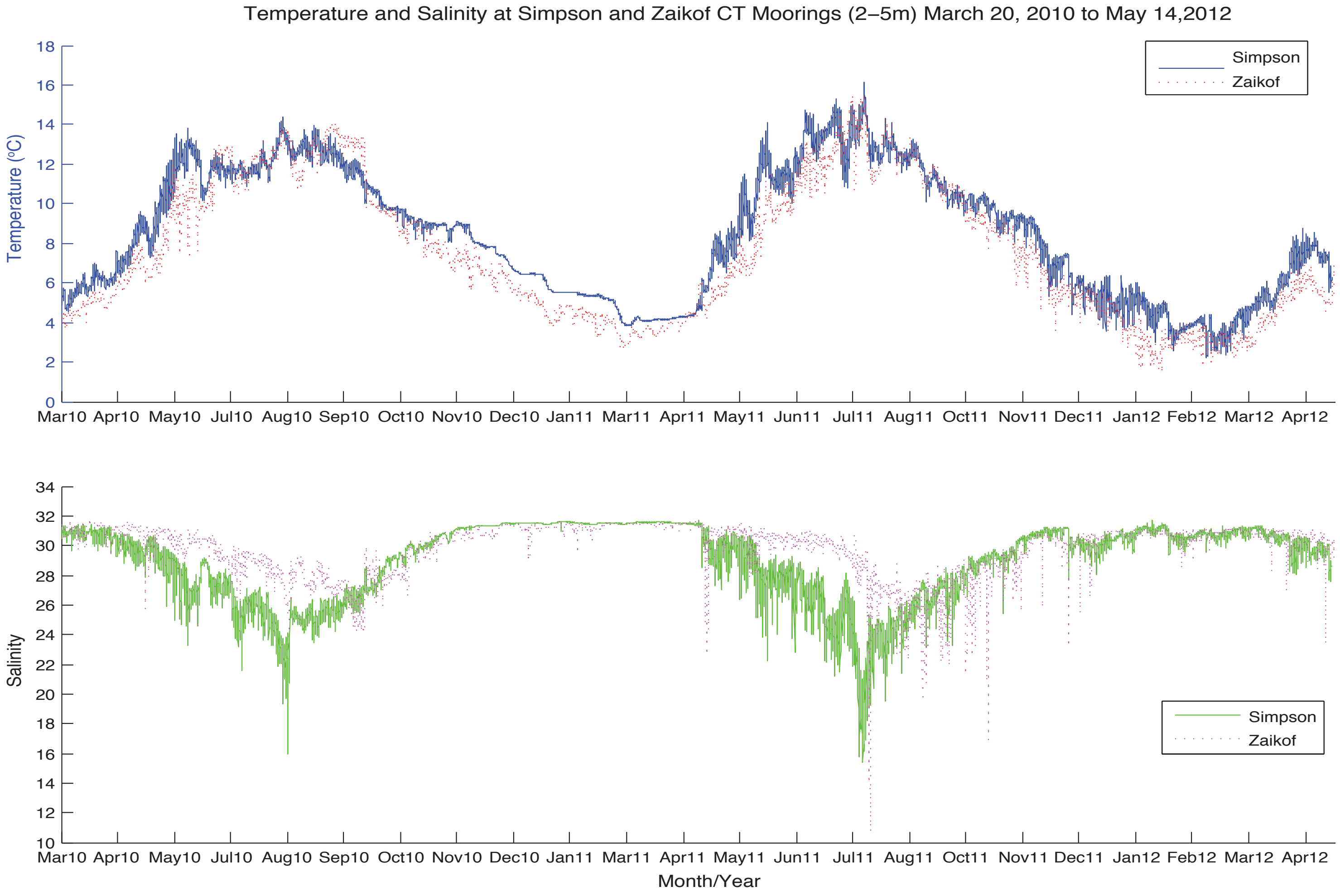

Fig. 5.8A. Temperature and salinity time series for the nearsurface (2-5m) CTs at Simpson and Zaikof. Both series extend over the full deployment period from March 2010 to May 2012, except for Simpson when the surface buoy pulled away due to sheet ice in late November 2010. From then until mid April 2011the CT depth was ~ 30m.

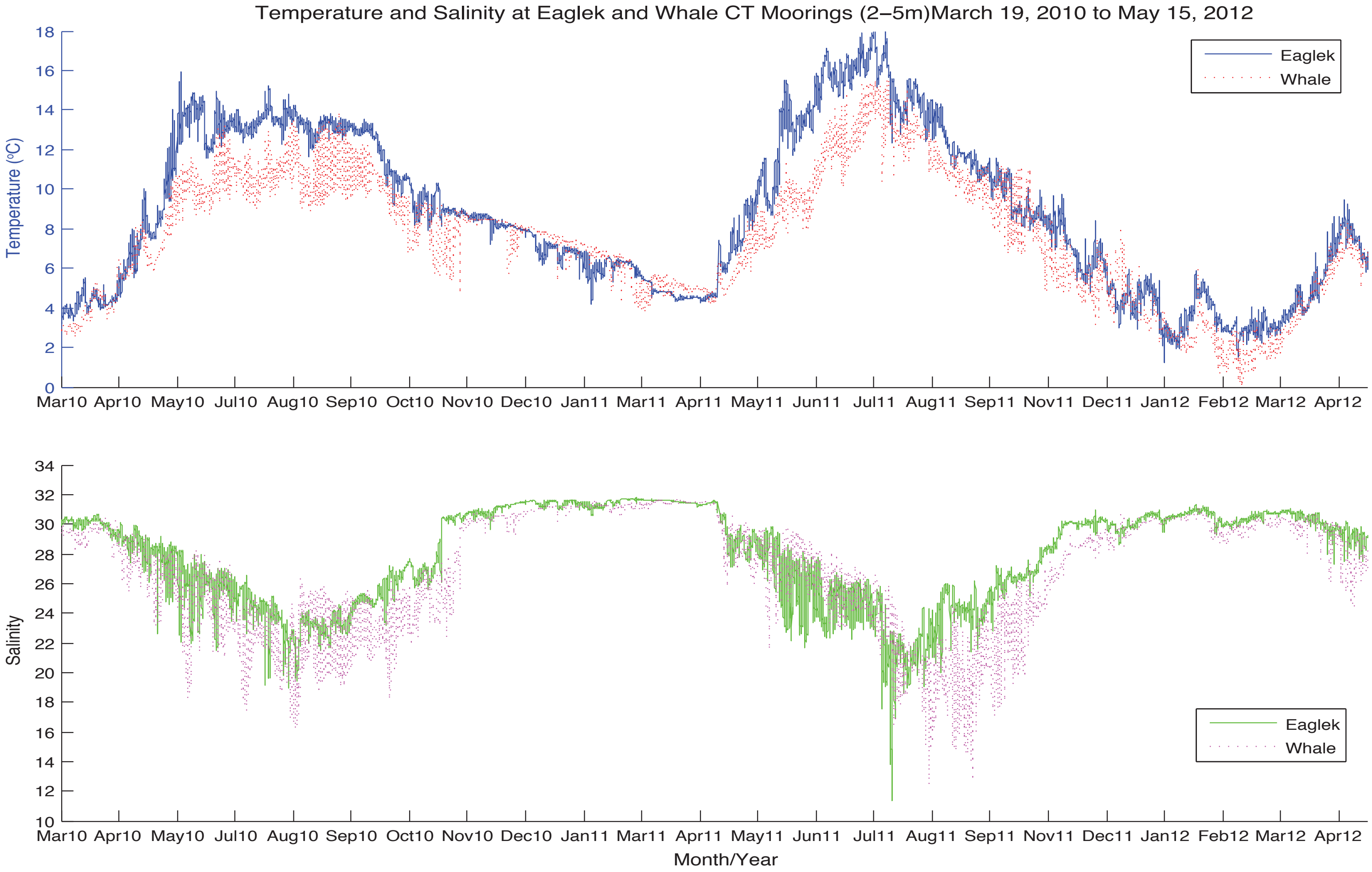

Fig.5.8B. Temperature and salinity time series for the nearsurface (2-5m) CTs at Eaglek and Whale. Both series extend over the full deployment period from March 2010 to May 2012, except for late October 2010 for Eaglek and November 2010 for Whale. From then until mid April 2011the CT depths were ~ 30m after the surface buoy pulled away due to sheet ice.

.

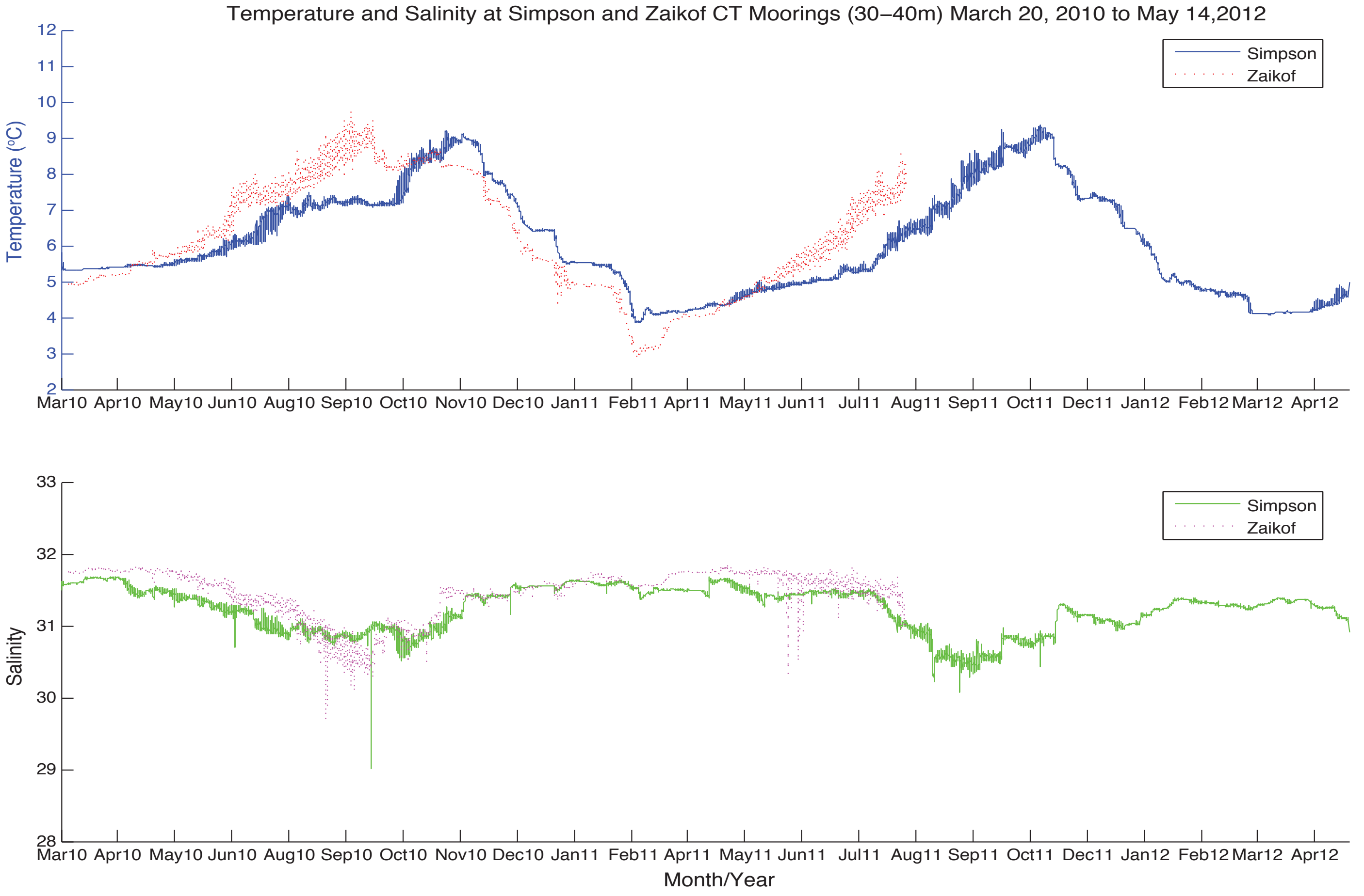

Fig. 5.8C. Temperature and salinity time series for the deep (30-50m) CTs at Simpson and Zaikof. All series, except Zaikof, extend over the full deployment period from March 2010 to May 2012. Zaiko's data were cut short due a failure in the instrument's data logger.

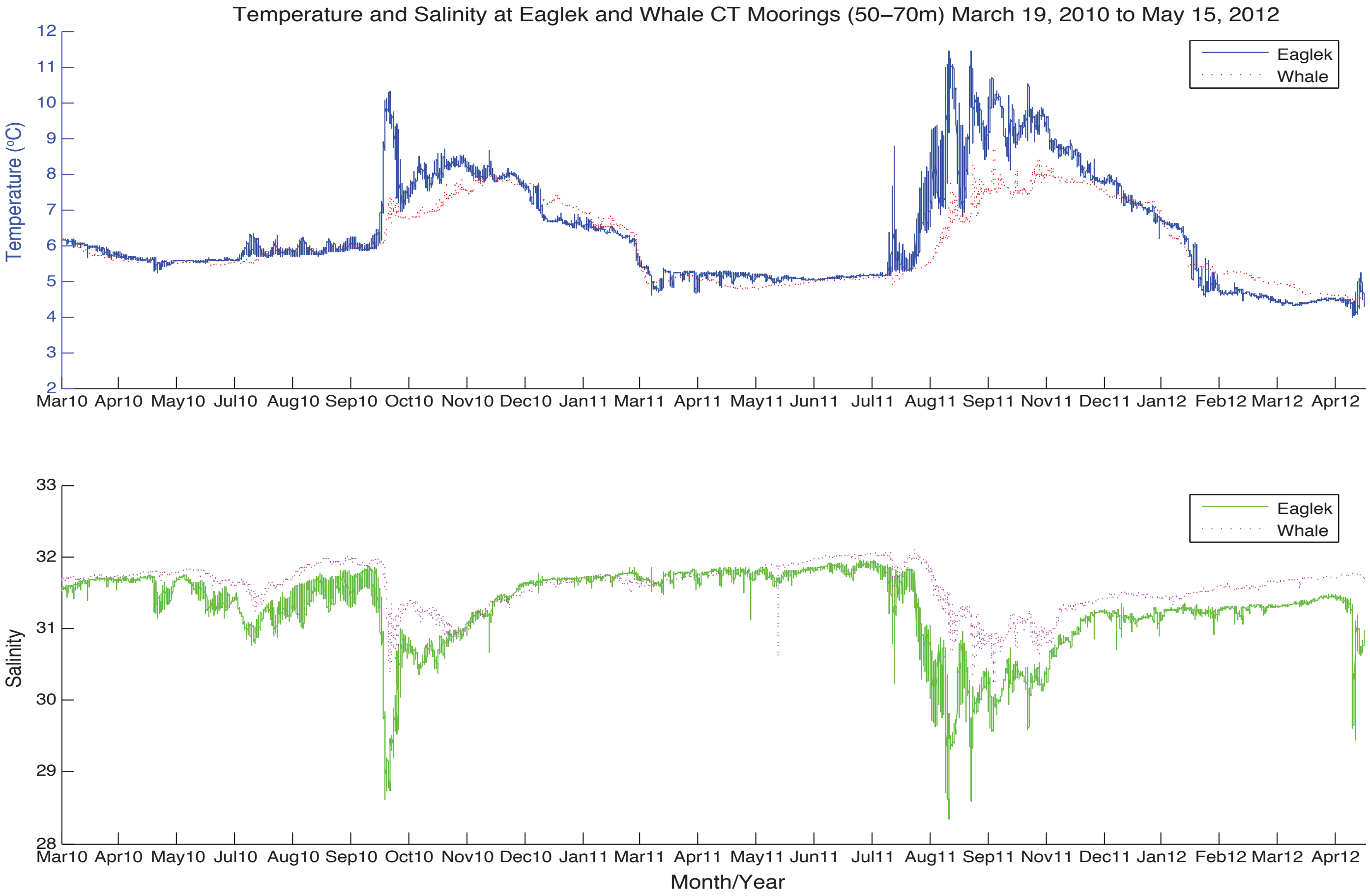

Fig. 5.8D. Temperature and salinity time series for the deep (30-50m) CTs at Eaglek and Whale. All series, extend over the full deployment period from March 2010 to May 2012.

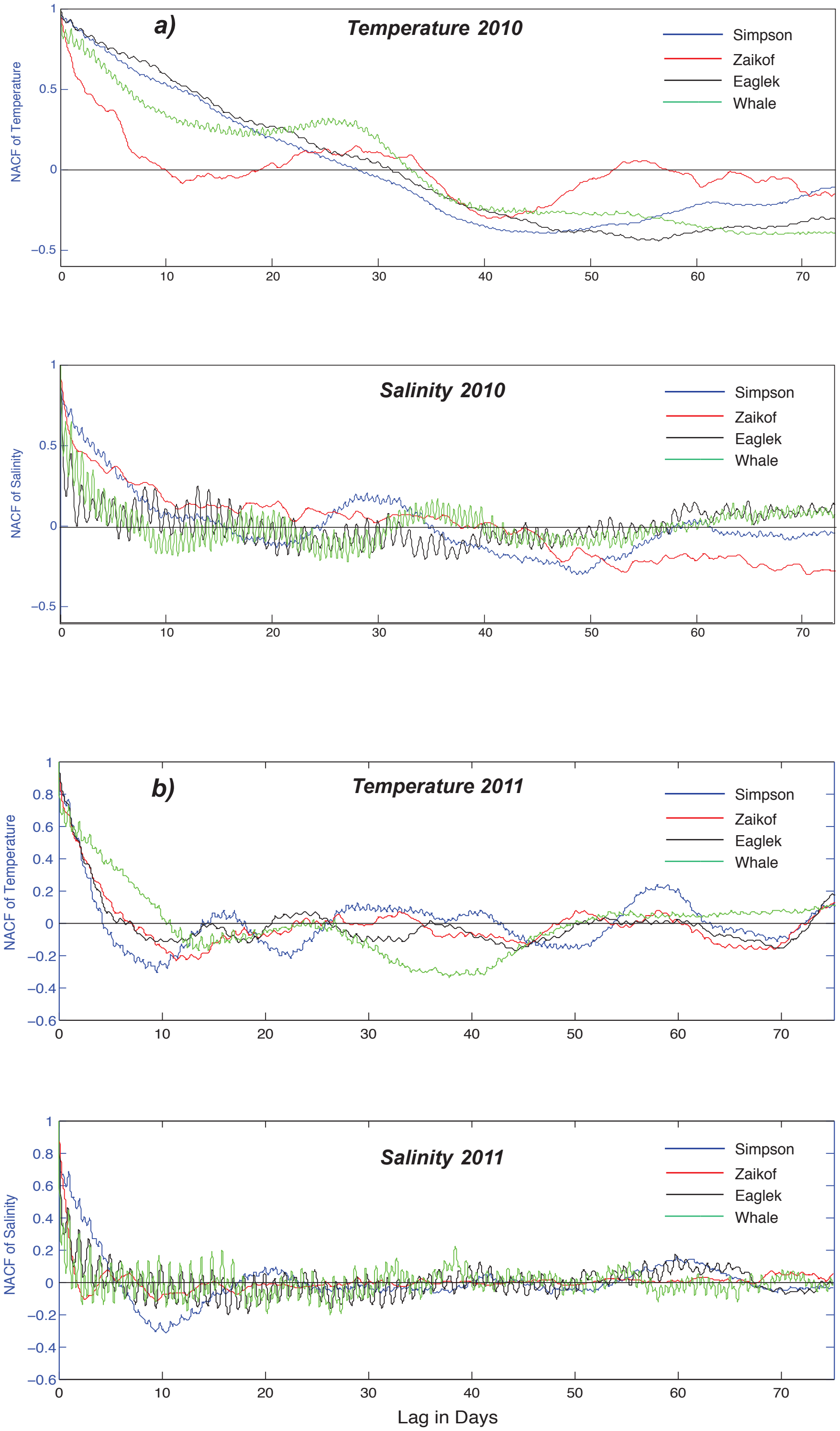

Fig. 5.9. Normalized Autocovariance Functions (NACFs) of temperature and salinity for hourly (a,b) and 40hr low-pass (c,d) data over the spring and summer of 2010 (top panels) and 2011 (bottom panels).

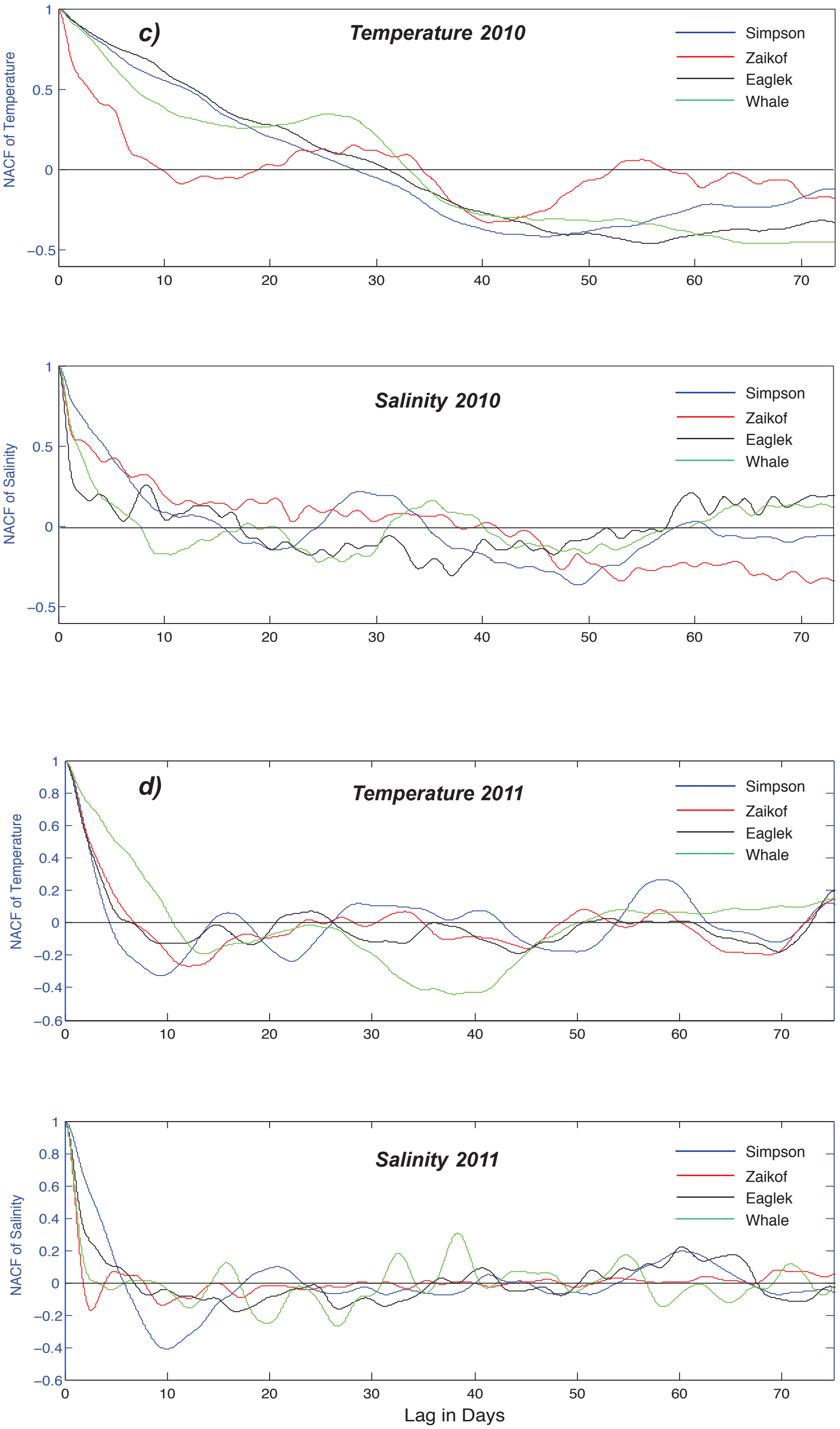
c)
Temperature 2010
Simpson
Zaikof
Eaglek
Whale
NACF of Temperature
1
0.5
0
−0.5
0
10
20
30
40
50
60
70
Salinity 2010
Simpson
Zaikof
Eaglek
Whale
NACF of Salinity
1
0.5
0
−0.5
0
10
20
30
40
50
60
70
d)
Temperature 2011
Simpson
Zaikof
Eaglek
Whale
NACF of Temperature
1
0.8
0.6
0.4
0.2
0
−0.2
−0.4
−0.6
0
10
20
30
40
50
60
70
Salinity 2011
Simpson
Zaikof
Eaglek
Whale
NACF of Salinity
1
0.8
0.6
0.4
0.2
0
−0.2
−0.4
−0.6
0
10
20
30
40
50
60
70
Lag in Days

Fig. 5.9 (cont.).

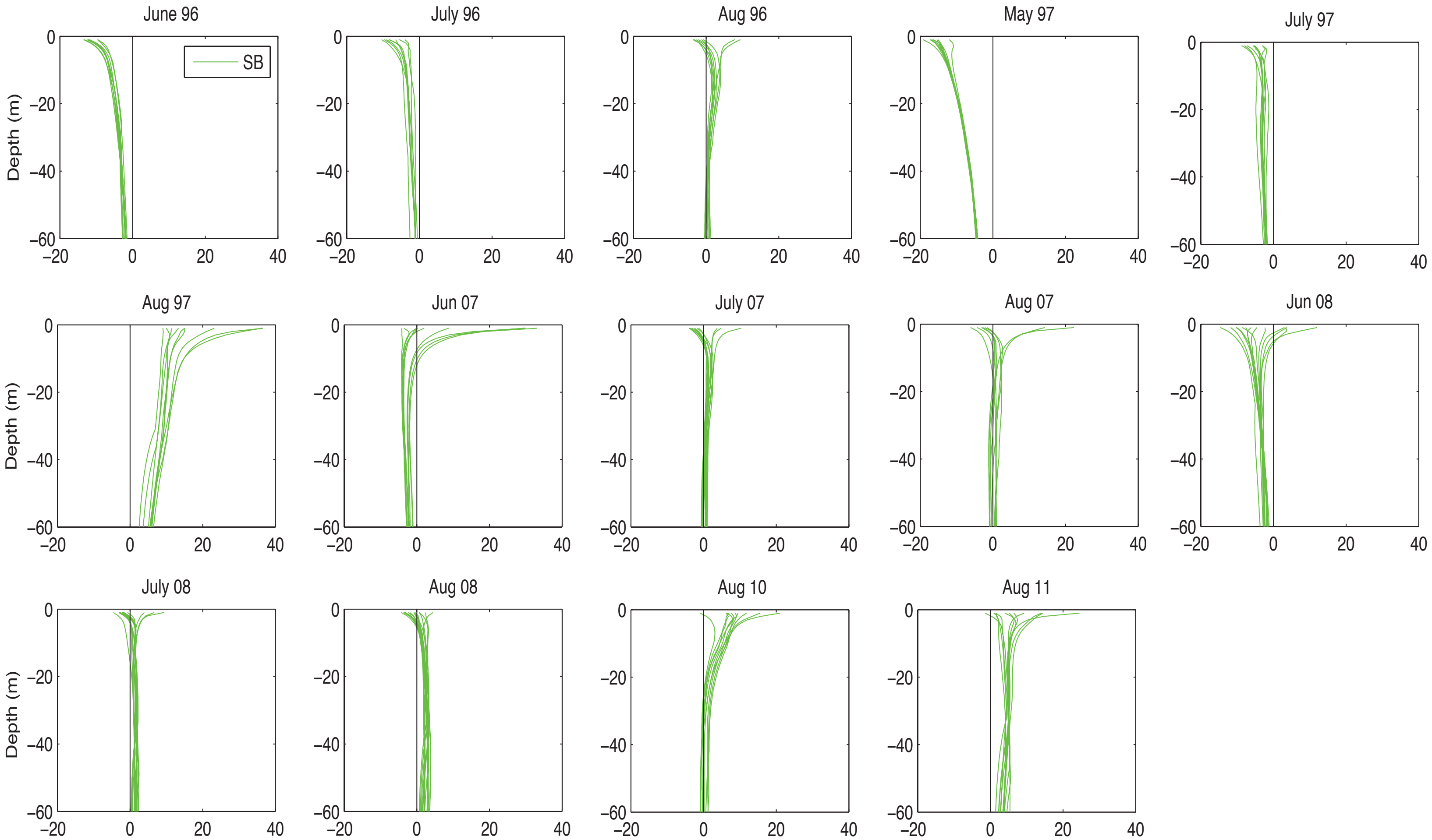

Fig. 5.10. Time series of FWCA at Simpson Bay from June 1996 to August 2011 showing a progression to higher freshwater content and stratification starting in June 2007. One positive anomaly occurs in 1997 due to high air temperatures and preciptation during August (Gay and Vaughan, 2001).

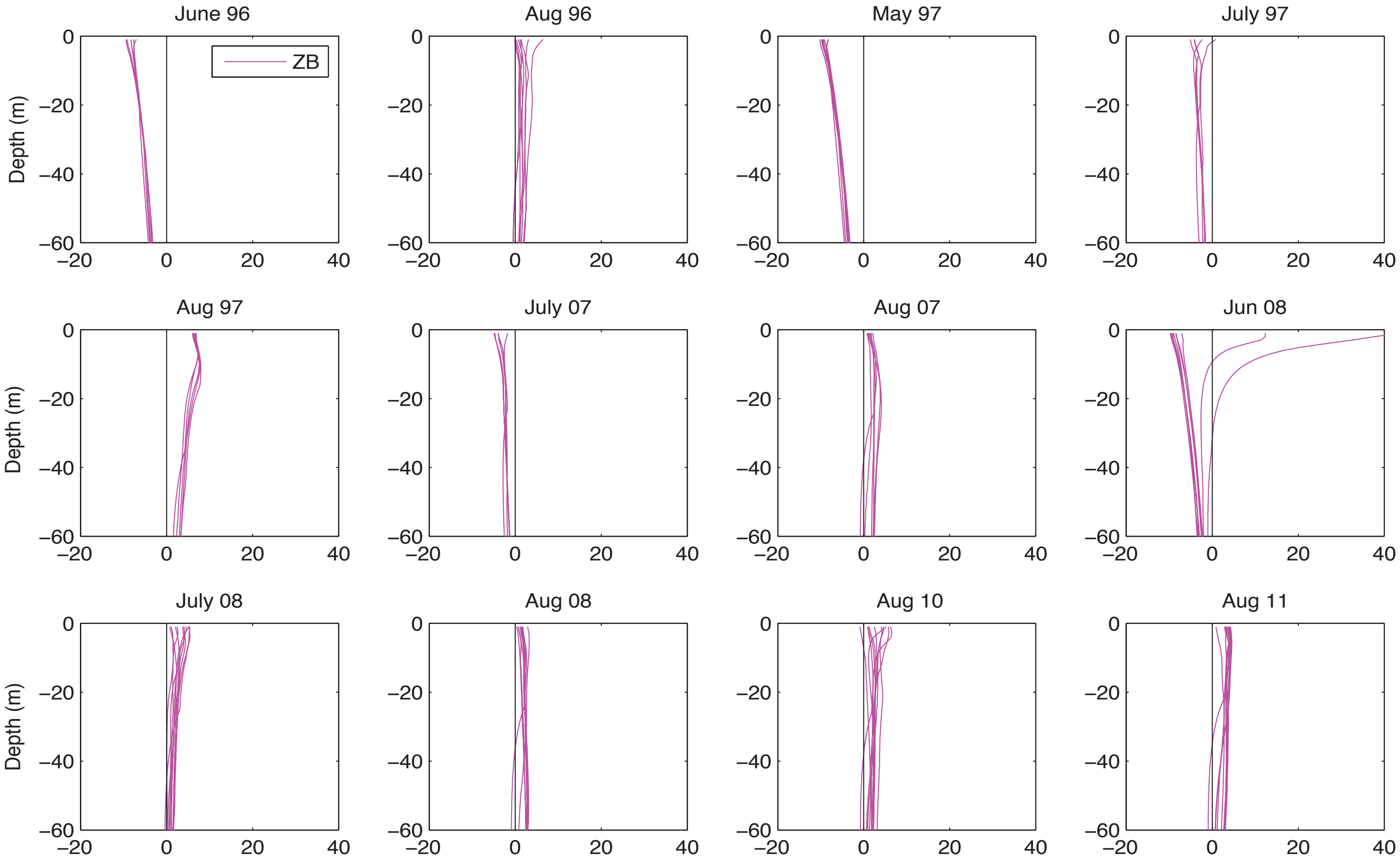

Fig. 5.11. Time series of FWCA at Zaikof Bay from June 1996 to August 2011 showing strong stratification from runoff in the inner basin in June 2008, and a progression to higher amounts of freshwater content throughout the water column in later years. One positive anomaly occurs in 1997 due to high air temperatures and preciptation during August (Gay and Vaughan, 2001).

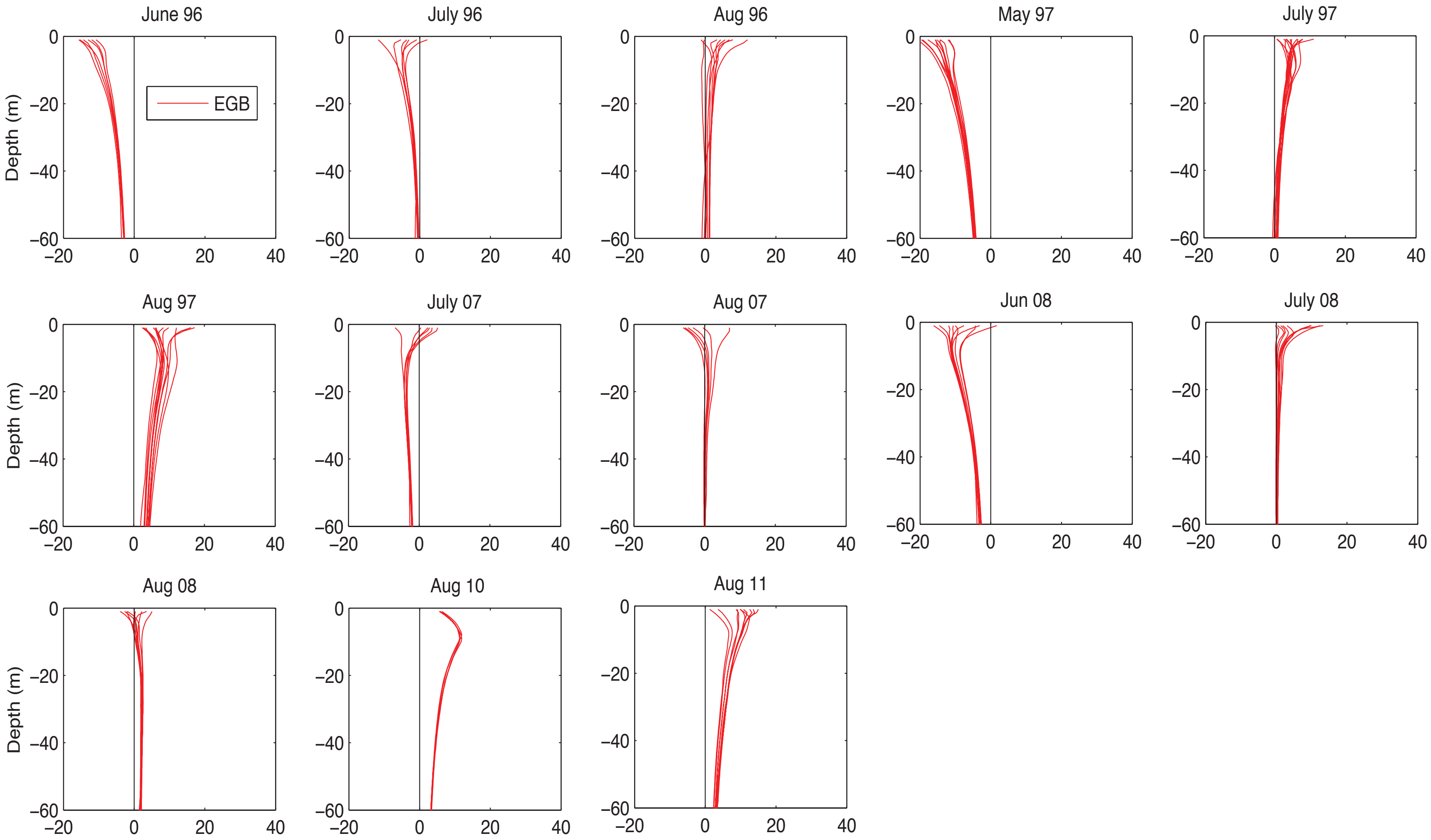

Fig. 5.12. Time series of FWCA at Eaglek Bay from June 1996 to August 2011 showing a progression to higher freshwater content and stratification starting in June 2007. One positive anomaly occurs in 1997 due to high air temperatures and preciptation during August (Gay and Vaughan, 2001).

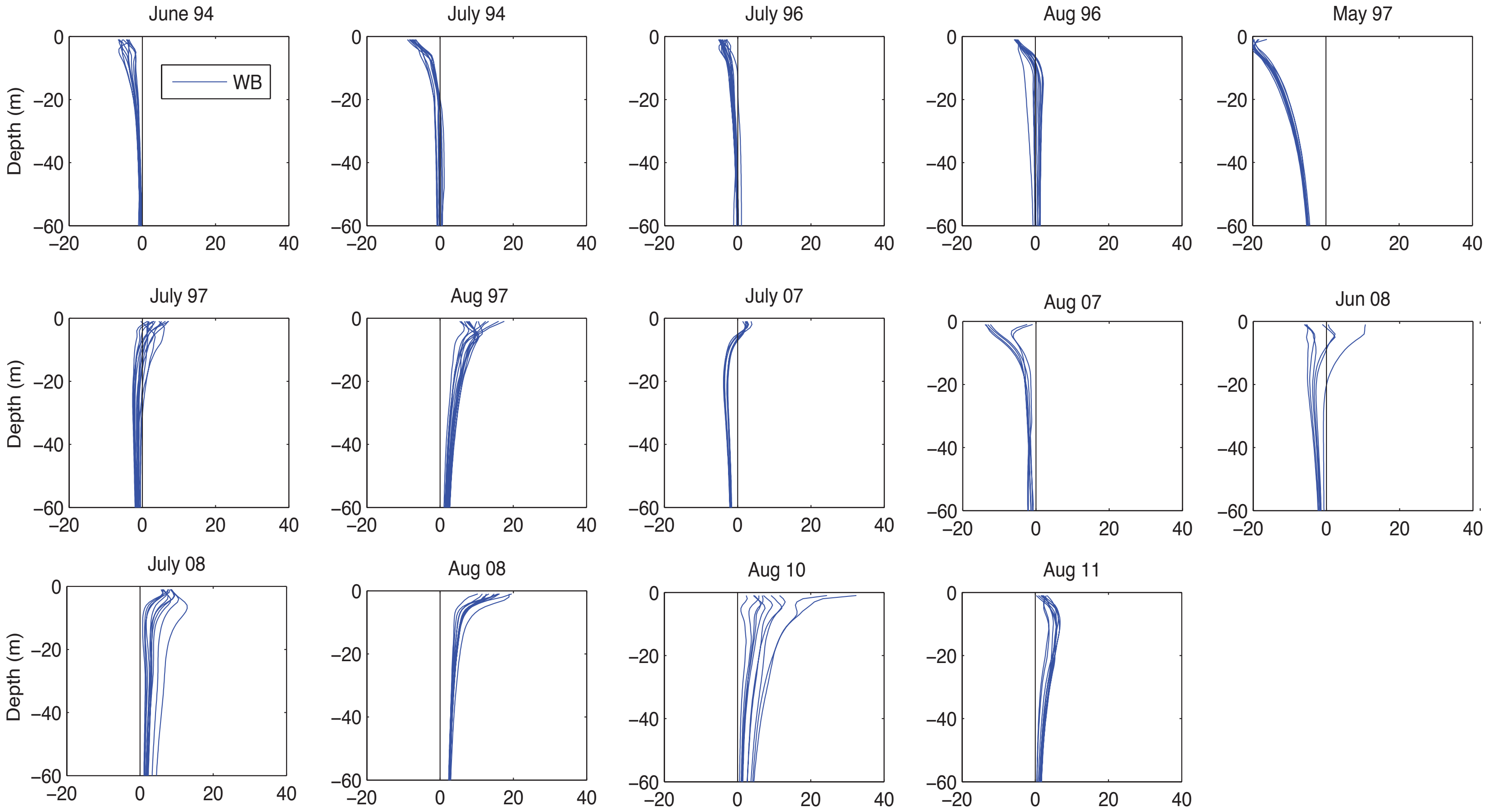

Fig. 5.13. Time series of FWCA at Whale Bay from June 1994 to August 2011 showing a progression to higher amounts of freshwater and stratification in 2008 and later years. One positive anomaly occurs in 1997 due to high air temperatures and preciptation during August (Gay and Vaughan, 2001).

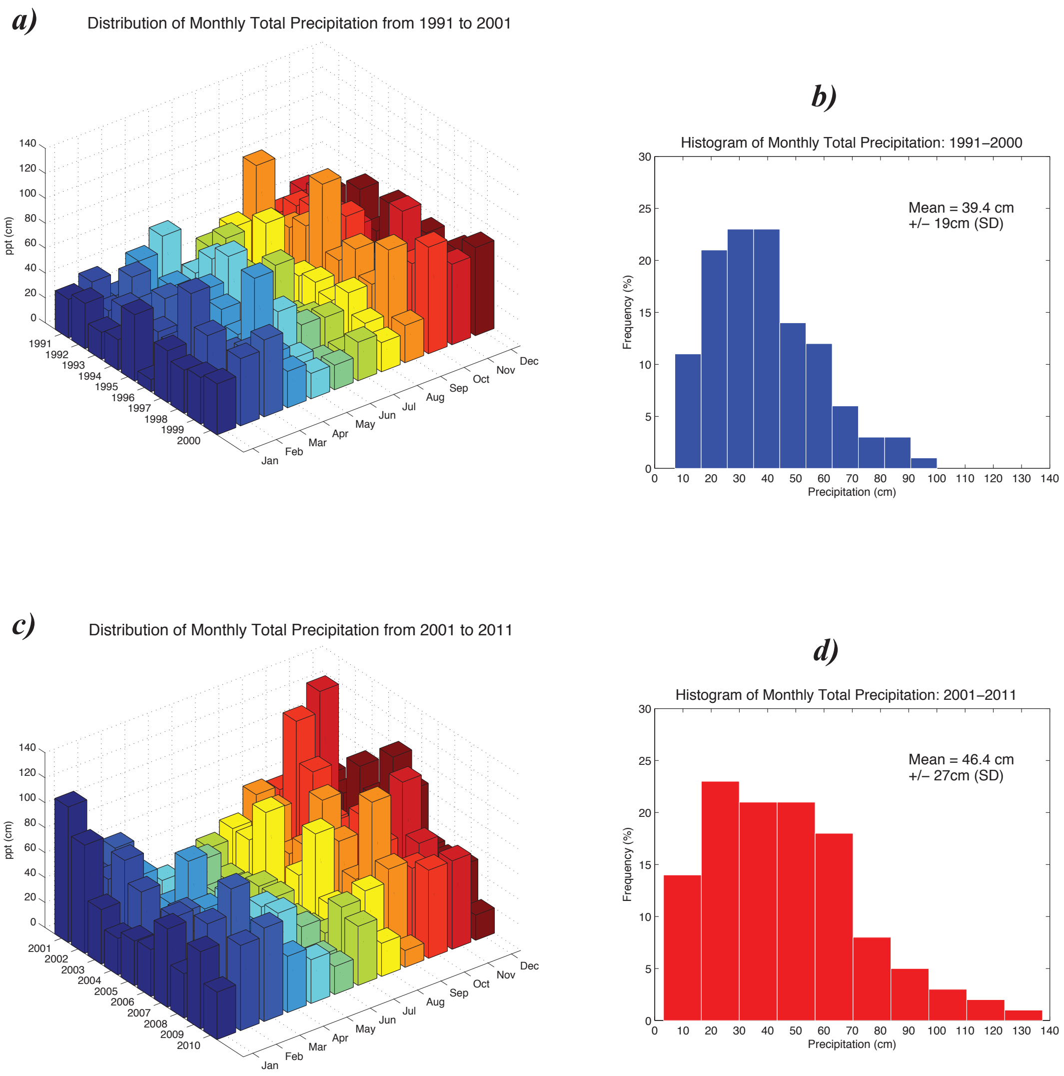

Fig. 5.14. Three-dimensional bar plots and histograms of monthly precipitation at Main Bay: a,b) 1991 to 2000; c,d) 2001 to 2010. Note that the decadal means are significantly different at the 98% level and the extreme events become more frequent in 2001 to 2010.

APPENDIX 3

OBSERVATION DATES, NUMBERS AND LOCATIONS OF OCEANOGRAPHIC STATIONS, WATERSHED CHARACTERISTICS AND ANCILLARY DATA

APPENDIX 3

Appendix 3.1. Observation dates and number of stations surveyed for fjords in Prince William Sound, Alaska May 1994 to March 1998.

Location	***Observation Period (month/year)***	***Stations Surveyed [1]***
Sub-Region 1:		
Herring Bay ^{f}	May, Jun, Jul 94,Oct/Nov 95	(1-14); (1-21); (1-5, 9-21); (1-21)
L. Herring Bay ^{f}	May, Jun, Jul 94	(1-12); (1-13); (1-13)
Drier Bay ^{f}	Jun, Jul 94, Mar, Jul 96	(1-11, 13-17); (same); (5-10, 14-19); (4-10, 14-19)
Long Channel ^{p}	Jul 94	(1-10)
Mummy Bay ^{sf}	Jul 94	(1- 9)
Little Bay	Jul 94	(1- 3)
Sub-Region 2:		
Culross Bay ^{f}	May 94	(1-8)
Southeast Perry I. ^{ns}	May, Jun 94	(1-6); (1-6)
South Bay	May, Jun 94	(1-8); (1-8)
West Twin Bay	May 94	(3-8)
Sub-Region 3:		
Main Bay ^{f}	May, Jun 94	(1-8, NPK1-2); (1-4, 6-12, NPK1-2)
Eshamy Bay ^{f}	May, Jun 94	(1-11); (1-7, 11)
Ewan Bay ^{sf}	Mar, Jul 96	(1-3); (1-3)
Paddy Bay ^{sf}	Mar, Jul 96	(1-5); (1-5)
Sub-Region 4:		
Nassau Fjord ^{gf}	Mar 96, Mar98	(1-2); (1-2)
Icy Bay ^{gf}	Mar, Jul 96	(1-5); (1-5)
Whale Bay ^{f}	Jun, Jul 94, Oct/Nov 95, Mar 96, Jul, Aug, Oct 96 Mar 97, Jul, Aug, Oct 97, Mar 98	(1-10); (1-10); (1-14); (1-3, 5, 7-12, 14, 16-17); (same); (5, 9, 14, 16-17); (1-3, 5, 7-12, 14-17); (1-3, 7-10, 12, 14, 17); (1-3, 5, 7-12, 14, 16-17); (same); (1-3, 5, 7-12, 16-17); (1-3, 5, 7, 9-12, 14-17)
Bainbridge Pass $^{f/p}$	Jun, Jul 94	(1-14); (1-10)
N. Flemming Isl. ^{ns}	Jun, Jul 94	(1-6); (1-7)
Sub-Region 5:		
U. Prince of Wales ^{p}	Jun, Jul 94	(1-14); (2-3, 4)
Shelter Bay ^{sf}	Jun	(1-12)
Sawmill Bay	Jul 94, Oct/Nov 95	(1-6); (1-7)
N. Elrington Pass ^{p}	Jul 94, Oct/Nov 95	(1-6, 1-9)
L. Bainbridge Pass ^{p}	Oct/Nov 95	(1-3)
N. & S. Twin Bays	Jul 94	(1-5)
Hogg Bay ^{sf}	Oct/Nov 95	(1-8)

Legend: f = fjord, gf = glacial fjord, sf = shallow fjord, p = pass, ns = near-shore region, all other locations are classified as shallow bays. 1 The station numbers surveyed at a given site for each monthly survey.

Appendix 3.1 (cont).

Location	***Observation Period (month/year)***	***Stations Surveyed*** [1]
Sub-Region 6:		
Eaglek Bay ^{f}	Oct/Nov 95, Mar, Jul,	(1-11); (1, 3, 5, 8, 10, 16); (same);
	Aug, Oct 96,Mar 97, Jul 97,	(3, 5, 8, 16); (1-11, 16); (same); (same)
	Aug 97 , Oct 97, Mar 98	(1-10, 16); (1-9, 11,16); (1, 3, 5, 6, 8-9, 10-11, 16)
Unakwik ^{gf} (outer)	Mar, Jul, Aug 96	(2-4); (2 -4); (1, 3-4)
Unakwik ^{gf} (inner)	Mar, Jul, Aug 96	(1-4); (5-7); (5-6)
Sub-Region 7:		
Jack Bay ^{f} (outer)	Oct/Nov 95, Mar, Jul 96	(1-4); (2, 4, 5, 7, 9); (2, 4, 5, 7, 9)
Jack Bay ^{f} (inner)	Oct/Nov 95, Mar, Jul 96	(10-12); (10-11); (10-11)
Galena Bay ^{f} (outer)	Mar, Jul 96	(4-6); (4-6)
Galena Bay ^{f} (inner)	Mar, Jul 96	(1-3); (1-3)
Sub-Region 8:		
Simpson Bay ^{sf}	Oct/Nov 95, Mar, Jul, Aug, Oct 96,	(3-7); (3-9); (3-9); (4-9); (4-9)
	Mar 97, Jul 97,	(1B-2B, 3-4, 6-9); (1B-2B, 3-9);
	Aug 97, Oct 97, Mar 98	(1B-2B, 3-9); (1B-2B, 3, 5-9); (1B-2B, 3-9)
Sheep Bay	Mar, Jul 96	(3-7); (3-9)
Port Gravina	Mar, Jul 96	(1-7); (1-7)
Sub-Region 9:		
Zaikof Bay	Oct/Nov 95, Mar 96,	(1-13); (2, 5, 8, 11, 13-14);
	Jun, Aug 96,	(2, 5, 14, 11, 13); (2, 4, 13-14);
	Oct 96, Mar 97,	(1-5, 7-9, 11, 13, 14); (1-6, 8, 11, 13-14)
	Jul 97, Aug 97,	(2, 8, 11, 13, 14); (2, 5, 8, 13, 14)
	Oct 97,	(1-6, 8, 11, 13, 14);
	Mar 98	(2-3, 5, 6, 8, 11, 13, 14)

Legend: f = fjord, gf = glacial fjord, sf = shallow fjord, p = pass, ns = near-shore region, all other locations are classified as shallow bays. 1 The station numbers surveyed at a given site for each monthly survey.

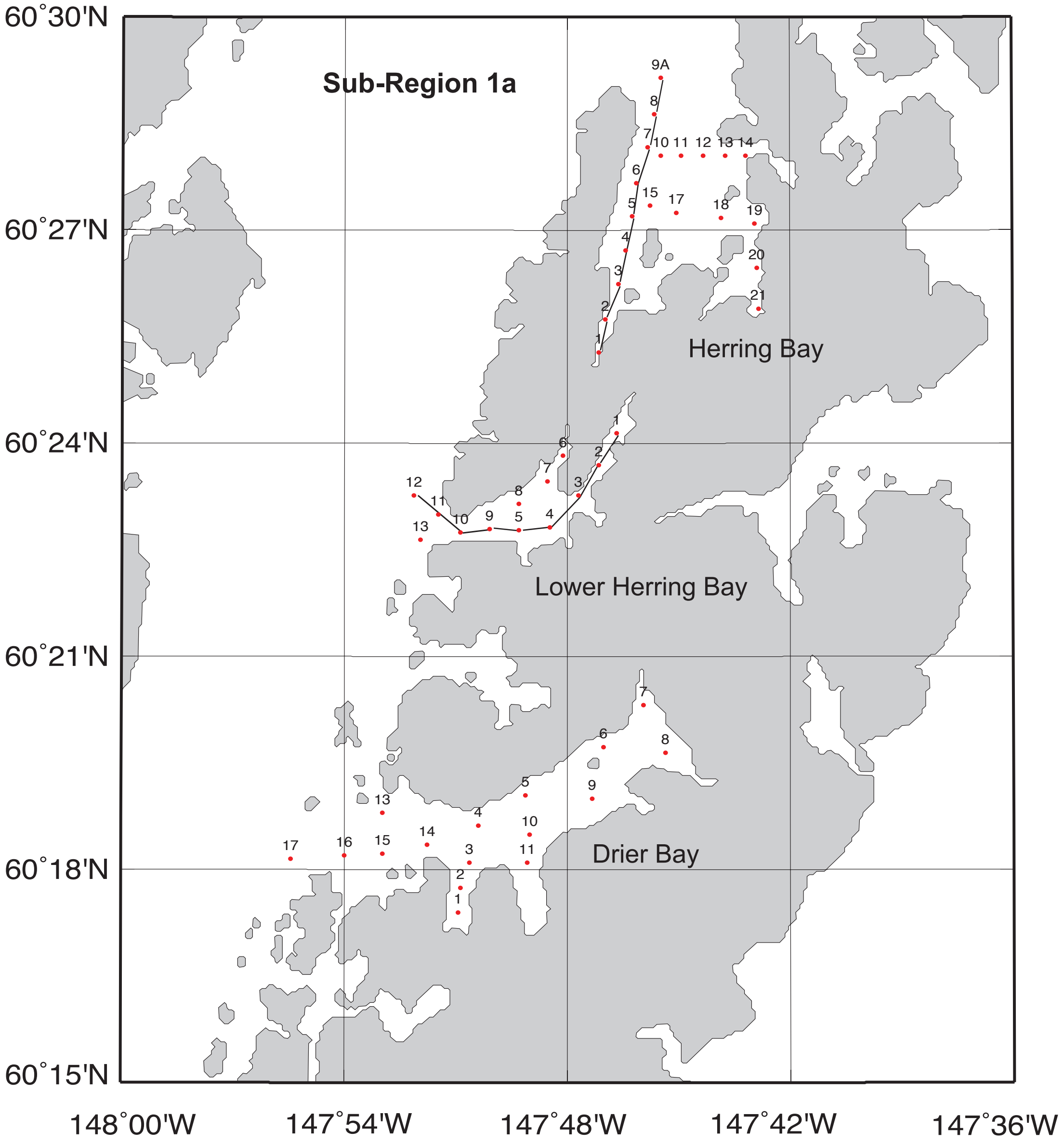

Appendix 3.2. Locations of oceanographic stations within fjords, bays and nearshore areas of Prince William Sound, Alaska surveyed from May 1994 to March 1998. Specific stations occupied during each cruise are listed in Appendix 3.1. Those shown above are for fjords within sub-region 1a surveyed in 1994 and 1996. The solid lines are transects in May and June 1994 shown in Fig. 2.18.

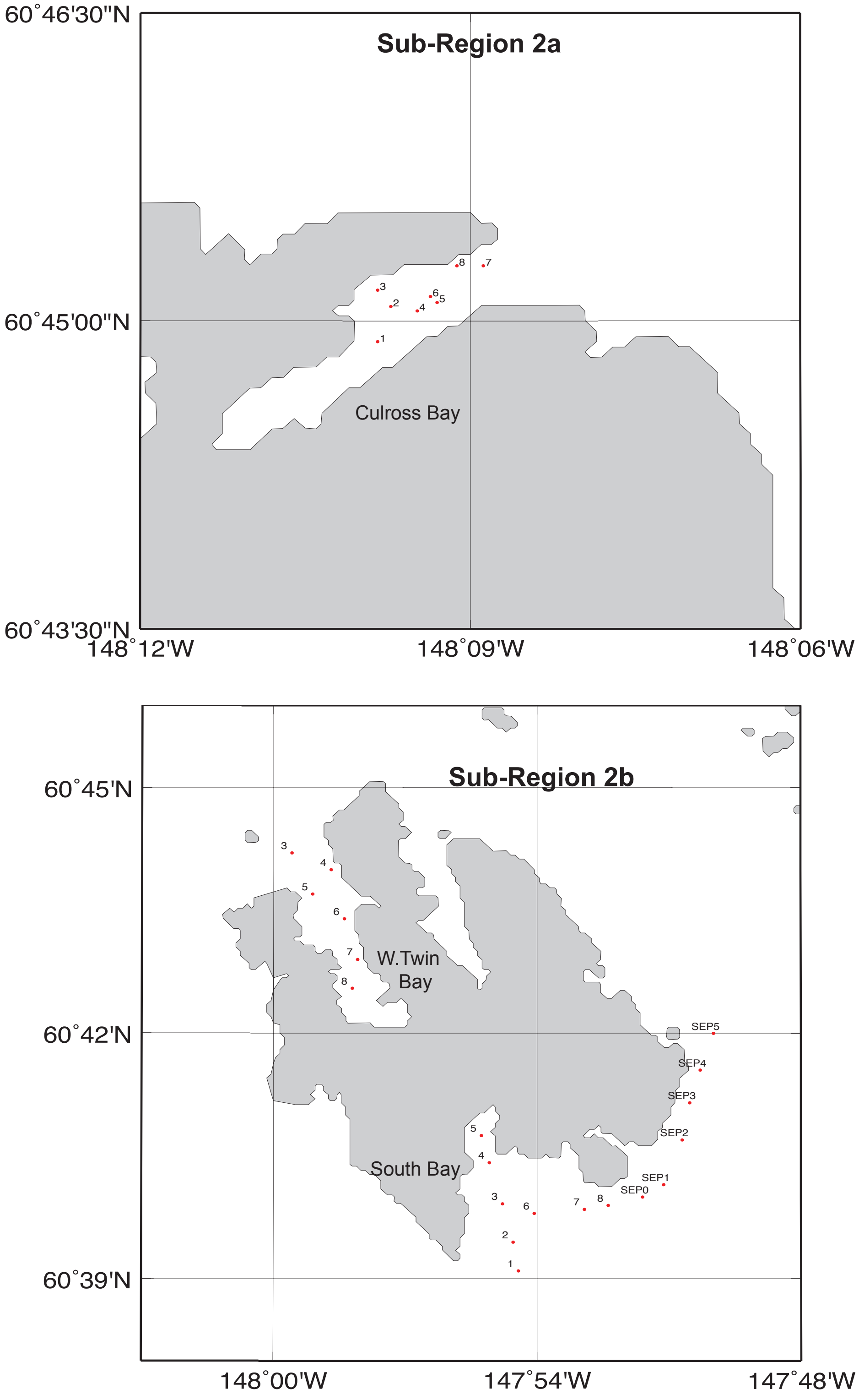

Appendix 3.2. (cont.). Locations of oceanographic stations surveyed in 1994 within one fjord in Sub-region 2a (Culross), two bays (W. Twin and South Bay) and one near-shore region (SEP) in Sub-region 2b.

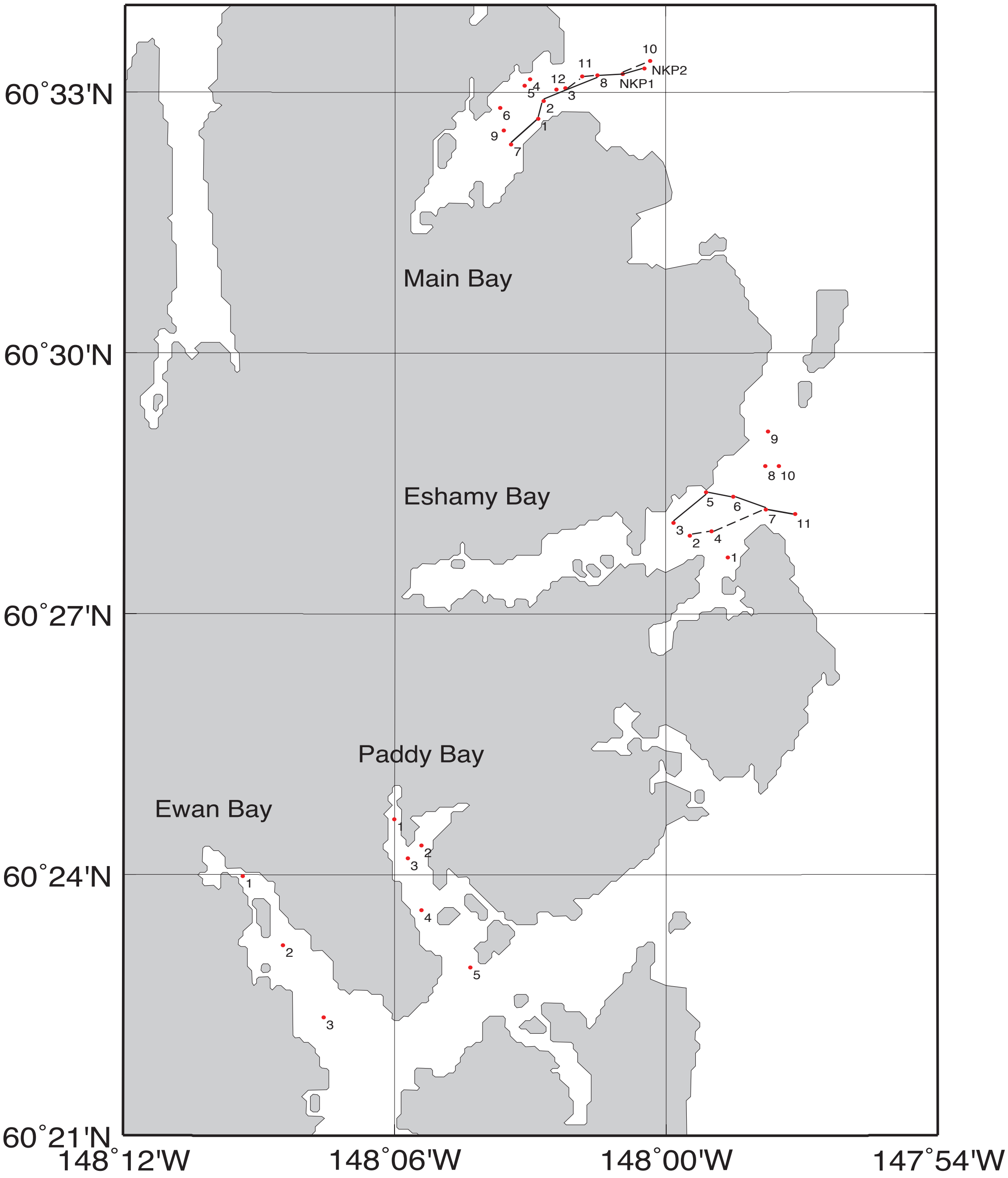

Appendix 3.2 (cont.). Locations of oceanographic stations within fjords in sub-region 3 surveyed in 1994 and in 1996. The solid and dashed lines are transects respectively in May and June 1994 shown in Fig. 2.18.

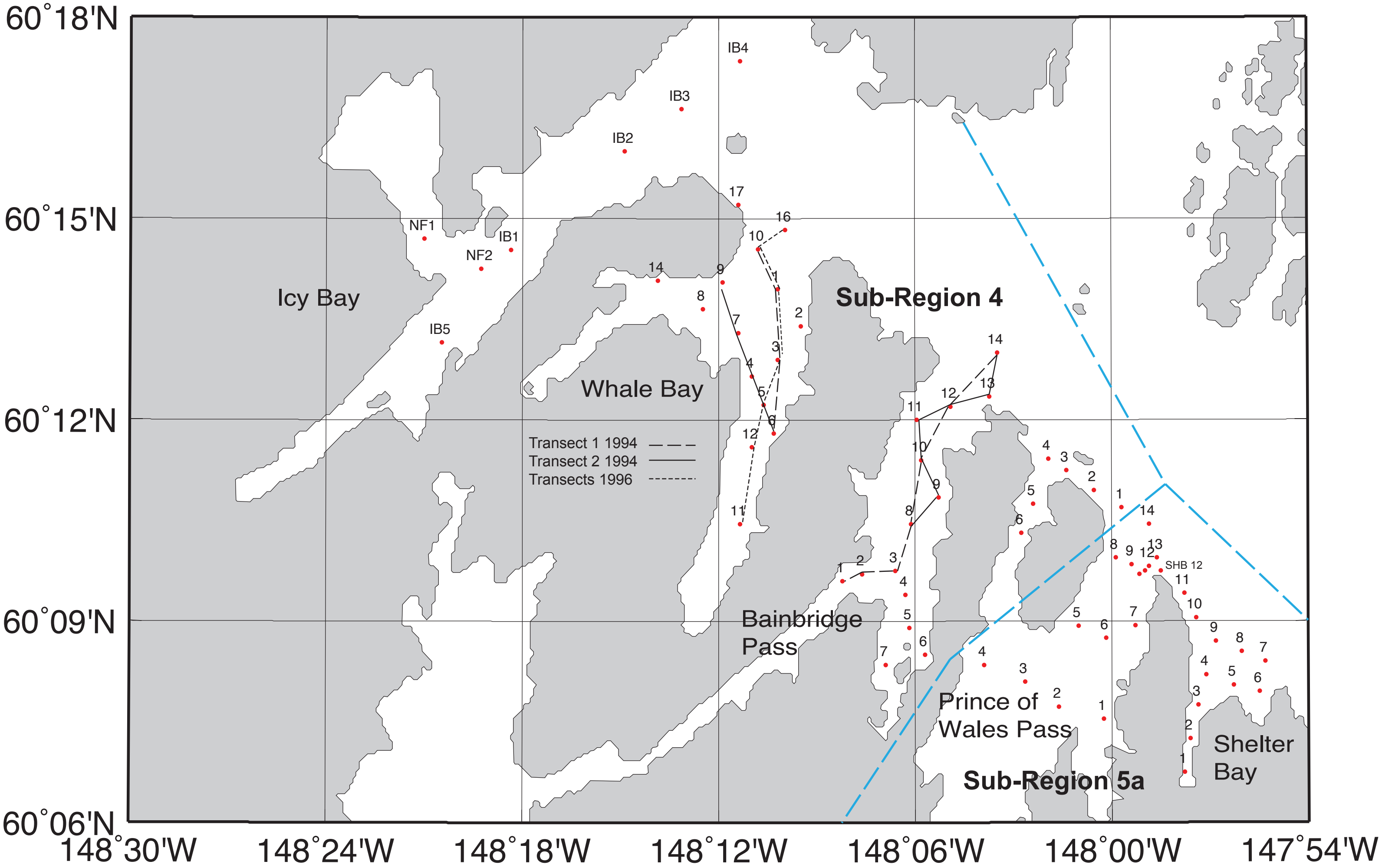

Appendix 3.2 (cont.). Locations of oceanographic stations within various fjords and passes in Sub-Regions 4 and 5a. Also shown are transects used in vertical sections of temperature in Fig. 2.20.

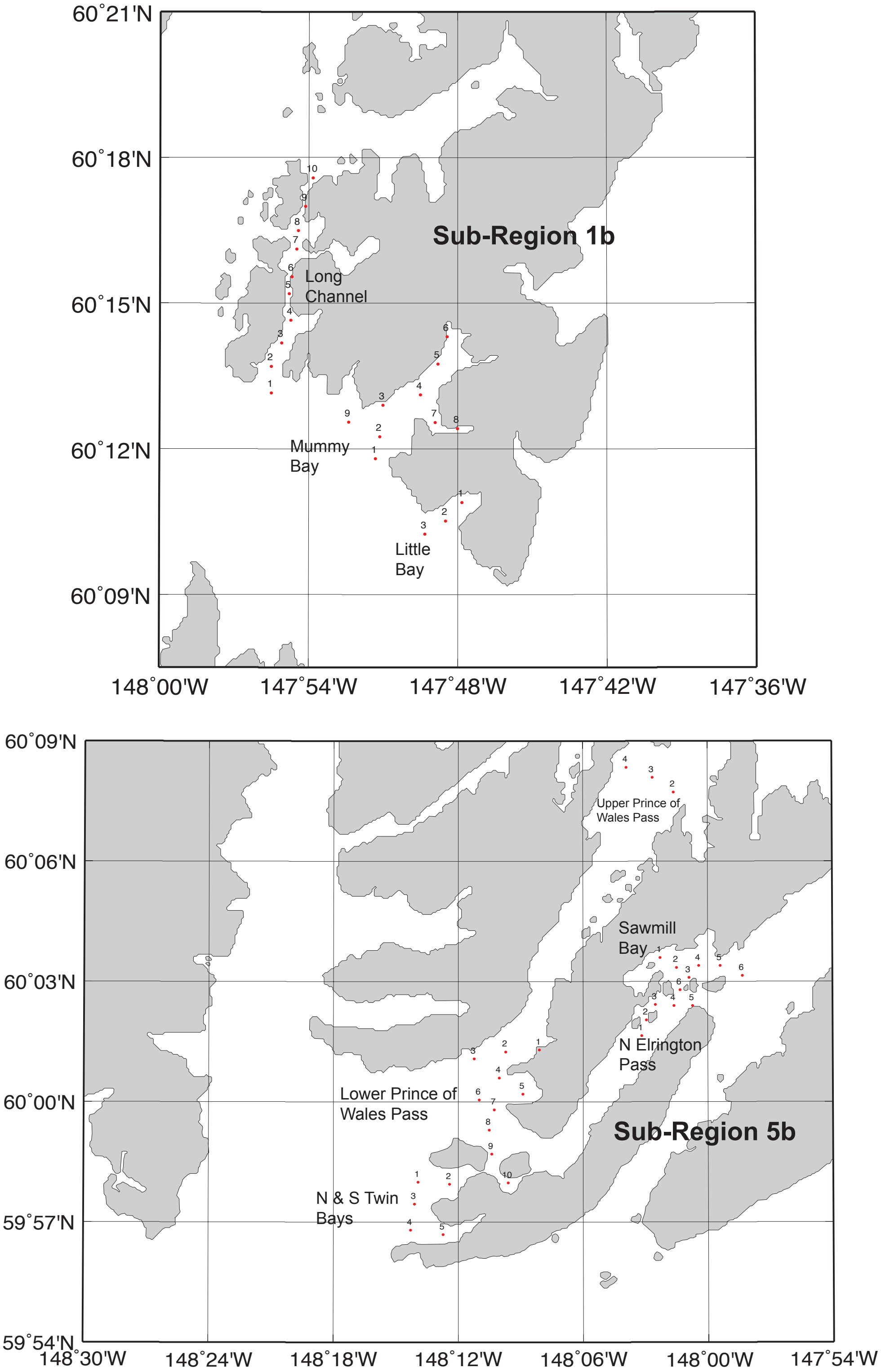

Appendix 3.2 (cont.). Locations of CTD casts conducted in July1994 within small fjords and passes in Sub-region1b and 5b.

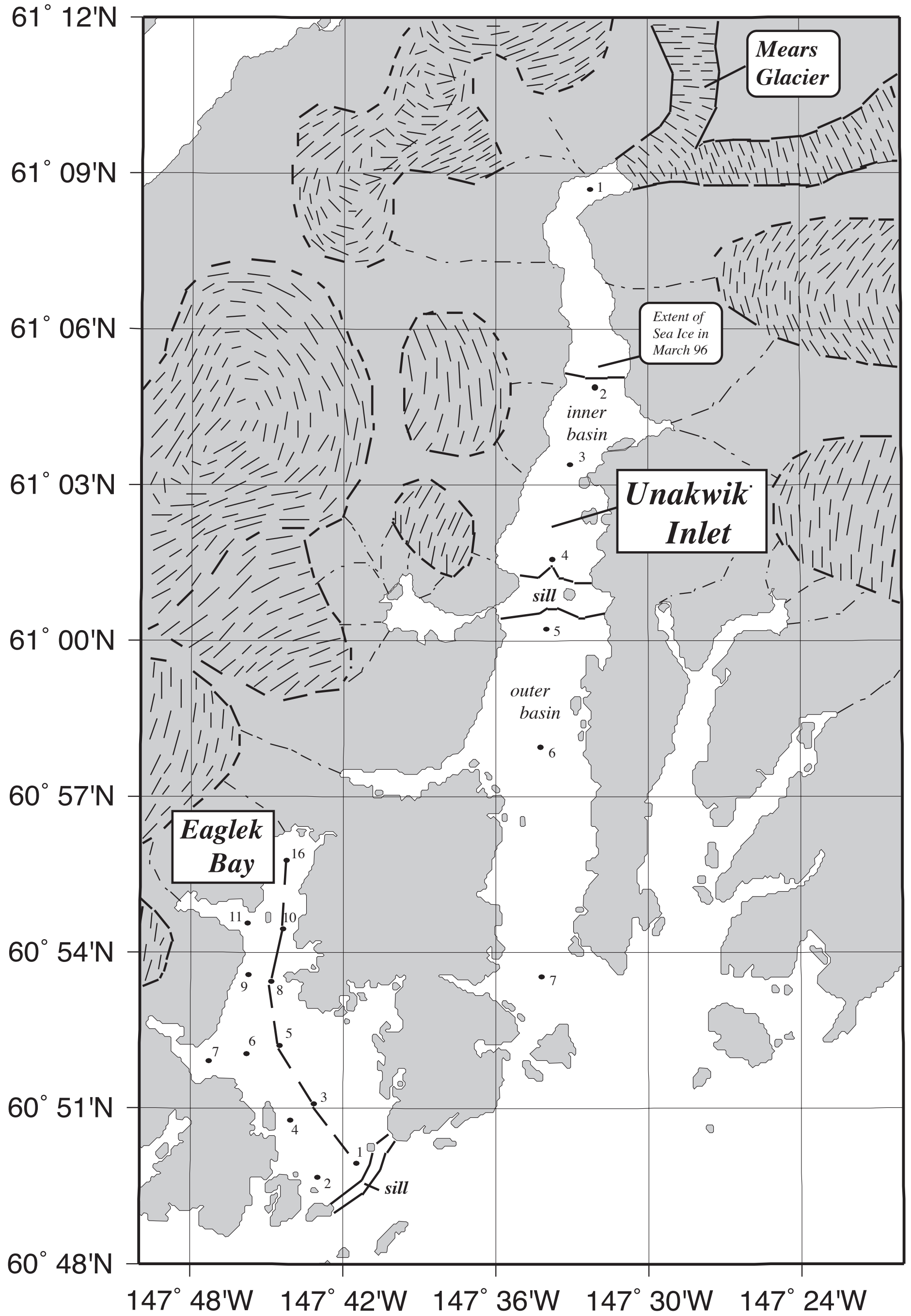

Appendix 3.2 (cont.). Locations of oceanographic stations within a small fjord (Eaglek) and a large glacial fjord (Unakwik Inlet) surveyed in 1996 in sub-region 6 (Northern PWS). Also shown are transects used in vertical sections of temperature in Fig. 2.21.

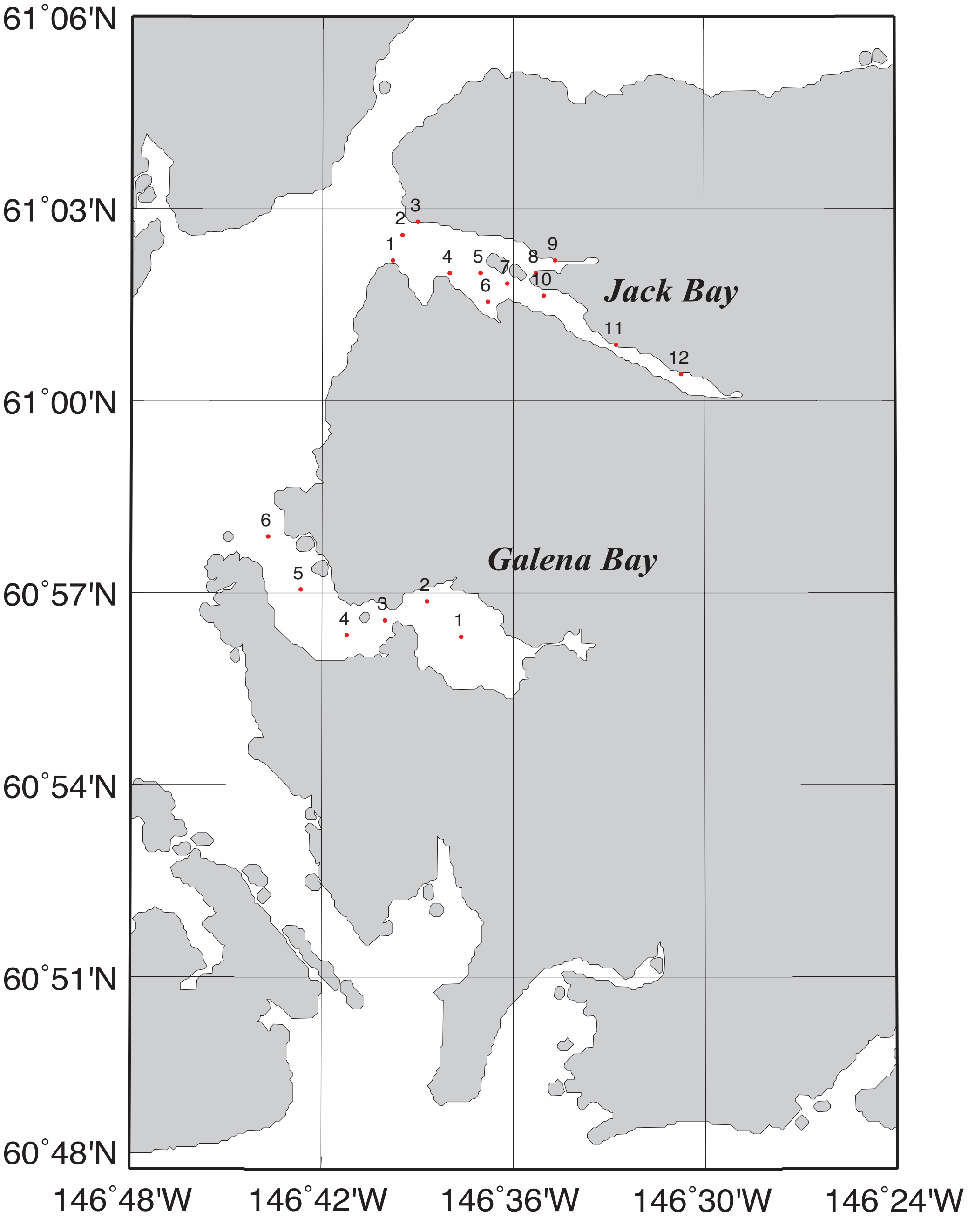

Appendix 3.2 (cont.). Locations of oceanographic stations within two small fjords (Jack and Galena) surveyed in 1996 in sub-region 7 (Northern PWS).

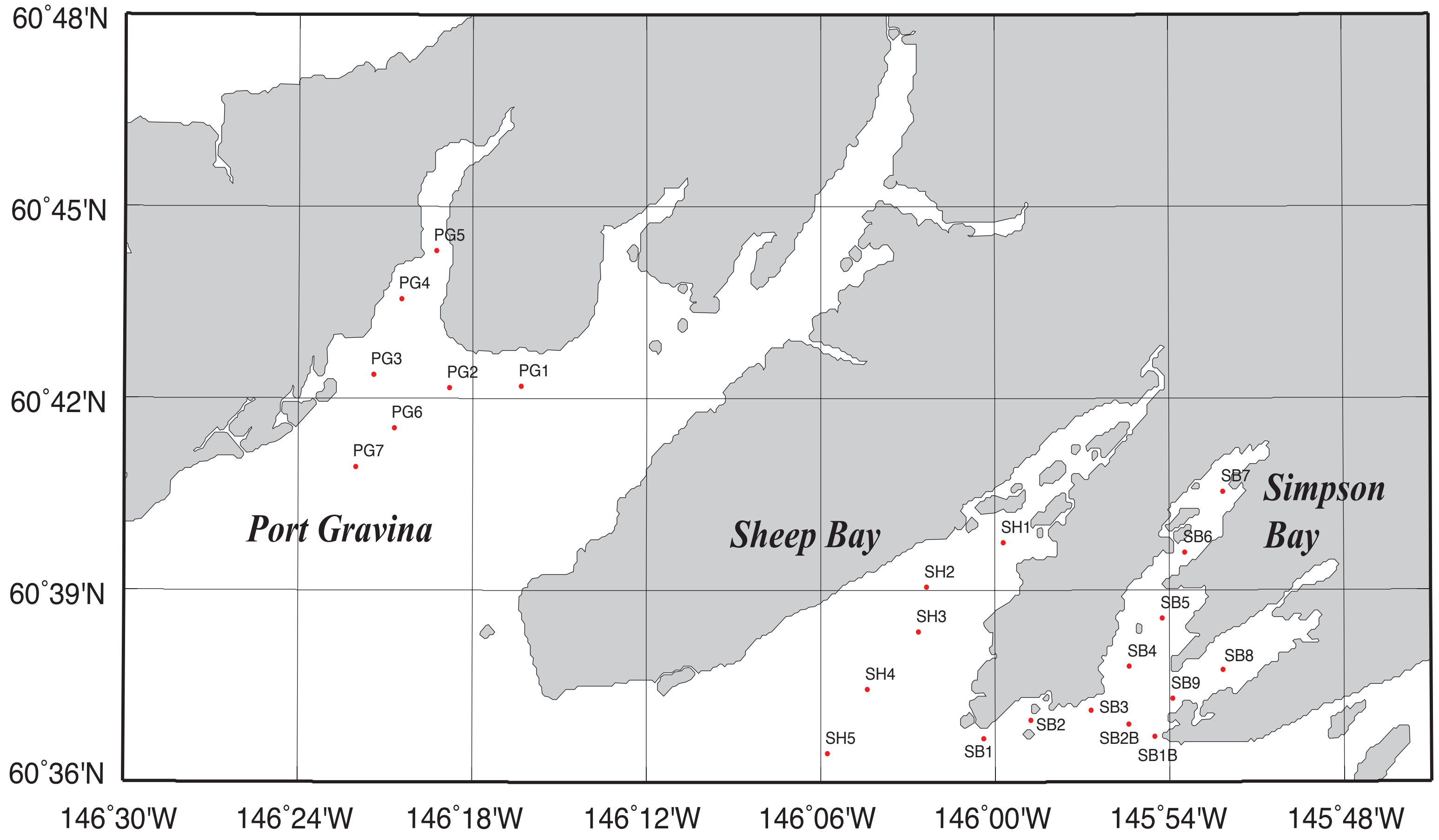

Appendix 3.2. (cont.). Locations of oceanographic stations within three shallow fjords surveyed in Eastern PWS (sub-region 8), including Port Gravina and Sheep Bay in 1996 and Simpson Bay in 1996, 1997 and 1998. The months and CTD stations occupied for each above site are given in Appendix 3.1.

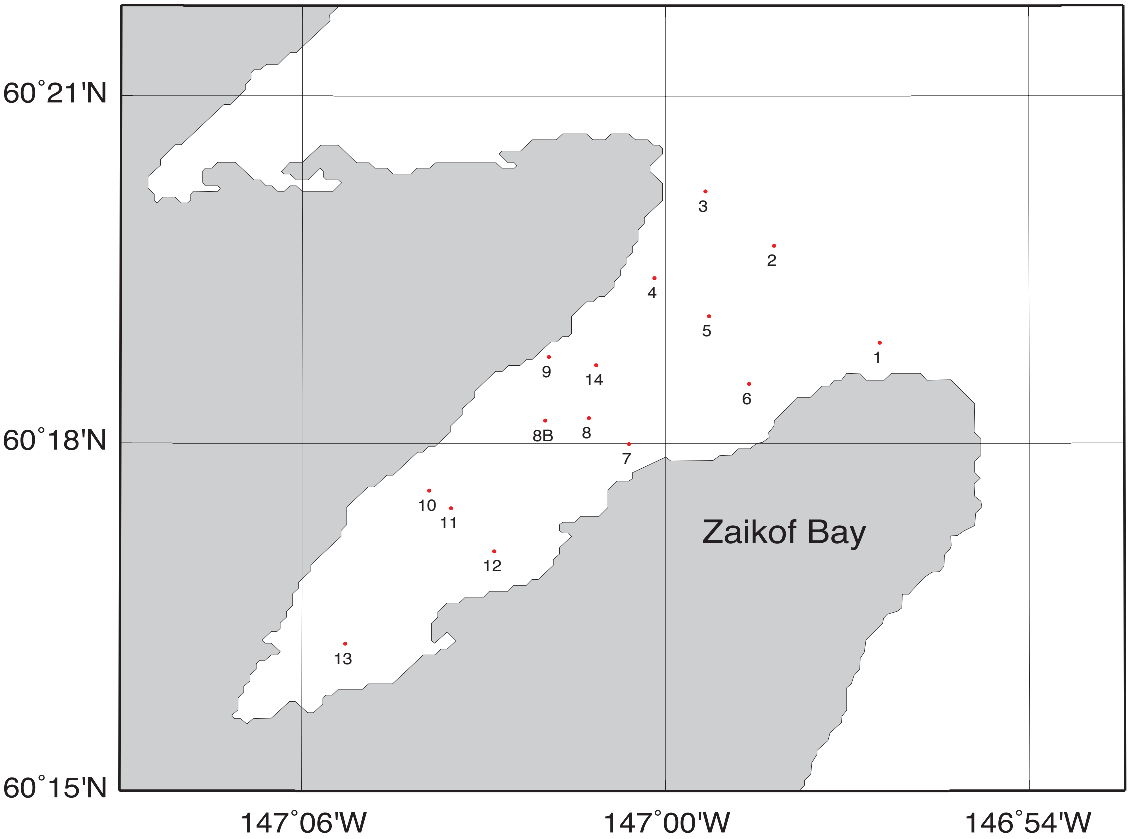

Appendix 3.2 (cont.). Locations of oceanographic stations surveyed within Zaikof Bay in South Central PWS (sub-region 9).

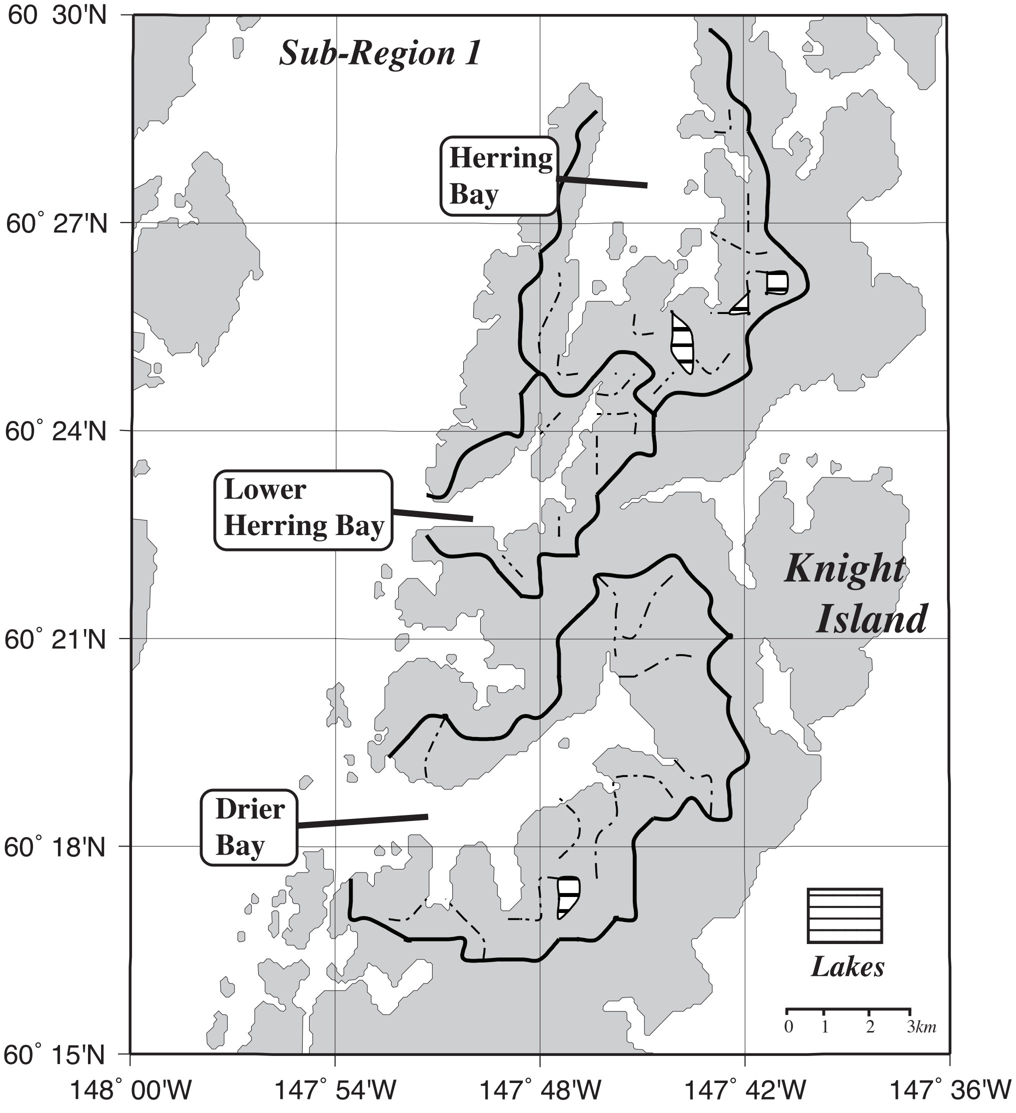

Appendix 3.3. Watershed characteristics of fjords and bays of Prince William Sound, Alaska surveyed from May 1994 to March 1998. Watersheds of fjords located in Sub-Region 1 are shown above. White areas with stripes denote lakes and small black lines denote drainages.

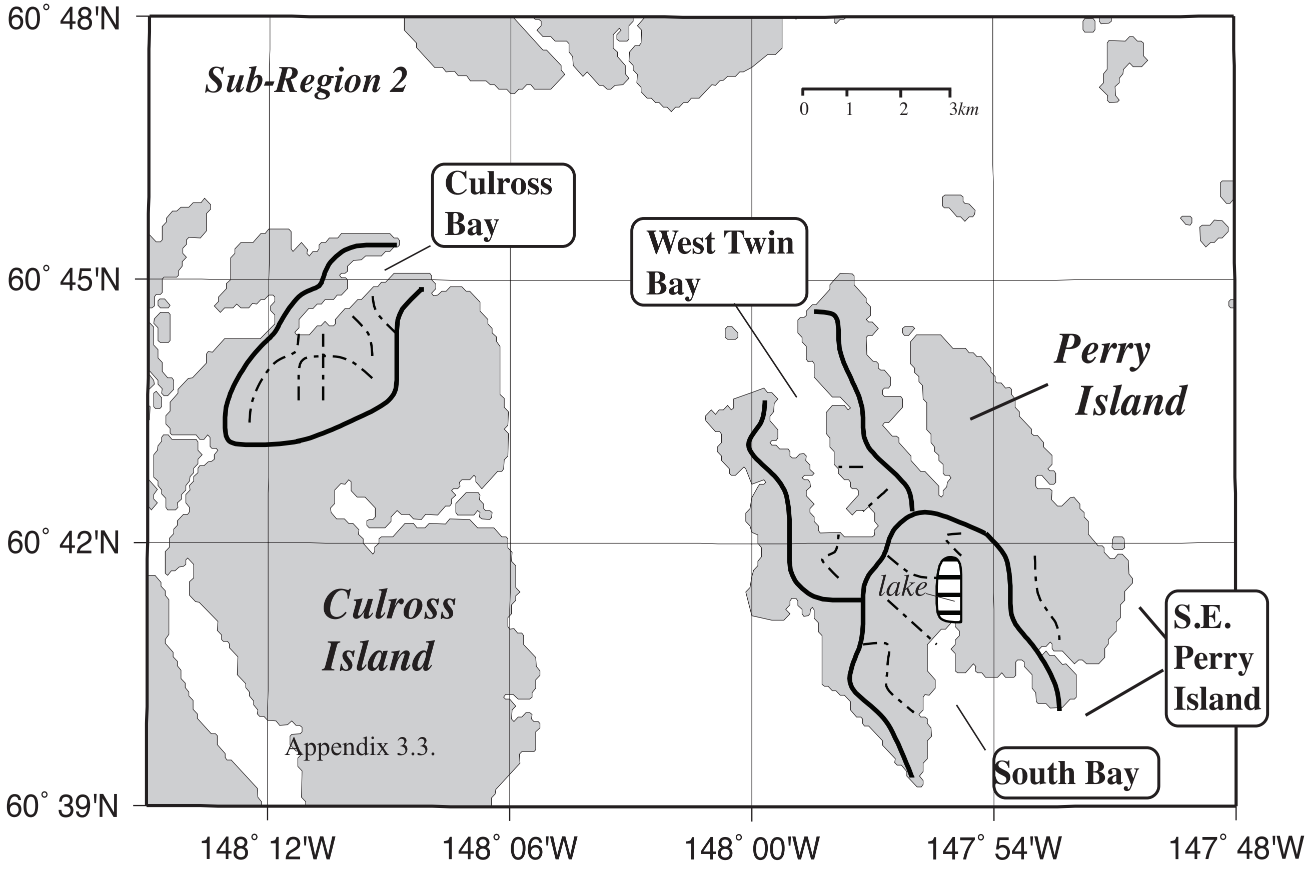

Appendix 3.3 (cont.). Watershed characteristics of fjords located in Sub-Region 2. White areas with stripes denote lakes and small black lines denote drainages.

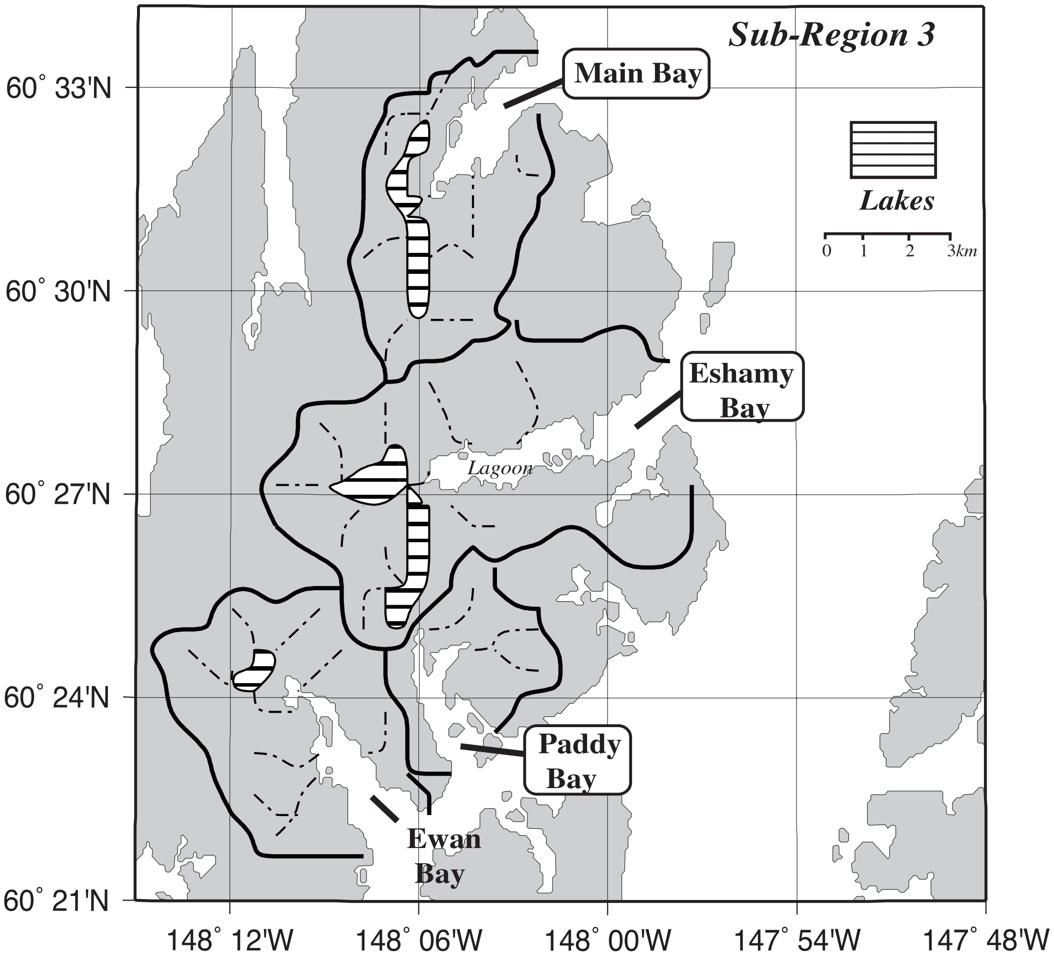

Appendix 3.3 (cont.). Watershed characteristics of fjords located in Sub-Region 3. White areas with stripes denote lakes and small black lines denote drainages.

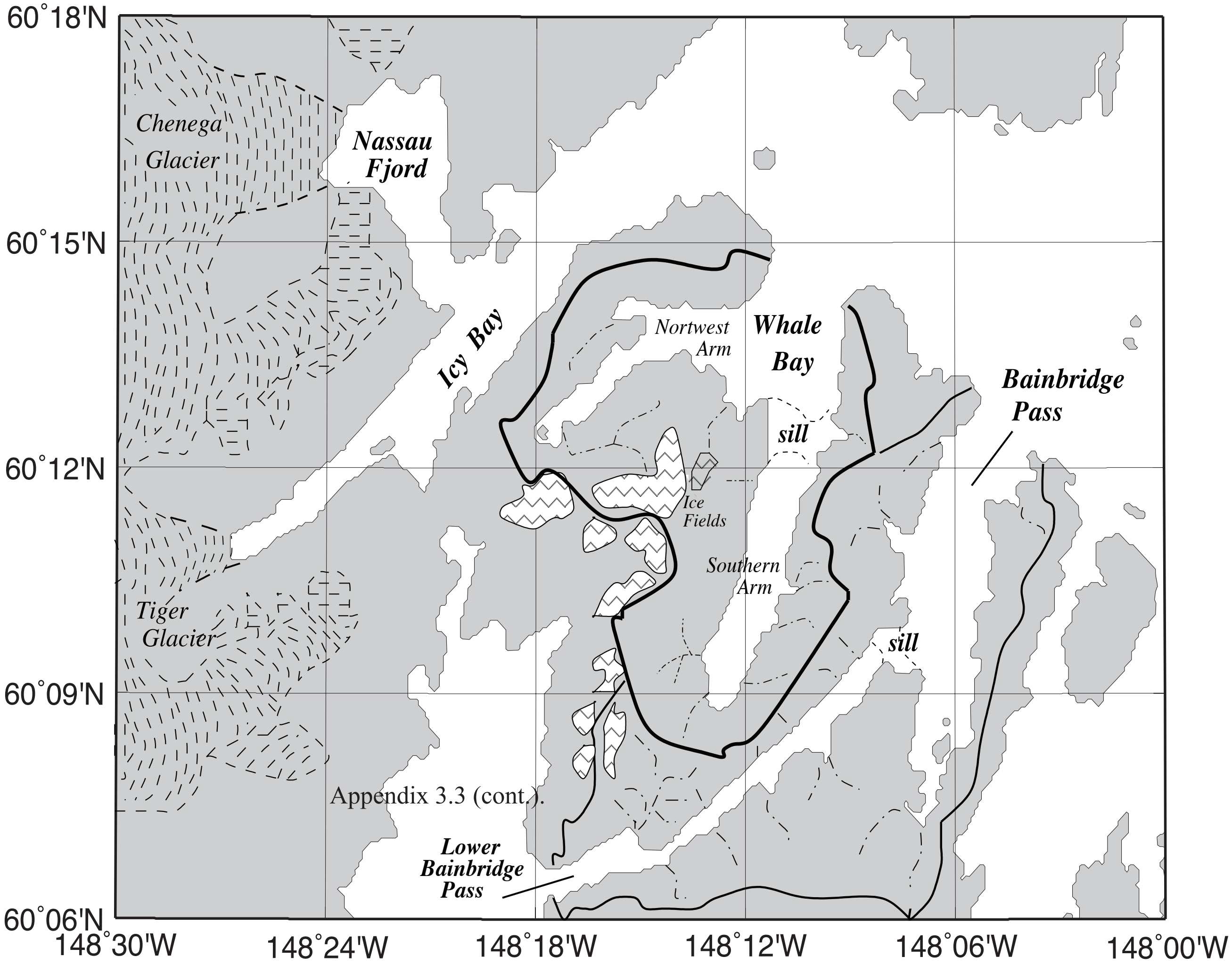

Appendix 3.3 (cont.). Watershed characteristics of fjords located in Sub-Region 4. White areas with stippling denote alpine glaciers, small black lines denote drainages, and large grey areas with dashed lines represent tidewater glaciers*.

*Watershed of Whale Bay reprinted with permission from "Seasonal hydrography and tidal currents of bays and fjords in Prince William Sound, Alaska" by Gay, S.M. III and S.L.Vaughan Fish. Oceanogr. 10 (Suppl. 1), 159-193, Copyright 2001 by John Wiley and Sons.

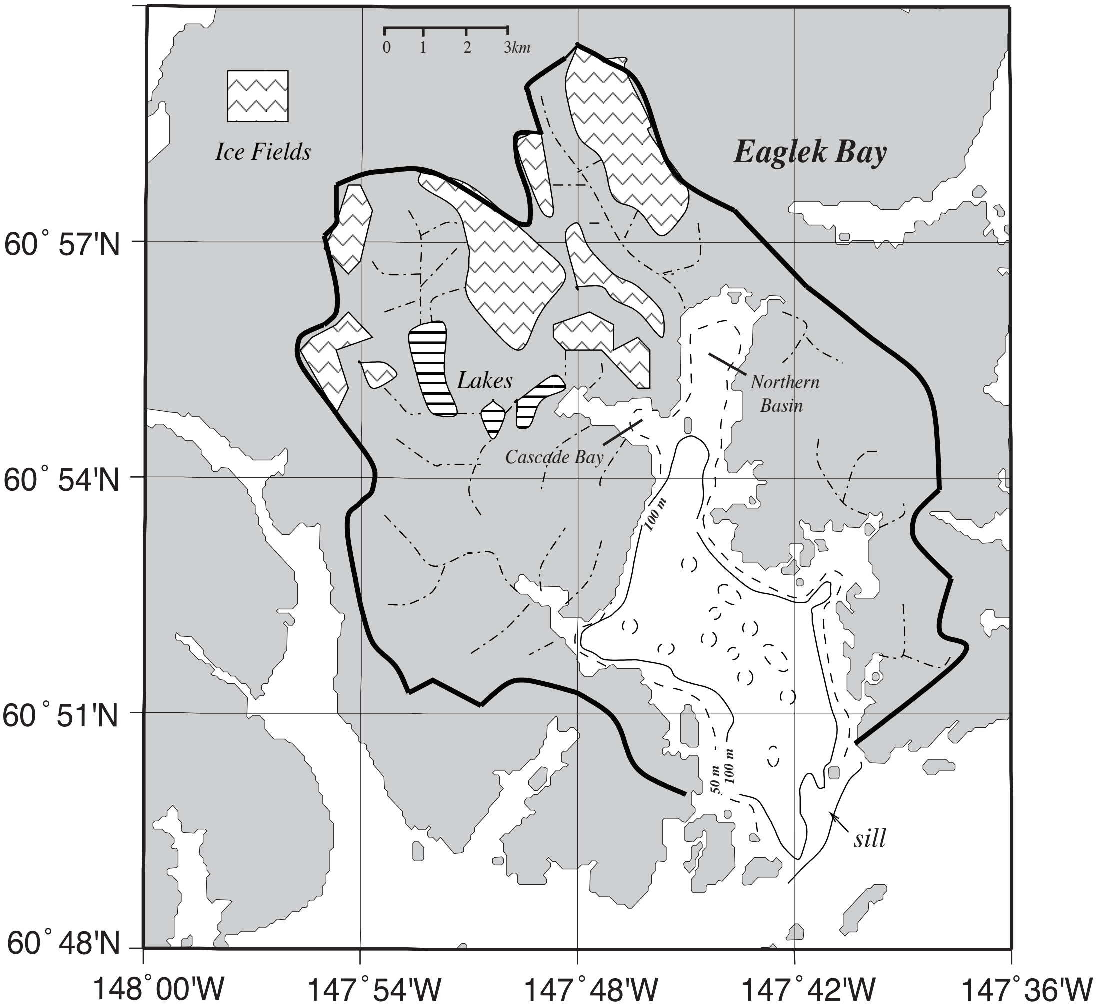

Appendix 3.3 (cont.). Watershed characteristics of Eaglek Bay located in Sub-Region 6. White areas with stripes and stippling denote lakes and alpine glaciers respectively, and small black lines denote drainages. Portions of the glacial watershed of Unakwik Inlet (not shown) are given in Appendix 3.2.*

*Watershed of Eaglek Bay reprinted with permission from "Seasonal hydrography and tidal currents of bays and fjords in Prince William Sound, Alaska" by Gay, S.M. III and S.L.Vaughan Fish. Oceanogr. 10 (Suppl. 1), 159-193, Copyright 2001 by John Wiley and Sons.

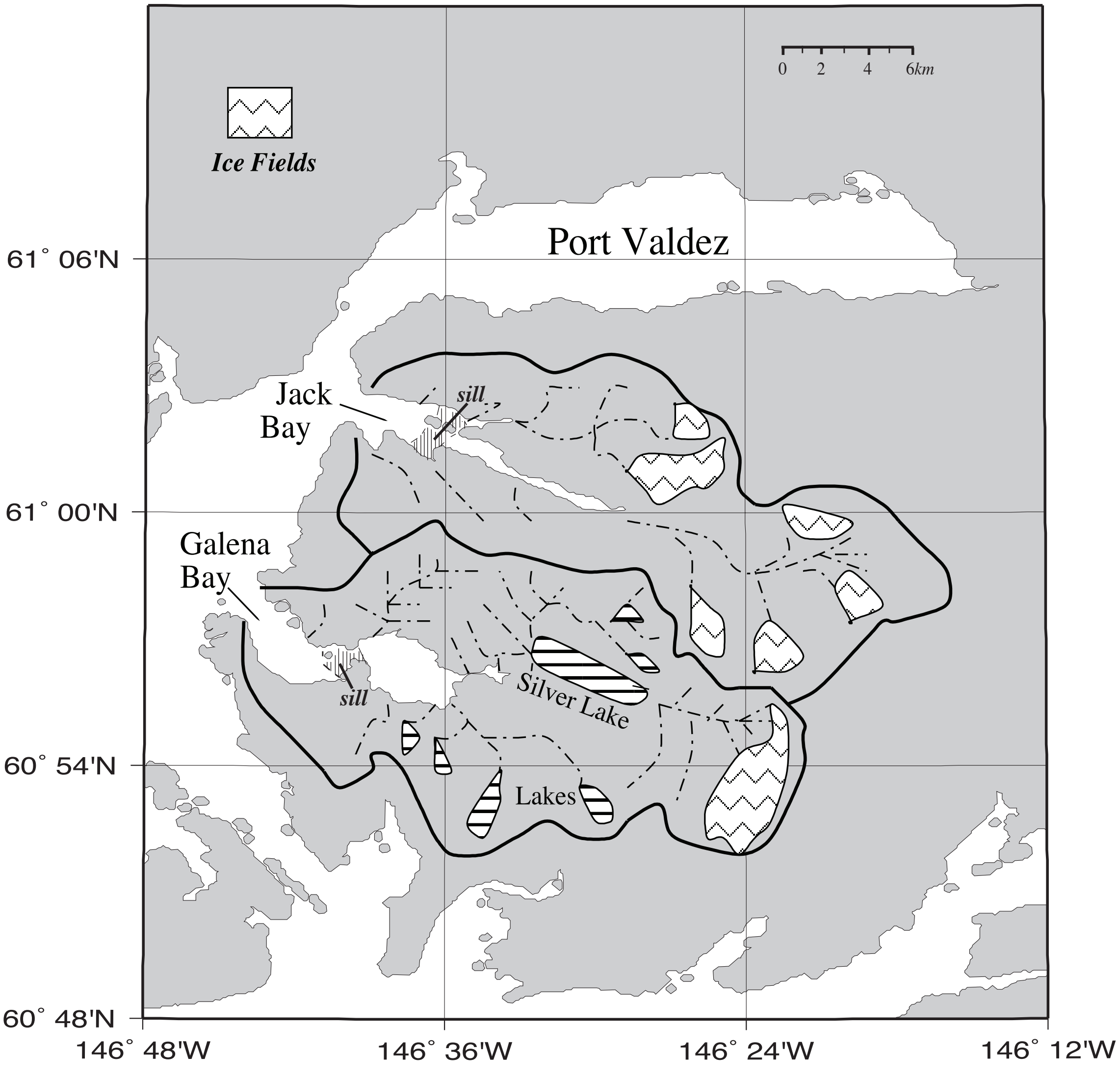

Appendix 3.3 (cont.). Watershed characteristics of Jack and Galena Bay, located in Sub-Region 7. White areas with stripes and stippling denote lakes and alpine glaciers respectively, and small black lines denote drainages.

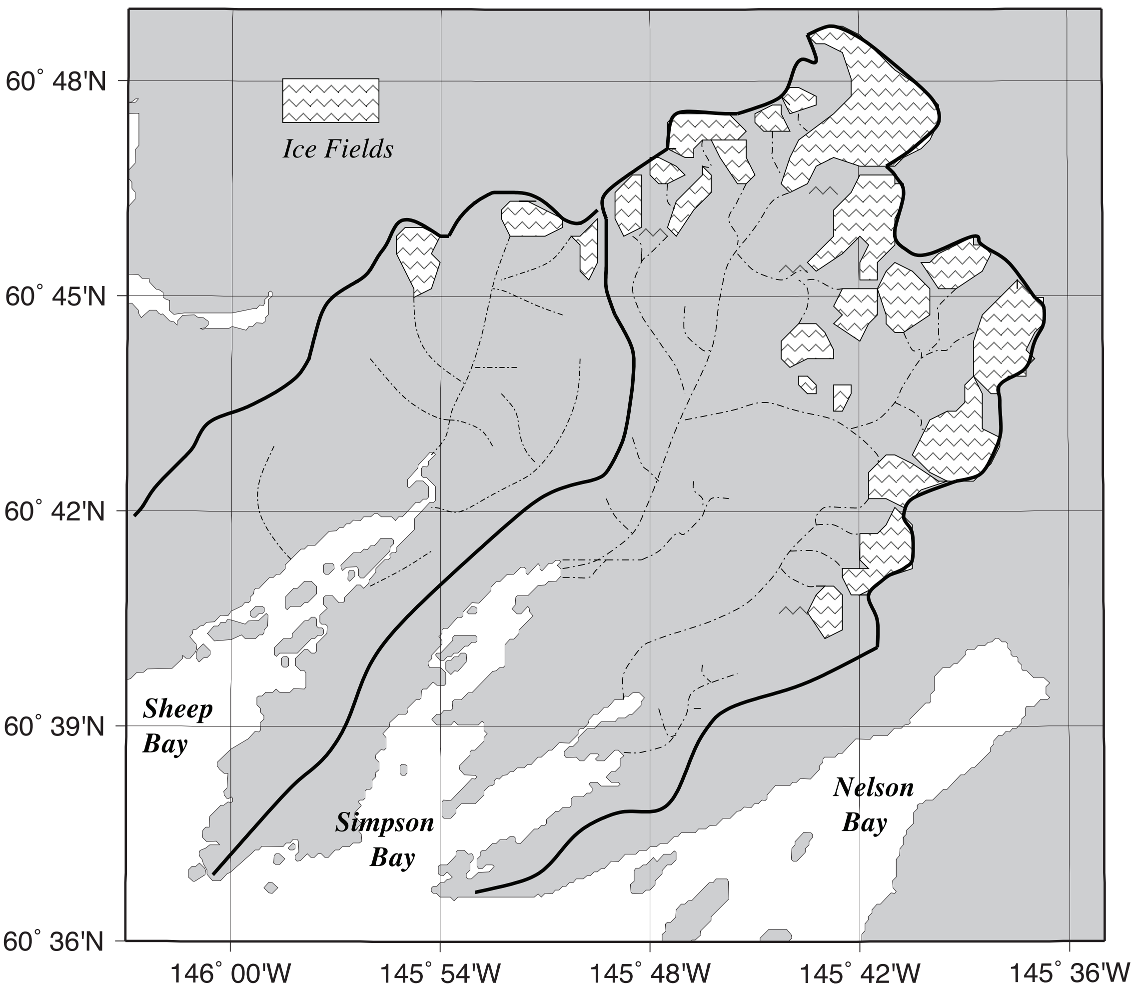

Appendix 3.3 (cont.). Watershed characteristics of Simpson and Sheep Bay, located in Sub-Region 8. White areas with stippling denote alpine glaciers and small black lines denote drainages*.

---

*Reprinted with permission from "Seasonal hydrography and tidal currents of bays and fjords in Prince William Sound, Alaska" by Gay, S.M. III and S.L.Vaughan Fish. Oceanogr. 10 (Suppl. 1), 159-193, Copyright 2001 by John Wiley and Sons.

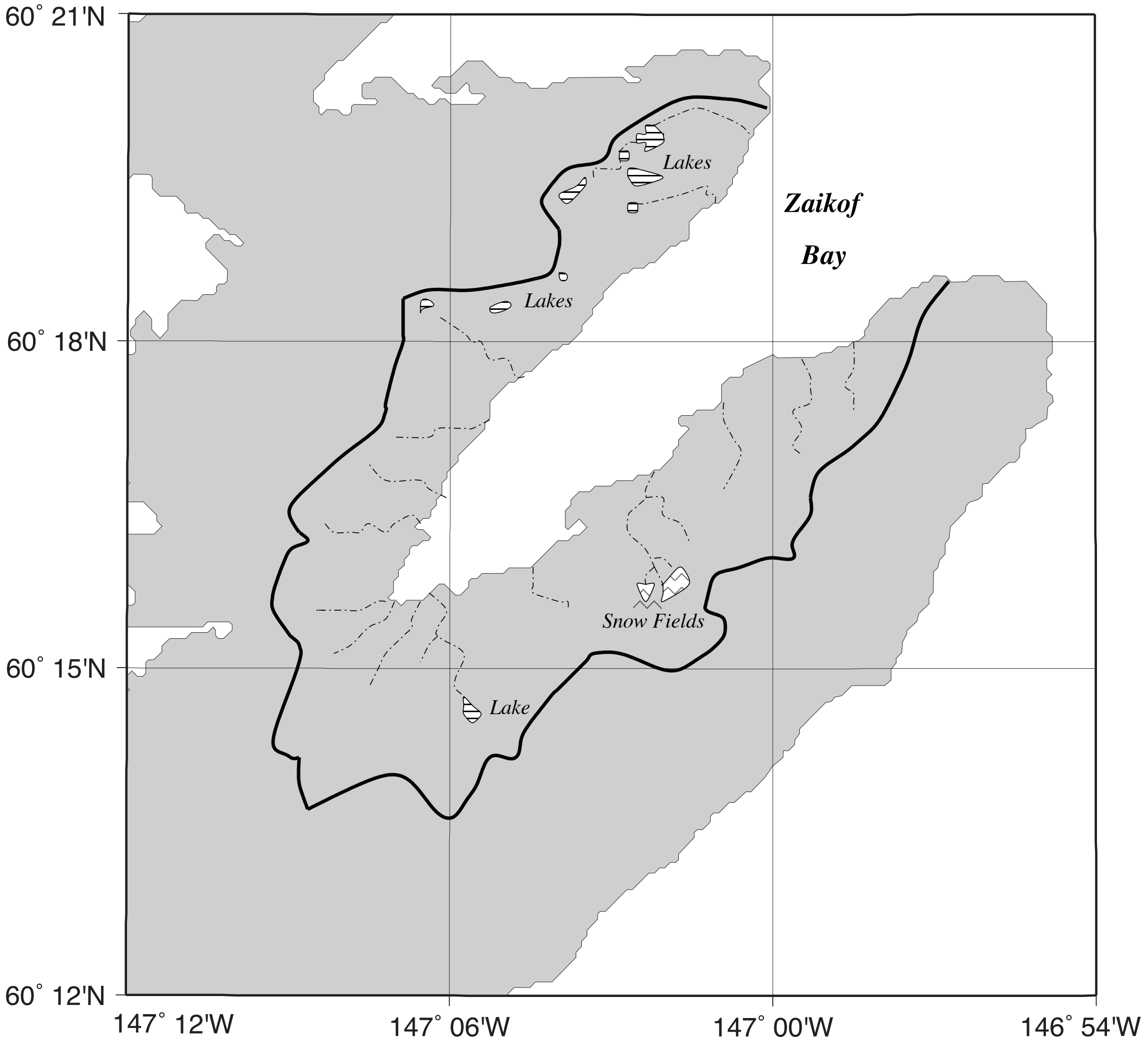

Appendix 3.3 (cont.). Watershed characteristics of Zaikof Bay, located in Sub-Region 9. White areas with stripes denote lakes and small black lines denote drainages.*

*Reprinted with permission from "Seasonal hydrography and tidal currents of bays and fjords in Prince William Sound, Alaska" by Gay, S.M. III and S.L.Vaughan Fish. Oceanogr. 10 (Suppl. 1), 159-193, Copyright 2001 by John Wiley and Sons.

Appendix 3.4. Transport Calculations for Section B (Across Outer Sill) Over Two Semidiurnal Tide Cycles on June 21 and 22, 2007 (*legend for parameters is at the bottom*).

Volume Transport and Flow Rates for Barotropic (Tidal) Flows

Tide	*section*	*start*	*end*	*dt(s)*	*dH(m)*	*Q1T**	*Qat*	*Qat2*	*Qat3*	*Ubt*
Flood1a	B	16:06:50	16:18:51	721	0.124	2321	1703	2002	2344	0.034
Flood1b	C	17:15:37	17:25:16	579	0.078	1815	1183	1434	1830	0.025
Ebb1a	B	21:15:09	21:27:24	735	-0.086	-1588	-1126	-1403	-1577	-0.021
Ebb1b	B	22:38:54	22:48:32	578	-0.093	-2162	-1633	-1935	-2148	-0.031
Flood2a	B	2:21:26	2:33:26	720	0.056	1045	803	944	1014	0.010
Flood2b	B	3:41:49	3:52:25	636	0.069	1464	1136	1288	1449	0.018
Flood2c	B	7:13:38	7:24:45	667	0.006	120	83	106	114	0.001
Ebb2a	B	8:32:35	8:46:24	839	-0.063	-1018	-878	-994	-1008	-0.012
Ebb2b	B	12:13:15	12:23:20	605	-0.061	-1367	-991	-1170	-1349	-0.017
Flood3a	B	13:28:00	13:37:14	554	0.009	213	158	179	198	0.002
Flood3b	B	16:26:41	16:38:07	686	0.104	2037	1498	1800	2049	0.029

Volume Transport and Flow Rates for Total and Baroclinic Flows

Tide	*section*	*Qyz (v')*	*Qyzb*	*Qyza*	*Qbcm*	*Qbcmb*	*Ubcm*	*Ubcmb*	*Qbct*	*Ubct*
Flood1a	B	2501	2883	2834	798	881	0.014	0.013	512	0.006
Flood1b	C	1866	2047	2188	683	613	0.013	0.010	373	0.005
Ebb1a	B	-1654	-1255	-1738	-528	149	-0.010	0.002	-149	-0.002
Ebb1b	B	-2113	-2350	-2775	-480	-415	-0.010	-0.007	-613	-0.009
Flood2a	B	1889	1633	1611	1085	689	0.018	0.010	566	0.008
Flood2b	B	1981	1868	2135	845	581	0.014	0.008	671	0.009
Flood2c	B	-293	445	-115	-210	339	-0.007	0.005	-235	-0.003
Ebb2a	B	-1132	-999	-1135	-254	-5	-0.003	0.000	-117	-0.002
Ebb2b	B	-894	-938	-1315	97	232	0.002	0.004	51	0.001
Flood3a	B	115	129	143	-43	-50	-0.001	-0.001	-70	-0.001
Flood3b	B	1977	2381	2474	480	581	0.008	0.008	437	0.005

Transect Measurement Areas and Percent of Total Section Area

Tide	*Axzm*	*Axzmb*	*Axz*	*redist*	*ledist*	*reAxz*	*leAxz*	*Axzt*	*pAxzm*	*pAxzmb*
Flood1a	57307	67396	67973	320	160	7840	2320	78133	0.734	0.863
Flood1b	52253	63356	64303	180	555	4500	11378	80181	0.652	0.790
Ebb1a	55025	68572	69414	220	160	5390	2800	77604	0.709	0.884
Ebb1b	50791	60198	60300	225	225	3713	3263	67275	0.755	0.895
Flood2a	60892	71560	72270	220	110	5280	1705	79255	0.768	0.903
Flood2b	62526	70874	71545	220	220	5720	3300	80565	0.776	0.880
Flood2c	53918	68416	68966	276	138	6072	2415	77453	0.696	0.883
Ebb2a	75182	85102	85948	20	50	350	850	87148	0.863	0.977
Ebb2b	55140	65063	65607	330	165	7920	2475	76002	0.726	0.856
Flood3a	57662	65355	65972	340	170	9180	2465	77617	0.743	0.842
Flood3b	59470	71464	72177	210	210	5145	3570	80892	0.735	0.883

* tide volume change rate based on dH * surface area of the main basin and northen arm by Noll et al. (2008) = 13.51 x 10^6 m^2

The same area based on Gay and Vaughan (2001) is (27.9 - 7.5) = 20.4km^2 = 20.4 x 10^6 m^2

Legend:
dt (sec) - time interval for the transect
dH (m) - tide height change during the transect
Q1T (m^3s^{-1}) *- total tidal volume flux during the transect*
Qat (m^3s^{-1}) *- tidal volume flux through the measured area*
Qat2 (m^3s^{-1}) *- tidal volume flux through the measured area and bottom layer*
Qa3 (m^3s^{-1}) *- tidal volume flux through the combined area (measured area, bottom layer and sides)*
Ubt ($m\ s^{-1}$) *- total barotropic tidal flow*

Qyz (m^3s^{-1}) *- volume transport based on v' through measured area of the transect*
Qyzb (m^3s^{-1}) *- volume transport through measured area and bottom layer*
Qyza (m^3s^{-1}) *- volume transport through entire section, adjusted for flow through sides*
Qbcm (m^3s^{-1}) *- baroclinic transport through measured area (Qyz - Qat)*
Qbcmb (m^3s^{-1}) *- baroclinic transport through measured area & bottom (Qyzb - Qat2)*
Ubcm ($m\ s^{-1}$) *- baroclinic flow through measured area (Qyz/Axzm)*
Ubcmb ($m\ s^{-1}$) *- baroclinic flow through measured area & bottom layer (Qyzb/Axzmb)*
Qbct (m^3s^{-1}) *- total baroclinic transport through the section (Qyza - Q1T)*
Ubct ($m\ s^{-1}$) *- total baroclinic flow through the section (Qbct/Axzt)*

Axzm (m^2) *- cross-sectional area of the measured region of the transect*
Axzmb (m^2) *- cross-sectional area of the measured & bottom layers of the transect*
Axz (m^2) *- cross-sectional area of the entire transect (surface to bottom)*
redist (m) - distance to shore on right (east) end of the transect
ledist (m) - distance to shore on leftt (west) end of the transect
reAxz (m^2) *- cross-sectional area of the right end region*
leAxz (m^2) *- cross-sectional area of the left end region*
Axzt (m^2) *-total cross-sectional area of the entire section (transect area and sides)*
pAxzm (%) - fraction of total area (Axzt) covered by the measured area of the transect
pAxzmb (%) - fraction of total area (Axzt) covered by the measured & bottom area of the transect

Appendix 3.5. Transport Calculations for Section B (Across Outer Sill) Over Two Semidiurnal Tide Cycles on July 16 and 17, 2007

Volume Transport and Flow Rates for Barotropic (Tidal) Flows

Tide	*section*	*start*	*end*	*dt(s)*	*dH(m)*	*Q1T**	*Qat*	*Qat2*	*Qat3*	*Ubt*
Flood1a	B	11:03:28	11:13:38	610	0.141	3116	2411	2732	3087	0.0407
Flood1b	B	14:25:47	14:37:10	683	0.103	2039	1567	1795	2024	0.0244
Ebb1a	B	18:36:11	18:47:18	667	-0.138	-2802	-2153	-2451	-2775	-0.034
Flood2a	B	22:36:16	22:46:33	617	0.073	1603	1180	1400	1590	0.0204
Flood 2c	B	2:44:13	2:55:02	649	0.070	1462	1045	1287	1451	0.0167
Ebb2b	B	6:47:17	6:56:28	551	-0.163	-3998	-2818	-3511	-3972	-0.0502
Flood3a	B	10:46:56	10:56:51	595	0.064	1454	1046	1269	1441	0.0189

Volume Transport and Flow Rates for Total and Baroclinic Flows

Tide	*section*	*Qyz (v')*	*Qyzb*	*Qyza*	*Qbcm*	*Qbcmb*	*Ubcm*	*Ubcmb*	*Qbct*	*Ubct*
Flood1a	B	5387	5627	5522	2976	2895	0.050	0.043	2406	0.032
Flood1b	B	3935	5380	5144	2369	3585	0.037	0.049	3105	0.038
Ebb1a	B	-2464	-2692	-3155	-311	-242	-0.005	-0.003	-353	-0.005
Flood2a	B	4649	4517	4899	3469	3116	0.060	0.045	3296	0.042
Flood2c	B	3090	4901	4625	2044	3614	0.033	0.047	3164	0.037
Ebb2b	B	-2972	-3602	-4283	-154	-91	-0.003	-0.001	-286	-0.004
Flood3a	B	3100	2793	2841	2054	1524	0.037	0.023	1388	0.018

Transect Measurement Areas and Percent of Total Section Area

Tide	*Axzm*	*Axzmb*	*Axz*	*redist*	*ledist*	*reAxz*	*leAxz*	*Axzt*	*pAxzm*	*pAxzmb*
Flood1a	59283	67171	67882	280	150	6720	2025	76627	0.7737	0.8766
Flood1b	64309	73683	74308	280	150	7140	2250	83698	0.7683	0.8803
Ebb1a	63419	72173	72983	280	150	7140	2400	82523	0.7685	0.8746
Flood2a	57990	68796	69436	280	150	7140	2175	78751	0.7364	0.8736
Flood 2c	62753	77264	77919	280	150	7420	2400	87739	0.7152	0.8806
Ebb2b	56098	69900	70408	280	150	6860	2325	79593	0.7048	0.8782
Flood3a	55430	67263	67923	280	150	7000	2100	77023	0.7197	0.8733

* tide volume change rate based on dH * surface area of the main basin and northen arm by Noll et al. (2008) = 13.51 x 10^6 m^2
The same area based on Gay and Vaughan (2001) is (27.9 - 7.5) = 20.4km^2 = 20.4 x 10^6 m^2

Appendix 3.6. Transport Calculations for Section B (Across Outer Sill) Over Two Semidiurnal Tide Cycles on August 18 and 19, 2007

Volume Transport and Flow Rates for Barotropic (Tidal) Flows

Tide	*section*	*start*	*end*	*dt(s)*	*dH(m)*	*Q1T*	*Qat*	*Qat2*	*Qat3*	*Ubt*
Flood1c	B	16:32:59	16:42:27	568	0.0287	682	452	597	729	0.014
Ebb1b	B	20:06:23	20:17:08	645	-0.1200	-2513	-1757	-2205	-2522	-0.033
Flood2a	B	0:23:46	0:36:39	773	0.0593	1036	677	906	983	0.008
Flood2b	B	1:38:54	1:49:19	625	0.0979	2117	1365	1852	2043	0.021
Flood2c	B	5:11:15	5:21:45	630	0.0201	432	285	381	481	0.011
Ebb2b	B	9:26:11	9:37:20	669	-0.0832	-1680	-1104	-1497	-1665	-0.019
Flood3a	B	13:46:02	13:57:43	641	0.1115	2350	1471	2077	2294	0.023
Flood3c	B	17:37:02	17:47:20	618	0.0008	17	11	15	63	0.005

Volume Transport and Flow Rates for Total and Baroclinic Flows

Tide	*section*	*Qyz (v')*	*Qyzb*	*Qyza*	*Qbcm*	*Qbcmb*	*Ubcm*	*Ubcmb*	*Qbct*	*Ubct*
Flood1c	B	1135	3039	2765	683	2441	0.013	0.034	2083	0.025
Ebb1b	B	-2444	-2966	-3634	-687	-762	-0.012	-0.010	-1121	-0.013
Flood2a	B	660	1011	1117	-17	105	0.000	0.002	81	0.002
Flood2b	B	2566	4711	4914	1201	2859	0.024	0.042	2798	0.038
Flood2c	B	1324	2102	1835	1039	1721	0.019	0.023	1404	0.016
Ebb2b	B	-1234	-2655	-3218	-129	-1158	-0.002	-0.015	-1538	-0.018
Flood3a	B	1100	2471	2355	-372	395	-0.007	0.005	5	0.001
Flood3c	B	128	955	637	118	941	0.002	0.013	620	0.007

Transect Measurement Areas and Percent of Total Section Area

Tide	*Axzm*	*Axzmb*	*Axz*	*redist*	*ledist*	*reAxz*	*leAxz*	*Axzt*	*pAxzm*	*pAxzmb*
Flood1c	53815	71129	71539	280	150	7140	2550	81229	0.6625	0.876
Ebb1b	58656	73586	74257	280	150	7140	2475	83872	0.6993	0.877
Flood2a	52258	69952	70716	280	150	7140	2175	80031	0.653	0.874
Flood2b	49817	67573	68200	280	150	6860	2175	77235	0.645	0.875
Flood2c	55076	73660	74233	280	150	6860	2325	83418	0.6602	0.883
Ebb2b	55738	75586	76098	280	150	6440	2250	84788	0.6574	0.892
Flood3a	52944	74738	75202	280	150	7140	2250	84592	0.6259	0.884
Flood3c	53771	75149	75690	280	150	7140	2400	85230	0.6309	0.882

* tide volume change rate based on dH * surface area of the main basin and northen arm by Noll et al. (2008) = 13.51 x 10^6 m^2
The same area based on Gay and Vaughan (2001) is (27.9 - 7.5) = 20.4km^2 = 20.4 x 10^6 m^2

Appendix 3.7. Transport Calculations for Section C (Above Outer Sill) Over Two Semidiurnal Tide Cycles on June 21 and 22, 2007

Volume Transport and Flow Rates for Barotropic (Tidal) Flows

Tide	*section*	*start*	*end*	*dt(s)*	*dH(m)*	*Q1T**	*Qat*	*Qat2*	*Qat3*	*Ubt*
Flood1a	C	15:56:24	16:06:25	601	0.104	2340	1675	1837	2382	0.036
Flood1b	C	17:15:37	17:25:04	567	0.076	1816	1173	1439	1831	0.026
Ebb1a	C	20:59:12	21:14:59	947	-0.100	-1425	-1016	-1197	-1419	-0.025
Ebb1b	C	22:50:39	23:01:46	667	-0.107	-2159	-1478	-1727	-2120	-0.026
Flood2a	C	2:09:22	2:21:17	715	0.047	896	539	628	821	0.009
Flood2b	C	3:52:36	4:00:53	497	0.055	1495	928	1145	1482	0.019
Flood2c	C	6:58:15	7:12:59	884	0.018	269	163	189	256	0.003
Ebb2a	C	8:52:43	9:04:24	701	-0.067	-1282	-793	-994	-1266	-0.016
Ebb2c	C	11:58:02	12:12:37	875	-0.100	-1549	-917	-1112	-1507	-0.018
Flood3a	C	13:37:22	13:44:13	401	0.012	413	224	280	368	0.004
Flood3b	C	16:26:41	16:38:07	472	0.071	2038	1371	1511	2090	0.030

Volume Transport and Flow Rates for Total and Baroclinic Flows

Tide	*section*	*Qyz (v')*	*Qyzb*	*Qyza*	*Qbcm*	*Qbcmb*	*Ubcm*	*Ubcmb*	*Qbct*	*Ubct*
Flood1a	C	1261	1298	1744	-414	-539	-0.008	-0.009	-596	-0.009
Flood1b	C	1832	2054	2377	659	615	0.013	0.010	561	0.007
Ebb1a	C	-782	-655	-1088	234	542	0.006	0.011	337	0.006
Ebb1b	C	-798	-694	-1187	680	1033	0.013	0.016	972	0.012
Flood2a	C	77	63	733	-462	-566	-0.010	-0.011	-163	-0.001
Flood2b	C	1283	1350	2045	356	204	0.007	0.003	551	0.007
Flood2c	C	381	581	-369	217	392	0.005	0.008	-100	-0.002
Ebb2a	C	-675	-795	-1058	119	199	0.002	0.003	224	0.003
Ebb2c	C	-964	-889	-1437	-48	223	-0.001	0.004	112	0.001
Flood3a	C	352	338	579	128	58	0.003	0.001	166	0.003
Flood3b	C	857	851	1320	-514	-659	-0.010	-0.012	-718	-0.010

Transect Measurement Areas and Percent of Total Section Area

Tide	*Axzm*	*Axzmb*	*Axz*	*redist*	*ledist*	*reAxz*	*leAxz*	*Axzt*	*pAxzm*	*pAxzmb*
Flood1a	52545	57624	58347	150	555	3675	11378	73399	0.716	0.785
Flood1b	50745	62257	63187	150	555	3750	11655	78592	0.646	0.792
Ebb1a	42889	50525	51127	220	160	5500	3520	60147	0.713	0.840
Ebb1b	54470	63635	64133	300	425	7350	8075	79558	0.685	0.800
Flood2a	44397	51782	52238	250	740	6125	15540	73903	0.601	0.701
Flood2b	49196	60755	61260	270	550	7020	11000	79280	0.621	0.766
Flood2c	45369	52561	55168	640	190	15360	4085	74613	0.608	0.704
Ebb2a	49379	61851	62490	250	520	6375	10920	79785	0.619	0.775
Ebb2c	46821	56797	57461	440	555	10560	11100	79121	0.592	0.718
Flood3a	39493	49356	49657	440	555	11660	11378	72695	0.543	0.679
Flood3b	51972	57280	57732	180	700	4500	15050	77283	0.673	0.741

* tide volume change rate based on dH * surface area of the main basin and northen arm by Noll et al. (2008) = 13.51 x 10^6 m^2
The same area based on Gay and Vaughan (2001) is (27.9 - 7.5) = 20.4km^2 = 20.4 x 10^6 m^2

Appendix 3.8. Transport Calculations for Section C (Above Outer Sill) Over Two Semidiurnal Tide Cycles on July 16 and 17, 2007

Volume Transport and Flow Rates for Barotropic (Tidal) Flows

Tide	*section*	*start*	*end*	*dt(s)*	*dH(m)*	*Q1T**	*Qat*	*Qat2*	*Qat3*	*Ubt*
Flood1a	C	11:14:09	11:21:22	433	0.099	3092	1979	2298	3128	0.046
Flood1b	C	14:14:21	14:25:31	670	0.118	2384	1401	1805	2378	0.030
Flood1c	C	15:17:30	15:26:00	510	0.013	346	219	261	344	0.004
Ebb1a	C	18:23:04	18:36:00	776	-0.156	-2723	-1634	-2054	-2708	-0.035
Ebb1b	C	19:28:41	19:35:45	424	-0.086	-2752	-1630	-2017	-2734	-0.038
Flood2a	C	22:22:02	22:36:00	778	0.077	1343	851	1002	1331	0.018
Flood2c	C	23:31:26	23:39:14	468	0.088	2549	1634	1943	2530	0.032
Flood2c	C	2:31:04	2:43:17	733	0.094	1726	975	1271	1718	0.022
Ebb2a	C	3:41:44	3:49:33	469	-0.009	-244	-157	-186	-243	-0.003
Ebb2b	C	6:33:46	6:46:54	788	-0.232	-3971	-2522	-2932	-3949	-0.055
Ebb2c	C	7:43:19	7:51:32	493	-0.133	-3651	-2316	-2766	-3624	-0.048
Flood3a	C	10:34:09	10:46:41	752	0.061	1094	632	834	1089	0.015

Volume Transport and Flow Rates for Total and Baroclinic Flows

Tide	*section*	*Qyz (v')*	*Qyzb*	*Qyza*	*Qbcm*	*Qbcmb*	*Ubcm*	*Ubcmb*	*Qbct*	*Ubct*
Flood1a	C	2052	2351	2833	73	53	0.0016	0.001	-259	-0.004
Flood1b	C	1943	2485	1937	542	680	0.0116	0.011	-448	-0.006
Flood1c	C	966	1299	977	747	1038	0.0147	0.017	631	0.008
Ebb1a	C	-1411	-1785	-3059	223	269	0.0048	0.005	-335	-0.005
Ebb1b	C	-1375	-1991	-2753	256	25	0.006	0.001	-1	0.000
Flood2a	C	1144	903	1593	293	-99	0.0062	-0.002	250	0.004
Flood2c	C	1940	2183	1924	306	240	0.006	0.004	-625	-0.008
Flood2c	C	1588	2669	2244	614	1398	0.0141	0.025	518	0.007
Ebb2a	C	595	796	-193	752	982	0.0141	0.016	51	0.001
Ebb2b	C	-1932	-2047	-3433	590	885	0.0128	0.017	539	0.007
Ebb2c	C	-1935	-2383	-3362	380	383	0.0078	0.007	289	0.004
Flood3a	C	931	224	1339	299	-610	0.0069	-0.011	245	0.003

Transect Measurement Areas and Percent of Total Section Area

Tide	*Axzm*	*Axzmb*	*Axz*	*redist*	*ledist*	*reAxz*	*leAxz*	*Axzt*	*pAxzm*	*pAxzmb*
Flood1a	46064	53493	53986	280	550	6720	11275	71981	0.640	0.7432
Flood1b	46698	60157	60367	280	550	7280	11825	79472	0.588	0.757
Flood1c	50881	60580	61206	280	550	7140	12100	80446	0.633	0.7531
Ebb1a	46310	58209	58646	280	550	7000	11550	77196	0.600	0.754
Ebb1b	42821	52964	53455	280	550	7280	11550	72285	0.592	0.7327
Flood2a	46949	55292	55954	280	550	6860	11275	74089	0.634	0.7463
Flood2b	51238	60910	61519	280	550	6860	11550	79929	0.641	0.762
Flood2c	43430	56639	56977	280	550	7560	12375	76912	0.565	0.7364
Ebb2a	53266	63271	63663	280	550	7000	12100	82763	0.644	0.7645
Ebb2b	46038	53535	53946	280	550	7280	11275	72501	0.635	0.7384
Ebb2c	48535	57966	58513	280	550	6720	11275	76508	0.634	0.7576
Flood3a	43433	57338	57653	280	550	6860	10725	75238	0.577	0.7621

Appendix 3.9. Transport Calculations for Section C (Across Outer Sill) Over Two Semidiurnal Tide Cycles on August 18 and 19, 2007

Volume Transport and Flow Rates for Barotropic (Tidal) Flows

Tide	*section*	*start*	*end*	*dt(s)*	*dH(m)*	*Q1T*	*Qat*	*Qat2*	*Qat3*	*Ubt*
Flood1	C	16:43:00	16:52:44	584	0.0212	490	320	423	543	0.011
Ebb1a	C	19:52:46	20:06:07	801	-0.145	-2453	-1370	-1839	-2500	-0.035
Ebb1b	C	21:04:16	21:12:12	476	-0.09	-2551	-1503	-1953	-2553	-0.034
Flood2a	C	0:09:58	0:23:30	812	0.042	699	382	509	538	0.002
Flood2b	C	1:49:36	1:57:07	451	0.0719	2155	1185	1627	2039	0.023
Flood2c	C	5:11:15	5:21:45	807	0.0375	627	362	475	651	0.010
Ebb2a	C	6:14:24	6:22:18	474	-0.015	-433	-248	-328	-436	-0.006
Ebb2b	C	9:13:22	9:25:44	742	-0.095	-1721	-1015	-1388	-1706	-0.021
Ebb2c	C	10:19:26	10:27:40	494	-0.047	-1297	-793	-1047	-1271	-0.015
Flood3a	C	13:32:57	13:45:37	760	0.1268	2253	1267	1712	2138	0.024
Flood3b	C	14:38:38	14:47:20	522	0.0905	2341	1320	1900	2307	0.027
Flood3c	C	17:28:19	17:36:29	490	0.0061	169	87	131	263	0.008

Volume Transport and Flow Rates for Total and Baroclinic Flows

Tide	*section*	*Qyz (v')*	*Qyzb*	*Qyza*	*Qbcm*	*Qbcmb*	*Ubcm*	*Ubcmb*	*Qbct*	*Ubct*
Flood1	C	900	1411	1027	580	988	0.0113	0.015	537	0.006
Ebb1a	C	-1616	-1751	-2269	-246	88	-0.0056	0.002	184	0.003
Ebb1b	C	-1879	-2366	-2611	-376	-412	-0.0082	-0.007	-60	-0.001
Flood2a	C	187	525	810	-195	16	-0.0048	0.000	112	0.004
Flood2b	C	1526	2457	3018	341	830	0.0081	0.014	864	0.013
Flood2c	C	1398	2417	2290	1036	1942	0.0231	0.033	1663	0.021
Ebb2a	C	520	543	306	768	870	0.0171	0.015	739	0.010
Ebb2a	C	-1183	-1207	-1242	-168	182	-0.0036	0.003	479	0.006
Ebb2c	C	-1168	-1150	-1064	-375	-104	-0.0078	-0.002	232	0.003
Flood3a	C	1673	2308	2532	407	597	0.0094	0.010	279	0.005
Flood3b	C	1476	2928	3154	156	1028	0.0034	0.016	813	0.011
Flood3c	C	333	1426	948	246	1295	0.0061	0.021	779	0.009

Transect Measurement Areas and Percent of Total Section Area

Tide	*Axzm*	*Axzmb*	*Axz*	*redist*	*ledist*	*reAxz*	*leAxz*	*Axzt*	*pAxzm*	*pAxzmb*
Flood1a	51480	67998	68227	241	400	6146	4400	78773	0.654	0.863
Ebb1a	44009	59062	59649	240	600	6240	12900	78789	0.559	0.750
Ebb1b	45733	59438	59924	200	600	5100	12600	77624	0.589	0.766
Flood2a	40398	53773	54428	200	700	5100	14350	73878	0.547	0.728
Flood2b	42162	57896	58364	200	644	5100	13202	76667	0.550	0.755
Flood2c	44930	58839	59518	220	600	5610	12600	77728	0.578	0.757
Ebb2a	44820	59168	59795	220	600	5830	12600	78225	0.573	0.756
Ebb2a	46730	63903	64386	120	600	2820	12000	79206	0.590	0.807
Ebb2c	48258	63664	64059	130	600	3120	11700	78879	0.612	0.807
Flood3a	43280	58483	59194	220	600	5500	12300	76994	0.562	0.760
Flood3b	45465	65427	65809	114	600	2223	12600	80632	0.564	0.811
Flood3c	40371	60809	61379	170	600	4335	12900	78614	0.514	0.774

Appendix 3.10. Tidal constituents at Cordova, Alaska NOAA CMAN station #9454050.

No.	constituent	amplitude	phase	speed	period (hrs)	days	definition
1	M2	4.773	290.2	28.98	12.42	0.518	Principal lunar semidiurnal onstituent
2	S2	1.627	322.2	30.00	12.00	0.500	Principal solar semidiurnal constituent
3	N2	0.977	265.9	28.44	12.66	0.527	Larger lunar elliptic semidiurnal constituent
4	K1	1.645	273.7	15.04	23.93	0.997	Lunar diurnal constituent
5	M4	0.181	13.8	57.97	6.21	0.259	Shallow water overtides of principal lunar constituent
6	O1	1.005	256.8	13.94	25.82	1.076	Lunar diurnal constituent
7	M6	0.035	115.4	86.95	4.14	0.173	Shallow water overtides of principal lunar constituent
8	MK3	0	0	44.03	8.18	0.341	Shallow water terdiurnal
9	S4	0.053	5.3	60.00	6.00	0.250	Shallow water overtides of principal solar constituent
10	MN4	0.054	331.1	57.42	6.27	0.261	Shallow water quarter diurnal constituent
11	NU2	0.186	269.5	28.51	12.63	0.526	Larger lunar evectional constituent
12	S6	0	0	90.00	4.00	0.167	Shallow water overtides of principal solar constituent
13	MU2	0.103	255.5	27.97	12.87	0.536	Variational constituent
14	2N2	0.115	239	27.90	12.91	0.538	Lunar elliptical semidiurnal second-order constituent
15	OO1	0.053	300.4	16.14	22.31	0.929	Lunar diurnal
16	LAM2	0.034	297.4	29.46	12.22	0.509	Smaller lunar evectional constituent
17	S1	0.064	61.7	15.00	24.00	1.000	Solar diurnal constituent
18	M1	0.053	289.1	14.50	24.83	1.035	Smaller lunar elliptic diurnal constituent
19	J1	0.094	287.7	15.59	23.10	0.962	Smaller lunar elliptic diurnal constituent
20	MM	0	0	0.54	661.31	27.555	Lunar monthly constituent
21	SSA	0	0	0.08	4382.91	182.621	Solar semiannual constituent
22	SA	0.431	254.2	0.04	8765.82	365.243	Solar annual constituent
23	MSF	0	0	1.02	354.37	14.765	Lunisolar synodic fortnightly constituent
24	MF	0.092	179.9	1.10	327.86	13.661	Lunisolar fortnightly constituent
25	RHO	0.032	249.4	13.47	26.72	1.113	Larger lunar evectional diurnal constituent
26	Q1	0.175	250.3	13.40	26.87	1.120	Larger lunar elliptic diurnal constituent
27	T2	0.092	313.8	29.96	12.02	0.501	Larger solar elliptic constituent
28	R2	0.013	323.5	30.04	11.98	0.499	Smaller solar elliptic constituent
29	2Q1	0.02	250.9	12.85	28.01	1.167	Larger elliptic diurnal
30	P1	0.51	271.2	14.96	24.07	1.003	Solar diurnal constituent
31	2SM2	0.014	132.8	31.02	11.61	0.484	Shallow water semidiurnal constituent
32	M3	0.023	277.8	43.48	8.28	0.345	Lunar terdiurnal constituent
33	L2	0.113	299.4	29.53	12.19	0.508	Smaller lunar elliptic semidiurnal constituent
34	2MK3	0.01	174.1	42.93	8.39	0.349	Shallow water terdiurnal constituent
35	K2	0.452	316.2	30.08	11.97	0.499	Lunisolar semidiurnal constituent
36	M8	0.012	186.7	115.94	3.11	0.129	Shallow water eighth diurnal constituent
37	MS4	0.108	97.1	58.98	6.10	0.254	Shallow water quarter diurnal constituent